



BRNO UNIVERSITY OF TECHNOLOGY

VYSOKÉ UČENÍ TECHNICKÉ V BRNĚ

FACULTY OF MECHANICAL ENGINEERING

FAKULTA STROJNÍHO INŽENÝRSTVÍ

ENERGY INSTITUTE

SUSTAINABLE PROCESS INTEGRATION LABORATORY

ENERGETICKÝ ÚSTAV

LABORATOŘ INTEGRACE PROCESŮ PRO TRVALOU UDRŽITELNOST

**COMPUTATIONAL HEAT TRANSFER WITH PHASE
CHANGES IN LATENT HEAT THERMAL ENERGY
STORAGE AND STEELMAKING**

VÝPOČTOVÉ MODELOVÁNÍ PŘENOSU TEPLA S FÁZOVÝMI PŘEMĚNAMI
V ÚLOHÁCH AKUMULACE TEPLA A VÝROBY OCELI

HABILITATION THESIS

HABILITAČNÍ PRÁCE

BRNO, 2019

Dr LUBOMÍR KLIMEŠ

ACKNOWLEDGEMENT

I WISH TO THANK the following people for their invaluable contribution to this thesis:

Associate Professor Dr Pavel Charvát for a great cooperation, his valuable thoughts and encouraging ideas, and for his immense enthusiasm attracting me to the research and computer modelling of latent heat thermal energy storage systems and phase change materials;

Professor Dr Josef Štětina for his overall long-term support, helpful comments and encouragement in academic and research activities, and for a great cooperation in the area of computer modelling of continuous steel casting;

My wife Tereza for her love, support, and forbearance.

The Author

Spring 2019 in Brno, the Czech Republic, and in Montreal, Canada.

Computational heat transfer with phase changes in latent heat thermal energy storage and steelmaking

ABSTRACT

Heat transfer and phase changes are encountered in many engineering applications and industrial processes. The thesis is aimed at the computational solution of heat transfer problems with phase changes in two technical areas: latent heat thermal energy storage with phase change materials and steelmaking by means of continuous steel casting. An insight into each area accompanied by the literature review of the current development in the field is provided, followed by several journal papers co-authored by the author of the thesis. Overall, ten journal papers published in peer-review journals having an impact factor in Web of Science are included in the thesis to demonstrate the author's contribution to the development in the fields. Achieved results indicate that the approach of computer modelling and developed models represent a viable way for effective design, optimisation, and control of the investigated systems.

Keywords: Heat transfer, phase change, computer modelling, latent heat thermal energy storage, phase change materials, continuous steel casting.

Výpočtové modelování přenosu tepla s fázovými přeměnami v úlohách akumulace tepla a výroby oceli

ABSTRAKT

Přenos tepla a fázové změny jsou významné děje zahrnuté v mnoha inženýrských aplikacích a průmyslových procesech. Tato práce je zaměřena na výpočtové modelování úloh přenosu tepla s fázovými přeměnami ve dvou technických aplikacích: akumulace tepla s využitím materiálů se změnou fáze a výroba oceli metodou plynulého odlévání. Pro každou oblast je v práci poskytnut přehled současného stavu vývoje a poznání, na který navazuje několik článků v časopisech, které demonstřují autorův přínos k vývoji v dané oblasti. Celkově je v práci zahrnuto deset článků, které byly publikovány v časopisech mající impakt faktor dle databáze Web of Science. Dosažené výsledky prokazují, že výpočtové modelování a vytvořené modely jsou vhodným nástrojem pro efektivní návrh, optimalizaci a řízení uvažovaných systémů.

Klíčová slova: Přenos tepla, změna fáze, výpočtové modelování, akumulace tepla, materiály se změnou fáze, plynulé odlévání oceli.

Contents

1	INTRODUCTION	9
2	PHASE CHANGE MODELLING AND UTILISATION OF SYSTEMS FOR LATENT HEAT THERMAL ENERGY STORAGE	13
2.1	Thermal energy storage	13
2.1.1	Sensible heat thermal energy storage	14
2.1.2	Latent heat thermal energy storage	15
2.2	Phase change materials	17
2.2.1	Types of phase change materials	18
2.3	Applications of latent heat thermal energy storage	19
2.3.1	Solar air heating and cooling systems with LHTES	20
2.3.2	Air-PCM heat storage units	21
2.3.3	Building structures integrating PCMs	25
2.4	Modelling of LHTES systems with PCMs	28
2.5	Author's contribution to the development of computer modelling and utilisation of systems for latent heat thermal energy storage	33
2.5.1	Numerical and experimental investigation of a PCM-based thermal storage unit for solar air systems	47
2.5.2	Front tracking in modelling of latent heat thermal energy storage: Assessment of accuracy and efficiency, benchmarking and GPU-based acceleration	57
2.5.3	PCM thermal energy storage in solar heating of ventilation air—Experimental and numerical investigations	73
2.5.4	Thermally activated wall panels with microencapsulated PCM: comparison of 2D and 3D models	85
2.5.5	Utilization of an air-PCM heat exchanger in passive cooling of buildings: A simulation study on the energy saving potential in different European climates	101
2.5.6	Energy demand of liquefaction and regasification of natural gas and the potential of LNG for operative thermal energy storage	119
3	PHASE CHANGE MODELLING AND PROCESS CONTROL IN STEEL PRODUCTION	135
3.1	Continuous steel casting	135
3.2	Computer modelling of continuous steel casting	137
3.2.1	Heat transfer and solidification models and phase change modelling	137
3.2.2	Modelling of specific phenomena related to continuous steel casting	142
3.2.3	Boundary conditions in continuous steel casting	146
3.2.4	Validation of thermal models for continuous steel casting	147
3.2.5	Computer models in optimal control and optimisation of casting process	147

3.3	Author's contribution to the development of modelling and control of continuous steel casting	151
3.3.1	A rapid GPU-based heat transfer and solidification model for dynamic computer simulations of continuous steel casting	159
3.3.2	Impact of casting speed on the temperature field of continuously cast steel billets	173
3.3.3	Two-stage stochastic programming approach to a PDE-constrained steel production problem with the moving interface	181
3.3.4	Unsteady model-based predictive control of continuous steel casting by means of a very fast dynamic solidification model on a GPU	205
4	CONCLUSIONS AND FURTHER WORK	211
	NOMENCLATURE	213
	LIST OF ABBREVIATIONS	215
	REFERENCES	216

1

Introduction

IN RECENT YEARS, A GREAT ATTENTION of researchers as well as politicians has been devoted to sustainable utilisation of energy, water, and other natural resources, and to minimisation of negative impacts of human activities to the natural environment. This includes the transition from fossil fuels to renewable resources of energy, improvement of energy efficiency, minimisation of water footprint as well as the reduction of production of emissions and greenhouse gases (especially CO₂), which mainly contribute to global warming. It was well reported that global warming represents a serious threat to the natural environment and can result in a wide range of harsh environmental impacts [3].

As for the utilisation of renewable energy resources, solar energy represents a renewable energy resource with a great opportunity for utilisation. Basically, there are two main forms of energy, into which the solar radiation can be converted: heat and electricity. The energy conversion of solar energy (radiation) to heat is easier than in case of electricity and there are many well-established applications available for this purpose. They include, for instance, solar heaters of air and water, which allow for solar heating of air and water and their further use for space heating and other utilisation in buildings. The second way—the energy conversion of solar energy to electricity—requires the use of solar cells, which convert solar radiation directly to electricity. Another example of the solar energy utilisation combining both heat and electricity together is the solar concentrated power generation (solar–thermal power plants). In the solar–thermal power plant, heliostats are used to concentrate solar radiation to a receiver. The receiver converts solar radiation to heat, which is used as a heat source in a thermodynamic cycle for electricity generation.

However, the main drawback of solar energy is that the energy demand usually does not meet the energy supply as these two are shifted in time. Moreover, solar energy is not evenly distributed over a day, nor over a year. Simply speaking, for instance, solar radiation is well available during a sunny

day, but at that time requirements for space heating are rather low. Instead, solar energy would be employed much more efficiently after the sunset when solar radiation is no more available but when a need for space heating arises. This implies that ways for thermal energy storage are a crucial issue for an efficient utilisation of solar energy.

There exist several approaches for thermal energy storage. Latent heat thermal energy storage (LHTES) and the use of phase change materials (PCMs) seem to be a promising way for mitigation of energy consumption applicable in buildings. It is well reported that buildings are responsible for about 40% of the total world energy consumption [35]. Moreover, heating, ventilating and air conditioning systems account for about 60% of energy consumed in buildings [53]. The principle of LHTES and PCMs is to employ the heat of fusion accompanying the phase change for the increase of the thermal storage capacity. There are numerous applications of LHTES systems and PCMs integrated in building structures. Examples include solar air heaters, heat storage units (allowing for energy storage, energy peak shaving, and for reduction of mismatch between the energy demand and energy supply mentioned above), and building structures with an integrated PCM, which allow, e.g., for an improved thermal comfort, for preventing a room from overheating and temperature fluctuations, and for the increase of thermal inertia of lightweight buildings.

The efficient utilisation, design, and optimisation of systems with LHTES and PCMs cannot be accomplished without the use of computer simulations. The computer models of these systems pertain to computational heat transfer with phase changes. Though great knowledge in this area is available, there is still an extensive research of such systems, which is mostly aimed at the transition of ideas and prototypes into practice.

As already mentioned at the beginning of this chapter, another current concern of researchers as well as politicians is the efficient use of natural resources, minimisation of emissions, and the reduction of the water consumption. Steel industry including ironmaking and steelmaking is an important industrial sector, which accounts for a huge consumption of energy, water, and natural resources—especially iron ores. It is reported that about 20.3 GJ of energy is required in all processes involved in the production of one tonne of steel [155]. Moreover, about 4 m³ of fresh water are consumed per one tonne of the crude steel output [148]. Considering the recent total world apparent steel production (i.e. finished steel products) of about 1,600 million tonnes [155], the steel industry represents a substantial consumer of vast amounts of energy and water. Therefore, even a reduction in the magnitude of 0.1% of the consumption of resources allows for significant savings.

At the moment, the steelmaking method of continuous steel casting is used for more than 98% of the total world steel production. The proper setup, the determination of casting parameters, and optimisation of the casting process with the aim to minimise quality issues (e.g. crack formation, centre-line segregation), the energy consumption, and the water use cannot be accomplished without the use of computer simulations. As in case of LHTES systems with PCMs, computer modelling of continuous steel casting pertains to computational heat transfer with phase changes. In fact, many issues, approaches, and conclusions are common and well applicable for computer modelling of LHTES systems with PCMs as well as for modelling of continuous steel casting, though these areas may seem to be rather distinct at the first glance.

The aim of this thesis is to provide an insight into the current development in computer mod-

elling of LHTES systems with PCMs as well as in computer modelling of continuous steel casting, and to demonstrate the author's contribution to these research fields. The thesis consists of two rather comprehensive chapters. Chapter 2 is devoted to LHTES systems, PCMs, and their computer modelling and utilisation in solar air systems with heat storage units and in building structures integrating PCMs. Chapter 3 is focused on continuous steel casting, its computer modelling, and the use of models for the casting process control and optimisation. Each of these two chapters first provides an overview of the current development in the field, which is followed by briefly commented journal papers co-authored by the author of the thesis demonstrating his contribution to the field. The presented overview in each chapter serves as a wider insight to the current state and development in the field, and it is not aimed at the assessment of the author's published papers with related works of other investigators. This is presented in each paper individually (mainly in the introduction section and/or in the section providing a review on the topic) with a proper identification of the contribution to the field as well as with the specified research gap and novelty covered by the paper.

Overall, the thesis contains ten journal papers co-authored by the author of the thesis. Each presented paper has been published in a peer-review journal having an impact factor according to Web of Science. Six papers are included in Chapter 2, while four papers in Chapter 3. Among the included ten papers, six papers are contained in the first quartile of mostly energy-related areas according to the Journal Citation Reports (JCR) and the journal impact factor (JIF) in Web of Science. Three papers are even included in the first decile, which contains top 10% journals in each category. The highest impact factor of the included papers is 9.18, and the sum of received citations to the included papers is 123 according to the Google Scholar.

2

Phase change modelling and utilisation of systems for latent heat thermal energy storage

ENERGY REPRESENTS A KEY INGREDIENT in the current technological and economic development of the society. As reported by many investigators, energy resources of non-renewable energy have become more and more limited. Together with the consideration of global warming, the trend and focus have moved to sustainable and renewable energy resources [25]. However, in the utilisation of renewable energy resources the crucial problem is that the energy demand very often does not meet the energy supply in the time scale. This is especially the case of solar and wind renewable energy. In such instances, mechanisms and technologies are needed to shift the energy supply and make it available in periods with the energy demand. Since the storage of higher forms of energy such as the electricity is rather difficult, the thermal energy storage with heat as the lowest form of energy is often utilised as heat is relatively easy to store. Moreover, heat is very often the required final form of energy supplied to customers, which makes the thermal energy a suitable way for energy storage.

2.1 THERMAL ENERGY STORAGE

Thermal energy storage (TES) is a way how to store energy in the form of heat—thermal energy. In the last 15 years, a great attention of researchers and investigators has been focused on the utilisation of TES for an efficient use of energy resources. Nazir et al. [103] reported that the number of papers on the topic of TES has increased about 10-times in the last 10 years. This has particularly been the case of renewable energy resources such as solar energy, where the TES can be used to balance between the energy demand and the energy supply.

There are basically three approaches applicable for the TES [18]: the sensible heat TES, the latent heat TES, and the thermochemical TES, but the most TES systems employ the first two approaches: the sensible and latent heat TES. As for the sensible heat TES, heat can be accumulated and stored in a material by means of increasing its temperature in the form of sensible heat. The sensibility here means that any change in the amount of heat accumulated to or released from the material causes a direct change of its temperature. On the other hand, the latent heat TES (LHTES) employs a phase change (including both changes with and without the change of the state) and its latent heat to store thermal energy. Examples of phase changes include the melting, solidification, boiling, condensation, sublimation, and desublimation. The term latent heat is frequently used, however it makes sense only in case of materials such as pure chemical elements (such as iron), which change the phase at a constant temperature. In such case, heat accompanying the phase change is indeed latent meaning "hidden" as it cannot be observed as a change of the temperature. In the majority of practical applications of TES, complex substances, composite materials, mixtures, and alloys are utilised rather than pure chemical elements. In such cases, the phase change does not occur isothermally but in a certain temperature interval (cf. iron and steel). Therefore, in these instances it is more precise to refer heat required for the phase change as the heat of fusion.

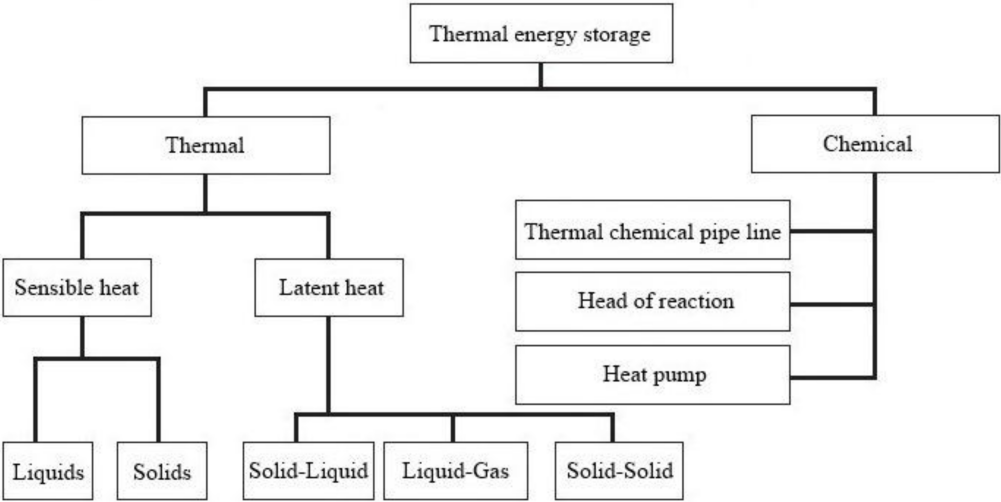


Figure 2.1: Ways for thermal energy storage [126]

Figure 2.1 demonstrates ways for thermal energy storage. As can be seen, the sensible heat TES is concerned with a single state only, typically with solids and liquids as in case of gases a number of impracticalities arise. On the other hand, the latent heat TES is accompanied with the phase change, typically including two states. Most applications involve the solid–liquid or the liquid–gas phase change, though there are also some technical solutions utilising the phase change in the single state such as the solid–solid phase change.

2.1.1 SENSIBLE HEAT THERMAL ENERGY STORAGE

The sensible heat TES is the most common approach for the thermal energy storage, which has been used by people since ancient times. The characteristic feature of the sensible heat TES is the change of the temperature of the storage medium during the heat storage and heat release processes. A change

of the temperature of the storage medium implies the change in the amount of heat transferred to or from it. In general, the amount of heat Q stored to or released from the heat storage medium can be determined from the First law of thermodynamics

$$dQ = mc_v dT + \left[T \left(\frac{\partial p}{\partial T} \right)_v - p \right] dV + p dV \quad (2.1)$$

or equivalently

$$dQ = mc_p dT + \left[V - T \left(\frac{\partial V}{\partial T} \right)_p \right] dp - V dp. \quad (2.2)$$

In most cases of TES, solid and liquid heat storage media are employed with the isobaric heat transfer. For such cases, Eq. (2.2) is reduced to $dQ = mc_p dT$, and therefore the amount of heat transferred to change the temperature of the storage media from T_i to T_f can be determined [18] as

$$Q = \int_{T_i}^{T_f} mc_p dT = \int_{T_i}^{T_f} \xi V c_p dT \quad (2.3)$$

where m is the mass of the heat storage medium, c_p is its heat capacity (also referred to as the specific heat) at constant pressure, and T is the temperature. As can be seen in Eq. (2.3), the amount of heat is proportional to the mass of the storage medium, its heat capacity, and to the temperature interval $T_f - T_i$ in which the heat transfer occurs. The operational range of the sensible heat TES is particularly limited by the temperature range in which the heat storage can take place. For instance, water, which is the most common heat storage medium for the sensible heat TES, can operate as the sensible heat storage medium between its freezing and boiling temperature. Similar conclusions apply to other materials as well.

A typical example of the system employing the sensible heat TES is a packed bed [131]. The packed bed is a container, which includes suitable form of particles of a packing material. Typically, the particles are solids such as rocks and pebbles. In the heat charging period, the heat transfer fluid (e.g. air, water, or flue gases) enters the packed bed with a high temperature and causes the rise of the temperature of the packing material due to the sensible heat, while the temperature of the heat transfer fluid decreases as the fluid passes through the bed. In the discharging period, the reverse process is used to release the heat from the packaging material to the heat transfer fluid.

2.1.2 LATENT HEAT THERMAL ENERGY STORAGE

Latent heat thermal energy storage (LHTES) represents a more efficient way how to store energy in the form of heat—thermal energy. In contrast to the sensible heat, the latent heat (heat of fusion) allows for the accumulation and release of a relatively large amount of heat in a narrow temperature interval, or even at a constant temperature. In other words, heat can be stored to a suitable material without increasing its temperature very much; instead of raising the temperature, the change of phase accompanied by the heat of fusion is utilised as a heat reservoir. This allows for a significantly larger thermal capacity of LHTES systems when considering the latent heat and the sensible heat TES in a fixed temperature interval. Due to these reasons, the attention of researchers and investigators has focused on the utilisation of LHTES for an efficient use of energy resources in the last 15–20

years. As already mentioned, this has particularly been the case of renewable energy resources such as solar energy, where the LHTES technique can be used to balance between the energy demand and the energy supply.

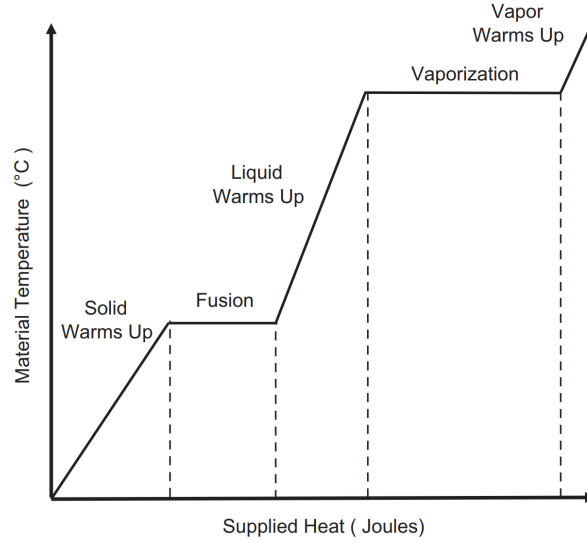


Figure 2.2: Dependence of the temperature on the heat transferred to a material [18]

Figure 2.2 demonstrates the influence of sensible heat and latent heat supplied to a storage material undergoing two phase changes: melting (fusion) of the solid to the liquid, and vaporisation of the liquid to the gas. The material, for which the plot in Figure 2.2 is shown, undergoes the phase changes isothermally as a pure chemical element. In case of a complex substance (a mixture), some raise of the temperature would be visible during the phase change processes. However, gradients of the phase change lines would be much smaller than gradients for sensible heat TES (all remaining lines in Figure 2.2). Applications of both the solid-liquid and liquid-gas phase changes can be found in the literature. However, the majority of LHTES systems utilises the solid-liquid transformation for its more suitable properties and behaviour mentioned e.g. in [38].

As for the quantification of heat stored in the latent heat TES material undergoing the isothermal phase change from the solid state to the liquid state, the amount of heat transferred to the material in the temperature range between T_i and T_f can be determined as [18]

$$Q = \int_{T_i}^{T_m} mc_p dT + m\Delta H_m + \int_{T_m}^{T_f} mc_p dT \quad (2.4)$$

where T_m is the phase change temperature and ΔH_m is the latent heat of the solid-liquid phase change (the heat of fusion). As for paraffins (organic phase change materials discussed in the following section), which are mostly considered in LHTES applications presented in this thesis, their heat of fusion is about 200 kJ/kg [43]. Thus, with the assumption of the specific heat of 2 kJ/kg·K [103] their heat storage capacity in the temperature range of 20 K including and excluding the phase change is about 240 kJ/kg and 40 kJ/kg, respectively. Considering two typical sensible heat storage media—pebbles (stone) and water—their specific heat is about 0.9 kJ/kg·K and 4.2 kJ/kg·K, respectively [28]. For the identical temperature range of 20 K, the TES capacity for pebbles and water is 18 kJ/kg and 84 kJ/kg, respectively. From this point of view, it is obvious that the heat of fusion

and the phase change play crucial roles for the thermal capacity available for TES. In other words, the LHTES allows for a higher heat storage density than in case of the sensible TES. Therefore, a smaller amount of the heat storage material is needed in case of the LHTES system, which implies lower requirements on space and its easier integration.

There are numerous designs and applications of LHTES and some of them are discussed in more detail in Section 2.3. In a general view, these systems for LHTES can be considered as heat exchangers: devices for heat transfer between a heat storage material changing the phase and a suitable heat transfer fluid. Such heat exchangers can be of different designs and concepts: including traditional closed-system heat exchangers [21] (e.g. the shell with a heat storage material inside and a heat transfer fluid flowing through the shell) as well as open systems such as wall panels with LHTES installed in the room and the ambient air interacting with the panels [67].

2.2 PHASE CHANGE MATERIALS

As explained in the previous section, the LHTES allows for a higher thermal capacity than in case of the sensible TES when considering the identical temperature range in both cases. Due to this reason, the LHTES has attracted a great attention of investigators and developers in the two last decades, which is confirmed by a vast number of original research papers as well as highly cited review papers on related topics, e.g. [2, 17].

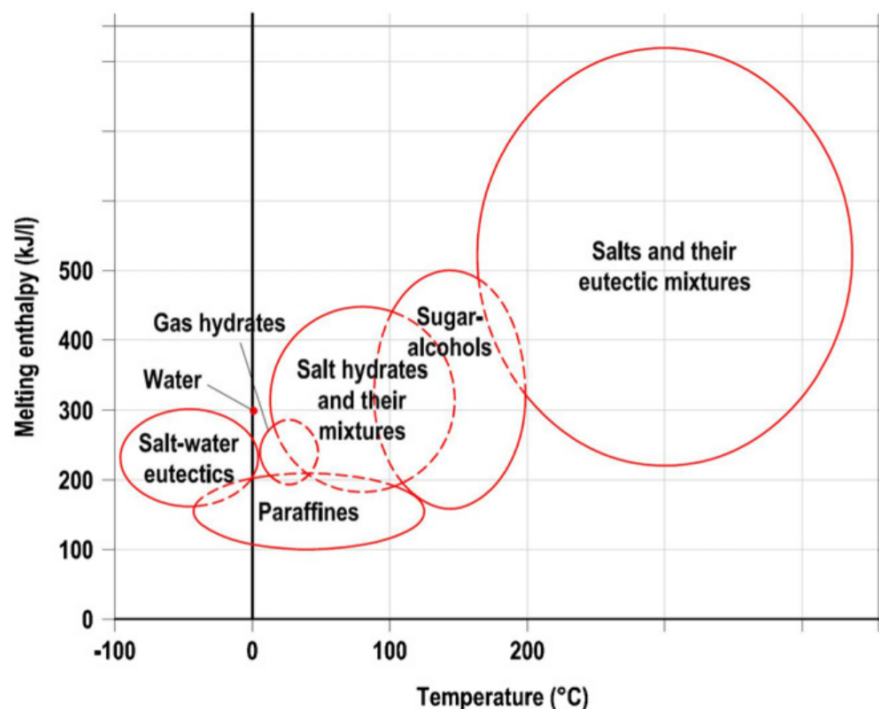


Figure 2.3: Temperature range and melting enthalpy of different groups of PCMs [11]

LHTES applications are based on the use of phase change materials (PCMs), which are able to change the phase in a desired temperature range [110]. In most cases, the solid-liquid phase change is employed. There is a wide range of PCMs available with various phase change temperatures suitable for low temperature applications ($-20\text{ }^{\circ}\text{C}$ to $5\text{ }^{\circ}\text{C}$), medium temperature applications between $5\text{ }^{\circ}\text{C}$

and 80 °C as well as for high temperature applications above 80 °C as shown in Figure 2.3. The largest sub-class with medium temperature applications is usually further split into two groups: medium low temperature applications between 5 °C and 40 °C, which typically include heating and cooling in buildings, and medium high temperature applications between 40 °C and 80 °C including solar air and water heating [31]. Figure 2.3 shows the temperature ranges for various types of PCMs. As for building-related applications of LHTES presented in this thesis, they fit into the medium low temperature category. PCMs suitable for those applications are discussed in more detail in the following sections.

The selection of a suitable PCM for a particular application should include the assessment of the following criteria [11]: (a) thermal criteria (a suitable phase change temperature and a high amount of the heat of fusion), (b) physical criteria (no phase segregation, high density and small volume expansion), (c) kinetic criteria (no supercooling and a sufficient crystallisation rate), and (d) chemical criteria (a long-term chemical stability, compatibility with other materials, non-toxicity, and no fire hazard).

2.2.1 TYPES OF PHASE CHANGE MATERIALS

The PCMs can be classified into three categories according to their chemical composition: organic, inorganic, and eutectic [11] as shown in Figure 2.4.

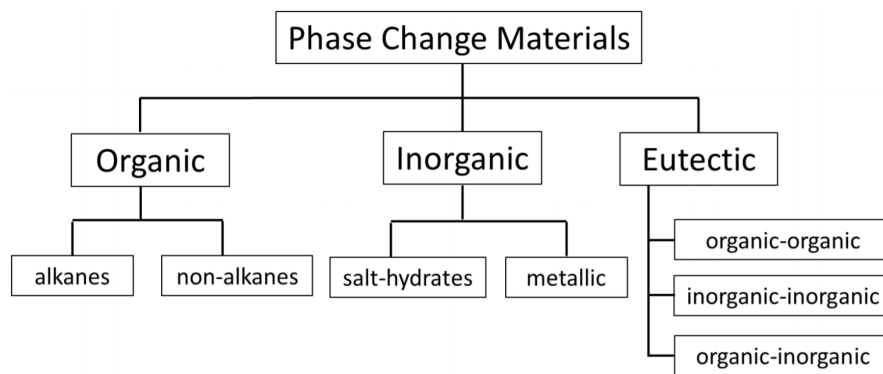


Figure 2.4: Types of PCMs according to their chemical composition [20]

The organic PCMs represent the majority of the PCMs used in applications operating in the medium low temperature range. Alkanes, often referred to as paraffins or waxes, are the typical and the most frequently utilised organic PCM. The alkanes are organic compounds consisting of carbon and hydrogen atoms according to the formula $\text{CH}_3(\text{CH}_2)_n\text{CH}_3$ with single carbon-carbon bonds only. The phase change temperature of paraffins depends on the number of carbons in the compound: the higher the number of the carbon atoms, the higher the phase change temperature. For example, $\text{C}_{12}\text{H}_{26}$ has the phase change temperature of about $-9\text{ }^\circ\text{C}$, while in case of $\text{C}_{44}\text{H}_{90}$ it is almost $86\text{ }^\circ\text{C}$ [29]. As it is rather difficult to prepare a paraffin consisting of only one alkane, commercially available PCMs usually consist of a mixture of paraffins. This implies that such a paraffin mixture allows for the phase change in a certain temperature range, which is dependent on the compounds and their mass ratios in the mixture. The paraffins are reported [11] to be inexpensive, chemically stable with no phase segregation, and available in a wide range of the phase change

temperatures. Drawbacks of paraffins are a low thermal conductivity making heat transfer slow, and relatively high volume changes during the phase change.

Besides the alkanes, the class of organic PCMs include other organic materials such as fatty acids, esters, alcohols, and glycols. They have very suitable properties for LHTES applications, however they are about three-times more expensive than paraffins. This makes them minor organic PCMs when considering the number of applications.

As for inorganic PCMs, salt hydrates are a typical representative of inorganic PCMs. They possess a high amount of the heat of fusion as well as a relatively high thermal conductivity (in comparison to paraffins), they are cheap and non-flammable. However, most of them are corrosive to the majority of metals, and they suffer from both supercooling and phase decomposition. Moreover, the salt hydrates degrade in cyclic operation meaning that the heat storage capacity decreases with the increasing number of phase change cycles [11]. The most known salt hydrate is the Glauber's salt $\text{Na}_2\text{SO}_4 \cdot \text{H}_2\text{O}$ with the phase change temperature range between 32°C and 35°C and with the heat of fusion of about 255 kJ/kg [81]. Another examples of inorganic PCMs include molten salts and metals, which are suitable for high temperature applications such as concentrated solar power generation, solar water heating systems, and industrial waste heat recovery. Lin et al. [81] reported on such high temperature applications and they also emphasised that though the most research works have been related to organic PCMs, there is currently an increasing trend towards inorganic PCMs in industrial applications due to e.g. an extremely high thermal conductivity in case of metals.

Eutectic PCMs are compounds consisting of two or more PCMs. The eutectics form blend crystals when they solidify [3]. According to components in the mixture, the eutectic can be of three types: organic–organic, organic–inorganic, and inorganic–inorganic. The eutectics do not suffer from phase separations and all the components of the mixture change the phase simultaneously. An example of the eutectic organic–organic PCM can be the mixture of the capric acid with the myristic acid, which form the PCM undergoing the phase change at 22.6°C accompanied by 154.8 kJ/kg of the latent heat [3]. On the other hand, $\text{Na}_2\text{CO}_3 \cdot \text{NaCl}$ is an inorganic–inorganic eutectic suitable for very high temperature applications as it has the solid-liquid phase change temperature of 637°C and the latent heat of 283 kJ/kg [81].

2.3 APPLICATIONS OF LATENT HEAT THERMAL ENERGY STORAGE

In the last 20 years, a vast number of research papers and studies have been published on the topic of LHTES applications. There are many research and application areas, which make use LHTES and PCMs. As already mentioned in the foregoing sections with the description of types and classification of PCMs, PCMs can be used for applications with very low temperatures such as in cryogenic cooling [138] to very high temperatures such as in concentrated solar power generation [81]. From the perspective of the present thesis and research papers published by the author of the thesis, two application areas of LHTES and PCMs are discussed in more detail in the following paragraphs: solar air heating and cooling systems using thermal storage units, and building structures integrating PCMs. All these applications have been studied with the aim of efficient energy utilisation and/or improvement of thermal comfort in buildings.

2.3.1 SOLAR AIR HEATING AND COOLING SYSTEMS WITH LHTES

Solar air heating and cooling are techniques, which can be used for heating, cooling and conditioning of air in buildings or in other applications [130]. Solar systems employ the renewable solar energy as a source of heat. The integration of the LHTES units with a PCM into the solar air system can benefit in the increase of its thermal performance. In particular for the space heating case, the use of a PCM allows to accumulate and store thermal energy during the day when the solar radiation is available. After the sunset, thermal energy stored in the PCM can subsequently be released and used for space heating [139]. This approach helps to meet the energy supply and demand, which do not occur at the same time. A simple and straightforward utilisation of the solar system for heating is the use of the flat plate solar collector coupled with a heat storage unit as shown in Figure 2.5. The air heated in the solar collector during the day is supplied by the fan to the heat storage unit, where heat is transferred from the air to the PCM, which melts as a consequence of heat transfer into it. The air exiting the storage unit is returned to the ambient environment. When the stored heat is needed, the cold ambient air flows through the heat storage unit and heat transfer occurs in the opposite direction: the PCM solidifies and the released heat is transferred to the air increasing its temperature. The heated air is then supplied to the room. Another design consists of the solar air heater (collector), which directly incorporates the heat storage medium and no separate heat storage unit is needed. A schematic of such design is illustrated in Figure 2.6 [9].

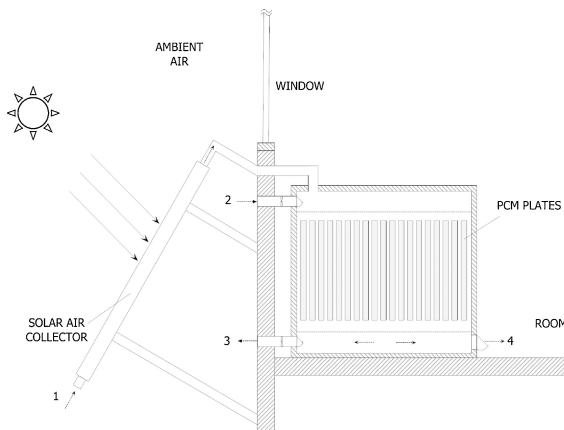


Figure 2.5: Schematic of the solar air system with the solar air collector and the heat storage unit [134]

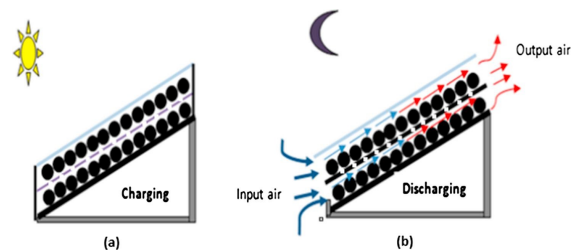


Figure 2.6: Schematic of the solar air heater with an integrated LHTES [9]

A similar principle can be utilised in case of cooling [105]. During the night when the ambient air temperature is lower than the desired room temperature, the ambient air is forced through the storage unit where the PCM solidifies and cold is stored. During the day, the ambient air temperature raising over the desired room temperature can be conditioned by means of the air flow through the storage unit. In this case, the cold stored in the PCM is released to the air, which decreases its temperature (i.e. heat from the air is transferred to the PCM, which causes its melting) [132].

Belmonte et al. [15] investigated the use of a fluidized bed with a PCM integrated into the solar air heating system with solar collectors for heating in a residential house. A parametric analysis investigating the influence of parameters to the thermal performance of the system was carried out. The authors used computer simulations in TRNSYS and they reported that the storage unit con-

taining 2000 kg of a PCM can cover about 50% of heating demands of a residential house in mild-winter climates. Abuska et al. [1] carried out a comparative experimental investigation of the solar air heater with an integrated PCM. The authors considered two cases of the heat storage material under various operational conditions and they compared them with the case without the PCM. It was reported that the use of the PCM allowed for about 9% increase of thermal efficiency, and the use of the aluminium honeycomb as an internal fin structure significantly reduced the charging-discharging time of the unit. Arfaoui et al. [9] presented a study into the use of the solar air heater with the integrated LHTES for the nocturnal use. Experimental investigations and energy analysis were performed. Two beds of encapsulated spherical capsules with a PCM were used as the heat storage material. The authors reported that the presented design allowed for the daily energy efficiency of about 47%.

Lin et al. [80] reported on the multi-objective optimisation of the air-PCM heat storage unit for solar air systems. The authors first performed experimental investigations, which were followed by the development of a computer model. A genetic algorithm was coupled with the computer model and an optimisation study was performed. The authors reported that the optimised heat transfer effectiveness can be improved by about 15% with the simultaneous reduction of the charging time by about 1.2 hour. Iten et al. [55] thoroughly reviewed air-PCM systems for LHTES in heating and cooling applications. The authors reported that passive systems (requiring no energy input) benefit in low initial and running costs, but their capability for heat storage is limited. On the other hand, active systems provide a much higher capability for heat storage with a rather low energy consumption of fans. Most research studies were aimed at the use of the heat storage with auxiliary sources such as air conditioning systems, heat pumps, and solar collectors. The applicability of some systems has been confirmed by received patents and their introduction to the market.

2.3.2 AIR-PCM HEAT STORAGE UNITS

Heat storage units are technical devices, which are designed to accumulate, store, and consequently release energy in the form of heat. In this section, the attention is focused on storage units, which employ air as the heat transfer fluid. As already explained in the foregoing paragraphs, the heat storage unit is often used as a part of the solar air heating system. However, the heat storage unit can also be used with other sources of energy. A system consisting of the electric heater and the heat storage unit [42] is an example how the LHTES system can be employed for the shift of peak demands of electricity, which are used for heating or cooling in buildings as well as in some industrial applications [122].

According to the purpose of the unit, heat as well as cold can be stored, frequently for space heating and cooling, respectively. The heat storage unit is actually a heat exchanger, which incorporates a suitable heat storage medium. As for the heat storage medium, two already discussed approaches can be utilised—the sensible heat TES (such as packed beds mentioned in Section 2.1.1) and the latent heat TES, which provides with a higher thermal capacity.

In recent years, various designs and types of the air-PCM heat storage units have been proposed, investigated, and analysed. In what follows, a brief description of some of them is provided. Their purpose is to illustrate the current research state and interest rather than to provide a comprehensive

description of the state-of-the-art, which can be found in review papers, e.g. in [4, 161].

Lopez et al. [89] introduced a computer model of the air-PCM heat exchanger with a PCM, which is suitable for the use in buildings for free cooling and peak load shaving in winter and in summer as shown in Figure 2.7. Thin PCM plates with air gaps between the plates were used as the heat storage medium. The authors emphasised that though the experimental investigation is applicable for the assessment of the thermal performance, computer simulations and computer model are needed for optimisation of the system and its proper design. For that purpose, the authors presented a computer model, which takes into consideration the heat conduction in the PCM plates and the heat transfer between the plates and the air flowing between them. The functionality of the model was validated by means of experimental data and a good agreement was reported.

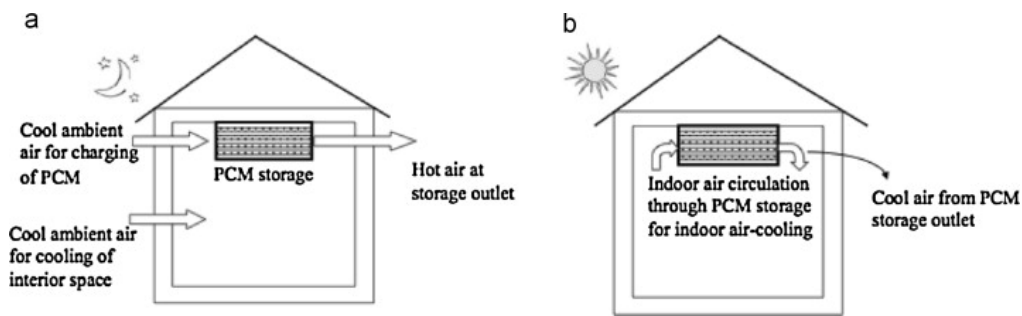


Figure 2.7: Use of air-PCM heat storage unit with LHTES for free cooling [89]

Sun et al. [136] experimentally investigated the heat charging process to the PCM plates by means of a wind tunnel as shown in Figure 2.8. A commercial PCM suitable for thermal storage applications in buildings was investigated. The authors assessed the influence of the inlet air temperature and velocity as well as the inclination angle of the PCM plates on the duration and the heat transfer rate during the phase change process. It was reported that the charging rate was more than doubled when the inlet air temperature was increased from 35 °C to 55 °C, but only about 9% increase was observed when the inlet air velocity increased from 4 m/s to 5 m/s. As for the inclination angle of the PCM panels, the best performance was reported for the inclination angle of 90° meaning the vertical position of the plates.

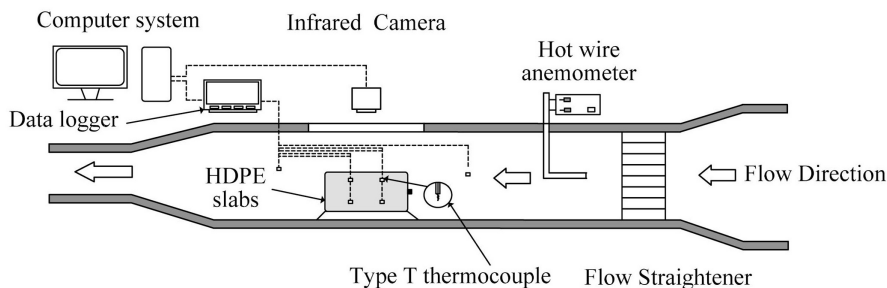


Figure 2.8: The system with a PCM heat storage medium investigated in [136]

Herbinger et al. [49] reported on a computational investigation of an air-PCM heat storage unit by means of computer simulations in COMSOL Multiphysics. The authors created a symmetric 3D model, which included the conductive and convective heat transfer and the laminar flow of air in the

channels surrounded by the PCM. Results indicated that a small size of channels and a high inlet air temperature allowed for higher heat transfer rates. On the other hand, it was reported that the inlet air velocity has only a minor influence to heat transfer rates during the heat charging and discharging processes. Halawa and Saman [44] reported a numerical study into the thermal performance of the thermal storage unit consisting of plates made of a PCM as shown in Figure 2.9. The unit was designed and proposed for space heating and its integration into the space heating and cooling system. A comprehensive parametric analysis was performed with the aim to assess effects of charge and discharge temperature differences, air mass flow rate, plate thicknesses, air gaps, and plate dimensions on the outlet air temperatures and heat transfer rates of the unit. The computer model developed as a type for TRNSYS simulation tool was used in the analysis. Besides the assessment of parameters to the thermal performance of the unit, the authors also concluded that the natural convection has a negligible effect to the considered design of the thermal storage unit.

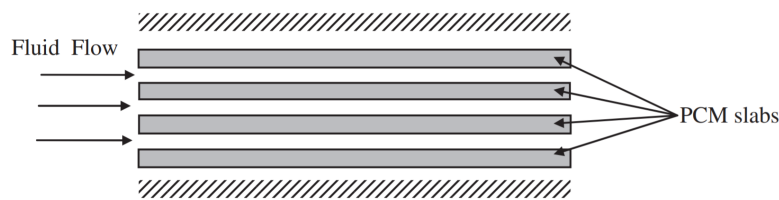


Figure 2.9: Schematic of air-PCM heat storage unit investigated in [44]

Arkar and Medved [10] presented a study into free cooling of buildings by means of the LHTES unit integrated into a ventilation system of the building. The cylindrical unit was filled with spheres containing a PCM. A computer model of the unit was implemented and used in the identification of parameters, which significantly influence the behaviour of the system. Simulation results indicated that the phase change temperature between 20 °C and 22 °C is the most suitable for the purpose of free cooling. The authors concluded that suitable thermal comfort conditions can be achieved with the use of 6.4 kg of a PCM per the square metre of the floor area. Liu and Tao [85] presented a theoretical optimisation model for a multi-stage heat storage unit with a PCM and with an unsteady heat transfer fluid inlet temperature as shown in Figure 2.10. The entransy theory was applied to the thermodynamic analysis and the optimisation procedure provided characteristics of optimal PCMs. The authors reported that the increase of the number of stages significantly improves the thermal behaviour of the heat storage unit. Moreover, the temperature fluctuations at the inlet substantially influence the optimal phase change temperatures in individual stages. The uniform outlet temperature of the heat transfer fluid can be achieved by the increase of the length of individual stages rather than by the increase of the number of stages. A similar analysis applied to the heat storage unit formed by a packed bed with particles filled with a PCM was reported in [76].

Farah et al. [37] reported a study aimed at the investigation of space cooling by means of the air-PCM heat storage unit coupled with the air source heat pump. The storage unit consisted of thin plates made of a PCM as shown in Figure 2.11. The authors developed a 2D computer model of the unit and verified it with the use of experimental data. A sensitivity analysis was carried out with the aim to assess the influence of uncertainties of the phase change temperature and of the inlet air temperature on computational results. It was reported that the uncertainty of these variables has a

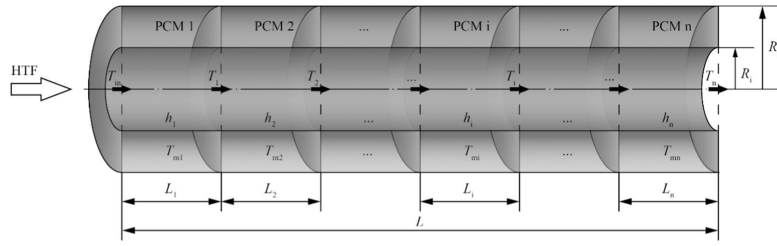


Figure 2.10: Multi-stage heat storage unit investigated in [85]

rather small effect on the electrical energy consumption and the power demand of the cooling system. Further, the authors reported that the use of the thermal storage unit in a proper configuration allowed for the reduction of the annual cooling energy required by the heat pump by about 25%.

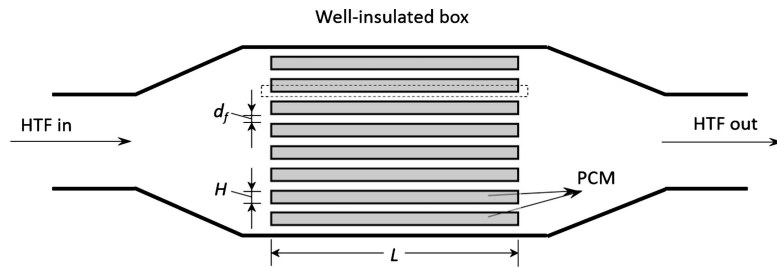


Figure 2.11: Heat storage unit used for space cooling investigated in [37]

Kumirai et al. [75] experimentally investigated an LHTES system consisting of commercially available containers with a PCM for space cooling as shown in Figure 2.12. Three PCMs were considered in the study: two paraffins and salt hydrate with the phase change temperature between 22 °C and 28 °C. The containers were positioned vertically with the gap of 15 mm. An analysis was carried out to investigate the influence of the inlet air temperature and the mass flow rate of the air through the system. It was found that the average thermal efficiency of the system decreased with the increased velocity of the air, and the cooling power increased with the flow rate and with the inlet air temperature. It was further reported that paraffins exhibited a faster and more intensive heat absorption than the considered salt hydrate.

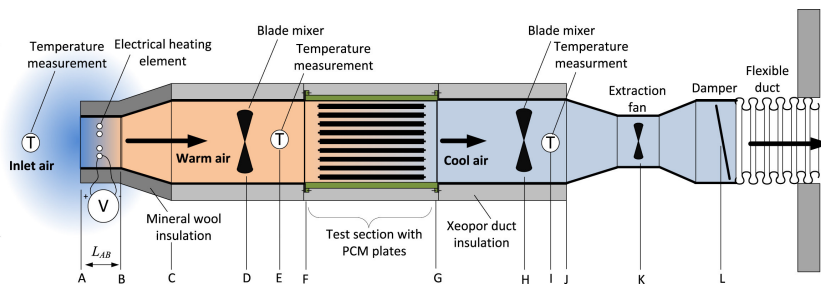


Figure 2.12: The top view of the heat storage system for space cooling analyzed in [75]

Waqas et al. [151] presented a study into the performance of the heat storage unit with a PCM in the form of plates. The computer model of the unit was developed and used for the analysis. The city of Islamabad was considered in the study. It was reported that the performance of the storage unit was maximal for the phase change temperature of about 29 °C in the summer season and for

about 21 °C in the winter season. The phase change temperature of 27.5 °C was identified as an optimum for the all-the-year operation of the unit. Moreover, it was concluded that the decrease of the heating capacity was not as sharp as the decrease of the cooling capacity. If, for instance, a PCM with the phase change temperature of 29 °C is used instead of 27.5 °C, the cooling capacity is increased by 15%, while the heating capacity is decreased only by 3%.

Iten et al. [56] reported on experimental investigations of an air-PCM thermal storage unit. The authors focused on the assessment of the inlet air temperature and velocity on the total thermal performance of the unit during the heat charging and discharging periods. It was reported that the increase of the inlet air velocity allowed for the reduction of time needed for charging and discharging, but not linearly. The inlet air temperature was identified as the most important parameter, which substantially influences the time (duration) needed for discharging. Rajagopal and Velraj [114] experimentally investigated an air-PCM heat storage unit for free cooling applications. The authors reported that based on charging experiments the decrease of the inlet air temperature has a higher influence on the reduction of the charging time (the solidification of the PCM) than the increase of the inlet air velocity. The investigated heat storage unit was capable to maintain a desired room temperature for about 8 hours with the assumed heat load of 0.5 kW.

2.3.3 BUILDING STRUCTURES INTEGRATING PCMS

The use of PCMs in building structures represents another frequent application of the LHTES. The main aim of the integration of PCMs in building structures is the improvement of thermal conditions, thermal comfort and environment in buildings. The integration of PCMs enables, for instance, the increase of thermal inertia of lightweight buildings, for the stabilisation of air temperature fluctuations, prevents overheating, and allows for the reduction of energy consumption needed for space heating and cooling. Dominantly, a vast number of research works can be found in relation to the integration of PCMs into walls and vertical building structures. However, the use of PCMs in horizontal building structures such as in floors (see e.g. [39, 8, 121]) and ceilings (see e.g. [152, 157, 57]) has also been widely reported. In the following text, several recent examples of achievements in the utilisation and integration of PCMs in vertical building structures are given and briefly commented to illustrate current research interests and objectives.

Besides the original research papers, there is a number of review papers on the topic of the integration of PCMs into building structures. Zhou et al. [166] provided a review of studies on LHTES in building applications including the use of PCMs, impregnation methods, current building solutions and the assessment of their thermal performance. Pomianowski et al. [112] reviewed PCM technologies applicable for buildings. Various PCM technologies were assessed from the view to improve the indoor environment, increase the thermal inertia and decrease the energy consumption in buildings. Further, an overview on available methods for a proper determination of thermal properties of PCMs, which play a key role in computer simulations, was provided. Rao et al. [117] published an overview of recent developments in the integration of PCMs with the mortar for the use in building applications. Various PCM–mortar combinations, thermal and mechanical properties of the PCM–mortar mixtures as well as their advantages and limitations were reviewed, summarised, and assessed. Akeiber et al. [3] reported on recent studies aimed at applications of PCMs for passive

cooling in buildings and building envelopes. Full-scale testing and numerical modelling were identified as the most frequent methods for the assessment of the use of PCMs in buildings. Konuklu et al. [73] reviewed recent advancements in the microencapsulation of PCMs and their use in building applications. The study provided an overview on test methods for microencapsulated PCMs as well as particular applications of microencapsulated PCMs in buildings including concrete, mortar, plaster, and other materials. Liu et al. [86] published an overview on macroencapsulated PCMs and their integration into building envelopes. The analysis provided insights into the material selection for macroencapsulation of PCMs, common macroencapsulation forms, and into the phase change process in these forms. Further, optimal locations for PCMs in building envelopes and the thermal performance enhancement were discussed.

De Gracia [26] presented a novel concept based on the dynamic use of PCMs in building envelopes as shown in Figure 2.13. The proposed solution allows to set up the position of the PCM layer inside the building envelope with respect to the insulation layer. The author provided a proof of concept for this technical solution based on computer simulations. The phase change temperature and the control of the position of the layer with the PCM were optimised using a particle swarm optimisation method. The simulation results indicated that the dynamic adjustment of the PCM layer significantly facilitates the solidification of the PCM, which allows for the use of a PCM with a lower phase change temperature.

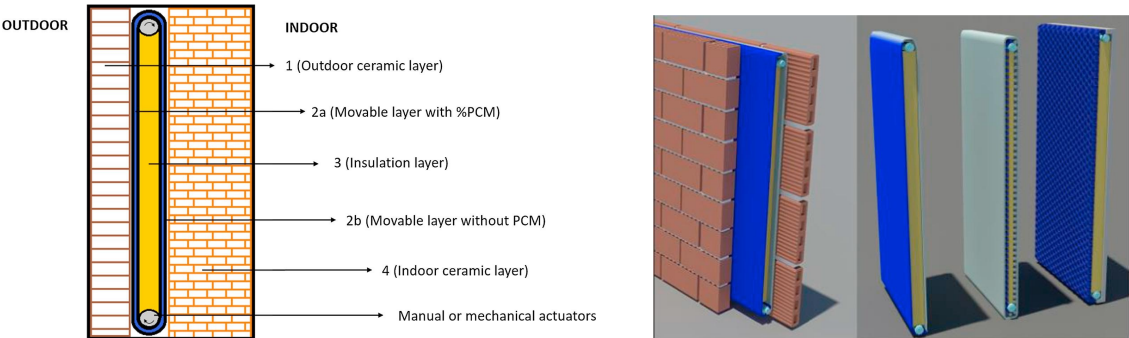


Figure 2.13: The schematic of the wall with the adjustable PCM layer investigated in [26]

Stritih et al. [135] investigated the use of a composite wall filled with different PCMs. The behaviour and thermal accumulation in the wall in the summer season were analysed by means of computer simulations in TRNSYS. It was reported that cooling requirements are, beside other factors, influenced by the wall material. Moreover, the authors emphasised that for the selection of a suitable PCM it is necessary to properly consider meteorological conditions in which the PCM wall is to be located. This is important not only from the view of the desired room temperature, but also due to heat discharging from the wall during the night. The achieved results indicated that the application of PCMs in walls can minimise the energy consumption in building and allow for achieving goals of net zero energy buildings. Xie et al. [156] reported that although PCM wallboards used in buildings have been extensively studied, further thermal performance analyses have to be carried out to enable their practical use. The authors analysed the application five PCM wallboards in the exterior wall of an air-conditioning room by means of computer simulations. The following parameters related to the thermal performance were analysed: the convective heat transferred from the

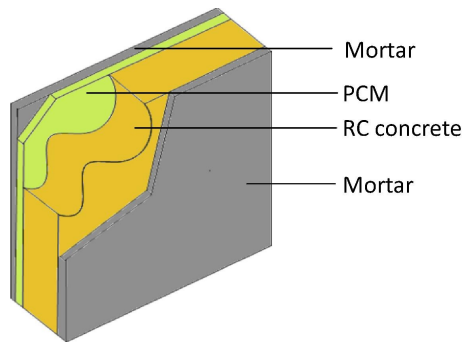


Figure 2.14: The wallboard with a PCM investigated in [96]

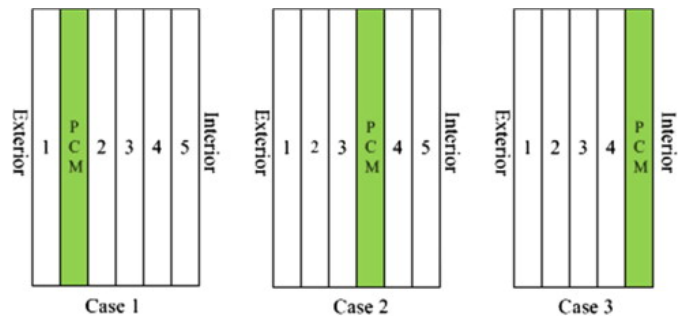


Figure 2.15: Optimal location of the PCM layer analysed in [167]

wall to the indoor air, the heat ratio, and relative thermal conductivity. The authors reported that the PCM wallboard with a good thermal performance in some seasons can have an average thermal performance in other seasons, and thus the thermal performance analysis over the entire year needs to be considered.

Saffari et al. [123] presented a simulation-based optimisation methodology based on the coupling of two simulation tools (EnergyPlus and GenOpt) with an innovative enthalpy–temperature function. The proposed method allows for the determination of the optimal phase change temperature, which enhances cooling, heating, and the annual total heating and cooling energy performance of a residential building in various climate conditions. Results showed that in case of a location with dominant cooling demands, the optimal phase change temperature is about 26 °C. On the other hand, the phase change temperature of about 20 °C allows for the maximisation of thermal performance in locations with dominant heating demands. Elnajjar [33] computationally investigated a wall made of bricks containing a PCM. The latent heat of fusion of the PCM was used to reduce heat load fluctuations and peak time shifting. A one-day and a seven-day analyses were carried out and the cyclic behaviour of the PCM in the building material was assessed. Results demonstrated that the selection of a suitable PCM requires at least the seven-day analysis evaluation. The author used the seven-day analysis for the determination of a PCM suitable for weather conditions in the United Arab Emirates and the possibility for about 30% energy savings was reported.

Mi et al. [96] analysed the influence of a PCM layer in the building envelope (shown in Figure 2.14) on energy consumption of a multistory office building. The computer model in EnergyPlus and a whole-year simulation were utilised and five locations with different climate conditions were considered in the study. The authors reported that energy savings are significant in cases with cold climate regions as well as in regions with hot summer and cold winter. It was already reported that though the use of PCM in wall structures is economically attractive in some locations, there are also locations in which the investment to the PCM cannot be recovered, and thus is not economically viable. Therefore, each installation has to be considered separately and properly addressed taking into account the whole-year conditions. Zwanzig et al. [167] investigated the potential of energy savings by means of the integration of PCM into the building envelope. The authors created a computational model of the wall, which was coupled with meteorological data applied for exterior boundary conditions. It was concluded that the thermal performance of the PCM highly depends

on weather conditions, which means that a suitable PCM has to be selected according to a particular climate region. The authors also analysed different locations of the PCM layer in the wallboard as shown in Figure 2.15. It was demonstrated that the optimal location of the PCM layer is a function of the thermal resistance between the PCM layer and the exterior boundary conditions.

Olivieri et al. [104] reported an experimental study into thermal properties of cementitious mortars incorporating microencapsulated PCMs, which were intended for the use in the building structure coupled with an integrated hydronic system, the so-called thermally activated building system (TABS). The TABS consisted of pipes embedded in the building element and a heat transfer fluid was actively used to transfer heat and/or cold to it. The TABS can be used in walls, ceiling, or floors. The activation of the thermal mass has a potential for reduction of the energy use in buildings. The advantages include its low temperature operation and the high thermal inertia, which allow for shaving of peak loads and for the shift of energy consumption to periods with low energy cost. The authors in [104] performed the characterisation of mortars with microencapsulated PCMs. The identified properties are crucial parameters for subsequent computer studies and optimisation procedures of the TABS application in buildings. Jobli et al. [63] computationally and experimentally analysed the thermal performance of a TABS with a PCM and embedded capillary tubes. The experimental element was built in a lab and a computer model was developed for the assessment of its long-term thermal performance. The authors reported that for a flow rate of the heat transfer fluid higher than a certain value, there was a good agreement between the model and experimental data. For lower flow rates, there were discrepancies and the authors proposed a correction factor methodology, which allowed for a sufficient accuracy of the model and its high computational performance.

2.4 MODELLING OF LHTES SYSTEMS WITH PCMs

It can be concluded from the overview of recent research works presented in the foregoing sections that computer modelling and numerical simulations play a crucial role in the research and development of systems and devices for LHTES with PCMs. Many investigators use computer simulations as an efficient and fast tool for the assessment, evaluation, and design optimisation of LHTES systems. The quantification of technical and economic feasibility of systems utilising LHTES and PCMs requires the development of proper computational models as well [6]. In the development of a model, several factors have to be considered and addressed. The model has to be reliable and provide results, which are in agreement with a real system being modelled. This means that validation and verification of the model are required before its use in simulations. Further, the model has to be computationally effective and sufficiently fast from the view of an intended application. The model should also be sufficiently robust and user-friendly, especially in cases when the finalised and ready-to-use model is applied by end-users rather than its developers. Taking all these factors together, the development and implementation of models for LHTES with PCMs are still challenging in certain views. This section aims at the summary of current trends and approaches, which have been applied to computer modelling of systems with PCMs for LHTES.

In general, computer modelling of systems for LHTES and including PCMs pertains to computational heat transfer with phase changes. In contrast to other research areas including the solu-

tion of heat transfer problems with phase changes, simpler and straightforward numerical methods and approaches are often used in the majority of models for LHTES in building applications rather than complicated, comprehensive, and computationally demanding techniques. This is also the case of solar air heating and cooling systems, thermal storage units consisting of commercially available plates with PCMs, and building structures with integrated PCMs discussed in this thesis. There are probably several reasons for it; the most important ones are that (1) in many cases the heat transfer problem can be simplified and considered as a 1D or 2D problem, (2) natural convection has often minor effects and can be neglected, and (3) models need to be computationally effective as they are frequently used for simulations of long-term periods, such as several weeks or months, or even a whole year. However, advanced methods such as CFD should be used in cases in which the geometry is rather complex and/or multiphysical phenomena such as heat conduction–convection with fluid flow have to be taken into consideration [5].

Agyenim et al. [2] thoroughly reviewed heat transfer and phase change formulations for LHTES systems. The authors concluded that the enthalpy method has been the most frequently utilised approach used for taking into account the phase change and the evolution of the heat of fusion. It was also pointed out that though only pure conduction was previously solely taken into consideration, current models also account for convection in the melt in cases where convection represents a non-negligible heat transfer mechanism. The authors reported that in case of modelling of PCMs and LHTES systems, the analysis is complex and includes the solid–liquid moving boundary problem. The position of the boundary (the interface between the phases) is unknown and needs to be determined as a part of the solution. The authors provided a list of research works related to computer modelling and the majority of them utilised a 1D or 2D solution by means of the enthalpy method as demonstrated in Figure 2.16. Besides the enthalpy method, some numerical models were enhanced/modified with the use of various computational techniques such as the Gauss-Seidel iterative procedure and the three-diagonal matrix algorithm (TDMA) solver.

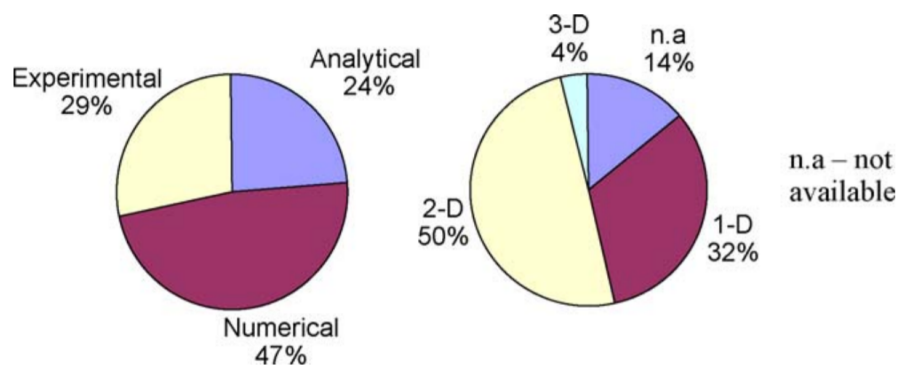


Figure 2.16: The share of research approaches on investigation of selected LHTES systems (left) and the considered dimensions (right) [2]

Al-Abidi et al. [5] provided an overview on papers, in which the CFD approach was applied for investigation of LHTES systems. The most frequently utilised CFD tool is ANSYS Fluent. The authors reported that the majority of researchers use the enthalpy formulation, in which the solid–liquid interface needs not be explicitly tracked. It was emphasised that the selection of the enthalpy formulation is mainly due to the following factors: (1) governing equations for two-phase problems

are similar to those containing the single phase only, (2) no explicit conditions have to be solved and satisfied at the phase interface, (3) the enthalpy formulation implicitly involves the mushy zone, and (4) the solution of the phase change problem with the enthalpy formulation is easier than in other cases. The authors also concluded that simulation results of the 2D model are generally similar to those of 3D model, and thus the use of 2D models allows for the reduction of computational costs.

Al-Saadi and Zhai [6] reviewed computer methods for modelling of PCMs embedded in building enclosures and they reported that only several numerical methods are applied including the enthalpy method, the heat capacity method, the temperature transforming model, and the heat source method. The authors provided a comparison of these methods with their advantages, disadvantages, and limitations. In particular, the enthalpy method was identified as the fast method if a proper scheme is selected and it allows for sharp as well as gradual phase changes. On the other hand, the enthalpy method can suffer from oscillations and requires a two-step solution as the enthalpy as well as the temperature values are unknown variables. The effective heat capacity was reported as intuitive and easy for programming, however it is not self-conservative (it may underestimate the heat of fusion) and it requires fine time and spatial discretization techniques for accurate results. The temperature transforming method was identified as an uncommon method without the evaluation of its pros and cons, while the heat source method suffers from numerical errors for a non-isothermal phase change over an temperature interval, which is the case of most PCMs. It was concluded that the effective (often also referred to as apparent) heat capacity method is mostly employed despite of its limitations.

Later, Al-Saadi and Zhai [7] investigated eight computational approaches for modelling of PCMs and LHTES systems, which were implemented in Matlab/Simulink. A linearised enthalpy method with a hybrid correction scheme was proposed as an improved method to existing numerical schemes. The authors utilised the EnergyPlus tool for the validation of the developed models, which were assessed for their computational efficiency and accuracy. Some methods including the effective heat capacity method were identified as rather sensitive to the range of the phase change, but quite robust in terms of the amount of heat of fusion. However, it was reported that a sufficiently small time step should be used for all the methods to gain accurate results. The proposed iterative and hybrid correction schemes were identified as computationally efficient and stable in terms of variations of PCM properties. It was further reported that the time step of up to 15 minutes can be utilised in simulations without significant numerical errors.

Liu et al. [82] presented a comprehensive review of mathematical models and numerical methods, which are applicable to the solution of phase change in LHTES systems. It was pointed out that it is important to weight the ratio between conduction and convection heat transfer in each stage of the system. The authors provided an overview on fixed grid methods widely applied to the solution of conduction-driven problems including the well-known enthalpy method and the effective heat capacity method. The authors also mentioned the use of adaptive grid methods such as the front tracking method [68], which are, however, used significantly less often in comparison to fixed grid methods. The authors further concluded that the integral method, the boundary fixing method, the enthalpy-porosity approach, and the equivalent thermal capacity method have been frequently used for solution of problems including natural convection. Numerical approaches to encapsulated

PCMs were also analysed in the paper. It was reported that current models for microencapsulated as well as for macroencapsulated PCMs have their limitations and a suitable method has to be selected according to a particular case.

Saffari et al. [124] reported an overview on whole-building energy simulation tools for passive cooling. It was emphasised by the authors that the application of PCMs has not always been as energy beneficial as expected. The effectiveness was identified as highly dependent on climatic conditions, on the phase change temperature as well as on the behaviour of occupants. The use of energy simulation tools is therefore a key procedure in the assessment of LHTES systems. Various computational tools were reviewed in this respect and it was found that EnergyPlus, TRNSYS, and ESP-r are dominantly used tools for simulations of thermal behaviour of buildings. In the majority of sub-models for LHTES systems applicable in the mentioned tools, either the enthalpy method or the effective heat capacity has been adopted. The authors further concluded that the 1D finite difference method with implicit, the semi-implicit Crank-Nicolson as well as with explicit time discretization schemes are the most commonly utilised approaches.

In accordance with the findings presented in the aforementioned papers, the enthalpy method (e.g. [89, 37, 151, 26, 156, 123]) and the effective heat capacity method (e.g. [49, 10, 135, 33]) represent the main and dominant two approaches applied by researchers and investigators to the solution of problems including solar air heaters, thermal storage units, and building structures integrating PCMs, which were discussed previously in Sections 2.3.1, 2.3.2, and 2.3.3. Due to the nature of these problems, 1D and 2D models with the dominant conduction heat transfer have often been adopted and used in these models.

As for the numerical discretization in the spatial domain, the mentioned models are often based on the use of the finite difference method, the control volume method, and the finite volume method. In the finite difference method, partial derivatives are replaced with their approximations by means of finite differences (more precisely by means of a suitable part of the Taylor's expansion), which allow for the transition from the partial differential equation to the algebraic equation. This transition is a key issue as algebraic equations (describing relations given in partial differential equations) are suitable for a direct solution by computers. The control volume method is based on partitioning of the spatial domain into elements—control volumes, for which the balance equation (more precisely the use of the First law of thermodynamics for an open system) in terms of heat and energy is established. Such the balance equation provides an algebraic equation, which allows for the determination of the temperature distribution and other quantities. Finally, the finite volume method requires partitioning as well—the domain is split into finite volumes over which the governing equation is integrated. The numerical integration (with the replacement of partial derivatives with their algebraic equivalents) results into algebraic equations and their solution then provides the distribution of desired quantities.

As for the approach to the time derivatives, all three basic methods have been applied in computer models of LHTES systems [82, 124]. These include the explicit time discretization, the implicit time discretization, and their combination such as the Crank-Nicolson scheme. Each has some advantages and drawbacks and the use of a particular method needs to be considered together with other factors, particularly with the discretization method and with the method applied to the solution of the phase

change. The explicit scheme is conditionally stable (meaning that the time step is strictly limited), but it is computationally inexpensive and allows for direct parallel computing. The implicit and the Crank-Nicolson schemes are, on the other hand, unconditionally stable (there is no restriction on the time step in terms of numerical stability), but they are computationally more expensive as they require the use of numerical methods for the solution of a set of equations. Moreover, simple and straightforward parallel processing discussed e.g. in [71] is not possible.

GENERAL FORMULATION OF A PHASE CHANGE PROBLEM. In case of the two-phase heat transfer problem driven by heat conduction, its solution consists of the time-dependent temperature distribution and of the time-dependent phase change location for the phase change problem with a moving interface [6]. In case of PCMs, the solid-liquid phase change is dominantly utilised. The temperature distribution of the solid phase is governed by the heat transfer equation

$$\varrho_s c_{p,s} \frac{\partial T_s}{\partial t} = \nabla \cdot (k_s \nabla T_s) \quad (2.5)$$

where ϱ is the density, c_p is the heat capacity, T denotes the temperature distribution, t is time, and k stands for the thermal conductivity. The subscript s indicates that the quantities are related to the solid phase. Similarly, for the liquid phase the governing equation is

$$\varrho_\ell c_{p,\ell} \frac{\partial T_\ell}{\partial t} = \nabla \cdot (k_\ell \nabla T_\ell) \quad (2.6)$$

which is the identical equation as in case of Eq. (2.5), only the temperature and the thermophysical properties of the liquid phase are used as indicated by the subscript ℓ . The balance on the interface between the phases as well as the behaviour of the interface (its movement and shape) are governed by the Stefan condition [6, 143]

$$k_s \frac{\partial T_s}{\partial n} - k_\ell \frac{\partial T_\ell}{\partial n} = \varrho \Delta H_m \frac{ds}{dt} = \varrho \Delta H_m v_n \quad (2.7)$$

where ΔH_m is the amount of the latent heat, s is the location of the interface, and v_n is the normal velocity of the interface. In general, the solution of the phase change problem requires the simultaneous solution of all three aforementioned equations (2.5), (2.6), and (2.7). This is, for example, the case of the front tracking method, which is discussed in detail in a paper [68] in Section 2.5. However, the widely used enthalpy method and the effective heat capacity method overcome this issue and they reduce Eqs. (2.5)–(2.7) into a single governing equation as explained below.

ENTHALPY METHOD. The method is based on the use of the enthalpy—a thermodynamically defined function, which allows for the inclusion of both the sensible heat and the heat of fusion. The enthalpy H can be defined [137] as a function of the temperature T according to

$$H(T) = \int_{T_{\text{ref}}}^T \left(\varrho c_p - \varrho \Delta H_m \frac{\partial f_s}{\partial \vartheta} \right) d\vartheta \quad (2.8)$$

where ϱ is the density, c_p is the heat capacity, f_s is the solid fraction, and T_{ref} is a reference temperature. The substitution of Eq. (2.8) to the heat transfer equations (2.5) and (2.6) requires no more

consideration of Eq.(2.7) as the evolution of the heat of fusion is now incorporated in the enthalpy and in Eq. (2.8), and the governing enthalpy-formulated heat transfer equation [137] reads

$$\frac{\partial H}{\partial t} = \nabla \cdot (k\nabla T). \quad (2.9)$$

As can be observed there are no subscripts s and ℓ in Eq. (2.9). It means that Eq. (2.9) serves as the governing equation for both the phases, which are not explicitly separated. However, it is worth pointing out that the thermal conductivity k is in fact a function of the local temperature.

EFFECTIVE HEAT CAPACITY METHOD. Similarly as in case of the enthalpy method, the effective heat capacity method uses the heat capacity c_p , often referred to as the specific heat, for the inclusion of the latent heat. The effective heat capacity then accounts for both the sensible heat and the heat of fusion, typically as a function of the local temperature $c_{\text{eff}}(T)$. The effective heat capacity is related to the enthalpy as [133]

$$c_{\text{eff}} = \frac{1}{\rho} \frac{\partial H}{\partial T} = c_p - \Delta H_m \frac{\partial f_s}{\partial T}. \quad (2.10)$$

Further, as in case of the enthalpy method, the Stefan condition given in Eq. (2.7) is transformed into Eq. (2.10) and the substitution of Eq. (2.10) into the heat transfer equations (2.5) and (2.6) leads to the governing effective-heat-capacity-formulated heat transfer equation

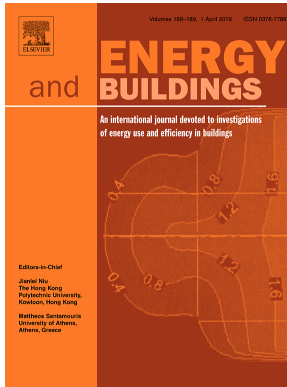
$$\rho c_{\text{eff}} \frac{\partial T}{\partial t} = \nabla \cdot (k\nabla T). \quad (2.11)$$

Similarly as in case of the enthalpy method, Eq. (2.11) accounts for both the phases, and ρ , c_{eff} , and k are functions of the local temperature.

The enthalpy method and the effective heat capacity method with their governing equations (2.9) and (2.11), respectively, represent the most frequently adopted methods for computer simulations of LHTES systems with PCMs. The reason for this is that both these methods are relatively simple, straightforwardly implementable and computationally efficient. It is reported that the enthalpy method offers a slightly better stability and a higher accuracy than in case of the effective heat capacity method, and the enthalpy approach does not require the use of additional techniques for the fulfilment of the energy conservation since the enthalpy method is known to be self-conservative [82, 124]. On the other hand, the enthalpy method requires a two-stage and usually less efficient solution as Eq. (2.9) contains two unknown variables H and T , which need to be sequentially solved in each time iteration. In case of the effective heat capacity method, the temperature T in Eq. (2.11) is the only unknown variable, which makes the method more straightforward.

2.5 AUTHOR'S CONTRIBUTION TO THE DEVELOPMENT OF COMPUTER MODELLING AND UTILISATION OF SYSTEMS FOR LATENT HEAT THERMAL ENERGY STORAGE

Six journal papers co-authored by the author of the thesis and published in peer-review journals having the impact factor in Web of Science are included in the thesis in order to demonstrate the author's contribution to the field of computer modelling and utilisation of systems for latent heat thermal energy storage. The included journal papers are:



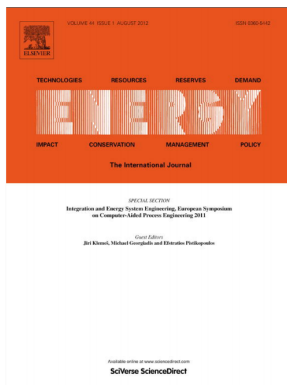
[21] Charvát P, Klimeš L, Ostrý M. 2014. Numerical and experimental investigation of a PCM-based thermal storage unit for solar air systems. *Energy and Buildings* 68: 488–497.

Author's contribution: 45%.

Metrics: $IF_{2014} = 2.88$. $CiteScore_{2014} = 4.21$. Citations: 77 (G Scholar).

Ranking: $2 \times QI$ ($2 \times DI$ as well)^a and Q2 in JCR 2014 WoS.

^aDI = the first decile = top 10% journals

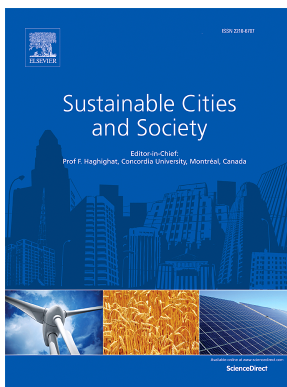


[68] Klimeš L, Mauder T, Charvát P, Štětina J. 2018. Front tracking in modelling of latent heat thermal energy storage: Assessment of accuracy and efficiency, benchmarking and GPU-based acceleration. *Energy* 155: 297–311.

Author's contribution: 70%.

Metrics: $IF_{2017} = 4.97$. $CiteScore_{2017} = 5.60$. Citations: 2 (G Scholar).

Ranking: $2 \times QI$ ($1 \times DI$ as well) in JCR 2017 WoS.



[134] Stritih U, Charvát P, Koželj R, Klimeš L, Osterman E, Ostrý M, Butala V. 2018. PCM thermal energy storage in solar heating of ventilation air—Experimental and numerical investigations. *Sustainable Cities and Society* 37: 104–115.

Author's contribution: 45% (considering authors from the Brno University of Technology only).

Metrics: $IF_{2017} = 3.07$. $CiteScore_{2017} = 3.55$. Citations: 11 (G Scholar).

Ranking: Q1 and $2 \times Q2$ in JCR 2017 WoS.



[67] Klimeš L, Charvát P, Ostrý M. 2019. Thermally activated wall panels with microencapsulated PCM: comparison of 2D and 3D models. *Journal of Building Performance Simulation* 12 (4): 404–419.

Author's contribution: 48%.

Metrics: $IF_{2017} = 2.60$. $CiteScore_{2017} = 2.20$. Citations: 0.

Ranking: Q1 in JCR 2017 WoS.

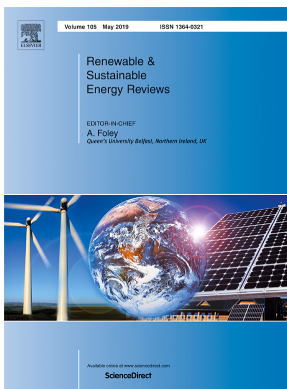


[22] Charvát P, Klimeš L, Zálešák M. 2019. Utilization of an air-PCM heat exchanger in passive cooling of buildings: A simulation study on the energy saving potential in different European climates. *Energies* **12** (6): article 1133.

Author's contribution: 30%.

Metrics: IF₂₀₁₇ = 2.68. CiteScore₂₀₁₇ = 3.15. Citations: 0.

Ranking: Q2 JCR 2017 WoS.



[113] Pospíšil J, Charvát P, Arsenyeva O, Klimeš L, Špiláček M, Klemeš JJ. 2019. Energy demand of liquefaction and regasification of natural gas and the potential of LNG for operative thermal energy storage. *Renewable and Sustainable Energy Reviews* **99**: 1–15.

Author's contribution: 20% (considering authors from the Brno University of Technology only).

Metrics: IF₂₀₁₇ = 9.18. CiteScore₂₀₁₇ = 10.54. Citations: 5 (G Scholar).

Ranking: 2 × Q1 (2 × DI as well) in JCR 2017 WoS.

CHARVÁT ET AL. [21]: NUMERICAL AND EXPERIMENTAL INVESTIGATION OF A PCM-BASED THERMAL STORAGE UNIT FOR SOLAR AIR SYSTEMS

The paper [21] was concerned with the numerical and experimental investigation of a PCM-based thermal storage unit, which was designed for the use in solar air systems. The heat storage unit consisted of 100 aluminium panels (CSM panels) filled with the commercially available PCM Rubitherm RT42. The purpose of the unit was space heating and the unit was designed to operate in two phases. In the charging phase during the day when the solar radiation is available, the hot air (e.g. supplied by a solar collector) is used to charge the PCM: heat is transferred from the air to the PCM, which melts and accumulates heat in the form of the sensible heat as well as of the latent heat of phase change (the heat of fusion). In the discharging phase when heat is needed and solar radiation is no more available (during the evening or the night), the cold air from the ambient environment is used to discharge the PCM in the CSM panels: heat is transferred from the PCM to the cold air, which causes the increase of its temperature. As a consequence of heat withdrawal from the CSM panels, the PCM solidifies and releases the heat of fusion accumulated in the charging period. The heated air is then delivered to the room for its space heating.

Both numerical and experimental investigations were performed and discussed in [21]. As for experimental investigations, the unit shown in Figure 2.17 was built and tested in a lab. As a source of heat, an electric heater coupled with the fan was used. Experimental data acquired in the unit testing were consequently used for the validation of the computer model. As for the computer

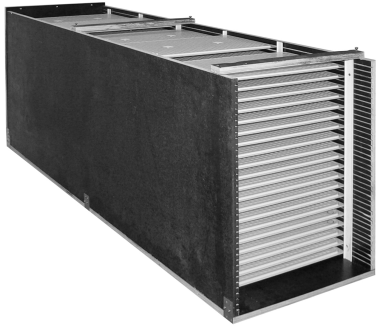


Figure 2.17: Photograph of the experimental unit without front and top walls revealing CSM panels [21]

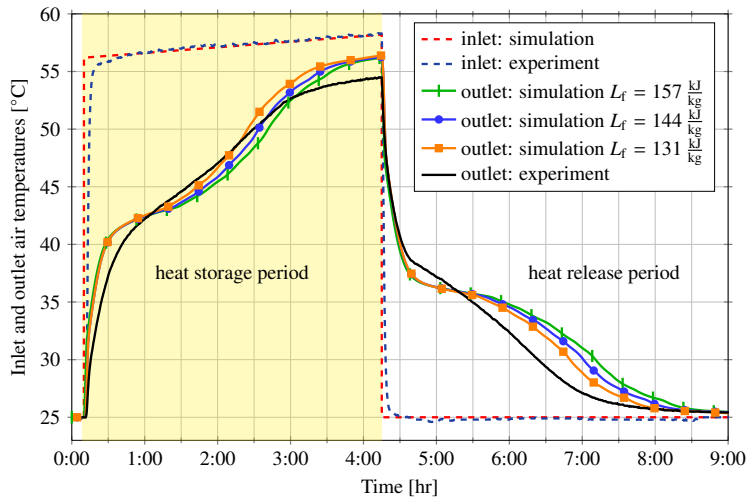


Figure 2.18: Comparison of experimental and simulation results [21]

model of the heat storage unit, a standalone model was first developed in MATLAB. After its testing, debugging, and validation, the model was re-implemented to the form of a so-called TRNSYS Type (a DLL library), which is suitable for the use in the TRNSYS simulation tool. The computer model was designed as a quasi 2D model (1D heat transfer was solved in the direction of the thickness of the CSM panels) and the effective heat capacity method was adopted for modelling of the phase change. The model was validated by means of acquired experimental data as shown in Figure 2.18. Once the model was validated, some case studies were performed in order to investigate operational parameters, setup, and thermal behaviour of the heat storage unit. Figure 2.19 demonstrates how the model can be used for optimal design of the thermal storage unit. The curves in Figure 2.19 show the outlet air temperature at distinct locations in the unit in the charging period. This gives information how the melting of the PCM progresses in time and how efficiently individual CSM panels are utilised for heat storage.

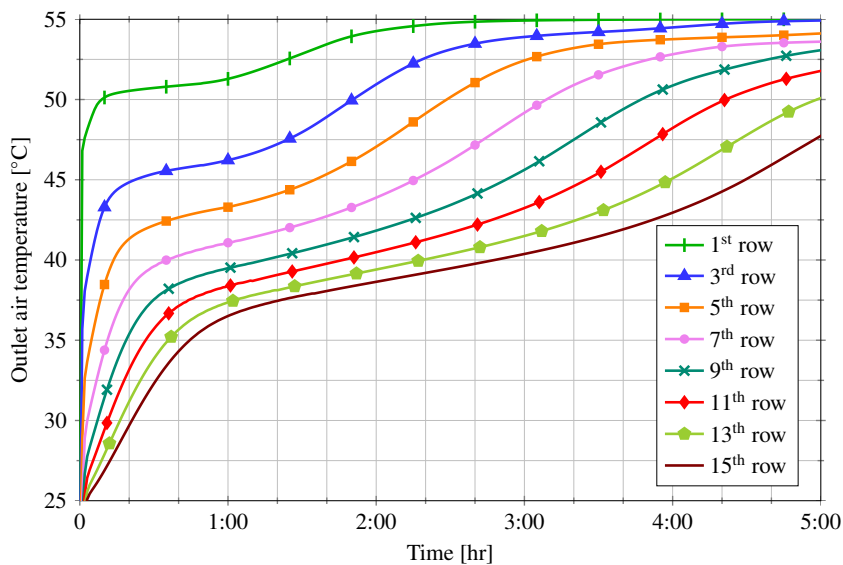


Figure 2.19: Use of the computer model for parametric investigation: outlet air temperature at different position in the unit [21]

The study [68] was aimed at the assessment of computer methods for phase change modelling applicable for latent heat thermal energy storage applications. Two kinds of methods were taken into consideration: interface capturing methods and interface tracking methods. As for methods based on interface capturing, the well known enthalpy method, the apparent heat capacity (frequently also referred to as the effective heat capacity method), and the temperature recovery method were incorporated into the study. Those interface capturing methods have dominantly been applied in computational heat transfer with phase changes as these methods are relatively simple and straightforward when considering their underlying principle and implementation. Such methods, however, primarily aim at the determination of the temperature distribution, and the location of the interface separating the phases is somehow determined from the temperature distribution, usually with the use of linear interpolation between nodes identified as nodes having distinct phases. On the other hand, interface tracking methods are proposed for the opposite strategy: first the interface location (the so-called front) and phase domains are accurately determined from the physical balance on the front, and the temperature distribution is consequently determined in the second step. The front tracking methods are reported to have a better accuracy than in case of the interface capturing methods.

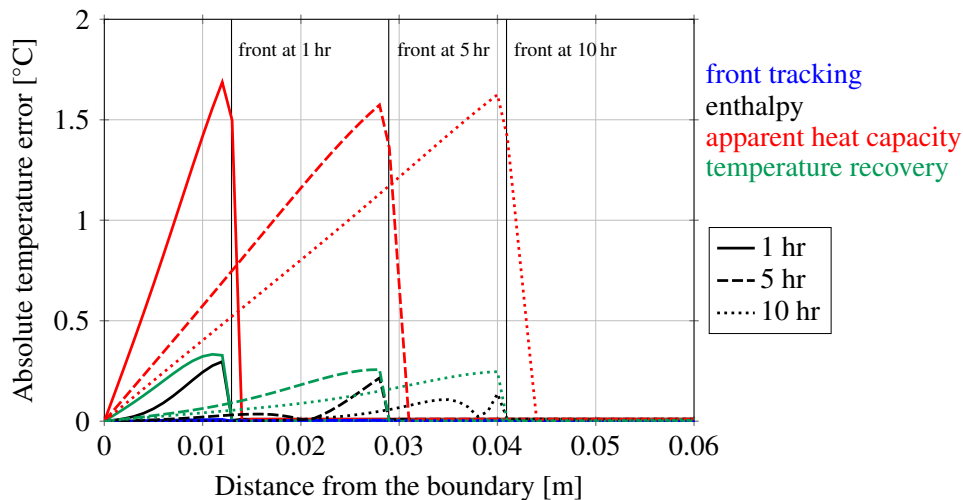


Figure 2.20: Assessment of the computational accuracy: absolute temperature errors as functions of the spatial distribution for the one-phase Stefan melting problem [68]

In the paper [68], the comparison of the interface capturing methods with the front tracking method was performed. The assessment was carried out in terms of the computational accuracy and efficiency. The two Stefan two-phase problems in the semi-infinite 1D domains were used for the assessment of accuracy as analytic (exact) solutions for these problems exist. Figure 2.20 and Figure 2.21 show the comparison of the computational accuracy in terms of the temperature error in dependence on the spatial coordinate, and in terms of the front location error in dependence on time, respectively. A more detailed analysis of the results revealed that the front tracking method allows for a superior computational accuracy when compared to other interface capturing methods

considered in the study: computational errors of the front tracking method were about two orders of the magnitude smaller than for other methods. However, the higher computational accuracy of the front tracking method is paid by its lower computational efficiency—the front tracking method was the slowest one when compared with interface capturing methods. Moreover, the implementation and coding of the front tracking method are substantially more challenging than in case of interface capturing methods. Due to the lower computational efficiency, the GPU-acceleration of the front tracking method, which was previously successfully proposed and applied by the author in [71], was utilised to enhance the computational performance. It was found that the GPU-acceleration allows for a significant speed-up of the front tracking method, which attains up to 27 (i.e. the GPU version is 27-times faster than the identical CPU version of the algorithm) in dependence on the computational grid density.

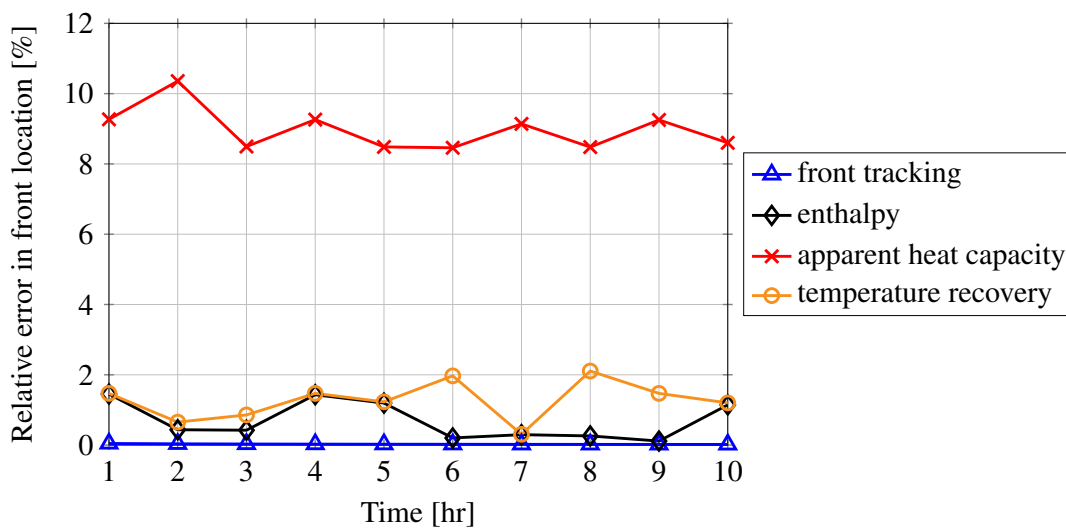


Figure 2.21: Assessment of the computational accuracy: relative error in the front location as the function of time for the one-phase Stefan melting problem [68]

STRITIH ET AL. [134]: PCM THERMAL ENERGY STORAGE IN SOLAR HEATING OF VENTILATION AIR—EXPERIMENTAL AND NUMERICAL INVESTIGATIONS

The paper [134] was aimed at the investigation of the latent heat thermal storage unit for solar heating of ventilation air. The article represents a result of the research cooperation between research teams from the Brno University of Technology and from the University of Ljubljana in Slovenia, which was established in Annex 31 ”Energy Storage with Energy Efficient Buildings and Districts: Optimisation and Automation” of the International Energy Agency. The study involved the investigation of the air-PCM storage unit with a similar design to the unit presented in [21]. Experiments as well as computer simulations were performed to assess the applicability of the air-PCM storage unit. The unit consisted of CSM panels filled with the PCM Rubitherm RT 22 HC and the unit was coupled with the solar collector.

Figure 2.22 shows the solar collector mounted on the exterior wall of a building (left) and the heat storage unit consisting of CSM panels filled with the PCM (right). The system was installed at the Faculty of Mechanical Engineering, University of Ljubljana in Ljubljana, Slovenia, where exper-

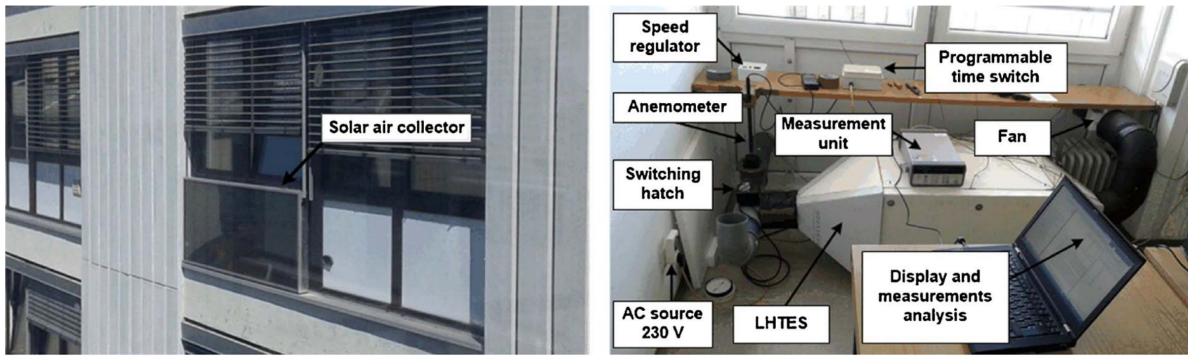


Figure 2.22: Experimental setup of the system with the solar air collector (left) and the heat storage unit (right) [134]

Experimental investigations took place. The computer model of the unit was developed by the research team at the Brno University of Technology. As the starting point, the model previously developed and tested in [21] was used. The model was further modified according to parameters of the storage unit located in Slovenia. Similarly as in [21], the quasi-2D structure of the model was proposed and implemented as a Type for the TRNSYS simulation tool. The effective heat capacity method was used for phase change modelling with the control volume method for the discretization of the governing heat transfer equation. The simulation model of the entire system consisting of the storage unit, the solar air collector, and other components was created in TRNSYS.

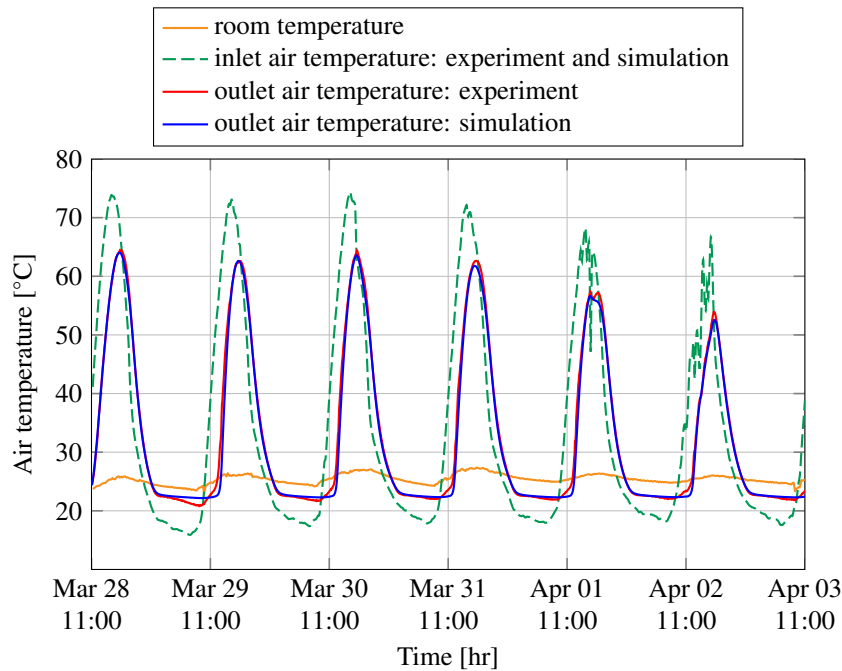


Figure 2.23: Comparison of the outlet air temperature: simulation vs. experiment [134]

The computer model was validated with the use of experimentally gained data by the team from Ljubljana. Figures 2.23 and 2.24 demonstrate that the agreement between the computer model and experimentally gained data was very good. Once the computer model was validated, the annual analysis of the performance of the heat storage unit was performed. The study was carried out for the heating season in Ljubljana from October to April. Weather data for a reference year available in the

TRNSYS tool and provided by Meteonorm were used. The analysis identified that the highest coverage ratio of ventilation heat loss was 92% and 89% in April and in October, respectively, which are the months when the transition of seasons occurs. When considering the system with and without LHTES, the average coverage ratio for the heating season was 67% and 53%, respectively. Further, the economic analysis was performed to evaluate the annual cost savings. It was found that in case operating costs for energy use were the only costs taken into consideration, the system with LHTES allowed for 68% annual savings when compared to district heating.

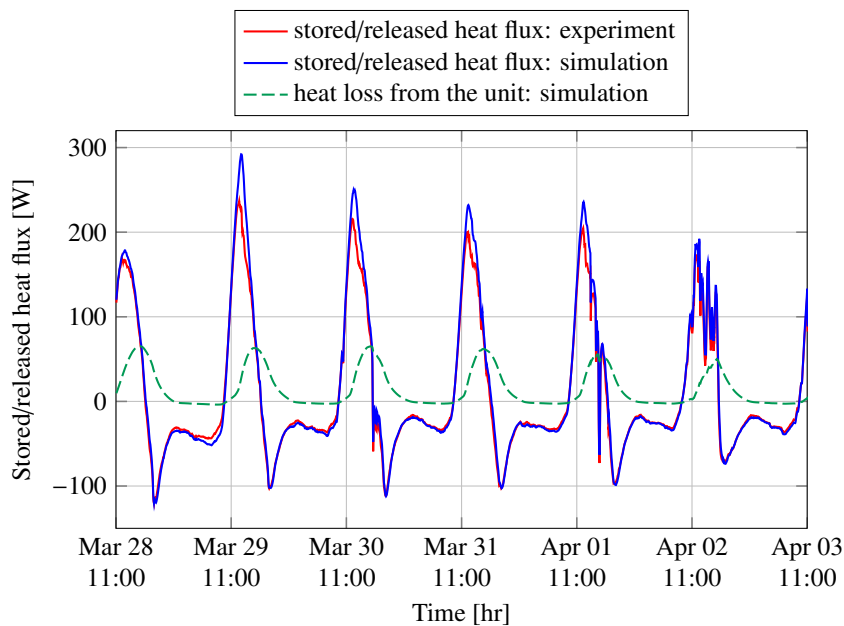


Figure 2.24: Comparison of the stored/released heat flux: simulation vs. experiment [134]

KLIMEŠ ET AL. [67]: THERMALLY ACTIVATED WALL PANELS WITH MICROENCAPSULATED PCM: COMPARISON OF 2D AND 3D MODELS

The article [67] was concerned with computer modelling of a thermally activated building system (TABS) with a PCM. The considered TABS was a wall panel, which contained a plaster with a microencapsulated PCM. In the plaster, plastic tubes were embedded to allow the heat transfer fluid (water in the considered case) to flow through the tubes and thermally interact with the plaster, see Figure 2.25. The thickness of the plaster was 15 mm and the embedded tubes made of polyethylene had the inner diameter of 2.25 mm with the pitch of 15 mm between the tubes. Two modifications of the wall panels were investigated: the panel with straight tubes having the supply pipe at the top of the panel and the return pipe at the bottom of the panel, and the panel with U-shaped tubes having both the supply and return pipes at the top of the panel as shown in Figure 2.26.

The main aim of the paper [67] was to create a fast and accurate model of the TABS for the use in the TRNSYS simulation tool. The motivation was that though some off-the-self commercial packages are available for the coupled heat transfer and fluid flow problem involved in the considered TABS operation, due to huge computational costs those computational tools are suitable for simulations of only one wall panel rather than for overall simulations and analyses of rooms and

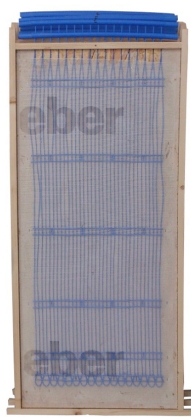


Figure 2.25: Photograph of the experimental TABS. Left: the TABS before the application of the plaster, right: the complete TABS [67]

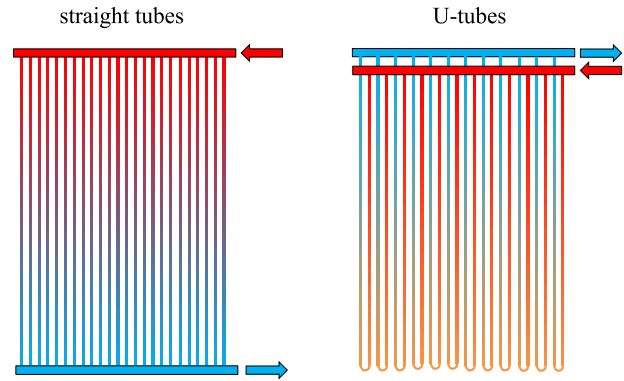


Figure 2.26: Two considered configurations of the TABS: straight and U-shaped tubes [67]

buildings employing a number of the TABS. Hence, a computationally efficient model for the considered TABS was proposed, developed, and tested. Its functionality in terms of accuracy and computational efficiency was assessed by means of the comparison with the model of the TABS created in the commercial FEM-based simulation software COMSOL Multiphysics. The developed model for TRNSYS was based on the quasi-2D approach, while the model in COMSOL was fully 3D. The model for TRNSYS was implemented in C++ and it used the control volume method for the spatial discretization. The effective heat capacity method was employed for the phase change modelling. The non-isothermal fluid flow in the tubes was solved by means of balance-based interactions between the 1D heat transfer sub-models for the plaster with the PCM and the sub-model for the fluid flow in the embedded pipes. On the other hand, the model in COMSOL considered 3D heat transfer with the effective heat capacity and the non-isothermal laminar fluid flow, which were coupled together by means of the multiphysical interface.

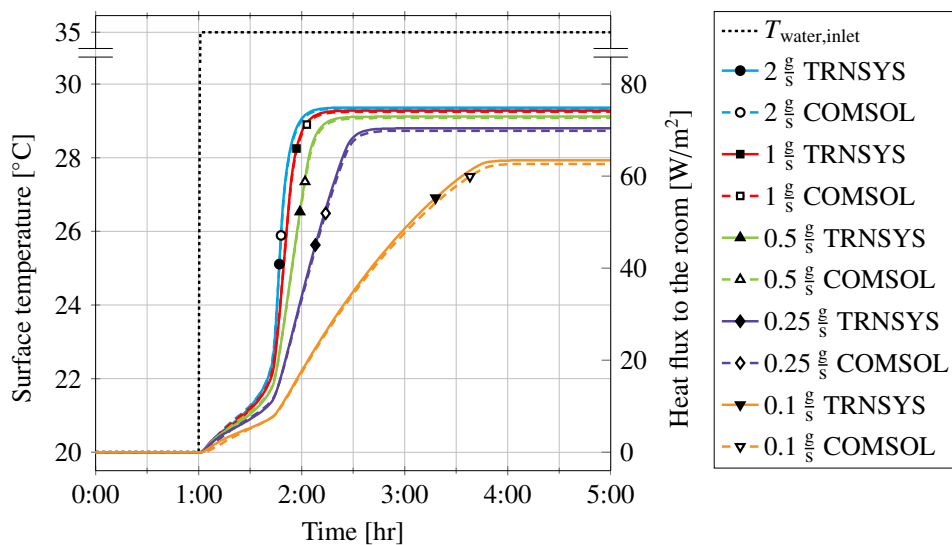


Figure 2.27: Surface temperature of the TABS with straight tubes: a very good agreement between the quasi-2D model for TRNSYS and the 3D model in COMSOL [67]

It was found that the model for TRNSYS is much faster than the model created in COMSOL,

which makes it applicable for TRNSYS simulations within large time scales. As for the computational accuracy, a very good agreement between the models was identified. In case of panels with the straight tubes, a very good accuracy was attained for all the considered flow rates of the heat transfer fluid. In case of panels with the U-shaped tubes, some discrepancies were observed for flow rates below 0.5 ml/s. However, it needs to be emphasised that such low flow rates are rather out of the range in practical applications. Figure 2.27 shows simulation results for the mean surface temperature of the TABS with a very good agreement between the quasi-2D model for TRNSYS and the 3D models in COMSOL. Figure 2.28 presents the same quantity for the case of the U-shaped tubes.

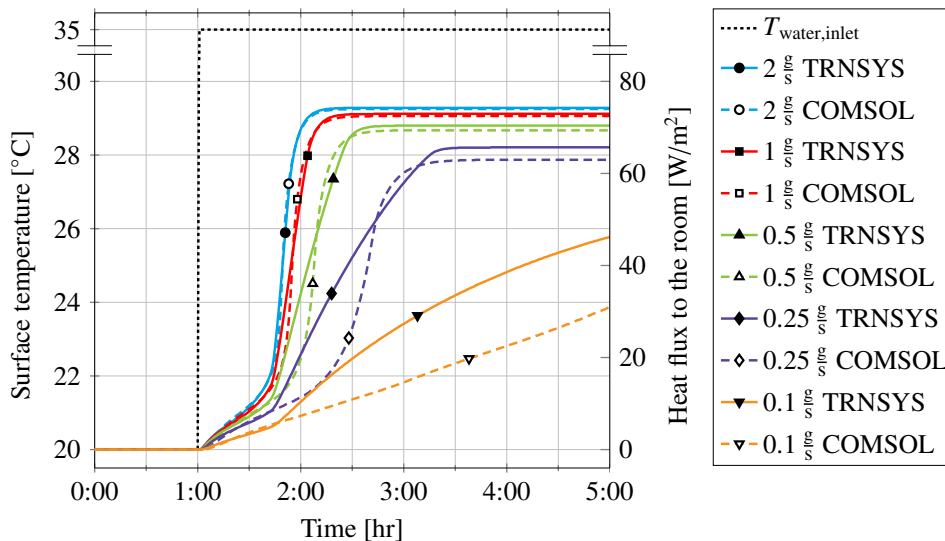


Figure 2.28: Surface temperature of the TABS with U-shaped tubes: a good agreement between the quasi-2D model for TRNSYS and the 3D model in COMSOL for flow rates above 0.5 ml/s with some discrepancies for lower flow rates [67]

CHARVÁT ET AL. [22]: UTILIZATION OF AN AIR-PCM HEAT EXCHANGER IN PASSIVE COOLING OF BUILDINGS: A SIMULATION STUDY ON THE ENERGY SAVING POTENTIAL IN DIFFERENT EUROPEAN CLIMATES

In the paper [22], the energy saving potential for passive cooling of buildings by means of the air-PCM cold storage unit previously studied experimentally as well as numerically in [21, 134] was investigated by means of computer simulations. During the daytime, the cold storage unit was utilised to cool down the outdoor air supplied to a building. On the other hand, heat stored in the PCM during the day was discharged (and thus cold was accumulated) to the outdoor environment during the night. One hundred CSM panels filled with the PCM were assumed as the cold storage medium in the storage unit with the PCM having the thermal storage capacity of 200 kJ/kg in the form of the heat of fusion in the temperature range of 4 K. The analysis was carried for sixteen cities in the Europe in the period between May 1 and September 30, and six mean phase change temperatures in the temperature range between 16 °C and 26 °C were taken into consideration. The temperature threshold of 20 °C was used as a switch for the utilisation and discharging of cold stored in the unit as shown in Figure 2.29. One of aims of the study was to determine the optimal mean phase change temperature for each location, ranging from Athens as the southernmost considered city to Helsinki as the northernmost considered city.

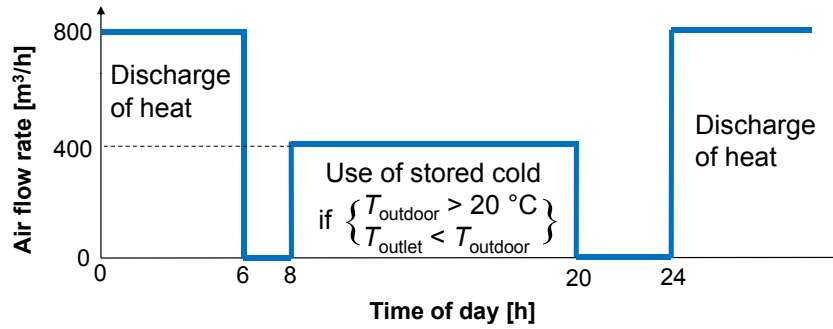


Figure 2.29: Operation of the cold storage unit: the temperature threshold and the charging and discharging flow rates [22]

The computer model of the air-PCM thermal energy storage unit previously developed by the authors [21] was used in the study. However, instead of the implementation for TRNSYS used in [21, 134], the model was coded in MATLAB. The results showed that the dependence of the energy saving potential on the location of the city was not as significant as could be expected. In case of Athens, approximately a 30% higher energy saving potential was identified in comparison to Helsinki. Madrid was identified as the city where the maximum energy saving potential of about 190 kWh can be obtained in the investigated period for the mean phase change temperature of 24 °C. The average value of the utilisation rate of the heat of fusion, which was defined as the ratio between the energy saving potential in a 24-hour cold storage cycle and the heat of fusion of the PCM accommodated in the storage unit, did not exceed 50% in any configuration, but in about 10 days the value of the utilisation rate of the heat of fusion exceeded 90% as shown in Figure 2.30. Further, the economic assessment of the use of the cold storage unit for passive cooling was performed. However, considering the price of 10 Euro per one CSM panel, the simple payback time of the cold storage unit would be well beyond the expected lifespan of the cold storage unit. Its economic viability is therefore crucially dependent on the price of the PCM: a significant reduction of its price would make PCM-based devices economically viable.

POSPÍŠIL ET AL. [113]: ENERGY DEMAND OF LIQUEFACTION AND REGASIFICATION OF NATURAL GAS AND THE POTENTIAL OF LNG FOR OPERATIVE THERMAL ENERGY STORAGE

The paper [113] was aimed at the assessment of energy demands of liquefaction and regasification processes of the natural gas (NG) and at the evaluation of the potential of the liquefied natural gas (LNG) for operative thermal energy storage. The paper is a result of the international cooperation between research teams from the Brno University of Technology and from the University of Paderborn in Germany.

In the last 30 years, the world trade volume of LNG has progressively been increasing year by year. A direct transport of the NG in the gaseous form suffers from some disadvantages (e.g. fixed network of pipelines is needed and much larger volumes of NG per 1 kg must be transferred than in case of the LNG), while the transport of NG in the liquid form as the LNG allows for higher flexibility and efficiency. That is the reason why the transport of LNG is a dominant way for the distribution of the NG over the world. The LNG process is fairly energy demanding and it consists of the liquefaction of the NG, transportation and storage of the LNG, and the regasification of the LNG into the NG.

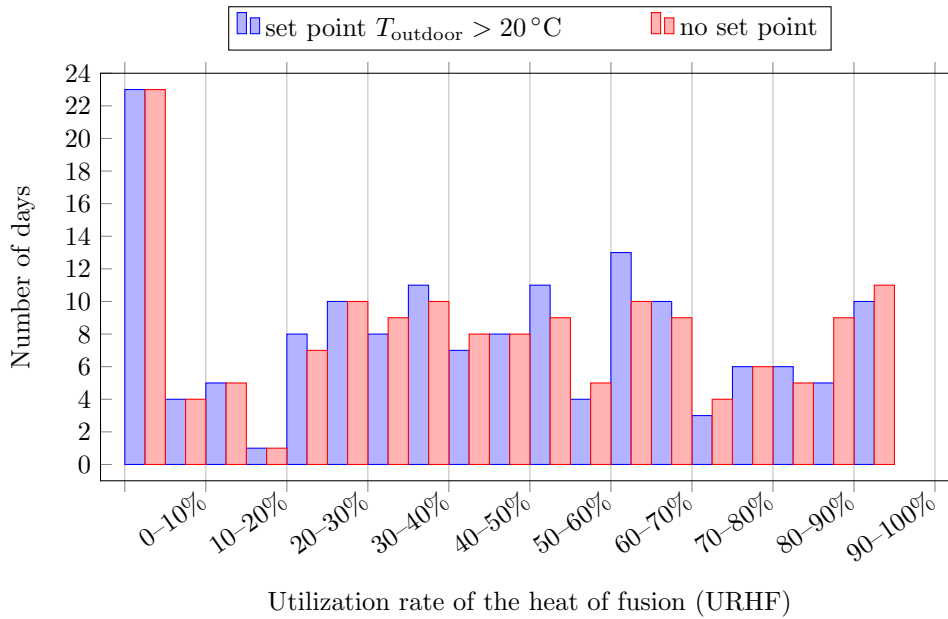


Figure 2.30: Utilisation rate of the heat of fusion for Madrid and the mean phase change temperature of 24°C , which maximised the overall energy saving potential [22]

Methods available for these three processes were analysed and assessed in the paper [113]. Figure 2.31 shows the energy flows as well as the three main processes with most frequent technologies applied in the LNG chain.

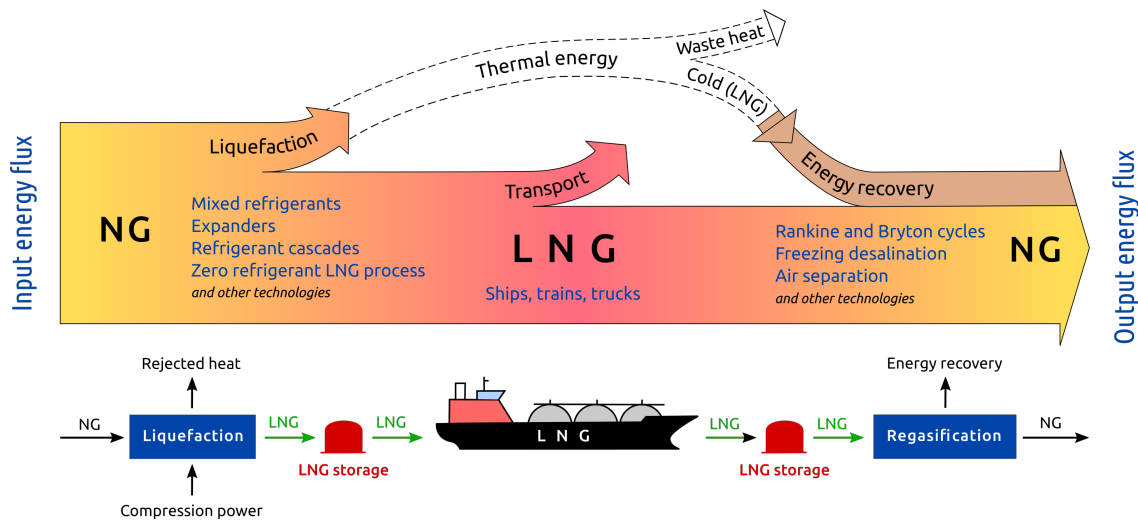


Figure 2.31: Process technologies and energy flows involved in the LNG process [113]

The study was particularly concerned with the assessment of the chain of energy transformations involved in the LNG process. Existing technologies and approaches were thoroughly reviewed and analysed. Two views to the process were evaluated: the utilisation of the LNG for direct thermal energy storage of cold, and the utilisation of the LNG for indirect storage of power. The results showed that the overall efficiency of the use of LNG for energy storage is significantly dependent on particular technologies involved in the chain of LNG process as well as on the total capacity considered in a particular case. If energy-efficient liquefaction and regasification technologies are

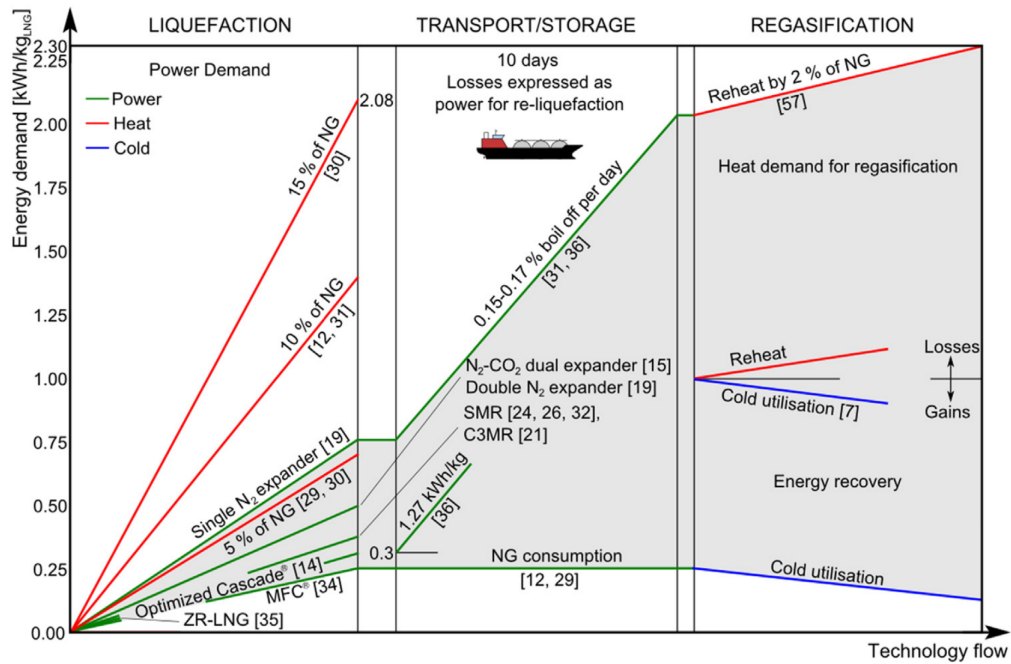
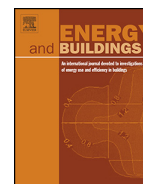


Figure 2.32: Analysis of energy demands in the LNG process [113]

employed, then it is possible to use the LNG as an energy storage medium in an effective way.

Figure 2.32 shows the diagram with the graphical representation of energy demands (grey area in the diagram) and gains in the LNG process. The upper piece-wise line boundary of the grey area represents the most energy demanding LNG process with about 2.3 kWh/kg_{LNG}, which corresponds to about 20% consumption of LNG. On the other hand, the lower piece-wise line boundary of the grey area indicates the LNG technology, which is the most effective in terms of minimum consumption of energy, as well as of maximum regeneration of energy from the cold stored in the LNG. This most effective LNG technology is represented by the MFC (Mixed Fluid Cascade) liquefaction process with the energy demand of about 0.25 kWh/kg_{LNG}, the transportation of the LNG without the need for the LNG re-liquefaction, and the energy recovery from the cold and the power generation in expanders and turbines during the regasification process.



Numerical and experimental investigation of a PCM-based thermal storage unit for solar air systems



Pavel Charvát^{a,*}, Lubomír Klimeš^a, Milan Ostrý^b

^a Brno University of Technology, Faculty of Mechanical Engineering, Energy Institute, Technická 2896/2, 616 69 Brno, Czech Republic

^b Brno University of Technology, Faculty of Civil Engineering, Institute of Building Structures, Veveří 331/95, 602 00 Brno, Czech Republic

ARTICLE INFO

Article history:

Received 6 April 2013

Received in revised form 4 October 2013

Accepted 9 October 2013

Keywords:

Thermal storage

Heat storage unit

Latent heat

Phase change materials

Solar air systems

ABSTRACT

A general problem of most solar thermal systems is the need for thermal storage in order to balance supply and demand of heat over a certain period of time. A possibility to employ latent heat of fusion in phase change materials (PCMs) for thermal energy storage in air-based solar thermal systems was investigated using laboratory experiments and numerical simulations. A heat storage unit containing 100 aluminium panels filled with a paraffin-based PCM was used in the investigations. The experiments were carried out in a lab environment with an electric air heater as a heat source. A numerical model of the unit was developed and implemented as a type in the TRNSYS 17 simulation tool. The results of the simulations with the developed model show a good agreement with experimental results. Subsequently, the model was used for a parametric study analysing the influence of certain parameters. The performed investigations showed a potential of the use of latent heat thermal storage in air-based thermal systems with a narrow temperature operation range.

© 2013 Elsevier B.V. All rights reserved.

1. Introduction

Solar air systems, though not as common as water-based solar systems, can be used in a number of applications. One of the most common applications is space heating or ventilation air heating [1]. Drying of various products is another area in which solar air systems can be used [2]. Solar heated air can also be used for regeneration of desiccant wheels in air-conditioning systems [3]. However, many of these applications require thermal energy storage in order to operate effectively [4]. Water can easily be used as a heat storage medium in water-based solar energy systems but it is usually less practical for air-based systems. Building structures can be employed as thermal storage mass in some solar applications utilizing air as a heat carrier but this approach is not applicable in all situations. The Tromb wall [5] is one of the examples of thermal storage integrated with building structures. Another possibility is the use of packed beds where solid materials (usually pebbles) are used for sensible heat storage [6]. Though rather simple to use, the packed beds containing sensible heat storage materials have certain disadvantages; they use a lot of space, they are difficult to clean and the thermal storage density is relatively small. With regard to the thermal storage density and operation

temperature range, latent heat thermal storage, which makes use of phase change of a heat storage material, offers certain advantages over sensible heat storage for many technical applications [7].

The materials used for latent heat thermal storage are generally referred to as phase change materials (PCMs). The phase change of a material provides a rather high thermal storage capacity and also energy storage density in a relatively narrow temperature interval around the phase change temperature. Though both the solid–liquid and the liquid–gas phase changes can be employed for latent heat storage, it is the solid–liquid phase change that is used in almost all the latent heat storage systems [8,9]. A large number of papers dealing with the phase change materials and their use in different technical applications, e.g. cold thermal energy storage [10], building integrated thermal storage [11], or air conditioning [12] have been published in recent years.

Various ways of integration of PCM-based heat storage in the air-based solar thermal systems have been reported. One of the simplest ways is the integration of the PCMs directly with the solar air collector [13]. Tyagi et al. [1] presented a review of a variety of solar air heating systems with and without thermal energy storage. Thermal energy storage in solar air systems is mostly intended to provide the heat storage capacity for hours or days. Since the volumetric thermal capacity of water is approximately 3500-times higher than that of air, it makes much more sense to use water-based solar systems when long-term (e.g. seasonal) thermal storage is needed and to employ water–air heat exchangers for air heating.

* Corresponding author. Tel.: +420 541143245.

E-mail addresses: charvat@fme.vutbr.cz (P. Charvát), klimes@fme.vutbr.cz (L. Klimeš), ostry.m@fce.vutbr.cz (M. Ostrý).

Nomenclature

c	specific heat at constant pressure ($\text{kJ kg}^{-1} \text{K}^{-1}$)
c_{eff}	effective heat capacity ($\text{kJ kg}^{-1} \text{K}^{-1}$)
f_s	solid fraction (-)
h	heat transfer coefficient ($\text{W m}^{-2} \text{K}^{-1}$)
H	enthalpy (kJ kg^{-1})
k	thermal conductivity ($\text{W m}^{-1} \text{K}^{-1}$)
L_f	latent heat of fusion (kJ kg^{-1})
\dot{m}	mass flow rate (kg s^{-1})
q	heat storage/release rate (W)
\dot{q}	convective heat flux (W m^{-2})
Q	internal source of heat (W m^{-3})
R	thermal resistance of the unit walls ($\text{m}^2 \text{K W}^{-1}$)
Re	Reynolds number
ρ	density (kg m^{-3})
τ	time (s)
t	temperature ($^{\circ}\text{C}$)
T	temperature (K)
x	spatial coordinate (m)

Abbreviations

CSM	compact storage module
PCM	phase change material

Subscripts

a	air
eff	effective
in	inlet
l	liquid
m	mean
out	outlet
s	solid
∞	free stream condition

Superscripts

c	congealing
m	melting

Several studies, both experimental and numerical, were carried out into latent heat thermal storage with air as a heat carrier. Hed and Bellander [14] reported mathematical modelling of a PCM-air heat exchanger for thermal storage in case of night cooling. The exchanger contained six horizontal layers of PCM in aluminium pouches with 8 mm air gaps between the layers. The length of the layers in the direction of airflow was 0.48 m. The air velocity of 4 m s^{-1} was considered in all air gaps. The model was implemented as a single node finite difference model. The heat loss to the ambient environment was neglected. The authors used the model to investigate the influence of the surface roughness on heat transfer in the heat storage unit, but the surface roughness is not described in detail what makes the results quite difficult to interpret. The authors concluded that the rough surface can significantly intensify heat transfer between the fluid and the heat storage material, but this intensification is subsequently paid for by a higher fan power. The increase of the fan energy consumption is not quantified in the paper.

Modelling and experimental validation of a similar arrangement of a PCM-air heat exchanger for free cooling applications was presented by Lopez et al. [15]. The authors considered an exchanger consisting of parallel horizontal PCM slabs with air gaps between the slabs. The simulation model was created in MATLAB with the use of control volume method. The same air flow rates were considered in all air gaps and thus only a half of the slab thickness with

a half of the air gap was modelled. The heat loss to the surroundings was neglected. The authors reported a good agreement between the results from the developed numerical model and the experimental data from the laboratory experiment. However, the phase change of the material (indicated by inflection points) is absent in the temperature curves during the heat storage and heat release periods. The temperature curves without inflection points are typical for sensible heat storage materials.

A quite extensive study of a PCM-air heat exchanger containing aluminium containers filled with a PCM (compact storage modules – CSM) was presented by Dolado et al. [16–18]. The authors studied a PCM-air exchanger in which the CSM panels were positioned vertically and the direction of air flow was also vertical with air supply at the top and air return at the bottom of the unit. The paraffin-based PCM RT27 was used in the investigations. The total weight of the PCM in the unit was 135 kg. Both empirical [16] and numerical [17] models of the investigated heat storage unit were developed. The numerical model of the PCM layer was developed with the use of finite difference method as a one-dimensional implicit formulation. An influence of thermophysical properties of the PCM as well as other parameters such as air flow rate, surface rugosity and thermal conductivity of the encapsulation material were numerically investigated with the developed model.

Halawa and Saman [19] reported the thermal performance analysis of a phase change thermal storage unit for space heating. The PCM used in the study was calcium chloride hexahydrate (referred to as PCM29 in the paper) with the melting temperature of 28°C . The PCM-air heat exchanger consisted of parallel slabs in a rectangular duct with air passing between the slabs. The authors analysed the influence of various parameters such as the air flow rate, the PCM slab thickness or the air gap on the performance of the unit. The adiabatic walls were considered for the unit but such an assumption is reasonable for a parametric study in which the influence of various design and operation parameters is investigated. However, the melting temperature of 28°C seems to be relatively low for space heating application. Though the parallel PCM slabs with the air channels between them is the most often considered configuration of a PCM-air heat exchanger, some other designs are also possible. Dubovsky et al. [20] presented an analytical model of a shell-and-tube PCM-air heat exchanger where a PCM was in the tubes and the air flowed inside the shell. According to Agyenim et al. [21], the shell-and-tube exchangers represent the most frequently studied case by the number of published papers, however, most of these cases are water-based systems.

As pointed out above, many of the models neglect the heat exchange between the thermal storage unit and the ambient environment [14,19]. Such simplification can be justified for thermal storage in passive cooling applications where the temperature difference between the PCM and the ambient air is rather small (usually less than 10 K) and the heat storage cycles are relatively short. In case of thermal storage for space heating, the temperature difference between the PCM and the ambient air can exceed 30 K, resulting in a non-negligible heat loss over a certain period of time. Another assumption often used in modelling of the storage units with PCM slabs is the same air flow rate in all air channels. This flow pattern can be achieved in laboratory experiments but it is less likely in case of the thermal storage units in actual building energy systems.

The aim of the study presented in this paper was to develop and validate a simulation model for the heat storage units comprising CSM panels filled with PCMs. The simulation model allows to take into account the distribution of air flow rates in different air channels as well as the heat exchange with the ambient environment. The model was used for a parametric study analysing the influence of certain parameters.

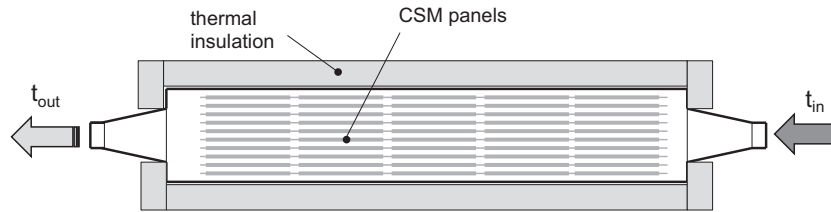


Fig. 1. Schematic of investigated heat storage unit.

2. Heat storage unit

The investigations were performed for a lab-scale model of a day-cycle thermal storage unit. On certain days, especially in spring and autumn, space heating or ventilation air heating may not be needed during the daytime when the outdoor temperature is relatively high and solar radiation is available but that need usually arises after the sunset. Also, some residential buildings do not need to be ventilated or heated to the comfort level during the day because occupants are not at home. These are the situations where a day-cycle thermal storage unit can be used in air-based solar systems. Solar heat can be stored in the heat storage unit during the day when the heat supply exceeds the heat demand and it can be released when otherwise. For that purpose the latent heat of phase change can favourably be utilized. The main advantage of thermal storage with the PCMs is the amount of heat that can be stored in a small temperature interval around the melting temperature. That amount of heat is generally larger than in the case of sensible heat storage operating in the same temperature range.

There is a number of both organic and inorganic PCMs that can be used for thermal storage in solar air heating systems. A paraffin-based PCM was selected for the presented study because paraffin is one of the most common organic PCMs. The advantage of paraffin-based PCMs is their availability with a wide range of melting temperatures. The PCM with the melting temperature of around 40 °C was chosen in this study with regard to the air temperature at the outlet of solar air heaters (collectors) and the supply air temperature for warm air heating. The conventional warm-air space heating systems usually use air supply temperature that is 20 K or even 30 K higher than the room temperature. The studied heat storage unit is supposed to be used in spring and autumn when the heat loss of a house is lower than the design heat loss and the air supply temperature can be lower to cover the heat loss. At the same time, the solar air heaters need to provide a higher air temperature than the melting temperature of the PCM in the heat storage unit. The efficiency of solar air heaters decreases with increasing temperature of heat transfer fluid; therefore, it makes sense to use PCMs with a melting temperature as low as (practically) possible for solar air space heating.

The CSM panels provide a rather easy and flexible approach to building thermal storage units of a desired thermal storage capacity. The CSM panels can be arranged in various ways in the units. The basic arrangement is a row of parallel CSM panels with an air channel between the two adjacent panels. In order to increase the capacity of the heat storage unit, the CSM panels can be added in all three spatial directions. However, even if the storage unit has the desired thermal capacity that capacity may not be available in operation due to various heat transfer constraints. The simplified energy balance calculations may underestimate problems with heat transfer between the heat transfer fluid and the heat storage materials.

The arrangement of the investigated heat storage unit can be seen in Fig. 1 and the photo of the unit is shown in Fig. 2. The unit contained 100 CSM panels filled with a PCM, see Fig. 3. The internal dimensions of the unit were 0.44 m × 0.62 m × 1.8 m. The CSM

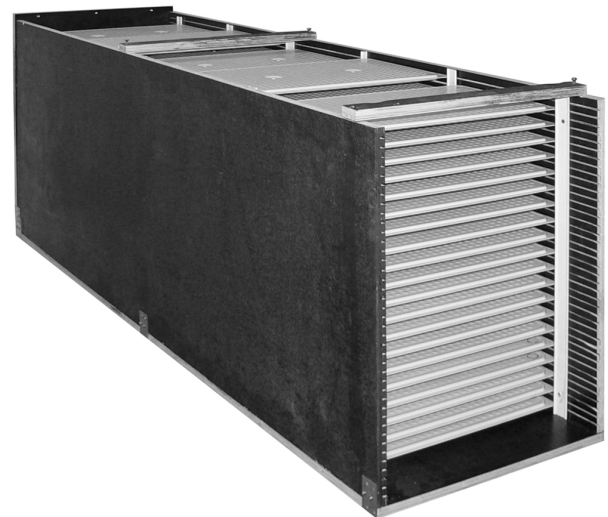


Fig. 2. The heat storage unit without front and top walls revealing CSM panels.

panels had the dimensions of 450 mm × 300 mm × 10 mm and each of them accommodated approximately 700 ml of Rubitherm RT42 paraffin-based PCM. The panels were arranged in 5 rows with 20 panels in each row. The CSM panels were positioned with the vertical distance of 30 mm from each other and there was a 20 mm air gap (air channel) between the panels. The PCM-based heat storage unit is a kind of PCM-air heat exchanger and the surface area density in case of the investigated unit was 53 m² m⁻³.

The properties of RT42 as specified in the product data sheet are summarized in Table 1 [22]. The product data sheet does not directly specify the latent heat of the solid–liquid phase change, but instead the heat storage capacity in a temperature interval around



Fig. 3. Rubitherm CSM panel.

Table 1
Thermophysical properties of Rubitherm RT42 [22].

Melting temperature range	38–43 °C main peak 41 °C
Congeeing temperature range	43–37 °C main peak 42 °C
Heat storage capacity in temp. range between 35 °C and 50 °C	174 kJ kg ⁻¹ (±7.5%)
Specific heat in both solid and liquid states	2 kJ kg ⁻¹ K ⁻¹
Density in solid state at 15 °C	880 kg m ⁻³
Density in liquid state at 80 °C	760 kg m ⁻³
Volume expansion in temp. range of phase change	14%
Heat conductivity	0.2 W m ⁻¹ K ⁻¹

the melting point (between 35 °C and 50 °C) is specified with the uncertainty of 7.5%. It means that the heat storage capacity of RT42 between 35 °C and 50 °C is $174 \pm 13 \text{ kJ kg}^{-1} \text{ K}^{-1}$.

As for the specific heat, it primarily depends on the chemical composition of a PCM. For the majority of commercially available PCMs, the specific heat in both the solid and liquid states is between $1 \text{ kJ kg}^{-1} \text{ K}^{-1}$ and $2.5 \text{ kJ kg}^{-1} \text{ K}^{-1}$ [21]. The specific heat in the solid and liquid state of Rubitherm RT42, specified in the product data sheet, is $2 \text{ kJ kg}^{-1} \text{ K}^{-1}$. However, Kenisarín and Mahkamov [23] reported the solid and liquid specific heats of Rubitherm RT42 of $1.8 \text{ kJ kg}^{-1} \text{ K}^{-1}$ and $2.4 \text{ kJ kg}^{-1} \text{ K}^{-1}$, respectively. Losada-Peréz et al. [24] determined the specific heats of Rubitherm RT42 experimentally with the use of the adiabatic scanning calorimetry method. They reported the specific heat of $3.5 \text{ kJ kg}^{-1} \text{ K}^{-1}$ and $2.3 \text{ kJ kg}^{-1} \text{ K}^{-1}$ in the solid and liquid state, respectively. Considering the specific heat of $2 \text{ kJ kg}^{-1} \text{ K}^{-1}$, the latent heat is $144 \text{ kJ kg}^{-1} \text{ K}^{-1}$, which is also consistent with the findings of Kenisarín and Mahkamov [23].

For the specific heat of $2 \text{ kJ kg}^{-1} \text{ K}^{-1}$ in both the solid and liquid states, as specified in the product data sheet, overall heat storage capacity of the panels (including the aluminium containers) was 11.8 MJ (3.3 kWh) in the temperature interval between 25 °C and 55 °C ($\Delta T = 30 \text{ K}$). If each of the panels was filled with 700 ml of water instead of Rubitherm RT42 then the total thermal storage capacity of the panels would be 9.7 MJ (2.7 kWh). It is obvious that the use of PCM-based thermal storage in this case only makes sense if the operation temperature interval is rather narrow. Water-based thermal storage (containers filled with water) operating in the temperature interval of $\Delta T = 45 \text{ K}$ would provide larger thermal storage capacity than the considered latent heat storage. Since each application may require different operation temperature interval, the melting temperature of a PCM needs to be chosen with regard to the application. There is a number of phase change materials with the melting temperature between 30 °C and 100 °C that can be used for thermal energy storage in solar air systems [25].

3. Experimental investigations

The experiments were carried out in a lab environment. The experimental set-up can be seen in Fig. 4. An electric heater substituting an air collector was used to heat up the air at the inlet of the unit. The electric heater had the maximum heating output of 2 kW. The heating output of the air heater could be controlled but the maximum output was used in most experiments. A fan with a flow rate control was used to maintain the constant flow rate through the heat storage unit. The fan allowed for the maximum air flow rate of $760 \text{ m}^3 \text{ h}^{-1}$. The data acquisition involved monitoring of the air flow rate through the unit as well as air temperature measurements at several locations. The resistance temperature probes Pt100 were used for the air temperature measurements and the anemometric probe was used for air flow rate measurements. An open-loop arrangement was used, it means that air passing through the unit was supplied outside of the lab. A thermally insulated flexible duct was used for this purpose. The storage unit itself was thermally insulated with polystyrene on the outside.

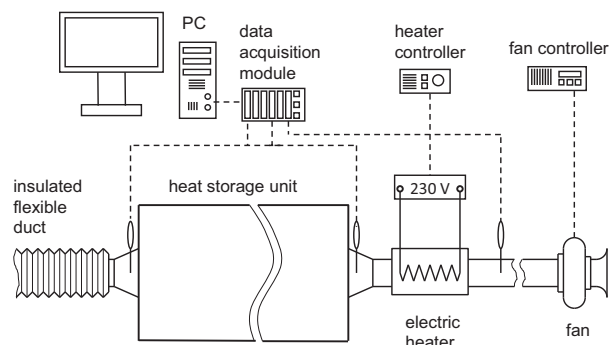


Fig. 4. Experimental set-up.

The application of thermal storage in solar air heating system means that the duration of thermal storage period is limited by availability of solar radiation. Space heating in central Europe is not generally needed in summer and conditions for solar air heating in winter are really poor. Moreover, there is not much need for thermal storage in solar air heating systems in winter because space heating is needed almost all the time and the days with clear sky are also those with low outdoor temperature. The biggest potential for thermal storage is in spring and autumn when some daytime solar gains can be moved to after sunset hours. The flow rate in the experimental case was a compromise between acceptably short heat storage period and the reasonable inlet air temperature. The average sunshine duration in early spring and late autumn is less than 5 h in Brno, Czech Republic (latitude 49.2° N) and it is probably not reasonable to expect higher solar air heater outlet temperature than 60 °C. It needs to be pointed out that the temperature at the outlet of a solar air heater changes during the day and a constant outlet temperature could only be achieved with variable air flow rate controlled with regard to solar radiation and outdoor air temperature.

The heat storage and release experiments were performed for a couple of weeks with only a few dozen phase change cycles. The change of PCM properties with the number of phase change cycles was reported by many authors. Rathod and Banerjee [26] published the review of papers on thermal stability of PCMs used in latent heat energy storage systems. The deterioration of thermophysical properties of the PCMs can significantly influence the long-term performance of heat storage. The change of the PCM properties can be taken into account in the numerical simulations as a change of thermophysical properties with time or a number of phase change cycles if such dependence is known.

4. Numerical investigations

4.1. Model concept

The numerical model of the heat storage unit was implemented as a one-dimensional transient heat transfer problem. The TRNSYS 17 simulation tool, which allows for transient simulations of energy systems and buildings, was used in the numerical investigations. The development of several latent heat storage models for TRNSYS has been reported by various authors in the last decade, e.g. [19,27,28]. The TRNSYS can be coupled with other simulation tools which increases its versatility. A coupling between TRNSYS and MATLAB was used for the development of the numerical model of the heat storage unit. Though convenient for the development of the model the coupling is not practical for actual simulations. The need for repeated calling of MATLAB from TRNSYS in each

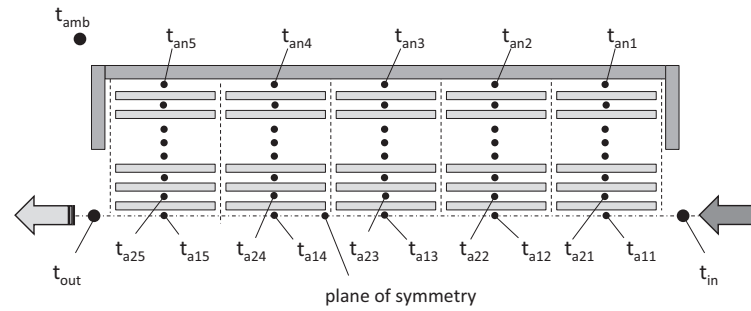


Fig. 5. Schematic of the numerical model.

time iteration profoundly increases the computational time. For that reason the numerical model developed in MATLAB was consequently recompiled with the use of C++ programming language to the form of the build-in TRNSYS module. The model of the unit can be used with other components available in the TRNSYS such as air heaters, solar collectors, and heat pumps. The schematic of the numerical model of the heat storage unit is shown in Fig. 5.

Since there are many geometrically same air channels (gaps) between the CSM panels, only several channels could be modelled in order to decrease the computational time. Actually, assuming the symmetry only the half of the channel with the half of the CSM panel thickness could be modelled. Such a basic model was tested but it did not represent the situation in the actual heat storage unit very well since the air flow rates vary in different air gaps. Therefore, a more realistic model as shown in Fig. 5 was implemented to address this issue. The air velocity profile in the heat storage unit was assumed symmetrical about the horizontal mid-plane of the unit. The variation of air velocities in the horizontal direction was neglected in the model. The heat loss of the unit was calculated from the temperature difference between the ambient air temperature and the air temperatures inside the unit close to the unit walls. The simulation of the phase change of PCM inside the CSM panels was the most time consuming part of the calculations and the computational time increased with the number of solved sections. The detail of the one of the sections (computational domains) is shown in Fig. 6. The number of nodes used for the calculations can be specified in the model together with the number of sections which should be solved for each panel. Regardless of the number of sections, each of them is solved as a 1D heat transfer problem. This assumption is based on the dimensions of the CSM panels where the thickness of the PCM layer is much smaller than its other two

spatial dimensions. Only one section per panel was calculated in the reported simulations.

4.2. Phase change modelling

The numerical model is based on the implementation of the 1D heat transfer equation that includes an internal source of heat [29]

$$\rho c \frac{\partial T}{\partial \tau} = \frac{\partial}{\partial x} \left(k \frac{\partial T}{\partial x} \right) + \dot{Q} \tag{1}$$

where ρ represents the density, c denotes the specific heat, k stands for the thermal conductivity, t is the time, T represents the temperature and x is the spatial coordinate (in the direction of the PCM layer thickness). The internal heat source of the latent heat of fusion \dot{Q} in Eq. (1) can be expressed as follows [30],

$$\dot{Q} = \rho L_f \frac{\partial f_s}{\partial \tau} \tag{2}$$

where L_f denotes the latent heat of fusion and f_s is the solid fraction that represents the ratio between the solid and liquid phases [30]. The effective heat capacity method [31] was adopted as an approach to modelling of the phase change. This method makes use of the effective heat capacity c_{eff} in order to comprise the latent heat of fusion. The effective heat capacity can be defined as follows [30],

$$c_{eff}(T) = \frac{1}{\rho} \frac{\partial H}{\partial T} = c - L_f \frac{\partial f_s}{\partial \tau} \frac{\partial \tau}{\partial T} \tag{3}$$

where H is the enthalpy of the material. Hence, the effective heat capacity is proportional to the slope of the enthalpy function with respect to the temperature. The substitution of Eq. (3) into Eq. (1) results in the governing equation of heat transfer in the phase change material as follows

$$\rho c_{eff} \frac{\partial T}{\partial \tau} = \frac{\partial}{\partial x} \left(k \frac{\partial T}{\partial x} \right). \tag{4}$$

A general dependence of the effective heat capacity on the temperature for a material undergoing a phase change can be seen in Fig. 7. The effective heat capacity coincides with the respective specific heats in the liquid and solid states of the material outside of the phase change temperature range. The effective heat capacity significantly varies when the material undergoes phase change as it comprises the absorption or the release of the latent heat. The temperature range of the phase change, in which both the solid and liquid phases simultaneously coexist and the solid fraction satisfies $0 < f_s < 1$, is commonly called the mushy zone [30]. Fig. 7 shows the effective capacity for a material with the hysteresis of melting and solidification that is rather typical for most of the PCMs. The hysteresis complicates numerical modelling of the PCM thermal behaviour when the material does not fully liquefy or

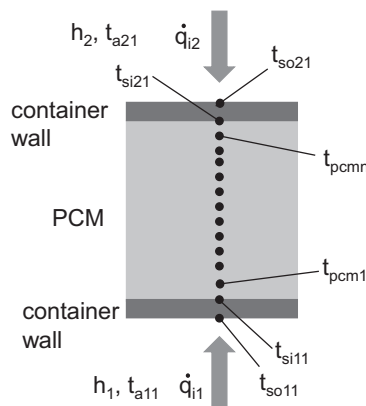


Fig. 6. Schematic of a computational domain.

Table 2
Parameters of effective heat capacity curves used in numerical simulations.

Case	c_m	Heat storage capacity between 35 °C and 50 °C	Latent heat of phase change
Lower uncertainty level (-7.5%)	51.1 kJ kg ⁻¹ K ⁻¹	161 kJ kg ⁻¹	131 kJ kg ⁻¹
Mean	56.2 kJ kg ⁻¹ K ⁻¹	174 kJ kg ⁻¹	144 kJ kg ⁻¹
Upper uncertainty level (+7.5%)	61.3 kJ kg ⁻¹ K ⁻¹	187 kJ kg ⁻¹	157 kJ kg ⁻¹

solidify during the working cycle. In the simulated thermal storage cycle the PCM fully liquefied during the heat storage period and fully solidified in the heat discharge period; therefore, one effective heat capacity curve was used for melting and a different one for solidification. The effective heat capacity of a PCM is usually determined experimentally, e.g. with the use of the differential scanning calorimetry method [32] or utilizing the thermal delay method [33]. A simplified approach as described by Kuznik et al. [34] was utilized in numerical simulations presented in this study. The effective heat capacity of Rubitherm RT42 was proposed in the form of the Gaussian-shape function. With both the solid and liquid specific heats of 2 kJ kg⁻¹ K⁻¹, the effective heat capacity function reads as follows,

$$c_{\text{eff}}(t) = 2 + c_m \exp \left\{ -\frac{(t - t_m)^2}{2.1} \right\} \quad (5)$$

where c_m is the maximum increment of the specific heat due to the latent heat. The mean temperature of the phase change t_m for melting and congealing was 41 °C and 40 °C, respectively. The effective heat capacity defined by Eq. (5) complies with the material properties stated in Table 1. Considering the uncertainty of ±7.5% for the heat storage capacity, two more $c_{\text{eff}}(t)$ curves were used in the numerical simulations. The parameters of the curves are presented in Table 2.

In comparison to the enthalpy method [35–37] that can also be used for modelling of phase change problems, the effective heat capacity approach requires only the primary unknown variable – the temperature – that is calculated directly from Eq. (4). A possibility to use an implicit discretization scheme, and therefore unlimited time step of simulation due to the unconditional numerical stability [29], is another advantage of the effective heat capacity approach. However, to ensure a desired accuracy the time step is still limited from the physical point of view due to a narrow temperature interval of the mushy zone where the effective heat capacity changes rapidly. The control volume method using the explicit scheme for the time derivative was utilized in order to solve the problem numerically [38]. Due to the conditional stability of the explicit time discretization, the time step of the simulation was carefully determined with the use of stability criteria in order to prevent numerical instability or even oscillations [39].

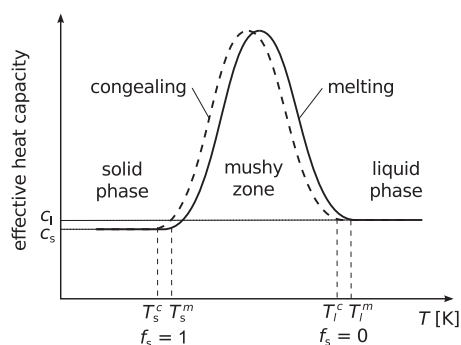


Fig. 7. Effective heat capacity.

In order to complete the mathematical model and to establish the well-posed problem, the initial and boundary conditions were provided. The initial condition was the uniform temperature for the entire heat storage unit. The convective heat flux according to the Newton’s law of cooling was used as the boundary condition at the surfaces of the panels, see Fig. 6. The heat transfer coefficient was determined with the use of the correlation for the fluid flow between two parallel planes [29]. The Reynolds number in the investigated cases was $Re \leq 1000$, which is generally laminar flow. In case of fully developed laminar flow the Nusselt number is constant and therefore the heat transfer coefficient does not depend on the Reynolds number. However, even in case of laminar flow the Nusselt number is not constant in the entry region where the flow is not yet fully developed meaning that the value of the heat transfer coefficient also depends on the distance from the channel entrance. The influence of entry region on the heat transfer coefficient was much more significant than the influence of the Reynolds number because the length of the entry region for the heat storage unit with 5 rows of CSM panels was longer than the length of the air gap (channel) between the CSM panels. The Nusselt number and therefore the heat transfer coefficient have smaller values in the fully developed laminar flow than in the entry region [29]. This fact can have implications in optimal design of heat storage units.

5. Results and discussion

Fig. 8 shows the measured and simulated air temperatures at the inlet and outlet of the heat storage unit during the heat storage and heat release periods in an experiment with the constant inlet air temperature. The situation with the constant air temperature is presented because it is rather illustrative for theoretical analyses. The constant air temperature at the inlet of the unit would probably be of a rare occurrence under real operating conditions of a solar air system, but for other heat sources such as air-to-air heat pumps the constant air temperature at the inlet is more plausible.

The heat storage period took place from 0:10 h to 4:15 h and the heat release period was between 4:15 h and 9:00 h. The air flow rate through the heat storage unit was 230 m³ h⁻¹ during the entire

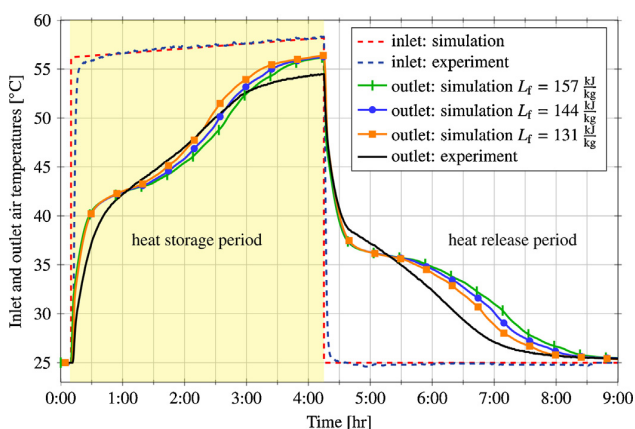


Fig. 8. Inlet and outlet air temperatures.

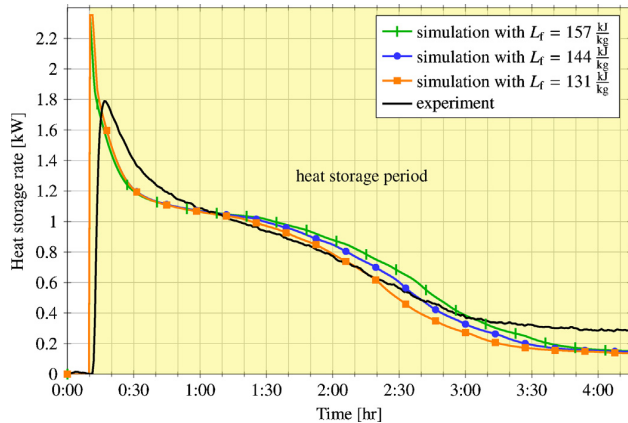


Fig. 9. Heat storage rate.

experiment. The experiment began from the constant temperature of the heat storage unit of 25 °C as can be seen from the inlet and outlet air temperatures during the first 10 min. In order to achieve this initial condition, the ambient air was circulated through the unit until there was no difference between the inlet and outlet air temperatures. Then the electric heater was switched on and almost constant inlet air temperature of 58 °C was maintained. At 4:15 h the heater was switched off and the heat release period began with the inlet air temperature of 25 °C. The numerical simulation used the same initial and boundary conditions in order to obtain comparable results.

5.1. Inlet and outlet air temperatures

As can be seen in Fig. 8, the outlet air temperature follows the increase of the inlet air temperature rather quickly at the beginning of the heat storage period when only sensible heat storage takes place. The onset of the melting process is clearly visible as the change in the time derivative of the outlet air temperature. Between about 0:30 h and 1:00 h, the time derivative of the outlet air temperatures (i.e. the slope of the air temperature increase) temporarily declines due to latent heat storage in the PCM. The same behaviour can be seen in the heat release period when the air temperature at the outlet initially decreases rather steeply, but when the air temperature drops to the congealing temperature of the PCM, the decrease of the air temperature slows down as the latent heat is released. The onset of melting and congealing does not occur in all panels at the same time and that is one of the reasons why there is not a temperature plateau (almost isothermal heat storage and release) so often shown in theoretical descriptions of latent heat storage. Another reason is a relatively wide melting range of RT42.

5.2. Heat storage and release rates

The heat storage rates for the situation shown in Fig. 8 can be seen in Fig. 9. The heat storage rate was obtained from the air mass flow rate \dot{m}_a and the difference between the inlet and outlet air temperatures

$$q_{in} = \dot{m}_a c_a (t_{in} - t_{out}) \quad (6)$$

where c_a is the specific heat of air at constant pressure and t_{in} and t_{out} are the air temperatures at the inlet and outlet of the unit as shown in Fig. 5. The discrepancies between the simulated and measured heat storage rates at the beginning of the unit operation (from 0:10 h to 0:30 h in Fig. 9) are mainly due to the electric air heater. The actual heater needed some time to reach the desired air temperature at the inlet of the heat storage unit and that is why the

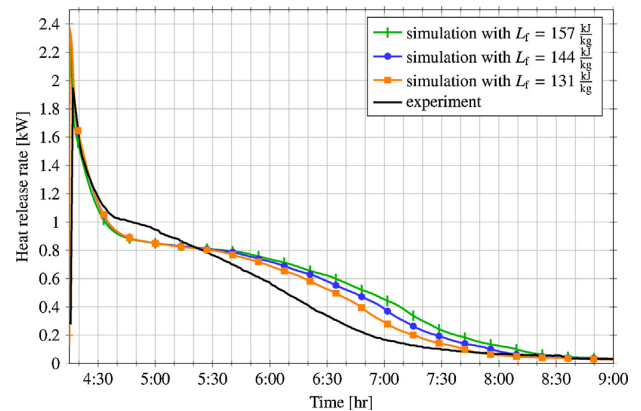


Fig. 10. Heat release rate.

peak in the heat storage rate from the experiment is not as sharp as in the case of numerical simulations where the inlet air temperature was reached in the first time step. The numerical model of the unit underestimated the heat loss to the surroundings. That is one of the reasons for increasing discrepancies between experimental and numerical results over longer periods of time. At a certain point during the heat storage period the air temperature difference between the inlet and the outlet of the unit is not because of the heat being stored in the unit but only due to the thermal loss of the unit.

The heat release rates can be seen in Fig. 10. Similarly to the heat storage period, the heat release rate was calculated as

$$q_{out} = \dot{m}_a c_a (t_{out} - t_{in}). \quad (7)$$

The air temperature at the inlet of the unit was 25 °C during the heat release period. The air flow rate was the same as in the case of the heat storage period. Again, there is a relatively good agreement between the numerical and experimental results at the beginning of the heat release period (sensible heat storage) but the discrepancies occur during the congealing of the PCM. The heat release rate peaks at around 2 kW at the beginning of the heat release period but it very quickly drops to around 1 kW when the sensible heat above the melting range is released.

5.3. Reasons for discrepancies

One-dimensional simulation models require simplification of the studied problem and that means that certain phenomena cannot be addressed in detail. In the case of the investigated unit the simplification mostly concerns the air flow inside the unit and the phase change of the PCM. Since the air flow in the unit cannot be modelled in detail, some assumption needs to be made about the air flow rates in particular air cavities (channels). The highest air flow rate for the studied arrangement was considered in the air cavity at the horizontal mid-plane (plane of symmetry) of the unit and it was assumed that the air flow rate in other air cavities decreased with their distance from the mid-plane (with the minimum air flow rates in the air channels adjacent to the walls of the storage unit). As for the phase change modelling, the 1D approach to heat transfer in the studied case seemed to be justified by the dimensions of the CSM panels where the thickness of the PCM layer was much smaller than other two spatial dimensions and the dominant heat flux could be expected in the direction of the PCM layer thickness. No convection was considered in the melted PCM. The horizontal position of the panels means that the melted PCM collects in the lower part of the panel and the air cavities (voids) may form between the PCM and the aluminium shell of the panel. That might increase the thermal

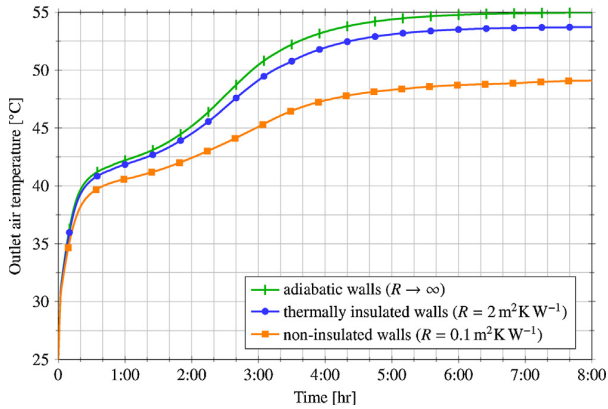


Fig. 11. Outlet air temperatures for different heat resistances of the unit walls.

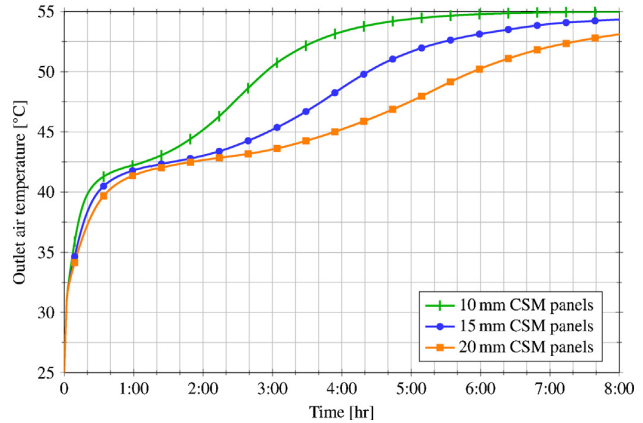


Fig. 12. Outlet air temperatures for different thicknesses of CSM panels.

resistance for heat transfer between the upper surface of the container and the PCM. No voids in the PCM were considered in the simulations. A 3D model of the panel would provide much better insight into the melting process [40,41] but for the computational constraints it would be almost impossible to model each CSM panel individually in 3D. The approach in which the results of a simplified 1D model are validated with experimental data and fine-tuning of the model is done based on that comparison is probably the most feasible approach for practical application of numerical simulations at the moment [16].

5.4. Further simulation results

The main advantage of the numerical simulations is that it is relatively easy to perform parametric studies analysing the influence of various design and operation parameters. The analyses of various parameters that influence the performance of the PCM-air heat storage unit can be found in [16] and [19]. It is obvious that with the increasing inlet air temperature or the increasing air flow rate, the necessary time for melting of PCM gets shorter. The influence, which is often neglected in the published studies, is the heat loss to the ambient environment. Fig. 11 shows the simulated outlet air temperature in the heat storage period for three levels of thermal resistance of the unit walls. The inlet air temperature was 55 °C, the ambient temperature was 25 °C and the air flow rate was 300 m³ h⁻¹. As can be seen the non-insulated unit has a rather high thermal loss. The thermal insulation with the resistance of 2 m²KW⁻¹ (roughly equivalent to 0.1 m of an insulation material with the thermal conductivity of 0.05 W m⁻¹ K⁻¹) rather significantly reduces the heat loss. In case of a thermally insulated unit, it is justifiable to use the assumption of adiabatic walls for the parametric studies with relatively short heat storage cycles.

The CSM panels are available with the thickness of 10 mm, 15 mm and 20 mm. The simulated outlet air temperatures during the heat storage period for the units containing CSM panels of the three thicknesses are shown in Fig. 12. The simulation was done for the inlet air temperature of 55 °C and the air flow rate of 300 m³ h⁻¹. The walls of the unit were considered adiabatic and the 20 mm air cavities between the panels were considered in all three cases.

The heat storage capacity of the unit can be increased by addition of CSM panels that can be added in parallel and in series. The number of panels in parallel does not influence the outlet air temperature as long as the air flow rate in each channel remains the same. The situation is different when the panels are added in series. In case of the units comprising CSM panels, the unit dimensions can only change in increments equivalent to dimensions of the panels. For the arrangement used in the tested unit, each row of CSM panels

extends the length of the unit by 0.3 m. Fig. 13 shows the simulated air temperatures behind the rows of the CSM panels in a unit with 15 rows of panels (15 × 20 panels). The walls of the unit were considered adiabatic, the inlet air temperature was 55 °C and the air flow rate was 300 m³ h⁻¹.

Most studies consider complete phase change cycles in which the whole amount of PCM completely changes phase from solid to liquid and vice versa [19,14]. However, especially in case of solar systems where the amount of available heat depends on solar radiation, which varies significantly from day to day, the partial melting can be commonplace in real-life operation. As can be seen in Fig. 13, the PCM in the first row of the CSM panels is fully melted in less than an hour while the PCM in the 15th row takes several hours to melt. It means that the PCM in the panels at the inlet of the unit would probably undergo more phase change cycles than the panels at the outlet in a real-life operation.

The heat storage rates for different numbers of rows can be seen in Fig. 14. For the constant inlet conditions the heat storage rate increases with the increasing number of rows. The increasing heat storage rate also means an increase of the effectiveness of the heat storage unit as a heat exchanger. A trivial conclusion would be that the infinite number of rows leads to the maximum effectiveness. Since the increase of the heat storage rate (and the effectiveness) is not proportional to the number of rows, an optimum arrangement of the CSM panels (a combination of panels positioned in parallel and in series) for a specific application can be found by means of multi-parametric optimization. It is important to choose appropriate optimization criteria (e.g. the pressure drop of the unit vs. the

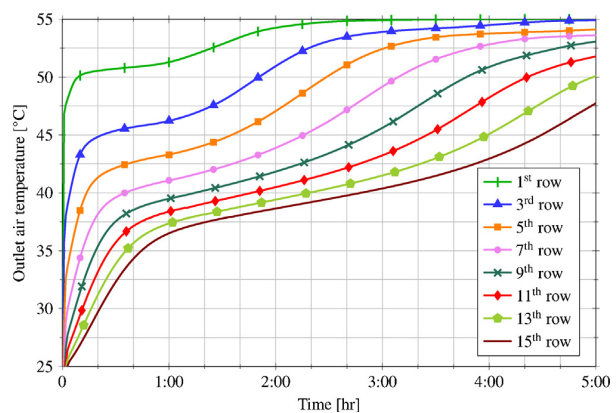


Fig. 13. Outlet air temperatures at different positions in the unit.

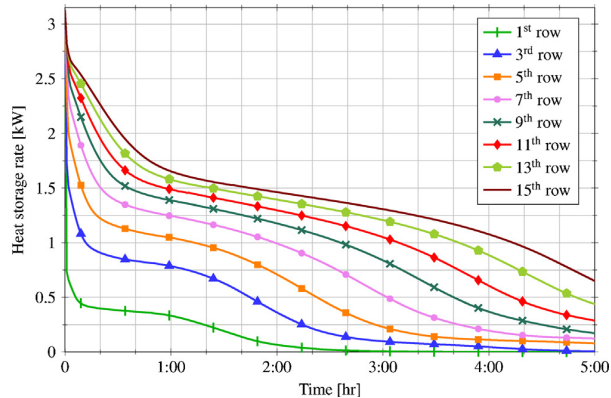


Fig. 14. Heat storage rates for different number of rows.

effectiveness) because the effectiveness as the only optimization criterion would lead to the infinite length of the unit.

6. Conclusions

Experimental and numerical investigations of a lab-scale latent heat storage unit for solar air systems were carried out. The experimentally investigated unit comprised 100 CSM panels filled with a paraffin-based PCM. A 1D simulation model of the unit was developed for the numerical investigations. The experimental and numerical results show relatively good agreement though the discrepancies occur when the PCM undergoes melting or congealing. The developed numerical model was used for a parametric study of the thermal behaviour of the unit. The investigated arrangement of the thermal storage unit is applicable in other thermal energy systems with air as a heat carrier fluid. Latent heat storage offers certain advantages over sensible heat storage and it attracts more attention even in the areas where it was not considered in the past. The increasing use of air-to-air heat pumps and variable refrigerant flow air-conditioning system contributes to peaks in electricity consumption. PCM-based thermal storage could be employed in some of these systems as a peak shaving measure.

Acknowledgements

The authors gratefully acknowledge financial support provided by the Czech Grant Foundation under contract number P101/11/1047, by the BUT FSI-J-13-1977 project for young scientists and by the ED0002/01/01 NETME project. The corresponding author is grateful to the EU COST Action TU0802: "Next generation cost effective phase change materials for increased energy efficiency in renewable energy systems in buildings (NeCoE-PCM)" for its sponsorship. The co-author, the holder of Brno PhD Talent Financial Aid sponsored by Brno City Municipality, also gratefully acknowledges that financial support.

References

- [1] V.V. Tyagi, N.L. Panwar, N.A. Rahim, R. Kothari, Review on solar air heating system with and without thermal energy storage system, *Renewable and Sustainable Energy Reviews* 16 (2012) 2289–2303.
- [2] S. Singh, S. Kumar, New approach for thermal testing of solar dryer: development of generalized drying characteristic curve, *Solar Energy* 86 (2012) 1981–1991.
- [3] A.E. Kabeel, Solar powered air conditioning system using rotary honeycomb desiccant wheel, *Renewable Energy* 32 (2007) 1842–1857.
- [4] P. Pinel, C.A. Cruickshank, I. Beausoleil-Morrison, A. Wills, A review of available methods for seasonal storage of solar thermal energy in residential applications, *Renewable and Sustainable Energy Reviews* 15 (2011) 3341–3359.

- [5] S. Jaber, S. Ajib, Optimum design of Trombe wall system in Mediterranean region, *Solar Energy* 85 (2011) 1891–1898.
- [6] D.L. Zhao, Y. Li, Y.J. Dai, R.Z. Wang, Optimal study of a solar air heating system with pebble bed energy storage, *Energy Conversion and Management* 52 (2011) 2392–2400.
- [7] Y. Dutil, D.R. Rousse, N. Ben Salah, S. Lassue, L. Zalewski, A review on phase-change materials: mathematical modeling and simulations, *Renewable and Sustainable Energy Reviews* 15 (2011) 112–130.
- [8] M.M. Farid, A.M. Khudhair, S.A.K. Razack, S. Al-Hallaj, A review on phase change energy storage: materials and applications, *Energy Conversion and Management* 45 (2004) 1597–1615.
- [9] B. Zalba, J.M. Marin, L.F. Cabeza, Review on thermal energy storage with phase change: materials, heat transfer analysis and applications, *Applied Thermal Engineering* 23 (2003) 251–283.
- [10] E. Oró, A. de Gracia, A. Castell, M.M. Farid, L.F. Cabeza, Review on phase change materials (PCMs) for cold thermal energy storage applications, *Applied Energy* 99 (2012) 513–533.
- [11] F. Kuznik, D. David, K. Johannes, J.J. Roux, A review on phase change materials integrated in building walls, *Renewable and Sustainable Energy Reviews* 15 (2011) 379–391.
- [12] B.M. Diaconu, S. Varga, A.C. Oliveira, Experimental assessment of heat storage properties and heat transfer characteristics of a phase change material slurry for air conditioning applications, *Applied Energy* 87 (2010) 620–628.
- [13] E.K. Summers, M.A. Antar, J.H. Lienhard, Design and optimization of an air heating solar collector with integrated phase change material energy storage for use in humidification–dehumidification desalination, *Solar Energy* 86 (2012) 3417–3429.
- [14] G. Hed, R. Bellander, Mathematical modelling of PCM air heat exchanger, *Energy and Buildings* 38 (2006) 82–89.
- [15] J.P.A. Lopez, F. Kuznik, D. Baillis, J. Virgone, Numerical modeling and experimental validation of a PCM to air heat exchanger, *Energy and Buildings* 64 (2013) 415–422.
- [16] P. Dolado, A. Lazaro, J.M. Marin, B. Zalba, Characterization of melting and solidification in a real scale PCM-air heat exchanger: numerical model and experimental validation, *Energy Conversion and Management* 52 (2011) 1890–1907.
- [17] P. Dolado, A. Lazaro, J.M. Marin, B. Zalba, Characterization of melting and solidification in a real-scale PCM-air heat exchanger: experimental results and empirical model, *Renewable Energy* 36 (2011) 2906–2917.
- [18] P. Dolado, J. Mazo, A. Lázaro, J.M. Marin, B. Zalba, Experimental validation of a theoretical model: uncertainty propagation analysis to a PCM-air thermal energy storage unit, *Energy and Buildings* 45 (2012) 124–131.
- [19] E. Halawa, W. Saman, Thermal performance analysis of a phase change thermal storage unit for space heating, *Renewable Energy* 36 (2011) 259–264.
- [20] V. Dubovsky, G. Ziskind, R. Letan, Analytical model of a PCM-air heat exchanger, *Applied Thermal Engineering* 31 (2011) 3453–3462.
- [21] F. Agyenim, N. Hewitt, P. Eames, N. Smyth, A review of materials, heat transfer and phase change problem formulation for latent heat thermal energy storage systems (LHTES), *Renewable and Sustainable Energy Reviews* 14 (2010) 615–628.
- [22] Rubitherm GmbH website, <http://www.rubitherm.de/> (accessed 15.06.13, under the topic: Products, Rubitherm RT).
- [23] M. Kenisarin, K. Mahkamov, Solar energy storage using phase change materials, *Renewable and Sustainable Energy Reviews* 11 (2007) 1913–1965.
- [24] P. Losada-Peréz, C.S.P. Tripathi, J. Leys, G. Cordoyiannis, C. Glorieux, J. Thoen, Measurements of heat capacity and enthalpy of phase change materials by adiabatic scanning calorimetry, *International Journal of Thermophysics* 32 (2011) 913–924.
- [25] A. Sharma, V.V. Tyagi, C.R. Chen, D. Buddhi, Review on thermal energy storage with phase change materials and applications, *Renewable and Sustainable Energy Reviews* 13 (2009) 318–345.
- [26] M.K. Rathod, J. Banerjee, Thermal stability of phase change materials used in latent heat energy storage systems: a review, *Renewable and Sustainable Energy Reviews* 18 (2013) 246–258.
- [27] F. Kuznik, J. Virgone, K. Johannes, Development and validation of a new TRNSYS type for the simulation of external building walls containing PCM, *Energy and Buildings* 42 (2010) 1004–1009.
- [28] M. Ibáñez, A. Lazaro, B. Zalba, L.F. Cabeza, An approach to the simulation of PCMs in building applications using TRNSYS, *Applied Thermal Engineering* 25 (2005) 1796–1807.
- [29] F.P. Incropera, D.P. DeWitt, T.L. Bergman, A.S. Lavine, *Principles of Heat and Mass Transfer*, 7th ed., Wiley & Sons, New York, 2013.
- [30] D.M. Stefanescu, *Science and Engineering of Casting Solidification*, 2nd ed., Springer, New York, 2009.
- [31] H.T. Yang, Y.Q. He, Solving heat transfer problems with phase change via smoothed effective heat capacity and element-free Galerkin methods, *International Communications in Heat and Mass Transfer* 37 (2010) 385–392.
- [32] G.H. Zhang, C.Y. Zhao, Thermal and rheological properties of microencapsulated phase change materials, *Renewable Energy* 36 (2011) 2959–2966.
- [33] E.D. Kravvaritis, K.A. Antonopoulos, C. Tzivanidis, Experimental determination of the effective thermal capacity function and other thermal properties for various phase change materials using the thermal delay method, *Applied Energy* 88 (2011) 4459–4469.
- [34] F. Kuznik, J. Virgone, J.J. Roux, Energetic efficiency of room wall containing PCM wallboard: a full-scale experimental investigation, *Energy and Buildings* 40 (2008) 148–156.

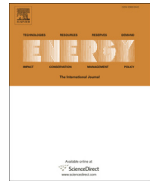
- [35] C.R. Swaminathan, V.R. Voller, A general enthalpy method for modeling solidification process, *Metallurgical Transactions B: Process Metallurgy* 23 (1992) 651–664.
- [36] M. Muhieddine, É. Canot, R. March, Various approaches for solving problems in heat conduction with phase change, *International Journal on Finite Volumes* 6 (2009) 66–85.
- [37] L. Klimeš, P. Charvát, M. Ostrý, Challenges in the computer modelling of phase change materials, *Materiali in Tehnologije* 46 (2012) 335–338.
- [38] F. Kreith, R.M. Manglik, M.S. Bohn, *Principles of Heat Transfer*, 7th ed., CL Engineering, Pacific Grove, 2010.
- [39] R.H. Pletcher, J.C. Tannehill, D. Anderson, *Computational Fluid Mechanics and Heat Transfer*, 3rd ed., Taylor and Francis, New York, 2011.
- [40] H. Shmueli, G. Ziskind, R. Letan, Melting in a vertical cylindrical tube: numerical investigation and comparison with experiments, *International Journal of Heat and Mass Transfer* 53 (2010) 4082–4091.
- [41] F.L. Tan, S.F. Hosseinizadeh, J.M. Khodadadi, L.W. Fan, Experimental and computational study of constrained melting of phase change materials (PCM) inside a spherical capsule, *International Journal of Heat and Mass Transfer* 52 (2009) 3464–3472.



ELSEVIER

Contents lists available at ScienceDirect

Energy

journal homepage: www.elsevier.com/locate/energy

Front tracking in modelling of latent heat thermal energy storage: Assessment of accuracy and efficiency, benchmarking and GPU-based acceleration

Lubomír Klimeš^{a,*}, Tomáš Mauder^b, Pavel Charvát^b, Josef Štětina^b^a Sustainable Process Integration Laboratory—SPIL, NETME Centre, Brno University of Technology, Technická 2896/2, 616 69 Brno, Czech Republic^b Energy Institute, Brno University of Technology, Technická 2896/2, 616 69 Brno, Czech Republic

ARTICLE INFO

Article history:

Received 1 February 2018

Received in revised form

28 April 2018

Accepted 2 May 2018

Available online 7 May 2018

Keywords:

Computational heat transfer

Front tracking method

GPU-based acceleration

Latent heat thermal energy storage

Phase change modelling

ABSTRACT

Computer simulations of phase change processes are of high importance in research and industry. The phase change of a material from solid to liquid and vice versa is commonplace in many technical applications from metal production to latent heat thermal energy storage. As for computer modelling, most investigators and engineers use well-known interface capturing methods because of their simplicity and straightforward implementation. However, these methods often suffer from lower computational accuracy. The paper investigates the use of the front tracking method which utilizes explicit tracking of the interface between the phases. The assessment of the computational accuracy shows that the front tracking method is about two orders of magnitude more accurate than interface capturing methods. The acceleration by means of the graphics processing units (GPUs) was utilized to enhance the computational efficiency of the front tracking method. The results demonstrate that the front tracking method and its GPU-based acceleration represent a powerful tool for fast and accurate modelling of phase change processes.

© 2018 Elsevier Ltd. All rights reserved.

1. Introduction

The mitigation of pollution, CO₂ emissions, greenhouse gas (GHG) content and the carbon footprint in the natural environment belongs to the main steps toward sustainability. The efficient utilization of non-renewable energy sources as well as their gradual replacement with renewable and sustainable energy sources are important strategies for the fulfilment of these goals. A recent research confirmed that the energy storage and, in particular, latent heat thermal energy storage (LHTES) can play an important role in effective utilization of energy sources, especially the renewable ones. Kenisarin and Mahkamov [17] reported that phase change materials (PCMs) and LHTES are a prospective technology for the utilization of solar energy. Similarly, Zhou et al. [51] published a comprehensive review on thermal energy storage in building applications and the authors concluded that the LHTES is a promising approach to effective utilization of renewable energy sources for the improvement of thermal comfort in buildings.

The LHTES and its applications include a wide range of devices and systems including thermal energy storage units, storage tanks and heat exchangers, thermally activated building structures, equipment for thermal protection of food and electronic devices and many others. The optimal design of such systems requires detailed analysis and examinations of involved phenomena. Since experimental investigations are usually rather expensive and time-consuming, many investigators use computer simulations instead. Since accurate simulation results are needed to design the LHTES systems appropriately, reliable and accurate simulation methods and models have to be used.

There are two distinct classes of computational methods for phase change problem with regard to the treatment of the interface between the phases: the methods based on interface capturing (IC) and the methods based on interface tracking (IT) [25]. In the IC methods, the temperature distribution is solved as a major quantity and only a minor effort is devoted to the location and translation of the interface between the phases. The interface is not tracked explicitly and it is usually determined from the temperature distribution—the interface is assumed to be near the isothermal surface corresponding to the phase change temperature. The enthalpy method and the apparent (often also referred to as effective) heat

* Corresponding author.

E-mail address: klimes@fme.vutbr.cz (L. Klimeš).

capacity method, both utilizing the Eulerian approach, are the typical IC methods. On the other hand, computational methods based on the IT principle are devised for the tracking of the interface between the phases. The interface is then called the front and these methods are also referred to as front tracking (FT) methods. It means that these methods include, in addition to IC methods, also the techniques that explicitly track the interface. In this context, the interface is represented by a finite number of points called markers, which are appropriately translated and precisely tracked [46]. The IT methods usually utilize the mixed Eulerian-Lagrangian modelling approach: the fixed Eulerian grid is used for the solution of the governing equation while the Lagrangian particles moving within the domain simulate the interface between the phases.

The IC methods, their principle and mathematical background, are rather simple and these methods are easily implementable into computer programs. Performing their code is relatively fast and requires no additional treatment. On the other hand, the IC methods suffer from lower accuracy. Nowadays, the IC methods are frequently utilized in modelling practice even though the FT methods outperform them in many respects. One of the reasons may be that only limited information about the accuracy, efficiency, and requirements of the FT method is available in the literature. This paper therefore presents a study into phase change modelling by means of the FT method. A comprehensive analysis including the assessment of the computational accuracy and efficiency was carried out. The results show that the FT method allows for two orders of magnitude higher accuracy in both the temperature and the interface location than three IC methods considered in the study: the enthalpy method, the apparent heat capacity method, and the temperature recovery method. The FT method and its processing was accelerated by means of the graphics processing units (GPUs). This allowed for a significant speed-up of the front tracking method.

2. Review of modelling approaches

2.1. Modelling of phase change problems

Liu et al. [27] reviewed mathematical models and numerical approaches for the computational investigation of LHTES and phase transformations in PCMs. The popular mathematical solutions were discussed and analysed. These included methods for the pure conduction as well as for the mixed conduction-convection. The authors reported that the enthalpy method and the effective heat capacity method, both pertaining to the category of IC methods, are the most frequently utilized methods. The very similar conclusions were also reported by Verma et al. [48], Dutil et al. [8], and Al-Saadi and Zhai [1]. König-Haagen et al. [20] thoroughly reviewed the use of the IC methods in the available literature including the enthalpy method, the apparent heat capacity method, and the heat source method. The authors implemented the methods and they used two Stefan problems for the assessment of their accuracy. The authors reported that good results were achieved with methods related to the enthalpy. Those methods were also sufficiently robust. On the other hand, the apparent heat capacity method led to results with the largest errors. However, it is well reported that the IC methods often suffer from lower computational accuracy. Namely, numerical oscillations may occur due to the poor fulfilment of the heat balance near the interface.

2.2. Front tracking in heat transfer and phase change modelling

Udaykumar et al. [46] presented a mixed Eulerian-Lagrangian method for the solution of fluid flow problems with moving boundaries. The method involves the solution of the governing

equations on an underlying Cartesian grid known as the Eulerian approach. On the other hand, the boundary moving within the domain is tracked explicitly by means of the marker particles. Those markers are translated using the Lagrangian approach in the normal direction to the boundary and their velocity is determined according to the Stefan condition. Later, Udaykumar et al. [47] presented finite difference formulation schemes for the FT method applicable in simulations of solidification problems with solid-liquid boundaries. The error analysis as well as sensitivity and stability issues were addressed. The authors demonstrated that their formulation of the FT method is able to solve the governing equations with the second-order accuracy while the location of the interface between the phases is determined with the first-order accuracy. Labonia et al. [23] reported a fundamental basis of the FT method in three dimensions. The method consists in the explicit interface tracking on a Eulerian fixed grid and it relies on the principles of the reconstruction and advection of the interface within the domain. The authors used the marker points for the representation of the moving interface and they provided a detailed mathematical description of the method. They demonstrated the applicability of the FT approach by means of several test problems.

Browne and Hunt [6] reported a study into the FT model applied to the simulation of the solidification and the grain growth of alloys. The authors considered a simple 2D square domain where the models for columnar and equiaxed solidifications were investigated. The heat transfer equation included the term for latent heat evolution. A dendrite tip kinetics law dependent on the local undercooling was used to govern the movement of the interface. The FT model was compared with the enthalpy based model and a good agreement was achieved. Li et al. [25] presented a detailed mathematical description for the FT method. The method solves the heat transfer equation on a fixed Eulerian grid and the heat transfer equation does not include the term for the latent heat evolution and the interface is not governed by kinetics laws. Instead, the interface between the phases moves within the domain according to the Stefan condition. The authors investigated a simple 1D case and a symmetrical 2D case in the cylindrical system. The simulated results were compared to available analytical solutions with a very good agreement between them and the method was identified as highly computationally effective. A more complicated solidification 2D case was consequently investigated numerically by means of the FT method and by the enthalpy method. The authors reported that a very good agreement was achieved at the beginning of the simulation. However, the discrepancies increased as the interface propagated in time and most of the domain became solid. McFadden and Browne [29] simulated the grain structure of metallic alloys with the use of the FT method. The heat transfer equation included the term for latent heat evolution and the movement of the interface was governed by the dendrite kinetics through the undercooling. In comparison to the previous work of the authors, the model included the non-linear latent heat treatment by means of the Scheil equation and the advanced method was used for the simulation of the initialization of the nuclei and of the grain impingement. The authors demonstrated the use of the method for the prediction of the equiaxed grain structure and of the columnar-to-equiaxed transition. A very good agreement between the simulation results and experimental data was reported. Pan and Yin [34] implemented a parallel FT method for the investigation of the multiphase flow of droplet collisions. The authors tested the MPI and OpenMP architectures for the parallel computing and they reported the speed-up between two and ten according to the size of the computational grid.

Recently, Mooney and McFadden [31] presented the verification of the 1D front tracking model for the Bridgman furnace

solidification problem. A previously developed model was utilized. The interface between the phases was governed according to kinetics laws. An available analytical solution from the literature was used for the verification of the model. The authors reported that the model is first-order accurate in space and asymptotically convergent. Seredyński et al. [39] presented a study into the use of the FT method and the immersed boundary method for the modelling of alloy solidification of single-component or semi-transparent materials. The model solves the momentum, energy and solute transport equations and the modified Stefan condition is used for the determination of the movement of the interface between the phases. Battaglioli et al. [4] investigated the Bridgman furnace solidification and the simulation of columnar growth by means of the FT method implemented in 2D. The heat transfer equation with the term accounting for the latent heat was utilized. Micro-segregation dendrite tip kinetics laws were used to govern the movement of the phase interface. The authors reported that the FT method allowed for a detailed analysis of thermal conditions influencing the grain structure. They also applied the method for the prediction of the columnar-to-equiaxed transition. Joybari et al. [16] developed a simplified FT method for thermal simulations of the horizontal shell and tube heat exchanger for latent heat thermal energy storage. The authors combined a fast and simple pure conduction model with a more complicated and computationally intense conduction-convection model both solved in Fluent. Based on simulation results, the authors derived correlations dependent on dimensionless parameters and a good agreement was reported.

2.3. Assessment of the review

The review shows that the IC methods, in particular the enthalpy method and the apparent heat capacity method, are frequently utilized in modelling of LHTES for their simplicity and straightforward implementation. The methods based on front tracking are discussed in the literature but their use in practical applications and in LHTES is rather rare as they are mostly used in theoretical studies. Moreover, the FT approach is claimed as an approach having a higher accuracy but only limited information on the assessment of the computational accuracy and its comparison to IC methods is available in the literature. Similar conditions also apply for the computational efficiency. The present study therefore aims at filling such gap and it provides the comparison and assessment of the computational performance of the FT approach and other frequently-applied IC methods.

3. Interface capturing and interface tracking

3.1. Interface capturing methods

Computational methods using the IC technique primarily focus on the solution of the heat transfer equation and on the determination of the temperature distribution [27]. The translation and evolution of the interface between the phases is not modelled in an explicit way and the behaviour of the interface is not governed by physical relationships as in case of FT [47]. The interface position, if needed, is usually localized from the temperature distribution using the assumption that the interface lies somewhere between the adjacent grid points with the temperature below and above the phase change temperature [25,1]. The location of the interface determined in such a way has no influence to the solution of the heat transfer equation. The IC methods include the Eulerian-based enthalpy method and the apparent (often also called the effective) heat capacity method, both the well-known and frequently utilized computational approaches, see e.g. Refs. [20,27]. Beside these two methods, the temperature recovery method is also briefly

discussed.

The IC methods are, in general, rather simple in terms of their mathematical formulation and coding. That explains their frequent use in various applications including the LHTES modelling. However, only a minor effort is devoted to the interface and its interaction with the governing equation. This may lead to a lower accuracy, especially in the vicinity of the interface [20].

3.1.1. Enthalpy method

The enthalpy method represents one of the most frequently utilized method for the modelling of heat transfer problems with the phase change. The method was first proposed by Eyres et al. [10]. The use of the method ranges from theoretical studies [32] to LHTES modelling [1] and to the modelling of metal production systems [44]. The enthalpy method was particularly studied by Swaminathan and Voller [41–43] who proposed an optimal scheme for the enthalpy method and they compared it with the effective heat capacity method. Swaminathan and Voller [42] reported the superiority of their proposed scheme which was demonstrated with the use of sample phase change problems.

A heat transfer problem with the phase change can be modelled by the general heat transfer equation comprising the term accounting for the internal heat source

$$\rho c_p \frac{\partial T}{\partial t} = \text{div}(k\nabla T) + \dot{g} \quad (1)$$

where ρ is the density, c_p is the heat capacity (also referred to as the specific heat) at the constant pressure, T denotes the temperature, t is time, k stands for the thermal conductivity, and \dot{g} is the internal source of heat. Generally speaking, the term \dot{g} can be used to represent any internal source of heat such as a heat sink or a heat generation sources including the latent heat release or accumulation. The governing Eq. (1) cannot be solved directly as it needs an additional treatment of \dot{g} . The enthalpy method incorporates \dot{g} by means of its inclusion to the thermodynamic state variable which is called the enthalpy. The enthalpy can be considered a form of energy which consists of both the sensible and the latent heats and it can be defined as a functional [42]

$$h(T) = \int_{T_{\text{ref}}}^T \left(\rho c_p - \rho L_f \frac{\partial f_s}{\partial \vartheta} \right) d\vartheta \quad (2)$$

where L_f is the amount of latent heat, T_{ref} is the reference temperature, and f_s is the solid fraction. The solid fraction $f_s \in (0, 1)$ expresses the ratio between the solid and the liquid phases and it is defined as $f_s = \frac{V_s}{V_s + V_l}$ where V_s is the volume of the solid phase and V_l is the volume of the liquid phase in the considered element, respectively. The source term accounting for the latent heat evolution can be expressed as [40]

$$\dot{g}_{\text{latent}} = \rho L_f \frac{\partial f_s}{\partial T} \frac{\partial T}{\partial t} \quad (3)$$

The substitution of Eq. (3) with the differentiated Eq. (2) into Eq. (1) leads to the enthalpy-based formulation of the heat transfer equation [42]

$$\frac{\partial h}{\partial t} = \text{div}(k\nabla T). \quad (4)$$

The formulation given in Eq. (4) is mathematically complete and it can now be numerically solved with the use of a proper computational method. On the other hand, instead of the unknown temperature in Eq. (1), the enthalpy-based formulation given in Eq.

(4) contains two unknown variables: the temperature and the enthalpy. Since both the quantities are coupled through the definition of the enthalpy given in Eq. (2), the computational solution is carried out per partes: the enthalpy is first resolved from the discretized Eq. (4), and then the temperature determined from the enthalpy according to Eq. (2). This two-step technique makes the numerical procedure more demanding.

A typical temperature-enthalpy relationship (curve) is presented in Fig. 1. The figure depicts a dependence for the non-isothermal phase change which is characteristic for alloys and non-crystalline matters that melt and solidify in a certain temperature interval. In case of the isothermal phase change, which is typical for transformations of pure substances and eutectic alloys, the phase change temperature interval adopts $\Delta T \rightarrow 0$ in the limit sense. The isothermal phase change may cause some numerical difficulties since the dependency of the enthalpy at the phase change temperature is not a function from the mathematical point of view. However, the enthalpy method can be adapted and applied for such isothermal cases, see e.g. Ref. [52].

3.1.2. Apparent heat capacity method

The apparent heat capacity method, often also referred to as the effective heat capacity method or the apparent capacity method, is another IC method frequently adopted for the solution of heat transfer problems with the phase change. The method was introduced by Hashemi and Sliepcevich [13]. Rather than introducing a new variable, the latent heat is incorporated into the Eq. (1) by means of the heat capacity c_p . In particular, the molecular heat capacity is appropriately extended by the latent heat. Such a modification of the heat capacity in the phase change temperature interval must be equivalent to the amount of the latent heat of the phase change. Therefore, it must hold that

$$\int_{T_s}^{T_\ell} c_{app}(T) dT = c_p(T_\ell - T_s) + L_f \tag{5}$$

where T_ℓ and T_s are the liquidus temperature and the solidus temperature, respectively. Using Eq. (2) it can be shown that the apparent heat capacity is related to the enthalpy in accordance to [40]

$$c_{app} = \frac{1}{\rho} \frac{\partial h}{\partial T} = c_p - L_f \frac{\partial f_s}{\partial T} \tag{6}$$

Though the apparent heat capacity is a function of temperature,

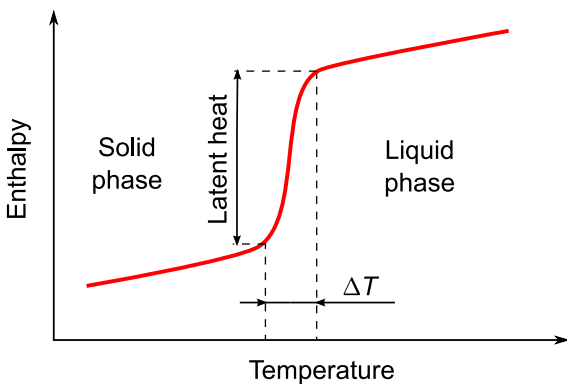


Fig. 1. A typical temperature-enthalpy relationship for the non-isothermal phase change.

a number of investigators (see e.g. Refs. [26,24]) adopted a simplified approach assuming its constant value proposed by Bonacina et al. [5]. Considering the apparent heat capacity as a function of the temperature, the investigators frequently adopt a bell-shaped function (see e.g. Ref. [22]) and polynomials (see e.g. Ref. [21]). A characteristic bell-shaped apparent heat capacity is shown in Fig. 2.

Obviously, the definition given in Eq. (5) is applicable only for the non-isothermal phase change for which $T_\ell - T_s > 0$. Indeed, in case of the isothermal phase change, the relationship in Eq. (5) is no longer numerically applicable since the apparent heat capacity approaches the Dirac delta function as $T_\ell - T_s \rightarrow 0$. König-Haagen et al. [20] reported that this issue of the apparent heat capacity method is usually overcome by the extension of the isothermal phase change temperature over a small temperature range.

The substitution of the apparent heat capacity defined in Eqs. (5) and (6) into Eq. (1) leads to

$$\rho c_{app} \frac{\partial T}{\partial t} = \text{div}(k \nabla T). \tag{7}$$

In comparison with the enthalpy method, Eq. (7) contains only one unknown variable which makes its solution easier and computationally straightforward. The form of Eq. (7) is also suitable for the implicit discretization in time, which can benefit in the unconditional numerical stability [40]. However, the apparent heat capacity methods is fairly sensitive to the selection of the time step, especially in case of a narrow temperature range of the phase change. It is well reported that a larger time step may lead to numerical inaccuracy due to the omission of the latent heat. Due to this reason some corrections are usually made to fulfil the energy conservation as discussed by Swaminathan and Voller [42].

3.1.3. Temperature recovery method

The temperature recovery method was first applied by Dusinberre [9] as the method for the solution of problems with the isothermal phase change. The modified method was later adopted for the solution of non-isothermal problems. Hong et al. [14] investigated the use of the temperature recovery method for simulations of the casting and metal solidification. Tszeng et al. [45] applied the method for the solidification modelling and the authors provided a detailed analysis of the numerical behaviour of the method. Recently, Mochnacki and Lara [30] utilized the temperature recovery method for the solidification analysis of pure metals and eutectic alloys. The authors reported a good effectiveness and a reasonable accuracy.

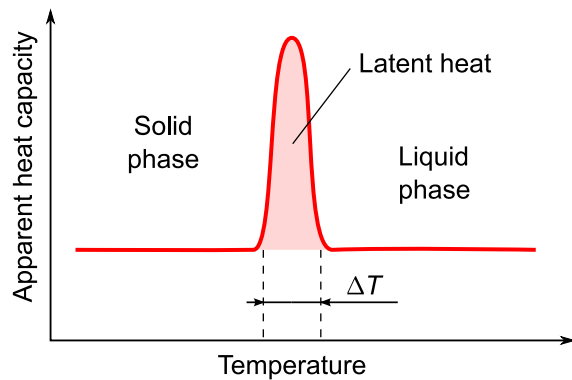


Fig. 2. A bell-shaped apparent heat capacity.

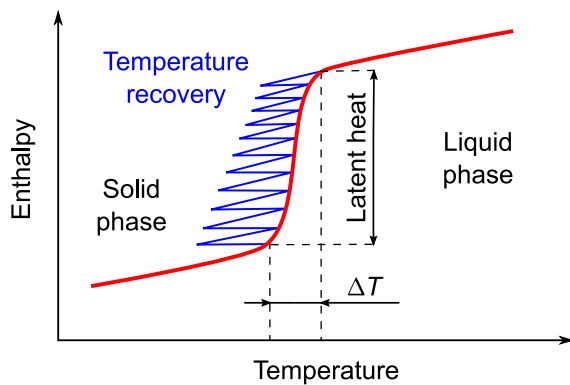


Fig. 3. Temperature recovery method.

The method uses the concept of the temperature reservoir for the inclusion of the latent heat of the phase change. The temperature recovery method considers Eq. (1) with $\dot{g} = 0$ which is solved for the temperature. The latent heat evolution is taken into account by means of the temperature reservoir R_i which is defined as the ratio between the amount of the latent heat and the heat capacity [30], $R_i = \frac{L}{c_p}$. The schematic of the principle of the temperature recovery in case of solidification is depicted in Fig. 3.

Let us consider the solidification process in a computational node i with the temperature T_i above the phase change temperature, $T_i > T_{pch}$. When the temperature T_i drops below the phase change temperature T_{pch} , the algorithm controls the level of the thermal reservoir R_i . If $R_i = 0$, the latent heat has already been completely released and the temperature $T_i < T_{pch}$ is accepted. Otherwise, the temperature reservoir is decreased by the temperature difference $T_{pch} - T_i$ and the actual temperature in the node i is recovered to the phase change temperature T_{pch} . The relation of the temperature reservoir to the enthalpy is demonstrated in Fig. 3. Each temperature recovery is shown in Fig. 3 as a teeth-shaped change and the collection of such teeth forms the saw-shaped release of the complete latent heat.

3.1.4. Comparison of the interface capturing methods

The advantage of the enthalpy method is a good accuracy and numerical stability. Further, the enthalpy method makes it possible to solve both the isothermal and non-isothermal phase change. Since the enthalpy defined in Eq. (2) and shown in Fig. 1 is a monotonically increasing function, the enthalpy method features a high level of the computational energy conservation. On the other hand, the presence of the enthalpy and the temperature in Eq. (4) makes its numerical solution more complicated.

The apparent heat capacity method is easily and straightforwardly implementable into computer programs since the Eq. (7) contains the temperature as the only unknown variable. The method has a good accuracy, however, the time step in both the formulations with explicit and implicit time discretizations needs to be carefully determined or another correction mechanism has to be implemented. In the former case, an improper setting of the time step can easily lead to numerical inaccuracy and oscillations since the concept of the apparent heat capacity has a low level of the energy conservation. Another drawback of the method is its limitation to the non-isothermal phase change. However, with a sufficiently small temperature interval of the phase change the method is also applicable for isothermal problems [20].

The temperature recovery method, along with other methods such as the heat source method, is used quite rarely in comparison

with the enthalpy method and the apparent heat capacity method. Some explanation can be derived from its properties: the temperature recovery method is relatively sensitive to the time step and the problems related to the numerical diffusion can arise near the phase change temperature. On the other hand, the method allows for a good computational accuracy and stability [28].

3.2. Interface tracking methods

Computational methods based on the IT (FT) approach, in comparison to the IC methods, incorporate techniques for explicit modelling (tracking) of the behaviour of the interface [25]. The solution of the heat transfer equation and the determination of the temperature distribution is closely coupled with the tracking of the interface between the phases [47]. In other words, the explicit tracking of the interface directly influences sub-domains in which the phases are located and for which the governing equations are solved.

Since a special treatment is devoted to the front, its location and movement within the domain, methods utilizing the FT technique are expected to be more accurate than the IC methods. A higher accuracy is particularly attained in the vicinity of the front due to its explicit tracking. Furthermore, a higher numerical stability, especially in cases with coarser spatial grids, was also acknowledged. On the other hand, these benefits are paid for by higher requirements of the FT methods. In particular, the mathematical background of the FT methods is significantly more complicated than in case of IC methods. This issue is also transmitted to coding—programming of the FT method is complicated, especially in boundary elements interacting with the boundary conditions. All these issues cause high computational difficulty and complexity; therefore, they lead to a lower computational performance. These are probably the main reasons why the FT method is not as widely used in practice as the enthalpy method or the apparent heat capacity method. The use of the FT method is in many cases limited to the theoretical studies rather than to practical applications.

The literature review on the FT methods presented in Section 2 has shown that there is a number of papers dealing with fundamental aspects or with theoretical problems [31,39]. Many papers consider the FT technique applied to problems with the alloy solidification in which the dendrite kinetics laws are used to govern the behaviour of the front, see e.g. Ref. [6]. However, such approach can be, in some sense, considered as an mixed approach of both the interface tracking and interface capturing as it partially utilizes the principle of the heat source method for the modelling of the latent heat evolution [20]. In this study, we limit the attention to the FT method originally proposed and theoretically investigated by Labonia et al. [23]. The method was also further investigated and examined by Li et al. [25]. The method is used to solve the heat transfer and the interface location; no effort is devoted to the investigation of the grain structure or solidification details such as the columnar-to-equiaxed transition. The considered FT method employs the Stefan condition evaluated at the front to govern the behaviour of the interface. Without the loss of generality, the solid-liquid phase change is assumed in the remainder of the paper.

The considered FT method utilizes the mixed Eulerian-Lagrangian approach. The governing heat transfer equation is solved in the fixed Eulerian grid while the front is tracked in the grid using the Lagrangian principle as shown in Fig. 4. In particular, the front is represented by massless points which are referred to as the markers. A proper junction of the markers such as a piecewise polynomial or splines then represents the front [25]. Such markers lie on the grid lines—boundaries of the mesh elements as shown in Fig. 4. The markers move in the grid as the front propagates in time. Let us consider a single shift of markers within the time period Δt .

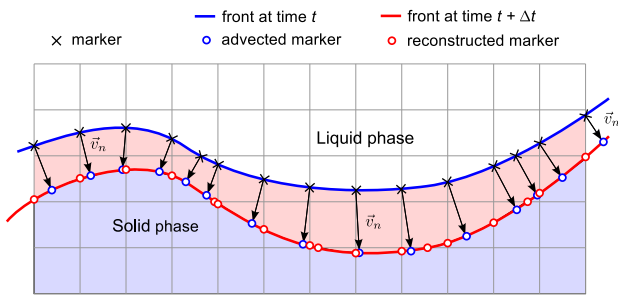


Fig. 4. Schematic of front tracking procedure.

The markers move in the normal direction with respect to the front and their velocity is determined from the Stefan condition [23,12]

$$k_s \frac{\partial T_s}{\partial \mathbf{n}} - k_l \frac{\partial T_l}{\partial \mathbf{n}} = \rho L_f \frac{ds}{dt} = \rho L_f v_n \tag{8}$$

assessing the energy balance at the interface where the subscripts s and l denote the solid and liquid phases, respectively, s is the location of the marker, and v_n is its normal velocity. Once the markers are advected in the normal direction, they do not necessarily lie on the grid lines. The advected markers and the front are analysed and the reconstructed markers lying on the grid lines are identified.

Once the front is determined, the FT method continues with the solution of the governing heat transfer equation. Since the evolution of the latent heat is incorporated through the Stefan condition, the heat transfer Eq. (1) with $\dot{g} = 0$ is solved. However, the Eq. (1) is solved in each phase separately and the solutions are coupled together by means of the interface.

Here, a brief overview on the main steps describing the principle of the considered FT method is provided. The reader is referred to [25,23] for a detailed background and implementation details. Let us consider a transient problem and a single calculation step of the FT method from the time instance t to the time instance $t + \Delta t$. The execution of the method can be described in four main steps as depicted in Fig. 4:

1. **Interface tracking.** The marker points are identified as points where the interface intersects the computational grid lines. For every marker the surface normals are determined. Special interface tracking treatment is required in case of the markers lying on the boundary grid lines.
2. **Evaluation of normal velocities of markers.** The temperature gradients in both the phases are determined for every marker by means of a transformation of coordinates. Then the Stefan condition given in Eq. (8) is evaluated in every marker and solved for the normal velocity v_n .
3. **Advection of markers and interface reconstruction.** Using the surface normals and normal velocities, the markers are advected. Since the advected markers do not necessarily lie on the grid lines, the reconstruction of the interface and the identification of the set of new markers are carried out. The updated markers determine the location of the interface and they define the regions occupied by phases.
4. **Solution of the heat transfer equation in each phase.** The procedure is completed with the solution of the governing Eq. (1) in the phases. A number of methodologies devised for the numerical solution of the heat transfer equation are available [1]. These include distinct formulations such as the finite differences, finite volumes, finite elements, and control volumes.

Various approaches are also applicable for the numerical approximation of the time derivative in the governing Eq. (1) such as explicit and implicit schemes, mixed schemes including the well-know Crank-Nicolson scheme or schemes based on the alternating direction technique [28].

A comparison of the computational procedures for the FT method and for the IC methods demonstrates the complexity of the FT method. Indeed, the FT method involves four steps mentioned above from which the first, second, and the third step are devoted to the interface tracking. The fourth step is devised to solve the thermal distribution. It is worth pointing out that the fourth step of the FT method is the only step considered in the IC methods as no effort is devoted to the determination of the interface. This also explains higher computational requirements of the FT method and its limited use in practical applications.

4. Assessment of computational performance

4.1. Stefan test problems

As mentioned in the previous sections, the FT method has a potential for a higher computational accuracy than the IC methods. Though there exist some studies (see e.g. Ref. [20]) assessing the IC methods, no study compares these methods with the methods based on the FT principle.

The accuracy of the computational methods cannot be appropriately assessed only by means of the comparison of their numerical results. Obviously, none of the computational solutions, even those computed under superior conditions, can be considered an exact solution and thus be used as an etalon. The same conclusion also applies to experimentally obtained data as they are influenced by various errors that have much higher magnitudes than the discrepancies between the results of different computational methods [19]. Instead, a phase change problem for which the analytical solution exists was utilized.

The Stefan problems considered in the semi-infinite domain represent a suitable tool for the assessment of the computational accuracy. The Stefan problems, initially proposed by the Slovenian physicist Jozef Stefan, are heat transfer problems with the phase change which consider the heat conduction as the only heat transfer mechanism. Analytical (exact) solutions for specific problems are available [12].

4.1.1. One-phase Stefan melting problem

The problem considers a semi-infinite material in the solid state which initially has the uniform temperature distribution corresponding with the phase change temperature $T(x, t = 0) = T_{pch}$. The Dirichlet condition specifying the temperature at the boundary $T(x = 0, t) = T_{bnd} > T_{pch}$ is applied as the boundary condition for $t > 0$. The material changes the phase from solid to liquid and the interface between the phases—the front—propagates within the material. The problem is schematically shown in Fig. 5.

The location $s(t)$ of the front is determined as [12]

$$s(t) = 2\psi \sqrt{\alpha_l t} \tag{9}$$

where $\alpha_l = \frac{k_l}{\rho_l c_l}$ is the thermal diffusivity of the liquid phase. The parameter ψ is dependent on the material properties and the boundary condition. Its value is determined as a solution of the transcendental equation

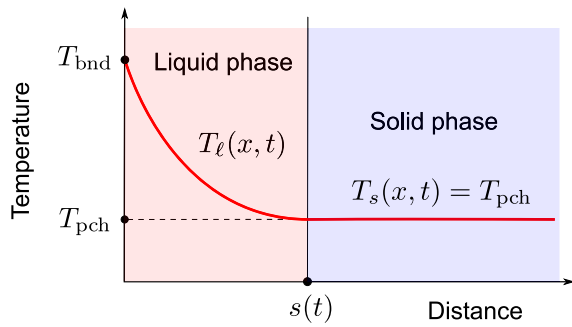


Fig. 5. One-phase Stefan melting problem.

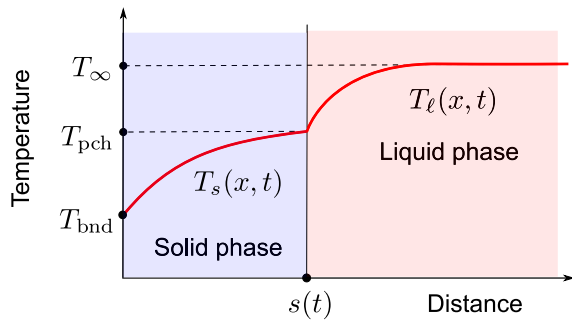


Fig. 6. Two-phase Stefan solidification problem.

$$\psi e^{\psi^2} \operatorname{erf} \psi = \frac{c_p (T_{\text{bnd}} - T_{\text{pch}})}{L_f \sqrt{\pi}} = \frac{1}{\sqrt{\pi}} \operatorname{Ste}_\ell \quad (10)$$

where Ste_ℓ is the Stefan number for the liquid phase. The temperature distribution in the liquid phase is then determined as [12]

$$T_\ell(x, t) = T_{\text{bnd}} + \frac{(T_{\text{pch}} - T_{\text{bnd}})}{\operatorname{erf} \psi} \operatorname{erf} \left(\frac{x}{2\sqrt{\alpha_\ell t}} \right) \quad (11)$$

while the temperature of the solid phase remains at the phase change temperature $T_s(x, t) = T_{\text{pch}}$.

4.1.2. Two-phase Stefan solidification problem

The two-phase Stefan problem refers to the semi-infinite problem in which the initial temperature differs from the phase change temperature. In particular, the solidification problem is considered with the uniform initial temperature $T(x, t = 0) = T_\infty > T_{\text{pch}}$, and with the Dirichlet boundary condition $T(x = 0, t) = T_{\text{bnd}} < T_{\text{pch}}$ for $t > 0$. The material therefore starts to solidify at the boundary and the front propagates within the material similarly to the previous case. The schematic of the two-phase Stefan solidification problem is shown in Fig. 6.

The front location is determined as

$$s(t) = 2\psi\sqrt{\alpha_s t} \quad (12)$$

where $\alpha_s = \frac{k_s}{\rho_s c_s}$ is the thermal diffusivity for the solid phase and ψ is the solution to the modified transcendental equation [12]

Table 1
Thermophysical properties of Rubitherm RT 28 HC [36].

	ρ_s [kg/m ³]	ρ_ℓ [kg/m ³]	c_p [J/kg K]	k [W/m K]	T_{pch} [°C]	L_f [J/kg]
Manufacturer	880	770	2000	0.2	27–29	215
This study	880	770	2000	0.2	28	215

$$\frac{e^{-\psi^2} + \frac{k_\ell}{k_s} \sqrt{\frac{\alpha_s}{\alpha_\ell}} \left(\frac{T_{\text{pch}} - T_\infty}{T_{\text{pch}} - T_{\text{bnd}}} \right) \frac{\exp\left(-\psi^2 \frac{\alpha_s}{\alpha_\ell}\right)}{\operatorname{erfc}\left(\psi \sqrt{\frac{\alpha_s}{\alpha_\ell}}\right)} = \frac{\psi \sqrt{\pi} L_f}{c_p (T_{\text{pch}} - T_{\text{bnd}})}$$

$$= \frac{\psi \sqrt{\pi}}{\operatorname{Ste}_s} \quad (13)$$

The temperature distribution in the solid phase is then determined as [12]

$$T_s(x, t) = T_{\text{bnd}} + (T_{\text{pch}} - T_{\text{bnd}}) \frac{\operatorname{erf}\left(\frac{x}{2\sqrt{\alpha_s t}}\right)}{\operatorname{erf} \psi} \quad (14)$$

and the temperature distribution in the liquid phase follows

$$T_\ell(x, t) = T_\infty + (T_{\text{pch}} - T_\infty) \frac{\operatorname{erfc}\left(\frac{x}{2\sqrt{\alpha_\ell t}}\right)}{\operatorname{erfc}\left(\psi \sqrt{\frac{\alpha_s}{\alpha_\ell}}\right)} \quad (15)$$

4.2. Computational accuracy

The described Stefan problems were solved with the use of the four considered methods: the FT method, the enthalpy method, the apparent heat capacity method, and the temperature recovery method. The reader is referred to the comprehensive study presented by König-Haagen et al. [20] for further comparison of IC methods. Their work includes the use of the heat source method as well as the modifications of the enthalpy method and the apparent heat capacity method.

The commercial phase change material Rubitherm RT 28 HC, which has been used in a number of practical applications in LHTEs, was considered in the study. The thermophysical properties of RT 28 HC declared by the manufacturer [36] are presented in Table 1. Since the study deals with the isothermal phase change, the constant phase change temperature was assumed as shown in Table 1.

All the computational methods adopted the identical spatial and time discretization setup: $\Delta x = 1$ mm and $\Delta t = 0.1$ s, respectively. The explicit time discretization was used in all the methods. Since the apparent heat capacity method is devised for the solution of non-isothermal phase change problems, the temperature range of the phase change was set to 28 ± 0.01 °C. The identical phase change temperature range was also applied to the enthalpy method.

4.2.1. One-phase Stefan melting problem

Initially, the material RT 28 HC was assumed in the solid state with the uniform temperature $T(x, t = 0) = T_{\text{pch}} = 28$ °C. The Dirichlet condition $T(x = 0, t > 0) = T_{\text{bnd}} = 50$ °C at the boundary with properties shown in Table 1 were applied. The computational results for the one-phase Stefan melting problem are presented in Figs. 7–10 and in Tables 2 and 3.

Fig. 7 shows the temperature distributions in the semi-infinite material in three various time instances: 1 h, 5 h, and 10 h. Solid lines are used for the exact temperature distributions given by Eq.

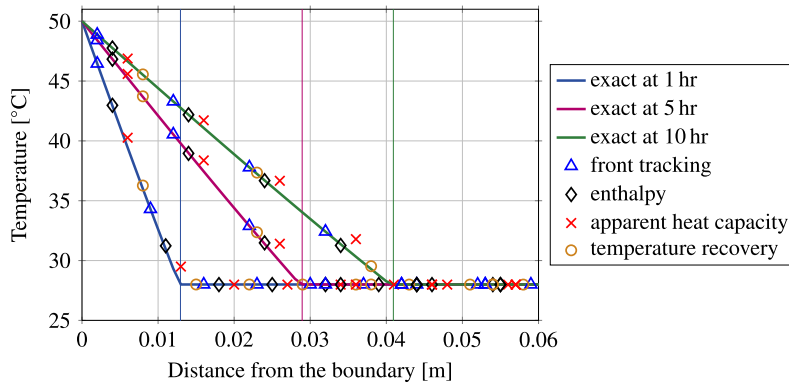


Fig. 7. Temperature distributions for the one-phase Stefan melting problem.

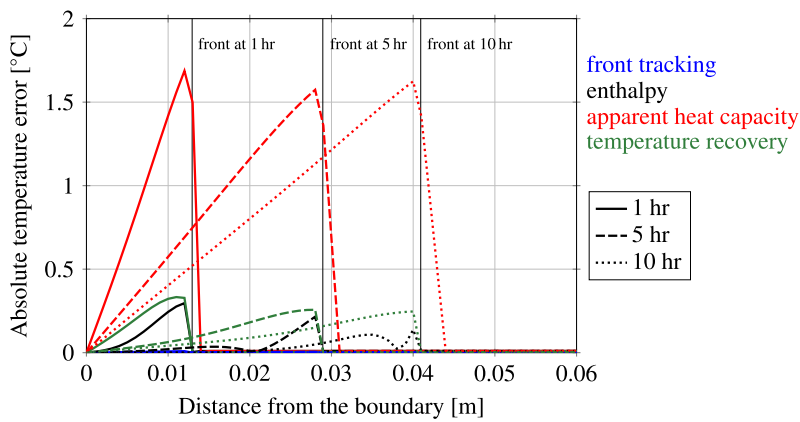


Fig. 8. Absolute temperature errors for the one-phase Stefan melting problem.

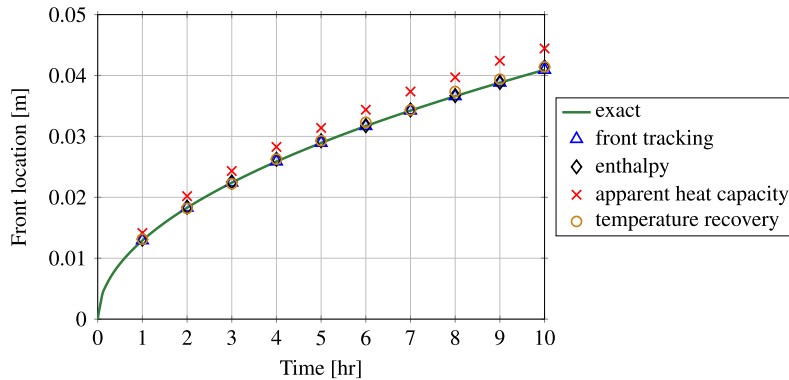


Fig. 9. Front location for the one-phase Stefan melting problem.

(11). Coloured markers represent the numerical solutions. As can be seen in Fig. 7, the FT method, the enthalpy method, and the temperature recovery method seem to provide results which are in a good agreement with the exact solutions. Only in case of the apparent heat capacity method, some deviations from the exact solutions are visible. Fig. 8 and Table 2 show the discrepancies in detail. Fig. 8 shows the absolute temperature error in the numerically gained solutions; the absolute temperature error is determined as $\Delta T_{err,abs} = |T_{exact} - T_{numerical}|$. In general, the temperature

errors shown in Fig. 8 peak near the front location. Such behaviour can be explained by the numerical violation of the energy conservation: violations especially occur in the vicinity of the interface between the phases due to the released or absorbed latent heat. The apparent heat capacity method had the maximum absolute temperature error of more than 1.5 °C, which was the largest error among the considered methods. The enthalpy method and the temperature recovery method exhibited similar temperature errors which peak at about 0.2–0.3 °C. As for the FT method, virtually no

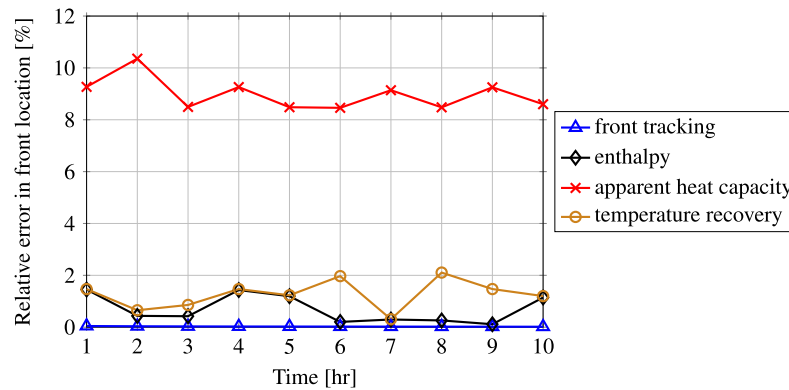


Fig. 10. Relative error in the front location for the one-phase Stefan melting problem.

Table 2
Computational errors in the temperature for the one-phase Stefan melting problem.

		Front tracking method	Enthalpy method	Apparent heat capacity method	Temperature recovery method
Absolute temperature error [°C]	Maximum	0.00896	0.2966	1.8185	0.3737
	Mean	0.00073	0.0183	0.2632	0.0331
Relative temperature error [%]	Maximum	0.0305	1.012	6.464	1.323
	Mean	0.0021	0.061	0.783	0.099

Table 3
Computational errors in the front location for the one-phase Stefan melting problem.

		Front tracking method	Enthalpy method	Apparent heat capacity method	Temperature recovery method
Absolute front location error [mm]	Maximum	0.0073	0.468	3.592	0.771
	Mean	0.0069	0.185	2.588	0.380
Relative front location error [%]	Maximum	0.045	1.45	10.36	2.11
	Mean	0.026	0.70	8.98	1.27

temperature error is observable in Fig. 8 meaning its superior accuracy.

Table 2 summarizes the temperature errors for all four computational methods. Beside the absolute temperature errors, the relative temperature errors were also evaluated. The relative temperature error was determined as

$$\Delta T_{\text{err,rel}} = \frac{|T_{\text{exact}} - T_{\text{numerical}}|}{T_{\text{exact}}} \quad (16)$$

Values in Table 2 confirm the previous conclusions and they demonstrate a superior accuracy of the FT method. Indeed, the FT method allows for about two orders of magnitude smaller temperature errors than the enthalpy method, which is comparable with the temperature recovery method. On the other hand, the apparent heat capacity method leads to the results with the largest errors.

Fig. 9 shows the computational results for the front location. Similar to the case of the temperature distribution, the FT method, the enthalpy method, and the temperature recovery methods provide results in a good agreement with the exact solution. Results gained with the use of the apparent heat capacity method clearly show disturbances and numerical inaccuracy.

The relative error of the front location is visually demonstrated in Fig. 10. The front location determined with the apparent heat capacity method is affected by the relative error of about 9%. Much better results are achieved with the enthalpy method and the temperature recovery method: with about 1–2% relative error. The FT method, similarly as in case of the temperature distribution,

shows an insignificant relative error in Fig. 9.

Table 3 shows an overview on computational errors related to the front location. Very similar conclusions as in case of Table 2 can be drawn. Results computed with the use of the FT method are influenced by errors which are about two orders of magnitude smaller than those of the enthalpy method and the temperature recovery method. The apparent heat capacity again leads to the results significantly influenced by numerical errors.

4.2.2. Two-phase Stefan solidification problem

Similarly as in case of the one-phase Stefan problem, the uniform temperature distribution $T(x, t = 0) = 50^\circ\text{C} > T_{\text{pch}}$ was assumed in the domain which corresponds to the liquid phase. The Dirichlet boundary condition $T(x = 0, t > 0) = T_{\text{bnd}} = 20^\circ\text{C} < T_{\text{pch}}$ and properties shown in Table 1 were applied. The computational results for the two-phase Stefan solidification problem are presented in Figs. 11–14 and Tables 4 and 5.

Fig. 11 shows the temperature distributions at 1 h, 5 h, and 10 h. Solid lines represent the exact temperature distributions according to Eqs. (14) and (15), coloured markers symbolize the numerical solutions. As can be seen in Fig. 11, all the computational methods show a good agreement with the exact solution including the apparent heat capacity method. Fig. 12 shows the absolute errors evaluated for the temperature distributions. The behaviour of the enthalpy method, the apparent heat capacity method, and the temperature recovery method is relatively similar: the absolute errors peak at about 0.4°C .

Slightly better accuracy was obtained in case of the enthalpy

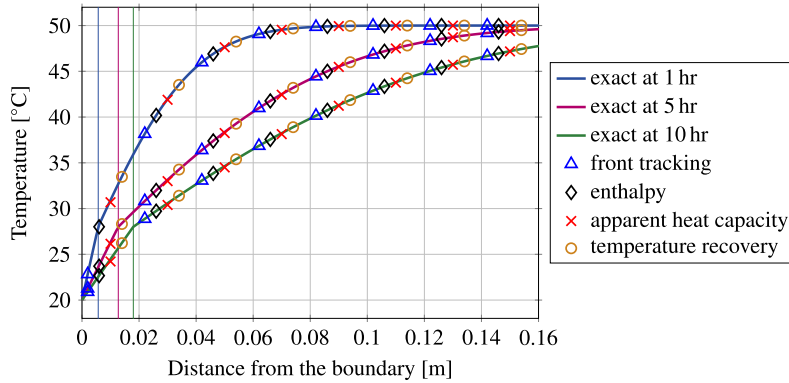


Fig. 11. Temperature distributions for the two-phase Stefan solidification problem.

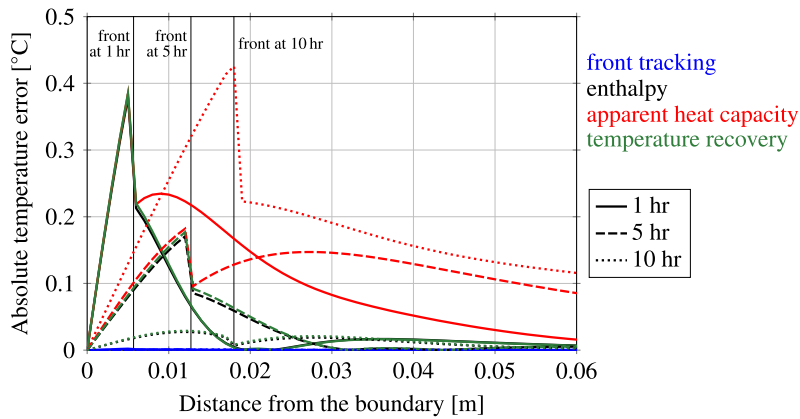


Fig. 12. Absolute temperature errors for the two-phase Stefan solidification problem.

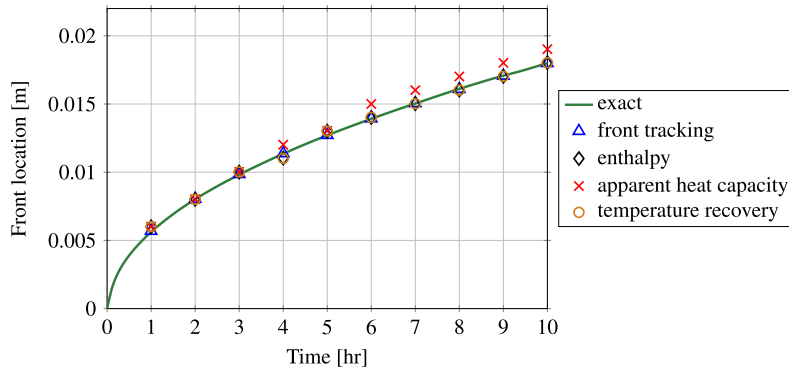


Fig. 13. Front location for the two-phase Stefan solidification problem.

method and the temperature recovery method than with the use of the apparent heat capacity method. As in case of the one-phase problem, no visible error is seen in Fig. 12 for the FT method. Table 4 presents the overall evaluation of the computational errors related to the temperature distribution. Conclusions similar to the one-phase problem can be drawn from Table 4: the FT method provides about two orders of magnitude better accuracy than the three IC methods. On the other hand, in case of the two-phase problem the accuracy of the apparent heat capacity method is

comparable with the enthalpy method and the temperature recovery method. The probable explanation lies in the less intensive heat transfer and lower heat fluxes between the ambient environment and the material through the boundary of the domain. Such conditions lead to better fulfilment of energy conservation than in case of the one-phase Stefan problem.

Fig. 13 shows the phase change front location. Almost identical behaviour as in case of the one-phase problem is observable in Fig. 13. The FT method, the enthalpy method, and the temperature

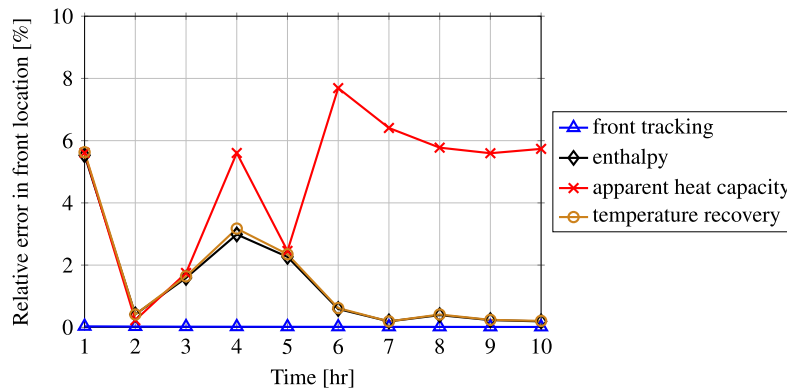


Fig. 14. Relative error in the front location for the two-phase Stefan solidification problem.

Table 4
Computational errors in the temperature for the two-phase Stefan solidification problem.

		Front tracking method	Enthalpy method	Apparent heat capacity method	Temperature recovery method
Absolute temperature error [°C]	Maximum	0.00221	0.3784	0.5234	0.3847
	Mean	0.000069	0.0023	0.0175	0.0024
Relative temperature error [%]	Maximum	0.0082	1.399	1.886	1.422
	Mean	0.0002	0.007	0.052	0.008

Table 5
Computational errors in the front location for the two-phase Stefan solidification problem.

		Front tracking method	Enthalpy method	Apparent heat capacity method	Temperature recovery method
Absolute front location error [mm]	Maximum	0.0022	0.340	1.071	0.361
	Mean	0.0021	0.138	0.641	0.143
Relative front location error [%]	Maximum	0.032	5.53	7.69	5.63
	Mean	0.018	1.44	4.68	1.49

recovery method provide results in a good agreement with the analytical (exact) solution. The results obtained with the apparent heat capacity method show visible disturbances causing the numerical inaccuracy.

The relative error of the front location is shown in Fig. 14. Again, similar behaviour of the methods can be deduced from these results. The relative error of about 5% in the front location is attained with the apparent heat capacity method. Better results are achieved with the enthalpy method and the temperature recovery method for which the relative error decreases with time. The FT method, as in the previous cases, exerts a negligible relative error in Fig. 14.

Table 5 shows the evaluation of computational errors in the location of the phase change front. Very similar conclusions as in previous cases can be drawn. The results obtained with the use of the FT method are influenced by errors which are about two orders of magnitude lower than those for the other methods. The enthalpy method and the temperature recovery method lead to results influenced by a similar level of numerical error. The apparent heat capacity method provided lower accuracy results than the other methods.

4.2.3. Assessment of computational accuracy

The results for Stefan problems demonstrate that the FT method allows for about two orders of magnitude better accuracy than the three considered IC methods. The maximum relative error influencing the temperature distribution and the front location obtained with the use of the FT method was about 0.03% and 0.045%, respectively. The enthalpy method and the temperature recovery

method provided comparable accuracy. The maximum relative error in the temperature distribution and in the front location determined with the use of the enthalpy method was about 1.40% and 5.53%, respectively. In case of the temperature recovery method, the maximum relative error in the temperature distribution and in the front location was about 1.42% and 5.63%, respectively. The worst results were obtained with the use of the apparent heat capacity method. In that case, the maximum relative error in the temperature distribution and in the front location was about 6.46% and 10.36%, respectively.

The performed simulations identified the FT method as the method with superior behaviour in terms of the computational accuracy. The good performance is especially owing to the explicit treatment of the interface between the phases by means of the Stefan condition. On the other hand, the use of the apparent heat capacity method showed large discrepancies in the computational results. The apparent heat capacity method is not intended for the isothermal phase change while the other three methods are more suitable or even devised to the isothermal case. The findings are in agreement with conclusions of other studies, see e.g. Ref. [20].

4.3. Computational efficiency

Beside the computational accuracy, the numerical methods can also be classified according to how much (wall-clock) time a method needs to complete a computation of a certain problem. This property is frequently referred to as the computational efficiency. Faster methods are often preferred by users as they are more

suitable for the process simulation and control. However, the computational efficiency is usually not a sole parameter and it has to be considered together with other parameters, especially with the computational accuracy since these two frequently compete with each other.

The previous study of the authors [28] investigated the influence of various discretization schemes to the computational accuracy and efficiency. The study compared the simple explicit scheme, the simple implicit scheme, and the alternating-direction explicit and implicit schemes. The influence of the time discretization scheme on the computational accuracy was identified as minor—with a reasonable discretization setup, numerical errors were kept at roughly the same magnitude for various schemes. On the other hand, the time discretization scheme directly influences the computational efficiency. Since the explicit schemes are conditionally stable, the size of the time step is strictly limited otherwise the method becomes divergent. On the contrary, the implicit schemes are known for their unconditional stability implying no limit to the time step [11]. However, the earlier results [28] demonstrated that the ratio between the computational times of various methods do not vary significantly with the time discretization scheme. Due to these reasons, the simple explicit time discretization scheme [2] was used to assess the computational efficiency. The simple explicit scheme has the second-order spatial accuracy and the first-order time accuracy [49]. The simple explicit scheme is also selected with regard to the parallel implementation discussed in the following section.

The relative computational time (RCT) per spatial node was used as a measure for the evaluation of the computational efficiency as it allows for the appropriate comparison of the results acquired for problems with the distinct duration and with the distinct number of computational nodes. The RCT per spatial node δt_{node} is a dimensionless ratio between the elapsed wall-clock time the method needs to complete the simulation t_{comp} and the simulated time period t_{sim} of the process

$$\delta t_{\text{node}} = \frac{1}{N} \frac{t_{\text{comp}}}{t_{\text{sim}}} \quad (17)$$

where N is the number of computational spatial nodes included in the model.

A set of simulations with various numbers of the spatial nodes was carried out with the use of the computer having the Intel Quad CPU 2.40 GHz, 8 GB RAM, and the Ubuntu 16.04 LTS system. The time step $\Delta t = 0.1$ s was set to all the methods. Table 6 shows the RCT per spatial node for all the methods.

As can be seen in Table 6 the apparent heat capacity method attains the lowest value of the RCT, meaning the method is the fastest one. The temperature recovery method and the enthalpy method have about 8% and 22%, respectively, higher values of the RCT than in case of the apparent heat capacity method. This can be explained by the additional numerical treatment for every spatial node: the transformation between the enthalpy and the temperature in case of the enthalpy method and the treatment of the temperature reservoir in case of the temperature recovery method. The highest value of the RCT was observed for the FT method. Indeed, the FT method required between two and 2.5-times more

computational time than the other methods. This makes the FT method the slowest method in the comparison. However, this conclusion was expectable as the FT method requires a number of operations related to interface tracking.

5. GPU acceleration of the front tracking method

The comparison of the computational accuracy and efficiency shows that the FT method has the superior computational accuracy in comparison to other methods. However, it has the lowest computational efficiency which makes it the slowest method. On the other hand the apparent heat capacity was identified as the fastest method but with poor computational accuracy. The enthalpy method seems to be a good compromise in terms of the accuracy and the efficiency, which is in agreement with conclusions drawn by König-Haagen et al. [20]. However, the increase of the computational accuracy of the FT method over the enthalpy method is significant. An obvious question arises; is there a way to improve the efficiency of the FT method?

5.1. Acceleration strategies

A number of approaches to enhance the computational efficiency exist. These range from the optimization of numerical codes, to the reduction of nested for-loops, to concurrent data processing. The parallel computing represents a way to accelerate computational models. Several approaches exist including the use of multiple central processor units (multi-CPU) and graphics processing units (GPUs). Pan and Yin [34] reported a study into the parallel computation of the FT method for multiphase flow simulations. The authors utilized the multi-CPU approach by means of the MPI architecture and they reported that the parallel model is two-times to ten-times faster than the non-parallel model. Jiang et al. [15] applied GPUs and a parallel algorithm to the solution of the partial differential equation for diffusion. The reported speed-up by the GPUs ranged up to 40. Klimeš and Stětina [18] developed a computational heat transfer and solidification model for the steel production and they utilized its implementation in CUDA/C++ suitable for processing by means of GPUs. The speed-up of the model acquired with the use of the GPU was almost 70. Motivated by results obtained with the use of GPUs, the GPU computing approach with the CUDA environment was applied for the acceleration of the FT method.

5.2. GPUs and parallel GPU programming

A graphics processing unit is a device intended for parallel processing. A GPU consists of a large number of computational units which are devised for the SIMD (single instruction multiple data) architecture: computational units concurrently perform an identical code but each unit processes different data [33]. From a computer component used originally in computer gaming, the GPUs have developed into the mature technology suitable for scientific parallel computing. Nowadays, GPUs fully support the double precision, contain thousands of computational units with the peak performance attaining 2 Tflops.

The FT method was accelerated for the use with NVIDIA GPUs.

Table 6
Computational efficiency of the methods.

	Front tracking method	Enthalpy method	Apparent heat capacity method	Temperature recovery method
Relative computational time per spatial node [—]				
Maximum	11.105×10^{-5}	5.231×10^{-5}	4.470×10^{-5}	4.823×10^{-5}
Mean	10.738×10^{-5}	5.079×10^{-5}	4.167×10^{-5}	4.484×10^{-5}

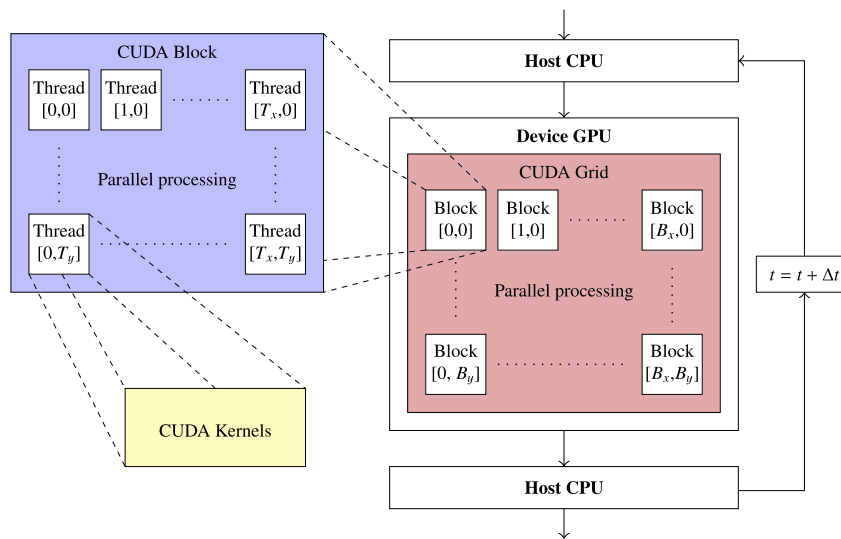


Fig. 15. Schematic of code processing with GPUs.

NVIDIA as a producer provides the CUDA architecture which serves as an interface between the GPU and the programmer. The GPU processing is controlled from the CPU which is referred to as the host while the actual parallel processing takes place at the GPU which is referred to as the device. The code written in CUDA, which is suitable for GPU processing, consists of kernels that represent a part of the code processed in parallel. The concurrent processing is performed by CUDA which launches the grid consisting of parallel blocks, each accommodating parallel threads. The schematic of the processing with the GPU is shown in Fig. 15. Further implementation details on CUDA and GPU programming are not discussed here and they can be found elsewhere, e.g. Ref. [7].

5.3. GPU implementation of the front tracking method

The FT method was implemented with the use of the control volume method and the explicit discretization scheme in time. The explicit discretization is crucial for the parallel GPU implementation as it leads to independent relationships allowing a straightforward parallelism of the solution. Two main classes of procedures for the parallel FT method were implemented. One consisted of the instructions and operations related to the interface tracking, advection of markers, evaluation of their normal velocities and of the Stefan condition, and to the interface reconstruction (steps 1–3 in the description of the FT method in Section 3.2). It is worth pointing out that a major part of operations related to front tracking is suitable in their nature for parallel processing as they can be performed independently on distinct markers.

The second class of procedures includes of the code implementing the parallel solution of the heat transfer equation in the phases (step 4 in the description of the front tracking method in Section 3.2). As mentioned earlier, the explicit formulation in time

allows for the straightforward parallelism since unknown values of temperatures in the computational nodes can be evaluated independently of each other. The details related to the parallel solution of the heat transfer equation were already published by the authors in their previous work [18], and therefore they are not discussed here.

5.4. Results and assessment of the GPU acceleration

The GPU-based implementation of the FT method was tested with the use of the GPU NVIDIA Tesla and Kepler. Distinct setups of the spatial discretization, and thus of the number of spatial nodes were analysed. The results of the GPU acceleration are presented in Table 7 for four computational grids with various numbers of spatial nodes. The GPU speed-up shown in Table 7 was determined as the dimensionless ratio between the absolute computational time of the non-parallel CPU-based FT method and the absolute computational time of the GPU-accelerated FT method as defined in Ref. [18].

As can be seen in Table 7, the speed-up for the coarse grid is almost negligible. The reason for this behaviour is that the performance of the GPU is lost in the data transfer and latency in the communication between the GPU and the host [37]. As the number of computational nodes increases, the parallel performance and computational capabilities of the GPU get into action. For the fine grid with 10^5 computational nodes, the GPU-accelerated model allows for the speed-up of about 11. The case with the finest tested mesh having 10^6 computational nodes led to the highest speed-up of about 27. The results in Table 7 demonstrate that the higher number of computational nodes leads to the higher value of the speed-up. The use of GPUs is therefore beneficial especially in cases with a large number of parallel threads. This conclusion is in

Table 7
GPU acceleration of the front tracking method.

	Coarse grid	Medium grid	Fine grid	Very fine grid
Number of computational nodes	10^3	10^4	10^5	10^6
GPU speed-up	1.1	4.2	11.4	27.3

agreement with the concept of GPU computing as well as with results of other investigators (see e.g. Refs. [50,34,28]). The results in Table 7 also demonstrate that the use of GPUs can mitigate the main drawback of the FT method: a lower computational efficiency discussed in the foregoing section.

6. Limitations and issues with front tracking

Though the FT method has many beneficial properties, there are some issues and difficulties, which are not often mentioned and discussed in the literature. A short discussion on such limitations and issues is provided below.

6.1. Existence of the interface

The FT method considered in the paper assumes that the front separating the phases is located in the domain at all times. This brings some difficulties especially in situations with only one phase in the initial state $t = 0$ with the assumption that another phase and the front will develop at $t > 0$. This issue can be overcome by several approaches. One of them is to consider kinetics laws and the local undercooling evaluation [31,4]. This technique can be used for the initialization of the front and its movement in its initial state. Once the front is developed, the method can switch to the use of the Stefan condition. Another approach is to utilize one of the IC method on a mesh with a high local refinement near the boundary. Such approach is then a hybrid combination of interface capturing and tracking. Since the IC methods do not require the existence of the interface at all times, a suitable IC method can be used to initialize the front. As in the previous case, once the front is established the algorithm can switch to the FT method.

6.2. Implementation in 3D

The implementation of the FT method in 3D is a fairly complicated problem. Most FT models reported in the literature are therefore implemented into computer programs in 1D and 2D though the mathematical formulation for 3D is available. Several approaches employing 1D and 2D methods can be used for the determination of solutions for 3D problems. The moving slice approach [38] is based on the use of the 2D model, which moves within the 3D domain. The 3D solution is then reconstructed from a set of the 2D solutions. The line-by-line method originally proposed by Patankar [35] is another approach applicable to the solution of 3D cases. The line-by-line method is based of the solution of 1D or 2D sub-problems in all three directions or planes, respectively. The 3D solution is then reconstructed from such solutions.

6.3. Isothermal and non-isothermal phase change

The FT method discussed in the paper is devised for the solution of phase change problems with the isothermal phase change. The method is therefore well applicable for pure materials (aluminium, copper, titanium etc.) that have the constant phase change temperature, or for materials with a narrow phase change temperature interval which can be approximated by the isothermal process. In cases with a wider phase change temperature interval, the interface governed by kinetics laws can be applied [6]. However, the presence of the mush (a mixture of two phases) makes the model more complicated as it involves the solution of the solidification process and the grain transitions (see e.g. Ref. [4]). This may discourage users aimed at the analysis of heat transfer only. Moreover, the use of the kinetics laws require the knowledge of various material properties (e.g. rate coefficients of solidification), which are not trivial to determine.

7. Conclusions

The use of the front tracking method for the solution of phase change problems was investigated. The analysis of the computational accuracy and computational efficiency was carried out for four computational methods including the front tracking method and three interface capturing methods: the enthalpy method, the apparent heat capacity method, and the temperature recovery method. The front tracking method was accelerated by means of the graphics processing units (GPUs). The following conclusions can be drawn from the study:

- the front tracking method has so far been rarely used in practical applications though its accuracy surpasses the interface capturing methods;
- the front tracking method is about two orders of magnitude more accurate in both the temperature and the interface location than the considered interface capturing methods;
- processing of the front tracking method is slower in comparison to interface capturing methods;
- unlike the interface capturing methods, the front tracking method retains high accuracy even in case of a rather coarse mesh;
- the GPU-based acceleration of the front tracking method allows for significant speed-up of calculations;
- the accelerated front tracking method is applicable for accurate and fast simulations in real time.

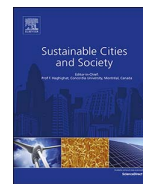
Acknowledgement

This paper has been supported by the project Sustainable Process Integration Laboratory—SPIL, No. CZ.02.1.01/0.0/0.0/15_003/0000456, funded by European Research Development Fund, Czech Republic Operational Programme Research, Development and Education, Priority 1: Strengthening capacity for quality research and by the project funded by the Czech Science Foundation under the number GA15-11977S.

References

- [1] Al-Saadi SN, Zhai Z. Modeling phase change materials embedded in building enclosure: a review. *Renew Sustain Energy Rev* 2013;21:659–73.
- [2] Anderson D, Tannehill JC, Pletcher RH. *Computational fluid mechanics and heat transfer*. third ed. Boca Raton: CRC Press; 2011.
- [3] Battaglioli S, Robinson AJ, McFadden S. Axisymmetric front tracking model for the investigation of grain structure evolution during directional solidification. *Int J Heat Mass Tran* 2017;115:592–605.
- [4] Bonacina C, Comini G, Fasano A, Primicerio M. Numerical solution of phase-change problems. *Int J Heat Mass Tran* 1973;16:1825–32.
- [5] Browne DJ, Hunt JD. A fixed grid front-tracking model of the growth of a columnar front and an equiaxed grain during solidification of an alloy. *Numer Heat Transf B-Fundam* 2004;45:395–419.
- [6] Cheng J, Grossman M, McKercher T. *Professional CUDA C programming*. first ed. Birmingham: Wrox; 2014.
- [7] Dutil Y, Rousse DR, Salah NB, Lassus S, Zaleski L. A review on phase-change materials: mathematical modeling and simulations. *Renew Sustain Energy Rev* 2011;15:112–30.
- [8] Dusanberre GM. *Numerical methods for transient heat flows*. *Trans ASME* 1945;67:703–12.
- [9] Eyres NR, Hartree DR, Ingham J, Jackson R, Sarjant RJ, Wagstaff JB. The calculation of variable heat flow in solids. *Phil Trans Roy Soc Lond Math Phys Sci* 240:1–57.
- [10] Farlow SJ. *Partial differential equations for scientists and engineers*. first ed. Mineola: Dover Publications; 1993.
- [11] Hahn DW, Özisik MN. *Heat conduction*. third ed. New York: Wiley; 2012.
- [12] Hashemi HT, Sliepcevich CM. A numerical method for solving two-dimensional problems of heat conduction with change of phase. *Chem Eng Prog Symp Ser* 1967;63:34–41.
- [13] Hong CP, Umeda T, Kimura Y. Numerical models for casting solidification: Part II. Application of the boundary element method to solidification problems. *Metall Trans B* 1984;15:101–7.
- [14] Jiang B, Dai W, Khaliq A, Carey M, Zhou X, Zhang L. Novel 3D GPU based

- numerical parallel diffusion algorithms in cylindrical coordinates for health care simulations. *Math Comput Simulat* 2015;109:1–19.
- [16] Joybari MM, Haghghat F, Seddegh S. Natural convection characterization during melting of phase change materials: Development of a simplified front tracking method. *Sol Energy* 2017;158:711–20.
- [17] Kenisarin M, Mahkamov K. Solar energy storage using phase change materials. *Renew Sustain Energy Rev* 2007;11:1913–65.
- [18] Klimeš L, Stětina J. A rapid GPU-based heat transfer and solidification model for dynamic computer simulations of continuous steel casting. *J Mater Process Technol* 2015;226:1–14.
- [19] Klimeš L, Mauder T, Charvát P, Stětina J. A front tracking method accelerated by graphics processing units for phase change modelling in latent heat thermal energy storage: a comparison with interface capturing methods. *Chem Eng Trans* 2017;61:1039–44.
- [20] König-Haagen A, Franquet E, Pernot E, Brüggemann D. A comprehensive benchmark of fixed-grid methods for the modeling of melting. *Int J Therm Sci* 2017;118:69–103.
- [21] Kravvaritis ED, Antonopoulos KA, Tzivanidis C. Experimental determination of the effective thermal capacity function and other thermal properties for various phase change materials using the thermal delay method. *Appl Energy* 2011;88:4459–69.
- [22] Kuznik F, Virgone J, Roux J-J. Energetic efficiency of room wall containing PCM wallboard: a full-scale experimental investigation. *Energy Build* 2008;40:148–56.
- [23] Labonia G, Timchenko V, Simpson JE, Garimella SV, Leonardi E, Davis GV. Reconstruction and advection of a moving interface in three dimensions on a fixed grid. *Numer Heat Transf B-Fundam* 1998;34:121–38.
- [24] Lamberg P, Lehtiniemi R, Henell A-M. Numerical and experimental investigation of melting and freezing processes in phase change material storage. *Int J Therm Sci* 2004;43:277–287.
- [25] Li C-Y, Garimella SV, Simpson JE. Fixed-grid front-tracking algorithm for solidification problems, Part I: method and validation. *Numer Heat Trans B-Fundam* 2003;43:117–41.
- [26] Li Y, Zhang Y, Li M, Zhang D. Testing method of phase change temperature and heat of inorganic high temperature phase change materials. *Exp Therm Fluid Sci* 2013;44:697–707.
- [27] Liu S, Li Y, Zhang Y. Mathematical solutions and numerical models employed for the investigations of PCMs' phase transformations. *Renew Sustain Energy Rev* 2014;33:659–74.
- [28] Mauder T, Charvát P, Stětina J, Klimeš L. Assessment of basic approaches to numerical modeling of phase change problems—accuracy, efficiency, and parallel decomposition. *J Heat Tran* 2017;139, 084502.
- [29] McFadden S, Browne DJ. A front-tracking model to predict solidification macrostructures and columnar to equiaxed transitions in alloy castings. *Appl Math Model* 2009;33:1397–416.
- [30] Mochnecki B, Lara S. Application of generalized finite difference method in numerical modelling of moving boundary problems. *Sci Res Inst Math Comput Sci* 2003;2:129–43.
- [31] Mooney RP, McFadden S. Order verification of a Bridgman furnace front tracking model in steady state. *Simulat Model Pract Theor* 2014;48:24–34.
- [32] Nedjar B. An enthalpy-based finite element method for nonlinear heat problems involving phase change. *Comput Struct* 2002;80:9–21.
- [33] Owens JD, Houston M, Luebke D, Green S, Stone EJ, Phillips JC. GPU computing. *Proc IEEE* 2008;96:879–99.
- [34] Pan K-L, Yin G-C. Parallel strategies of front-tracking method for simulation of multiphase flows. *Comput Fluids* 2012;67:123–9.
- [35] Patankar S. *Numerical heat transfer and fluid flow*. first ed. Boca Raton: CRC Press; 1980.
- [36] Rubitherm GmbH. Data sheet for RT 28 HC. Available at: www.rubitherm.de/under_Products_PCM_RT_line. Accessed on January 8, 2018.
- [37] Sanders J, Kandrot E. *CUDA by example: an introduction to general-purpose GPU programming*. first ed. Boston: Addison-Wesley Professional; 2010.
- [38] Sarler B, Vertnik R, Lorbiecka AZ, Vušanović I, Sencić B. A multiscale slice model for continuous casting of steel. In: IOP conference series: materials science and engineering, vol. 33; 2012. paper 012021.
- [39] Sereďyński M, Łapka P, Banaszek J, Furmański P. Front tracking method in modeling transport phenomena accompanying liquid-solid phase transition in binary alloys and semitransparent media. *Int J Heat Mass Tran* 2015;90:790–9.
- [40] Stefanescu DM. *Science and engineering of casting solidification*. third ed. New York: Springer; 2015.
- [41] Swaminathan CR, Voller VR. A general enthalpy method for modeling solidification processes. *Metall Trans B* 1992;23:651–64.
- [42] Swaminathan CR, Voller VR. On the enthalpy method. *Int J Numer Meth Heat Fluid Flow* 1993;3:233–44.
- [43] Swaminathan CR, Voller VR. Towards a general numerical scheme for solidification systems. *Int J Heat Mass Tran* 1997;40:2859–68.
- [44] Thomas BG. Review on modeling and simulation of continuous casting. *Steel Res Int* 2018;89, 1700312.
- [45] Tszeng TC, Im YT, Kobayashi S. Thermal analysis of solidification by the temperature recovery method. *Int J Mach Tool Manufact* 1989;29:107–20.
- [46] Udaykumar HS, Shyy W, Rao MM. ELAFINT: a mixed Eulerian-Lagrangian method for fluid flows with complex and moving boundaries. *Int J Numer Meth Fluid* 1996;22:691–712.
- [47] Udaykumar HS, Mittal R, Shyy W. Computation of solid-liquid phase fronts in the sharp interface limit on fixed grids. *J Comput Phys* 1999;153:535–74.
- [48] Verma P, Goel V, Singal SKV. Review of mathematical modeling on latent heat thermal energy storage systems using phase-change material. *Renew Sustain Energy Rev* 2008;12:999–1031.
- [49] Yang WY, Cao W, Chung T-S, Morris J. *Applied numerical methods using MATLAB*. first ed. New York: Wiley; 2005.
- [50] Yang C, Xu Q, Liu B. GPU-accelerated three-dimensional phase-field simulation of dendrite growth in a nickel-based superalloy. *Comput Mater Sci* 2017;136:133–43.
- [51] Zhou D, Zhao CY, Tian Y. Review on thermal energy storage with phase change materials (PCMs) in building applications. *Appl Energy* 2012;92:593–605.
- [52] Zivkovic B, Fujii I. Analysis of isothermal phase change of phase change material within rectangular and cylindrical containers. *Sol Energy* 2001;70:51–61.



PCM thermal energy storage in solar heating of ventilation air—Experimental and numerical investigations



Uroš Stritih^a, Pavel Charvat^b, Rok Koželj^{a,*}, Lubomir Klimes^c, Eneja Osterman^a, Milan Ostry^d, Vincenc Butala^a

^a University of Ljubljana, Faculty of Mechanical Engineering, Aškerčeva 6, 1000 Ljubljana, Slovenia

^b Brno University of Technology, Faculty of Mechanical Engineering, Technická 2896/2, 61669 Brno, Czech Republic

^c Sustainable Process Integration Laboratory - SPIL, NETME Centre, Brno University of Technology, Technická 2896/2, 61669 Brno, Czech Republic

^d Brno University of Technology, Faculty of Civil Engineering, Veverí 331/95, 60200 Brno, Czech Republic

ARTICLE INFO

Keywords:

Energy storage
Phase change materials (PCM)
Experiments
TRNSYS

ABSTRACT

Heating of ventilation air accounts for a significant part of energy consumption in buildings. The paper presents the use of latent heat thermal energy storage (LHTES) heated with a hot air solar energy collector mounted on the facade of the office building at the Faculty of Mechanical Engineering in Ljubljana where experiments have been carried out. The numerical model of the LHTES unit was developed at the Brno University of Technology, implemented as a type in the TRNSYS simulation tool and validated with experimental results. With the use of the developed model the annual savings of the unit were calculated.

1. Introduction

Ventilation heat loss significantly contributes to the energy consumption of buildings. A good indoor air quality is a very important aspect of healthy and comfortable indoor environment and as a result, ventilation is unavoidable in most building environments. There are a number of measures that can be used to decrease the impact of ventilation on energy consumption of a building. Waste heat recovery is increasingly used in building ventilation systems. Another option of energy saving is solar heating of ventilation air. The solar air heating systems are not as widespread as the solar hot water heating systems. On the other hand, solar air heaters are relatively simple devices that can be easily used for heating of ventilation air. In comparison to water-heating solar collectors, the efficiency of solar air heaters (solar air collectors) decreases somewhat steeper with the increasing temperature difference between the ambient temperature and the fluid temperature in collector (Kramer, Thoma, Mehnert, & Fahr, 2014). As a result, the solar air heaters applied for heating of ventilation air operate under more favourable conditions than solar air heaters used for space heating. In the ventilation (fresh) air heating operation of a solar air heater, the outdoor air is drawn into the air heater and the warm air is supplied to the ventilated space. In the space heating operation, the indoor air usually passes through the solar air heater and returns to the indoor environment. The mean air temperature in the solar air heater in case of ventilation air heating operation is lower than the mean air

temperature in case of space heating operation. That translates into the higher efficiency of the solar air heater in the ventilation air heating operation.

Thermal energy storage can be taken into account when the final energy consumption is in the form of heat. Many solar air heating systems operate without thermal energy storage. However, similar to water-based solar heating systems, thermal energy storage mitigates the mismatch between the heat supply and heat demand, and thus it contributes to the higher operation efficiency of solar heating systems. Rock beds and pebble beds represent a typical way of heat storage in solar air heating systems. This kind of sensible heat storage can operate in a wide temperature range from sub-zero temperatures to temperatures of several hundred degrees of Celsius but the energy density is relatively small, especially in narrow temperature ranges. The amount of heat stored in the sensible heat storage medium depends on the weight of the medium, its specific heat capacity and the difference between the initial and final temperature. On the other hand, LHTES can be used when a narrow temperature range of heat or cold storage is required. In latent heat storage systems the temperature of the medium changes only in a narrow temperature range since the medium undergoes a phase change transformation. Materials for LHTES are called Phase Change Materials (PCMs). The phase change from the solid to liquid state and vice versa is mostly used in LHTES (Shukla, Buddhi, & Sawhney, 2009).

In order to be used as latent heat storage media, the PCMs must

* Corresponding author.

E-mail address: rokkozelj1@gmail.com (R. Koželj).

<https://doi.org/10.1016/j.scs.2017.10.018>

Received 31 July 2017; Received in revised form 13 October 2017; Accepted 13 October 2017

Available online 13 November 2017

2210-6707/ © 2017 Elsevier Ltd. All rights reserved.

Nomenclature	
A	Surface area (m^{-2})
a_0	Optical efficiency (-)
a_1	First order coefficient of the efficiency curve (-)
a_2	Second order coefficient of the efficiency curve (-)
c	Specific heat ($J kg^{-1} K^{-1}$)
F_R	Heat removal efficiency factor (-)
h	Heat transfer coefficient ($W m^{-2} K^{-1}$)
H	Length of leading edge (m)
I	Global solar irradiation ($W m^{-2}$)
j	Number of computational domain (-)
k	Thermal conductivity ($W m^{-1} K^{-1}$)
N	Number of iterations (-)
\dot{m}	Air mass flow rate ($kg s^{-1}$)
n	Number of nodes (-)
P	Perimeter (m)
\dot{Q}	Heat flux (W)
Q	Heat (J)
R	Thermal resistance ($m^2 K W^{-1}$)
T	Temperature (K)
t	Time (s)
U	Overall thermal loss coefficient ($W m^{-2} K^{-1}$)
y	Spatial coordinate (-)
ΔT	Temperature difference (-)
Δx	Length of the section (m)
<i>Greek letters</i>	
α	Absorptance (-)
η	Solar thermal collector efficiency (-)
ρ	Density ($kg m^{-3}$)
τ	Transmittance (-)
<i>Subscripts</i>	
a	Ambient
eff	Effective
exp	Experimental
f	Fluid
glob	Global
in	Inlet
ins	Inside
int	Internal
loss	Heat loss
L	Linear dependency
m	Mean
max	Maximum
n	Normal on surface
out	Outlet
outs	Outside
p	Constant pressure
pch	Phase change
PCM	Phase change material
R	Removal
sol	Solar collector
T	Tilted surface
use	Useful
vent	Ventilation
λ	Short-wavelength
<i>Acronyms</i>	
CSM	Compact storage module
EPS	Expanded polystyrene
LHTES	Latent heat thermal energy storage
PCM	Phase change material
PMMA	Poly(methyl methacrylate)
TISS	Thickness insensitive spectrally selective paint
TRNSYS	TRaNsient system simulation

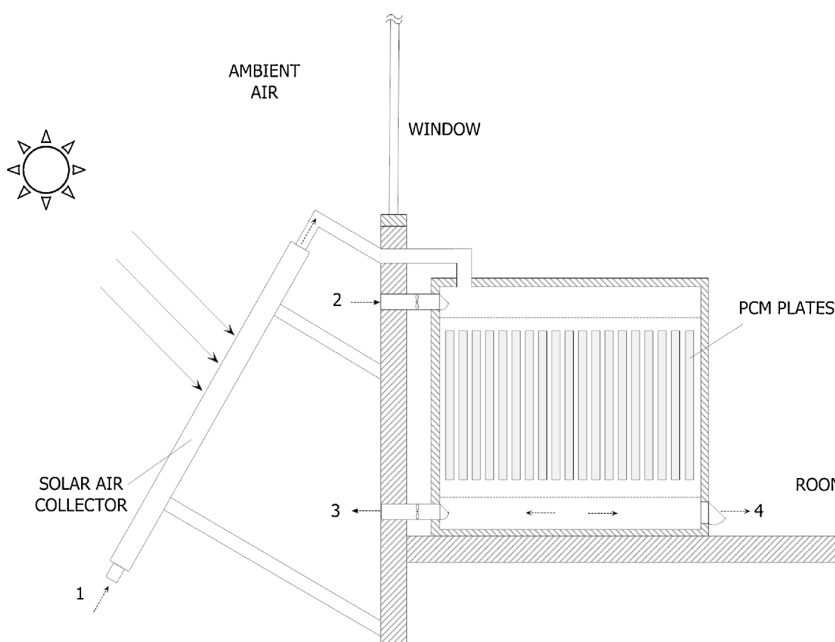


Fig. 1. Schematic of the system.

exhibit certain thermodynamic, kinetic and chemical properties (Tyagi and Buddhi, 2007). The PCM should have a suitable melting temperature, desirable heat of fusion and thermal conductivity required by the practical application (Zhou, Zhao, & Tian, 2012). In the building sector LHTES can be employed for both heat and cold storage. In either case, LHTES is used to balance supply and demand of heat or cold with respect to time and also with respect to power (Sharma, Tyagi, Chen, & Buddhi, 2009). Pardiñas, Alonso, Diz, Kvalsvik, and Fernández-Seara (2017) pointed out that the PCMs in LHTES systems contribute to a higher density of heat storage equipment compared to systems using sensible heat storage only. This approach allows for a reduction in the size of heat storage system.

Numerical simulations are often used in design and optimization of LHTES systems using PCMs as the storage media. Dutil, Rousse, Salah, Lassue, and Zalewski (2011) presented a review on mathematical modelling and simulations of phase change materials and they stated that the problem of predicting the behaviour of PCM-based systems is difficult due to its inherent nonlinear nature at moving interfaces, for which displacement rate is controlled by the latent heat lost or absorption at the boundary.

Heim and Clarke (2004) implemented a numerical model of the PCMs in the ESP-r control volume approach. They used the effective heat capacity method and added the effect of the phase transition to the energy balance equation via a material property substitution. They considered a PCM-gypsum composite as a heat storage building material. Belmonte, Izquierdo-Barrientos, Molina, and Almendros-Ibáñez (2016) reported a numerical simulation of fluidized bed thermal energy storage for an air-based solar heating system. TRNSYS was used as a simulation tool in the study with the model of fluidized bed created in MATLAB. The parametric simulation study included not only the solar air heating system with fluidized bed thermal storage but also a single-zone model of a house. Another study of LHTES in solar air heating was presented by Arkar, Šuklje, and Medved. In this case the LHTES unit was made of two concentric corrugated aluminum tubes where the space between the tubes was filled with microencapsulated PCM and the air passed through the inner tube. Bony (2007) presented a model of PCMs based on the enthalpy method. The model accounts for phase change hysteresis, subcooling and heat transfer by conduction and convection in the PCMs. The model was implemented as a TRNSYS type of a heat storage water tank.

2. System description

A concept of the investigated system, shown in Fig. 1, consists of the solar air collector, the LHTES unit, ductwork and a fan. The system has two basic modes of operation; the heating mode (heating season) and the cooling mode (cooling season). In the heating mode, thermal storage is charged during daytime with the warm air from the solar air collector. The solar air collector is installed on the external wall of an office. Warm air is transported by a fan from the solar air collector to the LHTES unit, where it gives off heat and the PCM melts. From sunset to sunrise, or when the solar radiation intensity is insufficient, the heat stored in the LHTES unit can be used to heat the air – the PCM solidifies and gives off heat to the passing air. The air is then supplied to the space at the temperature that reduces the risk of thermal discomfort.

The operation of the system in the cooling mode consists of two

consecutive cycles. The first cycle, the rejection of heat from the LHTES unit, is carried out at night. The cool outside air is supplied to the LHTES unit to reject heat from the PCM which solidifies and in this way stores cold. The second cycle is used during daytime when the outside warm air enters the LHTES unit. The outdoor air cools down in the LHTES unit before it is supplied to the room. In this cycle the PCM melts.

The test rig was set up in order to experimentally investigate the operation of the LHTES unit. The casing of the unit was made of 8 mm thick PMMA. The external dimensions of the LHTES unit were 0.725 m x 0.460 m x 0.420 m. The LHTES unit was thermally insulated with 50 mm thick EPS. The LHTES unit contained 29 compact storage modules (CSM) filled with paraffin Rubitherm RT22HC which has the melting range between 20 °C and 23 °C and the melting peak temperature of 22 °C. The heat capacity of RT22HC between 14 °C and 29 °C is 200 kJ/kg ± 7.5%. The phase change temperature interval of the PCM was chosen in a way to ensure maximum melting and solidification during the operation of the LHTES unit (the LHTES unit was to be used for both heat and cold storage). During the discharge of heat, the PCM should be able to keep air temperature within the comfort level. The proposed melting point for the Slovenian climate is between 22 °C and 23 °C.

The dimensions of the CSM plates were 0.45 m x 0.30 m x 0.15 m and they were horizontally positioned in the LHTES unit (the longer side perpendicular to the air flow direction). The distance (air gap) between the panels was 10 mm. The average mass of the filled CSM plate was 1361 g, the weight of RT22HC in the CSM plate was 1003 g and the volume of each panel was 1.42 L. Approximately 9% of the CSM plate volume is empty in order to compensate for the volume expansion of the liquid PCM and to avoid deformation of the CSM plate due to higher pressure. The amount of PCM was adapted to the empty space that was available below the window in the office room for the convenient placement of the LHTES. The average ventilation heating load per day according to the test reference year for Ljubljana in the heating season is 4920 kJ/day. Since the heat capacity in the phase change range of the used PCM is 200 kJ/kg and the PCM in one CSM plate weights 1003 g, the LHTES unit would need 25 CSM plates. In order to cover the heat load of ventilation losses in the coldest days, 29 CSM plates were used with the overall heat capacity of 5817 kJ.

In the heating mode (heating season), the outdoor air enters the solar air collector at the point 1 (see Fig. 1) during daytime. The warm air from the solar air collector flows to the LHTES unit where the heat is stored. The heat stored in the LHTES unit can then be used for heating of ventilation air when solar radiation is not available. In the cooling mode (cooling season), the outside air enters the LHTES unit through the opening in the facade (point 2) and passes through the LHTES unit. At night, the cool outdoor air discharges the heat from the LHTES unit whereby the cold is stored in the PCM and air can then be supplied to the room for night cooling (point 4) or redirected outdoors (point 3). During daytime, when cooling demand occurs the outdoor air is cooled down in the LHTES unit before entering the room at the point 4.

The solar air heating collector, a commercial product of SolAir company, has been installed in the considered system. The solar air collector has an area of 1.638 m² and has been mounted vertically on the parapet below the office window. The tilt angle of the solar air collector is thus 90°. The solar absorber plate is made of aluminium

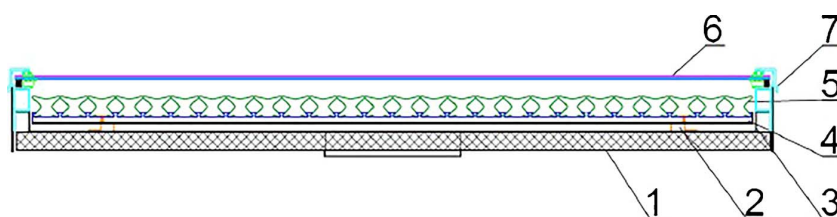


Fig. 2. Structure of the solar air collector (SolAir, 2016).

with the fin thickness of 0.2 mm and with the fin width of 30 mm. Solar absorptance of the absorber is 93% with the tolerance of $\pm 2\%$. Its hemispherical emittance is 35% with the tolerance of $\pm 3\%$. The absorber is painted with a black thickness insensitive spectrally selective (TISS) paint. The air flow channels are connected with no spacing in between and the solar air collector is connected to the LHTES unit inside of the office. The glazing of the solar air collector is made of the extruded solid polycarbonate sheets with the thickness of 4 mm and with the solar transmittance of $90\% \pm 1\%$. Thermal insulation is made of polyethylene and it is located on the backside of the solar air collector while there is no sidewise insulation (SolAir, 2016). The goal in the study was to obtain as much solar gains as possible to have enough heat for air heating. The size of the solar air collector was therefore adapted to the parapet below the office window so that the solar air collector occupied the available space below the window.

In Fig. 2, the structure of the installed solar air collector is shown where elements in the figure are:

- thermal insulation (foamed closed-pore polyethylene) (1),
- spacer made of a heat-resistant plastic (2),
- back assembly of galvanized steel sheet (3),
- absorber holder – stainless sheet (4),
- aluminium absorber (5),
- polycarbonate sheets Macrolux® (6),
- double wall aluminium case (7).

The performance measurements of the solar air collector were done at Fraunhofer Institute for Solar Energy Systems ISE in Freiburg, Germany. Power output of a solar air collector has been obtained through measurements under the steady-state conditions with the calorimetry method. The efficiency of the solar air collector reduced to an aperture area with radiation of normal incidence is 0.703. The value is obtained at the solar irradiation on the solar air collector plane of 961 W m^{-2} , thermal power output of 1290 W and air mass flow rate of 250 kg/h. Fig. 3 shows the power output per solar air collector unit over temperature difference (between the mean air temperature in the solar air collector ϑ_m and the ambient air temperature ϑ_a) at 1000 W m^{-2} of solar irradiation (Fraunhofer, 2014).

3. Experimental investigations

The experimental system shown in Fig. 4 was placed in the office building of Faculty of Mechanical Engineering, University in Ljubljana. The dimensions of the office were $4.0 \text{ m} \times 3.0 \text{ m} \times 2.8 \text{ m}$.

Fig. 5 shows the experimental setup of the thermal energy storage system where measurements of temperature and velocity were

performed. The air temperature was measured with thermocouples at nine locations in the system. The air velocity was measured with an anemometer in the outlet duct of the system where the best conditions for the measurement were established (measurement in a round duct). Since the fan speed was kept constant, the air flow rate was also constant in the system.

The experiments were performed with the constant air flow rate through the LHTES unit which, as already mentioned, was achieved through the constant fan speed. The LHTES unit stored heat during daytime and released it during nighttime by transporting it outdoors. Therefore, the fan operated the whole time and the switching hatch directed the air to the outlet duct of the system which led to outdoors. As a result, maximum heat flows were achieved because the LHTES unit completely released the latent heat during the night time and accumulated the maximum capacity of the latent heat during daytime when solar radiation was present. Thereby the complete response of the LHTES unit was obtained and according to which the computer model can be validated. The system was tested and monitored for several months. The data for the time period of six sunny days in the spring were used for the validation of the numerical model of the LHTES unit. Fig. 6 shows the measured air temperatures for the mentioned time period: the room air temperature (relevant for calculating heat losses of the LHTES unit), the inlet air temperature of the solar air collector, the inlet air temperature of the LHTES unit (which is essentially the outlet air temperature from the solar air collector) and the outlet air temperature of the LHTES unit.

The inlet air temperature of the solar air collector was mainly between $6 \text{ }^\circ\text{C}$ and $34 \text{ }^\circ\text{C}$ with the average temperature of $18 \text{ }^\circ\text{C}$. On March 28 the temperature increased up to $45 \text{ }^\circ\text{C}$. The reason for such high amplitudes was the position of the solar air collector near the envelope of the building. The building envelope (facade) was heated by solar radiation and that is why the surrounding air was also heated by radiation from the building envelope. The location of the solar air collector on the building facade is favorable from the energy performance point of view as the air temperature close to the facade tends to be higher (sometimes significantly) than the outdoor air temperature.

The peaks of the outlet air from the solar collector were around $70 \text{ }^\circ\text{C}$ across all days. The maximum reached $74 \text{ }^\circ\text{C}$ while the minimum temperature was $14 \text{ }^\circ\text{C}$. The maximum outlet temperature from the LHTES unit was $65 \text{ }^\circ\text{C}$ and the minimum temperature was $21 \text{ }^\circ\text{C}$ which means that the temperature level is high enough for heating the air for ventilation of the room.

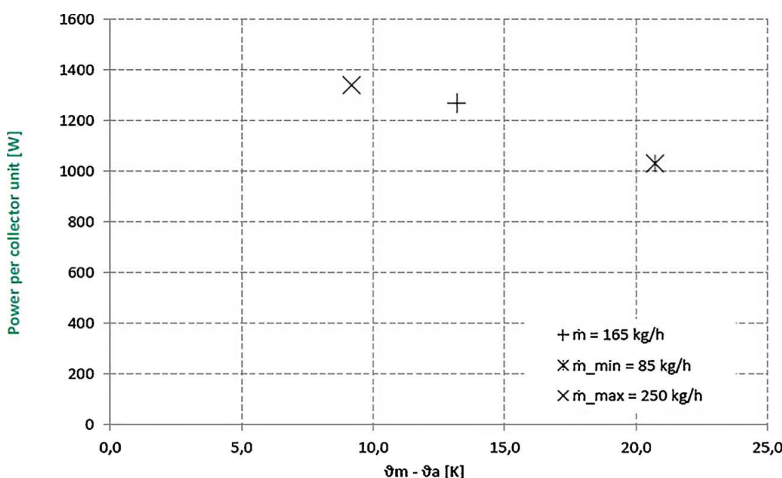


Fig. 3. Power output per solar air collector unit (Fraunhofer, 2014).

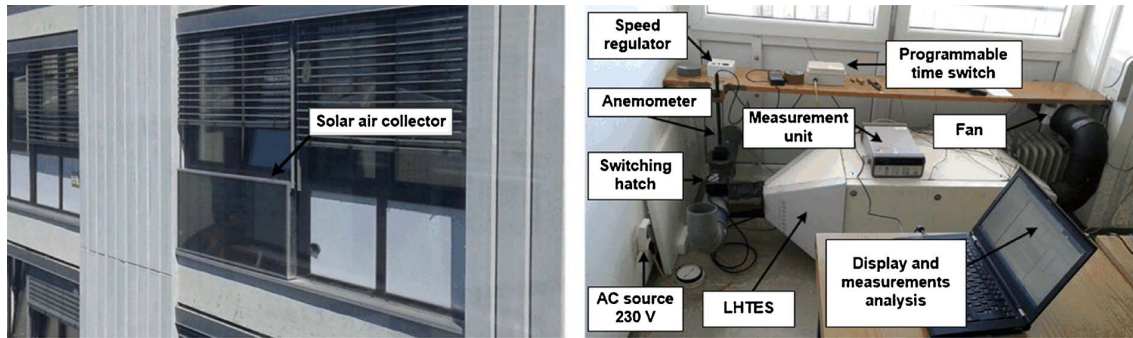


Fig. 4. The LHTES unit with CSM plates (left) and solar air collector (right) of the experimental system.

4. The model of latent heat storage unit in TRNSYS

4.1. Modelling approach, simplifications, assumptions

The model of the LHTES unit was devised as quasi one-dimensional. The mass flow rate of air was assumed to be the same in all air gaps (channels) between the CSM panels. Heat conduction in the PCM was considered only in the direction of the thickness of the CSM panels. Such assumption was based on the dimensions of the CSM panels. The thickness of the panels is much smaller than their other two spatial dimensions and the highest temperature gradient is in the direction of the thickness. Heat transfer between the air and the surface of the CSM panels was calculated by means of correlations for fluid flow between parallel planes. Though the experimental LHTES unit presented in the paper contained two rows of CSM panels the simulation model is not limited to this configuration.

4.2. Concept of the model

The TRNSYS 17 was used as a simulation tool. The model of LHTES unit was implemented as a TRNSYS type. A number of models for thermal energy storage systems were implemented and applied by

various researchers, see e.g. (Al-Saadi & Zhai, 2015; Lu, Liu, Huang, & Kong, 2014; Halawa & Saman, 2011). The model was created as a standalone TRNSYS type in the form of a DLL library. The C++ programming language was used for its implementation. The LHTES unit consists of a number of geometrically identical air channels, which are constituted by gaps between the CSM panels installed in the LHTES unit. As the same air flow rates were considered in all air channels only one air channel between a pair of adjacent CSM panels was modelled. The simulation of heat conduction and phase changes of the PCM inside the CSM panels was the most time consuming part.

4.3. Modelling of heat transfer, phase change, and of the latent heat storage unit

As mentioned above, the TRNSYS model of the LHTES unit utilizes a sub-model which solves the 1D heat conduction equation for the temperature distribution. The latent heat of phase change was taken into account with the use of the effective heat capacity method which relies on the artificial increase of the specific heat in the temperature range of the phase change. The governing equation expressed for one direction reads

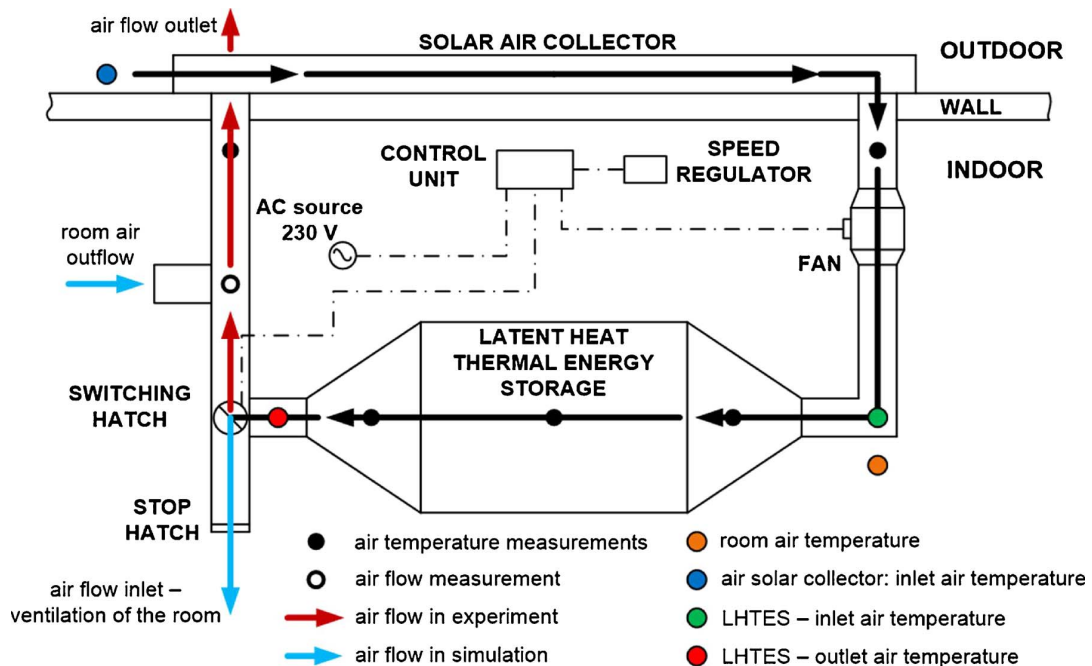


Fig. 5. Experimental setup.

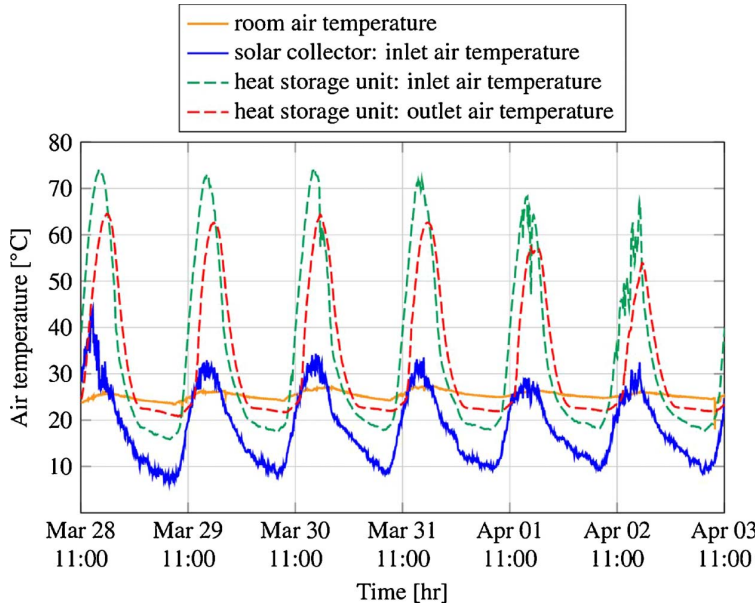


Fig. 6. Measured air temperatures.

$$\rho c_{\text{eff}} \frac{\partial T}{\partial t} = \frac{\partial}{\partial y} \left(k \frac{\partial T}{\partial y} \right) \quad (1)$$

where ρ is the density, c_{eff} as a function of the temperature is the effective heat capacity, k is the thermal conductivity, t is the time, T is the temperature to be determined and y is the spatial coordinate in the direction perpendicular to CSM panels. The reader is referred to the previous work (Charvát, Klimeš, & Ostrý, 2014) for more details on the modeling approach. The application of the LHTES unit model in a TRNSYS simulation involves the use of two distinct time steps. The TRNSYS iterates in time with the use of the global time step Δt_{glob} which is specified by a user. However, the model of the LHTES unit numerically approximates the time derivative in Eq. (1) by means of the explicit time discretization which is conditionally stable. The conditional stability necessitates that the maximum time step for the numerical solution is strictly limited. The maximum time step $\Delta t_{\text{int,max}}$ can be determined from the stability criteria and it is usually significantly smaller than the global time step used in the TRNSYS. The model of LHTES unit therefore uses the internal time step Δt_{int} which is determined as

$$\Delta t_{\text{int}} = \frac{\Delta t_{\text{glob}}}{N_{r,\text{int}}} \quad (2)$$

and

$$N_{r,\text{int}} = \frac{\Delta t_{\text{glob}}}{\Delta t_{\text{int,max}}} \quad (3)$$

is rounded to the closest higher integer. The quantity $N_{r,\text{int}}$ represents the number of the internal time iterations within one global time iteration.

The 1D heat transfer submodel serves as a basic modelling element of the LHTES unit. Let us assume a particular air channel (gap) through

the LHTES unit as shown in Fig. 7. Such air channel is formed by several pairs of (adjacent) CSM panels. The considered air channel can be divided into n sections in the longitudinal direction where each air node (red circle in Fig. 7) represents a particular section.

The detail of a section (a computational domain) of the CSM panel is shown in Fig. 8. The number of nodes used for the calculations can be specified in the model together with the number of sections which should be solved for each panel.

The solution of the thermal behavior in each section includes the use of the 1D heat transfer submodel. The calculation starts in the first section where the air node temperature is considered the same as the inlet temperature $T_{\text{air},1} = T_{\text{air,in}}$. The air node temperature $T_{\text{air},2}$ is calculated from the inlet air temperature $T_{\text{air},1}$, the heat flux to/from the adjacent CSM panels $Q_{\text{PCM},1}$ and the heat loss to the surroundings $Q_{\text{loss},1}$. Then the procedure continues with the next section until the last n -th section is resolved. The schematic of the procedure is shown in Fig. 9.

The heat $Q_{\text{PCM},j}$ transferred (stored or released) between the PCM in the CSM panel and the air flowing in the j -th section in the internal time iteration (during the internal time step Δt_{int}) is determined as

$$Q_{\text{PCM},j} = 2H \Delta x_j h_{\text{ins}} (T_{\text{air},j} - T_{\text{PCM},j}) \Delta t_{\text{int}} \quad (4)$$

where H is the total length of the leading edge of all CSM panels, Δx_j is the length of the j -th section, h_{ins} is the heat transfer coefficient at the surface of the CSM panels, $T_{\text{air},j}$ is the temperature of air and $T_{\text{PCM},j}$ is the surface temperature of the CSM panel filled with the PCM. The heat loss of the j -th section during the internal time step Δt_{int} is determined as

$$Q_{\text{loss},j} = \Delta x_j P \left(\frac{T_{\text{air},j} - T_{\text{ambient}}}{\frac{1}{h_{\text{ins}}} + \frac{R}{h_{\text{outs}}}} \right) \Delta t_{\text{int}} \quad (5)$$

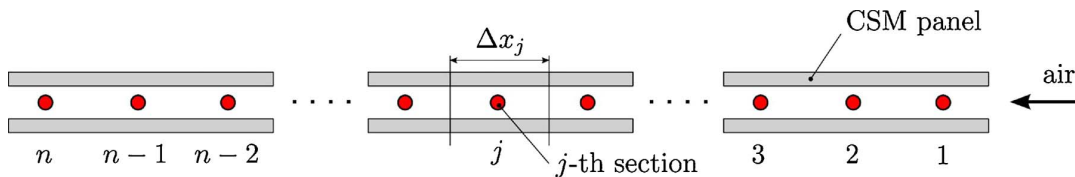


Fig. 7. Schematic of the air flow channel with sections.

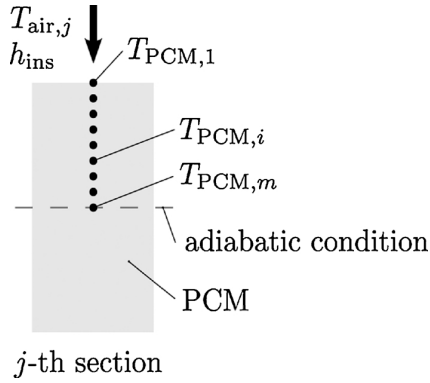


Fig. 8. Schematic of the computational domain of the CSM panel.

Where P is the perimeter of the LHTES unit in the plane perpendicular to the length of the section (to the air flow direction), $T_{ambient}$ is the ambient temperature, R is the thermal resistance of the wall of the LHTES unit including the thermal insulation and h_{outs} is the heat transfer coefficient at the outer surface of the LHTES unit.

The temperature of air flowing in the air channel in the j -th section is then updated according to the energy balance

$$T_{air,j} = T_{air,j-1} - \frac{Q_{loss,j-1} + Q_{PCM,j-1}}{\dot{m}_{air} c_p \Delta t_{int}} \quad (6)$$

Where \dot{m}_{air} is the mass flow rate of the air through the LHTES unit and c_p is the specific heat of air at the constant pressure. As for the first section with $j = 1$, Eq. (6) is replaced by $T_{air,1} = T_{air,in}$ with the assumption that the temperature of air in the first section is equal to the inlet air temperature.

5. Computer model of solar air collector

5.1. General description of solar air collector model

The model implemented in Type 1b for a flat-plate solar collector from the standard TRNSYS library was used for the solar air collector performance modeling. Therefore, the description of the mathematical model in this section is a summary from the TRNSYS manual (TRNSYS, 2014). This model uses a quadratic efficiency equation that is a generalization of the Hottel-Whillier equation. This component models the thermal performance of a solar collector using theoretical relationships. The results from the standard efficiency testing need to be provided – efficiency as a function of solar irradiation (I_T) and temperature difference between the heat transfer fluid (HTF) and ambient temperature (ΔT). The HTF temperature according to European Standards on solar collectors is an average temperature where the model assumes that the efficiency versus the $\Delta T/I_T$ curve can be modeled as a quadratic function. There are also corrections applied to the slope, intercept and curvature parameters to account for the presence of a heat exchanger.

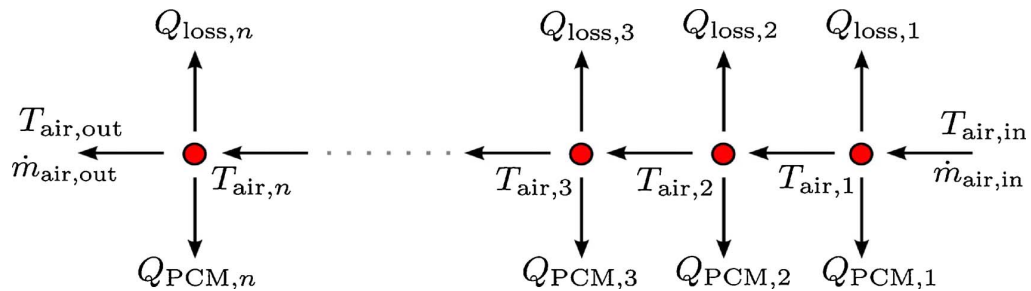


Fig. 9. Schematic of the interaction between the 1D heat transfer submodel, flowing air and surroundings.

There are five possibilities for considering the effects of off-normal solar incidence in Type 1. A second order quadratic function is used to compute the incidence angle modifier in Type 1a. Coefficients of the function are supplied by the ASHRAE or by an equivalent test.

5.2. Mathematical description

A general equation for solar thermal collector efficiency η is obtained from the Hottel-Whillier equation

$$\eta = \frac{Q_{use}}{A I_T} = \frac{\dot{m} c_p (T_{outlet} - T_{inlet})}{A I_T} = F_R (\tau_\lambda \alpha_\lambda)_n - F_R U_{sol} \frac{T_{average} - T_{ambient}}{I_T} \quad (7)$$

Where η is the ratio between the useful energy gain from the solar collector Q_{use} and the global solar irradiation incidenting on the solar collector (tilted surface) I_T with the solar collector aperture area A . The difference between the outlet temperature of the fluid from the solar collector T_{outlet} and the inlet temperature of the fluid to the solar collector T_{inlet} multiplied with the mass flow \dot{m} of the fluid and its specific heat c_p gives the useful energy gained from the solar collector. The optical efficiency a_0 is the product of the short-wave transmittance of the solar collector cover τ_λ and the short-wave absorptance of the absorber plate α_λ at the normal incidence multiplied with the overall solar collector heat removal efficiency factor F_R . Because the overall thermal loss coefficient of the solar collector per unit area U_{sol} is not exactly constant, a better expression is obtained by taking into account a linear dependency of the thermal loss coefficient $U_{sol/L}$ on the temperature difference $T_{average} - T_{ambient}$ presented in Eq. (8).

$$\eta = F_R (\tau_\lambda \alpha_\lambda)_n - F_R U_{sol} \frac{T_{average} - T_{ambient}}{I_T} - F_R U_{sol/L} \frac{(T_{average} - T_{ambient})^2}{I_T} \quad (8)$$

Eq. (8) can be rewritten as

$$\eta = a_0 - a_1 \frac{\Delta T}{I_T} - a_2 \frac{\Delta T^2}{I_T} \quad (9)$$

which is the general solar collector thermal efficiency equation used in Type 1b where a_0 , a_1 and a_2 are coefficients that have to be specified in the model. The coefficient a_0 is the maximal efficiency of the solar collector and depends on optical properties of the glazing and of the absorber; that is why it is called the optical efficiency. The coefficient a_1 is the slope of the efficiency curve. It represents heat losses of the solar collector and is equal to the negative value of the first-order coefficient in the solar collector efficiency equation. The coefficient a_2 then equals to the negative value of the second-order coefficient in the efficiency equation.

Particular values of the coefficients were obtained from test measurements and determined according to equations presented above. The thermal efficiency used for the definition of other parameters refers to the aperture area of the solar air collector and it was obtained from test measurements.

The temperature difference ΔT in Eq. (9) refers to the average

temperature between the inlet and the outlet of solar collector and it equals to the difference between the average solar collector fluid temperature $T_{average}$ and the ambient temperature $T_{ambient}$ as shown in Eq. (10).

$$\Delta T = T_{average} - T_{ambient} \tag{10}$$

6. Validation of the numerical model

In the first step of the study, the computer model of the LHTES unit presented in Section 4 was validated by means of the data acquired experimentally with the use of the setup described in Sections 2 and 3. The data from the six consecutive sunny days (March 28 to April 3, 2017) were used for model validation. Thermocouples were used for the measurement of the air temperature at the inlet and at the outlet of the LHTES unit. The volume flow rate of the air at the inlet of the LHTES unit was determined from the measured air velocity in the inlet duct by means of an anemometer. During the entire six-day period, the air flow rate was maintained at 37 m³/hr, which corresponds to 43 kg/hr.

The model in TRNSYS was configured in agreement with the experimental setup. The experimentally measured inlet air temperature was used as the inlet air temperature in the simulations. The initial temperature of the CSM panels filled with the Rubitherm RT22HC was set to 23 °C. The thermal conductivity of 0.2 W m⁻¹·K and the density of 730 kg/m³ were used for the PCM. The effective heat capacity of the PCM was considered as a function of temperature

$$c_{eff}(T) = 2 + 136 \exp\left(-\frac{(T - T_{pch})^2}{0.5}\right) \tag{11}$$

which corresponds to the phase change temperature interval between 20 °C and 23 °C with the latent heat of 200 kJ/kg reported by the manufacturer of the material (Rubitherm, 2016). The thermal resistance of the insulated outer wall of the LHTES unit was set to 0.5 m² K/W.

The measured air temperatures at the inlet of the LHTES unit and the measured and simulated outlet air temperatures for the six-day period are presented in Fig. 10.

As can be seen in Fig. 10, a fairly good agreement between the experimental measurement and the simulation was achieved. Some minor discrepancies are visible mainly in locations where the derivative

of the inlet air temperature attains its maximum values, i.e. in inflection points of the inlet air temperature curve. The maximum absolute deviation between the simulated and measured outlet air temperatures from the unit was 9.69 K. This maximum occurred on March 29 at about 1:15PM. Though the value of the maximum absolute deviation is quite high, the agreement between the simulated and experimental results, shown in Fig. 10, is overall very good. The temperature deviation has its maxima in time instances for which the derivative (the steepness) of the temperature curve is very high. In other words, almost vertical temperature curves lead to such a high value of the absolute deviation. The mean absolute deviation between the simulated and measured outlet air temperatures from the unit is 0.33 K which implies a good agreement between the data.

Fig. 11 presents heat fluxes which were stored or released in the LHTES unit. The experimental stored/released heat flux was calculated from the inlet and outlet air temperatures as

$$\dot{Q}_{exp} = \dot{m}c_p(T_{air,inlet} - T_{air,outlet}) \tag{12}$$

The heat flux obtained from Eq. (12) includes the heat loss of the LHTES unit. In case of the simulation it was possible to obtain stored/released heat flux and the heat loss of the LHTES unit separately. The stored/released heat flux was directly computed by the developed TRNSYS Type 256 from the actual temperature of air flowing through the LHTES unit and the surface temperature of the CSM panels. The heat loss, in Type 256, was calculated from the U-value of the LHTES unit envelope and the difference between the air temperature in the LHTES unit and the ambient temperature. For better comparison with experimental results the heat flux obtained from the simulation, shown in Fig. 11, includes the heat loss of the LHTES unit. Similarly to the outlet air temperatures, a good agreement was achieved between the experimental data and the simulation results. Some discrepancies are present near peaks of the heat fluxes.

Fig. 12 presents the daily-evaluated amounts of heat stored in or released from the heat storage LHTES unit for the considered six-day period. Only a complete 24-h days were investigated and those are presented in Fig. 12. The amount of heat stored in or released from the LHTES unit was determined as an integral value of the heat fluxes presented in Fig. 11,

$$Q_{stored} = \int_{t \in t_{storage}} \dot{Q} dt \tag{13}$$

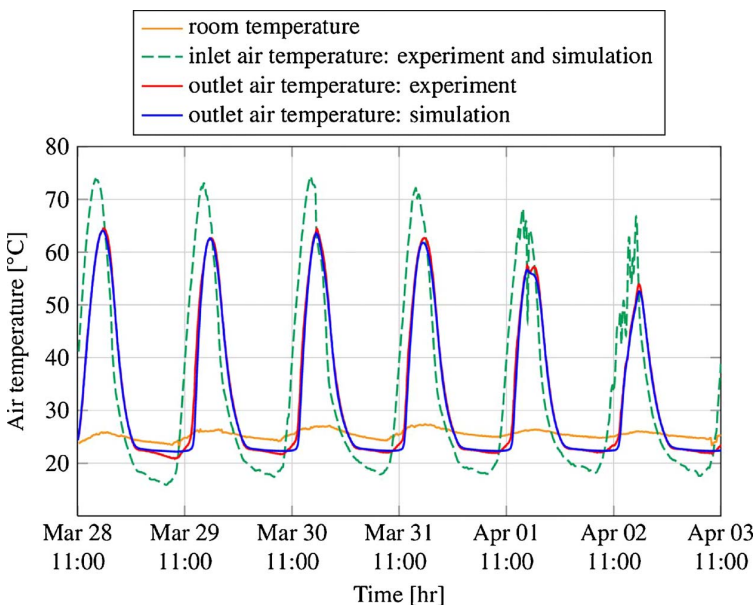


Fig. 10. Comparison of the outlet air temperatures from the LHTES unit.

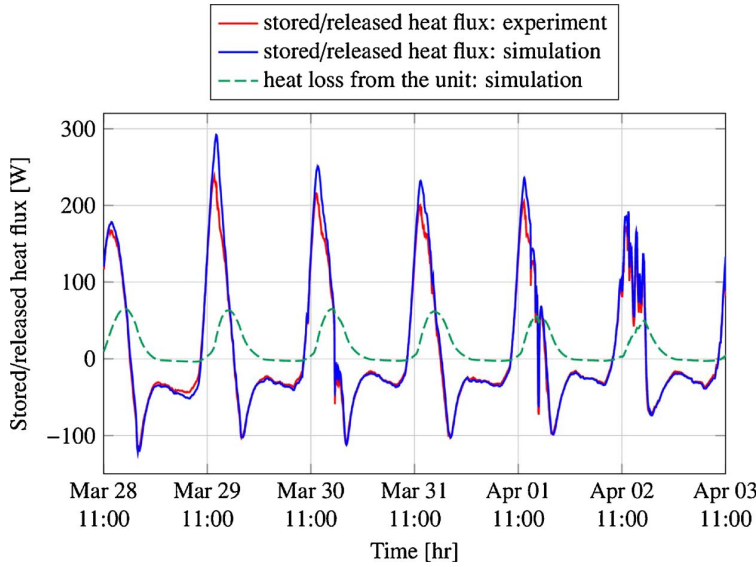


Fig. 11. Comparison of stored and released heat flux in the LHTES unit.

and

$$Q_{\text{released}} = \int_{t \in t_{\text{release}}} \dot{Q} dt \quad (14)$$

where t_{storage} corresponds to the time intervals in which the heat is stored in the LHTES unit (positive heat fluxes in Fig. 11) while t_{release} corresponds to the time intervals in which the heat is released from the LHTES unit (negative heat fluxes in Fig. 11). As can be seen in Fig. 12, a relatively good agreement was achieved between the experimental data and simulation results. Reasons for difference between the simulation and the experiment are discrepancies near the peaks of the heat fluxes shown in Fig. 11.

7. Annual analysis

The developed and validated TRNSYS model was used in the second step of the study for the annual analysis of the performance of LHTES unit. The annual simulation was performed for the heating season (from October to April) in Ljubljana, Slovenia, using weather data file distributed with TRNSYS 17. These data were obtained from the

Meteonorm. The simulation was performed for the ventilation of the office room where the system was assumed to operate from 8:00 to 16:00. The annual analysis was carried out only for the heating season because the analysis of the cooling season with the validated numerical model of the considered system was already presented by Osterman, Butala, and Stritih (2015).

Simulation results for the heating season are presented in the organized diagram on Fig. 13. The exterior temperature represents the temperatures of outdoor air which has a direct influence on ventilation loss. The collector outlet temperature is the inlet air temperature in the office room with the use of the solar air collector but without the LHTES unit. The LHTES outlet temperature is the inlet air temperature in the office room with the use of the solar air collector and the LHTES unit. As can be seen in Fig. 13 the temperature level at the outlet of the LHTES unit is higher than the temperature level at the solar air collector outlet. The area between the LHTES outlet and the collector outlet curves indicates the energy potential of the heat storage in the LHTES unit in the ventilation system. In annual analysis the comparison between ventilation system with solar air collector with LHTES unit and

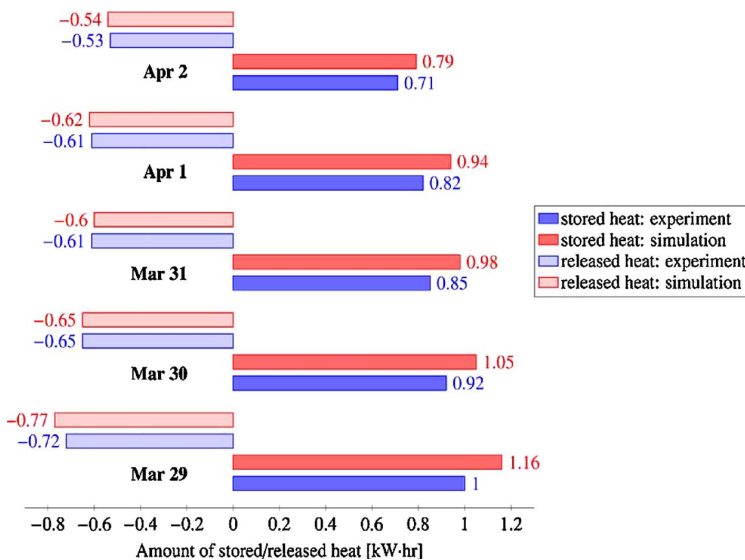


Fig. 12. Comparison of the amount of heat in heat storage and heat release periods.

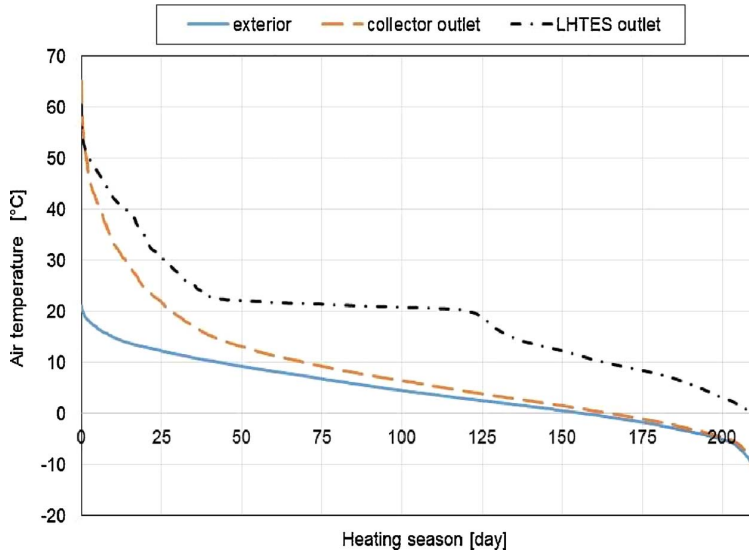


Fig. 13. Air temperatures for the heating season.

without LHTES unit was made.

Fig. 14 presents the ventilation air temperatures supplied to the room. It can be seen that the LHTES unit increases the average temperature of the ventilation air supplied to the room. The distance between the curves implies on the stored or released heat in the PCM storage. In time instances where the solar air collector curve is higher than the LHTES unit curve, heat will be stored in the LHTES unit. On the other hand, in case the solar air collector curve is lower than the LHTES unit curve, then heat will be released from the LHTES unit. The time when the air from the LHTES unit has the temperature around 20 °C represents about 36% of the total ventilation time. This shows the impact of the LHTES unit on the indoor thermal comfort. Parts of the curves where the temperature is above 20 °C represent excess heat – the system provides more heat than it is necessary to cover the ventilation heat loss and that excess heat can be utilized to cover the transmission heat loss of the room.

Table 1 shows the stored and released heat for each month during the heating season for the operating hours (8:00 to 16:00). If the stored heat is higher than the released heat, it means that in average for a considered month the outlet temperature of the solar air collector has a higher temperature than at the outlet of PCM storage. If the released heat is higher than the stored heat then the opposite conclusion applies. The stored heat has the highest value in March and April as well as the lowest value of the released heat what is the consequence of the highest solar radiation and of the highest outside temperature in the heating season. The stored heat has the lowest value in December meaning that December was the month with the lowest solar radiation and, according to ventilation losses in Table 2, the second coldest month. The highest value of the released heat was in January (9 kWh) and with the comparison to the stored heat in that month (7 kWh) it can be concluded that January was a cold month; and according to ventilation losses from Table 2 it is seen that January was the coldest month. The same applies for February but the stored heat is higher than the released heat meaning that the solar radiation was very high.

The energy balance analysis was carried out from obtained hourly-average values of temperatures from the simulation. First, the ventilation losses Q_{vent} were calculated with the use of following Eq. (15).

$$Q_{vent} = \sum_{i=1}^n \dot{m}c_p(T_{room} - T_{exterior,i})\Delta t \quad (15)$$

where T_{room} is the constant temperature of air in the room (20 °C), $T_{exterior,i}$ is the outside air temperature, \dot{m} is the average mass flow rate

of air through the system defined from velocity measurements and Δt is the time interval. Afterwards the total heat Q_{total} gained from the system was calculated according to Eq. (16).

$$Q_{total} = \sum_{i=1}^n \dot{m}c_p(T_{outlet,i} - T_{exterior,i})\Delta t \quad (16)$$

where $T_{outlet,i}$ presents the outlet air temperature of the solar air collector or of the LHTES unit. The difference between the total heat gained without the use of the LHTES unit and the total heat gained with the use of the LHTES unit represents the stored heat (if the value of the difference is positive) or the released heat (if the value of the difference is negative). The temperature of air supplied to the room is of a significant importance for maintaining indoor thermal comfort. If the supplied air temperature is higher than the room temperature the excess heat occurs and is therefore subtracted from the total heat gained from the system, thus this excess heat presents waste heat to the environment. This represents the measure of the useful heat which is in this case the same as ventilation losses. If the temperature of air supplied to the room is smaller than the room temperature then total heat gained is smaller than ventilation losses. In this case the useful heat of the system is the same as total heat gained of the system and additional heating is required.

Table 2 shows the results for which the energy balance of the

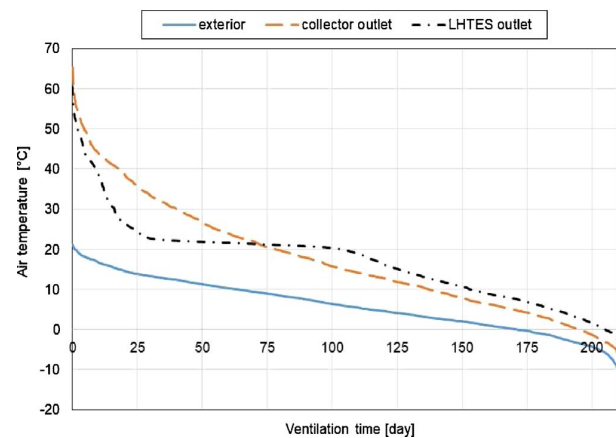


Fig. 14. Ventilation air temperatures for the ventilation period.

Table 1
Stored and released heat in the simulation.

Month	Stored heat [kWh]	Released heat [kWh]
October	9	7
November	6	8
December	5	8
January	7	9
February	9	8
March	10	6
April	11	5
Σ	56	51

Table 2
Energy balance of the system.

Mon	Required heat [kWh]	Useful heat [kWh]		Additional heating [kWh]	
		Ventilation losses	No storage	Storage	No storage
Oct	23	16	20	7	3
Nov	41	16	22	25	19
Dec	58	19	26	39	32
Jan	61	23	30	38	31
Feb	46	24	31	22	16
Mar	37	23	28	14	10
Apr	23	19	22	4	2
Σ	290	140	178	150	112

Table 3
Coverage ratio and time ratio.

Month	Coverage ratio [%]		Time ratio for total coverage [%]		Time ratio when T < 15 °C [%]	
	No storage	Storage	No storage	Storage	No storage	Storage
Oct	69%	89%	53%	80%	23%	8%
Nov	39%	54%	26%	34%	69%	58%
Dec	32%	44%	17%	21%	78%	72%
Jan	37%	49%	19%	21%	75%	70%
Feb	53%	66%	29%	36%	58%	46%
Mar	62%	74%	47%	65%	37%	27%
Apr	81%	92%	64%	81%	15%	4%
AVG	53%	67%	36%	48%	51%	41%

Table 4
Economic analysis.

	Solar air collector	LHTES unit	District heating
Investment [€]	500	770	10000
Lifetime	25	25	25
Amortization annual costs [€/a]	20	31	400
Required energy for additional heating [kWh/a]	150	112	290
Costs of energy source for additional heating [€/a]	8	6	16
Auxiliary electrical energy [kWh/a]	9	9	80
Operating costs [€/a]	9	7	21
Annual costs [€/a]	29	37	421
Annual savings according to district heating [€/a]	392	383	–
Annual savings regarding operating costs only [%]	58%	68%	–
Annual savings regarding all costs [%]	93%	91%	–
Return period [year]	1	2	–

ventilation system is presented. Ventilation losses represent the losses without the solar air collector and without the LHTES unit in the

ventilation system. Based on these results, the evaluation of the effectiveness of the ventilation system was assessed. The effectiveness was calculated as the coverage ratio ε of ventilation losses according to Eq. (17). Since the average ventilation heat losses per month was 61 kWh and the heating load (heat losses minus heat gains) of the office was 51 kWh, the investigation focused only on the ventilation losses of the office room.

$$\varepsilon = \frac{Q_{use}}{Q_{vent}} \quad (17)$$

where Q_{use} is equivalent to Q_{vent} for $T_{outlet,i} > T_{room}$ meaning that the excess heat is rejected. If $T_{outlet,i} < T_{room}$ then Q_{use} is equivalent to Q_{total} and additional heating is required.

Results of the coverage ratio of ventilation losses with and without the LHTES unit are presented in Table 3, where are also results of the time ratio when ventilation losses are completely covered. In the last two columns in Table 3 are results of the time ratio when the outlet temperature of the system (supplied air temperature to the room) is less than 15 °C. From obtained results it can be seen that the ventilation system with the LHTES unit achieves a greater effectiveness throughout the entire heating season than ventilation system without the LHTES unit. The highest coverage ratio of ventilation losses is in the transitional period between seasons in April (92%) and October (89%). The lowest coverage occurs in December (44%) in agreement with the previous conclusion that December was the month with the lowest solar radiation and with the second coldest temperature. The average coverage ratio throughout the heating season of the system with the LHTES unit is 67% and 53% of the system without the LHTES unit.

The coverage ratio can also be interpreted as energy savings of the system according to the required heat for covering total ventilation losses without an additional system. The amount of additional heat required for covering the difference between ventilation losses and the useful heat gained from the additional system is presented in Table 2.

A basic economic analysis of the experimental system is presented in Table 4 and compared to heating from the district heating system. Only the price of energy source was taken into account without additional costs of network charge and other monetary contributions that are included in the overall cost of energy source.

8. Conclusions

A numerical model of the LHTES unit (air-PCM heat exchanger) was implemented as a TRNSYS type and it has been validated with experimental data. The simulation of the annual performance of the solar ventilation air heating system with and without LHTES was conducted for a Test Reference Year for Ljubljana. The simulation results show that the highest coverage ratio of ventilation heat loss was in the transitional period between seasons – April (92%) and October (89%). The lowest coverage occurred in December (44%) as it was the month with the lowest solar radiation gain and the second lowest outdoor air temperature. The average coverage ratio in the heating season for the system with and without LHTES was 67% and 53%, respectively.

Annual cost savings, in comparison to district heating, with all costs considered were 91% for the system with LHTES and 93% for system without LHTES. The evaluated return of investment was one year for the system without LHTES and two years for the system with LHTES. If only operating costs for the energy use were taken into account, without consideration of the amortization costs of investment, then the annual savings for the system without LHTES were 58% and those for system with LHTES were 68%. Savings of the system with LHTES regarding only operating costs in comparison to the system without LHTES were 24%.

Acknowledgement

On the Slovenian side this study was financially supported by the

Slovenian Research Agency through the research program P2-0223. On the Czech side study was supported by the Czech Science Foundation project No. 15-19162S “Research and development of heat storage media based on the phase change materials for higher energy performance of buildings” and by the project Sustainable Process Integration Laboratory – SPIL, No. CZ.02.1.01/0.0/15_003/0000456, funded by European Research Development Fund, Czech Republic Operational Programme Research, Development and Education, Priority 1: Strengthening capacity for quality research.

References

- Al-Saadi, S. N., & Zhai, Z. (John) (2015). A new validated TRNSYS module for simulating latent heat storage walls. *Energy and Buildings*, *109*, 274–290.
- Arkar, C., Šuklje, T., Vidrih, B., & Medved, S. (2016). Performance analysis of a solar air heating system with latent heat storage in a lightweight building. *Applied Thermal Engineering*, *95*, 281–287.
- Belmonte, J. F., Izquierdo-Barrientos, M. A., Molina, A. E., & Almendros-Ibáñez, J. A. (2016). Air-based solar systems for building heating with PCM fluidized bed energy storage. *Energy and Buildings*, *130*, 150–165.
- Bony, C. (2007). Comparison between a new trnsys model and experimental data of phase change materials in a solar combisystem. *Building & simulation conference: 2*, (pp. 371–378).
- Charvát, P., Klimeš, L., & Ostrý, M. (2014). Numerical and experimental investigation of a PCM-based thermal storage unit for solar air systems. *Energy and Buildings*, *68*, 488–497.
- Dutil, Y., Rousse, D. R., Salah, N. B., Lassue, S., & Zalewski, L. (2011). A review on phase-change materials: mathematical modeling and simulations. *Renewable and Sustainable Energy Reviews*, *15*(1), 112–130.
- Fraunhofer Institute for Solar Energy Systems ISE, Freiburg, Germany. Test report according to EN 12975-1:2006+A1:2010/EN ISO 9806:2013 (2016).
- Halawa, E., & Saman, W. (2011). Thermal performance analysis of a phase change thermal storage unit for space heating. *Renewable Energy*, *36*(1), 259–264.
- Heim, D., & Clarke, J. A. (2004). Numerical modelling and thermal simulation of PCM-gypsum composites with ESP-r. *Energy and Buildings*, *36*(8), 795–805.
- Kramer, K. S., Thoma, C., Mehnert, S., & Fahr, S. (2014). Testing solar air-heating collectors. *Energy Procedia*, *48*, 137–144.
- Lu, S., Liu, S., Huang, J., & Kong, X. (2014). Establishment and experimental verification of PCM room's TRNSYS heat transfer model based on latent heat utilization ratio. *Energy and Buildings*, *84*, 287–298.
- Osterman, E., Butala, V., & Stritih, U. (2015). PCM thermal storage system for ‘free’ heating and cooling of buildings. *Energy and Buildings*, *106*, 125–133.
- Pardiñas, Á.Á., Alonso, M. J., Diz, R., Kvalsvik, K. H., & Fernández-Seara, J. (2017). State-of-the-art for the use of phase-change materials in tanks coupled with heat pumps. *Energy and Buildings*, *140*, 28–41.
- Rubitherm (2016). *Data sheet*. Berlin: Rubitherm Technologies GmbH Accessible on: https://www.rubitherm.eu/media/products/datasheets/Techdata_RT22HC_EN_29062016.PDF.
- Sharma, A., Tyagi, V. V., Chen, C. R., & Buddhi, D. (2009). Review on thermal energy storage with phase change materials and applications. *Renewable and Sustainable Energy Reviews*, *13*(2), 318–345.
- Shukla, A., Buddhi, D., & I. Sawhney, R. (2009). Solar water heaters with phase change material thermal energy storage medium: A review. *Renewable and Sustainable Energy Reviews*, *13*(8), 2119–2125.
- SolAir. Solar air collector. Solair d.o.o., Celje (2016).
- TRNSYS 17 manual, Mathematical Reference, Volume 4; Solar Energy Laboratory, University of Wisconsin-Madison (2014).
- Tyagi, V. V., & Buddhi, D. (2007). PCM thermal storage in buildings: A state of art. *Renewable and Sustainable Energy Reviews*, *11*(6), 1146–1166.
- Zhou, D., Zhao, C. Y., & Tian, Y. (2012). Review on thermal energy storage with phase change materials (PCMs) in building applications. *Applied Energy*, *92*, 593–605.



Thermally activated wall panels with microencapsulated PCM: comparison of 1D and 3D models

L. Klimeš ^{a,b,*}, P. Charvát ^b and M. Ostrý^c

^aSustainable Process Integration Laboratory, NETME Centre, Brno University of Technology, Technická 2896/2, 61669 Brno, Czech Republic; ^bDepartment of Thermodynamics and Environmental Engineering, Brno University of Technology, Technická 2896/2, 61669 Brno, Czech Republic; ^cInstitute of Building Structures, Brno University of Technology, Veveří 331/95, 60200 Brno, Czech Republic

(Received 4 August 2017; accepted 29 October 2018)

The paper deals with the comparison of the one-dimensional (1D) and three-dimensional (3D) models of a thermally activated wall panel with a microencapsulated phase change material. The 3D model was created in the off-the-shelf simulation tool COMSOL Multiphysics. The 1D model was an in-house developed TRNSYS type. The main advantage of the 1D model is the short computation time but it comes at the expense of lower accuracy and less detailed results. In most building performance simulations, however, detailed knowledge of the temperature distribution over the surface of a wall is not important. For this reason, the results of both models were compared in terms of the mean surface temperature of the wall panels, the outlet water temperature, and the overall heating and cooling capacity of the panels. The two models provided very similar results for the practical range of water flow rates. The mass flow rate of water had a relatively small influence on the mean surface temperature and the heating and cooling capacity of the panels. For the one-tube mass flow rates of water between 0.25 and 2 g/s, the mean surface temperature was in the range of 28–29.5°C in the heating scenario and 21–21.5°C in the cooling scenario, with the heating and cooling capacity ranges of 65 W/m² to 75 W/m² and 35 W/m² to 40 W/m², respectively.

Keywords: thermally activated building structure; phase change material; latent heat thermal energy storage; TRNSYS; COMSOL multiphysics

1. Introduction

Current energy policies in many developed countries promote the use of renewable energy sources. Since some of these sources, such as wind or solar radiation, are naturally variable, energy storage needs to be used in order to balance the supply and demand of energy. A new term ‘energy flexible buildings’ was introduced in this context (Reynders et al. 2018). A significant part of energy consumption in buildings is in the form of thermal energy (heating and cooling), therefore, it makes sense to use thermal energy storage (TES) in buildings. TES in buildings can be part of building energy systems, usually as heat and cold storage tanks, or it can be integrated with building structures. This concept has led to the combination of a thermally-activated building system (TABS) with TES in phase change materials (PCMs). Latent heat thermal energy storage (LHTES) integrated with the TABS increases the energy flexibility of a building, as reported by a number of investigators, e.g. (Park et al. 2014).

The TABS have attracted a lot of attention in connection with low-temperature heating and high-temperature cooling in buildings. Large surface areas in the TABS

make it possible to bring the heat transfer fluid (HTF) temperature closer to the room temperature than in case of other systems, such as fan coil units (Lehmann et al. 2011). That makes TABS suitable for the use with heat pumps and other low exergy heating and cooling sources.

Chilled water systems, which are also commonly used in buildings, operate with the HTF (usually water) temperature between 4°C and 7°C (supply HTF temperature). The temperature of the HTF in high-temperature cooling systems is much higher (e.g. 18°C as considered in the present study). In some cases or locations, groundwater can be used as an HTF in high-temperature cooling systems directly. This makes it possible to avoid mechanical cooling altogether. In most cases however, the main advantage of high-temperature cooling is that the cooling machinery (heat pumps, chillers, etc.) can operate with a higher coefficient of performance as the HTF does not need to be cooled to low temperatures.

A certain disadvantage of the TABS is that they need to be considered in an early stage of building design and their application in building retrofits is more complicated. However, a highly applicable option for building retrofits

*Corresponding author. Email: klimes@fme.vutbr.cz

seems to be the use of wall and ceiling panels that can be mounted on the surfaces of existing building structures. The efficiency and performance of a TABS is strongly dependent on its thermal capacity. Generally, the larger the thermal mass the larger the amount of thermal energy that can be stored in the structure. Therefore, the thermal mass enhances the energy flexibility of space heating or cooling and also stabilizes the indoor environment in terms of temperature fluctuations. The integration of PCMs into building structures seems to be a promising way of increasing the thermal capacity of the structures (Parameshwaran et al. 2012). The latent heat of fusion accompanying the phase change allows for a significant increase in thermal capacity.

TES, and especially LHTEs, integrated with building structures have recently attracted the attention of many researchers and investigators. The paper presented by de Gracia and Cabeza (2015) reviewed building structures that employ TES. The authors reported that TES allows for the reduction of heating and cooling demands, while also reducing peak shaving and increasing energy efficiency. Heier, Bales, and Martin (2015) published a detailed study on various TES technologies used in different types of buildings. The authors analysed active and passive systems, including TABS, for their suitability for residential and commercial buildings. Tatsidjoudoung, Pierres, and Luo (2013) provided a comprehensive review on both organic and inorganic materials suitable for TES in building applications. They reported that PCMs have, in comparison to materials for sensible heat storage, higher energy storage density and various melting temperatures that allow for different levels of use in buildings. Zhou, Zhao, and Tian (2012) published an overview on the available methods for integration of PCMs into building structures. The direct incorporation, immersion, and encapsulation methods were described and compared. The authors concluded that microencapsulated PCMs do not suffer from leakage and that the microencapsulation is easier and more economic than other ways of incorporating PCMs into building structures.

Many investigators developed and tested one-dimensional (1D) models of TABS, which were then used for thermal analyses and optimization of building systems. The present paper deals with the comparison of 1D and three-dimensional (3D) models of the thermally activated wall panel with a plaster containing a microencapsulated PCM (MPCM). The idea behind is to use the 1D model in practical applications as it is much faster than the 3D model. The 1D model was developed and implemented as a standalone C++ library for TRNSYS (referred to as a type in the TRNSYS environment). The detailed 3D model, including coupled heat transfer with phase changes and fluid flow phenomena, was built in the off-the-shelf FEM software COMSOL Multiphysics. The results of the models are in fairly good agreement.

2. TABS in building simulation tools

Several building simulation tools provide models of thermally activated building structures or systems. However, some of these models are only usable with sensible heat storage materials. Romani, de Garcia, and Cabeza (2016) presented a comprehensive review on simulation and control strategies of TABS. Literature relating to radiant floors and ceilings, core slabs, pipe-embedded envelopes, and general TABS were included in the study. The authors concluded that computer models and dynamic simulations are essential for the accurate assessment of TABS performance. Since numerical simulations of TABS are time-consuming and complex, a number of simplified models have been developed, mostly based on the finite difference method (FDM) and the finite element method (FEM). Romani, de Garcia, and Cabeza (2016) reported that FDM models are often developed for integration in building simulation environments such as ESP-r, TRNSYS, and EnergyPlus, while more computationally demanding FEM models are built and solved separately in commercial software.

2.1. Systems with sensible heat TES

A comparison of embedded-tube radiant floor models in building performance simulation (BPS) tools was presented by Brideau et al. (2016). The authors used TRNSYS, ESP-r, and EnergyPlus to simulate the behaviour of a hydronic radiant floor and they compared the results with the FEM performed with the LISA software. The authors reported discrepancies between the results of the BPS tools. Park et al. (2014) numerically investigated thermal comfort and energy consumption of TABS combined with a radiant floor heating system and a packed air conditioning system in the conventional and low-thermal-load residential buildings. The authors created their model of the investigated room in EnergyPlus and they applied the model in the thermal performance study. The authors concluded that the proposed system is a feasible solution when applied to low-thermal-load buildings with a lower energy consumption. Schmelas, Feldmann, and Bollin (2017) carried out a case study into the savings through the adaptive predictive control of TABS. They created a resistance-capacitance (RC) model of TABS. The authors reported that although the RC model is relatively simple, it is very appropriate for the proposed model-based predictive control which relies on a multiple linear regression. Saelens, Parys, and Baetens (2011) presented a study into energy and comfort performance of TABS including occupant behaviour. They created a model of a typical office floor in TRNSYS with the use of the multi-zone building type. The authors reported that the implementation of occupant behaviour into the model had a significant influence on cooling demands and thermal comfort in comparison with a model with the idealized cooling and standardized user

behaviour. The reduction of peak requirements for cooling by means of TABS was presented by Rijkssen, Wise, and van Schijndel (2010) who investigated a concrete floor with embedded pipes. The model was created in TRNSYS with the use of the multi-zone building type combined with a floor heating system. The authors compared simulation results with experimentally gathered data and a good agreement was achieved. Yu et al. (2014) carried out a comparison of an analytical solution, a two-dimensional (2D) simulation, and a simulation in EnergyPlus for a hollow core concrete deck. The 2D model was created in a commercial software while an integrated system module for TABS was utilized in EnergyPlus. They pointed out that neglected thermal resistances in the EnergyPlus module lead to overestimation of the cooling and heating capacity. The authors proposed a simple modification of the module improving its accuracy.

2.2. Systems with latent heat TES

The simulation of the TABS becomes more complex when the thermally activated structure is combined with latent heat TES. A simulation model in such cases needs to account for transfer and storage of latent heat. There are three basic approaches to the modelling of phase change problems: the enthalpy method, the effective heat capacity method (sometimes referred to as the apparent heat capacity method), and the temperature recovery method. Each of these basic approaches can be combined with a variety of numerical methods as reported by Mauder et al. (2017).

Pomianowski, Heiselberg, and Jensen (2012) investigated a TABS consisting of hollow core concrete ceiling decks incorporating a PCM for TES. The influence of a concrete layer with a microencapsulated PCM in the decks was analysed. The 2D model of the TABS was created in COMSOL Multiphysics. The effective heat capacity method was used for the phase change modelling. The authors reported that the use of PCMs in TABS had promising potential, but they also pointed out that theoretical assumptions on the thermal properties of the concrete with PCM overestimated its performance when compared with the results obtained experimentally. Mazo et al. (2012) reported the modelling of a radiant floor system with a PCM. The authors used the 1D FDM with the effective capacity method applied for PCM modelling. The authors compared the results of their model with the results of ESP-r but only for a case without PCM and without thermal activation. A numerical model for walls with PCMs, implemented in TRNSYS, was presented by Delcroix, Kummert, and Daoud (2017). The developed model used an explicit FDM for the solution of the conductive heat transfer equation and the enthalpy method was employed to address the temperature dependent heat capacity of the PCM. Both the phase change hysteresis and supercooling of the PCM were considered in the model.

Weinläder, Klinker, and Yasin (2016) reported on the experimental testing of two designs of cooling ceilings containing PCM. The two designs differed in the position of the PCM relative to the pipes for the HTF. The authors only reported the results for the passive cooling operation mode where both types of ceiling exhibited similar performance in terms of cooling power at various room temperatures and room cooling loads. Lachheb et al. (2017) reported a computational study on the thermal behaviour of a hybrid plaster accommodating a microencapsulated PCM. The authors created their computational 1D model based on the enthalpy method formulated by means of the finite volume method. The model was validated against data from the literature and was consequently used for an analysis of the thermal performance. Borreguero et al. (2011) investigated gypsum wallboards containing various contents of a microencapsulated PCM. The authors created a 1D computer model based on the apparent heat capacity method and they used the model for the thermal testing of wallboards with PCMs. The authors reported that a wallboard containing 5% of microcapsules allowed for the reduction of the wallboard thickness by 8.5% while maintaining the same comfort conditions.

2.3. Implications for the development of the present models

The review of existing works shows that a number of computer models for various TABS and building systems with and without PCMs have been developed. The enthalpy method and the effective (or apparent) heat capacity method are frequently utilized in case of PCM modelling. Furthermore, the majority of the models are implemented in 1D due to the fact that the dominant heat flux in TABS is in one direction. Such models are sufficiently accurate and fast enough to make them applicable for design, optimization, and even real-time control applications.

In the present paper, a 1D computer model of thermally activated wall panels with a microencapsulated PCM is proposed and implemented as a TRNSYS type. The wall panels considered in the study were a variant of actual wall panels investigated at the Brno University of Technology. A 3D FEM model, created in COMSOL Multiphysics, was used for the validation of the 1D TRNSYS model.

3. Thermally activated wall panels with PCM

In the present paper, the considered TABS with latent heat TES consisted of wall panels with embedded plastic tubes for the liquid HTF, the distribution system for the HTF, and a reversible air-to-water heat pump for heating and cooling of the HTF. The TABS was intended for use in lightweight buildings; therefore, the panels were designed to be mounted on the indoor surfaces of the building structures. The panels increase the energy flexibility of a building, such as in the case of a heat pump powered

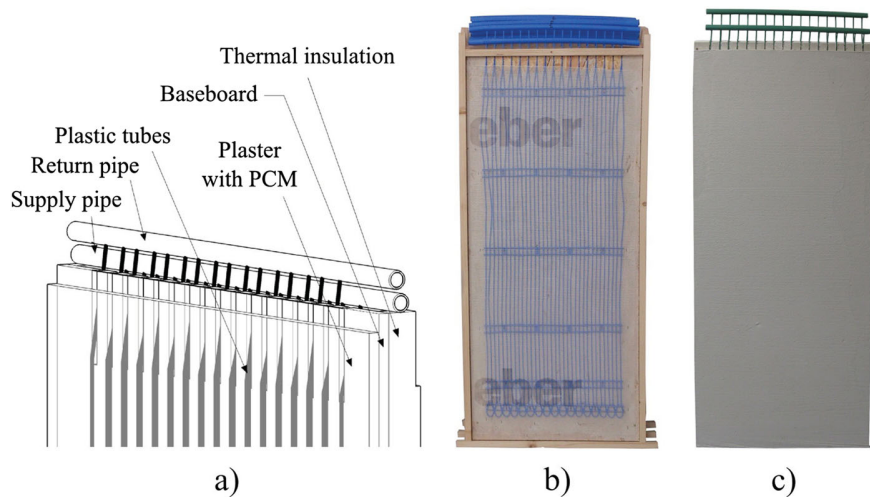


Figure 1. Wall panels: (a) the schematic, (b) the panel before application of the plaster, (c) the finished panel.

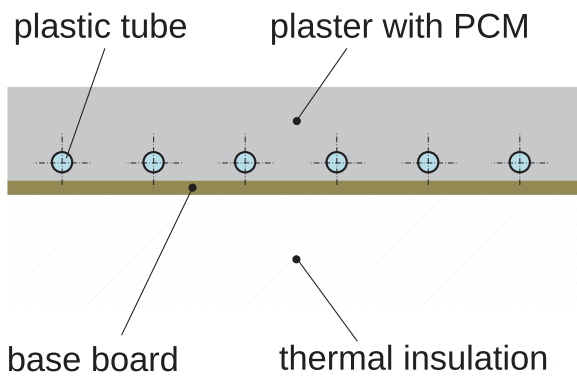


Figure 2. Horizontal cross-section of the wall panel.

by solar photovoltaics. A schematic view of the panel is shown in Figure 1(a).

The wall panels consisted of baseboards with a thermal insulation layer on the side facing the wall and a layer of plaster with the microencapsulated PCM on the side facing the room. The plastic tubes for the HTF were embedded in the layer of plaster. The horizontal cross-section of the considered wall panel is shown in Figure 2. The plaster layer was 15 mm thick. Each panel contained 17 plastic tubes connected in the U-shaped manner with the supply and return pipe on one side of the panel. The embedded tubes had an inner diameter of 2.25 mm and a wall thickness of 0.5 mm. A picture of the experimental wall panel before the application of the MPCM plaster is presented in Figure 1(b) while Figure 1(c) shows a finished wall panel prepared for installation on the wall.

The panels were tested in an experimental room at the Brno University of Technology. A reversible air-to-water heat pump was used as a source of heating and cooling water. The description of the experiment was reported by Ostrý, Charvát, and Klubal (2016). A thermal imaging system was used for the monitoring of the temperature

of the room-facing surfaces of the panels. The results of thermal imaging were used in the validation of the TRN-SYS model (Charvát et al. 2015). A good agreement was achieved between the surface temperatures obtained from the experiment and from the simulation.

4. Simulation approaches and models

The goal of the present study was the comparison of the simulation results obtained with the 1D and 3D models. The models were compared in terms of the outlet water temperature, the mean surface temperature, and the heat flux between the panels and the surrounding (indoor) environment. The comparison was done for both steady-state and transient boundary conditions in the heating and cooling operation of the panels.

Two configurations of the embedded plastic tubes, shown in Figure 3, were considered. In the first configuration, the supply pipe for the HTF was at the top of the panel and the return pipe at the bottom with the embedded tubes running straight from the supply pipe to the return pipe. Each of the plastic tubes was 2 m long in this configuration. In the second configuration, the supply pipe and the return pipe were at the top of the panel and the embedded tubes were connected in the U-shaped manner (U-tubes). This was the configuration of the experimental panels described in Section 3. As can be seen in Figure 3, for the same height of the panel the U-tubes were twice as long as the straight tubes, it means that each tube was 4 m long.

The pressure drop of the panels was not analysed in this study but it is evident that the pressure drop of the panel with the U-shaped tubes is higher than that of the panel with the straight tubes. The tubes have a very small inner diameter and the water flow in the tubes is laminar for the practical range of the water flow rates. The critical Reynolds number ($Re_D = 2000$, the onset of transition to turbulent flow) is reached for the water velocity

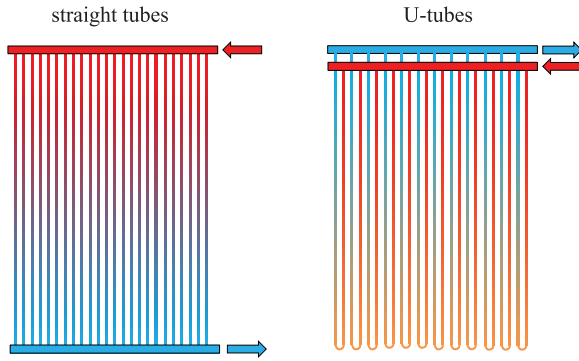


Figure 3. Embedded tube configurations.

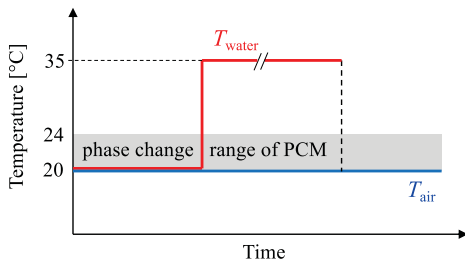


Figure 4. Heating scenario.

of about 0.63 m/s corresponding with a mass flow rate of about 0.0025 kg/s in one tube.

Both the heating and cooling operation of the panels was simulated. Different phase change temperature intervals of the PCM were considered in the heating and cooling scenarios. In the practical application, the wall panel would likely be used for both heating and cooling, and thus, only one phase change range of a PCM could be used to provide TES in both heating and cooling operations. Consideration of different phase change temperature intervals in the heating and cooling scenarios insured that the PCM would be fully melted in the steady-state heating operation and fully solidified in the steady-state cooling operation.

The temperature interval of phase change from 20°C to 24°C was considered in the heating scenario. In this case, the ambient (room) air temperature was set to 20°C throughout the simulation. The initial plaster temperature was the same as the ambient temperature. A step change in the water temperature was introduced as shown in Figure 4. The mass flow rate of water was constant during the simulations and the initial water temperature was set to be the same as the ambient temperature (20°C) before being increased to 35°C. After reaching the steady-state operation, the water flow was turned off and the temperature of the panel decreased as heat was discharged to the ambient environment.

The cooling operation scenario was defined in a similar manner. The ambient air temperature was set to 26°C and the phase change range of the PCM was between 22°C and

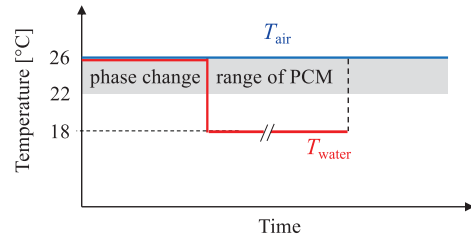


Figure 5. Cooling scenario.

26°C. The water temperature changed from 26°C to 18°C as shown in Figure 5.

4.1. Phase change modelling

The effective heat capacity method (Voller 1996) was used in both the 1D and 3D models. This means that the latent heat of the encapsulated PCM was included in the specific heat capacity of the mixture of plaster and PCM. Most PCMs melt and solidify in certain temperature intervals rather than at a constant temperature. The temperature interval of the phase change $\Delta T_{pch} = 4$ K was considered in both the heating and cooling scenarios, as shown in Figures 4 and 5. The curve of the effective heat capacity as a function of the temperature T was expressed with the following equation (Kuznik, Virgone, and Roux 2008):

$$c_{eff}(T) = c_0 + c_m \exp \left\{ -\frac{(T - T_{pch})^2}{\sigma} \right\}, \quad (1)$$

where c_0 is the specific heat, c_m is the maximum increment of the specific heat due to the latent heat, T_{pch} is the mean temperature of phase change (the peak of effective heat capacity), and σ is a parameter that influences the width of the phase change temperature range. Equation (1) can be used not only for a PCM but also for a mixture of a PCM with other materials, such as the presented case of the microencapsulated PCM embedded in the gypsum plaster. The effective heat capacity described by Equation (1) with $c_0 = 1550$ J/kg · K, $c_m = 48500$ J/kg · K and $\sigma = 1.1$ K² was used for both the heating and cooling scenarios. As already mentioned above, the mean phase change temperature T_{pch} in Equation (1) was set to 22°C and 24°C in the heating and cooling scenarios, respectively. The corresponding amount of latent heat was then 90 kJ/kg. The curves of effective heat capacity for the heating and cooling scenarios are shown in Figure 6.

Equation (1) provides a flexible approximation of the distribution of effective heat capacity in a certain temperature range. As change in the T_{pch} does not influence the melting range or latent heat, Equation (1) is suitable in situations where the influence of T_{pch} is to be investigated independently of other parameters.

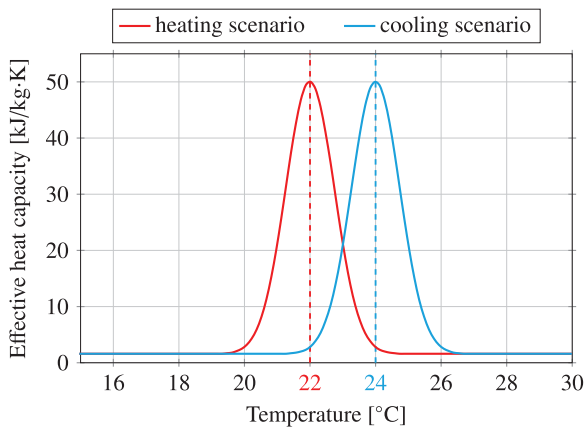


Figure 6. Effective heat capacity of the PCM.

4.2. Discussion on the use of the effective heat capacity method

As mentioned in the introduction, the effective heat capacity method together with the enthalpy method are the most frequent modelling approaches used in a variety of applications (Al-Saadi and Zhai 2013). The advantages and drawbacks of these methods are well documented in the literature. Muhieddine, Canot, and March (2009) reported that the enthalpy method requires two primary variables to be consecutively solved in each time step prolonging the calculation time. The enthalpy method may also suffer from temperature fluctuations as demonstrated by the same authors. Alternatively, the effective heat capacity method considers the temperature as the only primary variable and eliminates the occurrence of temperature fluctuations. Not without its weaknesses, the effective heat capacity is sensitive to the size of the time step and improper adjustment of the time step can lead to a violation of energy conservation. Delcroix, Kummert, and Daoud (2017) demonstrated such behaviour, though they used excessively large time steps which could not be applied in practice. Another drawback of the effective heat capacity method is its inability to address an isothermal phase change as it leads to the singularity behaviour (Hu and Argyropoulos 1996). In practice, the PCMs used for TES in buildings usually change the phase in relatively wide temperature intervals rather than isothermally which mitigates this drawback. However, the enthalpy method is self-conservative as the enthalpy is a monotonically-increasing function of temperature, and thus the enthalpy method can be used to model an isothermal phase change when the effective heat capacity method cannot (Swaminathan and Voller 1992).

In the present simulation study, both the 1D model in TRNSYS and the 3D model in COMSOL Multiphysics employed the effective heat capacity method. The main reason was to have two models with the same modelling approach, but also because COMSOL Multiphysics straightforwardly allows for phase change modelling only by means of the effective heat capacity. The in-house 1D

Table 1. Thermophysical properties of the plaster with the microencapsulated PCM.

Property	
Density	677 kg/m ³
Thermal conductivity	0.176 W/m-K
Specific heat capacity	1550 J/kg-K
Latent heat capacity	90 kJ/kg

model in TRNSYS adopts a rather small time step and an internal control mechanism described later is used to mitigate drawbacks of the effective heat capacity method.

4.3. Assumptions and materials

Heat conduction was assumed to be the dominant heat transfer mechanism in the plaster with the microencapsulated PCM. Inside the tubes, heat and mass transfer occurs in the HTF due to convection. The heat exchange between the panels and the surrounding environment is accomplished by convection and radiation. Though the developed TRNSYS model allows for calculation of radiative heat transfer from the surface of the panel, the radiative heat flux was assumed to be included in the convective heat flux through the value of heat transfer coefficient.

Water was used as the HTF in the study. The plaster with the PCM was a mixture of the gypsum plaster and the microencapsulated PCM. Micronal DS 5040 X, a product of BASF/Microtek Labs, was the MPCM used in the study. Micronal DS 5040 X consists of a paraffin-based PCM encapsulated in polymethylmethacrylate polymer. The capsules have a diameter between 50 μm and 300 μm (Micronal 2018).

The considered plaster with the MPCM consisted of 70 wt.% of the plaster and 30 wt.% of Micronal DS 5040 X. From the macroscopic view, the mixture forms a homogeneous material which can be applied on walls, ceilings, and other building surfaces like an ordinary gypsum plaster. For this reason, the plaster with the MPCM is considered and modelled as a homogeneous material, such as in the work by Lachheb et al. (2017). The thermophysical properties of the plaster with the Micronal MPCM were determined experimentally and they are presented in Table 1.

5. 1D model in TRNSYS

All heat transfer problems encountered in the real world are 3D and their transformation to a 1D case requires certain simplifications. In the case of the wall panels, the heat conduction from the embedded tubes to the surrounding plaster is 3D. The simplification to a 1D problem meant that heat conduction was considered only in one direction—the direction of the thickness of the plaster, as seen in

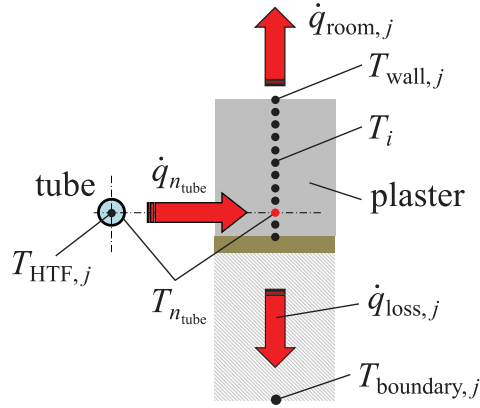
Figure 7. 1D conduction in the j -th section.

Figure 7. The baseboard and the thermal insulation layer were modelled as thermal resistances.

It is obvious that the temperature of the HTF changes in the direction of the flow due to heat transfer between the fluid and the plaster. Therefore, a single 1D model of the panel cannot be used for the modelling of the entire wall panel. Instead, the panel is partitioned into several sections in the fluid flow direction and a collection of coupled 1D models for each section is considered as shown in Figure 8.

5.1. Governing equations for 1D model

The TRNSYS model consists of a set of 1D models for heat conduction in the wall panel, coupled with the 1D model for energy balance in the fluid flow in the embedded tubes. The model was written in the C++ programming language and implemented as a TRNSYS type.

5.1.1. Heat transfer model in the wall panel

The effective heat capacity method applied to the 1D heat transfer equation in the wall panel leads to the governing equation (Voller 1996):

$$\rho c_{\text{eff}} \frac{\partial T}{\partial t} = \frac{\partial}{\partial x} \left(k \frac{\partial T}{\partial x} \right), \quad (2)$$

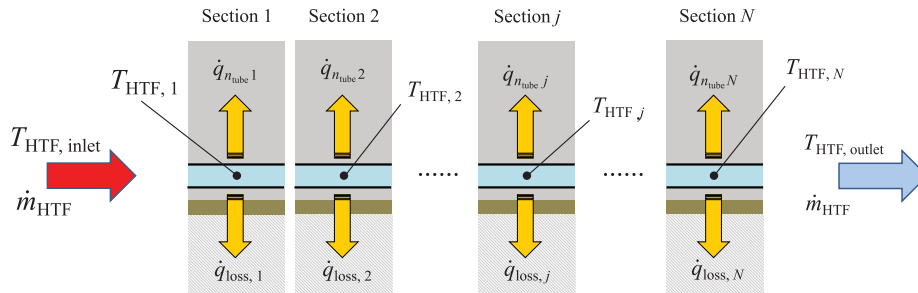


Figure 8. Schematic of the 1D heat transfer and fluid flow model in TRNSYS.

where ρ is the density, c_{eff} is the effective heat capacity, T is the temperature, t is time, k denotes the thermal conductivity, and x is the spatial variable. Equation (2) was transformed into a numerical model by means of the forward-time central-space (FTCS) discretization (Pletcher, Tannehill, and Anderson 2011). Though the forward-time (explicit) method of the discretization implies a conditional numerical stability, the determination of the temperature distribution requires only the successive evaluation of the discretized equations rather than the solution of a set of equations (Kreith, Manglik, and Bohn 2011).

For internal nodes i , the explicit formula for the temperature in time $t + \Delta t$ incorporates the heat conduction from the neighbouring nodes and it reads:

$$T_i^{t+\Delta t} = T_i^t + \frac{\Delta t}{\rho c_{\text{eff}} \Delta x_i} \left[\frac{k_{i-1/2}}{\Delta x_{i-1/2}} (T_{i-1}^t - T_i^t) + \frac{k_{i+1/2}}{\Delta x_{i+1/2}} (T_{i+1}^t - T_i^t) + \dot{q}_i \right], \quad (3)$$

where $k_{i\pm 1/2}$ denotes the thermal conductivity between the nodes i and $i \pm 1$, Δx_i is the 1D volume corresponding to the node i , and $\Delta x_{i\pm 1/2}$ is the distance between the nodes i and $i \pm 1$. Patankar (1980) proposed the thermal conductivity between two neighbouring nodes i and $i \pm 1$ as their geometric mean and such approach was successfully applied by a number of investigators. The \dot{q}_i is the heat flux transferred to or from the node. In the model of the wall panel, \dot{q}_i in Equation (3) represents the heat flux transferred from the HTF through the wall of the tube to the node i of the plaster. Obviously, \dot{q}_i equals zero for all the nodes except the node $i = n_{\text{tube}}$ which geometrically corresponds with the location of the tube.

The heat flux transferred between the HTF and the plaster is determined as:

$$\dot{q}_{n_{\text{tube}}} = \frac{U}{P} (T_{\text{HTF},j}^t - T_i^t), \quad (4)$$

where U is the overall heat transfer coefficient of the tube, and $P = 15 \text{ mm}$ is the pitch of the tubes (the distance between two adjacent tubes in the panel). The $T_{\text{HTF},j}^t$ is the temperature of the HTF with j representing the index of the location in the direction of the fluid flow. The overall

heat transfer coefficient of the tube wall (Kreith, Manglik, and Bohn 2011) can be expressed as:

$$U = \frac{2\pi}{\frac{2}{d_{\text{tube}} h_{\text{tube}}} + \frac{1}{k_{\text{tube}}} \ln\left(\frac{D_{\text{tube}}}{d_{\text{tube}}}\right) + \frac{1}{k_{\text{plaster}}} \ln\left(\frac{P}{\pi d_{\text{tube}}}\right)}, \quad (5)$$

where d_{tube} and D_{tube} are the inner and outer diameter of the tube, respectively. Furthermore, h_{tube} is the heat transfer coefficient at the inner surface of the tube, and k_{plaster} and k_{tube} are the thermal conductivity of the plaster with PCM and of the plastic tube, respectively. In the boundary nodes, the convective heat transfer to the ambient environment is also taken into account. For the boundary node facing the room $i = 1$, the explicit formula for the temperature is:

$$T_1^{t+\Delta t} = T_1^t + \frac{\Delta t}{\rho c_{\text{eff}} \Delta x_1} \times \left[h_{\text{wall}} (T_{\infty}^t - T_1^t) + \frac{k_{1/2}}{\Delta x_{1/2}} (T_2^t - T_1^t) \right], \quad (6)$$

where h_{wall} is the heat transfer coefficient between the boundary (surface) and the ambient environment (room). The restriction to the size of the time step can be derived from the stability condition for a 1D case (Bergman et al. 2011) as:

$$\text{Fo}(1 + \xi \text{Bi}) \leq \frac{1}{2}, \quad (7)$$

where $\text{Fo} = k\Delta t/\rho c\Delta^2 x$ is the Fourier number, $\text{Bi} = h\Delta x/k$ is the Biot number, Δt is the time step, Δx is the spatial discretization step (the distance between the spatial nodes), and h is the heat transfer coefficient of the convection at the surface. The ξ is the binary function of the node location; $\xi = 0$ for internal nodes while $\xi = 1$ for boundary (surface) nodes. Then the time step is estimated as:

$$\Delta t \leq \min_i \frac{\rho c \Delta^2 x}{2(k + \xi h \Delta x)}, \quad (8)$$

where the minimum is evaluated over all the boundary and internal nodes i . As some parameters in Equation (8) are not the same in all nodes, the values leading to the minimal time step should be considered. In particular, the value c_0 from the effective heat capacity in Equation (1) should be used as a representative value of the heat capacity. As can be seen from Equation (8), boundary nodes are usually more restrictive on the time step than the internal nodes.

The plaster with the encapsulated PCM, as described in Section 4, was considered in the study. The heat transfer coefficient between the plaster and the ambient environment was set to $8 \text{ W/m}^2 \cdot \text{K}$. The thickness of the plaster was 15 mm and 31 nodes were used in the spatial discretization in the thickness direction implying that the Δx was 0.5 mm. The substitution of these parameters into Equation (8) estimates the feasible time step to be about 0.7 seconds. Since the effective heat capacity method is relatively sensitive to the time step and a higher simulation

accuracy was required, the time step was set to 0.1 second. It is worth pointing out that this time step was an internal time step adopted in the TRNSYS type of the wall panel. It means that the time step was internally used for the solution of Equation (2) regardless of the global (main) time step used in TRNSYS. Besides a very small time step, the 1D model also adopts a phase change detection control, proposed by Delcroix, Kummert, and Daoud (2017), preventing the violation of energy conservation. The mechanism controls the temperature change within one time step and compares it with the distribution of the effective heat capacity. If the change in the temperature is so large that it would lead to the incorrect detection of phase change, a correction of the nodal temperature by means of a corresponding amount of latent heat is applied.

5.1.2. Heat transfer model in the HTF

The temperature of the HTF in the plastic tubes changes along the length of the tube. To account for this, the tube with the respective part of the wall panel is partitioned into several sections and each section is coupled with the separate 1D heat transfer model of the wall panel as shown in Figure 8. The HTF temperature (water temperature in the studied case) was calculated using the energy balance shown in Figure 8. At the beginning of the simulation, the HTF temperature is initialized to the HTF inlet temperature as $T_{\text{HTF},j} = T_{\text{HTF,inlet}}$ in all the sections $j = 1, \dots, N$ where N is the number of sections used for the partition of the panel. During the simulation, the HTF temperature is iteratively updated in two steps. First, the values of the HTF temperature are transferred between sections in the direction of the HTF flow through the tube. In particular,

$$T_{\text{HTF},j}^{t+(1/2)\Delta t} = T_{\text{HTF},j-1}^t \quad (9)$$

is set for the sections $j = 2, \dots, N$. The inlet HTF temperature is then assigned to the ‘empty’ first section as $T_{\text{HTF},1}^{t+(1/2)\Delta t} = T_{\text{HTF,inlet}}$. The procedure then continues with the solution of the temperature distribution in the wall panel. In the second step, the HTF temperature takes into account the heat transfer between the fluid and the surrounding plaster with the PCM as

$$T_{\text{HTF},j}^{t+\Delta t} = T_{\text{HTF},j}^{t+(1/2)\Delta t} - \frac{U \cdot L_{\text{section}}}{\dot{m}_{\text{HTF}} c_{\text{HTF}}} \left(T_{\text{HTF},j}^{t+\frac{1}{2}\Delta t} - T_{n_{\text{tube}},j}^t \right) \quad (10)$$

for all the sections $j = 1, \dots, N$ where L_{section} is the length of the section in the direction of the fluid flow.

5.2. Further assumptions for 1D model in TRNSYS

It was assumed that the mass flow rate of the HTF and the inlet HTF temperature were the same for all tubes embedded in one wall panel. Therefore, only one tube and the respective part of the panel was modelled. As 1D heat conduction was considered in the direction of the plaster, it

was not possible to model the tube itself. Only the corresponding heat flux in Equation (4) was used as an input in the computational node where the tube was located (a heat source in the node). The heat flux from the HTF to the plaster was calculated with the assumption that the temperature of the outer surface of the tube was the same as the temperature of the plaster at the position of the tube (node temperature). Correlations from the literature (Bergman et al. 2011) were used in Equation (5) to calculate the heat transfer coefficient h_{tube} on the internal side of the tubes.

5.3. Outputs of the 1D model in TRNSYS

As already mentioned, the 1D model cannot be used for detailed simulations of the spatial temperature distribution in the wall panel. The model is rather intended for the prediction of the overall heat transfer between the panels and the surrounding environment. The outputs of the 1D model include the mean surface temperature of the panel, the mean heat flux exchanged between the panel and the ambient environment, and the outlet temperature of the HTF. On the other hand, the 1D model in TRNSYS was much faster than the 3D model in COMSOL Multiphysics.

5.4. Energy conservation test

A simple energy conservation test was conducted to assess the accuracy of the modelling approach. The adiabatic boundary condition was applied on the surface of the panel facing the room, as well as the surface facing the wall. It was found that both the heat flux to the room and the heat flux to the wall (heat loss) were equal to zero and all heat delivered/rejected by the flowing water was stored in/released from the PCM plaster. The total amount of heat stored in or the plaster for the step change of water temperature (as shown in Figures 4 and 5) can easily be calculated analytically and compared with the numerical results. A very good agreement between the analytical and numerical results was achieved in this test. The modelled part of the panel with the straight tubes had an overall heat capacity of 34.42 kJ in the temperature interval between 20°C and 35°C. The amount of heat stored in this segment of the 1D model was 34.40 kJ. It means that the difference was less than 0.1%. In the cooling scenario where the temperature interval was between 26°C and 18°C, the heat capacity of the modelled part of the panel was 31.21 kJ and the amount of heat rejected in the 1D model in TRNSYS was 31.14 kJ. It means that the difference was about 0.2%. Such differences indicate fairly good fulfillment of energy conservation in the 1D model.

6. 3D Model in COMSOL multiphysics

The 3D model was created in the COMSOL Multiphysics simulation software. The COMSOL Multiphysics is an off-the-shelf FEM-based simulation tool which allows for

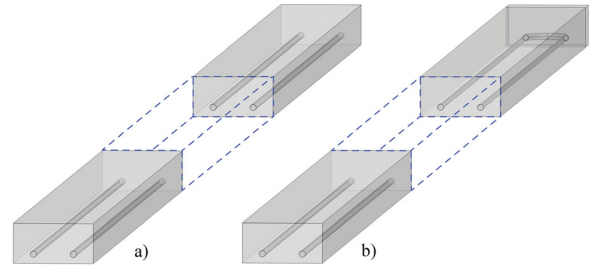


Figure 9. Schematic of the 3D model in COMSOL Multiphysics: (a) segment with two straight tubes and (b) segment with one U-tube.

numerical investigations of various kinds of problems including multiphysical phenomena. Two versions of the 3D model were created: one for the panel with the straight tubes and the other for the panel with the U-tubes. Since these wall panels can be considered as a periodical repetition of segments with a single straight tube or U-shaped tube, respectively, only a single segment of the tube with a width of 30 mm and containing either two straight tubes or one U-tube was modelled. The schematic of the considered geometry is shown in Figure 9.

The heat transfer and fluid flow phenomena were modelled by means of the built-in heat transfer and laminar flow modules, respectively. The variable fluid temperature, due to the heat transfer between the fluid and the panel, was assumed in the flow direction. Both the heat transfer and laminar flow modules were coupled to each other by means of the multiphysical non-isothermal flow interface.

The heat transfer module solved the heat transfer both in the panel with the PCM and in the water flowing in the tubes (Bergman et al. 2011):

$$\rho c_{\text{eff}} \frac{\partial T}{\partial t} + \rho c_{\text{eff}} \mathbf{u} \nabla T = \nabla \cdot (k \nabla T), \quad (11)$$

where \mathbf{u} is the velocity vector of the HTF. The fluid flow module was used to simulate the laminar incompressible fluid flow in the tube by means of the Navier–Stokes equations (Versteeg and Malalasekera 2007):

$$\rho \left(\frac{\partial \mathbf{u}}{\partial t} + \mathbf{u} \cdot \nabla \mathbf{u} \right) = \nabla p + \nabla \cdot (\mu (\nabla \mathbf{u} + (\nabla \mathbf{u})^T)) + \rho \mathbf{g} \quad (12)$$

and of the continuity equation:

$$\nabla \cdot (\rho \mathbf{u}) = 0, \quad (13)$$

where p is the HTF pressure, μ is the dynamic viscosity of the HTF, and \mathbf{g} is the standard gravity.

As for the boundary conditions in the 3D model, their definitions are needed for both the heat transfer and the fluid flow. The surface of the panel facing the ambient environment was subjected to the heat convection with the defined heat transfer coefficient. Adiabatic and periodic boundary heat transfer conditions were applied to longitudinal sides of the segments with the straight tubes and

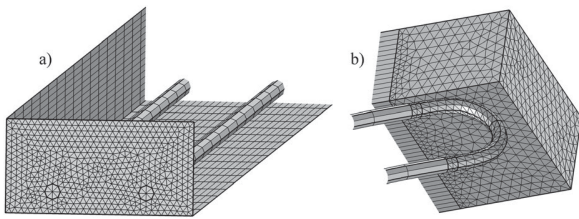


Figure 10. Structure of the computational mesh: (a) triangular 2D mesh of the face used for the generation of prismatic 3D elements by means of sweeping and (b) detail of the U-shaped elbow meshed with the use of tetrahedral elements.

U-tubes, respectively. The COMSOL Multiphysics implements the periodic boundary condition at two surfaces A and B such that $T_A = T_B$ and $\dot{q}_A = -\dot{q}_B$ (COMSOL 2012), which is the case with the segment with the U-tube. The pressure inlet and mass flow rate outlet conditions were applied at the tube with the HTF and the no-slip fluid flow condition was defined at the inner surfaces of the tubes.

Due to the specific slim geometry of the domain with its dominant dimension in the flow direction, the swept computational mesh was created. The faces of the segments shown in Figure 10 were meshed with the use of triangular 2D elements that were consequently used in the swept procedure to create 3D prismatic elements. In case of the panel with the U-tube, the part of the segment containing the U-shaped elbow of the tube (see Figure 10) was meshed with the use of tetrahedral elements as the swept mesh was not applicable. The size of the swept elements was selected to be finer in the normal direction to the surface of the panel and coarser in the water flow direction, according to the assumed variation of the temperature and heat fluxes in the panel. Therefore, most elements of the mesh were prisms with the dominant dimension in the fluid flow direction. The mesh for the segment with two straight tubes and with the U-tube consisted of 338,400 and 362,472 elements, respectively.

6.1. Outputs of the 3D model in COMSOL multiphysics

In comparison to the 1D model in TRNSYS, the 3D model in COMSOL Multiphysics allows for fairly detailed simulations of the thermal and fluid flow behaviour of the panel. The outputs of the 3D model included the transient 3D temperature distribution in the panel, the spatially-dependent heat flux between the panel and the ambient environment, the outlet temperature of the HTF, and the pressure drop in the tubes. Several hours of computation time were needed for one hour of wall-clock time simulation, as the 3D model in COMSOL Multiphysics is very computationally demanding.

7. Results and discussion

The main goal of the comparison of the 1D and 3D models was to assess the effect of the simplification of the

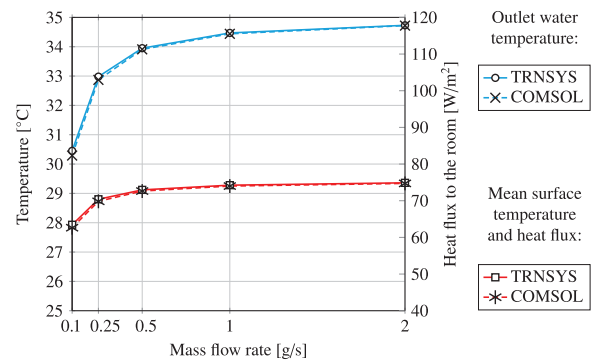


Figure 11. Steady-state heating: straight tubes.

3D problem to the 1D problem and the impact it had on the results. The temperature distribution over the surface of the thermally activated structure is not usually important in BPSs since the room is quite often represented by a single node. Instead, the most important results are the mean surface temperature, the heat transfer rate between the structures and the ambient environment, and the outlet water temperature. All simulations were carried out with the assumption that the height of the wall panels was 2 m. Thus, the embedded tubes were 2 m long in the panel with the straight tubes and 4 m long in the panel with the U-tubes. Water was considered as the HTF in all cases. In this paper, the water mass flow rates in all figures are for one embedded plastic tube. The simulations were carried out for five mass flow rates: 0.1 g/s, 0.25 g/s, 0.5 g/s, 1 g/s, and 2 g/s. The water velocities in the plastic tube corresponding to the maximum and minimum mass flow rates (0.1 g/s and 2 g/s) are 0.025 m/s and 0.5 m/s, respectively. The practical operating range of the panels (based on flow rates) is well within these limits. As the panels have a height of 2 m and contain 34 straight tubes, the surface area of the panels is about 1 m². The mass flow rate of 0.5 g/s in one tube means that the total mass flow rate is about 61 kg/hr for the overall wall panel.

7.1. Results of steady-state operation

The steady-state heating scenario was calculated with an inlet water temperature of 35°C and an ambient air temperature of 20°C. The average temperature of the panel surface facing the room, the outlet water temperature, and the average heat flux for the wall panel with the straight tubes are presented in Figure 11.

As can be seen, there is a very good agreement between the results of the 1D and 3D models. Since convection was the only mechanism of heat transfer considered on the surface facing the room and both the ambient air temperature and the heat transfer coefficient were considered constant, the heat flux to the room is only a function of surface temperature. The mean surface temperature and the mean heat flux density do not increase very much for mass flow rates

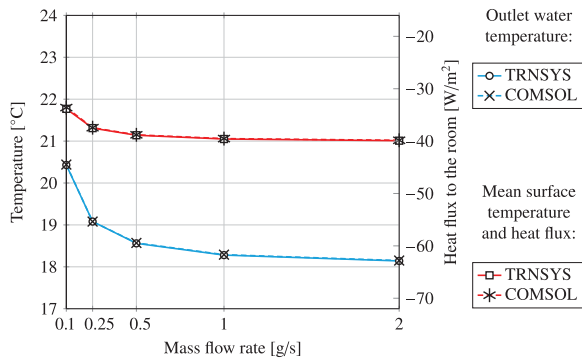


Figure 12. Steady-state cooling: straight tubes.

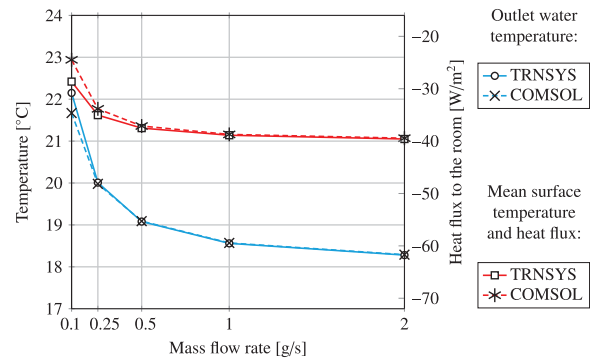


Figure 14. Steady-state cooling: U-tubes.

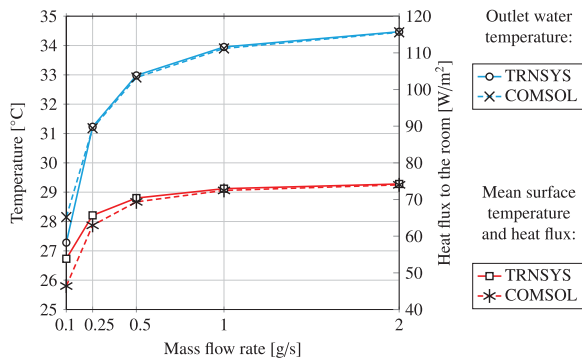


Figure 13. Steady-state heating: U-tubes.

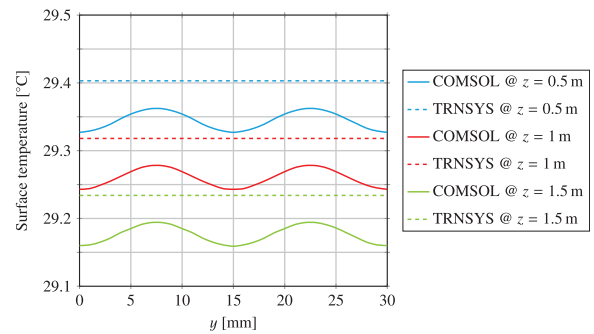


Figure 15. Temperature profiles across the surface of the wall panel: straight tubes.

of water above 0.5 g/s. Since the pressure drop of the tubes increases with the square of the water flow rate, it would not make much sense in practice to increase the flow rate above a certain value in the steady-state operation of the panels.

The results for the steady-state cooling scenario are shown in Figure 12. The water inlet temperature of 18°C and the ambient air temperature of 26°C were considered in this case. The agreement between the two models is very good, as was the case with the heating scenario.

The results for the heating operation of the panel with the U-tubes are presented in Figure 13. There is a discrepancy between the results of the 1D and 3D models for the mass flow rates lower than 0.5 g/s, though the results are still in fairly good agreement. The discrepancy in this case is rather logical as the 1D model does not address the heat transfer between the adjacent tubes.

The cooling mode operation of the panels with the U-tubes shown in Figure 14 exhibited the largest discrepancies between the 1D and 3D models. There was a relatively small difference between the inlet water temperature and the ambient temperature in the cooling mode (as shown in Figure 5) that were then translated into large relative differences. Similar to other simulated cases, the discrepancies increase with the decreasing water flow rate.

Figure 15 shows the surface temperature across the surface of the modelled segment of the wall panel with

straight tubes in the heating scenario. The temperatures were determined from cross-sections of the segment; each cross-section was in the x - y plane (perpendicular to the flow direction) at a specified distance from the water inlet. The chart shown in Figure 15 is for the water mass flow rate of 1 g/s and the temperature profiles are at the distance of 0.5 m, 1.0 m, and 1.5 m from the water inlet. Since the 1D model does not account for the heat flow between the adjacent tubes, the surface temperatures in the sections are constant. The surface temperatures in case of the 3D model have a sine wave-like profile. However, the differences between maximum and minimum temperatures in case of the 3D model temperature profiles are rather small and thus their approximation with the constant temperature (1D model) is justifiable.

The surface temperature profiles for the wall panel with U-tubes are presented in Figure 16. Again, the 1D model does not account for the heat flow between the adjacent tubes. Due to the decrease of water temperature in the direction of water flow and the averaging effect of the 1D approach, the entire surface of the panel has almost constant temperature in case of 1D model. The 3D model reveals the asymmetry of the surface temperature profile due to the heat flow between the adjacent tubes. Nonetheless, the absolute difference between the results of the 1D and 3D models of about 0.1 K is still very good.

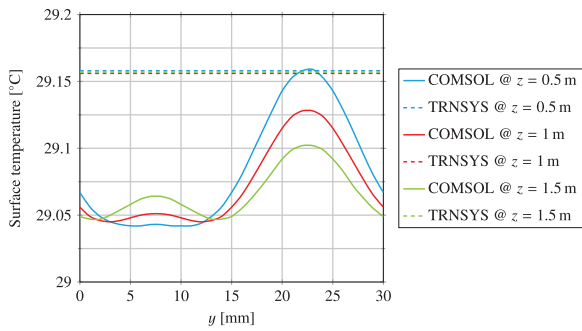


Figure 16. Temperature profiles across the surface of the wall panel: U-tubes.

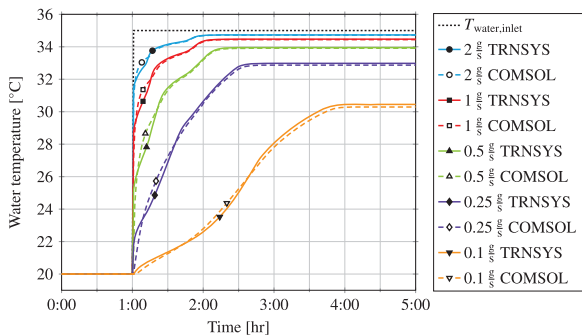


Figure 17. Outlet water temperature: straight tubes.

It needs to be stressed that the good agreement between the 1D and 3D models is for the geometry, the thermophysical properties, and the operating conditions of the wall panels considered in this study. Should any of these characteristics change significantly, from those considered in the study, the accuracy of the 1D model would need to be tested.

7.2. Transient results – heating scenario

The transient simulations show the dynamic behaviour of the wall panels in heating and cooling operation. The outlet water temperatures for the panel with the straight tubes in the heating scenario are shown in Figure 17. The step change of water temperature took place 1 hour after the start of the simulation. The presence of the PCM increased the surface temperature in the early stages of the heating operation. As can be seen, the response time of the wall panel depended on the mass flow rate of water. For the mass flow rates of water greater than 0.25 g/s the panel reached the steady-state operation in less than 1.5 hours. However, when the water flow rate was 0.1 g/s, it took almost 3 hours to reach the steady-state operation.

Figure 18 shows the mean surface temperature of the wall panel and the heat flux to the ambient environment. The agreement between the results of the 1D model and the 3D model is very good. The mass flow rate of water influences the dynamic behaviour of the panel but it has

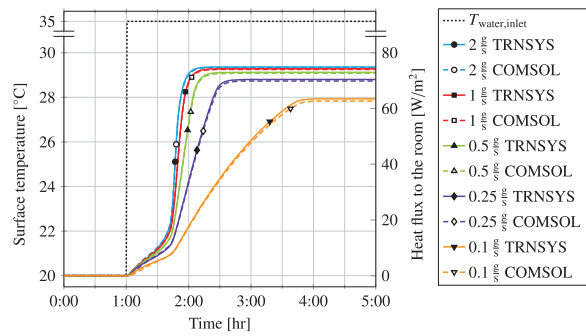


Figure 18. Surface temperature and heat flux: straight tubes.

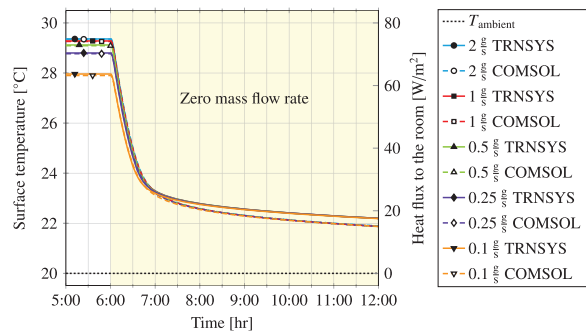


Figure 19. Heat discharge at zero mass flow rate: straight tubes.

a much smaller effect on the steady-state operation. The increase in water mass flow rate from 0.1 to 2 g/s shortened the time needed to reach the steady-state conditions from almost 3 hours to about 1 hour. Despite this, the steady-state heat flux increased by only 19% from 63 to 75 W/m².

The discharge of heat from the panel when water flow is turned off is shown in Figure 19. Both the mean surface temperature and the heat flux from the panel drop rather quickly. Even though the heat discharge process starts from different initial states, given by the steady-state conditions for different flow rates, the results for different flow rates are rather similar. The mean surface temperature at the beginning of the heat discharge was above the phase change temperature range of the PCM. Due to heat storage in the PCM, the heat flux to the room decreased rather slowly when the surface temperature entered the melting range of the PCM. When the heating water was turned off, the mean heat flux to the room remained above 20 W/m² for almost 4 hours.

The outlet water temperature in the heating mode, for the wall panel with the U-tubes, is presented in Figure 20. The discrepancies between the 1D and 3D models are larger than in the case of the panel with the straight tubes and increase with decreasing water flow rate. The agreement between the results is still fairly good for mass flow rates above 0.25 g/s.

The mean surface temperature and the heat flux from the surface are shown in Figure 21. The level of discrepancy between the results is similar to the discrepancies

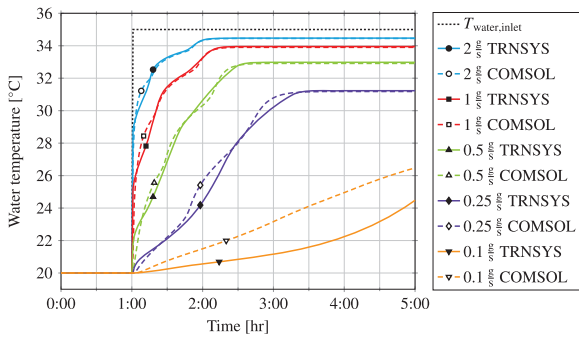


Figure 20. Outlet water temperature: U-tubes.

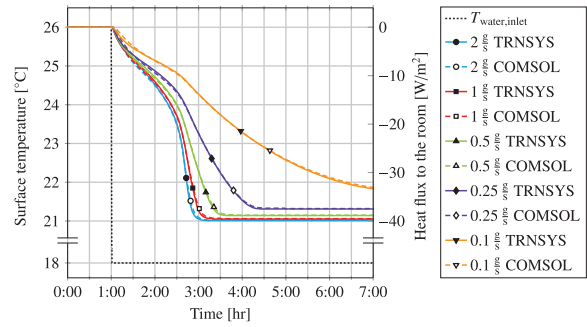


Figure 23. Transient cooling: straight tubes.

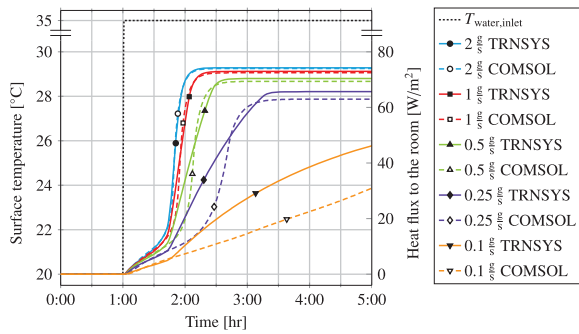


Figure 21. Surface temperature and heat flux: U-tubes.

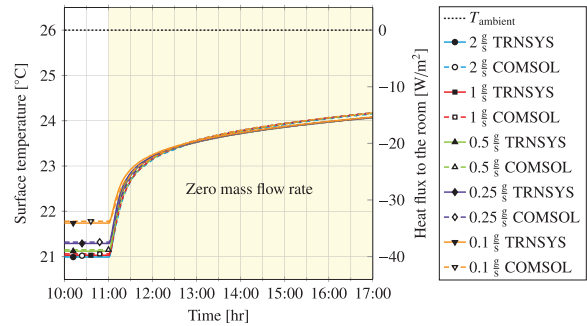


Figure 24. Heat absorption at zero mass flow rate: straight tubes.

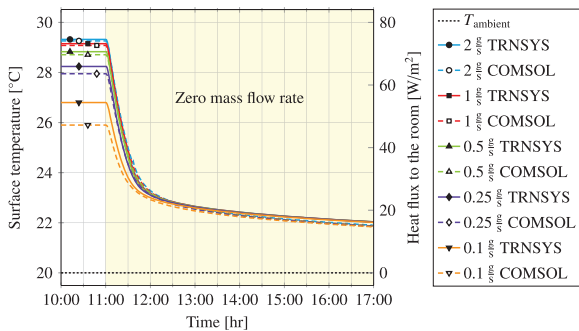


Figure 22. Heat discharge at zero mass flow rate: U-tubes.

in the case of the outlet water temperature shown in Figure 20. For that reason, only the mean surface temperature and the heat flux will be shown in other simulated cases.

Figure 22 shows the end of the heating operation when the flow rate of heating water drops to zero. The discrepancies between the results of the 1D and 3D models are larger than in case of the panel with the straight tubes. The discrepancies between the 1D and 3D models for steady-state operation were shown in Figure 13. These discrepancies can also be seen in Figure 22 for the steady-state operation between 10:00 and 11:00.

7.3. Transient results – cooling scenario

The results for the cooling operation of the panel with the straight tubes can be seen in Figure 23. A longer period of time is needed to reach the steady-state cooling operation than the heating operation. The results of the 1D and 3D models are again in a fairly good agreement.

The increase of the surface temperature and the decrease of the heat flux, when the mass flow rate of cooling water drops to zero, can be seen in Figure 24. It took almost 8 hours to reach steady-state operation with the water mass flow rate of 0.1 g/s. The implication is that such small mass flow rates of cooling water would be quite impractical in the real-life operation of the panels.

The largest discrepancy between the results of the 1D and 3D models occurred in the transient cooling scenario with the U-tube panel, as shown in Figure 25. Good agreement was achieved only for the mass flow rates higher than 1 g/s. With the decreasing flow rate the discrepancy increased significantly. The adopted simplification to the 1D heat transfer problem, when considering the panel with the U-tubes, is much less realistic than in case of the panel with the straight tubes. Unlike with straight tubes, the heat flux between adjacent tubes is not negligible in the case of the panel with U-tubes.

Though the discrepancies of the results in both the steady-state and transient cooling operations of the panel with the U-tubes were relatively large, the results are in rather good agreement when the cooling water is turned

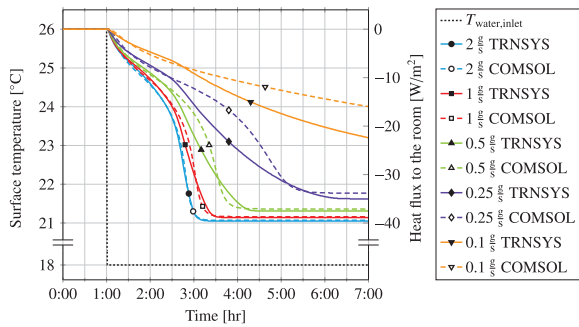


Figure 25. Surface temperature and heat flux: U-tubes.

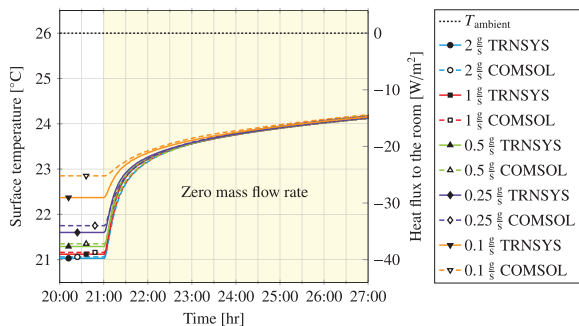


Figure 26. Heat absorption at zero mass flow rate: U-tubes.

off as in Figure 26. The cooling capacity of the panels decreased quickly when the cooling water was turned off but the absolute value of the heat flux remained between 20 W/m^2 and 15 W/m^2 for several hours as the the heat flux from the room was absorbed in the PCM.

8. Conclusion

The results of the 1D and 3D models of the thermally-activated wall panel with a PCM were compared in terms of the mean surface temperature, the outlet water temperature and the mean heat flux density. Very good agreement was achieved for the panel with the straight tubes as the discrepancies were practically insignificant – even for small mass flow rates of water. The discrepancies were larger for the panel with the U-tubes as the 1D model did not account for heat transfer between the adjacent tubes. The discrepancies also increased with decreasing water mass flow rate. However, significant discrepancies only occurred with small mass flow rates of water that would not be encountered in normal real-life operation of the wall panels.

The mean surface temperature of the panels directly influences their heating and cooling capacity. Due to the rather low thermal conductivity of the plaster with PCM, the tube configuration and the mass flow rate of water had a rather small influence on the mean surface temperature. Moving the tubes for the HTF closer to the room-facing surface of the plaster would decrease thermal resistance

between the HTF and the indoor environment and it would also lead to a higher heating and cooling capacity of the panels. The optimization of the position of the tubes, relative to the room-facing surface, will be the focus of further studies. The constant values of the ambient air temperature and the heat transfer coefficient on the surface of the panel were justifiable for the comparison of the models. However, time-dependent values of boundary conditions need to be considered for practical simulations. The pressure drop of the panel was not analysed in this study. As the pressure drop, and thus the pump power, increases with an increasing flow rate of HTF, an optimal flow rate in terms of the heating and cooling capacity and corresponding pump power for a particular panel can be found. As could be expected, at the same mass flow rate of water, the wall panels with the straight tubes had a higher heating and cooling capacity than the panels with U-tubes.

The developed 1D TRNSYS model of the wall panel can be used with other models available in TRNSYS (e.g. with a heat pump). The use of the model with other TRNSYS types allows for the simulation of more complex scenarios than the ones presented in the paper. The developed models can also be used for optimization of the panels in terms of both design and operation. A relatively good accuracy and short computation time make a 1D TRNSYS model a suitable tool for optimization where dozens or even hundreds of simulations need to be executed in the search for an optimal design. In terms of design optimization, the future work will focus on other parameters such as the influence of the position of the embedded tubes in the plaster, thermophysical properties of the plaster with the PCM, and the pressure drop of the tubes.



Disclosure statement

No potential conflict of interest was reported by the authors.

Funding

This work was supported by the Czech Science Foundation under the contract 18-19617S *Hysteresis of the temperature-enthalpy curve during partial phase change of latent heat storage materials* and by the project *Sustainable Process Integration Laboratory* – SPIL, No. CZ.02.1.01/0.0/15_003/0000456, funded by European Research Development Fund, Czech Republic Operational Programme Research, Development and Education, Priority 1: Strengthening capacity for quality research.

ORCID

L. Klimeš  <http://orcid.org/0000-0003-2133-3587>
P. Charvát  <http://orcid.org/0000-0003-1571-923X>

References

- Al-Saadi, S. N., and Z. Zhai. 2013. "Modeling Phase Change Materials Embedded in Building Enclosure: A Review." *Renewable and Sustainable Energy Reviews* 21: 659–673. doi:10.1016/j.rser.2013.01.024.

- Bergman, T. L., A. S. Lavine, F. P. Incropera, and D. P. DeWitt. 2011. *Fundamentals of Heat and Mass Transfer*. New York: John Wiley & Sons.
- Borreguero, A. M., M. L. Sánchez, J. L. Valverde, M. Carmona, and J. F. Rodríguez. 2011. "Thermal Testing and Numerical Simulation of Gypsum Wallboards Incorporated with Different PCMs Content." *Applied Energy* 88: 930–937. doi:10.1016/j.apenergy.2010.08.014.
- Brideau, S. A., I. Beausoleil-Morrison, M. Kummert, and A. Wills. 2016. "Inter-Model Comparison of Embedded-Tube Radiant Floor Models in BPS Tools." *Journal of Building Performance Simulation* 9 (2): 190–209. doi:10.1080/19401493.2015.1027065.
- Charvát, P., L. Klimeš, M. Ostrý, and J. Štětina. 2015. "A Validated TRNSYS Model of Thermally Activated Layer with Phase Change Material." Paper presented at the ASME 2015 International Mechanical Engineering Congress and Exposition, Houston, TX, USA, November 13–19.
- de Gracia, A., and L. F. Cabeza. 2015. "Phase Change Materials and Thermal Energy Storage for Buildings." *Energy and Buildings* 103: 414–419. doi:10.1016/j.enbuild.2015.06.007.
- Delcroix, B., M. Kummert, and A. Daoud. 2017. "Development and Numerical Validation of a New Model for Walls with Phase Change Materials Implemented in TRNSYS." *Journal of Building Performance Simulation* 10 (4): 422–437. doi:10.1080/19401493.2017.1280087.
- COMSOL. 2012. *Heat Transfer Module: User's Manual*.
- Heier, J., C. Bales, and V. Martin. 2015. "Combining Thermal Energy Storage with Buildings – A Review." *Renewable and Sustainable Energy Reviews* 42: 1305–1325. doi:10.1016/j.rser.2014.11.031.
- Hu, H., and A. Argyropoulos. 1996. "Mathematical Modelling of Solidification and Melting: A Review." *Modelling and Simulation in Materials Science and Engineering* 4: 371–396. doi:10.1088/0965-0393/4/4/004.
- Kreith, F., R. M. Manglik, and M. S. Bohn. 2011. *Principles of Heat Transfer*. Stamford: Cengage Learning.
- Kuznik, F., J. Virgone, and J. J. Roux. 2008. "Energetic Efficiency of Room Wall Containing PCM Wallboard: A Full-Scale Experimental Investigation." *Energy and Buildings* 40 (2): 148–156. doi:10.1016/j.enbuild.2007.01.022.
- Lachheb, M., Z. Younsi, H. Naji, M. Karkri, and S. B. Nasrallah. 2017. "Thermal Behavior of a Hybrid PCM/Plaster: A Numerical and Experimental Investigation." *Applied Thermal Engineering* 111: 49–59. doi:10.1016/j.applthermaleng.2016.09.083.
- Lehmann, B., V. Dorer, M. Gwerder, F. Renggli, and J. Tödtli. 2011. "Thermally Activated Building Systems (TABS): Energy Efficiency as a Function of Control Strategy, Hydronic Circuit Topology and (Cold) Generation System." *Applied Energy* 88: 180–191. doi:10.1016/j.apenergy.2010.08.010.
- Mauder, T., P. Charvat, J. Stetina, and L. Klimes. 2017. "Assessment of Basic Approaches to Numerical Modeling of Phase Change Problems—Accuracy, Efficiency, and Parallel Decomposition." *Journal of Heat Transfer* 139 (8). article number 084502. doi:10.1115/1.4036081.
- Mazo, J., M. Delgado, J. M. Marin, and B. Zalba. 2012. "Modeling a Radiant Floor System with Phase Change Material (PCM) Integrated into a Building Simulation Tool: Analysis of a Case Study of a Floor Heating System Coupled to a Heat Pump." *Energy and Buildings* 47: 458–466. doi:10.1016/j.enbuild.2011.12.022.
- Muhieddine, M., E. Canot, and R. March. 2009. "Various Approaches for Solving Problems in Heat Conduction with Phase Change." *International Journal on Finite Volumes* 6 (1): 19–38.
- Ostrý, M., P. Charvát, and T. Klubal. 2016. "Thermally Activated Structures using Latent Heat Storage Technique." Paper presented at the 11th IIR Conference on Phase Change Materials and Slurries for Refrigeration and Air Conditioning, Karlsruhe, Germany, May 18–20.
- Parameshwaran, R., S. Kalaiselvam, S. Harikrishnan, and A. Elayaperumal. 2012. "Sustainable Thermal Energy Storage Technologies for Buildings: A Review." *Renewable and Sustainable Energy Reviews* 16: 2394–2433. doi:10.1016/j.rser.2012.01.058.
- Park, S. H., W. J. Chung, M. S. Yeo, and K. W. Kim. 2014. "Evaluation of the Thermal Performance of a Thermally Activated Building System (TABS) According to the Thermal Load in a Residential Building." *Energy and Buildings* 73: 69–82. doi:10.1016/j.enbuild.2014.01.008.
- Patankar, S. 1980. *Numerical Heat Transfer and Fluid Flow*. Washington: CRC Press.
- Pletcher, R. H., J. C. Tannehill, and D. Anderson. 2011. *Computational Fluid Mechanics and Heat Transfer*. Washington: CRC Press.
- Pomianowski, M., P. Heiselberg, and R. L. Jensen. 2012. "Dynamic Heat Storage and Cooling Capacity of a Concrete Deck with PCM and Thermally Activated Building System." *Energy and Buildings* 53: 96–107. doi:10.1016/j.enbuild.2012.07.007.
- Micronal DS 5040 X. 2018. "Product Sheet of the Microencapsulated Phase Change Material Micronal DS 5040 X Produced by BASF/Microtek Labs." <http://www.microteklabs.com/micronal>.
- Reynders, G., R. A. Lopes, A. Marszał-Pomianowska, D. Aelenei, J. Martins, and D. Saelens. 2018. "Energy Flexible Buildings: An Evaluation of Definitions and Quantification Methodologies Applied to Thermal Storage." *Energy and Buildings* 166: 372–390. doi:10.1016/j.enbuild.2018.02.040.
- Rijksen, D. O., C. J. Wise, and A. W. M. van Schijndel. 2010. "Reducing Peak Requirements for Cooling by using Thermally Activated Building Systems." *Energy and Buildings* 42: 298–304. doi:10.1016/j.enbuild.2009.09.007.
- Romani, J., A. de Garcia, and L. F. Cabeza. 2016. "Simulation and Control of Thermally Activated Building Systems (TABS)." *Energy and Buildings* 127: 22–42. doi:10.1016/j.enbuild.2016.05.057.
- Saelens, D., W. Parys, and R. Baetens. 2011. "Energy and Comfort Performance of Thermally Activated Building Systems including Occupant Behavior." *Building and Environment* 46 (4): 835–848. doi:10.1016/j.buildenv.2010.10.012.
- Schmelas, M., T. Feldmann, and E. Bollin. 2017. "Savings through the Use of Adaptive Predictive Control of Thermo-Active Building Systems (TABS): A Case Study." *Applied Energy* 199: 294–309. doi:10.1016/j.apenergy.2017.05.032.
- Swaminathan, C. R., and V. R. Voller. 1992. "A General Enthalpy Method for Modeling Solidification Processes." *Metallurgical Transactions B* 23 (5): 651–664. doi:10.1007/BF02649725.
- Tatsidjodoung, P., N. L. Pierres, and L. Luo. 2013. "A Review of Potential Materials for Thermal Energy Storage in Building Applications." *Renewable and Sustainable Energy Reviews* 18: 327–349. doi:10.1016/j.rser.2012.10.025.
- Versteeg, H. K., and W. Malalasekera. 2007. *An Introduction to Computational Fluid Dynamics: The Finite Volume Method*. Essex: Pearson Education.
- Voller, V. R. 1996. "An Overview of Numerical Methods for Solving Phase Change Problems." Chap. 9 in *Advances in Numerical Heat Transfer*. Washington: CRC Press.

- Weinläder, H., F. Klinker, and M. Yasin. 2016. "PCM Cooling Ceilings in the Energy Efficiency Center-Passive Cooling Potential of Two Different System Designs." *Energy and Buildings* 119: 93–100. doi:10.1016/j.enbuild.2016.03.031.
- Yu, T., P. Heiselberg, B. Lei, and M. Pomianowski. 2014. "Validation and Modification of Modeling Thermally Activated Building Systems (TABS) using EnergyPlus." *Building Simulation* 7 (6): 615–627. doi:10.1007/s12273-014-0183-6.
- Zhou, D., C. Y. Zhao, and Y. Tian. 2012. "Review on Thermal Energy Storage with Phase Change Materials (PCMs) in Building Applications." *Applied Energy* 92: 593–605. doi:10.1016/j.apenergy.2011.08.025.

Article

Utilization of an Air-PCM Heat Exchanger in Passive Cooling of Buildings: A Simulation Study on the Energy Saving Potential in Different European Climates

Pavel Charvát ¹ , Lubomír Klimeš ^{2,*}  and Martin Zálešák ¹ 

¹ Department of Thermodynamics and Environmental Engineering, Brno University of Technology, Technická 2896/2, 61669 Brno, Czech Republic; charvat@fme.vutbr.cz (P.C.); 162098@vutbr.cz (M.Z.)

² Sustainable Process Integration Laboratory—SPIL, NETME Centre, Brno University of Technology, Technická 2896/2, 61669 Brno, Czech Republic

* Correspondence: klimes@fme.vutbr.cz; Tel.: +420-54114-3241

Received: 4 February 2019; Accepted: 19 March 2019; Published: 22 March 2019



Abstract: The energy saving potential (ESP) of passive cooling of buildings with the use of an air-PCM heat exchanger (cold storage unit) was investigated through numerical simulations. One of the goals of the study was to identify the phase change temperature of a PCM that would provide the highest energy saving potential under the specific climate and operating conditions. The considered air-PCM heat exchanger contained 100 aluminum panels filled with a PCM. The PCM had a thermal storage capacity of 200 kJ/kg in the phase change temperature range of 4 °C. The air-PCM heat exchanger was used to cool down the outdoor air supplied to a building during the day, and the heat accumulated in the PCM was rejected to the outdoors at night. The simulations were conducted for 16 locations in Europe with the investigated time period from 1 May–30 September. The outdoor temperature set point of 20 °C was used for the utilization of stored cold. In the case of the location with the highest ESP, the scenarios with the temperature set point and without the set point (which provides maximum theoretical ESP) were compared under various air flow rates. The average utilization rate of the heat of fusion did not exceed 50% in any of the investigated scenarios.

Keywords: energy conservation; latent heat thermal energy storage; phase change materials; passive cooling

1. Introduction

Many countries, especially in Europe, have adopted a number of requirements on the energy performance of buildings in the last several decades in order to make the building stock more energy efficient [1]. The early energy saving policies focused mainly on energy consumption for space heating. The requirements on the thermal resistance of building envelopes have been repeatedly tightened. As a result, the transmission heat loss of newly-built and renovated buildings has decreased significantly and so has the amount of energy needed for space heating. As the transmission of heat loss decreased, the ventilation heat loss and its impact on the energy consumption of buildings became more important. Consequently, various approaches to the reduction of ventilation heat loss have been introduced. Mechanical ventilation with heat recovery has become more common in many types of buildings, and various energy saving strategies for building ventilation were developed. “Build tight—ventilate right” [2] is becoming a widely-adopted approach in the building sector. The air tightness testing is now a rather standard procedure during building construction, particularly in the case of passive buildings.

Well thermally-insulated buildings with a high air tightness level brought about problems with thermal comfort during the warm part of year. This is one of the factors contributing to the increasing demand for space cooling in Europe [3]. The actual energy consumption for space cooling in buildings is more difficult to determine than the energy consumption for space heating. The energy consumption for space heating can often be obtained or estimated based on the amount of consumed heat or fuels. On the other hand, the energy used for space cooling is mostly in the form of electricity and needs to be obtained from consumption of electricity [4]. Nonetheless, the consumption of energy for space cooling in buildings is becoming a concern even in climates where space cooling was not an issue several decades ago [5]. This development brought about an interest in passive cooling of buildings. Many studies have been conducted in this area since the beginning of the 21st Century. Artmann et al. [6] assessed the climatic potential for passive cooling of buildings by night-time ventilation. The analysis was carried out for 259 locations in Europe. The authors concluded that there was a “very significant” potential for passive cooling by night-time ventilation in Northern Europe. In Central and Eastern Europe and some parts of Southern Europe, the authors assessed the potential of this passive cooling technique as “significant”. However, the authors pointed out that “floating building temperature is an inherent necessity of this passive-cooling concept”. Passive cooling by night-time ventilation is thus mostly suitable for the buildings that are not occupied at night and where low air temperatures and relatively high air velocities during night-time ventilation would not cause discomfort.

Another issue with passive cooling of buildings by night-time ventilation is thermal energy storage. For this passive cooling technique to work effectively, cold needs to be stored at night in order to be available for the next day. Cold is usually stored in the building structures, and thus, night-time ventilation works best in buildings with high thermal mass. As many new buildings consist of light-weight building structures, additional thermal mass needs to be provided for passive cooling to work effectively [7].

Some of the problems of passive cooling of buildings (e.g., lightweight construction or large swings in indoor air temperature) could be mitigated by the use of cold storage units. The cold can be stored in the cold storage unit at night and then utilized during the day. This approach has been used in mechanical cooling systems for decades in the form of ice storage. The use of cold storage in passive cooling makes it possible to avoid supplying large volumes of cool outdoor air into the building at night and thus compromising thermal comfort. Cold can be stored in the cold storage unit at night and utilized the following day.

A number of studies have been conducted in the area of energy saving with latent heat thermal energy storage (LHTES) under various climatic conditions. Arkar and Medved [8] reported investigations of PCM-based LHTES integrated into the ventilation system for free cooling of a building. The LHTES unit was a cylindrically-packed bed comprising spherical containers filled with the encapsulated RT20 paraffin-based PCM (Phase Change Material). A mathematical model of the LHTES unit was created as a 2D continuous-solid-phase packed-bed model. The model was validated with the experimental results obtained for the packed bed with spheres of two diameters; 50 mm and 37.6 mm. The developed model was then used to obtain the multi-parametric temperature-response function of the LHTES unit in the form of a Fourier series. The temperature-response function allowed for calculation of the outlet air temperature of LHTES in the case that the inlet air temperature was approximated with a smooth periodic function. The thermal-response function was then used in the TRNSYS simulation tool for the investigation of free cooling in the case of a low-energy house. In the studied case, 6.4 kg of PCM per m² of floor area was found as an optimum value. The same authors [9] investigated the correlation between the local climate and the free-cooling potential of LHTES. The same packed bed LHTES, as in the previous paper [8], was considered. The climatic data of six cities in Europe were used in the study, and the simulated time period was from 1 June–31 August. The free-cooling potential was assessed in terms of the cooling degree hours (CDH). As no building characteristics or cooling set point were considered, the adopted approach provided the maximum theoretical cooling potential for the specific climatic conditions and the ratio between the

air flow rate and the mass of the PCM. The authors concluded that the wide melting range of a PCM was not a disadvantage in free cooling of buildings. The optimum melting temperature of PCM was 2 °C above the average outdoor air temperature at the location in the investigated time period, and the optimum ratio between the mass of PCM and the air flow rate was $1\text{--}1.5 \frac{\text{kg}}{\text{m}^3/\text{h}}$.

Chen et al. [10] investigated the energy saving potential of a ventilation system with a latent heat thermal energy storage (LHTES) unit under different climates in China. The authors used an in-house-developed model of the LHTES unit (air-PCM heat exchanger). The LHTES unit consisted of 20 parallel PCM slabs, which were 1.5 m long, 0.5 m wide, and 0.01 m thick. The air gaps between the slabs were 0.01 m high. The thermophysical properties of $\text{CaCl}_2 \cdot 6\text{H}_2\text{O}$ were considered in the study with the exception of the melting temperature. The optimal melting temperature for each location was obtained by simulations. An isothermal phase change of the PCM was considered. The simulations were done for eight cities in China for the time period from 1 June–31 August. The average outdoor air temperature in the studied locations varied from 21.3 °C (city of Harbin) to 28.0 °C (city of Guangzhou). The study showed that the optimal PCM melting temperature varied from 21 °C in the case of Harbin to 29 °C in the case of Guangzhou. The average utilization rate of the heat of fusion of the PCM ranged from 0.09 in Shanghai to 0.24 in Beijing. Beijing was also the location with the highest electricity savings (87 kWh).

Costanzo et al. [11] used the EnergyPlus simulation tool to investigate the contribution of the PCM mats, installed behind the plasterboards, on the energy need for cooling and also thermal comfort in an air-conditioned office building with a large glass area. The PCM considered in the study was a fatty acid-based organic material. Three commercially-available variants of the material with the peak melting temperatures of 23 °C, 25 °C, and 27 °C were considered. The non-isothermal phase change without hysteresis with the melting range of about 2 °C was assumed. The summer climatic conditions of three cities in Europe (Rome, Vienna, and London) were used in the study. The authors concluded that the peak values of the operative temperature were reduced by about 0.2 °C when the PCM was used in comparison to a basic scenario without the PCM. The average reduction of the peak cooling load was around 10%, and the cooling energy need was reduced by 6%–12%.

An inverse method to estimate the average air flow rate through the air-PCM heat exchanger in free-cooling operation was proposed in [12]. The air-PCM heat exchanger (HEX) consisted of PCM slabs separated by air gaps. The air flow rate was estimated with the use of experimentally-obtained temperatures at the exit of the heat exchanger. MATLAB and COMSOL Multiphysics were used in the simulations. Considering the plane symmetry, only a half of the PCM slab thickness and a half of the air gap were modeled. Different apparent heat capacity curves were considered in melting and congealing of the PCM (i.e., phase change hysteresis). The authors reported fairly good agreement between the measured air flow rates and the air flow rates obtained by the proposed inverse method. The investigation was the first step in the optimization of the air flow rates with regard to the melting and congealing processes.

The goal of the present simulation study was to assess the energy saving potential of passive cooling of buildings, with the use of an air-PCM heat exchanger, when considering a cooling set point that would allow addressing both the ventilation cooling load and the internal cooling loads. In the study conducted by Chen et al. [10], the temperature set point for the utilization of stored cold was 26 °C as the ventilation cooling load was addressed. Moreover, an isothermal phase change of the PCM was assumed, which is rather rare in the case of most real-life PCMs. A lower temperature set point makes it possible to utilize the stored cold for the removal of indoor cooling loads, and it leads to higher utilization rates of the available cold storage capacity of the air-PCM HEX. In the simulation study presented by Medved and Arkar [9], no temperature set point was considered for the utilization of stored cold. Such an approach provides the maximum theoretical utilization rate of cold storage capacity, but it overestimates the real-life potential of passive cooling (particularly in cold climates). These issues were the motivation for the present simulation study, and the authors aimed at taking them into account. The air-PCM HEX considered in the present study was different from the one (a

packed bed) considered in [9]. The present study revealed significant difference between the “optimal” ratio between the mass of the PCM and the air flow rate in the case of the air-PCM HEX consisting of parallel PCM slabs (panels) and the cylindrically-packed bed of spherical containers filled with the encapsulated PCM [9].

2. Simulated Scenario

The need for space cooling in buildings depends on many factors; most of them building-specific (thermal resistance of the building envelope, area of glazing, ventilation rates, internal heat gains, cooling set point, etc.). Certain assumptions about the operation of cold storage had to be made in order to assess the energy saving potential of passive cooling with an air-PCM heat exchanger (air-PCM HEX) without considering building-specific parameters. The actual amount of cold that can be stored in and released from an air-PCM heat exchanger depends on the temperature of air passing through the air-PCM HEX. In the case of passive cooling, the outdoor air flows through the air-PCM HEX during both rejection of heat (at night) and utilization of cold (during the day). For that reason, the outdoor air temperature was the most important factor in the study. The lower the outdoor air temperature, the larger the amount of cold that can be stored in the air-PCM HEX. On the other hand, when the outdoor air temperature is below a certain value during the day, the outdoor air does not need to be cooled down in the air-PCM HEX. For these reasons, it was assumed that the cold stored in the air-PCM HEX would be utilized only when the outdoor air temperature is above 20 °C. Though the set point of 20 °C seems arbitrary, there are justifiable reasons for choosing this value in the case of passive cooling. Many buildings may need space cooling when the outdoor air temperature is above 20 °C because of the internal heat gains, solar heat gains, and other factors. On the other hand, when the outdoor air temperature is below 20 °C, unconditioned outdoor air can be supplied to a building to provide passive cooling. With the upper limit of a good thermal comfort level at about 26 °C, the supply air temperature below 20 °C provides sufficient cooling capacity in many cases. Once again, cooling loads are very building-specific, and a thorough analysis of a particular case would be needed before actual application of passive cooling with cold storage.

The energy saving potential of the air-PCM HEX in passive cooling was determined from the mass flow rate of air and the difference between the outdoor air temperature and the outlet air temperature of the air-PCM HEX. The investigations were performed for 16 locations in Europe (described in Section 4) and for the time period from 1 May–30 September. Six nominal phase change temperatures of PCM were considered (16 °C, 18 °C, 20 °C, 22 °C, 24 °C, and 26 °C). The phase change temperature of the PCM providing the highest energy saving potential for a particular location could thus be identified.

An air-PCM heat exchanger, described in detail in the next section, was considered in the study. The simulated scenario was as follows. The rejection (discharge) of heat from the air-PCM HEX took place at night between midnight and 6:00. The air flow rate through the heat exchanger was 800 m³/h during the discharge phase. The air passing through the air-PCM HEX during the discharge (rejection) of heat was assumed to return to the outdoor environment. The cold stored in the air-PCM HEX was utilized during the day. Several conditions were set for the utilization of the stored cold. The outdoor air would be supplied to a building through the air-PCM HEX between 8:00 and 20:00, but only if the outdoor air temperature was above 20 °C and the outlet air temperature of the air-PCM HEX was lower than the outdoor air temperature. When the air was supplied to a building through the air-PCM HEX, the air flow rate was 400 m³/h (Figure 1). The simulation model of the air-PCM HEX allows for the calculation of the heat loss/gain to/from the surrounding environment, but the adiabatic walls of the exchanger were considered in the study. Considering a relatively small temperature difference between the inside of the air-PCM HEX and the ambient environment in the passive cooling operation, almost adiabatic walls can be achieved in practice with an appropriate level of (inexpensive) thermal insulation.

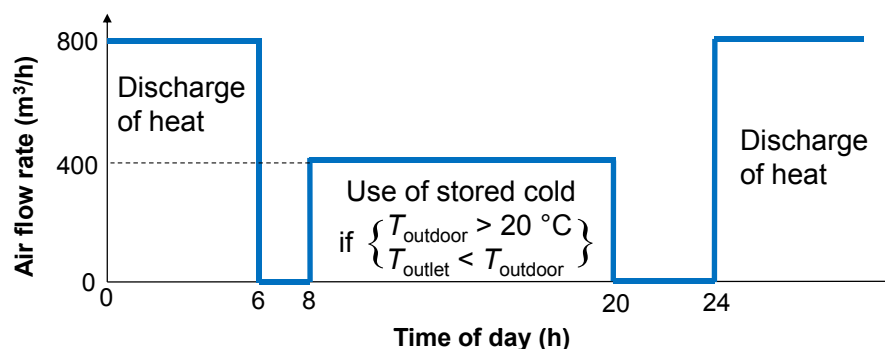


Figure 1. Operation of cold storage.

3. Model of the Air-PCM Heat Exchanger

The model of the air-PCM HEX, previously developed by the authors [13], was used in the study. The exchanger (heat storage unit) consisted of aluminum panels filled with a PCM. The unit contained a total of 100 CSM panels (compact storage modules) in five rows of 20 panels with each CSM panel containing 0.5 kg of the PCM (the total weight of the PCM was 50 kg). A schematic of the air-PCM heat exchanger can be seen in Figure 2. The configuration with 100 panels arranged in five rows of twenty panels was chosen because it was previously investigated both experimentally and numerically [13].

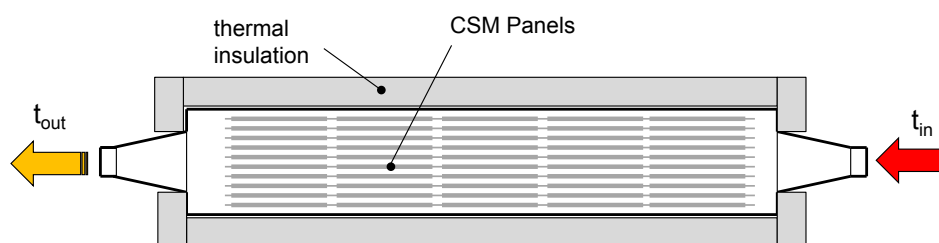


Figure 2. Schematic of the air-PCM heat exchanger. CSM, compact storage module.

The application of such a or similar designs of the latent heat thermal energy storage (LHTES) unit for cold storage has been investigated by many researchers; see, e.g., [14]. The main advantage of the design is its flexibility. The overall thermal energy storage capacity of the air-PCM HEX increases with the number of compact storage modules (panels). The doubling of the number of CSM panels in the air-PCM HEX theoretically doubles its overall thermal energy storage capacity. However, not all arrangements of the CSM panels provide the same performance of the air-PCM HEX. The heat charging and discharging characteristics can be adjusted by the arrangement of the panels in columns and rows.

A PCM exhibiting non-isothermal phase change, but without a phase change hysteresis was considered in the study. The thermophysical properties of the PCM are shown in Table 1. Though no specific PCM was considered in the study, the thermophysical properties were similar to those of paraffin-based PCMs [15]. The model of the heat storage unit was devised as quasi-two-dimensional. It consisted of a set of sub-models of the CSM panels, which were coupled with an energy-balance sub-model for the air flowing between the panels. The sub-model of the CSM panel was devised for the 1D solution of heat conduction in the CSM panel. The conductive heat transfer in the PCM was considered only in the direction of the thickness of the CSM panel (perpendicular to the air flow), while the conductive heat transfer in the other two dimensions was not taken into consideration (as the dominant temperature gradient was in the direction of the thickness of the CSM panel). The effective heat capacity method was used for the phase change modeling. The governing heat transfer equation solved by the sub-model of the CSM panel reads [16]:

$$\rho c_{\text{eff}} \frac{\partial T}{\partial \tau} = \frac{\partial}{\partial x} \left(k \frac{\partial T}{\partial x} \right) \quad (1)$$

where ρ is the density, c_{eff} is the effective heat capacity, T is the temperature, τ denotes time, k is the thermal conductivity, and x is the spatial coordinate. The bell-shaped effective heat capacity defined as a function of the temperature was adopted (e.g., [17]):

$$c_{\text{eff}}(T) = c_0 + c_m \exp \left\{ -\frac{(T - T_{\text{mpc}})^2}{\sigma} \right\} \quad (2)$$

where c_0 is the heat capacity outside the temperature range of the phase change, $c_m = 110 \text{ kJ/kg}$ is the increment of the heat capacity corresponding to the latent heat of the phase change, T_{mpc} is the mean phase change temperature, and $\sigma = 1.05 (\text{°C})^2$ is a parameter characterizing the range of the phase change. The curve of the effective heat capacity according to Equation (2) for the PCM with these parameters, with $T_{\text{mpc}} = 22 \text{ °C}$ and other properties shown in Table 1, can be seen in Figure 3.

Table 1. Thermophysical properties of the PCM considered in the CSM panels

Parameter	Value
Phase change temperature range	$\langle T_{\text{mpc}} - 2, T_{\text{mpc}} + 2 \rangle \text{ °C}$
Mean phase change temperature T_{mpc}	$\{ 16, 18, 20, 22, 24, 26 \} \text{ °C}$
Amount of latent heat	200 kJ/kg
Specific heat	2 kJ/kg °C
Thermal conductivity	0.2 W/m °C
Density	730 kg/m ³

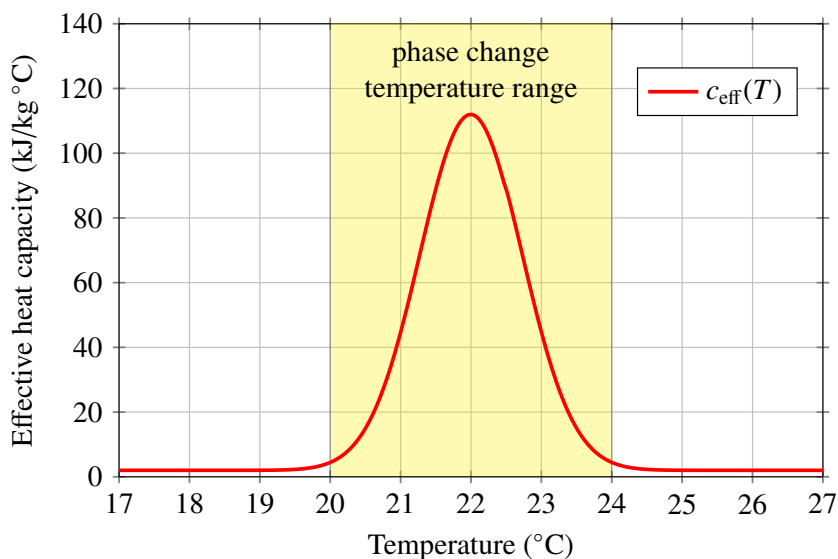


Figure 3. The curve of the effective heat capacity for the considered PCM.

Equation (2) provides a flexible approximation of the distribution of the effective heat capacity of PCMs. Even though most PCMs have an asymmetrical distribution of the effective heat capacity with regard to the mean phase change temperature [18], the approximation by Equation (2) is far more realistic than the assumption of an isothermal phase change considered in some phase change models [19].

The 1D sub-models of heat conduction in the CSM panels interact with each other, as well as with the air flowing in the channel by means of the sub-model of the air flow in the channel. The idea is that each 1D sub-model of the CSM panel is coupled with one node of the air flow sub-model by means of the CSM-air boundary condition. The sub-model of the air flow is devised for the solution of the movement of air in the channel including heat transfer interactions with the sub-models of the CSM panels. A description of this approach was already published by the authors of the paper, and is not repeated here. Readers interested in a detailed description are referred to [20].

4. Considered Locations

The climate in Europe varies significantly, not only with the latitude, but also with other factors such as altitude or the proximity of the sea or ocean. Considering the assumptions and simplifications adopted in the simulated passive cooling scenario, the main factor in the study was the ambient (outdoor) air temperature, which influences the potential of LHTES in passive cooling of buildings. Since the total energy saving potential increases with the number of buildings adopting a particular energy saving measure, only the locations of densely-populated areas were considered in the study. To keep the selection of the locations relatively simple, four cities with their latitude above 55° N were chosen to represent the cold European climate; eight cities with their latitude between 45° N and 55° N represented the mild to cool regions, where the majority of the European population lives; and four cities with their latitude below 45° N represented warm European climates.

Figure 4 shows the boxplots of outdoor air temperature of four cities located above the 55th parallel. A box plot is a graphical representation of numerical data by means of their quartiles. The red horizontal line indicates the median, and the blue box represents values in the second and third quartile (between the 25th and 75th percentiles). The whiskers reach the most extreme values (maximum and minimum values), which are not considered outliers, while the outliers are plotted individually as red plus signs. The outliers had values that were 1.5-times the interquartile range below the 25th percentile or above 75th percentile.

The locations above the 55th parallel provide very good potential for passive cooling of buildings by the supply of unconditioned outdoor air into a building. As can be seen, the outdoor temperature rarely exceeds 20°C . For that reason, the potential for the use of cold storage in passive cooling is rather limited, as will be further demonstrated by the results of the study.

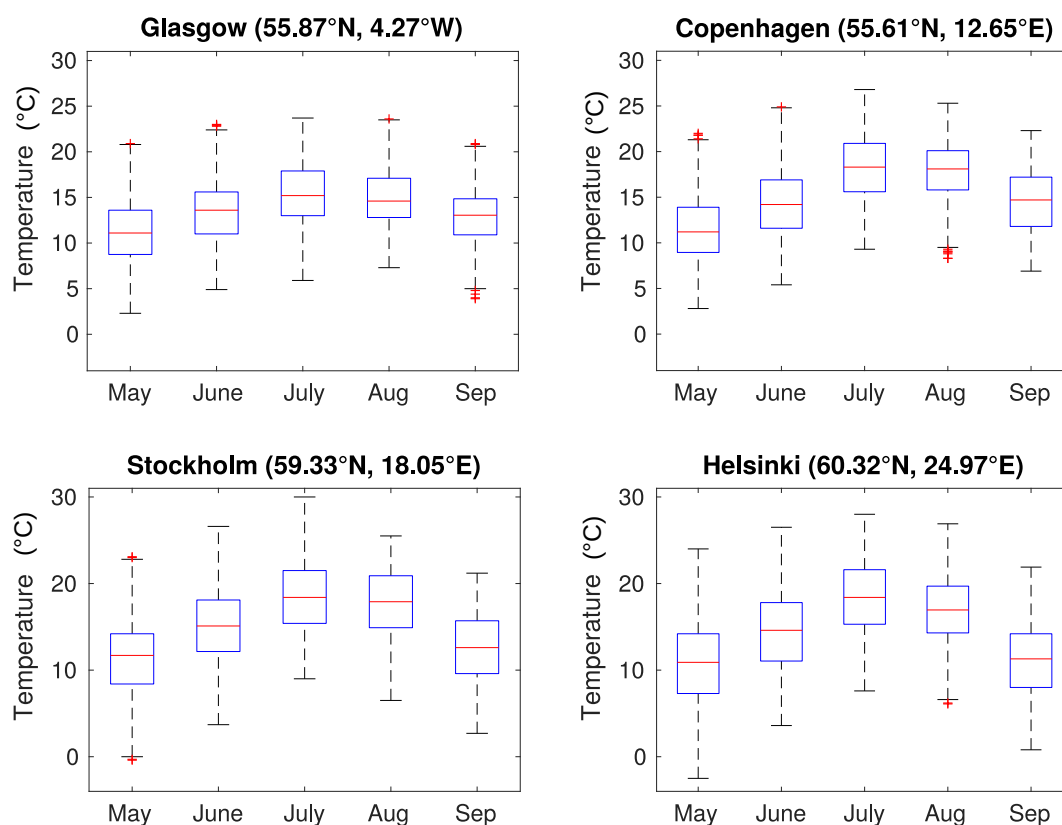


Figure 4. Outdoor air temperatures in the cities located above the 55th parallel.

The box plots of outdoor air temperatures for eight cities located between the 45th and 55th parallels are shown in Figures 5 and 6.

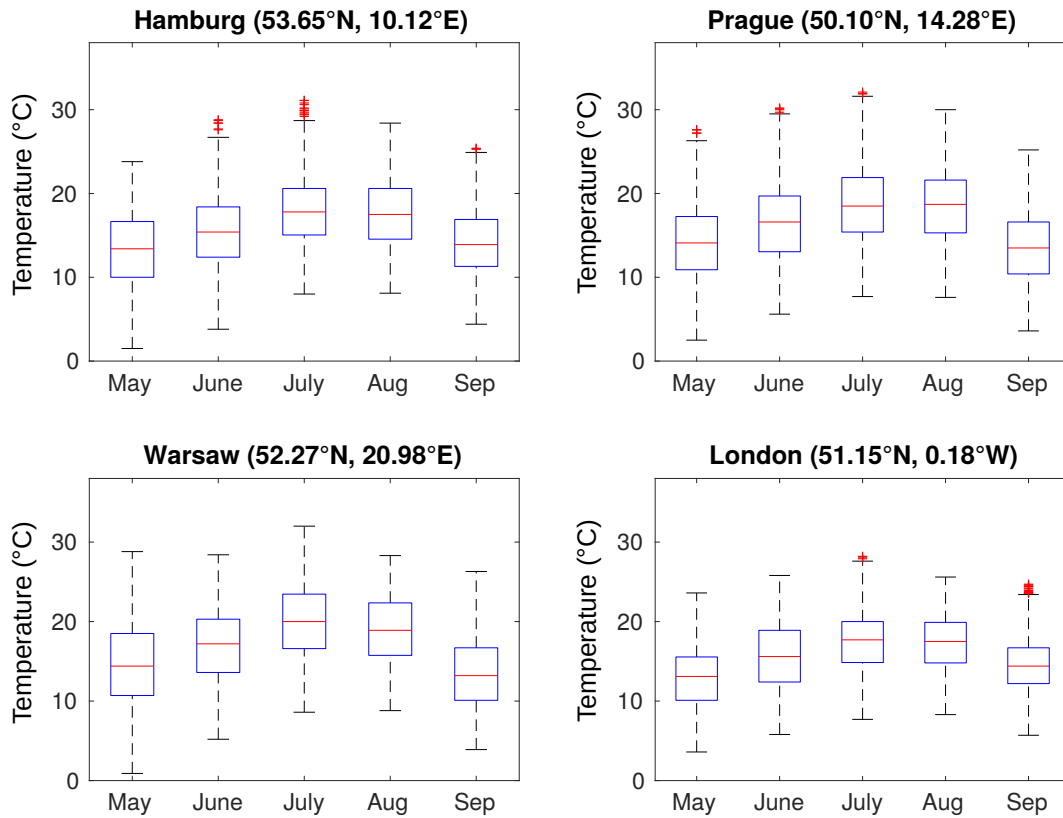


Figure 5. Outdoor air temperatures in the cities located between the 50th and 55th parallels.

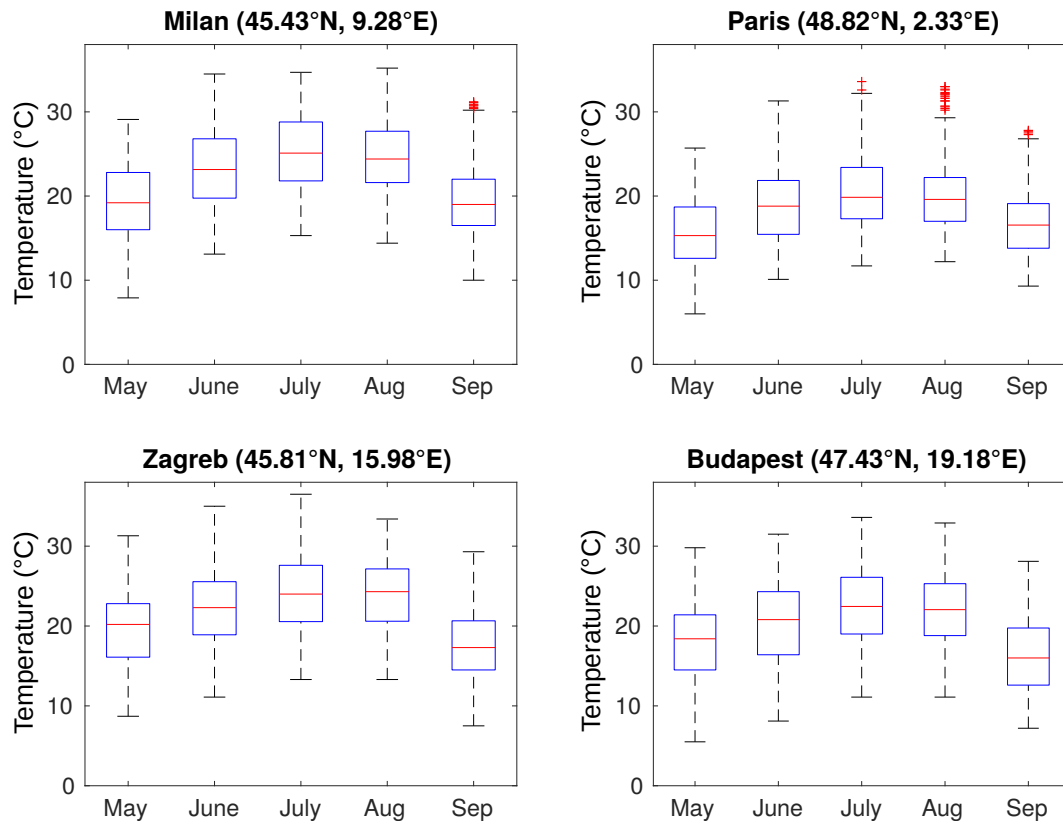


Figure 6. Outdoor air temperatures in the cities located between the 45th and 50th parallels.

The outdoor air temperatures for the four cities located below the 45th parallel are shown in Figure 7. Unlike in case of the four cities above the 55th parallel, there is a high potential for utilization

of cold storage in the south of Europe. The problem is the rejection of heat at night as the air temperatures remain rather high all day long.

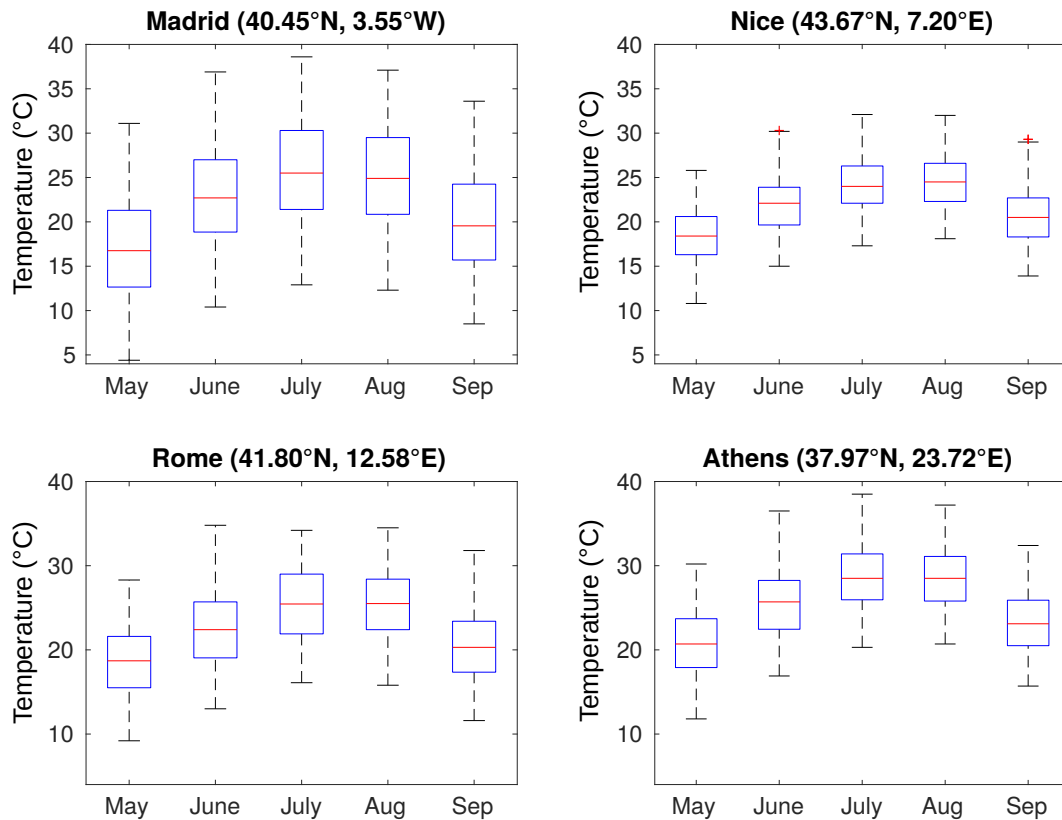


Figure 7. Outdoor air temperatures in the cities located below the 45th parallel.

5. Results and Discussion

The considered air-PCM HEX could store 10,000 kJ (2.78 kWh) of heat or cold in the phase change temperature range of the PCM (Figure 3). The specific heat of the PCM was 2 kJ/kg °C and, thus, 100 kJ/°C could be stored in the form of sensible heat outside of the phase change temperature range. Cold storage in the air-PCM HEX worked in daily cycles, and this means that the maximum amount of cold theoretically available for passive cooling on one day was about 3 kWh. This total heat storage capacity could not be exploited every day as passive cooling was not needed on some days or the heat accumulated in the PCM could not be fully rejected at night.

The amount of cold available for passive cooling of a building was evaluated from the mass flow rate of air \dot{m}_{air} and the temperature difference between the outlet air temperature of the air-PCM HEX T_{outlet} and the outdoor air temperature T_{outdoor} according to:

$$\dot{Q} = \dot{m}_{\text{air}} c_{p,\text{air}} (T_{\text{outdoor}} - T_{\text{outlet}}) \quad (3)$$

where \dot{Q} is the time-dependent heat transfer rate in which cold is transferred from the HEX to the building. The amount of cold (energy saving potential (ESP)) was obtained as:

$$\text{ESP} = \int_{t \in \mathcal{T}} \dot{Q} dt \quad (4)$$

where \mathcal{T} is the set of time instances during the day satisfying the conditions $T_{\text{outdoor}} > 20^\circ\text{C}$ and $T_{\text{outlet}} < T_{\text{outdoor}}$ for the utilization of cold from the air-PCM HEX, as explained in Section 2.

The utilization rate of the heat of fusion utilization rate of the heat of fusion (URHF) was obtained as the ratio between the ESP in a 24-h cold storage cycle and the heat of fusion of the PCM in the air-PCM HEX:

$$\text{URHF} = \frac{\text{ESP}_{24}}{m_{\text{PCM}}H_m} \quad (5)$$

where m_{PCM} is the weight of the PCM in the air-PCM HX and H_m is the enthalpy of fusion of the PCM. Table 2 shows the results for the cities located above 55° N. The largest energy saving potential was in case of Helsinki (82.4 kWh) for the PCM with the nominal phase change temperature of 18 °C. This phase change temperature provided also the largest energy saving potential at other two locations, Copenhagen and Stockholm. Despite a lower latitude than Helsinki and Stockholm and a similar latitude to Copenhagen, the ESP in the case of Glasgow was rather small (proximity of the ocean influencing summer temperatures, as could be seen in Figure 4).

Table 2. Energy saving potential in kWh (cities above 55° N).

		Nominal Phase Change Temperature of PCM (°C)					
		16	18	20	22	24	26
Glasgow	May	2.0	1.3	0.7	0.2	0.1	0.1
	June	6.1	5.3	3.0	1.1	0.3	0.2
	July	12.0	11.0	7.0	2.3	0.8	0.6
	August	15.5	13.4	8.4	3.3	1.2	0.9
	September	1.2	0.8	0.4	0.1	0.1	0.1
	Total	36.8	31.8	19.4	7.0	2.4	1.9
Copenhagen	May	3.3	2.3	1.2	0.4	0.2	0.2
	June	13.1	14.5	10.6	4.9	1.5	0.7
	July	17.4	24.4	25.2	17.1	7.5	2.9
	August	14.8	21.4	20.2	11.5	3.9	1.3
	September	4.3	5.4	3.3	1.0	0.3	0.3
	Total	52.9	68.0	60.5	35.0	13.5	5.3
Stockholm	May	7.1	5.2	3.0	1.2	0.4	0.3
	June	13.8	16.8	17.1	10.5	4.7	1.8
	July	20.6	28.7	30.7	24.1	14.0	6.6
	August	18.9	26.3	25.5	14.1	5.2	1.6
	September	4.0	2.7	1.4	0.4	0.2	0.2
	Total	64.4	79.7	77.6	50.4	24.5	10.6
Helsinki	May	7.0	5.3	3.1	1.3	0.5	0.3
	June	14.1	14.2	10.8	5.8	2.8	1.3
	July	25.6	33.7	33.5	23.3	11.4	4.3
	August	21.4	26.1	19.9	11.1	4.3	1.8
	September	4.4	3.0	1.7	0.7	0.3	0.3
	Total	72.5	82.4	69.0	42.2	19.3	7.9

The energy saving potentials for the cities between 50° N and 55° N are shown in Table 3. Warsaw was the location with the highest energy saving potential of LHTES in passive cooling; 126.5 kWh for $T_{\text{mpc}} = 20$ °C. The situation for Prague, another city located inland, was rather similar. The energy saving potential in the case of London and Hamburg was influenced by the proximity of the sea, which reduced daily temperature swings.

The energy saving potential of LHTES did not improve very much in the case of the cities located between 45° N and 50° N as demonstrated in Table 4. All four cities in this latitude range were located inland. The highest energy saving potential was reached in the case of Milan; 148.5 kWh for $T_{\text{mpc}} = 24$ °C. The phase change temperature providing the largest energy potential shifted to higher values.

Table 3. Energy saving potential in kWh (cities between 50° N and 55° N).

		Nominal Phase Change Temperature of PCM (°C)					
		16	18	20	22	24	26
London	May	8.7	6.8	3.9	1.5	0.6	0.4
	June	21.2	21.3	16.4	8.0	2.6	1.3
	July	19.9	22.6	19.6	12.0	6.4	3.2
	August	22.9	26.3	19.6	10.4	4.2	1.8
	September	8.2	10.5	8.1	4.1	1.6	0.6
	Total	80.9	87.5	67.6	36.1	15.4	7.3
Hamburg	May	10.0	8.2	4.7	1.7	0.7	0.5
	June	15.8	17.1	15.4	10.3	5.2	2.2
	July	20.0	25.9	25.8	18.9	11.6	6.3
	August	19.9	26.8	26.9	19.0	10.2	4.5
	September	8.7	9.2	7.3	3.8	1.7	0.7
	Total	74.4	87.1	80.1	53.6	29.3	14.3
Prague	May	17.4	18.5	14.3	7.7	3.4	1.6
	June	17.8	21.3	21.2	17.1	10.6	5.7
	July	23.2	29.2	31.2	24.7	16.3	8.9
	August	24.5	32.6	34.1	25.3	14.9	7.3
	September	13.0	14.6	12.3	6.5	2.7	1.1
	Total	96.0	116.3	113.1	81.4	47.9	24.5
Warsaw	May	20.1	20.9	18.1	12.6	7.5	3.9
	June	22.9	24.4	22.2	17.3	9.2	4.1
	July	23.0	30.1	35.9	33.9	24.6	14.5
	August	23.0	32.4	38.3	29.1	14.9	5.5
	September	13.3	13.9	12.1	6.5	2.8	1.2
	Total	102.3	121.8	126.5	99.4	59.1	29.2

The best energy saving potential among all investigated locations was obtained for Madrid; 188.7 kWh for $T_{mpc} = 24$ °C (Table 5). Other locations below the 45th parallel did not provide much better energy saving potential than the studied locations with the latitude between 45° N and 55° N, but for different reasons. Rejection of heat accumulated in the PCM was a problem in the case of Nice, Rome, and Athens, as can be seen from the rather narrow interquartile temperature ranges (Figure 7).

As mentioned earlier, the overall thermal energy storage capacity of the air-PCM HEX in the phase change temperature range of the PCM was 2.78 kWh. For the time period from 1 May–September 30, this means the theoretical ESP of about 425 kWh. This potential can only be exploited if the PCM completely melts and solidifies in every cold storage cycle (this means every single day). This cannot be achieved in the considered passive cooling operation, where the daily outdoor temperature swings do not always overlap with the phase change temperature range of the PCM. As a result, the heat of fusion cannot be fully taken advantage of in each cold storage cycle. The largest amount of stored cold utilized during the entire investigated time period was 188.7 kWh in the case of Madrid. This means a utilization rate of the heat of fusion (URHF) of about 44%. This value of URHF is higher than the URHF reported for different climates in China [10]. However, the authors considered an isothermal phase change of PCM, which is not an advantage in passive cooling according to [9]. Furthermore, the authors considered a higher temperature set point for the utilization of stored cold, as they focused on the reduction of ventilation cooling load.

Table 4. Energy saving potential in kWh (cities between 45° N and 50° N).

		Nominal Phase Change Temperature of PCM (°C)					
		16	18	20	22	24	26
Paris	May	11.4	14.5	14.2	8.6	3.5	1.2
	June	16.0	21.4	20.8	16.0	10.1	5.5
	July	10.1	19.1	25.4	24.7	18.7	11.6
	August	11.7	19.2	24.3	21.6	15.1	9.4
	September	13.3	12.0	10.4	8.0	3.9	1.7
	Total	62.5	86.3	95.1	78.7	51.2	29.4
Milan	May	21.8	32.6	35.7	30.7	20.2	10.1
	June	7.5	15.3	25.8	34.3	35.8	30.2
	July	2.8	5.8	13.1	26.4	37.2	42.1
	August	4.2	9.2	17.1	26.7	35.7	37.6
	September	14.4	24.1	30.5	25.7	19.6	12.3
	Total	50.7	87.0	122.3	143.9	148.5	132.3
Zagreb	May	16.3	21.2	23.5	21.5	17.3	11.5
	June	9.8	15.0	19.5	22.8	21.4	18.9
	July	4.6	9.0	15.8	23.9	30.3	30.3
	August	5.3	10.8	16.8	21.7	25.2	26.9
	September	12.5	16.3	14.9	12.0	7.8	3.9
	Total	48.4	72.2	90.5	102.0	101.9	91.6
Budapest	May	24.8	26.7	26.9	23.9	14.6	7.2
	June	23.3	31.7	35.7	30.5	23.0	16.4
	July	11.8	20.3	29.4	35.7	36.6	30.6
	August	11.9	21.3	29.7	34.5	34.0	24.7
	September	21.7	21.7	19.0	13.6	6.6	3.1
	Total	93.5	121.6	140.7	138.2	114.7	81.9

The largest amount of cold utilized in one cold storage cycle (this means during one day) in all locations during the entire investigated time period was 2.67 kWh, meaning URHF of about 95% (Milan, $T_{mpc} = 16$ °C, 13 May). In the vast majority of the cold storage cycles, only a small fraction of the available heat storage capacity was utilized. If the considered air-PCM HEX was used for cold storage in an all-air air-conditioning system, it would be theoretically possible to utilize the entire amount of heat of fusion in the cold storage cycle. Another interesting result of the study is the relatively small difference in the energy saving potential between locations at markedly different latitudes: Helsinki (82.4 kWh) and Athens (107 kWh). Helsinki (latitude 60.32° N) was the northernmost location considered in the study, while Athens (latitude 37.97° N) was the southernmost location.

The amount of cold that can be stored in the air-PCM HEX (and later utilized) depends on the mass flow rate of air. Small mass flow rates of air mean that the available cold storage capacity cannot be fully utilized. On the other hand, large airflow rates lead to the increases of the necessary fan power and thus decrease the energy efficiency of cold storage. The fan power was not considered in the study, as it depends on the actual integration of the air-PCM HEX in the ventilation or air-conditioning systems.

Table 5. Energy saving potential in kWh (cities below 45° N).

		Nominal Phase Change Temperature of PCM (°C)					
		16	18	20	22	24	26
Madrid	May	27.6	31.2	31.7	26.0	17.2	9.1
	June	15.9	25.6	34.6	42.3	44.6	38.1
	July	5.6	10.4	19.6	33.1	45.8	54.4
	August	6.9	13.0	23.0	36.2	48.6	53.7
	September	22.8	32.9	41.3	39.4	32.5	22.3
	Total	78.9	113.2	150.1	176.9	188.7	177.7
Nice	May	12.5	20.0	20.5	12.1	4.4	1.6
	June	3.1	10.1	21.2	24.0	16.1	10.1
	July	1.4	2.4	7.5	18.7	29.7	23.8
	August	1.4	2.0	6.5	17.5	27.2	24.7
	September	5.4	13.9	23.8	21.9	12.9	5.3
	Total	23.8	48.4	79.4	94.1	90.3	65.4
Rome	May	24.2	32.3	33.0	26.2	14.7	6.6
	June	7.9	17.1	27.6	33.5	30.4	25.2
	July	2.5	6.2	14.4	27.9	40.6	44.3
	August	2.8	6.4	13.1	24.8	36.8	41.5
	September	12.4	22.3	32.3	30.7	21.3	12.5
	Total	49.9	84.2	120.4	143.1	143.9	130.2
Athens	May	12.0	22.4	30.1	30.3	22.8	11.3
	June	1.9	4.3	10.7	21.8	30.3	29.2
	July	1.8	1.8	2.0	3.6	10.3	23.3
	August	1.8	1.8	1.9	3.8	10.4	24.6
	September	2.2	6.0	15.5	29.1	28.0	18.6
	Total	19.7	36.3	60.2	88.5	101.8	107.0

Table 6 shows the ESP and the URHF for Madrid under various air flow rates in the considered scenario with the temperature set point of 20 °C for the utilization of cold. Both the ESP and the URHF increase with the increasing air flow rates. Table 7 shows the results for the same scenario, but without the temperature set point. The energy saving potential was obtained from Equation (4), but without the condition $T_{\text{outdoor}} > 20\text{ °C}$. The obtained values of the ESP and URHF were the theoretical maximums that can be reached under the considered conditions. As can be seen, neither the ESP nor the URHF increased very much. The main reason is the frequent occurrence of outdoor air temperatures above 20 °C during the daytime (8:00–20:00) in the studied time period.

Table 6. Energy saving potential (ESP) in kWh for Madrid at various air flow rates for the temperature set point $T_{\text{outdoor}} > 20\text{ °C}$. The percentage in brackets is the utilization rate of the heat of fusion (URHF).

Air Flow Rate (m ³ /h)		Nominal Phase Change Temperature of PCM (°C)					
Daytime	Night	16	18	20	22	24	26
100	200	71.4 (16.8%)	94.7 (22.3%)	118.0 (27.7%)	133.8 (31.5%)	139.2 (32.7%)	130.1 (30.6%)
200	400	76.5 (18.0%)	106.7 (25.1%)	138.3 (32.5%)	161.0 (37.9%)	170.0 (40.0%)	159.9 (37.6%)
400	800	78.9 (18.5%)	113.2 (26.6%)	150.1 (35.3%)	176.9 (41.6%)	188.7 (44.4%)	177.7 (41.8%)
800	1600	79.8 (18.9%)	116.3 (27.4%)	155.9 (36.7%)	185.2 (43.5%)	197.7 (46.5%)	186.4 (43.8%)

Table 7. Energy saving potential (ESP) in kWh for Madrid at various air flow rates without the temperature set point. The percentage in brackets is URHF.

Air Flow Rate (m ³ /h)		Nominal Phase Change Temperature of PCM (°C)					
Daytime	Night	16	18	20	22	24	26
100	200	81.9 (19.3%)	105.5 (24.8%)	127.1 (29.9%)	140.1 (32.9%)	142.8 (33.6%)	131.8 (31.0%)
200	400	90.4 (21.3%)	120.6 (28.4%)	150.2 (35.3%)	168.7 (39.7%)	174.2 (41.0%)	161.3 (37.9%)
400	800	94.6 (22.3%)	128.7 (30.3%)	163.1 (38.3%)	185.0 (43.5%)	192.9 (45.4%)	178.7 (42.0%)
800	1600	96.4 (22.7%)	132.5 (31.2%)	169.1 (39.8%)	193.0 (45.4%)	201.9 (47.5%)	187.1 (44.0%)

Figure 8 shows the comparison of the ESP and the URHF, in the case of Madrid, for the daytime air from rates from 50 m³/h–1000 m³/h (the air flow rates at night were twice higher, from 1000 m³/h–2000 m³/h) for the scenarios with and without the temperature set point. The results in Figure 8 are shown for the nominal phase change temperature $T_{mpc} = 24$ °C. The chart shows a rather significant influence of the air flow rate below about 400 m³/h (0.125 kg of PCM per 1 m³/h of the air flow rate). This PCM mass to air flow rate ratio is significantly lower than the 1–1.5 $\frac{\text{kg}}{\text{m}^3/\text{h}}$ reported in [9]. However, it needs to be emphasized that a very different type of air-PCM HEX (cylindrical packed bed) was used in that study. Furthermore, the PCM considered in the study had a smaller melting enthalpy and a wider temperature phase change range than the PCM considered in the present study. This only demonstrates the difficulty of providing quantitative recommendations that would be generally applicable in a latent heat thermal energy storage. Fortunately, with the current state of knowledge and many available models and simulation tools, it is possible to investigate the performance of a particular design of LHTES under a given set of operating conditions.

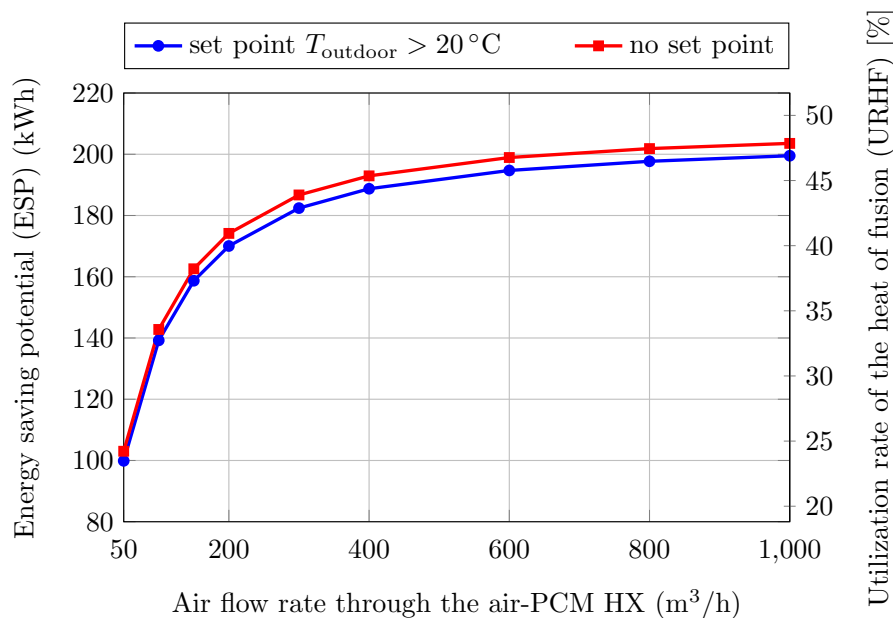


Figure 8. Energy saving potential (ESP) and the utilization rate of the heat of fusion (URHF) for Madrid and the nominal phase change temperature $T_{mpc} = 24$ °C.

The comparison of the URHF for Madrid in the case of the scenarios with and without the temperature set point, in the form of histograms, is shown in Figure 9. Each bar of the histogram represents a URHF range of 5%. The histograms are for the daytime air flow rate of 400 m³/h and

the nominal phase change temperature of the PCM $T_{mpc} = 24\text{ }^{\circ}\text{C}$. As can be seen, the URHF did not exceed 95% in either of the scenarios, but on about 10 days, the URHF was over 90%. As already mentioned earlier, the outdoor temperature set point had only a small impact on both the ESP and the URHF in the case of Madrid.

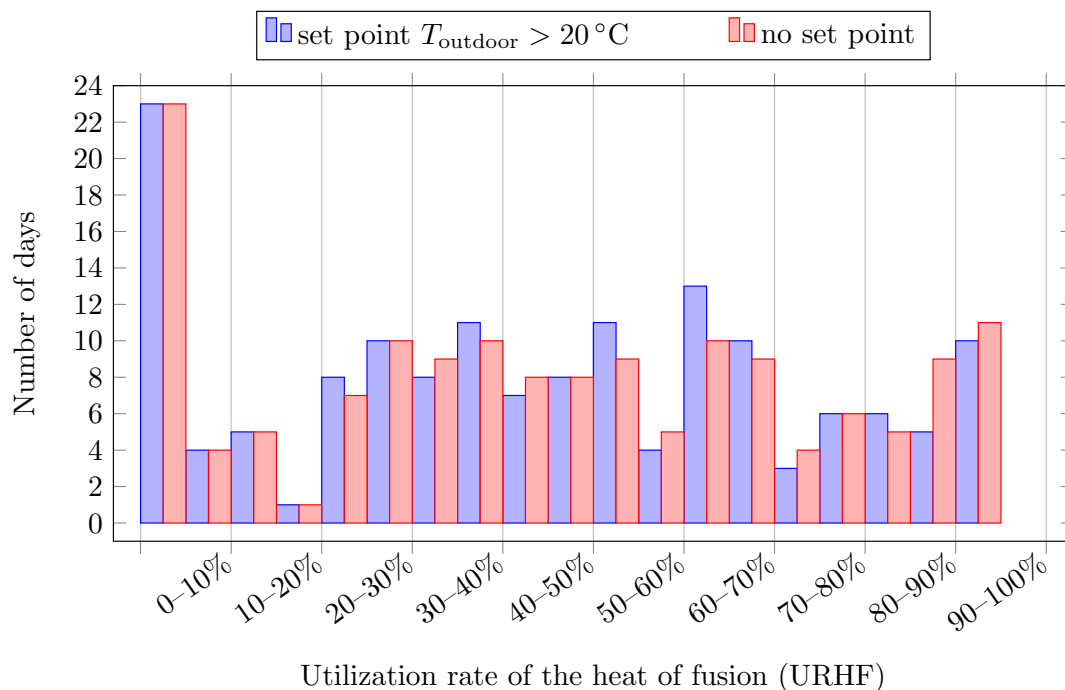


Figure 9. Histogram of the utilization rate of the heat of fusion (URHF) for Madrid and the nominal phase change temperature $T_{mpc} = 24\text{ }^{\circ}\text{C}$; each bar represents a range of 5%.

6. Economic Considerations

Despite many studies demonstrating the energy-saving potential of the PCMs in heat and cold storage, the real-life application of PCM-based LHTES is still lagging behind its potential. One of the reasons is the current economic viability of many solutions employing the PCMs. The economic considerations presented in this section concern only the system investigated in the present paper. A thorough analysis needs to be carried out in each particular case.

Economically, passive cooling is most cost effective if it makes it possible to avoid installation of a mechanical cooling system. In such a case, the benefit of both lower capital costs and lower operating costs can be exploited. If mechanical cooling needs to be installed anyway, the economic benefits of passive cooling are related to lower operating costs and possibly the downsizing of the mechanical cooling system, which can save some capital costs. The more complex the passive cooling system is (e.g., when it includes latent heat thermal energy storage), the less advantage in terms of capital costs it offers in comparison to relatively inexpensive mass-produced air-conditioners.

In the present study, the energy saving potential of passive cooling of buildings with the use of an air-PCM HEX (cold storage unit) was investigated. The economic question was whether the potential energy savings could pay for the cost of the considered air-PCM HEX. The most expensive part of the heat exchanger are the CSM panels. Considering the cost of 10 Euro per panel the total cost of the panels in the air-PCM HEX would be 1000 Euro. The shell of the heat exchanger, thermal insulation, dampers, and other fittings for connecting the heat exchanger to a ventilation system might cost about 200 Euro. The largest amount of stored cold utilized in the entire investigated time period was 188.7 kWh. If a vapor compression cooling system with the coefficient of performance of three ($COP = 3$) were used for space cooling, the reduction of cooling demand due to LHTES would translate to a savings of about 63 kWh of electricity. With the average price of electricity in the EU being about

0.2 Euro/kWh, the simple payback time would be well beyond the expected lifespan of the air-PCM heat exchanger.

7. Conclusions

As expected, the energy saving potential (ESP) of the air-PCM heat exchanger for cold storage in passive cooling of buildings depends on the climatic conditions. However, the differences between some locations were not as significant as could be expected. The energy saving potential in the case of Athens was only about 30% higher than the ESP in the case of Helsinki. The influence of the air flow rates on the ESP was rather significant. In the considered configuration of the air-PCM HEX and the investigated operating conditions, the ESP decreased rather significantly below about 400 m³/h.

The average utilization rate of the heat of fusion (URHF) was lower than 50% in all investigated cases. The main reason for that was the daily outdoor temperature swing that does not always overlap (straddle) the phase change temperature range of the PCM. Nonetheless, the URHF exceeded 90% on some days. In the case of Madrid (the location with the highest average ESP), the outdoor temperature set point of 20 °C for the utilization of cold during daytime had only a small influence on the overall ESP, which was very close to the theoretical maximum (without considering any set point). The main reason was the frequent occurrence of outdoor air temperatures above 20 °C during the utilization of cold, which made the set point condition inconsequential most of the time.

From the economic point of view, the considered way of cold storage (an air-PCM heat exchanger) was not economically viable even in the climates with the most favorable conditions.

Author Contributions: Conceptualization, P.C.; methodology, P.C. and L.K.; software, L.K. and M.Z.; formal analysis, P.C., L.K., and M.Z.; investigation, P.C., L.K., and M.Z.; writing, original draft preparation, P.C. and L.K.; writing, review and editing, P.C. and L.K.; visualization, L.K. and M.Z.; supervision, P.C.; funding acquisition, P.C. and L.K.

Funding: This research was funded by the project Sustainable Process Integration Laboratory (SPIL), funded as Project No. CZ.02.1.01/0.0/15_003/0000456, by the European Research Development Fund and by the project Computer Simulations for Effective Low-Emission Energy funded as Project No. CZ.02.1.01/0.0/0.0/16_026/0008392 by the Operational Programme Research, Development and Education, Priority Axis 1: Strengthening capacity for high-quality research.

Conflicts of Interest: The authors declare no conflict of interest.

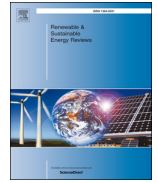
References

1. Mata, E.; Sasic Kalagasidis, A.; Filip Johnsson, F. Contributions of building retrofitting in five member states to EU targets for energy savings. *Renew. Sustain. Energy Rev.* **2018**, *93*, 759–774. [[CrossRef](#)]
2. Perera, E.; Parkins, L. *Build Tight—Ventilate Right*; Building Services, Chartered Institution of Building Services Engineers: London, UK, 1992; pp. 37–38.
3. Connolly, D. Heat Roadmap Europe: Quantitative comparison between the electricity, heating, and cooling sectors for different European countries. *Energy* **2017**, *139*, 580–593. [[CrossRef](#)]
4. Gouveia, J.P.; Seixas, J.; Mestre, A. Daily electricity consumption profiles from smart meters—Proxies of behavior for space heating and cooling. *Energy* **2017**, *141*, 108–122. [[CrossRef](#)]
5. Patronen, J.; Kaura, E.; Torvestad, C. Nordic heating and cooling: Nordic approach to EU's Heating and Cooling Strategy. *TemaNord* **2017**, *532*, 1–110. [[CrossRef](#)]
6. Artmann, N.; Manz, H.; Heiselberg, P. Climatic potential for passive cooling of buildings by night-time ventilation in Europe. *Appl. Energy* **2007**, *84*, 187–201. [[CrossRef](#)]
7. Del Pero, C.; Aste, N.; Paksoy, H.; Haghighat, F.; Grillo, S.; Leonforte, F. Energy storage key performance indicators for building application. *Sustain. Cities Soc.* **2018**, *40*, 54–65. [[CrossRef](#)]
8. Arkar, C.; Medved, S. Free cooling of a building using PCM heat storage integrated into the ventilation system. *Sol. Energy* **2007**, *81*, 1078–1087. [[CrossRef](#)]
9. Medved, S.; Arkar, C. Correlation between the local climate and the free-cooling potential of latent heat storage. *Energy Build.* **2008**, *40*, 429–437. [[CrossRef](#)]

10. Chen, X.; Zhang, Q.; Zhai, Z. Energy saving potential of a ventilation system with a latent heat thermal energy storage unit under different climatic conditions. *Energy Build.* **2016**, *118*, 339–349. [[CrossRef](#)]
11. Costanzo, V.; Evola, G.; Marletta, L.; Nocera, F. The effectiveness of phase change materials in relation to summer thermal comfort in air-conditioned office buildings. *Build. Simul.* **2018**, *11*, 1145–1161. [[CrossRef](#)]
12. Ousegui, A.; Marcos, B.; Havet, M. Inverse method to estimate air flow rate during free cooling using PCM-air heat exchanger. *Appl. Therm. Eng.* **2019**, *146*, 432–439. [[CrossRef](#)]
13. Charvát, P.; Klimeš, L.; Ostrý, M. Numerical and experimental investigation of a PCM-based thermal storage unit for solar air systems. *Energy Build.* **2014**, *68*, 488–497. [[CrossRef](#)]
14. Osterman, E.; Butala, V.; Stritih, U. PCM thermal storage system for ‘free’ heating and cooling of buildings. *Energy Build.* **2015**, *106*, 125–133. [[CrossRef](#)]
15. Pielichowska, K.; Pielichowski, K. Phase change materials for thermal energy storage. *Prog. Mater. Sci.* **2014**, *65*, 67–123. [[CrossRef](#)]
16. Agyenim, F.; Hewitt, N.; Eames, P.; Smyth, M. A review of materials, heat transfer and phase change problem formulation for latent heat thermal energy storage systems (LHTESS). *Renew. Sustain. Energy Rev.* **2010**, *14*, 615–628. [[CrossRef](#)]
17. Kuznik, F.; Virgone, J.; Roux, J.J. Energetic efficiency of room wall containing PCM wallboard: A full-scale experimental investigation. *Energy Build.* **2008**, *40*, 148–156. [[CrossRef](#)]
18. Iten, M.; Liu, S.; Shukla, A. Experimental validation of an air-PCM storage unit comparing the effective heat capacity and enthalpy methods through CFD simulations. *Energy* **2018**, *155*, 495–503. [[CrossRef](#)]
19. Muhieddine, M.; Canot, E.; March, R. Various approaches for solving problems in heat conduction with phase change. *Int. J. Finite Vol.* **2009**, *6*, 1–20.
20. Stritih, U.; Charvát, P.; Koželj, R.; Klimeš, L.; Osterman, E.; Ostrý, M.; Butala, V. PCM thermal energy storage in solar heating of ventilation air—Experimental and numerical investigations. *Sustain. Cities Soc.* **2018**, *37*, 104–115. [[CrossRef](#)]



© 2019 by the authors. Licensee MDPI, Basel, Switzerland. This article is an open access article distributed under the terms and conditions of the Creative Commons Attribution (CC BY) license (<http://creativecommons.org/licenses/by/4.0/>).



Energy demand of liquefaction and regasification of natural gas and the potential of LNG for operative thermal energy storage

Jiří Pospíšil^{a,*}, Pavel Charvát^b, Olga Arsenyeva^c, Lubomír Klimeš^a, Michal Špiláček^a, Jiří Jaromír Klemeš^a

^a Sustainable Process Integration Laboratory – SPIL, NETME Centre, Faculty of Mechanical Engineering, Brno University of Technology, Technická 2896/2, 61669 Brno, Czech Republic

^b Energy Institute, Faculty of Mechanical Engineering, Brno University of Technology, Technická 2896/2, 61669 Brno, Czech Republic

^c Faculty of Mechanical Engineering, University of Paderborn, Pohlweg 55, D-33098 Paderborn, Germany



ARTICLE INFO

Keywords:

Liquefied natural gas
LNG
Regasification
Energy storage
Cooling
Power

ABSTRACT

The world trade volume of Liquefied Natural Gas (LNG) is increasing year by year. Unlike gaseous natural gas (NG), which is transported through a fixed network of pipelines, LNG offers more flexibility to both the exporters and the importers as it can be transported between any pair of exporting and receiving LNG terminals. The LNG process, consisting of liquefaction, transportation, storage, and regasification of LNG, is accompanied by certain energy demands. The paper focuses on the evaluation of the chain of energy transformations involved in the LNG process. Based on the review of existing information, the entire process is evaluated from the view of the potential use of LNG for direct storage of cold and indirect storage of power. The analysis of the existing data shows that the overall efficiency of using LNG for operative energy storage depends very much on the technologies involved and on the overall capacity of the particular technology. The combination of energy-efficient liquefaction technologies and regasification technologies with energy recovery makes it possible to employ LNG as an energy storage medium even when transported over large distances.

1. Introduction

Worldwide consumption of natural gas (NG) has been steadily growing in recent years. There are several factors that have together contributed to the intense use of NG in many applications. Developed countries are calling for the decrease in the environmental impact of combusting fossil fuels for transportation, electricity production, heat, and cold. The use of NG is advantageous because NG has the lowest emissions per released Joule of energy among all fossil fuels. Kumar et al. [1] reported that CO₂ emissions from stroke engines running on NG dropped by around 20% and by 80% for NO_x. Combustion of carbon and oil emits significantly more pollutants, which has recently lead to restrictions on the use of these fuels. The future low-carbon power industry is supposed to renounce carbon and oil completely. The vacancy left by carbon and oil in the energy market has been taken by NG and renewable energy sources. However, increased use of renewable energy

sources is limited by the availability of energy storage leading to NG being preferred to produce electrical energy. Another factor contributing to the popularity of NG is the price of produced energy. The price includes not only the cost of the NG itself but also the price of the technologies necessary for energy transformation as well as for the subsequent minimisation of environmental impact, ecological fees, and carbon credits. Thanks to the composition of methane, the combustion of NG emits the smallest amount of CO₂ per unit of released energy out of all fossil fuels.

The vast availability of NG further promotes its use. New technologies for the extraction and transportation of NG, developed in the last several decades, contribute to the increasing worldwide demand for NG. The deposits of NG in the Earth's crust are assumed to be relatively sufficient and the prices are expected to be stable for several years. The broad application potential of NG is another benefit of this fuel and NG can be used in all plants that use a combustion process to produce

Abbreviations: AGFCS, Automotive gas-filling compressor station; BC, Brayton cycle; C3MR, Propane mixed refrigerant; CCS, Carbon capture system; CHP, Combined heat and power; CNG, Compressed natural gas; COP, Coefficient of performance; DMR, Dual mixed refrigerant; FLNG, Floating liquefied natural gas; FSRU, Floating storage regasification units; HFO, Heavy fuel oil; JT, Joule-Thomson; LNG, Liquefied natural gas; MCFC, Molten carbonate fuel cell; MFC, Mixed fluid cascade; NG, Natural gas; ORC, Organic Ranking cycle; RC, Rankine cycle; SMR, Single mixed refrigerant

* Corresponding author.

E-mail address: jiri.pospisil@vutbr.cz (J. Pospíšil).

<https://doi.org/10.1016/j.rser.2018.09.027>

1364-0321/ © 2018 Elsevier Ltd. All rights reserved.

electrical energy, heat and, indirectly, cold. The NG-plants producing electrical energy are units with flexible operations and outstanding operating parameters. These plants have been in high demand because they complement renewable energy systems that inherently cannot provide stable and uninterrupted supply of electricity. Natural gas is a fuel suitable for road transport, railroad transport, and shipping transport. Consumption of NG in road transport has increased thanks to compressed natural gas (CNG), used particularly in personal vehicles and city buses. The use of liquified natural gas (LNG) as a fuel has gradually spread to cargo transport as well. The popularity of LNG is reflected in the growing number of trucks running on LNG. Song et al. [2] reported that there were 100,000 trucks running on LNG that consumed around 5 Gm³ of NG. That number is very small compared to the number of diesel trucks but still it represents a non-negligible share (about 2.4%) of heavy-duty vehicles.

These facts, combined with a good shelf life and the relatively easy transportation of LNG over long distances, have to lead to serious growth in the global trade of this fuel. LNG represents the energy source with the most intensive development in the world. Dong et al. [3] made a brief historical overview of world's LNG consumption from 1964 (when the production reached 80,000 t) to 2004 (the consumption of 0.1318 Gt). The latter number corresponds with the production reported by Kirillov et al. [4]. On the other hand, NG consumption predicted for 2010 was higher (2.5 Gt). This major increase in consumption reflects accelerating growth of the global market with NG. Overall annual growth from 1970 to 2004 is said to be 20.34% and 7.31% from 1994 to 2004. Zhang et al. [5] applied gravity modelling to LNG trade flows to analyse the factors and mechanisms that influence LNG trade. Factors such as economics, supply and demand, price, energy structure, trade feasibility, and politics were considered. The analysis was carried out for a period of time from 2004 to 2015. The global LNG trade increased from 177.09 Gm³ in 2004 to 302.25 Gm³ in 2015. Fig. 1 presents the LNG trade volumes published by International Gas Union [6] for 1990–2016 with the identification of a number of LNG exporting and importing countries.

Kanbur et al. [7] state that if the current trends continue, the worldwide consumption of LNG will increase by 1.7–2.2% every year, making NG the second most important energy source by 2030. Its predicted growth of consumption is 39% between 2010 and 2030 [8]. The same source predicts that in 2030, natural gas may cover 25% of energy demand in the world. Nowadays, one-third of all the worldwide trade with NG is transported in the form of LNG [9]. Paltrinieri et al. [10] report that the worldwide rise in the consumption of LNG is predicted to be 1.3% per year with the exact numbers of 3.2 Tm³ NG in 2010 to 5.2 Tm³ NG in 2040, while the EU only had a steady 2% rise per year in the last 10 years. The study further informs about the current state of LNG terminals where there are 60 terminals operating in 18 countries and 180 terminals under construction. Yoon et al. [11] confirm the ongoing growth in consumption and importance of NG as one of the world's most important energy source. The advantages of this source are stressed here, namely the “cleanness” resulting from the fact that a) combustion of LNG produces virtually no particulate matter due

to the absence of nucleation particles; b) it produces less gaseous emissions than other fossil fuels, such as NO_x and CO₂, thanks to better mixing of the fuel and oxidiser; and c) regasified LNG produces insignificant amounts of sulphurous emissions thanks to the liquefaction process that removes most of the sulphur that NG might contain. The economic profitability of transportation of NG in the form LNG over long distances is also mentioned. The number of regasification plants is reported to be over 100 in the year 2018, meaning the number of plants almost doubled from 60 plants reported in 2015 [10].

Many deposits of NG are in remote off-shore locations; therefore, long under-sea pipelines would have to be built for delivering NG to coastal liquefaction terminals. Since the mid-1990s, investors started projects on the building of floating LNG facilities (FLNG). The company Shell started operation of the first worldwide FLNG facility in 2011. FLNG technology can unlock off-shore NG resources that are technically difficult to extract or too small for building a pipeline connection to a shore. FLNG facilities utilise similar technologies for LNG liquefaction, storage, and offloading as the on-shore plants. There are two main design constraints on FLNG in comparison to the on-shore plants. The FLNG technology needs to be rather compact, due to limited space, and it needs to withstand the movements of the vessels or the floating platforms that it is installed on.

The main advantage of LNG for transportation and storage is that LNG occupies 600-times less volume than gaseous NG. The density of LNG is approximately 400 kg/m³. LNG is kept at almost atmospheric pressure and at the temperature of – 162 °C during transportation and storage. Liquefaction of NG is an energy-demanding process and based on the performance evaluation of real-life liquefaction terminals, the energy need of the process was determined to be equivalent of up to 10% of the supplied NG [12]. The energy spent on the liquefaction process is not entirely wasted. A certain part of it can be recovered by the utilisation of cold from LNG. The amount of usable cold is given by thermophysical properties of NG and corresponds to 830 kJ/kg of LNG [9]. This cold energy can be recovered during the regasification process, see Fig. 2. Regasification is carried out either in port terminals before NG is transported via gas lines or directly before the use of NG. With respect to the amount of LNG transported worldwide, Agarwal et al. [13] quantified the global amount of cold energy at 12 GW per annum. The exploitation of cold from LNG is quite limited at present. Most of the available cold is wasted during the regasification process when LNG is heated up by water or ambient air [9].

Wasting of cold results in higher prices of NG and it reduces the overall efficiency of this primary energy source. That is why promising ways of utilising cold from LNG in the regasification process should be explored and implemented. Several theoretical studies have recently focused on potential applications of cold energy in power, heat, and cold production, see Fig. 3. Many papers have been published lately, discussing various parts of the LNG chain (conversion, transportation, and utilisation). However, most papers failed to grasp the details of energy requirements and energy gains of the LNG technology. The share of energy consumed, and energy recovered during the LNG treatment is influenced by the current state of the relevant technologies. And these

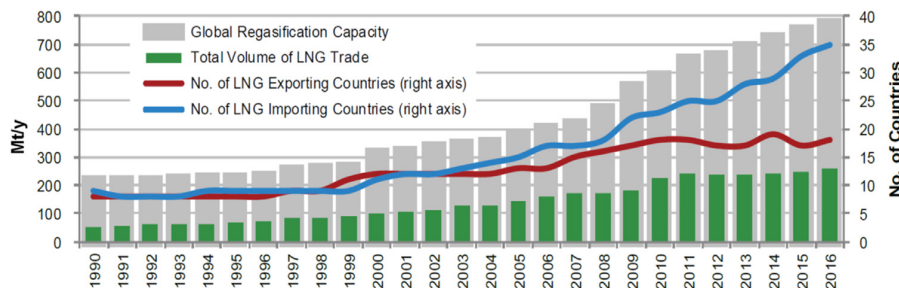


Fig. 1. LNG trade volumes for 1990–2016 (adapted from [6]).

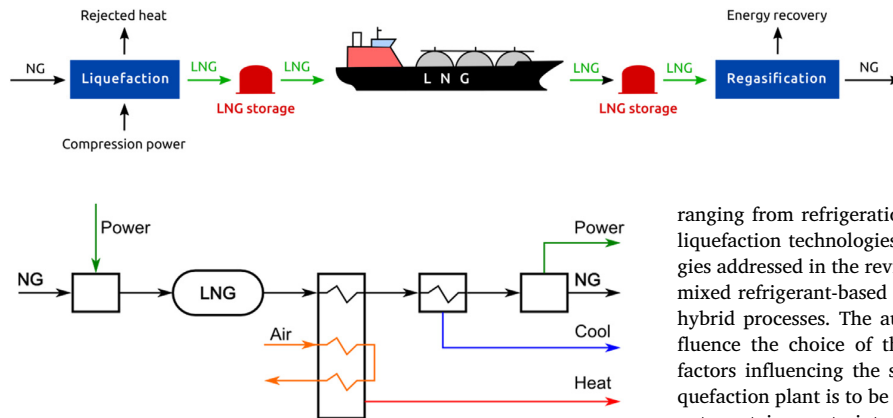


Fig. 2. LNG process.

Fig. 3. Energy flows in the LNG process.

technologies have undergone a major change lately. The consumption of energy for processing of 1 kg of LNG generally decreases with the increasing capacity of the LNG technology (larger LNG liquefaction trains, larger LNG tankers, larger storage tanks, etc.). Since the capacities have increased considerably recently, it is worth re-evaluating the efficiency of the LNG technologies.

The present review analyses and summarises information on LNG technology that has been published recently. Particular chapters tackle partial processes of the LNG technology and evaluate their energy demands. The content and conclusions of papers of various authors published about the topic are listed here. The available sources provided data on the consumption of electricity and gas in the LNG processes. Energy intensity of individual conversions is later utilised to evaluate the overall energy intensity of the LNG technology and to evaluate the current potential of recovering the cold energy. This review also provides information from various documented installations and theoretical studies.

The goal of this review is to present the energy demands of the LNG process including liquefaction, regasification, and relevant transportation and storage. The major share of the paper is focused on the potential of energy recovery and useful exploitation of the cold energy. An overview of the energy intensity of relevant technologies, found in papers of other authors, is given in the textual part of this review. Several sources allow for direct quantification of energy demand of a given process, other sources deal with the general optimisation of the technology and analyse the influence of various parameters on energy consumption. The authors of this paper gathered information on the energy intensity of individual processes within the LNG technology that have been published in the cited papers. This information is presented here in the form of comprehensive tables. To make the energy intensity of LNG technology clear and understandable, the data are also presented in the form of diagrams and charts to show the energy intensity of the LNG process. The whole LNG process is studied in terms of energy efficiency. Acquired data on the energy intensity of liquefaction and regasification allow the evaluation of the potential for using the LNG storage tanks for alternative energy storage.

2. Technologies for liquefaction of NG

Liquefaction is the most energy-demanding part of the LNG supply chain. Several liquefaction processes are currently in use or under consideration in the LNG industry and differ in their complexity and energy demands, see Fig. 4. The suitability and the energy efficiency of a particular liquefaction process depend on many factors including the liquefaction train size.

Khan et al. [14] presented an extensive review of NG liquefaction and optimisation technologies. The authors addressed several issues

ranging from refrigeration principles employed in NG liquefaction, to liquefaction technologies, to process plant optimisation. The technologies addressed in the review included the expander-based technologies, mixed refrigerant-based technologies, cascade-based technologies, and hybrid processes. The authors presented a number of factors that influence the choice of the liquefaction technology. One of the main factors influencing the selection of the technology is whether the liquefaction plant is to be built onshore or offshore. Offshore installation puts certain constraints on the liquefaction technology (space limitations, handling of refrigerant, vessel movements, etc.) that may not constrain an onshore installation in the same way.

A review on trends in the floating liquefied NG technologies was presented by Won et al. [16]. Among other issues, the authors discuss the advantages and disadvantages of onshore and offshore NG liquefaction facilities. The onshore liquefaction plants are often built in remote areas where both the technology and the workforce need to be transported. That has a negative impact on the engineering procurement and construction costs. On the other hand, the floating (offshore) liquefaction plants are built in well-configured shipyards where the workforce is readily available. The authors admit that when large LNG storage is needed it is usually much cheaper in case of onshore plants with the abundance of space than in the case of offshore plants where space is limited. Six nations, Argentina, Brazil, Kuwait, the UAE, the UK, and the USA, operate floating liquefaction plants. Though the offshore liquefaction plants have certain advantages over onshore plants, the countries with the high potential for LNG production (Russia, Iran, Qatar) are not planning construction of large offshore plants in the near future.

The whole liquefaction process, no matter what liquefaction technology is used, consists of these steps [3]: (i) NG is cleaned in a gas treatment plant to remove contaminants like sulphur, CO₂, and water. (ii) NG is cooled down to separate heavier hydrocarbons (with more than three carbon atoms). These hydrocarbons are then used to produce petroleum products. The chemical composition of various LNGs is presented in Table 1. (iii) After the two previous purification steps the NG is cooled down to $-162\text{ }^{\circ}\text{C}$ and liquefied. LNG is then shipped to the destination. At the destination, LNG can be regasified or used directly.

There are three frequently used principles of NG liquefaction [4]. (i) Cryo-generators – using the reverse Stirling cycle (among others) with hydrogen or helium to provide cooling power that can achieve temperatures as low as $-258\text{ }^{\circ}\text{C}$ [17]. (ii) Cryogenic liquids - nitrogen or oxygen have boiling point below the boiling point of NG. Technologies for the production of liquid nitrogen are time-proven and available. (iii) Cascade cycle - this technology uses a cascade of heat exchangers, each with a different medium. All the media are liquefied by compression and have a different boiling point with the last one in the cascade having the boiling point below the boiling point of NG. The cascade cycle and its variants are the most used technology in large LNG plants.

Khan et al. [18] reported optimisation of the dual mixed refrigerant (DMR) process using the commercial Aspen HYSYS[®] simulation tool and the Peng–Robinson state equation for the thermodynamic properties. Two different ambient conditions were considered to investigate the influence of the geographical location on the performance of the DMR process. In the first scenario, the ambient temperature of $25\text{ }^{\circ}\text{C}$ was considered together with the intercooler discharge temperature of $30\text{ }^{\circ}\text{C}$. In the second scenario, both the ambient temperature and the intercooler discharge temperature of $38\text{ }^{\circ}\text{C}$ were considered. The flow

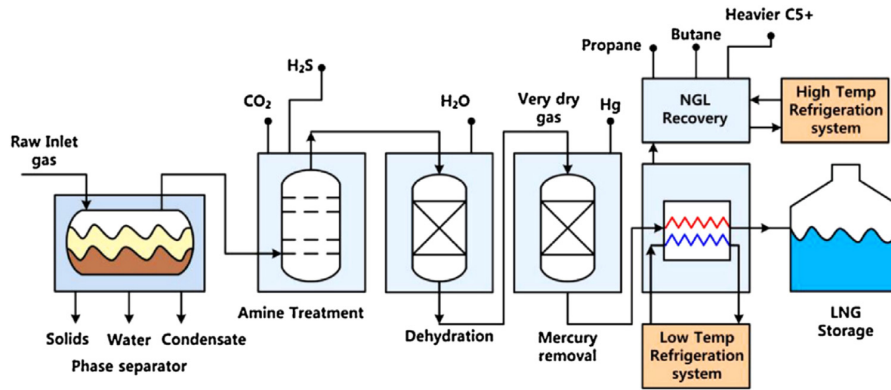


Fig. 4. Block diagram of a typical liquefaction plant (adapted from [15]).

Table 1
Chemical components of various LNGs in the world (adapted from [7]).

Terminal	Methane	Ethane	Propane	Butane	Nitrogen
Abu Dhabi	87.07	11.41	1.27	0.14	0.11
Alaska	99.80	0.10	N.A.	N.A.	N.A.
Algeria	91.40	7.87	0.44	0.00	0.28
Australia	87.82	8.30	2.98	0.88	0.01
Brunei	89.40	6.30	2.80	1.30	0.00
Indonesia	90.60	6.00	2.48	0.82	0.09
Malaysia	91.15	4.28	2.87	1.36	0.32
Oman	87.66	9.72	2.04	0.69	0.00
Qatar	89.87	6.65	2.30	0.98	0.19
Trinidad	92.26	6.39	0.91	0.43	0.00
Nigeria	91.60	4.60	2.40	1.30	0.10

rates of individual components and the suction and discharge pressures of the cold-mixed refrigerant and the warm-mixed refrigerant were the main optimising variables. Single and multi-objective optimisation of the DMR process was conducted with the objectives of minimising both the specific compression energy and the heat exchanger size. The authors concluded that the single objective optimisation with the minimisation of specific compression energy resulted in a 36% saving when compared to the base case. The multi-objective optimisation led to 24% saving when compared to the base case, but the heat exchanger size was reduced by only 3%.

Using computer simulations, nitrogen-based single and dual expander processes were investigated by Khan et al. [19]. The authors used the Aspen HYSYS® simulation software in their study. The main focus of the study was to make the nitrogen-based turbo-expander technologies more competitive with traditional technologies. After analysing the improvement opportunities for energy efficiency, the optimisation of the processes was carried out. The compression energy requirement of the single nitrogen expander process was optimised by varying the low operating pressure and the flow rate of nitrogen. The authors reported an optimum compression energy of 0.7449 kW/kg_{LNG} in the single expander process. Two-step optimisation was used in case of the dual expander process. In the first step, the pressure levels and the nitrogen split fraction were optimised. In the second step, the post-expansion temperatures and the flow rate of nitrogen were optimised with regard to the minimum energy consumption. A minimum compression power of 0.5007 kW/kg_{LNG} was reported in this case.

Han and Lim [20] have reported an improvement of the C3MR liquefaction process. The C3MR process involves precooling NG to -30 °C, using propane as a refrigerant, with the final cooling achieved in the main heat exchanger by a mixed refrigerant that is a mixture of methane, ethane, propane, and nitrogen, see Fig. 5. The reported improvement, named the AP-X™ process, utilises a nitrogen expander loop. In this process, the NG exits the main heat exchanger with a

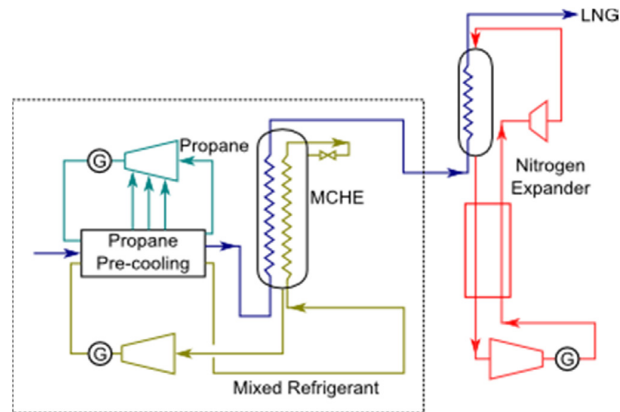


Fig. 5. Diagram of AP-XTM Process (adapted from [20]).

temperature of around -115 °C and is liquefied in the nitrogen expander loop. It is stated that this improvement can increase the train capacity from 5 MTPA to 10 MTPA. The power requirements of the improved cycle were not reported in the paper, but it was stated that the process must be optimised to provide satisfactory efficiency.

Ali et al. [21] have created an optimisation algorithm that greatly reduces the power consumption of the liquefaction process. The application of optimisation algorithms reduced power consumption from 0.4584 kWh/kg_{LNG} to 0.2681 kWh/kg_{LNG}, which means a reduction of 41.5%. Dhameiliya and Agrawal [22] stated that, in general, roughly 400 kWh of energy is needed to produce 1 t of LNG. That means 0.4 kWh/kg of LNG. On the other side, if fully utilised, i.e. without energy losses, 1 kg_{LNG} can provide 0.24 – 0.25 kWh of cold.

Ghorbani et al. [23] investigated the use of trigeneration in the Mixed Fluid Cascade (MFC) liquefaction process. The investigations were done numerically with the use of HYSYS® and MATLAB software. The pre-cooling vapour compression refrigeration cycle in the MFC was replaced with a water-ammonia absorption cycle. The process was combined with a power plant consisting of a high-temperature Molten Carbonate Fuel Cell (MCFC), a gas turbine, and a Stirling engine. A reforming reactor was employed to produce hydrogen for the MCFC. The MCFC operated at the temperature of 650 °C. The heat from the MCFC was used in the Stirling engine to produce electricity. The heat rejected from the Stirling engine, together with the heat from the flue gas of the turbine, was reused in the process. The specific power consumption of the proposed modified MFC process was 0.162 kWh/kg_{LNG}.

The energy efficiency enhancement of a single mixed refrigerant (SMR) process by replacement of the conventional Joule-Thomson (JT) valve with a hydraulic turbine was presented by Qyyum et al. [24]. The

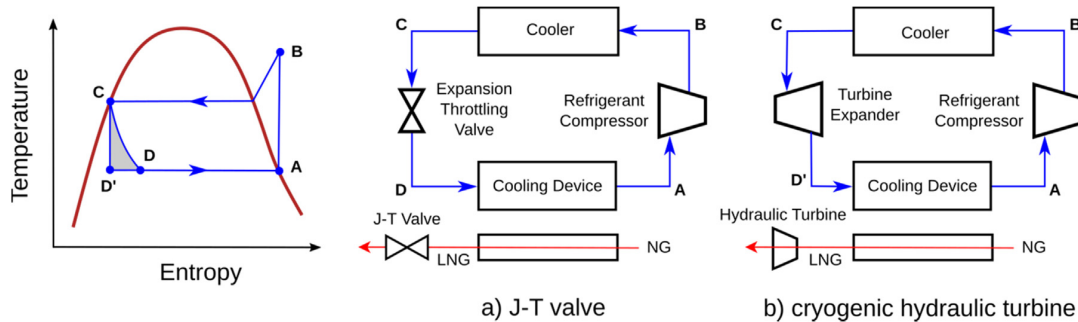


Fig. 6. Replacement of Joule-Thomson valve with a hydraulic turbine (adapted from [25]).

authors used a modified coordinate descent optimisation method, implemented in Microsoft Visual Studio, coupled with a rigorous Aspen HYSYS® model. As the replacement of the JT valve with a turbo-expander is not feasible in SMR, the JT valve was replaced by a hydraulic turbine. The expansion of the JT valve is isenthalpic and thus energy inefficient. On the other hand, the expansion in the hydraulic turbine has isentropic expansion efficiencies over 90% making it possible to recover energy from the expansion process. In the studied SMR process the recovered energy was used for a compressor in the NG feed. The optimised enhanced SMR process required 16.5% less specific compression power compared to the base case.

The development and industrial testing of a cryogenic hydraulic turbine for NG liquefaction process were presented by Chen et al. [25]. The hydraulic turbine was used as a replacement for the JT valve (Fig. 6). The hydraulic turbine with a flow rate of 40 m³/h was developed for energy recovery during the throttling and depressurisation of LNG or mixed refrigerant. The design inlet pressure of the turbine was 4.27 MPa and the rotation speed 2800 rpm. The authors report experimental results for three flow rates (30, 32, and 35 m³/h) with extrapolation for the design flow rate of 40 m³/h. At the flow rate of 35 m³/h, the turbine had the power production capacity of 8.3 kW and it improved the LNG production by an average of 2%.

Nguyen [26] presented a study into NG liquefaction systems that are suitable for small-scale applications. Three refrigeration systems were considered in this study: an SMR system, a single reverse Brayton cycle (BC) with expanders, and a dual reverse BC with expanders. The authors created computational process models in Aspen Plus based on three different thermodynamic models for the calculation of refrigerant properties and power consumption. Five cases based on NG compositions in five European countries were investigated. The authors performed the system optimisation with the aim of finding a trade-off between the power consumption and the size of the systems. The system using the SMR was identified as the most efficient of the three refrigeration systems. The SMR-based system required 1–2 MJ to produce 1 kg_{LNG} and had a coefficient of performance for cooling (COP_{cooling}) of about 0.85, an exergetic efficiency of 33%, and a thermal conductance (of the heat exchanger network used in the liquefaction process) of 250 kW/K. Alternatively, the systems based on the expanders required around 2.5–5 MJ/kg_{LNG}, had a COP_{cooling} of about 0.46, an exergetic efficiency of 15%, and a thermal conductance of 75 kW/K. The comparison between the results showed that the use of different thermodynamic models can cause a minor error (about 1%) in the power consumption of the systems, but the error can peak at about 20% for the thermal conductance of heat exchanger networks.

Kuz'menko et al. [27] discussed the possibility of using automobile gas-filling compressor stations (AGFCS) for NG liquefaction using the open Klimenko cycle. The authors argued that the AGFCS already have the equipment needed to compress NG to 20 MPa and since they never operate at full capacity the unused capacity could be used for NG liquefaction. As the AGFCSs are usually built near highways, the

transportation of the produced LNG would be relatively easy. The proposed plant, using the open Klimenko cycle, could have the production capacity of up to 850 kg/h of LNG. The authors compared the proposed plant to a plant using a K-127 refrigeration machine. They conclude that the plant using the Klimenko cycle would reduce the capital cost by 50% and the unit power consumption by 8%.

Gerasimov et al. [28] commented on the utilisation of small-scale cryogenic systems for energy supply in remote areas. The authors compared gas-piston engines and gas turbines fed by LNG for the co-generation of energy. The presented project of small-scale LNG technology was developed for Tomsk Transgaz Company. This project made use of the AGFCS, utilising the throttle system liquefaction with pre-cooling to – 40 °C. The real-life installation of this liquefaction technology consumed 0.7–0.8 kWh/kg_{LNG}. The production capacity of the plant was below 1 t/h of LNG. Kandiyoti [12] reports that the liquefaction process consumes 9–10% of the NG. Ulvestad and Overland [29] investigated how much NG was consumed to cover energy demands in the processes of established LNG technologies. Their investigations showed that 5–6% of the NG is consumed by the liquefaction process. Selfors et al. [30] state that 5–15% of the NG is consumed by the liquefaction process. Jung et al. [31] report that the liquefaction process consumes 9% of the incoming NG.

The number of papers dealing with the modification and optimisation of NG liquefaction processes shows that the specific power consumption of liquefaction is an important factor in the overall energy efficiency of using LNG as an energy carrier or an energy storage medium. Some of the proposed modifications [23] are rather complex and their application in the near future is not very likely.

Table 2 shows the specific power consumption for the different liquefaction processes. The type of the process is not the only factor influencing the specific consumption. Generally, the larger the plant the lower the specific consumption. Table 3 collects the energy demand of the liquefaction processes expressed as a portion of the incoming NG. The NG demand of the liquefaction process is dependent on the liquefaction technology. However, none of the original sources of the data presented in Table 3 referred to a specific liquefaction technology. Therefore, the data in Table 3 merely demonstrate that the NG demand for the liquefaction process ranges, in general, between 5% and 15%.

3. Technologies for transport and storage of LNG

Because LNG has a large energy volume density, it is very advantageous for transport and storage. Transport of LNG over long distances is done almost exclusively in ships. The loading and unloading of LNG in port terminals is a periodic process that requires enough capacity of the LNG port storage tanks. Creating sufficiently large capacities is necessary to maintain stable supplies of LNG as well as to offset fluctuations in the supply and demand of LNG. Other reasons for sufficiently large storage tanks include the creation of secure supplies of fuels that are located close to the site of NG consumption in case the

Table 2
Power demand of liquefaction processes.

Process	Specific compression power kWh/kg _{LNG}	Source
LNG Liquefaction Plants		
Pure refrigerant cascade (ConocoPhillips Optimised Cascade®), capacity 5.2 Mt/y	0.29–0.35	[14]
MFC® (mixed-fluid cascade), LNG plant in Hammerfest, Norway capacity 4.3 MTPA	< 0.250	[34]
ZR-LNG® FLNG capacity 1 MTPA	0.304	[35]
Simulation results		
Single Mixed Refrigerant	0.3807	[32]
	0.3179	[24]
	0.28–0.56	[26]
N ₂ -CO ₂ dual expander	0.4945	[33]
Single N ₂ expander	0.7449	[19]
Dual N ₂ expander	0.5007	[19]
Automobile gas-filling compressor stations, capacity 1 MTPA	0.7–0.8	[28]
Modified open Klimentko cycle	0.753	[27]
System with expander	0.7–1.4	[26]
General expression to liquefaction	0.25–0.4	[22]
C3MR	0.46–0.27	[21]

Table 3
NG demand of liquefaction processes.

Energy consumption of liquefaction expressed as consumption of NG income	Source
10% of NG	[12]
5–6% of NG	[29]
5–15% of NG	[30]
9% of NG	[31]

regular supplies are disrupted [28]. LNG then serves as a safe backup fuel replacing gaseous and liquid fuels normally used in combustion turbines, stroke engines, and boilers.

LNG storage tanks are cylindrical high-volume containers which store LNG under atmospheric pressure (with the boiling point of LNG at – 162 °C). LNG storage tanks have a simple design with a high-quality thermal insulation that wraps the external shell of the tank. Thermal insulation reduces heat gains from the surrounding environment but cannot fully prevent it. This undesired heat flow causes the LNG to boil off. Boil-off gas must be extracted from the tank so that the internal pressure does not rise. Boil-off gas, which is gaseous NG, can be utilised in the same manner as NG, e.g. in NG-fed combustion engines. If the utilisation of boil-off gas is not attainable or technically feasible, boil-off gas can be vented into the atmosphere.

The energy efficiency of LNG transport is evaluated based on the amount of boil-off gas. Its quantity directly depends on the time necessary for transport. Boil-off gas can be used as fuel for engines of transporting ships and Jung et al. [31] state that 0.17% of boil-off LNG is used daily for the ship demands. Kwak et al. [36] dealt with the use of boil-off gas for LNG-fuelled ships during long-distance transport and long-term storage. The boil-off rate of LNG in storage tanks was quantified as 0.15% per day. Boil-off gas can be utilised as a fuel for thermal engines. If there is no demand for boil-off gas it needs to be reliquefied. The reverse BC is frequently employed for this purpose with nitrogen as a convenient working fluid. The refrigeration temperature necessary for reliquefaction of boil-off gas is significantly lower than the liquefaction temperature of NG due to the composition of boil-off gas which contains predominantly light components of LNG [37]. Recent intensive research focuses on the efficiency of the refrigeration BC that operates with nitrogen as the working fluid. Extending the BC with the process of pre-cooling is presented in [36]. Utilising the multistage expander [38] does not improve the efficiency of reliquefaction for

Table 4
Boil-off rate of LNG during long-distance transport.

Transport / storage	The boil-off rate of NG/d	Source
1 d storage	0.15%	[36]
	0.08%	[6]
20 d transport	0.3%	[12]
9 d transport	0.22%	[29]
1 d ship transport	0.17%	[31]

Table 5
Power consumption and cost impact of CO₂ BOG reliquefaction processes.

Process	Power consumption kW	Fuel consumption t/y	Fuel cost USD/y
Two-stage BOG reliquefaction cycle	105.1	137.1	41,125
CO ₂ BOG reliquefaction process utilising LNG fuel as a refrigerant	5.9	7.7	2309
CO ₂ BOG reliquefaction process utilising LNG fuel as a chilling fluid	4.5	5.8	1,76

nitrogen working fluid. Reliquefaction of boil-off gas in large-scale systems is addressed in many papers (Table 5). A significantly smaller number of contributions deal with reliquefaction of boil-off gas in small applications. Kwak et al. [36] describes a small-scale application that may be employed in LNG-fuelled ships, see Fig. 7. The specific energy consumption of these applications is quantified as 1.27 kWh per reliquefaction of 1 kg of boil-off gas.

Ulvestad and Overland [29] carried out a detailed comparison of two major transport methods for NG, namely pipeline transport and the transport of LNG. Gaseous NG is transported in pipelines and LNG in tankers. Comparison of expensiveness for various transportation methods is a popular and common topic of many papers. Pipelines are a cheaper option for transport over short distances while transport over long distances is more economical in tankers, see Fig. 8. Stevens et al. [39] defined the break-even distance as 5000 km; however, a shorter distance is given by Mäkinen [40] who defines the break-even at 4000 km for land pipes and 2000 km for offshore gas lines.

Raj et al. [42] calculate the fuel consumption for several scenarios where LNG is transported by a ship (LNG carrier). In these scenarios, different carriers with different characteristics and the following operating conditions were considered: (i) the engines consume all the boil-off gas and diesel fuel covers the rest of the power requirements, (ii) all power requirements are met by diesel fuels and boil-off gas is reliquefied in onboard reliquefaction plants, (iii) diesel fuels function only as a backup power source and in case the boil-off gas cannot

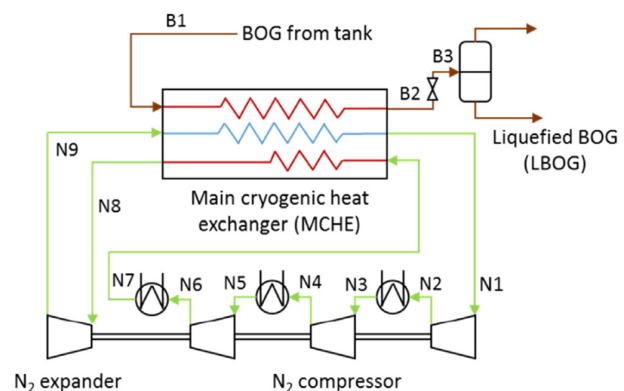


Fig. 7. Brayton cycle with the pre-cooling extension (adapted from [36]).

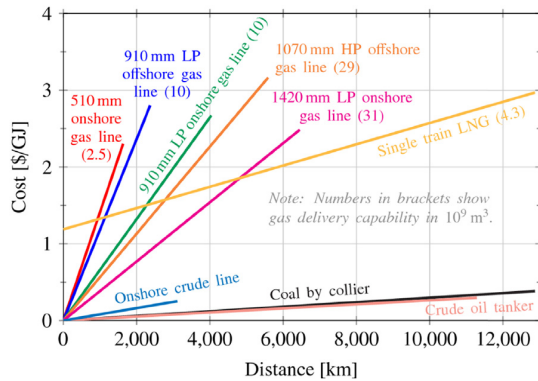


Fig. 8. Costs of fossil fuel transport (adapted from [41]).

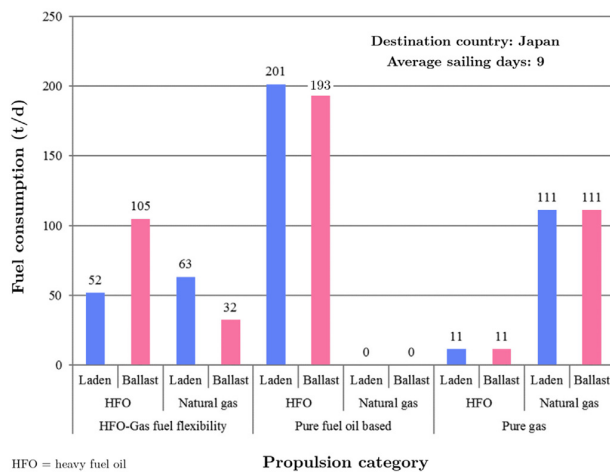


Fig. 9. Fuel consumption per day with different propulsion systems (adapted from [42]).

provide enough power, a forced boil-off is commenced. All of these scenarios were also considered for laden and ballast options. The point of origin was Port Kitimat, Canada, and the destination ports were in Japan, China, and India. Fig. 9 displays the fuel consumption for Japan as the destination.

Kandiyoti [12] identifies consumption of twenty-day LNG transport as up to 6% of transported LNG but many reports state even lower consumption for LNG transformation. These reports frequently fail to evaluate the entire process and focus instead on the particular processes in the LNG value chain. The report from Ulvestad and Overland [29] presents the relative amount of primary NG consumed to cover energy demands in the transport of LNG. It shows that 1–2% of NG is consumed during the mid-distance transport of LNG (Table 4).

There is a significant difference in the conditions for utilisation of

LNG in coastal areas and in landlocked countries. A detailed study published by Pfoser et al. [43] discussed perspectives of the use of LNG in landlocked countries. The study compares the potential of replacing fossil fuels with LNG in Austria which is a landlocked country and has no LNG infrastructure. The study shows a realistic demand for LNG using a survey conducted among consumers in various industries and sectors. A major reason for using LNG quoted by the respondents is the ecological and environmental impact. Combustion of NG represents one of the cleanest combustion processes. Combustion of NG produces almost exclusively water vapours and carbon dioxide. Production of greenhouse gases from engines fuelled by NG represents the primary production of greenhouse gases.

Zhang et al. [5] list the LNG technology as a doable method of energy storage. However, the undesired leak of gas from LNG technology is a significant local source of greenhouse gas emissions. If tanks storing LNG leak, the gas is wasted as it scatters in the air. Ulvestad and Overland [29] state that a single LNG facility became the fourth major producer of greenhouse gases in Norway. Gilbert and Sovacool [44] analysed the climate impact exporting LNG from the USA to Asia. Methane - the main component of NG - is a powerful greenhouse gas. The leakage of NG during production and transportation can lead to greater greenhouse gas emissions than combusting the NG. The authors investigated four of the largest LNG importers in 2013 (China, Japan, India, and South Korea) and identified eleven potential uses of LNG imported to Asia from the USA. The authors developed a bounded hybrid lifecycle-energy strategy analysis based on the normalised emissions and selected end uses of LNG. Three leakage scenarios were considered in the study: 1.45%, 2.93%, and 5.87% of NG leaked. The authors concluded that the probable increase in global greenhouse gas emissions was a result of LNG exports. They point out that, while uncertainty remains, methane leakage, additional energy demand, and decreased domestic coal displacement could thwart potential climate benefits of LNG exports in the long term. In the authors' opinion, the possible solutions to this problem are in the hands of policymakers.

4. Technologies for regasification

Technologies used in the chain of LNG transformations are characterised by significant energy consumption (liquefaction) or energy losses (storage and transport). These issues were addressed in the previous sections of this paper. The regasification is a process in which the LNG is transformed back into gaseous NG. The regasification of LNG releases the significant potential of cold energy, equivalent to 200 kWh of electricity per ton of LNG [45]. Since a large amount of heat is needed for the vaporisation of LNG, seawater, ambient air or other heat sources can be used together with waste heat from other industrial sites in the regasification process. Usually, all the wasted heat of the whole liquefaction-storage-regasification process goes to the LNG vaporisation, where a big amount of heat is needed. The regasification process is a key step in LNG utilisation with a significant potential for energy regeneration [13], see Fig. 10. The energy flows shown in Fig. 10 are addressed in more detail in Fig. 14 and Fig. 15. The majority of

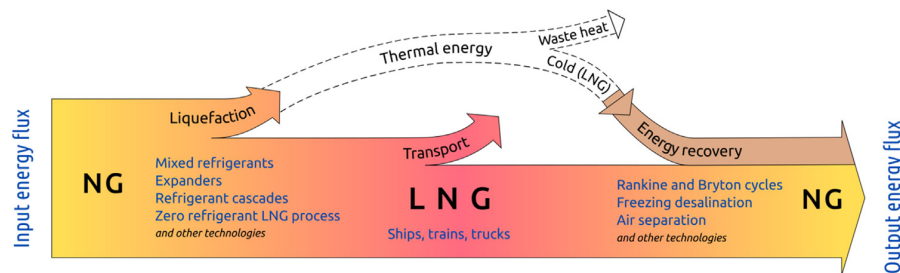


Fig. 10. Energy flows in the LNG process.

regasification plants are operated without any energy regenerative technology. The LNG is boiled off by a convenient source of heat available in particular geographical conditions. The climate-related factors such as ambient air temperature, relative humidity, wind speed, and seawater temperature are considered for LNG regasification technologies around the world. For example, ambient air can be used in fluid vaporisers located in a warmer location (i.e., India, Spain, South America). In this sense, the global climatic effect can positively influence utilising cold energy in the future. In colder geographical conditions, the sea water or active heating of LNG can be utilised. Gas-heated vaporisers consume some portion of LNG for heat generation. Consumption of NG for gas-heated vaporisers is quantified by different authors in the range of 1% [29] to 2.5% [31]. Jung et al. [13] published a review on the available active and passive vaporisers utilised in the LNG regasification terminals. The paper collects data from diverse sources and provides a basis for quantitative design of future installations. The review introduces the submerged combustion vaporisers, open rack vaporisers, intermediate fluid vaporisers, shell and tube vaporisers, and ambient air vaporisers.

Atienza-Márquez et al. [46] carried out a study into cold recovery from the regasification process of LNG with a focus on polygeneration applications. In the first part of the work, the authors provided an overview of the existing literature related to cold recovery opportunities from the LNG regasification and to technologies and applications for the LNG regasification. The authors concluded that most of the LNG regasification plants and facilities worldwide do not recover the cold during the LNG regasification, which means that the great amount of energy supplied to LNG during liquefaction is wasted. A limited interest in providing energy to third parties or their fluctuating demands is among the reasons for such behaviour. The literature review further shows that the cold recovery from the LNG can be utilised in various ways.

The global potential of possible cold production from LNG was identified as nearly 12 GW [6]. The cold production utilises less than 1% of the regasification global potential [13]. This is influenced by the limited requirements for cold delivery in the vicinity of LNG terminals equipped with regasification technology. The cold energy is frequently wasted without utilisation of its “cold” potential. This is a great challenge for the further development of LNG technology with regard to the outlook for future development of consumption. Paltrinieri et al. [10] have reported that the worldwide rise in consumption of LNG is predicted to be 1.3% per year with the exact numbers of 3.2 Tm^3 in 2010 to 5.2 Tm^3 in 2040, while the EU had a steady 2% rise per year in the last 10 years. The current state of LNG terminals has also been reported, with 60 operating in 18 countries and 180 under construction. In response to optimistic forecasts of LNG use, several theoretical works have been published over the past ten years, addressing the utilisation of cold energy. In this area, the authors' attention is focused in two directions. The first direction is the direct regeneration of cold energy by putting in place the appropriate technology to produce a useful form of energy (cold, heat). The second direction is the development of technologies that allow the indirect use of cold energy in a variety of processes. In evaluating the benefits of these applications, the savings of conventional energy sources by using cold energy are assessed. The cold energy of LNG can be recovered during regasification in many processes like seawater desalination, cold storage, cryogenic crushing, cold power generation, inlet air-chilling for gas turbines, producing of liquid nitrogen or air, etc.

4.1. Direct utilisation of cold energy

The majority of LNG terminals use simple vaporisation technologies and benefits can be gained by connecting the LNG vaporisers with technologies that utilise cold energy [50]. Atienza-Márquez et al. [46] mentioned some other applications that make use of the cold recovery from the LNG regasification such as cryogenic air separation, seawater

desalination and the refrigeration and cooling in the food industry and commercial sector. Lee et al. [47] investigated a system combining cryogenic energy storage with the regasification of LNG. The cold recovered during the LNG regasification was employed for the liquefaction of air during peak-off times. In case of demands at peak-on times, the liquefied air can be used for direct expansion to provide shaft work and electricity. The system consists of an LNG direct expansion/generation subsystem and of a cryogenic energy subsystem. The regasification takes place in nine heat exchangers: five of them are used for the liquefaction of air, and the remaining four exchangers use the seawater to gasify the LNG which directly expands in turbines and powers the compressors in the air liquefaction section. The authors created a computational model of the system in the commercial tool Aspen HYSYS®. The model was consequently used for the analysis and assessment of the system. The authors reported that their proposed system has a round-trip efficiency of about 95% which is higher than the 75% that is typical for recently reported cryogenic energy systems. However, the specific work output is only about $161 \text{ kJ/kg}_{\text{LNG}}$. The analysis showed that the heat exchange efficiency between the LNG and air was about 52%. The energy efficiency for the regasification, air storage, and air release was about 31%, 94%, and 71%, respectively. The overall energy efficiency is then approximately 34%.

The authors further carried out the analysis based on the second law of thermodynamics with the aim of evaluating the exergy efficiency. The exergy efficiency for the LNG regasification, air storage, and air release sections were about 55%, 94%, and 61%, respectively. This means that there is a room for further improvements and optimisation, especially in the case of the LNG regasification process and the conversion of the liquid air into shaft work and electricity in the direct expanders. The authors reported the overall exergy efficiency of the proposed system to be about 33%. About 29% of the exergy is destructed by pumps and 17% of the exergy is lost by heating seawater in the LNG regasification process. During the air storage (air liquefaction), only about 6% of exergy was lost in compressors. As for the air release (air direct expansion), about 12% of exergy is destructed in pumps and heaters while about 27% of exergy is lost due to heat exchange with seawater. A thermodynamic analysis revealed that only about 33% of the LNG cold is transferred to the air and that more than 500 kJ of cold per $1 \text{ kg}_{\text{LNG}}$ is still wasted to the seawater. The authors concluded that the thermodynamic and exergy analysis provided an insight into the system and allowed for the identification of possibilities for further improvement and optimisation leading to higher values of the exergy efficiencies.

Lin et al. [9] dealt with utilising cold energy for the seawater freezing desalination process. This process requires significant energy for refrigeration. The evaporation of LNG can be utilised by these processes as a source of economical cold in coastal locations. The cold energy flux of $830 \text{ kJ/kg}_{\text{LNG}}$ is produced during the regasification process. Lin et al. [9] investigated the freezing desalination process, utilising the LNG cryogenic exergy. Design of such equipment and results from the experimental set-up are presented. The salt removal rate is close to 50% per one cycle freezing desalination. The production capacity of freshwater is theoretically quantified as 6.5 kg water per $1 \text{ kg}_{\text{LNG}}$. Cravalho et al. [48] quantified the theoretical maximum freshwater output of the freezing desalination system to be about $6.7 \text{ kg/kg}_{\text{LNG}}$. Freezing desalination requires less energy and lower temperature in comparison with thermal desalination. Lin et al. [9] presented an internal refrigeration loop utilising working coolant R410A, see Fig. 11. From experimentation, a production rate of 2 kg of fresh water per 1 kg of LNG was determined.

Kanbur et al. [7] reviewed several technologies that utilised the cold energy from the LNG revaporisation process, and reported the following:

(i) The seawater desalination process can benefit from LNG cold energy, reportedly with 50% lower energy demand than processes based on reverse-osmosis. According to the conducted study, a $1 \text{ kg}_{\text{LNG}}$

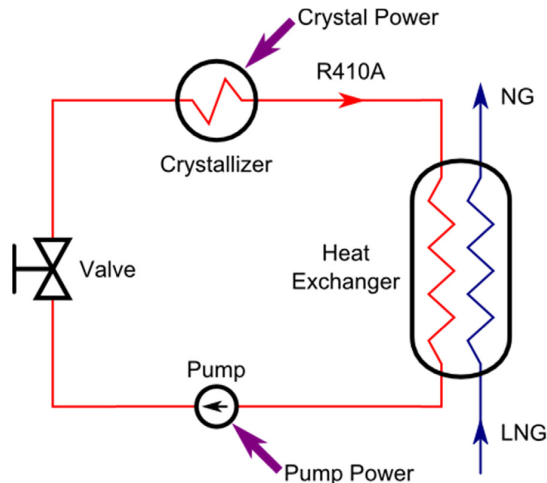


Fig. 11. Freezing desalination with internal refrigeration loop (adapted from [9]).

has enough cold energy to produce 2 kg of ice from seawater with almost no additional energy requirements.

(ii) Air separation is another process which allows direct utilisation of the cold energy recovery from the LNG regasification. Mehrpooya et al. [75] presented a study in which the authors proposed two systems utilising LNG cold energy for the cryogenic air separation and oxygen production. The power consumption of the conventional air separation process was reported to be about 575 kWh/kNm³-O₂. One of the proposed systems, with a two-column configuration employing the cold recovery from the LNG, required an estimated 305 kWh/kNm³-O₂. Another proposed system, which used the LNG cold for the feed air pre-cooling, consumes only about 140 kWh/kNm³-O₂, which reduced its power consumption by about 75% in comparison to the conventional air separation process.

(iii) Cold storage systems can directly use the LNG cold energy e.g. food industry.

(iv) In waste incineration plants, when the LNG stream is utilised as a heat sink of the Rankine cycle (RC) and water in the RC is mixed with ammonia, there is a reported 1.53 times higher thermal efficiency. The product of the plants remains the same and the product of the LNG stream is NG and electricity. This technique is not exclusive to the waste incineration sector only, LNG cold energy can be utilised in the power generation sector in general.

(v) The LNG temperature is low enough to liquefy carbon dioxide from a flue gas stream, thus effectively removing it from the stream for deposition or further usage (e.g. Sabatier reaction). The works conducted in this field have all shown a promising technology when utilising LNG cold energy for CO₂ capture. One of the mentioned methods utilises combined BC and RC, combusting LNG with pure oxygen from an air separation unit which is also utilising LNG cold energy. The resulting energy efficiency is stated to be 65.5%, having 22% higher efficiency than the conventional cycle and almost zero CO₂ production.

Yoo [49] proposes two new carbon capture systems (CCS) on carriers by utilising LNG cold energy. These systems are compared to the original system and show a great reduction in the required power consumption (Fig. 12).

4.2. Integration of the regasification process in power generation plants

The application of LNG as a fuel in a power plant provides the opportunity to use the waste heat of the exhaust gases and LNG cold energy in a combined system. The high-temperature heat can be obtained directly from NG combustion or from flue gases after the gas turbine.

The commonly used technologies for LNG vaporisation are open rack vaporisers, where the major operating costs are associated with pumping and treatment operations, and submerged combustion vaporisers, where the low-pressure NG is burnt to heat the water. When integrating with LNG regasification, two types of thermodynamic cycles can be applied: cycles that use the heat from the environment and produce work; or cycles that use the high-temperature heat obtained from fuel combustion. The integration could involve the implementation of an additional closed cycle with a secondary working fluid using in an organic Rankine cycle (ORC) or the direct expansion of NG to generate power in a turbine and proposing to use waste heat from the power plant for LNG vaporisation. These techniques can be implemented separately or together. Most of the works are based on the thermodynamic and/or exergy analysis of the integrated processes, estimating the efficiency of the integrated cycles. The following power cycles are considered in the literature: the direct expansion cycle, the RC, the BC, the absorption power cycle, the Stirling cycle, and a combination of these cycles.

Fernández et al. [51] considered different thermal cycles for producing power with boil-off gas or regasified NG. In the last ten years, numerous papers described a great variety of such applications involving two or four-stroke engines with internal combustion, steam turbines, gas turbines, combined cycles, and ORCs. A special category includes operating propulsion systems on board of vessels transporting LNG. These propulsion systems are fed by boil-off gas and excess of shaft work is utilised for necessary reliquefaction of boil-off gas. As a convenient solution, Fernández et al. [51] combined a two-stroke low-pressure engine with a dual fuel system. This engine has a good thermal efficiency and it complies with actual emission regulations without needing additional flue gas treatment. The engine revolutions per minute are suitable for the direct connection of the engines with the compressors of reliquefaction technology.

Atienza-Márquez et al. [46] carried out a review of the literature focused on the various ways of cold recovery. This mainly includes the electric power generation by means of an RC or a BC, where the cold from the LNG regasification is used as a heat sink for the cycle. A thermal efficiency of about 25–30% was reported for the combined transcritical RCs. The BCs, which are suitable for high-temperature heat sources (i.e., from biomass combustion), allow for a thermal efficiency of about 70–80%. The authors propose and computationally investigate a polygeneration plant for LNG cold recovery. Their polygeneration plant is a cascade of facilities consisting of (1) the low-temperature transcritical RC with argon as the working fluid, seawater as the heat source, and LNG as the heat sink; (2) the high-temperature transcritical RC with CO₂ as the working fluid, biomass boiler as the heat source, and LNG as the heat sink; (3) the district cooling network with CO₂ as the heat transfer fluid providing three temperature levels for cooling; and (4) an LNG direct expansion unit. The investigators created an analytical model of the plant which was implemented in Engineering Equation Solver (EES). A number of operational scenarios were computationally investigated with the conclusion that the most beneficial is the one with all facilities (1)–(4) in service. For the reported case with an LNG mass flow rate of 30 kg/s, the electricity saving was about 81 kWh/t_{LNG}, the net electric power was 4.5 MW, the refrigeration capacity was 9 MW, the seawater consumption decreased by about 68%, and approximately 35,000 t/y of CO₂ emissions was avoided. The investigators also analysed the influence of the operating LNG pressure. Though a higher LNG pressure allows for higher net electrical power, the refrigeration capacity, the seawater consumption, electricity saving, and other performance characteristics get worse. The authors, therefore, recommend a lower LNG pressure in cases with higher district cooling demands and a higher LNG pressure in cases with higher electricity demands.

The selection of a working fluid for an RC, or of several fluids for a number of cycles in the system, affects the integration performance. Such fluids as ammonia, an ammonia-water mixture, ethane, freon,

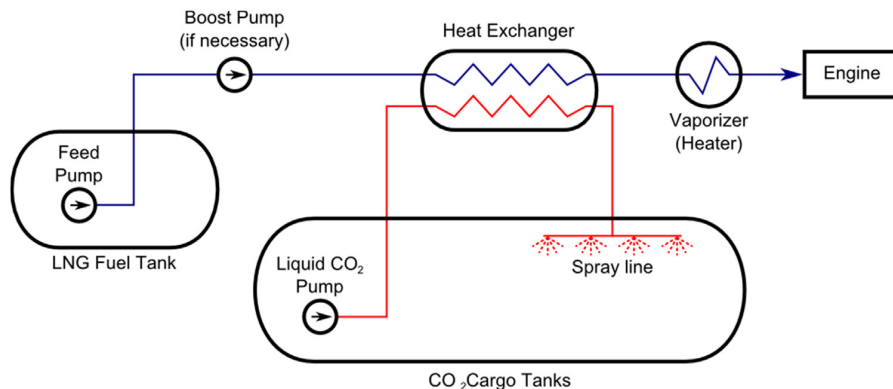


Fig. 12. Schematic diagram of CO₂ reliquefaction utilising LNG fuel (adopted from [49]).

R23, R134a, C₂ hydrocarbons or their mixture, a mixture of propane and tetrafluoromethane (CF₄), or steam for an RC are considered [52]. Another possibility of integration is the combination of LNG regasification facilities with BC power, but the high operating temperatures limit its application, and the combination of a BC with an RC is more promising. To provide the comparison of the various integration systems with different thermodynamic cycles from an energy point of view, the approach proposed in [53] can be made, using such evaluation parameters as the thermal efficiency and the specific power performance. The possibility of integrating an ammonia top RC and LNG bottom cycle in a cascade was proposed by Arcuri et al. [54]. The top cycle generates the electricity in an ocean thermal energy conversion plant, and the bottom cycle uses heat from the top cycle through the direct expansion for producing additional electricity or gives its heat for LNG regasification process. The reported net electric power was 14.23 MW with a thermal efficiency equal to 8.1%. The comparison with the real RC without integration revealed a 17.5% higher thermal efficiency with 11 MW of electric power production. The lack of combustion processes helps to avoid CO₂ emissions.

The integration of low-pressure steam from a pulverised coal power plant with a CO₂ capture unit and cold energy from LNG regasification with a multicomponent ORC was proposed in [55]. It was suggested to use the heat captured from the pulverised coal power plant for pre-heating the working fluid, thus reducing the energy consumption for CO₂ liquefaction. The ORC in the observed system is used as the bottom cycle, enabling it to receive more power from the cold LNG. The analysis of possible working fluids such as propane, an ammonia-water mixture, and a ternary mixture R601-R23-R14, revealed the better performance of the last one. The reported maximal power generation was 74.10 MW and the thermal efficiency of ORC equal to 23.7%.

A system, which consists of an open LNG regasification cycle, an oxy-fuel power generation cycle, and an RC with ammonia-water as the working fluid is described in [56]. The exergy efficiency of the proposed process is 59.4%. The exergoeconomic analysis done in the work provided the exergy efficiency and investment cost of the process components.

Kaczmarek and Stachel [57] studied an ORC with a working fluid condenser cooled by a very low-temperature fluid. The proposed model is based on the LNG regasification by the submerged combustion vaporiser method, in which a portion of the gas is combusted to provide the heat for the process, which comes to 1.5–2.0% of the degasified LNG, reducing the efficiency of LNG regasification. The ORC evaporator type uses the heat of seawater to evaporate the LNG. The implemented evaporator and preheater, installed in the LNG line, are heated up by the seawater, providing additional heat to the NG after the regasification. Ethane, propane, butane, and isobutene were studied as working fluids. The power and efficiency of the RC with these working fluids at different condensation temperatures can be seen in Fig. 13.

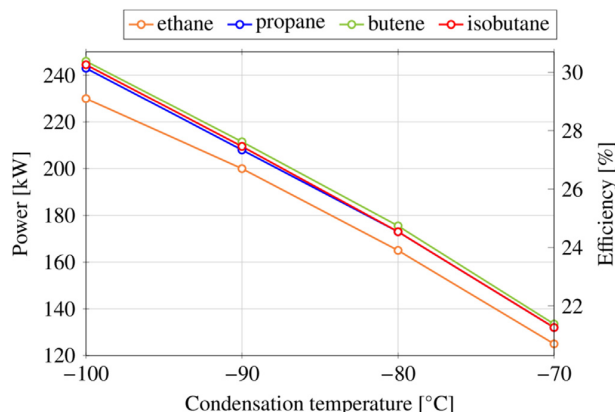


Fig. 13. The power and efficiency of the Rankine cycle at different condensation temperatures (adapted from [57]).

The power and efficiency of the ORC in Fig. 13 are relatively high. The performance generally improves with the decreasing condensation temperature of the working fluid, which is not surprising. The authors suggested utilising the heat from the exhaust fumes of the gas turbine instead of a low-temperature heat source.

A waste heat recovery and utilisation system for a combined heat and power (CHP) plant fuelled with LNG were studied in [58]. The proposed low-grade heat recovery cycle consist of gas and steam turbines from the combined cycle; a subsystem of heat recovery from the steam turbine with LNG vaporisation; the subsystem that recovers both the sensible heat and the exhaust gas heat from the heat recovery steam generator; and the subsystem for hot water utilisation, which receives waste heat from the exit flue gas. There are several advantages of the proposed integrated system: (a) The pressure in steam condenser can be reduced, as the cold energy from LNG vaporisation is used for condensing the steam from the steam turbine. (b) Electricity for the water pump can be saved as no seawater for LNG vaporisation is required. (c) The waste heat of the exit flue gas can be used for heating the water, which can then be sent to the heating system, or to heat the natural gas. (d) There are fewer pollutant emissions from the flue gas as they remain in the condensed water. The efficiency of the fuel utilisation for the proposed combined cycle reaches 62.88%. The heat recovery per kg of flue gas is 86.27 kJ/s and the low-quality waste heat is used to vaporise LNG. With the waste heat utilisation system, about 300 t/h of LNG can be heated to 208 °C in the heat recovery steam generator. The savings of seawater are 12,000 t/h, reducing the electric power for pumping seawater by 1 MW.

Stradioto et al. [59] analysed the possible energy integration of LNG terminals and a power plant. The potential of using waste heat from a

combined cycle gas turbine power plant in the regasification process was considered. The work aims to simultaneously increase the efficiency of the power system and the LNG regasification process. Two scenarios were analysed: 1) integrate the LNG regasification with the inlet air cooling of the BC, and 2) integrate the LNG regasification with inlet air cooling as well as the heat rejection from the RC. The electrical efficiency of the proposed cycles was better than for the non-integrated cycle, with that the first case having an efficiency of 55.54% and the second case having an efficiency of 58.31%, with a gain of 6.32% and 9.90%, respectively. When including the energy for regasification, the efficiency was 62.76% in the first case and 86.34% in the second case. The analysed cases showed higher efficiency when utilising the heat rejected from the RC. The return on investment was also improved by 18.57%.

Moghimi and Khosravian [60] modelled a combination of an ORC, a Stirling cycle, and direct expander turbines. The reported exergy efficiency was 27.98% in the case of the argon ORC, 20.86% in case of the Stirling cycle, and 12.90% in case of the turbines. The maximum efficiency of the proposed integration was 54.25%. The output power was 355.72 kW.

An attempt to compare the performance of different thermodynamic cycles used with LNG regasification was made in [53]. The systems with heat received from LNG combustion showed high-efficiency levels. The combined systems with a gas turbine and a closed BC had the highest exergy efficiency (47–54%) due to their high thermal efficiencies of about 60%. The specific electrical power was 1.7 MW per kilogram per second of regasified LNG. The combined cycles with several RCs in a cascade sometimes have an efficiency level close to zero. In case of a gas turbine, combined cycles have high turbine costs associated with operating with the increasing flow volumes. The RCs with low-temperature heat have higher values of “net” exergy efficiency.

Cascade RCs with a direct expansion power unit were proposed in [61] and [62]. In these works, the LNG regasification process receives heat rejected from each RC. García et al. [62] investigated the RC working at quasi-critical condensation conditions at low relative temperatures. It is proposed, in addition to heat from seawater or ambient air, to use additional heat sources such as heat from combustion engines of floating storage regasification units (FSRUs) or heat from the compressor of the liquefaction process. The working fluids of the RC were argon and methane. The reported maximum energy efficiency of power production was 235.00 kW/kg_{LNG} with an exergetic efficiency of 42.70%.

The integration of a power plant with a closed BC (which operates by the combustion of NG), and cold LNG exergy used for the cooling of the compressor inlet, was investigated by Gómez et al. [63]. The analysed exergy efficiency of the proposed integration is 59.08% with a specific power of 1.746 MW per kilogram per second of LNG.

The integration of LNG regasification with a direct expansion power cycle with a multistage turbine and recovery heat exchanger was analysed by Franco and Casarosa [64]. Compared to the simple direct expansion, which is not feasible from an energy recovery perspective, the proposed system is less complex than the system based on an ORC, having at the same time a similar power production, equal to 120 kJ/kg of NG. The output power of the system was 11.40 MW.

Gómez et al. [65] presented an integration of an LNG regasification process and thermal power plant together with CO₂ capture from the flue gases. The proposed power plant configuration recovers the LNG cold energy through a closed BC and direct expansion and captures CO₂ through an oxy-fuel combustion system and a RC, which operates with the flue gases themselves under quasi-critical condensation conditions. It was pointed out that the LNG composition affects the available exergy, providing higher values for higher CH₄ concentrations in the mixture. The energy efficiency was 65.07% and the exergy efficiency was 53.70%, with a global efficiency of approximately 55.29%. The maximum efficiency ensured power production of 1.650 MW per kilogram per second of LNG.

Zhao et al. [66] analysed an integrated power plant and LNG regasification with CO₂ capture. The power generation system had two parallel twin-staged ORCs with LNG used as a heat sink and flue gas used as a heat source. For the LNG regasification, the pressure was 1.0 MPa with the CO₂ capture of 0.15 MPa, and had a reported maximum network output of 119.42 kW. The integration of the proposed scheme with a magnesite processing plant in China showed the exergy efficiency of 57% while producing 62.03 GWh of electricity.

Some works are devoted to the integration of LNG regasification with electricity production for the FSRU. The integrated heat recovery system, which recovers both the cold energy of LNG and the exhaust gas from the diesel generator for the FSRU, was analysed by Lee and Choi [67]. The LNG vaporisation process, which uses the heat from seawater, is under consideration. Authors make the thermodynamic analysis of the integrated heat recovery system of exhaust gas and LNG. The LNG processing capacity observed in the study is 198.26 kg/s, while the FSRU needs the electricity for LNG regasification process and for on-board utilities. The electricity is produced by two diesel generators with an output of 8.55 MW each, generating the electricity of 12.825 MW. The exhaust gas released in the ambient air comes to 26.8 kg/s with a temperature of 351 °C. For the waste heat recovery, three alternative schemes based on an ORC were investigated: the cycle with primary RC, the cycle with primary and secondary RCs with seawater, and the cycle with primary and secondary RCs with exhaust gas. The received maximum net output was 9.728 MW for the first case, with additional 1.142 MW (or 11.74%) for the second case, and 2.347 MW (or 22%) for the third case. The third case also showed the maximal thermal efficiency. It demonstrated the advantages of the exhaust gases integration; however, the influence of the working fluids was not investigated.

Soffiato et al. [68] analysed the waste heat recovery from an ORC on board of an LNG carrier. The carrier has four diesel generators, two of which have the nominal electrical output equal to 11,000 kW, while the other two produce 5500 kW. Three cases for engines cooling systems were analysed together with three configurations of an ORC, namely simple, regenerative, and two-staged, with six variants of working fluids: R-134a, R-125, R-236fa, R-245ca, R-245fa, R-227ea. The two-stage ORC showed the best characteristics with the highest net power of 820.3 kW, which increased the carrier power output to a 3.50%. The power output also increased when the waste heat was used in the ORC, increasing it maximally by about 2.48%.

Lee et al. [47] proposed and computationally investigated a system for energy storage and generation which employs the use of liquid air and LNG. The off-peak electricity from the grid and the cold from a thermal medium is used to liquify the air. The Linde-Hampson liquefaction process was considered. At on-peak times, the liquid air and LNG are regasified with the cold transferred to the thermal medium, pressurised, and burned in two turbines operating in a BC. The authors created a computational model of the adiabatic system in Aspen HYSYS®. A case with the following parameters was considered: 8 h charging at 60 MW, 8 h reserve, and 8 h generation of on-peak electricity using LNG at about 122 MW. The authors reported a round trip and storage efficiency of about 64% and 73%, respectively. These values were higher than those for systems considered in the comparison. An exergy efficiency of approximately 62% was attained. As for the economic assessment, the authors estimated that the levelised cost of energy ranged between 143 \$/MWh to 190 \$/MWh. Though the thermodynamic efficiencies were reported slightly lower in the case of the use of NG instead of LNG, the levelised cost of energy was reduced by 13%. The authors concluded that the proposed system, utilising the liquid air energy storage, is an economic and viable alternative to facilities using the compressed air, especially considering geographical limitations and environmental impacts.

Morosuk and Tsatsaronis [69] performed an investigation of co-generation systems with the aim to generate electricity while regasifying the LNG. Some novel concepts were proposed and compared to the base case which consisted of a system based on open and closed

BCs of the gas turbines, with the combustion of NG used as the heat source and the LNG regasification process as the heat sink. The open-cycle gas turbine burns LNG and its flue gases expand in the turbine. The flue gases exiting the open-cycle turbine are used as the heat source for the closed-cycle gas turbine which operates with nitrogen. The nitrogen exiting the close-cycle turbine is used as a heat source for the regasification of LNG. The regasified NG then expands in the turbine and produces shaft work. The authors derived some modifications of that system and created computational models using GateCycle, Gatex, and EES software. Modifications, such as the inclusion of an additional nitrogen-based close-cycle gas turbine or the use of a combined (RC-BC) cycle with gas and steam turbines, were proposed. The authors reported that the proposed systems (modifications of the base case) allowed for the increase of the energy efficiency from 68% to 86% (even to 95% in case of the combined cycle) by minimisation of exergy losses from 6.2 MW to 2.6 MW (even to 2.0 MW in case of the combined cycle). The overall exergy efficiency increased from 52.6% to 54.3%. The CO₂ emissions of produced electricity increased from 0.145 CO₂/kWh to 0.19 CO₂/kWh while the CO₂ emissions per 1 kg_{LNG} decreased from 0.09 CO₂/kg_{LNG} to 0.067 CO₂/kg_{LNG}. The specific electricity generation was maximal for the base case with 2.23 MWhel/kg_{LNG} and minimal for the combined cycle with 1.02 MWhel/kg_{LNG}.

4.3. Integration of LNG regasification process in alternative applications

Small-scale (from 0.5 to 10 t/h) regasification technologies for different applications were compared by Gerasimov et al. [28]. These systems are advantageous in locations where laying gas pipe is unfavourable. The small LNG systems can provide a power production system with the necessary fuel reserve. In remote locations, local distribution of LNG enables the construction of self-contained heat and power generating stations. Different technologies are utilised for co-generation of power and heat from LNG in these stations. The gas-piston engines are typically installed with a power capacity of 0.8–3 MW, whereas gas turbines are usually installed in bigger plants with capacities above 15 MW. The majority of decentralised systems are fed by LNG engaged gas-piston engines. The cited efficiency of power production of the installed engines is 40–60%.

Lee and Choi [67] presented an assessment of heat recovery systems applicable to the regasification process of LNG in a vessel equipped with an FSRU. The authors considered three systems with two-stage heat exchangers for the LNG regasification: (a) a system with the RC operating with the first-stage exchanger, using seawater as the heat source; (b) a system which extends the system (a) with a second RC between the first and second-stage exchangers using seawater as the heat source; and (c) a system which consists of identical components as the system (b), but instead of using seawater for the second RC's heat source, flue gases produced by diesel generators are used. Those systems were compared to a case in which two diesel generators were used to generate electricity with a power output of about 13 MW. The authors created computational models in Aspen HYSYS® with the use of the Peng-Robinson equation of state. It was reported that using system (a), more than 75% of the required electricity could be produced by the RC (about 9.8 MW). Using system (b), an improvement of about 12% in the net power generated by the second RC (about 1.15 MW) was obtained. System (c) was identified as the most effective since it doubled the power generated by the second RC to about 2.35 MW. The authors also evaluated the thermal and exergy efficiencies and compared them to the Carnot efficiency. The thermal efficiencies were 5.9%, 6.5%, and 7.4% for the system (a), (b), and (c), respectively. The utilisation of the flue gases (system (c)) allowed for an improvement in the thermal efficiency by about 13% in comparison to the identical system employing seawater as the heat source.

Thermoelectric modules can also be used for converting cold energy into power [70]. The efficiency of this process is dependent on the hot and cold side temperatures, heat flux through the thermoelectric

module, and the properties of thermoelectric materials. The drawback of thermoelectric generators is their low conversion efficiency in comparison with the theoretical thermal engine. It restricts their applications to a few special cases where the geometry of thermoelectric modules adapts to the geometrical requirements of the application [71]. For evaluation of these applications, a complex one-dimensional model was developed by Jeong [70]. The model is able to identify the maximum energy conversion ratio in specific conditions of LNG regasification. The maximum conversion ratio is quantified as 8%, but real installations operate with the conversion ratios significantly lower (2–5%).

4.4. Support of heat and electricity demand

Many countries rely heavily on NG as a fuel for power generation, district heating, and other purposes. Some of those countries even have legislation that require a certain capacity of gas storage in case of interrupted NG supply. The utilisation of LNG can improve energy independence together with making the NG market more competitive. The use of LNG for heating integrated with electricity-heat-gas networks can continually support the heating demand even in peak periods or in case of disrupted supply of gaseous NG.

Some of the works propose models to analyse the heating demand of separate houses in a particular region. This analysis is conducted in combination with the investigation of the requirements for gas and electricity used for heating, dealing with a central or decentralised level. The central level assumes proper daily and hourly timescales with satisfying the demand using energy storage systems. The integration of LNG into the multi-energy systems or hybrid energy networks can provide the steady operation of the electricity network together with district heating networks. The integration of CHP plants with LNG regasification is possible by the utilisation of cold from the LNG in cooling of the condensers in the RC, which increases the overall efficiency of the CHP plants. During regasification, NG increases in volume by a factor of approximately 600, while changing temperature from –162 °C to the ambient temperature, thus providing a large amount of cold exergy [46]. The direct expansion of NG in a CHP plant turbine can interconnect the supply and demand of electricity [72]. By using this technology, it is possible to employ LNG not only for heating but also for power generation.

The integration of an LNG regasification unit with a waste-to-energy plant was presented by Cardona et al. [73]. The paper analyses a case study in the Netherlands. The capacity of the regasification plant is 60–800 t/d of LNG. The waste-to-energy plant utilises 2200 t/d of residual waste and generates about 550 kWh_{el}/t with an efficiency of 15%. The waste heat produced at 73% efficiency can be used for the heating demand of the neighbouring houses, which rely on NG for heating. The considered waste-to-energy plant operates with an RC utilising cold from LNG, which increases the power generating efficiency to 25% and provides additional low-potential heat. To meet the electricity demand, NG is expanded under high pressure. The analysis of the proposed integration showed a decrease of the efficiency of the expander with a decrease of the electricity production. However, the investigated technique does not provide an increase in operational flexibility. The authors suggest that the combining the ORC with a Stirling cycle can provide more advantages.

Clegg and Mancarella [74] proposed a model to ensure the heating and electricity demand for steady operation of energy system under the extreme weather condition. The work shows the possibility of integrating the LNG terminals with renewable energy sources like wind and solar generation in the UK, providing a detailed analysis of NG distribution over the region. The presented scenario can define the NG demand for the coldest winter day, which corresponds to peak heat demand.

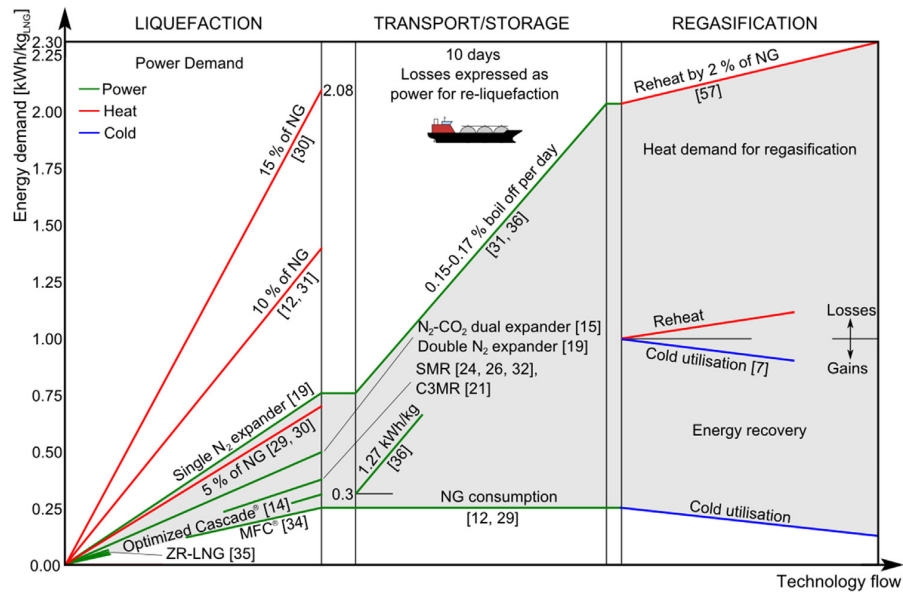


Fig. 14. Energy demands of LNG process.

5. Summary of reviewed technologies

Different studies and papers commented on the energy consumption for LNG technologies in the past fifteen years. There are significant differences between the results of these studies. Kandiyoti [12] identified that the LNG processes involving liquefaction, shipping, and regasification consume 20% of the initial NG. Another study [29] evaluated the consumption of entire chain of LNG technology from the dataset of ship owner Trygve Seglem. The energy consumption of the entire chain of processes is in the range of 20–25% of NG.

The energy consumptions of sub-processes in the LNG technology have been identified from the literary sources referred to in the previous part of this contribution. Tables, charts and diagrams are used to present the data in a condensed and clear manner as it was not possible to create a summary table in the chapter dealing with LNG regasification and cold energy utilisation. The absolute efficiency of the presented technologies is frequently not expressed. Instead, the authors of these studies commonly presented a relative change of the power production efficiency due to utilising of LNG cold energy.

The energy requirements of the LNG process are graphically summarised in Fig. 14. The diagram shows the energy demands and gains of the entire LNG process. The grey area indicates the extent of the energy demand of the LNG technology. The upper border of “the grey area” is characterised by the LNG process with the highest energy consumption. This is 2.3 kWh/kg_{LNG} for the entire LNG technology which corresponds to a consumption of approximately 20% of NG. The lower border corresponds with the LNG process with the minimum consumption of energy and maximum regeneration of cold energy. This technology connects highly efficient MFC liquefaction technology [34], transport of LNG without reliquefaction, and maximum cold utilisation during the regasification process. The lower border represents a chain of processes that are idealised in many steps. This borderline identifies the potential of the chain of technologies for energy recovery. Different energy forms are indicated by different line colours.

A number of studies indicate the energy needs of LNG technology indirectly. They use the corresponding consumption of NG during LNG transformations and transport, see Fig. 15. This consumption is most often expressed as the ratio of the consumed NG and the input amount of NG for the LNG process. This expression allows a practical assessment of the chain of transformation technologies in cases where all

power is generated by using NG. As can be seen, the liquefaction is the most energy demanding part of the LNG process, consuming the equivalent of between 5% and 15% of NG going through the process. The improvement of the effectiveness of liquefaction processes has the highest potential for decreasing the energy demand of the entire LNG process. Transportation and storage represent relatively small energy demand. Though storage of LNG is more energy demanding than storage of gaseous NG, it can be offset by the lower energy demand for long distance transportation of LNG as could be seen Fig. 8. The boil-off makes LNG generally unsuitable for long-term (more than a few weeks) energy storage. Nonetheless, in situations where the consumption of NG is about the same as the amount of boil-off gas, LNG could be used as an energy storage medium. LNG could, for example, replace oil-based fuels in power generation on islands and in some remote locations on the shores with access for LNG tankers.

Regasification of LNG is the process with the highest potential for energy recovery. Though the recovered energy is in the form of heat or cold, it can be used in power generation and thus increase the efficiency of power production. When the cold energy of LNG is utilised then the energy demand of regasification is virtually zero, as shown in Fig. 14. If waste heat is used for regasification the regasification energy demand is close to zero. The energy most demanding situation is the burning of NG to reheat LNG.

The subsequent processes used for energy recovery during the LNG regasification process cannot be correctly addressed in the diagram in Fig. 15. For correct quantification, it is necessary to consider all forms of energy together, as shown in Fig. 14.

6. Conclusions

Liquefied natural gas (LNG) is a promising fuel and energy carrier. Natural gas (NG) is much cleaner fuel than oil and coal, and thus it will play an important role in the transition from fossil fuels to other energy sources. LNG is also a form of energy storage where cold can be recovered and utilised during the regasification process. LNG has certain advantages in comparison to the gaseous NG. For example, the liquefaction process removes most of the impurities contained in NG and makes it an even cleaner fuel. The significant reduction in volume makes it possible to transport LNG effectively over long distances, contributing to the flexibility of the NG market. With the boil-off rate as

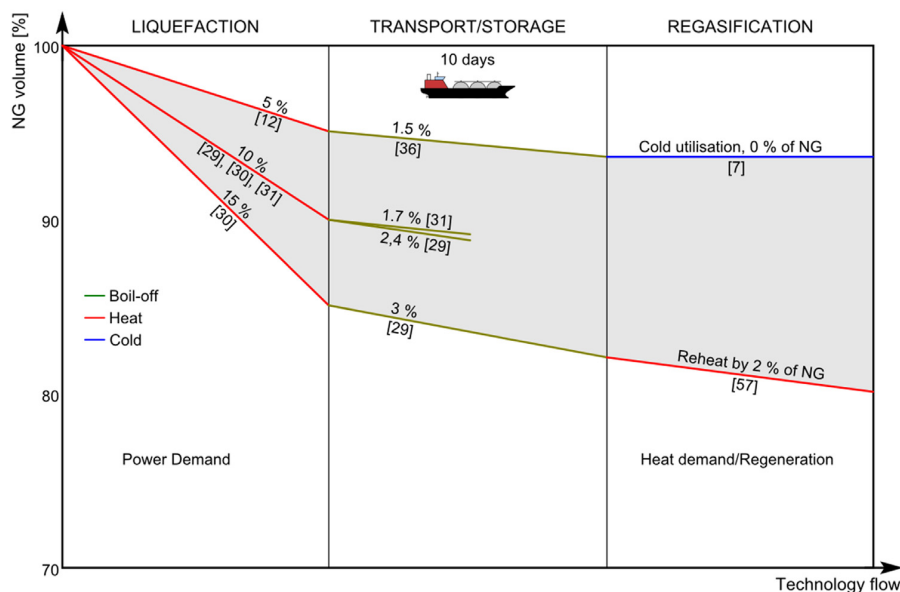


Fig. 15. Natural gas consumption of LNG process.

low as 0.08% per day, the transport of NG in the liquefied form by LNG carriers is more energy efficient than the transport of compressed NG in gas pipelines where gas turbines are used to drive the compressors.

Though the liquefaction process is quite energy demanding, the application of various energy recovery technologies in the regasification process makes it possible to recover a significant part of the energy used. The literature review presented in this paper shows a number of techniques and technologies for energy recovery during the regasification process. An application of such techniques makes LNG not only a fuel but also a medium for thermal energy storage. The effectiveness of LNG, as a thermal energy storage (basically cold storage) medium, increases with the decreasing power demand of the liquefaction process and with the decreasing losses during transportation and storage. As the specific power consumption depends on both the liquefaction technology and the plant capacity, the high capacity liquefaction plants utilising energy-efficient liquefaction processes have the highest potential for applications of energy recovery technologies in the regasification of LNG. Some liquefaction plants in operation have a specific consumption of less than 0.25 kWh/kg_{LNG}, with theoretically proposed technologies achieving even lower values. Certain estimates of the overall energy efficiency of the LNG process, based on the literature review, were presented in this paper. However, many of the possible energy recovery technologies found in the literature are only in the concept or experimental stage and their practical applicability needs to be further investigated.

Acknowledgement

This paper has been supported by the project Sustainable Process Integration Laboratory - SPIL, No. CZ.02.1.01/0.0/0.0/15_003/0000456, funded by European Research Development Fund, Czech Republic Operational Programme Research, Development and Education, Priority 1: Strengthening capacity for quality research.

References

- [1] Kumar S, Kwon H-T, Choi K-H, Lim W, Cho JH, Tak K, et al. LNG: an eco-friendly cryogenic fuel for sustainable development. *Appl Energy* 2011;88:4264–73. <https://doi.org/10.1016/J.APENERGY.2011.06.035>.
- [2] Song H, Ou X, Yuan J, Yu M, Wang C. Energy consumption and greenhouse gas emissions of diesel/LNG heavy-duty vehicle fleets in China based on a bottom-up model analysis. *Energy* 2017;140:966–78. <https://doi.org/10.1016/J.ENERGY.2017.09.011>.
- [3] Dong L, Wei S, Tan S, Zhang H. GTL or LNG: which is the best way to monetize “stranded” natural gas? *Pet Sci* 2008;5:388–94. <https://doi.org/10.1007/s12182-008-0063-8>.
- [4] Kirillov NG. Analysis of modern natural gas liquefaction technologies. *Chem Pet Eng* 2004;40:401–6. <https://doi.org/10.1023/B:CAPE.0000047655.67704.dc>.
- [5] Zhang H-Y, Xi W-W, Ji Q, Zhang Q. Exploring the driving factors of global LNG trade flows using gravity modelling. *J Clean Prod* 2018;172:508–15. <https://doi.org/10.1016/J.JCLEPRO.2017.10.244>.
- [6] International Gas Union. World LNG Report 2016; 2016. www.igu.org/publications/2016-world-lng-report [Accessed 23 April 2018].
- [7] Kanbur BB, Xiang L, Dubey S, Choo FH, Duan F. Cold utilization systems of LNG: a review. *Renew Sustain Energy Rev* 2017;79:1171–88. <https://doi.org/10.1016/J.RSER.2017.05.161>.
- [8] British Petroleum. BP Statistical review of world energy 2016; 2016. www.bp.com/content/dam/bp/pdf/energy-economics/statistical-review-2016/bp-statistical-review-of-world-energy-2016-full-report.pdf [Accessed 23 April 2018].
- [9] Lin W, Huang M, Gu A. A seawater freeze desalination prototype system utilizing LNG cold energy. *Int J Hydrog Energy* 2017;42:18691–8. <https://doi.org/10.1016/J.IJHYDENE.2017.04.176>.
- [10] Paltrinieri N, Tugnoli A, Cozzani V. Hazard identification for innovative LNG regasification technologies. *Reliab Eng Syst Saf* 2015;137:18–28. <https://doi.org/10.1016/J.RESS.2014.12.006>.
- [11] Yoon B, Shin J, Lee S. Technology assessment model for sustainable development of LNG terminals. *J Clean Prod* 2018;172:927–37. <https://doi.org/10.1016/J.JCLEPRO.2017.10.187>.
- [12] Kandiyoti R. (Rafael). *Pipelines: flowing oil and crude politics*. London, UK: I.B. Tauris; 2008.
- [13] Agarwal R, Rainey T, Rahman S, Steinberg T, Perrons R, Brown R. LNG regasification terminals: the role of geography and meteorology on technology choices. *Energies* 2017;10:2152. <https://doi.org/10.3390/en10122152>.
- [14] Khan MS, Karimi IA, Wood DA. Retrospective and future perspective of natural gas liquefaction and optimization technologies contributing to efficient LNG supply: a review. *J Nat Gas Sci Eng* 2017;45:165–88. <https://doi.org/10.1016/J.JNGSE.2017.04.035>.
- [15] Khan MS, Chaniago YD, Getu M, Lee M. Energy saving opportunities in integrated NGL/LNG schemes exploiting: thermal-coupling common-utilities and process knowledge. *Chem Eng Process Intensif* 2014;82:54–64. <https://doi.org/10.1016/J.CEP.2014.06.001>.
- [16] Won W, Lee SK, Choi K, Kwon Y. Current trends for the floating liquefied natural gas (FLNG) technologies. *Korean J Chem Eng* 2014;31:732–43. <https://doi.org/10.1007/s11814-014-0047-x>.
- [17] Stirling Cryogenics. Stirling Cryogenerators - Products; n.d. www.stirlingcryogenics.com/en/products/cryocoolers [Accessed 27 April 2018].
- [18] Khan MS, Karimi IA, Lee M. Evolution and optimization of the dual mixed refrigerant process of natural gas liquefaction. *Appl Therm Eng* 2016;96:320–9. <https://doi.org/10.1016/J.APPLTHERMALENG.2015.11.092>.
- [19] Khan MS, Lee S, Getu M, Lee M. Knowledge inspired investigation of selected parameters on energy consumption in nitrogen single and dual expander processes of natural gas liquefaction. *J Nat Gas Sci Eng* 2015;23:324–37. <https://doi.org/10.1016/J.JNGSE.2015.02.008>.
- [20] Han C, Lim Y. LNG processing: from liquefaction to storage. *Comput Aided Chem Eng* 2012;31:99–106. <https://doi.org/10.1016/B978-0-444-59507-2.50013-5>.
- [21] Ali W, Qyyum MA, Qadeer K, Lee M. Energy optimization for single mixed refrigerant natural gas liquefaction process using the metaheuristic vortex search

- algorithm. *Appl Therm Eng* 2018;129:782–91. <https://doi.org/10.1016/J.APPLTHERMALENG.2017.10.078>.
- [22] Dhameliya H, Agrawal P. LNG cryogenic energy utilization. *Energy Procedia* 2016;90:660–5. <https://doi.org/10.1016/J.EGYPRO.2016.11.238>.
- [23] Ghorbani B, Shirmohammadi R, Mehrpooya M, Mafi M. Applying an integrated trigeneration incorporating hybrid energy systems for natural gas liquefaction. *Energy* 2018;149:848–64. <https://doi.org/10.1016/J.ENERGY.2018.02.093>.
- [24] Qyum MA, Ali W, Long NVD, Khan MS, Lee M. Energy efficiency enhancement of a single mixed refrigerant LNG process using a novel hydraulic turbine. *Energy* 2018;144:968–76. <https://doi.org/10.1016/J.ENERGY.2017.12.084>.
- [25] Chen J, Hua Y, Su Q, Wan X, Li Z. Development and industrial tests of the first LNG hydraulic turbine system in China. *Nat Gas Ind B* 2016;3:283–90. <https://doi.org/10.1016/J.NGIB.2016.12.005>.
- [26] Nguyen T-V, Rothuizen ED, Markussen WB, Elmegegaard B. Thermodynamic comparison of three small-scale gas liquefaction systems. *Appl Therm Eng* 2018;128:712–24. <https://doi.org/10.1016/J.APPLTHERMALENG.2017.09.055>.
- [27] Kuz'menko IF, Dovbish AL, Darbinyan RV, Peredel'skii VA, Lyapin AI. Efficient natural gas liquefaction plant based on AGFCs by using open klimenko cycle. *Chem Pet Eng* 2003;39:216–20. <https://doi.org/10.1023/A:1024294601975>.
- [28] Gerasimov VE, Kuz'menko IF, Peredel'skii VA, Darbinyan RV. Introduction of technologies and equipment for production, storage, transportation, and use of LNG. *Chem Pet Eng* 2004;40:31–5. <https://doi.org/10.1023/B:CAPE.00000024132.28963.56>.
- [29] Ulvestad M, Overland I. Natural gas and CO₂ price variation: impact on the relative cost-efficiency of LNG and pipelines. *Int J Environ Stud* 2012;69:407–26. <https://doi.org/10.1080/00207233.2012.677581>.
- [30] Selfors A, Thorsen K, Hofstad K, Fagerlund K, Wiggen T. Natural gas: a general introduction. Norwegian Directorate of Hydropower and Energy, Oslo, Norway; 2004.
- [31] Jung Y, Yokobori K, Doi N, Peng H, Wang Z, Sinygin O. Natural gas pipeline development in Northeast Asia. Tokyo, Japan: Asia Pacific Energy Research Centre; 2000.
- [32] Khan MS, Lee M. Design optimization of single mixed refrigerant natural gas liquefaction process using the particle swarm paradigm with nonlinear constraints. *Energy* 2013;49:146–55. <https://doi.org/10.1016/J.ENERGY.2012.11.028>.
- [33] Khan MS, Lee S, Hasan M, Lee M. Process knowledge based opportunistic optimization of the N₂-CO₂ expander cycle for the economic development of stranded offshore fields. *J Nat Gas Sci Eng* 2014;18:263–73. <https://doi.org/10.1016/J.JNGSE.2014.03.004>.
- [34] The Linde Group. LNG Technology; 2008. <www.linde-engineering.com/internet.global.lindeengineering.global/en/images/LNG_1_1_e_13.150dpi_NB19.4577.pdf?V=8>. [Accessed 24 April 2018].
- [35] Gasconsult Limited. ZR-LNG™ Natural Gas Liquefaction Process for FLNG; 2014. <www.gasconsult.com/wp-content/uploads/2014/05/ZR-LNG-FLNG-Datasheet.pdf>. [Accessed 24 April 2018].
- [36] Kwak D-H, Heo J-H, Park S-H, Seo S-J, Kim J-K. Energy-efficient design and optimization of boil-off gas (BOG) re-liquefaction process for liquefied natural gas (LNG)-fuelled ship. *Energy* 2018;148:915–29. <https://doi.org/10.1016/J.ENERGY.2018.01.154>.
- [37] Shin Y, Lee YP. Design of a boil-off natural gas reliquefaction control system for LNG carriers. *Appl Energy* 2009;86:37–44. <https://doi.org/10.1016/J.APENERGY.2008.03.019>.
- [38] Romero Gómez J, Romero Gómez M, Lopez Bernal J, Baaliña Insua A. Analysis and efficiency enhancement of a boil-off gas reliquefaction system with cascade cycle on board LNG carriers. *Energy Convers Manag* 2015;94:261–74. <https://doi.org/10.1016/J.ENCONMAN.2015.01.074>.
- [39] Stevens P. Transit troubles pipelines as a source of conflict a chatham house report. London, UK: Royal Institute of International Affairs; 2009.
- [40] Mäkinen H. The future of natural gas as the European Union's energy source – risks and possibilities. Turkey, Finland: Pan-European Institute; 2010.
- [41] Jensen J. The development of a global LNG market. Is it Likely? If so When? Oxford, UK: Oxford Institute for Energy Studies; 2004.
- [42] Raj R, Ghandehariun S, Kumar A, Geng J, Linwei M. A techno-economic study of shipping LNG to the Asia-Pacific from Western Canada by LNG carrier. *J Nat Gas Sci Eng* 2016;34:979–92. <https://doi.org/10.1016/J.JNGSE.2016.07.024>.
- [43] Pfoser S, Aschauer G, Simmer L, Schauer O. Facilitating the implementation of LNG as an alternative fuel technology in landlocked Europe: a study from Austria. *Res Transp Bus Manag* 2016;18:77–84. <https://doi.org/10.1016/j.rtbm.2016.01.004>.
- [44] Gilbert AQ, Sovacool BK. US liquefied natural gas (LNG) exports: boom or bust for the global climate? *Energy* 2017;141:1671–80. <https://doi.org/10.1016/J.ENERGY.2017.11.098>.
- [45] Li S, Wang B, Dong J, Jiang Y. Thermodynamic analysis on the process of re-gasification of LNG and its application in the cold warehouse. *Therm Sci Eng Prog* 2017;4:1–10. <https://doi.org/10.1016/J.TSEP.2017.08.001>.
- [46] Atienza-Márquez A, Bruno JC, Coronas A. Cold recovery from LNG-regasification for polygeneration applications. *Appl Therm Eng* 2018;132:463–78. <https://doi.org/10.1016/J.APPLTHERMALENG.2017.12.073>.
- [47] Lee I, Park J, Moon I. Conceptual design and exergy analysis of combined cryogenic energy storage and LNG regasification processes: cold and power integration. *Energy* 2017;140:106–15. <https://doi.org/10.1016/J.ENERGY.2017.08.054>.
- [48] Cravalho EG, McGrath JJ, Toscano WM. Thermodynamic analysis of the re-gasification of LNG for the desalination of sea water. *Cryog (Guildf)* 1977;17:135–9. [https://doi.org/10.1016/0011-2275\(77\)90272-7](https://doi.org/10.1016/0011-2275(77)90272-7).
- [49] Yoo B-Y. The development and comparison of CO₂ BOG re-liquefaction processes for LNG fueled CO₂ carriers. *Energy* 2017;127:186–97. <https://doi.org/10.1016/J.ENERGY.2017.03.073>.
- [50] Koku O, Perry S, Kim J-K. Techno-economic evaluation for the heat integration of vaporisation cold energy in natural gas processing. *Appl Energy* 2014;114:250–61. <https://doi.org/10.1016/J.APENERGY.2013.09.066>.
- [51] Fernández IA, Gómez MR, Gómez JR, Insua AB. Review of propulsion systems on LNG carriers. *Renew Sustain Energy Rev* 2017;67:1395–411. <https://doi.org/10.1016/J.RSER.2016.09.095>.
- [52] Sun H, Zhu H, Liu F, Ding H. Simulation and optimization of a novel Rankine power cycle for recovering cold energy from liquefied natural gas using a mixed working fluid. *Energy* 2014;70:317–24. <https://doi.org/10.1016/J.ENERGY.2014.03.128>.
- [53] Invernizzi CM, Iora P. The exploitation of the physical exergy of liquid natural gas by closed power thermodynamic cycles. *Overv Energy* 2016;105:2–15. <https://doi.org/10.1016/J.ENERGY.2015.09.020>.
- [54] Arcuri N, Bruno R, Bevilacqua P. LNG as cold heat source in OTEC systems. *Ocean Eng* 2015;104:349–58. <https://doi.org/10.1016/J.OCEANENG.2015.05.030>.
- [55] Lee U, Kim K, Han C. Design and optimization of multi-component organic Rankine cycle using liquefied natural gas cryogenic energy. *Energy* 2014;77:520–32. <https://doi.org/10.1016/J.ENERGY.2014.09.036>.
- [56] Mehrpooya M, Sharifzadeh MMM, Zonouz MJ, Rosen MA. Cost and economic potential analysis of a cascading power cycle with liquefied natural gas regasification. *Energy Convers Manag* 2018;156:68–83. <https://doi.org/10.1016/J.ENCONMAN.2017.10.100>.
- [57] Kaczmarek R, Stachel AA. Effectiveness of operation of Organic Rankine Cycle installation applied in the liquid natural gas regasification plant. *J Eng Phys Thermophys* 2017;90:729–35. <https://doi.org/10.1007/s10891-017-1622-x>.
- [58] Shi X, Che D. Thermodynamic analysis of an LNG fuelled combined cycle power plant with waste heat recovery and utilization system. *Int J Energy Res* 2007;31:975–98. <https://doi.org/10.1002/er.1293>.
- [59] Stradioto DA, Seelig MF, Schneider PS. Performance analysis of a CCGT power plant integrated to a LNG regasification process. *J Nat Gas Sci Eng* 2015;23:112–7. <https://doi.org/10.1016/J.JNGSE.2015.01.032>.
- [60] Moghimi M, Khosravian M. Exergy optimization for a novel combination of organic Rankine cycles, Stirling cycle and direct expander turbines. *Heat Mass Transf* 2018;1–13. <https://doi.org/10.1007/s00231-017-2270-6>.
- [61] Ferreiro García R, Carbia Carril J, Romero Gomez J, Romero Gomez M. Power plant based on three series Rankine cycles combined with a direct expander using LNG cold as heat sink. *Energy Convers Manag* 2015;101:285–94. <https://doi.org/10.1016/J.ENCONMAN.2015.05.051>.
- [62] García RF, Carril JC, Gomez JR, Gomez MR. Combined cascaded Rankine and direct expander based power units using LNG (liquefied natural gas) cold as heat sink in LNG regasification. *Energy* 2016;105:16–24. <https://doi.org/10.1016/J.ENERGY.2015.09.051>.
- [63] Gómez MR, García RF, Gómez JR, Catoira ADM. Cold exergy recovery during LNG regasification through a closed Brayton cycle. *Int J Exergy* 2014;14:484. <https://doi.org/10.1504/IJEX.2014.062921>.
- [64] Franco A, Casarosa C. Thermodynamic analysis of direct expansion configurations for electricity production by LNG cold energy recovery. *Appl Therm Eng* 2015;78:649–57. <https://doi.org/10.1016/J.APPLTHERMALENG.2014.11.062>.
- [65] Romero Gómez M, Romero Gómez J, López-González LM, López-Ochoa LM. Thermodynamic analysis of a novel power plant with LNG (liquefied natural gas) cold exergy exploitation and CO₂ capture. *Energy* 2016;105:32–44. <https://doi.org/10.1016/J.ENERGY.2015.09.011>.
- [66] Zhao L, Dong H, Tang J, Cai J. Cold energy utilization of liquefied natural gas for capturing carbon dioxide in the flue gas from the magnesite processing industry. *Energy* 2016;105:45–56. <https://doi.org/10.1016/J.ENERGY.2015.08.110>.
- [67] Lee S, Choi BC. Thermodynamic assessment of integrated heat recovery system combining exhaust-gas heat and cold energy for LNG regasification process in FSRU vessel. *J Mech Sci Technol* 2016;30:1389–98. <https://doi.org/10.1007/s12206-016-0246-y>.
- [68] Soffiato M, Frangopoulos CA, Manente G, Rech S, Lazzaretto A. Design optimization of ORC systems for waste heat recovery on board a LNG carrier. *Energy Convers Manag* 2015;92:523–34. <https://doi.org/10.1016/J.ENCONMAN.2014.12.085>.
- [69] Morosuk T, Tsatsaronis G. Comparison of novel concepts of cogeneration systems used to regasify liquefied natural gas (LNG). *J Nat Gas Sci Eng* 2016;34:1434–45. <https://doi.org/10.1016/J.JNGSE.2016.08.021>.
- [70] Jeong ES. Optimization of power generating thermoelectric modules utilizing LNG cold energy. *Cryog (Guildf)* 2017;88:29–35. <https://doi.org/10.1016/J.CRYOGENICS.2017.10.005>.
- [71] Min G, Rowe DM. Design theory of thermoelectric modules for electrical power generation. *IEE Proc - Sci Meas Technol* 1996;143:351–6. <https://doi.org/10.1049/ip-smt:19960714>.
- [72] Miyazaki T, Kang Y, Akisawa A, Kashiwagi T. A combined power cycle using refuse incineration and LNG cold energy. *Energy* 2000;25:639–55. [https://doi.org/10.1016/S0360-5442\(00\)00002-5](https://doi.org/10.1016/S0360-5442(00)00002-5).
- [73] Cardona JM, Dam J, Rooij Mde. Role of lng in an optimized hybrid energy network: Part 1. Balancing renewable energy supply and demand by integration of decentralized LNG regasification with a CHP. Hanzhoheschool Groningen, The Netherlands; 2017.
- [74] Clegg S, Mancarella P. Integrated electricity-heat-gas network modelling for the evaluation of system resilience to extreme weather. 2017 IEEE Manchester PowerTech, IEEE; 2017, p. 1–6. doi:<http://dx.doi.org/10.1109/PTC.2017.7981133>.
- [75] Mehrpooya M, Kalhorzadeh M, Chahartaghi M. Investigation of novel integrated air separation processes, cold energy recovery of liquefied natural gas and carbon dioxide power cycle. *J Clean Prod* 2016;113:411–25.

3

Phase change modelling and process control in steel production

METAL PROCESSING AND STEEL PRODUCTION represent an important industrial application, in which the phase change and the latent heat significantly influence the solidification of metals, and mechanical and physical properties of finished products. At the moment, more than 98% of the total world production (TWP) of steel, aluminium, as well as copper is cast by means of the continuous casting method [155]. As for shares in the production, China with about 50% of the TWP is a dominant producer of steel, followed by Japan, USA, India, and Russia with considerably lower shares on the TWP production of 7%, 5.5%, 5%, and 4.3%, respectively [155]. Though the TWP of steel is increasing every year, steelmakers at steel plants rather aim at the production of high-quality and high-alloyed steel grades having an extra added value for customers [141]. Examples of such grades include steel grades, which are used for the production of shells of boilers and pressure vessels, micro-alloyed steel grades, or highly resistant steel grades for the use in off-shore constructions in aggressive salt water on coast sides. Another view includes environmental impacts of the steel production to the natural environment and their minimisation. This includes the reduction of the water consumption and of the carbon trace, and the decrease of emission generation during the steel production.

3.1 CONTINUOUS STEEL CASTING

The continuous casting method [90] shown in Figure 3.1 is based on uninterrupted casting of the molten steel into the water-cooled mould, from which a semi-continuous steel strand with the solidified shell on its surface, but with a liquid core continues to the secondary cooling zone. In the

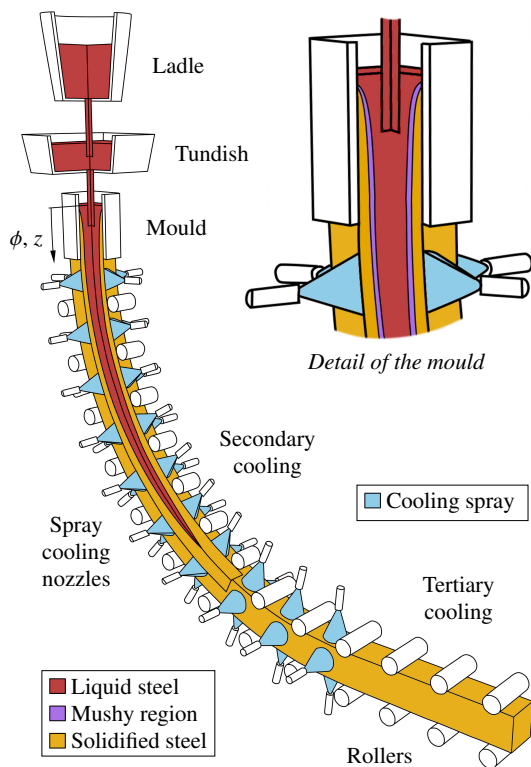


Figure 3.1: Schematic of continuous steel casting [71]

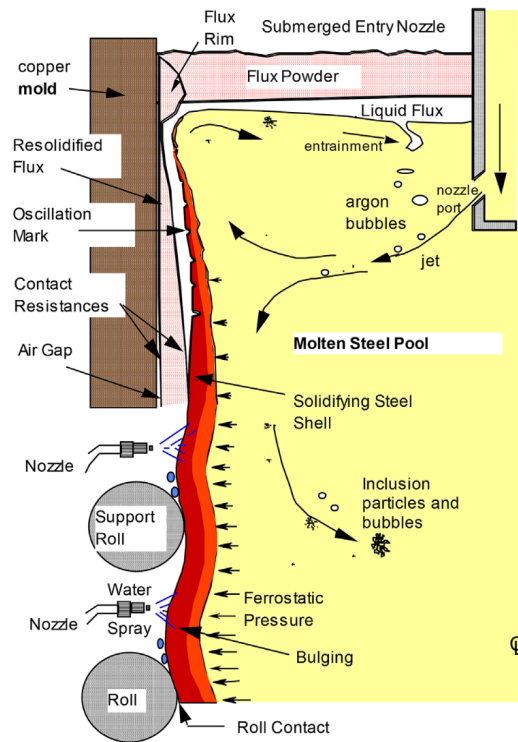


Figure 3.2: Multiphysical phenomena in continuous steel casting [140]

secondary cooling zone, the solidification and cooling proceed due to water or air-mist spraying nozzles, which withdraw heat from the steel strand by means of the forced convection, and due to radiation to the ambient environment. The cooling process and its distribution in the mould and in the secondary cooling zone greatly influence the quality of steel products, including material as well as mechanical properties. A great attention is paid by steelmakers to surface and internal defects [97, 34], which may cause the rejection of the cast strand from next processing, meaning a higher scrap ratio, and thus a lower yield.

Recently, the production of high quality steel grades in a way reducing impacts to the natural environment cannot be accomplished without deep knowledge of the solidification process and its computer simulation and prediction. The literature review [141] on the current state-of-the-art in the steel production demonstrates that the casting process with no support in terms of computer simulations and of process control by means of computer models is inefficient, with a high occurrence of quality defects and other issues. Therefore, computer models are currently widely utilised at steel plants for monitoring of casting process, for the investigation of influences of process parameters, for the determination of optimal casting parameters, and for the real-time casting control and optimisation. The current research in the field of computer simulations of continuous steel casting mainly focuses on the development of models taking into account specific phenomena, such as the fluid flow prediction of the melt in the mould and in the liquid core of steel strand [107], fluid flow induced by the electromagnetic stirring [95], coupled thermal-mechanical phenomena encountered in the soft reduction method [58], or coupled thermal-mechanical-material phenomena in the prediction of cracks and other defects [111], which can arise during the production due to an improper

setup of the casting machine and due to improper operational parameters of the casting process. Another issue is computer modelling of near-net-shape casting [90], in which a very high casting speed requires special numerical techniques providing the numerical stability of computer models.

3.2 COMPUTER MODELLING OF CONTINUOUS STEEL CASTING

A number of researchers and investigators have contributed to the field of computer modelling of continuous steel casting and to the use of computer models in the casting control and optimisation. This section briefly summarises some achievements and the current state-of-the-art. It is worth mentioning that published papers and studies can be assessed and split from two points of view: some studies and approaches are at the moment rather general and/or theoretical, while other studies are directly related to particular steel plants and steel producers, where ideas and proposed methodologies are straightforwardly tested and analysed in the real casting process. When considering the purpose of the models, they can be split into two main groups [141]: simpler and fast models for the use in real-time monitoring, control, and optimisation of the casting process, and more complicated and complex models, which enable detailed analyses and simulations of multiple phenomena. However, such detailed models are computationally expensive and often very slow, which makes them not applicable for the real-time use.

3.2.1 HEAT TRANSFER AND SOLIDIFICATION MODELS AND PHASE CHANGE MODELLING

Computer modelling of continuous steel casting consists of the numerical solution of a coupled multiphysical problem incorporating heat transfer, mass transfer with fluid flow, and phase changes [90] as demonstrated in Figure 3.2. The heat transfer phenomena are rather obvious: the primary task in continuous steel casting is a controlled transformation—the solidification—of the liquid steel into semi-finished products in the solid state. During the solidification, a vast amount of heat needs to be withdrawn from the strand to the ambient environment. As for the heat transfer mechanisms, all three kinds are taken into account: heat conduction as the dominant heat transfer mechanism in the solidifying strand, while heat convection and radiation are crucial mechanisms serving as boundary conditions (forced convection induced by spray nozzles in the secondary cooling zone, and natural convection and radiation in the tertiary cooling zone [24]). A typical output of a heat transfer model for continuous steel casting includes the transient temperature distribution in the cast strand and information about the location of the solidification interface. Figure 3.3 illustrates an example of such output.

As for mass transfer and fluid flow, they are mostly involved in the mould and in the liquid core of the strand. Especially in the investigation of electromagnetic stirring and submerged entry nozzles, fluid flow needs to be solved. However, since the viscosity of the liquid steel is rather high, a number of authors of computers models for continuous steel casting have applied a simplified approach, in which the fluid flow is solved and accounted indirectly, often by means of the concept of effective thermal conductivity [91, 93], instead of the direct solution of the Navier-Stokes equations. A direct solution of the fluid flow takes place particularly in specific models of the mould, where the strand exiting the mould is not further considered and simulated. The reason for such approach is rather

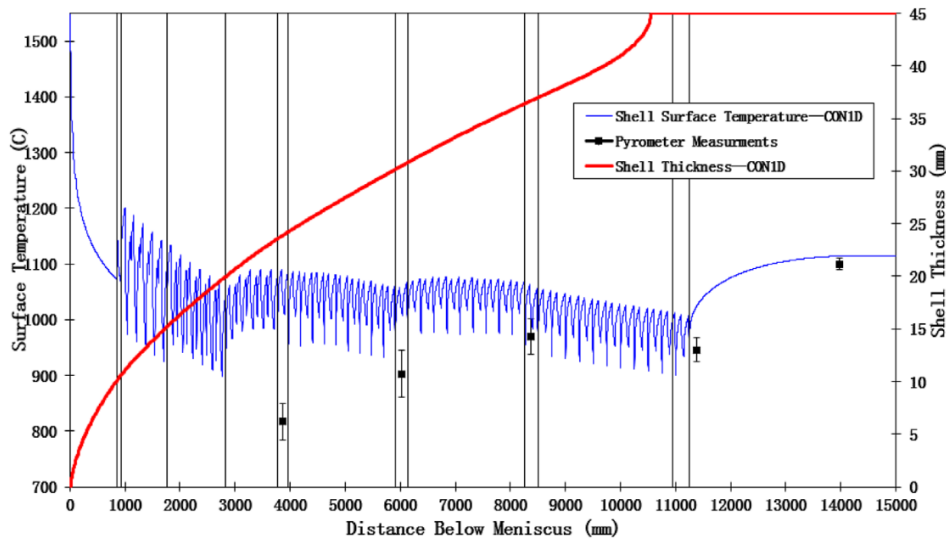


Figure 3.3: A typical output of heat transfer and solidification models of continuous steel casting: temperature distribution and location of solidification front with experimentally determined surface temperatures by means of pyrometers [109]

straightforward: fluid flow modelling is computationally fairly demanding and not applicable for real-time use. It is also worth pointing out that the mass transfer is also implicitly incorporated in continuous steel casting by its nature: since the casting process is continuous and in the form of the semi-infinite strand, the mass transfer to the mould in the form of the liquid steel occurs continuously as well.

Another important aspect in the solidification of steel and its computer modelling is the phase change. The phase change, besides the influence to mechanical and physical properties and to the structure, is accompanied by the release of a large amount of heat in a relatively narrow temperature interval. Such heat is referred to as the latent heat or, more precisely, as the heat of fusion. In case of low-alloyed carbon steel grades, there are usually two phase changes during the solidification: the liquid-to-solid phase change (the solidification itself) and solid-to-solid transformations in the solid state accompanied by changes of the structure [142].

Though the currently utilised computer models particularly include the above mentioned phenomena, their list to the relation of continuous steel casting is not complete as illustrated in Figure 3.2. Nowadays, there are challenging efforts to develop even more complex models, which would encompass multidisciplinary effects ranging from multiphase turbulent flow and electromagnetic effects to particle entrapment to clogging and to segregation and micro-structure formation [141]. In particular, some research papers have been published on the topic of coupling between the thermal model and the stress-strain model. Such the thermal-mechanical model can simulate the distribution of both thermal and mechanical stresses, which are directly related to the formation of cracks and other quality issues. Another proposed simulation approach combines the thermal model with the structural model. The thermal-structural model is able to simulate and predict microscopic solidification phenomena such as the initialisation and the growth of dendrites. However, at the moment these models are rather at the development stage as reported in [141]. Their limitations are particularly the complexity and computational expenses.

From the discussion presented above, it is obvious that computer modelling of continuous steel

casting is a complicated problem. The complexity of the models is also given by a wide range of both length and time scales included in continuous steel casting [141]. For instance, the creation of the solid shell and nucleation of grains in the mould involve a size scale much less than one millimetre but it is well reported that these phenomena have an influence to the centre-line segregation, which occurs more than ten meters away from the mould [141].

THERMAL MODELS WITH PHASE CHANGE

In heat transfer modelling of continuous steel casting, there are two main categories of modelling approaches applied by investigator and developers of the models. The first category consists of mathematical and numerical methods, which are rather simpler and straightforwardly implementable. Methods from this category [137, 133] are frequently utilised in both academia and industry, and they represent the majority of the models. Another category includes advanced simulation methods, which are challenging from mathematical as well as programming/implementation point of view. Such methods [146, 78] are superficial in some aspects when compared to standard methods; however their complexity, requirements, and computational costs are well beyond the standard methods. Such models are utilised predominantly in academia for research purposes with a rather limited use in industrial applications at steel plants.

When considering straightforward methods for implementation of the thermal model with the phase changes, the enthalpy method [137] and the effective heat capacity method [133] are two frequently utilised techniques. Both the methods are grid-based under the Euler principle, well suitable and thus frequently applied to computer modelling of continuous steel casting.

ENTHALPY METHOD. The method is based on the use of the thermodynamic enthalpy, which allows for the inclusion of both the sensible heat and the heat of fusion. The enthalpy H can be defined [137] as a function of the temperature T according to

$$H(T) = \int_{T_{\text{ref}}}^T \left(\varrho c_p - \varrho \Delta H_m \frac{\partial f_s}{\partial \vartheta} \right) d\vartheta \quad (3.1)$$

where ϱ is the density, c_p is the heat capacity at constant pressure, ΔH_m is the heat of fusion, f_s is the solid fraction and T_{ref} is a reference temperature. The substitution of Eq. (3.1) to the heat transfer equation [54] (as already explained in Section 2.4) and the consideration of the strand movement during the casting process lead to the governing enthalpy-formulated heat transfer equation [137]

$$\frac{\partial H}{\partial t} = \nabla \cdot (k \nabla T) + v_z \frac{\partial H}{\partial z} \quad (3.2)$$

in the Cartesian coordinate system (x, y, z) with the assumption of z being the casting direction. In Eq. (3.2), t is time, v_z is the casting speed, and k stands for the thermal conductivity.

EFFECTIVE HEAT CAPACITY METHOD. The method uses the heat capacity c_p , often referred to as the specific heat, for the inclusion of the heat of fusion. The effective heat capacity accounts as a

function of the temperature $c_{\text{eff}}(T)$ for both the sensible heat and the heat of fusion. The effective heat capacity is related to the enthalpy as [133]

$$c_{\text{eff}} = \frac{1}{\rho} \frac{\partial H}{\partial T} = c_p - \Delta H_m \frac{\partial f_s}{\partial T}. \quad (3.3)$$

Similarly as in case of the enthalpy method, the substitution of Eq. (3.3) to the heat transfer equation [54] and taking into account the casting speed lead to the governing effective-heat-capacity-formulated heat transfer equation [128]

$$\rho c_{\text{eff}} \frac{\partial T}{\partial t} = \nabla \cdot (k \nabla T) + v_z \rho c_{\text{eff}} \frac{\partial T}{\partial z}. \quad (3.4)$$

The governing equations (3.2) and (3.4) formulated with the use of the enthalpy method and the effective heat capacity method, respectively, are the most frequently implemented techniques in computer models of continuous steel casting, both in research papers (e.g. [109, 128, 52]) as well as in industry (e.g. ProCAST software [98]). The reason is that both the methods are relatively simple, straightforwardly implementable and computationally efficient. Especially in case of the explicit formulation of the time discretization, their numerical solution does not require the solution of the set of equations, which might be an issue in case of a large number of computational nodes. As for the numerical formulation and the transition between the partial differential equations (3.2) and (3.4), and algebraic equations suitable for the numerical solution, the well-known and robust finite difference method, the finite volume method, and the control volume method (all already discussed in Section 2.4) can be applied.

As in case of modelling of LHTES systems, the enthalpy method offers a slightly better stability and accuracy than the effective heat capacity method, and it does not require methods for the energy conservation control since the enthalpy approach is self-conservative [102]. On the other hand, the enthalpy method requires a two-stage and computationally less effective solution for the two unknown variables H and T , while in case of the effective heat capacity method, T is the only unknown variable solved for.

Besides the enthalpy method and the effective heat capacity method, several other techniques are employed for computer modelling of continuous steel casting. However, their use is, in comparison to the enthalpy method and the effective heat capacity method, substantially less frequent in practical applications.

TEMPERATURE RECOVERY METHOD. It is based on the concept of the temperature reservoir, which prevents the solidification until all the heat of fusion is released [32]. The method was tested by several authors and it was reported that the temperature recovery method is rather sensitive to the time step, and some numerical disturbances in the solution can occur near the phase interface under certain conditions. On the other hand, the temperature recovery method allows for a good computational accuracy [100].

SLICE-BASED METHOD. Another approach applied to continuous steel casting is the use of the slice model [127]. The idea is based on the use of a 2D slice, which travels in imaginary way through

the actual 3D domain in the casting direction. The advantage of such approach is the computational efficiency; it is much less expensive to solve a set of 2D problems than to consider a fully 3D model. On the other hand, a crucial drawback of the method is that it is not designed and straightforwardly applicable for transient simulations, which is often the case in process control and optimisation.

MESH-LESS (MESH-FREE) METHODS. The concept of mesh-free methods is based on the use of no mesh in the domain. Instead of the structural grid, the mesh-less nodes are intentionally distributed within the domain with the density according to the desired accuracy of the solution. This allows for a great refinement of the computational domain according to requirements of the user. However, the mesh-less methods suffer from a lower computational stability and from other issues related to the definition of boundary conditions [145, 146].

FRONT TRACKING METHODS. These methods are based on a completely different idea than the grid-based methods such as the enthalpy method or the effective heat capacity method. The front tracking methods employ the mixed Eulerian-Lagrangian approach and they explicitly track the interface (referred to as the front) between the phases by means of Lagrangian mass-less markers, which moves in the Eulerian grid [78]. In case of the solid-liquid phase transition, the movement of the phase interface is governed by the Stefan condition describing the balance at the interface. The main aim of these methods is the exact determination of the domains occupied by the phases, from which the temperature distribution is determined as a consequence. This approach is therefore opposite to the technique used e.g. in the enthalpy method. The advantage of the front tracking methods is their substantially higher accuracy and the capability for microscopic modelling of solidification including the growth of dendrites and the formation of individual grains [12]. On the other hand, the front tracking methods are fairly complicated in principle as well as in implementation and this limits their wider use. A more detailed information about the front tracking technique is provided in Section 2.4 and in [68].

The thermal models are the most important simulation tool for the casting control and optimisation. The reason is that the temperature history and the location of the solidification front (iso-solidus and iso-liquidus cones) are directly connected to properties of final products as well as to the formation of defects. In contrast to most models aiming at specific phenomena as discussed in the foregoing section, thermal models are capable to operate in real time or even faster, which is crucial for the process optimisation and casting control. Therefore, a number of models with a different level of complexity and computational efficiency have been developed in the last two decades. Examples of the most well-known include the models CON1D [109], TEMPSIMU3D [91, 92], and models presented in [145] and [47].

Though the attention of investigators is at the moment focused mainly on modelling of specific phenomena, there is still an effort to the development devoted to the thermal models of continuous casting. For instance, a method for the reduction of complexity of the model for continuous steel casting was proposed by Mitchell and Vynnycky [99]. The authors claimed that the proposed technique allows for recovery of some fluid flow interactions only from the solution of the heat transfer model. Another example is the paper presented by Bratu et al. [16], in which the authors enhanced

the heat transfer and solidification model by taking into account the convective heat transfer at the solid-liquid interface in the solidification region. The method for estimation of the heat transfer coefficient of cooling nozzles from experimentally measured surface temperatures was reported by Luo et al. [94]. The authors used particle swarm optimisation techniques and they demonstrated that the proposed method allows for a significant reduction of large disturbances in source data. Recently, Mosayebidorchen and Gorji-Bandpy [101] published an analysis on the topic of local and averaged-area heat transfer and phase change in continuous steel casting. Various aspects and behaviour of heat transfer and solidification in continuous steel casting were discussed. Another study carried out by Hetmaniok et al. [50] focused on the restoration of cooling conditions in continuous steel casting by means of a computer model and artificial intelligence algorithms. The authors demonstrated that the nature-based algorithms can effectively be utilised in the solution of an inverse heat transfer problem. Zhang et al. [163] studied effects on evenly distributed cooling in the secondary cooling zone on the temperature and stress fields in continuous steel casting of round billets. They reported that a proper design of the number of segments and of the length of the cooling zone can avoid sharp fluctuations in the temperature at the spray cooling position. Vertnik and Šarler [146] presented a mesh-less method for the solution of an industrial benchmark test of continuous steel casting. The authors compared their mesh-less model based on local radial basis functions with a model implemented in ANSYS Fluent and a very good agreement was identified. Han et al. [45] carried out a numerical analysis of temperature and structure distributions in continuous casting of copper pipes. The authors utilised the heat transfer model created in the simulation software ProCAST and they reported that higher cooling water flow rates in the secondary cooling zone had a positive effect to the macrostructure of pipes. Hietanen et al. [51] aimed at the solidification, heat transfer, and fluid flow modelling in continuous steel casting by means of an advanced modelling approach. The authors utilised ANSYS Fluent and an in-house heat transfer model TEMPSIMU_{3D}, and they reported that the effective thermal conductivity taking into account fluid flow patterns of the liquid core can be applied in a sufficient accuracy only in region of the solidification end, whereas it is not applicable in locations where the liquid fraction is high.

3.2.2 MODELLING OF SPECIFIC PHENOMENA RELATED TO CONTINUOUS STEEL CASTING

As already explained above, the thermal model including the phase change is an underlying platform for the determination of the temperature distribution and solidification of cast steel strands. However, a number of other phenomena, which are coupled to each other, are encountered in continuous steel casting as well. This section briefly mentions some of them, which have an importance from specific points of view.

FLUID FLOW MODELLING

When leaving the heat transfer and solidification phenomena aside, fluid flow is one of the most important issues considered in modelling of continuous steel casting [160]. The consideration of the fluid flow is particularly important in a detailed modelling of the mould and of the part of the strand directly below the mould, including e.g. the system for electromagnetic stirring. A number

of investigators have utilised off-the-shelf CFD models such as ANSYS Fluent and ProCAST, see e.g. [19, 95, 107, 59]. The very frequently employed approach is the solution of the steady-state single-phase flow by means of the Reynolds Averaged Navier-Stokes method, which can be coupled with various turbulence models such as $k-\varepsilon$ and $k-\omega$ SST [141].

Applications of the fluid flow modelling in continuous steel casting mainly include the fluid flow pattern in the mould and in the submerged entry nozzle (which is used to feed the liquid steel from the tundish to the mould), the submerged entry nozzle clogging, the argon gas injection to the nozzle preventing it from clogging, the investigation of meniscus level fluctuations in the mould and slag entrainment, and the analysis of effects of electromagnetic stirring [141].

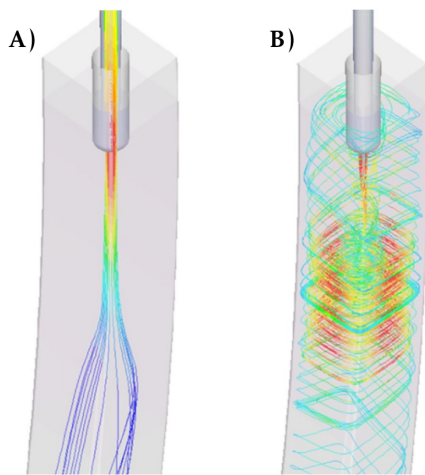


Figure 3.4: Simulated fluid flow pattern in the mould (A) without and (B) with electromagnetic stirring [90]

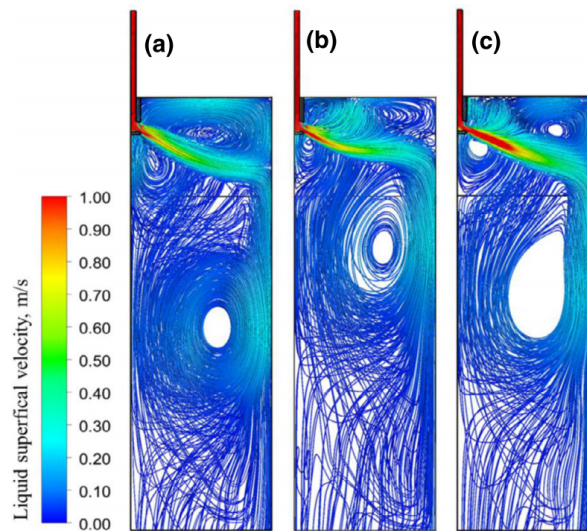


Figure 3.5: Simulated fluid flow pattern in the mould (a) without and (b, c) with gas injection (cases (b) and (c) account for the bubble size of 0.5 mm and 1 mm, respectively) [87]

Figure 3.4 shows an example of CFD results from the analysis [90], which was aimed at the investigation of influences of electromagnetic stirring below the mould on the fluid flow pattern in the liquid core. Figure 3.5 demonstrates the use of CFD for the investigation of fluid flow under the influence of gas injection (argon) to the submerged entry nozzle [87].

THERMAL-MECHANICAL MODELLING

Coupled thermal-mechanical modelling is required for the investigation of phenomena in continuous steel casting, which are related to the temperature as well as to the stress-strain distribution. In such cases, the total strain is determined as a sum of elastic, plastic, and thermal stress components. Examples of issues, which require the consideration of thermal-mechanical modelling include the crack formation caused by hot tearing [119], surface shape problems, bulging of the strand between rolls due to ferrostatic pressure, unbending of the strand in case of radial casters, and the soft reduction for the reduction of the centre-line porosity [141].

Some methodologies for the solution of the stress-strain distribution in the strand having the free surface in the mould were developed and tested, including the separation of the stress between the solid and liquid phases [77], the accommodation of the shrinkage in the centre of the computational

domain [74], and the mixed Lagrangian-Eulerian formulation [36]. Another reported issue in the thermal-mechanical modelling of continuous steel casting is an accurate experimental determination of steel properties, especially at higher temperatures relevant to the casting process and including the creep region [141]. Moreover, the validation of the coupled thermal-mechanical models is not, in contrast to the thermal models, an easy and routine task and it requires investigations at steel plants by means of residual stress measurements. Currently, there is a rather small number of thermal-mechanical models applicable for continuous steel casting [19].

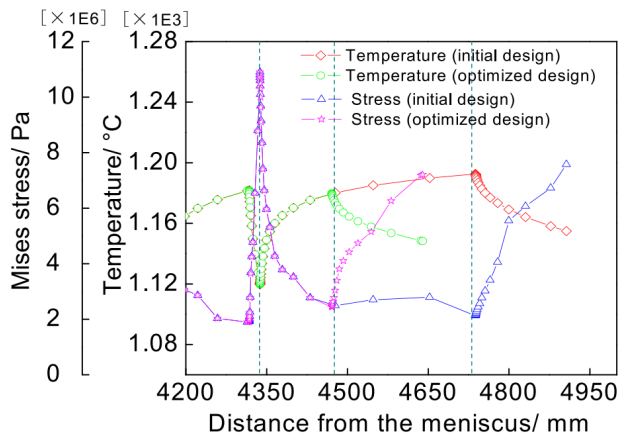


Figure 3.6: Relation between the temperature and the stress distribution in continuous steel casting of round billets [163]

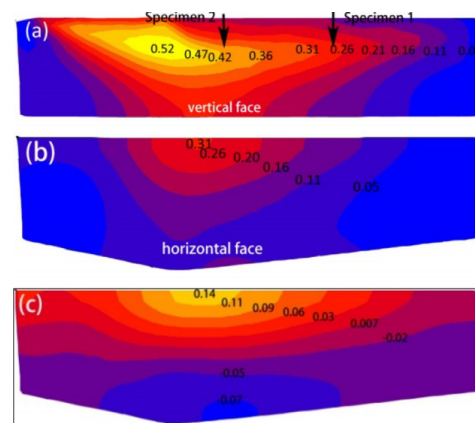


Figure 3.7: Strain distribution during pretreatment process for continuous casting [79]

Figure 3.6 presents an example of simulation results [163], which were gained with the use of the coupled thermal-elastic-plastic stress model for continuously cast round billets. The plots show the correlation between the temperature distribution and the von Mises stress in the secondary cooling zone. A computationally determined strain distribution is shown in Figure 3.7 [79]. In that case, a commercial simulation software MSC Marc was used for the simulation of thermal-mechanical phenomena.

SEGREGATION

Macrosegregation represents one of the very serious issues, which cannot be mitigated or removed from final products by means of subsequent processing (e.g. rolling) as in case of internal cracks, voids, and porosity [141]. Therefore, the prediction of macrosegregation has a great potential for the improvement of casting efficiency and for the minimisation of scraped products having quality issues. However, modelling of microsegregation is reported to be very difficult as it includes the solution of interactions in a very small length scale corresponding to the dendrite size. Though several models for the local solution of the macrosegregation of steel have been developed during last decades, Thomas [141] reported in his review that modelling of macrosegregation is still in its infancy and a great effort will be required to improve the models into the level suitable for the industrial use.

Figure 3.8 shows an example of recent computational results from the analysis [60] of centre-line segregation influenced by the soft reduction. The authors created a thermal-mechanical model, which was used for the prediction of carbon segregation of continuously cast strands. The model allowed for the determination of a suitable location for the soft reduction mechanism and a relatively

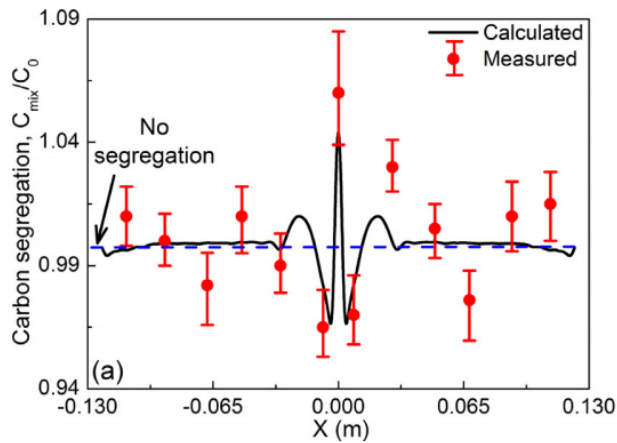


Figure 3.8: Prediction of carbon segregation influenced by soft reduction [60]

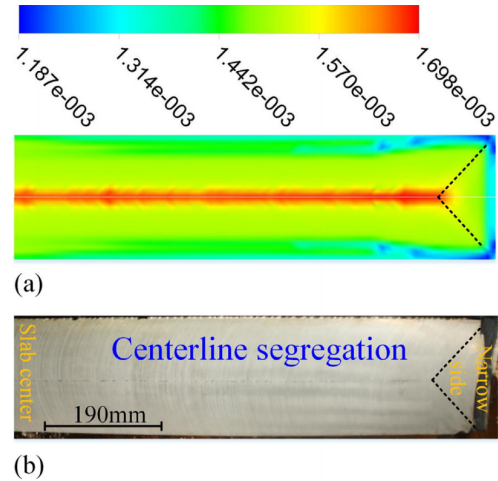


Figure 3.9: Simulation of centre-line segregation [23]

good agreement between simulation and experimental results was achieved. The study [23] was aimed at the prediction of the centre-line segregation by means of a computer model for the solute distribution. Figure 3.9 presents a comparison of the simulated prediction of the carbon distribution and its relation to the experimentally determined centre-line segregation.

MACROSTRUCTURE AND MICROSTRUCTURE

At the moment, the majority of the models for continuous steel casting uses macroscale modelling. In order to improve the accuracy of prediction of defects such as cracks and segregation, the current macroscale models will require their extension to microscale [141]. However, microstructure modelling and simulation of the grain formation is a fairly difficult problem on very small length scales. Currently, some models exist for the prediction of the transition between the columnar to equiaxed dendrites [93], secondary dendrite arm spacing [165], and the delta ferrite to austenite phase transformation [158]. The development of models for the microstructure prediction is limited especially due to the microscale nature requiring extremely fine computational grids in 3D as well as due to a difficult experimental determination of material properties characterising interactions between dendrites and inter-facial domain [141]. Figure 3.10 illustrates an example of morphology of macrostructure gained with the use of CAFE and SDAS models [41]. The figure on the left shows simulation results, while the figure on the right was gained from an experimental investigation.

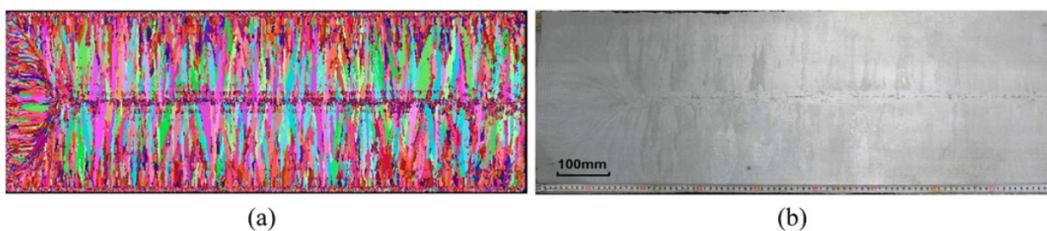


Figure 3.10: Morphology of macrostructure: comparison of simulation and experimental results [41]

3.2.3 BOUNDARY CONDITIONS IN CONTINUOUS STEEL CASTING

A very important issue in modelling of continuous steel casting is a proper determination of boundary conditions, which describe conditions between the strand and the ambient environment. In particular, the quality and accuracy of boundary conditions directly influence computational results provided by models: simulation results can be at most as accurate as inputs to the models are. In continuous steel casting, heat transfer boundary conditions in the mould and in the secondary cooling zone are of interest as these two parts are responsible for the majority of the heat withdrawal from the strand [128]. A simpler solution to the boundary conditions, which is quite frequently utilised (e.g. [115]), is the use of empirical correlations available in the literature for the determination of the local heat flux from the mould and for the heat transfer coefficient characterising the heat removal by spray nozzles. As for the cooling nozzles, such correlations are functions of mainly the water spray density generated by the nozzle, and only a limited number of correlations take into account other parameters, such as the casting speed and the distance of the nozzle from the surface.

An alternative to empirical correlations is the use of data gained experimentally under actual casting conditions. The utilisation of the hot plate method coupled with a solution to the inverse heat transfer problem [118] allows for the determination of realistic values of the heat transfer coefficient, which takes into consideration the local water spray density, the coolant pressure and temperature, and the relative movement and distance of the nozzle to the cooled surface. The heat transfer coefficient determined in such a way also accounts for the Leidenfrost effect, for the formation of the steam barrier at the cooled surface, and for distinct boiling regimes in the interaction coolant–surface [153]. Obviously, experimentally determined boundary conditions provide a higher level of realistic information, significantly overcome empirical correlations in terms of precision and complexity, and allow for a higher overall accuracy of the models.

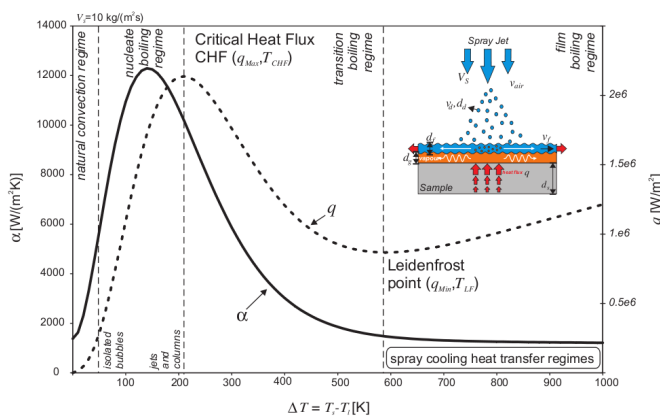


Figure 3.11: Leidenfrost effect and the dependence of the heat transfer coefficient on the surface temperature [153]

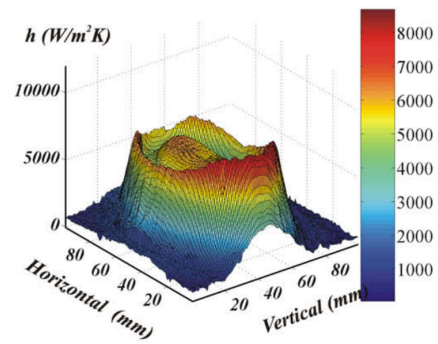


Figure 3.12: Experimentally determined heat transfer coefficient for a water cooling nozzle [147]

Figure 3.11 shows various regimes of heat transfer between the hot surface and the water spray impinging the surface [153]. The necessity for the inclusion of the Leidenfrost effect into the heat transfer coefficient is clearly demonstrated as a significant increase of the heat transfer coefficient below the Leidenfrost temperature. Figure 3.12 illustrates a complexity of an experimentally determined heat transfer coefficient for a cooling nozzle in certain operational conditions [147].

3.2.4 VALIDATION OF THERMAL MODELS FOR CONTINUOUS STEEL CASTING

Since the models of continuous steel casting are created for simulations of a real industrial process, their validation and verification are important tasks in their development. Most authors utilise validation by means of experimentally gained data from steel plants. Typically, thermocouples are installed in walls of the mould as well as in its water inlet and outlet. Non-contact measurements of the surface temperature of steel strands by means of pyrometers (as shown in Figure 3.13 from [101]) and thermoscanners along the caster represent another important source of data for validation of the models. The calibration of the models is usually performed by a trial-and-error method (e.g. [84]), or by an inverse technique [30]. Some investigators have also utilised the validation of the predicted solid shell thickness by means of nail shooting experiments [88, 58] as shown in Figure 3.14.

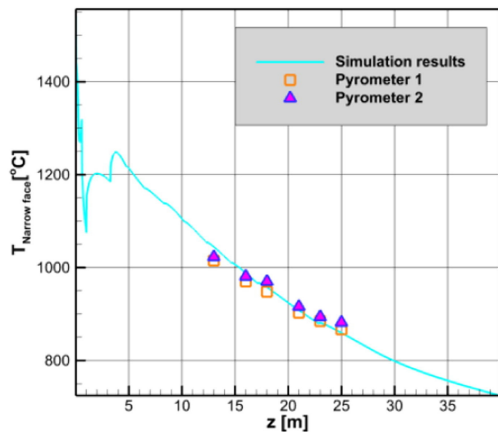


Figure 3.13: Validation of thermal model by means of pyrometers [101]

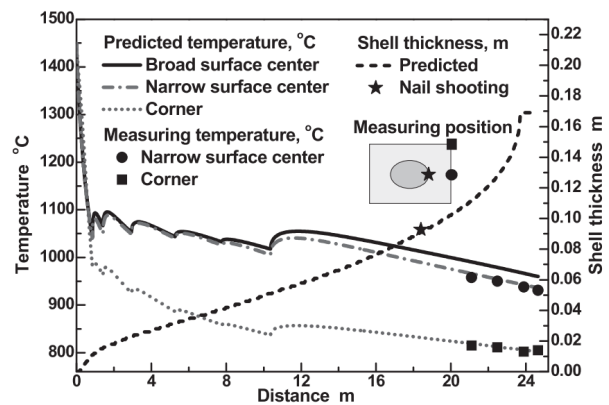


Figure 3.14: The use of nail shooting for validation of shell thickness [58]

3.2.5 COMPUTER MODELS IN OPTIMAL CONTROL AND OPTIMISATION OF CASTING PROCESS

The main purpose of computer models of industrial processes is usually their use for process monitoring, control and optimisation, and for investigation of case studies. This also applies to continuous steel casting, which includes the use of a wide range of computer models for casting control and optimisation. Since the dynamic casting control makes sense especially in real time (in the so-called on-line operation), rather simpler and sufficiently fast computer models are used for this purpose. On the other hand, the models can also be utilised in the off-line mode for the pre-calculation and determination of optimal casting parameters, and for case studies, which are usually aimed at the investigation of a particular issue. In such instances, the models and algorithms using them are slower than the wall-clock time (even substantially), and therefore the real time control is not possible. This is especially the case with more comprehensive models taking into account multiphysical phenomena such as fluid flow or thermal-mechanical phenomena as discussed in the foregoing sections. Powerful computational hardware and a huge amount of the computational time are essential ingredients to perform such simulations.

As for mathematical and control methods employed for the casting control, three main categories can be defined. One category includes methods, which are based on the use of traditional optimisation techniques of the operational research known as mathematical programming. However, these

methods have been applied in practice in a limited range only. The reason is that the computer models of continuous steel casting are fairly comprehensive and they include a large number of unknown variables, which need to be determined by an optimisation algorithm. However, the dimension of such domains often exceeds the capability of optimisation solvers.

Another category is formed by meta-heuristics and nature-inspired algorithms, which are, in comparison to mathematical programming, more robust and efficient when used for the optimal control of continuous steel casting. Meta-heuristics, instead of searching for an exact and global optimum, are searching for some better solution than the actual one is. Due to their stochastic nature, these algorithms often have a higher efficiency, and they allow for a simple escape from a local extreme. These properties make them a widely applied approach in the control of continuous steel casting.

The third category contains the rest of various algorithms and approaches, which do not fit to any of the previous two categories. In particular, it includes PID-based regulation methods, techniques employing the fuzzy approach, learning optimisation, and the model-based predictive control. In the following, some recent papers published on the topic of control and optimisation of continuous steel casting across all three above mentioned categories are reviewed and discussed.

USE OF MATHEMATICAL PROGRAMMING TECHNIQUES

Methods based on mathematical programming have been mainly utilised in scheduling problems. Jiang et al. [61] presented a solution of the scheduling problem for continuous steel casting, which consisted of cost and penalty objectives. The authors proposed a prediction-based online soft scheduling algorithm and they reported that the algorithm outperforms other algorithms and allows for an approximate determination of the cost objective. In further work, Jiang et al. [62] presented a multi-stage dynamic soft scheduling algorithm, which was based on an improved differential evolution. The uncertainty was taken into account by means of the scenario-based approach and the decomposition was used for the solution of the problem. Similarly as in [61], the authors reported that the proposed algorithm is more efficient than other algorithms.

Bellabdaoui and Teghem [14] applied a mixed-integer linear mathematical programming model to scheduling in continuous steel casting. The authors created analytic and deterministic models, which were solved by means of the OMPartners software. The applicability of the model was tested and the authors concluded that the model allows for a significant reduction of the production time. Bartz-Beielstein and Zaeferrer [13] investigated the use of surrogate models in optimisation of continuous steel casting. The authors reviewed and analysed methods for continuous as well as for discrete optimisation problems. As for discrete problems, several strategies were proposed how to deal with discrete data structures, and a new method based on the combination of surrogate information via stacking was developed.

USE OF META-HEURISTICS AND NATURE-BASED ALGORITHMS

The range of applications of meta-heuristics in optimisation of continuous steel casting is rather wide ranging from scheduling to the process control. Santos et al. [125] created a control system based on heuristic search techniques and a genetic algorithm. The aim was to maximise the produc-

tion rate and the system was proposed to determine optimal parameters including water flow rates in the secondary cooling zone. The system consisted of a heat transfer model for continuous steel casting, which was coupled with a genetic algorithm. The authors presented a detailed analysis of their system, which was designed for off-line casting control. The applicability of the system was demonstrated with the use of experimental data, and it was shown that modifications suggested by the model led to the reduction of the water consumption and to an assured strand quality. Hetmaniok et al. [50] proposed a method for the restoration of cooling conditions in the mould and in the secondary cooling zone. The method utilised a solution of an inverse heat transfer problem and temperature measurements were used as inputs to it. The authors employed the alternating phase truncation method for the solution of a direct heat transfer problem, and the ant colony algorithm and the artificial bee colony algorithm were used for the minimisation of errors between simulation and experimental results. A good agreement and efficiency of the method were reported.

Hao et al. [46] investigated strong uncertainties in the scheduling problem for continuous steel casting and they proposed a two-layered approach for its solution. The particle swarm optimisation and another heuristic approach were used in the algorithm. The authors reported that the proposed algorithm provides a significantly better solution when compared to other methods for problems containing strong uncertainties. Peng et al. [108] utilised an improved artificial bee colony algorithm for the scheduling problem of continuous steel casting. The ability for exploration as well as exploitation of the algorithm were improved by introducing new parameters and a superior behaviour of the proposed algorithm was reported. Similarly, Pan [106] reported on a combined co-evolutionary artificial bee colony algorithm, which was used for the solution of a coupled charge-cast scheduling problem. Two swarms of individuals were used together with an improved strategy for onlookers and with an enhanced neighbourhood operator. The authors concluded that the proposed algorithm is effective and capable for the solution of scheduling problems. Wang et al. [149] utilised a particle swarm approach for optimisation of the secondary cooling zone in the continuous steel casting process. The authors emphasised a necessity for the correct and appropriate determination of heat transfer boundary conditions in the secondary cooling zone. They applied a particle swarm optimisation algorithm coupled with the heat transfer model and with surface temperature measurements for the determination of the optimal heat transfer coefficient in the secondary cooling zone. An experimentally determined shell thickness was used to assess the accuracy, and the authors reported that the proposed algorithm converges fast and possesses a strong global search efficiency.

USE OF OTHER CONTROL ALGORITHMS

Petrus et al. [109] presented a control algorithm of spray cooling in the secondary cooling zone by means of a 1D finite difference heat transfer model of continuously cast steel strands. The authors reported that the algorithm is capable for the real-time operation. The algorithm was based on a decentralised controller coupled with a bank of proportional-integral controllers with an anti-windup mechanism. The algorithm also utilised an adaptive set-point generation taking into account measured heat fluxes in the mould. Examples of simulations were used for the demonstration of control ability. Furtmüller et al. [40] addressed the stabilisation of dynamic bulging (large oscillations of the level in the mould) by means of an adaptive robust stabilisation. The adaptive control method

was proposed for the reduction of dynamic bulging without slowing down the casting process. The mould was modelled as a system of differential equations. Bulging was considered stochastic and the system was solved by means of an adaptive compensation of oscillations. The proposed method was validated with the use of experiments and its good applicability was reported. Liu and Xie [83] proposed a control system based on the fuzzy self-adaptive PID regulator, which aimed at the improvement of the billet quality and stability in the secondary cooling. The authors compared the system with another system based on the water distribution and superheat. They performed simulations as well as experimental investigations and it was reported that the fuzzy self-adaptive PID regulator outperformed other two considered controllers.

Hou et al. [52] employed a dynamic secondary cooling control model, which was based on a thermal-transition computation method and on the PID controller. The system was capable to adjust the flow rates of water in the secondary cooling zone and maintained the surface temperature of strands in a desired range. The authors reported that the system was enhanced by means of stabilisation of the secondary cooling flow, and the model was successfully applied at several continuous casting steel plants in China. He et al. [48] presented a breakout prediction and control system for the mould in continuous steel casting. The model was based on a logic judgement for the prediction of stickers. The model used real-time data from thermocouples installed with a high density in the mould walls. Results indicated that the model allows for a precise and in-time prediction of stickers and it has a good robustness. After sticking alarm, dynamic control strategies are proposed by the system to prevent the breakout. The system was tested at a steel plant and a very good efficiency in the prediction was reported. You et al. [159] presented an iterative learning control method for the control of the steel level in the mould of continuous steel casting process. The method considered the presence of disturbances, noise, and initial errors. The proposed algorithm was based on the use of a P-type learning rule with a forgetting factor and switching mechanism. The system was tested with experimental data, which confirmed its validity.

Rao et al. [116] utilised a teaching-learning-based approach for the parameter optimisation of casting parameters in continuous steel casting. The proposed model described a multi-objective multi-constrained problem and the authors reported that the proposed approach is more efficient when compared to the solution gained by means of the genetic algorithm. Wang et al. [150] presented a control algorithm for spray cooling in continuous steel casting, which was based on the use of the model-based predictive control method coupled with a particle swarm optimisation technique. The authors got their inspiration in the papers [71, 70] since they created a GPU-based heat transfer model adopted from [71], and they used it in the model-based control algorithm as proposed in [70]. Wang et al. [150] further implemented a weighted least-squares modified conjugate gradient method for the identification of heat transfer coefficients in boundary conditions. The authors reported that the proposed control system has a good computation performance and a satisfactory control performance. Zhang et al. [162] proposed an open-loop dynamic spray cooling control model for continuous steel casting, which was based on tracking of the casting speed and of the strand temperature. These two objectives were monitored and evaluated in slices into which the strand was split. The algorithm evaluated a heat transfer model of cast steel billets and used it as a numerical sensor. The authors compared their dynamic control algorithm with another algorithm,

and they reported that their dynamic control model enabled for a significant reduction of temperature fluctuations in controlled points. Moreover, the authors consequently applied their model at a steel plant and the occurrence of strand defects, such as mid-way cracks, was significantly reduced.

3.3 AUTHOR'S CONTRIBUTION TO THE DEVELOPMENT OF MODELLING AND CONTROL OF CONTINUOUS STEEL CASTING

Four journal papers co-authored by the author of the thesis and published in peer-review journals having the impact factor according to Web of Science are included in the thesis in order to demonstrate the author's contribution to the field of computer modelling, control, and casting analyses of continuous steel casting, which are based on the use of computer models. The journal papers included in the thesis are:

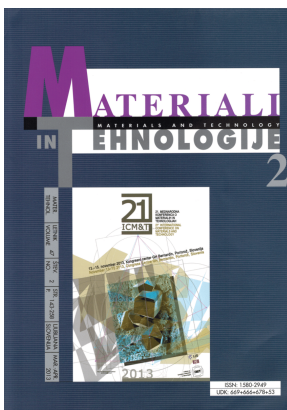


[71] Klimeš L, Štětina J. 2015. A rapid GPU-based heat transfer and solidification model for dynamic computer simulations of continuous steel casting. *Journal of Materials Processing Technology* 226: 1–14.

Author's contribution: 80%

Metrics: $IF_{2015} = 2.36$. $CiteScore_{2015} = 2.90$. Citations: 19 (G Scholar).

Ranking: $2 \times Q_1$ and Q_2 in JCR 2015 Web of Science.

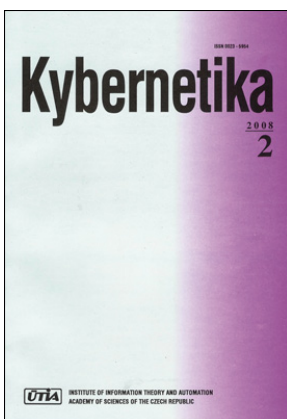


[72] Klimeš L, Štětina J, Buček P. 2013. Impact of casting speed on the temperature field of continuously cast steel billets. *Materials and Technology* 47 (4): 507–513.

Author's contribution: 75%

Metrics: $IF_{2013} = 0.56$. $CiteScore_{2013} = 0.69$. Citations: 6 (G Scholar).

Ranking: Q_4 in JCR 2014 Web of Science.



[69] Klimeš L, Popela P, Mauder T, Štětina J, Charvát P. 2017. Two-stage stochastic programming approach to a PDE-constrained steel production problem with the moving interface. *Kybernetika* 53 (6): 1047–1070.

Author's contribution: 50%

Metrics: $IF_{2017} = 0.63$. $CiteScore_{2017} = 0.62$. Citations: 0.

Ranking: Q_4 in JCR 2017 Web of Science.



[70] Klimeš L, Štětina J. 2014. Unsteady model-based predictive control of continuous steel casting by means of a very fast dynamic solidification model on a GPU. *Materials and Technology* 48 (4): 525–530.

Author's contribution: 80%

Metrics: IF₂₀₁₄ = 0.55. CiteScore₂₀₁₄ = 0.89. Citations: 3 (G Scholar).

Ranking: Q4 in JCR 2013 Web of Science.

KLIMEŠ AND ŠTĚTINA [71]: A RAPID GPU-BASED HEAT TRANSFER AND SOLIDIFICATION MODEL FOR DYNAMIC COMPUTER SIMULATIONS OF CONTINUOUS STEEL CASTING

The most significant achievement to the field of modelling and control of continuous steel casting was reported in [71]. The paper presented the development and benchmarking of the dynamic heat transfer and solidification model for continuous steel casting, which was designed for the use with graphics processing units (GPUs). A highly parallel code was proposed and implemented in CUDA/C++, which allowed for a very significant computational acceleration of the model in comparison to the state-of-the-art sequential CPU-based models for continuous steel casting. The parallel implementation was attained by means of the explicit-time discretization of the governing heat transfer equation, which was solved with the use of the enthalpy method and discretized by the application of the control volume method. In contrast to many models for continuous steel casting published in the literature, the developed GPU-based model utilised experimentally determined boundary conditions in the mould (heat fluxes quantified by means of thermocouples embedded in walls of the mould) as well as for spray cooling in the secondary cooling zone (heat transfer coefficients estimated by means of the hot plate method and of a solution to the inverse heat transfer problem in Heat Transfer and Fluid Flow Laboratory in Brno). The functionality of the model was validated as well as verified according to experimental data (surface temperature measurements by pyrometers) from a steel plant and to an exact solution of the Stefan two-phase solidification problem, respectively. The computational performance of the GPU-based model was assessed for several computational grids consisting of various numbers of computational nodes. It was found that the use of GPUs allowed for the acceleration (when compared to the identical CPU-based model) between 33× and 68× for the grid having 100 thousand and 5 million computational nodes, respectively.

Figure 3.15 demonstrates the acceleration provided by the GPU-based model in terms of the absolute computational time. It is worth pointing out that the vertical axis in Figure 3.15 is in a logarithmic scale. Figure 3.16 emphasises the advantage of the GPU-based model in case it is used in real-time control algorithms as a numerical sensor. In this case, the relative computational time is used to emphasise the necessity of fast models for their use in real-time optimisation and control systems. The reason is that in real-time control, the model needs to be faster or even much faster than the real wall-clock time as the control algorithm may require several evaluations of the model

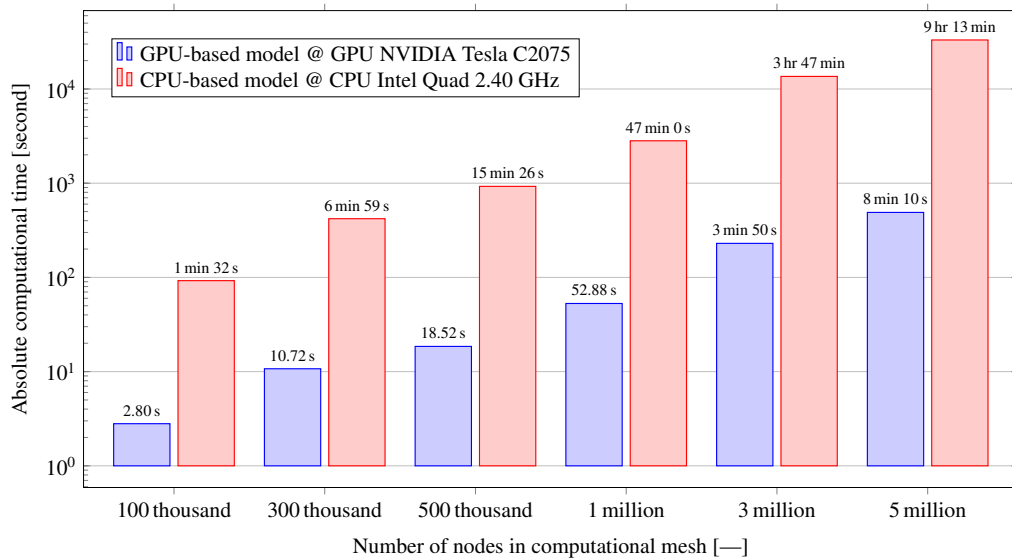


Figure 3.15: Comparison of the GPU-based model with the equivalent CPU-based model – evaluation of the absolute computational time [71]

in order to determine the optimal control strategy for the next time instance. The paper [71] was already adopted by other authors [150], who re-implemented and adopted the model in their research work.

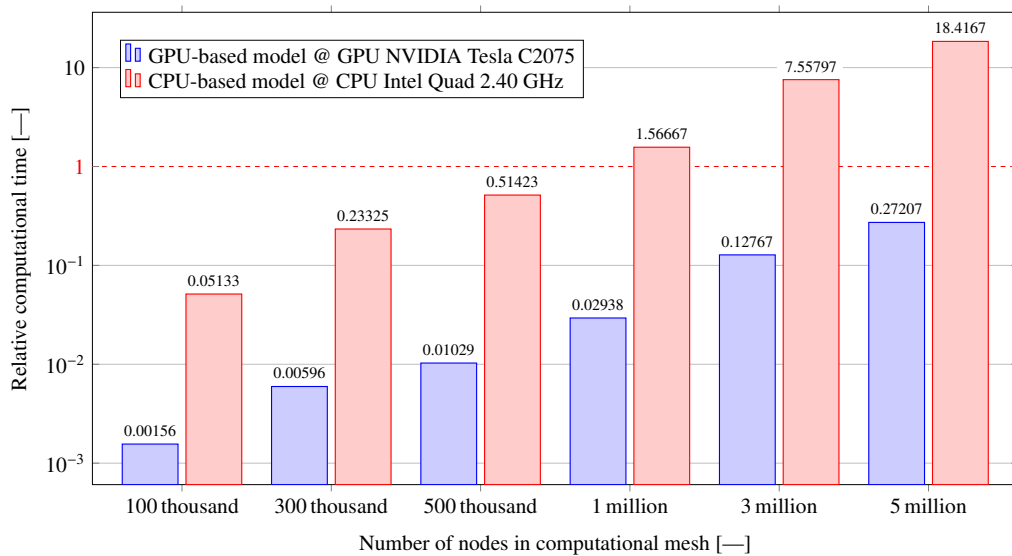


Figure 3.16: Comparison of the GPU-based model with the equivalent CPU-based model – evaluation of the absolute computational time [71]

KLIMEŠ ET AL. [72]: IMPACT OF CASTING SPEED ON THE TEMPERATURE FIELD OF CONTINUOUSLY CAST STEEL BILLETS

The paper [72] was aimed at an analysis of thermal and solidification conditions in continuous casting of steel billets. The heat transfer and solidification model, which was based on the enthalpy

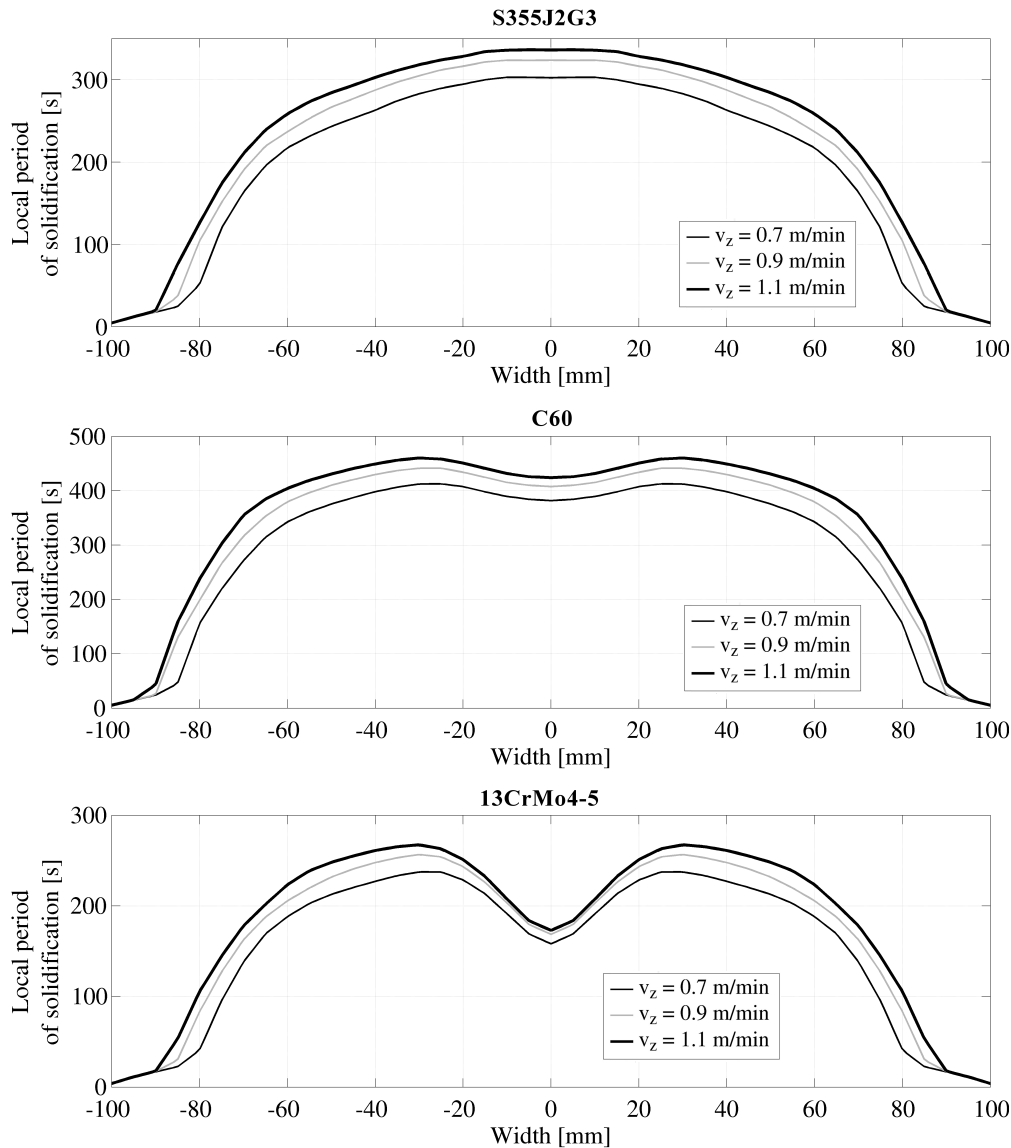


Figure 3.17: Computationally determined local time of solidification for various steel grades [72]

method and on the control volume discretization, was presented in the paper and its capabilities for the investigation of casting conditions were demonstrated. Similarly as in [71], the model employs experimentally determined boundary conditions in the mould as well as in the secondary cooling zone with spray cooling, and the functionality of the model was validated by means of experimental investigation and pyrometer measurements. In the paper [72], surface and corners temperatures, solidification regions, shell thickness, and the local period of solidification were computationally analysed for various casting speeds by means of the computer model. Such analysis can help metallurgists and operators of casters for the improvement of the strand quality and for the reduction of the occurrence of defects and quality issues. In particular, the temperature distribution at corners of the cast billets is directly related to the thermal stress and to the formation of cracks. Moreover, knowledge of the location of iso-solidus and iso-liquidus cones defining the distribution of the liquid and solid phases and their relationship to the location of the unbending point is crucial for the prediction of both internal and surface quality issues as reported in the literature.

Figure 3.17 shows the local time of solidification, which expresses the duration of solidification across the strand cross-section. As can be seen from Figure 3.17, the local time of solidification for the carbon steel grade S355J2G3 has a typical parabolic character. However, in case of the alloyed steel grade 13CrMo4-5, the parabolic behaviour has a local drop in the centre of the billet, which can indicate a tendency to issues in the central part of the steel strand.

KLIMEŠ ET AL. [69]: TWO-STAGE STOCHASTIC PROGRAMMING APPROACH TO A PDE-CONSTRAINED STEEL PRODUCTION PROBLEM WITH THE MOVING INTERFACE

The paper [69] was concerned with techniques of mathematical programming for the optimal control of continuous steel casting under uncertainty. In particular, the stochastic programming approach, which uses random variables with a known probability distribution, was used for modelling of randomness. It is worth pointing out that almost all papers presented in the literature review in Section 3.2.5 were aimed at the solution of deterministic control problems, while the optimisation model presented in [69] allows for the consideration of random events.

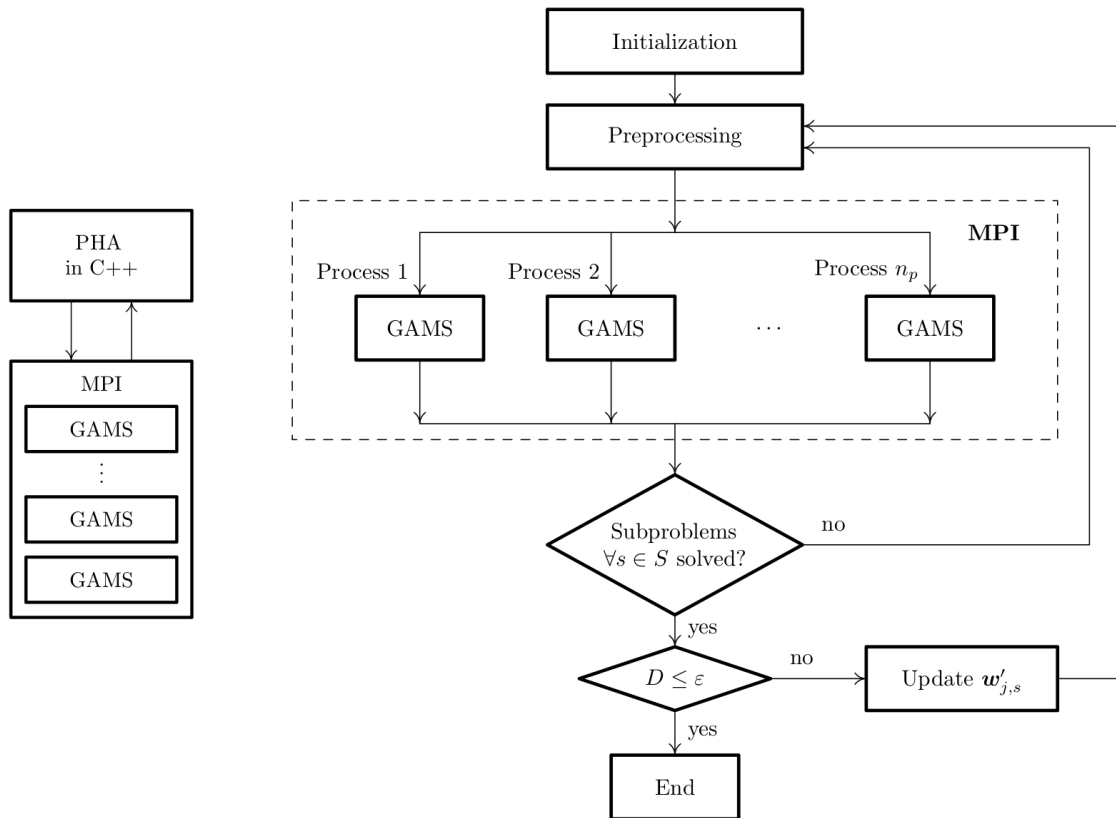


Figure 3.18: The block diagram and the flow chart of the parallel implementation of the progressive hedging algorithm [69]

The paper considered a two-stage decision making problem in the steel production. The randomness was used for modelling of a failure of the water pump in a loop in the secondary cooling zone, which would cause a sudden stop of spray cooling in the corresponding cooling loop. The scenario-based approach was utilised for modelling of randomness and the optimisation model was built in the general algebraic modelling system GAMS. The effective heat capacity method was used for the

description of heat transfer and solidification of the steel strand, and the control volume method was applied to the formulation of discretized equations.

The scenario-based two-stage stochastic problem was solved with the use of the progressive hedging algorithm proposed in [120, 154], which was implemented as a standalone application written in C++. Since the solution of individual scenario-based problems was independent to each other, a decomposition and parallel solution was proposed and implemented by means of the message passing interface (MPI) API. The schematic of the implemented system is shown in Figure 3.18. The parallel decomposition was identified as an effective method for the reduction of the computational time needed for the solution of the problem. The stochastic optimisation problem with an uncertain fault of the pump was used for the demonstration of applicability of the proposed approach. The solution of the model resulted in a two-stage solution answering the following questions: "How to set up the casting speed and cooling conditions in the secondary cooling zone at the beginning of the casting process, which would maximise the casting rate, but taking into consideration a failure of the pump with a given probability? And in case the failure of the pump indeed happens, how to change the casting parameters to maintain the casting process in operation?" The optimisation case study was performed to answer these questions and the practicability of the determined solution was evaluated and assessed by means of quantitative characteristics.

KLIMEŠ AND ŠTĚTINA [70]: UNSTEADY MODEL-BASED PREDICTIVE CONTROL OF CONTINUOUS STEEL CASTING BY MEANS OF A VERY FAST DYNAMIC SOLIDIFICATION MODEL ON A GPU

The paper [70] presented a dynamic control for continuous steel casting, which was based on the model-based predictive control approach and on the use of the rapid GPU-based heat transfer and solidification model presented in [71]. The very fast GPU-based model was a crucial part of the model-based predictive control mechanism: the control system used the GPU-based model for prediction of the future thermal behaviour of the strand in the so-called prediction (time) horizon.

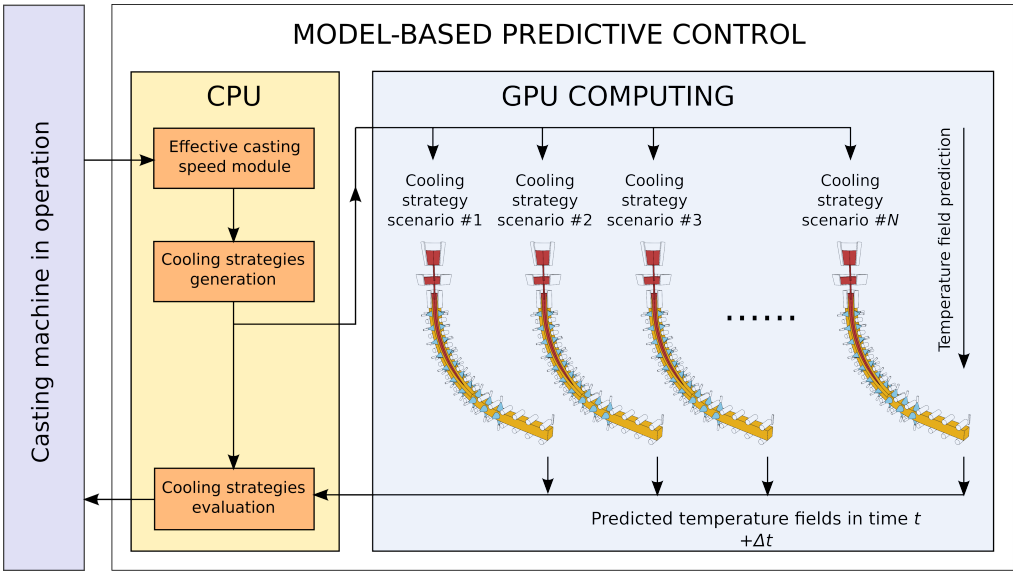


Figure 3.19: The schematic of the proposed MPC-GPU control system for continuous steel casting [70]

The underlying principle of the model-based predictive control was the fast evaluation of several cooling strategies (cooling scenarios), which were proposed and generated with the use of the effective casting speed. Since the GPU-based model is much faster than the wall-clock time, the GPU-based model allows for the pre-calculation and for the assessment of several cooling scenarios in real time. The schematic of the concept of the proposed model-based predictive control system is shown in Figure 3.19. It was shown that the proposed system has a good capability for the control of dynamic cases with strong changes of process parameters. The concept of the control system was further extended and validated in [66] where several case studies with dynamic changes of the casting speed were investigated, including the on-the-fly replacement of the tundish and the dynamic intervention of the breakout prediction system. The applicability and the proof of concept of the proposed control system were also confirmed by other investigators [150], who were motivated by results presented in [70, 71] and who re-implemented and extended the proposed control system by means of its coupling with a nature-inspired optimisation algorithm.



Contents lists available at ScienceDirect

Journal of Materials Processing Technology

journal homepage: www.elsevier.com/locate/jmatprotec

A rapid GPU-based heat transfer and solidification model for dynamic computer simulations of continuous steel casting

Lubomír Klimeš^{a,b,*}, Josef Štětina^{a,b}^a Brno University of Technology, Energy Institute, Technická 2896/2, 616 69 Brno, Czech Republic^b NETME Centre, Technická 2896/2, 616 69 Brno, Czech Republic

ARTICLE INFO

Article history:

Received 16 April 2015

Received in revised form 10 June 2015

Accepted 11 June 2015

Available online 23 June 2015

Keywords:

Continuous casting

Computational model

Heat transfer and solidification

Graphics processing unit (GPU)

CUDA

Parallelization

ABSTRACT

The paper presents a GPU-based model for continuous casting of steel. The model provides rapid computation capabilities required for real-time use in the casting control and optimization. The fully three-dimensional formulation of the heat transfer and solidification model is based on the control volume method and it allows for very fast transient simulations of the thermal behaviour of cast strands. The developed model has been verified on Stefan problem and validated with industry measurements. Heat transfer conditions in the mould and secondary cooling were determined experimentally in lab-scale experiments. The computational model is implemented as highly-parallel with the use of the NVIDIA CUDA architecture, which enables to launch the model on graphics processing units (GPUs) allowing for its great acceleration. The acceleration can be evaluated with the use of the relative computational time, which is the dimensionless ratio between the computational time that the model needs to compute the simulation and the wall-clock time of the real casting process being simulated. The relative computational time of the presented GPU-based computational model is between 0.0016 for a coarse mesh and 0.27 for a very fine mesh. The corresponding multiple of the GPU-acceleration, which is the ratio between the computational time of the GPU-based model and of the CPU-based model for the identical simulation, is between 33 and 68.

© 2015 Elsevier B.V. All rights reserved.

1. Introduction

Continuous casting is a primary method for steel production. The method currently accounts for 95% of the total world steel production. Steelmakers aim at the control of thermal behaviour of cast strands in the casting process as a number of quality and productivity issues (e.g. surface and internal defects) are caused due to improper setup of the mould and/or of the secondary cooling. Monitoring of the strand temperature and thermal stress is rather difficult to perform owing to high temperatures and severe environment. Ma et al. (2009) used pyrometers for the surface temperature measurement and they reported a substantial fluctuation of measured temperatures, which makes the measurement inapplicable.

A number of researchers and steelmakers therefore tend to utilize computational models for continuously cast steel strands.

Finite difference, finite volume, and finite element methods have frequently been used for the model implementation. Chen et al. (2014) emphasized the necessity for accurate determination of heat transfer conditions to ensure reliable computational results. Yang et al. (2014) reported that a number of computer models for continuous casting have been developed. Some of these models were created only for steady-state simulations. Many developed models are designed for control and optimization of casting and they are, however, capable to operate only in offline mode as simulators due to limits in computational efficiency and accuracy. Šarler et al. (2012) reported that simulations performed with the use of some sophisticated multiscale and multiphysics models can last even several days. As for the online models capable to operate in real-time, most of them are rather simple and only implemented in 1D or 2D. Louhenkilpi et al. (2005) concluded that attention has recently turned to the development of three-dimensional models for real-time simulations in the process control. Yoon (2008) reported the recent trend towards near-net-shape casting, which requires computationally demanding models with fine meshes.

Meng and Thomas (2003) developed a one-dimensional transient heat transfer model of the strand coupled with a two-dimensional steady-state heat transfer model of the mould. The

* Corresponding author at: Brno University of Technology, Energy Institute, Technická 2896/2, 616 69 Brno, Czech Republic.

E-mail addresses: klimes@fme.vutbr.cz (L. Klimeš), stetina@fme.vutbr.cz (J. Štětina).

Nomenclature

α	thermal diffusivity (m^2/s)
c_p	specific heat at constant pressure ($\text{J}/\text{kg K}$)
Γ	set of boundary points
D	diameter (m)
δ	distance (m)
Δ	size of discretization step, difference
e_{MRE}	mean relative error
ϵ	emissivity (–)
f_s	solid fraction (–)
\dot{g}	source of heat (W/m^3)
H	total enthalpy (kJ/m^3)
h	heat transfer coefficient ($\text{W}/\text{m}^2 \text{K}$)
k	thermal conductivity ($\text{W}/\text{m K}$)
L	length (m)
L_f	latent heat of fusion (kJ/kg)
m	coefficient of multiplication (–)
\dot{m}	mass flow rate (kg/s)
N_s	number of control volumes (volume elements) (–)
N_t	number of time steps (–)
Φ	coefficient in the del operator (–)
ψ	parameter (–)
q	heat transfer rate (W)
\dot{q}	heat flux (W/m^2)
r, ϕ, ω	cylindrical coordinates system (m, rad, m)
ρ	density (kg/m^3)
s	position of the solid–liquid interface (m)
S	area (m^2)
σ	Stefan–Boltzmann constant ($\text{W}/\text{m}^2 \text{K}^4$)
σ	standard deviation
T	temperature (K)
t	time (s)
ϑ	parameter (–)
v	casting speed (m/min)
x, y, z	Cartesian coordinate system (m, m, m)
ξ	spatial coordinate (m or rad)
ξ	vector of spatial coordinates (m, m or rad, m)

Abbreviations

CPU	central processing unit
CUDA	compute unified device architecture
GPU	graphics processing unit
SIMD	single instruction multiple data

Subscripts

0	initial
∞	ambient
c	convective
cast	casting
eff	effective
ℓ	liquid
latent	latent (related to fusion)
m	mean
M	mould
MC	meniscus of casting
move	movement
nat	natural
r	radiative
R, roll	roller
s	solid
STC	secondary and tertiary cooling
surf	surface
T	torch
w	water

coupled model was formulated with the use of the finite difference method and it addressed metallurgical phenomena such as slag in the mould and effects of oscillation marks. The authors, however, admitted that a more advanced 3D transient simulation tool was needed since their model allowed for simulations of time-averaged behaviour, which were not sufficient for practical use. [Fic et al. \(2000\)](#) adopted the front tracking boundary element method. For simplicity the model was implemented as steady-state and linear with the natural convection neglected. Two-dimensional computational domain oriented longitudinally in the casting direction was used. Such configuration, however, is not suitable for the thermal analysis at the edges of the strand, which are prone to cracking. Further, the model was assembled with an assumption that the phase change takes place at a constant temperature, which is rather unrealistic in case of steel. [Louhenkilpi et al. \(2013\)](#) presented the thermal model, which consists of two submodels for the strand and for the mould. The model is three-dimensional and is formulated with the use of the finite difference method. The model integrates upwinding and ghost point numerical techniques in order to improve its numerical behaviour and stability. The authors reported that the model was sufficiently fast for real-time applications. [Šarler et al. \(2012\)](#) developed a quasi three-dimensional slice model, which calculates a 2D heat transfer in the strand cross-section as it moves within the strand. Due to the quasi 3D approach, the model neglects all interactions in the longitudinal direction of casting and accounts only for those perpendicular to the casting direction. The authors reported that the model allowed for fast computations with a satisfactory accuracy.

Some authors evaluated the computational performance of the models and their applicability for real-time simulations with the use of the relative computational time. This dimensionless time represents the ratio between the computational time that the model needs to compute the simulation and the wall-clock time of the real casting process being simulated. [Mauder et al. \(2015\)](#) developed a fully three-dimensional transient model for continuous casting slabs. The finite difference method was used for the formulation of the model. The authors reported a good accuracy of their model with the relative computational time of about 0.7. [Yang et al. \(2014\)](#) developed a two-dimensional slice heat transfer model with the use of the finite volume method. A multiple non-uniform grid allowed for high accuracy calculations in real time with the relative computational time of about 0.25. The authors reported unconditional numerical stability for constant thermophysical properties, which is, however, not the case in the practice.

It can be concluded that only relatively simple computational models are used in real-time applications as they require the relative computational time of less than one. However, some authors (e.g. [Mauder et al., 2015](#); [Santos et al., 2003](#)) presented optimization and control algorithms, which perform repetitive evaluations of the model in an iterative loop. In other words, such applications require the relative computational time significantly less than one. An intrinsic effort of developers is therefore to create computational models, which are physically advanced, accurate, reliable, and also very fast.

The present paper reports the development of a rapid computational model for continuous casting of steel, which greatly fits for real-time use. The control volume method is used for the formulation of the model, which is fully three-dimensional. The model allows for transient simulations of the thermal behaviour of the complete strand from the mould to the torch. The developed model has been verified on Stefan problem, validated with the industry measurements, and it utilizes experimentally determined heat transfer conditions in the mould and secondary cooling. The model is implemented as highly-parallel by means of the NVIDIA

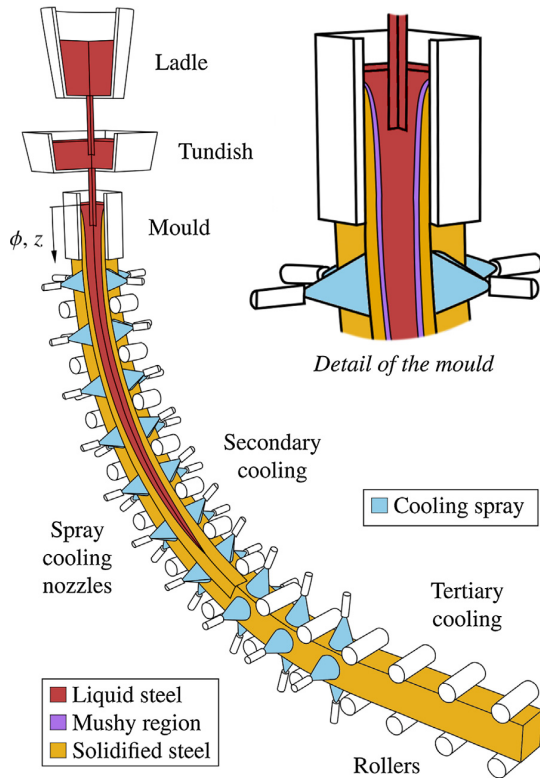


Fig. 1. A schematic of the continuous casting machine with the detail of the mould and of the solid–mushy–liquid interface.

CUDA architecture, which enables to launch the model on graphics processing units (GPUs).

2. Continuous steel casting

The principle of continuous casting is shown in Fig. 1. In steelworks, molten steel from a furnace or from a converter is transferred in ladles to the continuous casting machine. Liquid steel is poured from the ladle to the tundish, which is used as a melt storage for homogenization. The melt flows from the tundish through the submerged entry nozzle to the mould where primary heat withdrawal takes place. The mould, which is made of copper for its high thermal conductivity, is cooled by water flowing through it. The main objective of the mould is to withdraw a sufficient amount of heat, which induces the formation of the solid shell. As steel solidifies within a temperature range rather than at a constant temperature, a heterogeneous mixture of both the solid phase and the melt forms at the phase interface, see the detail of the mould in Fig. 1. Such a heterogeneous mixture is called the mushy region.

The strand with the solid shell at the surface, but still liquid inside (with the so-called liquid pool), exits the mould and enters to the secondary cooling. A number of water and/or air-mist cooling nozzles are installed within the secondary cooling, which gradually cool the strand down as it passes through the machine. Simultaneously, the solid shell thickness grows up and reduces the liquid pool as the steel solidifies. The tertiary cooling follows the secondary cooling. In tertiary cooling the heat withdrawal is only due to radiation and natural convection to the ambient. At the end of tertiary cooling, the semi-infinite strand is periodically cut with the use of a torch to slabs or billets for next processing.

3. Computational model for continuous steel casting

3.1. Mathematical formulation

The governing equation of heat transfer and solidification for continuous casting strands (e.g. Stefanescu, 2008) reads

$$\rho c_p \frac{\partial T}{\partial t} = \text{div}(k \nabla T) + \dot{g}_{\text{latent}} + \dot{g}_{\text{move}} \quad (1)$$

where T is temperature, t is time, ρ is density, c_p denotes specific heat at constant pressure, and k stands for thermal conductivity. The term \dot{g}_{latent} represents an internal source of heat due to the latent heat of phase changes. The last term \dot{g}_{move} in Eq. (1) reflects heat transfer owing to the movement of the strand through the casting machine.

A number of methods have been developed for the treatment of the latent heat of phase changes incorporated in the term \dot{g}_{latent} , e.g. the enthalpy method, the apparent specific heat method, or the temperature recovery method. Idelsohn et al. (1994) provided a comprehensive review on methods for modelling of phase change problems and their discretizations. The enthalpy method is utilized for the formulation of the presented computational model since the method is stable, self-conservative, and it allows for its straightforward parallelism (Muhieddine et al., 2009). The main feature of the enthalpy method is coupling of the latent heat of phase changes with the sensible heat into the temperature-dependent thermodynamic total enthalpy $H(T)$. It is defined (e.g. Stefanescu, 2008) as

$$H(T) = \int_0^T \left(\rho c_p - \rho L_f \frac{\partial f_s}{\partial \theta} \right) d\theta \quad (2)$$

where L_f is the latent heat of phase changes and $f_s \in (0, 1)$ is the solid fraction, which is equal to the fraction of the solid phase. In case of steel the latent heat

$$\dot{g}_{\text{latent}} = \rho L_f \frac{\partial f_s}{\partial T} \frac{\partial T}{\partial t}. \quad (3)$$

The differential energy transfer due to the movement of the strand through the casting machine can straightforwardly be formulated by means of the differential change of the total enthalpy as

$$\dot{g}_{\text{move}} = v_{\text{cast}} \Phi_{\text{cast}} \left(\frac{\partial H}{\partial \xi_{\text{cast}}} \right) \quad (4)$$

where v_{cast} is the casting speed of the strand in the casting machine along the spatial coordinate ξ_{cast} . The Φ_{cast} is the coefficient in the del operator corresponding to the term of the casting direction. For the Cartesian coordinate system $\Phi_{\text{cast}} = 1$ with $\xi_{\text{cast}} = z$ while $\Phi_{\text{cast}} = \frac{1}{r}$ with $\xi_{\text{cast}} = \phi$ in case of the cylindrical coordinate system. The differentiation of Eq. (2) and its substitution together with Eqs. (3) and (4) to Eq. (1) lead to the resulting enthalpy-formulated governing equation for heat transfer and solidification of the cast strand

$$\frac{\partial H}{\partial t} = \text{div}(k \nabla T) + v_{\text{cast}} \Phi_{\text{cast}} \left(\frac{\partial H}{\partial \xi_{\text{cast}}} \right). \quad (5)$$

So far, the derived governing Eq. (5) takes into account only heat and mass transfer due to the solidification and the strand movement. As for the fluid flow inside the liquid pool, a number of authors (e.g. Fic et al., 2000) neglect this phenomenon and justify this approach by the high viscosity of liquid steel. It was shown (e.g. Ji et al., 2013) that the precise treatment of fluid flow phenomena is computationally very demanding and is important rather in case of a detailed study of the mould behaviour. A simple, but usually sufficient approach for fluid flow modelling inside the liquid pool is to introduce an effective thermal conductivity k_{eff} to Eq. (5). The

effective thermal conductivity is an artificially increased value of the physical thermal conductivity due to fluid motion and heat transfer enhancement inside the liquid pool. We have utilized the relationship $k_{\text{eff}} = k[1 + m(1 - f_s)]$ as [Ha et al. \(2001\)](#) where k is the physical thermal conductivity and m is a multiplier. The value m determined by a number of simulations carried out during the model validation was set to 1.15.

3.2. Initial and boundary conditions

As the governing Eq. (5) is a partial differential equation of the second-order in space and first-order in time, the initial and boundary conditions are required to correctly complete the mathematical formulation of the model. The initial temperature distribution of the strand, which is used at the beginning of a simulation, reads

$$T|_{t=0} = T_0(\xi) \quad (6)$$

where ξ is the vector of spatial coordinates; for the Cartesian coordinate system $\xi = [x, y, z]$ while for the cylindrical coordinate system $\xi = [r, \phi, \omega]$. The boundary conditions apply for $t > 0$ and they define the heat withdrawal at the boundaries of the strand. Three kinds of boundary conditions, namely the Dirichlet, Neumann, and the Robin condition, arise in the model formulation. The surface temperature at the meniscus of casting in the mould is equal to the casting temperature T_{cast}

$$T|_{\xi \in \Gamma_{\text{MC}}} = T_{\text{cast}}(\xi, t) \quad (7)$$

where Γ_{MC} is the meniscus of casting in the mould. At the boundary Γ_{M} corresponding to the mould, the heat flux is usually defined as

$$-k \frac{\partial T}{\partial \mathbf{n}}|_{\xi \in \Gamma_{\text{M}}} = \dot{q}(\xi, t). \quad (8)$$

Eq. (8) also applies at the boundary Γ_{R} where rollers are positioned, see [Fig. 1](#). A special case of Eq. (8) further occurs at the end of the strand Γ_{T} where the torch cuts the semi-infinite strand to slabs or billets. Here, the heat flux is $\dot{q} = 0$ due to the adiabatic boundary. The most complicated boundary conditions are those in the secondary and tertiary cooling Γ_{STC} where $\Gamma_{\text{STC}} = \Gamma \setminus \{\Gamma_{\text{MC}} \cup \Gamma_{\text{M}} \cup \Gamma_{\text{R}} \cup \Gamma_{\text{T}}\}$ with Γ being the set of all boundaries of the strand. Here, heat transfer from the strand is due to forced and natural convection as well as due to radiation. Hence,

$$-k \frac{\partial T}{\partial \mathbf{n}}|_{\xi \in \Gamma_{\text{STC}}} = h(T - T_{\text{c},\infty}) + \sigma \epsilon (T^4 - T_{\text{r},\infty}^4) \quad (9)$$

where h is the heat transfer coefficient, σ is the Stefan–Boltzmann constant and ϵ is the emissivity of the surface. In case of forced convection by spray cooling, the ambient temperature $T_{\text{c},\infty}$ is equal to the temperature of cooling water. In case of natural convection, the ambient temperature $T_{\text{c},\infty}$ is equal to the temperature of the ambient air. An analogy for ambient temperatures applies in case of radiation.

A number of approximate empirical formulae have been published for the heat transfer coefficient beneath the spraying nozzles in the secondary cooling. Some approximations are also available for the heat flux in the mould and for the emissivity indicated in Eqs. (8) and (9). [Shimada and Mitsutsuka \(1966\)](#) first proposed that the heat transfer coefficient for cooling nozzles is mainly dependent on the impingement water flux density, and their empirical relationship has widely been used by other researchers (e.g. [Yang et al., 2014](#)). In case of heat transfer in the mould, [Savage and Pritchard \(1954\)](#) first suggested that the withdrawn heat flux is proportional to the square root of the casting speed. Their empirical formula has been adopted by a number of researches (e.g. [Gonzalez et al., 2003](#)). These empirical formulae are, however, only approximate and they incorporate several constants and/or parameters, which are rather difficult to determine for a particular case. Experimental



Fig. 2. Experimental mould in a lab with installed thermocouples.

measurements were therefore carried out to more precisely assess the heat withdrawal in case of the particular installed mould and spray cooling nozzles.

The heat withdrawal from the mould was measured in a lab environment with the use of the actual mould operated at the casting machine by means of methodology presented by [Pyszkó et al. \(2012\)](#). The thermocouples installed at the mould shell, see [Fig. 2](#), were used to measure the shell temperature. A number of experiments were carried out for distinct water flow rates through the mould. The local heat flux was consequently determined from the measured temperatures using the computational heat transfer analysis. The resultant heat flux at 15 characteristic locations is pictured in [Fig. 3](#) for a particular water flow rate through the mould. The bilinear interpolation is used to approximate the heat flux at remaining locations.

The cooling characteristics of the spray cooling nozzles were determined by means of lab-scale experiments carried out with the use of a hot-plate model presented by [Raudenský and Horský \(2005\)](#). [Fig. 4](#) shows a photo taken during the hot-plate experiment. The method comprises a steel plate incorporating thermocouples, which are positioned in holes drilled at the plate. The plate is initially heated up in a furnace to about 1200 °C. Consequently, the plate is installed to the experimental stand where it remains at a steady position. The tested cooling nozzle then repeatedly moves back and forth along the surface and it sprays the surface,

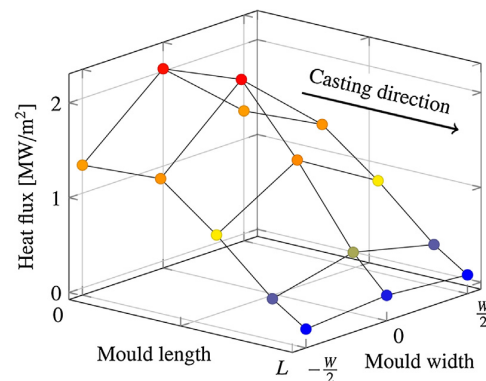


Fig. 3. Heat flux distribution in the mould determined by experiments.



Fig. 4. The hot-plate experiment used for the assessment of cooling nozzle characteristics.

which gradually cools down. The acquisition system retrieves time-dependent temperatures from thermocouples, which are installed at the plate. At the final step of the procedure, the heat transfer coefficient of the cooling nozzle is determined from the experimental data by means of the computation of the inverse heat transfer problem investigated by Raudenský et al. (2002). Fig. 5 shows the distribution of the heat transfer coefficient for a cooling nozzle.

As for the emissivity in the boundary condition given by Eq. (9), its value is often assumed constant in the range between 0.8 and 0.9 (e.g. Gonzalez et al., 2003). Some empirical correlations for the emissivity of the steel surface at elevated temperatures have been published by Touloulian et al. (1972). These correlations are applied by other researchers (e.g. Hardin et al., 2003). We assessed the emissivity experimentally in order to obtain more precise and reliable results as the radiation is responsible up to about 30% of the total heat withdrawal from the strand. The hot-plate method with no cooling nozzle was used for the determination of the emissivity. In this case the heat is transferred from the plate only by means of radiation and natural convection. Subtracting the natural convection yields to the surface temperature-emissivity polynomial relationship

$$\epsilon = 0.7883 + 3.3375 \cdot 10^{-4} T_{\text{surf}} - 4.0179 \cdot 10^{-7} T_{\text{surf}}^2. \quad (10)$$

The heat transfer coefficient in areas outside of spray cooling, where cooling is due to natural convection, is almost constant and virtually negligible in comparison to the forced convection of spray cooling and to the radiation. The empirical formula $h_{\text{nat}} = 0.84 (T_{\text{surf}} - T_{\infty})^{1/3}$ given by Hardin et al. (2003) was used in estimation of the heat transfer coefficient for natural convection. As for the heat withdrawal due to rollers, the heat balance estimation presented by

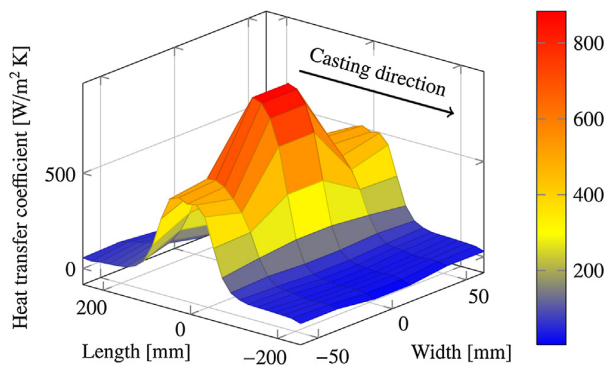


Fig. 5. The heat transfer coefficient for a spray cooling nozzle.

Mauder et al. (2015)

$$q_{\text{roll}} = h_{\text{roll}} \pi D L \vartheta_c (T_{\text{roll}} - T_{\infty}) + \sigma \epsilon \pi D L \vartheta_r (T_{\text{roll}}^4 - T_{\infty}^4) + \dot{m}_w c_w \Delta T \quad (11)$$

was used to quantify the heat transfer between rollers and the strand in the presented model. The estimation given in Eq. (11) is based on the assumption that the heat transfer rate withdrawn through the roller can be approximated as the sum of heat transfer rates from the roller to the ambient by means of the convection, radiation, and water flowing through the roller. The parameter $\vartheta \in (0, 1)$ accounts for the particular location of the roller and for its surrounding.

3.3. Thermophysical properties of steel

Temperature-dependent thermophysical properties of steel – the total enthalpy, the thermal conductivity, the density, and the specific heat are important inputs to the computational model. Moreover, these material characteristics are not only functions of the temperature, but also of the chemical composition. Experimental investigations of thermophysical properties in a lab environment are generally expensive and time-consuming. The presented computational model utilizes thermophysical properties determined by means of the commercial interdendritic solidification software IDS developed by Miettinen et al. (2010). The IDS is a complex grey-box model, which combines empirical or semi-empirical models with fundamental physically-based models. The IDS allows for the definition of the chemical composition of steel and for the solidification conditions. Results of the IDS have been validated and a good agreement was reported. Fig. 6 shows the temperature-dependence of the total enthalpy, the thermal conductivity, the density, and of the specific heat for a low carbon steel 9SMN28, which is used hereafter in the model validation.

4. GPU-based implementation of the model

4.1. A brief overview on GPUs

A graphics processing unit, a GPU, is a computer device intended for parallel data processing. Although primarily designed for the use in computer graphics and image rendering, GPUs are nowadays widely used for massive parallel computing in science and engineering. In the last years, graphics processing units have encountered a vast development and a steep rise of their computational performance. In 2008, the theoretical peak performance of high-end GPUs in double precision was about 80 GFlops¹ provided by about 250 of computing units incorporated in one GPU. The value increased to about 700 GFlops in 2012. Nowadays in 2015, the theoretical peak performance in double precision has attained approximately 1.5 TFlops for high-end GPUs, which incorporate about 3000 of computing units. GPU computing offers a huge computational performance with a very favourable ratio between the price and the performance of GPUs.

A GPU is generally a device designed for the use in Single Instruction Multiple Data (SIMD) architecture, in which a number of computing units concurrently perform an identical set of operations but each unit with different data. Nowadays, a high-end GPU consists of thousands of elementary computing units, so-called stream processors, which are arrayed into stream multiprocessors (Owens et al., 2008). GPUs are especially effective in cases having a high value of ratio between the number of performed arithmetic

¹ Flops is a unit of computational performance meaning Floating-point Operations Per Second.

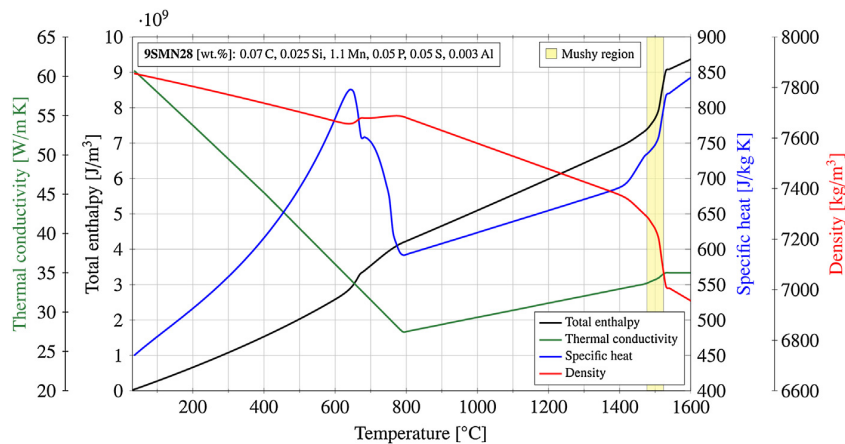


Fig. 6. Temperature-dependent total enthalpy, thermal conductivity, specific heat, and density for a low carbon steel 9SMN28.

operations and the number of memory operations. A computational problem, which is about to be computed with the use of a GPU, have to be parallelizable. It means that there has to be a computer formulation of the problem that allows for splitting the problem into independent procedures. The parallel formulation of the problem is therefore a necessary condition for the use of GPUs.

GPUs have been utilized in a number of various computational problems. Many papers were published on topics related to multi-body molecular dynamics (e.g. Cheng et al., 2015), image processing (e.g. Galizia et al., 2015), and to Monte Carlo simulations (e.g. Goldsworthy, 2014). Some papers have recently been published on the topic of the GPU use in heat transfer problems. Jiang et al. (2015) developed a parallel algorithm for solving the diffusion partial differential equation in cylindrical coordinates. They utilized the finite difference Crank-Nicolson scheme and the local one-dimensional approach for the model formulation intended for the use on GPUs. Rong et al. (2014) developed a three-dimensional parallel heat transfer model for the calculation of fluid flow and heat transfer characteristics in a pipe with embedded porous media. Ansoni et al. (2015) investigated the acceleration of the inverse heat transfer problem by means of parallel computing with the use of GPUs and multi-core CPUs. The authors developed a gradient method for solving sparse linear systems on GPUs. Fu et al. (2012) used a GPU for the computation of a 3D heat transfer problem with natural convection between two horizontal plates. The authors adopted preconditioning and dual time stepping. All the mentioned authors reported that the use of GPUs allowed for the acceleration of computations. The multiple of acceleration between parallel GPU-based and serial CPU-based implementations was from 2 (rather small) presented by Ansoni et al. (2015) to 40 (very high) reported by Jiang et al. (2015). It is therefore obvious from these results that GPUs and their use can greatly enhance the performance of computational models.

4.2. Programming GPUs with CUDA

In the present paper we employ the GPU produced by NVIDIA, which provides the CUDA platform for programming NVIDIA GPUs. The CUDA (Compute Unified Device Architecture), first released in 2006, is an application programming interface (API) used for the communication between a programmer, a CPU, and a GPU. The CUDA is accessible to developers in several programming languages including C/C++ and Fortran, and it is supported in MATLAB. We utilized the CUDA/C++, which is an extension of the C++ language allowing the programmer to create codes for massive computations with GPUs.

In GPU programming, the GPU, which is referred to as a device, is used as a co-processor. It performs a huge amount of computations by means of a parallel thread execution of a set of instructions referred to as a kernel (Wilt, 2013). The kernel is not a complete program as it incorporates only operations performed in parallel manner. The CPU, which is referred to as a host, sequentially controls the program flow and launches the kernel on a GPU. A program for GPUs thus consists of two parts, each running either on the host or on the device. An execution of the kernel instructs the GPU, which launches a large number of threads executing an identical code of the kernel but each thread with different data. The CUDA environment launches parallel threads in a grid, which consists of thread blocks, each incorporating a specific number of threads. Fig. 7 shows the arrangement of the GPU-based computation.

Specific CUDA methods are accessible to each thread allowing for identification of the thread in the grid. The CUDA also provides methods for thread synchronization and for thread-to-thread communication by means of the shared memory. A number of special kinds of memory are accessible to threads at distinct levels of thread hierarchy. However, from the performance point of view, data transfer needs to be minimized as frequent memory operations between the host and the device can enormously reduce the computational performance of GPUs.

4.3. Numerical formulation

The control volume method (e.g. Kreith et al., 2011) was adopted for the numerical formulation and discretization of the mathematical model described in Section 3. An explicit numerical scheme was used for the discretization of the time derivative in the governing Eq. (5). The explicit scheme is conditionally stable and the size of the time step is therefore limited. Nevertheless, the explicit formulation of the governing equation leads to independent relationships that can be used for a straightforward parallel computation of the model. This is one of the features that are responsible for a recent increase in use of explicit methods. The explicit formulation is therefore essential for launching the presented model on graphics processing units.

The numerical formulation by means of the control volume method requires to mesh the strand into appropriate volume elements, so-called control volumes. Cuboid control volumes (rectangular parallelepipeds) are meshed at the straight part of the strand incorporating tertiary cooling, see Figs. 1 and 8. On contrary, curvilinear control volumes having the shape of a sector of a hollow cylinder are used for mesh in the radial part, which consists of the mould and secondary cooling. The transient conservation of

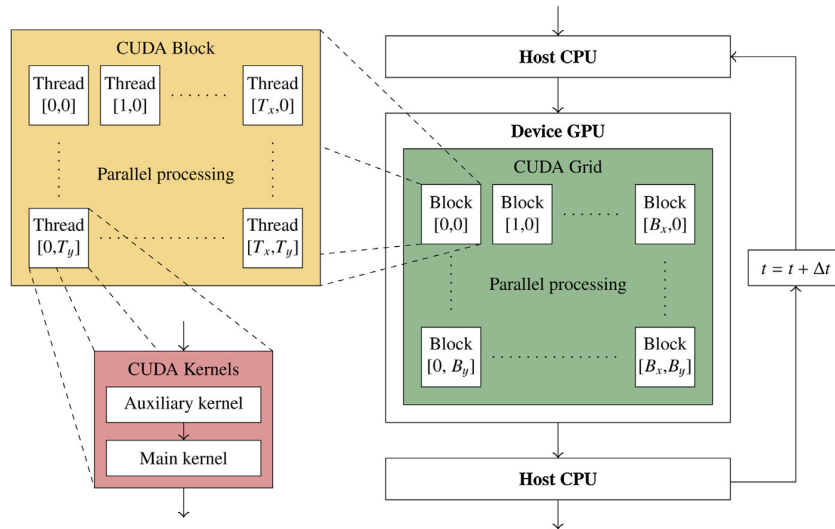


Fig. 7. A schematic and flowchart of the GPU-based implementation in CUDA for the computational model of continuous steel casting.

energy is then applied to each control volume. This leads to a set of algebraic equations allowing for the computation of an unknown temperature distribution. Nonetheless, in case of the enthalpy formulation used in the governing Eq. (5), both the total enthalpy and the temperature are unknown variables. It is therefore necessary to solve the coupled temperature-enthalpy problem. However, the use of the explicit discretization scheme in time allows for the separation of the coupled problem into two sequentially-linked subproblems. First, the unknown total enthalpy is calculated from the conservation of energy. The unknown temperature is

consequently determined from the value of the total enthalpy with the use of the temperature-enthalpy relationship shown in Fig. 6.

Considering the cuboid control volume (i, j, k) in the Cartesian coordinate system shown in Fig. 8, the explicit formula for the computation of the total enthalpy $H_{i,j,k}^{t+\Delta t}$ at the time instance $t + \Delta t$ reads

$$H_{i,j,k}^{t+\Delta t} = H_{i,j,k}^t + \frac{\Delta t}{\Delta x \Delta y \Delta z} (q_x^\pm + q_y^\pm + q_z^\pm) + v_{\text{cast}} \Delta t \frac{H_{i,j,k-1}^t - H_{i,j,k}^t}{\Delta z} \quad (12)$$

where Δt , Δx , Δy , and Δz are the sizes of time and spatial discretization steps, respectively. The q denotes the heat transfer rate, which enters the control volume in the spatial direction indicated in the subscript. The plus-minus sign in the superscript of q is used to explicitly emphasize that the resultant heat transfer rate q^\pm is given as the sum of two heat transfer rates $q^\pm = q^+ + q^-$ where q^+ is the rate in the positive direction of the spatial coordinate while q^- is that in the negative direction, see Fig. 8. The heat transfer rate q is given by the Fourier law as

$$q = k_{\text{eff}} S \frac{\hat{T} - T_{i,j,k}^t}{\delta} \quad (13)$$

where S is the area of the control volume the heat is transferred through, \hat{T} is temperature in the adjacent control volume, and δ is the distance between the node of the adjacent control volume corresponding to the temperature \hat{T} and the node of the control volume (i, j, k). The particular values of k_{eff} , S , \hat{T} , and δ for the cuboid control volume are listed in Table 1. The effective thermal conductivity in Eq. (13) between two adjacent control volumes is calculated as the harmonic mean value proposed by Patankar (1980) as presented in

Table 1 Values of k_{eff} , S , \hat{T} , and δ for the determination of heat transfer rates: cuboid control volume in the Cartesian coordinate system.

q	\hat{T}	k_{eff}	S	δ
q_x^\pm	$T_{i\pm 1,j,k}^t$	$\frac{2k_{i\pm 1,j,k}k_{i,j,k}}{k_{i\pm 1,j,k} + k_{i,j,k}}$	$\Delta y \Delta z$	Δx
q_y^\pm	$T_{i,j\pm 1,k}^t$	$\frac{2k_{i,j\pm 1,k}k_{i,j,k}}{k_{i,j\pm 1,k} + k_{i,j,k}}$	$\Delta x \Delta z$	Δy
q_z^\pm	$T_{i,j,k\pm 1}^t$	$\frac{2k_{i,j,k\pm 1}k_{i,j,k}}{k_{i,j,k\pm 1} + k_{i,j,k}}$	$\Delta x \Delta y$	Δz

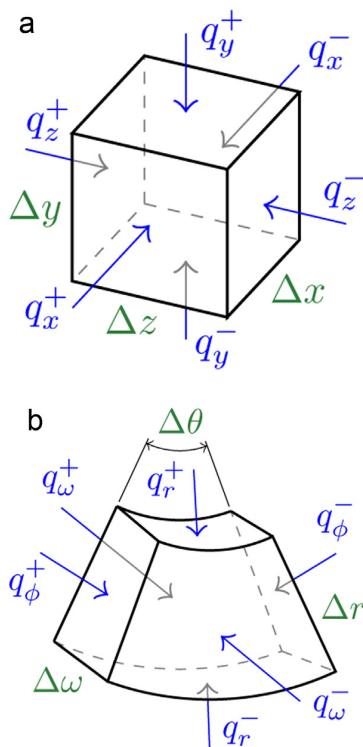


Fig. 8. Cuboid (left) and curvilinear cylindrical (right) control volumes used for the numerical formulation of the model.

Table 2

Values of k_{eff} , S , \hat{T} , and δ for the determination of heat transfer rates: curvilinear control volume in the cylindrical coordinate system.

q	\hat{T}	k_{eff}	S	δ
q_r^\pm	$T_{i\mp 1,j,k}^t$	$\frac{2k_{i\mp 1,j,k}^k k_{i,j,k}}{k_{i\mp 1,j,k}^k + k_{i,j,k}}$	$r \mp \frac{\Delta r}{2}$	Δr
q_ϕ^\pm	$T_{i,j\mp 1,k}^t$	$\frac{2k_{i,j\mp 1,k}^k k_{i,j,k}}{k_{i,j\mp 1,k}^k + k_{i,j,k}}$	$\Delta r \Delta \omega$	$r \Delta \omega$
q_ω^\pm	$T_{i,j,k\mp 1}^t$	$\frac{2k_{i,j,k\mp 1}^k k_{i,j,k}}{k_{i,j,k\mp 1}^k + k_{i,j,k}}$	$r \Delta r \Delta \omega$	$\Delta \omega$

Table 1. Note that the subscript “eff” is omitted in **Tables 1 and 2** due to lucidity.

As for the curvilinear control volume (i, j, k) in the cylindrical coordinate system shown in **Fig. 8**, the explicit formula for the computation of the total enthalpy $H_{i,j,k}^{t+\Delta t}$ at the time instance $t + \Delta t$ reads

$$H_{i,j,k}^{t+\Delta t} = H_{i,j,k}^t + \frac{\Delta t}{r \Delta r \Delta \phi \Delta \omega} \left(q_r^\pm + q_\phi^\pm + q_\omega^\pm \right) + v_{\text{cast}} \Delta t \frac{H_{i,j,k-1}^t - H_{i,j,k}^t}{r \Delta \phi} \quad (14)$$

where Δr , $\Delta \phi$, and $\Delta \omega$ are the sizes of the spatial discretization steps. The heat transfer rates q_r , q_ϕ , q_ω in Eq. (14) are given by Eq. (13) with the particular values of k_{eff} , S , \hat{T} , and δ listed in **Table 2**. The final step required for the determination of the desired temperature distribution $T_{i,j,k}^{t+\Delta t}$ is the enthalpy-temperature search, which gives the temperature corresponding to the calculated value of the total enthalpy. The dependence of the total enthalpy on the temperature is determined with the use of the IDS model as the thermophysical properties shown in **Fig. 6**.

As the explicit formulation of the model is conditionally stable, the stability criterion for all the control volumes is used to determine the maximum size of the time discretization step as a way to avoid numerical instabilities or even oscillations. The stability criterion reads

$$\Delta t \leq \left(\sum_{i=1}^3 \frac{k}{\rho c_{\text{eff}}} \left(\frac{2 - m_i}{\Delta \xi_i^2} \right) + \sum_{i=1}^3 \frac{h}{\rho c_{\text{eff}}} \left(\frac{m_i}{\Delta \xi_i} \right) + \frac{v_{\text{cast}}}{\xi_{\text{cast}}} \right)^{-1} \quad (15)$$

where $\Delta \xi_i$ is a corresponding element of the spatial vector with the sizes of spatial discretization ($\Delta \xi = [\Delta x, \Delta y, \Delta z]$ for the Cartesian coordinate system and $\Delta \xi = [\Delta r, r \Delta \phi, \Delta \omega]$ for the cylindrical coordinate system). The quantity c_{eff} used in Eq. (15) is the effective specific heat defined as $c_{\text{eff}} = \frac{1}{\rho} \frac{\partial H}{\partial T}$ (Stefanescu, 2008). The substitution of the total enthalpy given in Eq. (2) to the definition of the effective specific heat leads to

$$c_{\text{eff}} = \frac{1}{\rho} \frac{\partial H}{\partial T} = c_p - L_f \frac{\partial f_s}{\partial T}. \quad (16)$$

The effective specific heat c_{eff} is used in Eq. (15) instead of the physical specific heat c_p as the effective specific heat takes into account the release of the latent heat when steel undergoes the phase change. The use of c_p instead of c_{eff} in Eq. (15) could cause an incorrect determination of the maximum size of the time step for simulations.

The m_i in Eq. (15) is a binary parameter used to include the convection into the stability criterion for boundary control volumes. In case the boundary control volume has its surface corresponding to a spatial axis ξ_i exposed to the convection, then $m_i = 1$. Otherwise $m_i = 0$, which holds for all the interior control volumes. The stability criterion given by Eq. (15) should be evaluated for all the control volumes and the minimum value of Δt is then used for computer simulations. From the stability point of view, the most restrictive control volumes are usually boundary volumes within the mould

and the secondary cooling as the heat fluxes attains high values here.

4.4. Implementation in CUDA/C++

The most computationally demanding part of the model is the iterative in-the-loop calculation of the transient temperature distribution of the cast strand according to Eqs. (12) and (14). Moreover, this requires the enthalpy-temperature search to determine the temperature. A sequential CPU-based implementation of the model, which has almost solely been used for models of continuous casting, incorporates three nested loops, one for each spatial coordinate in 3D. Considering another loop required for iterations in time, four nested loops are needed for the computation of the transient temperature distribution. From the computational point of view, nested loops belong to common bottlenecks of the computational efficiency. In a strict sequential approach, the computing unit has to perform $N_t \times N_s$ sequential operations to complete the simulation where N_t is the number of time steps and N_s is the number of volume elements. Consider the spatial mesh with 10^6 volume elements, a casting process lasting 30 min of the wall-clock time and the time step of 0.2 s. The simulation of the process then requires 9000 time steps, which means almost 10^{10} evaluations of Eqs. (12) and (14) in total.

The explicit formulation, however, does not require sequential processing in nested loops. Indeed, the evaluation of Eqs. (12) and (14) for a time instance $t + \Delta t$ requires only the temperature distribution in the time instance t , which is known. In fact, the evaluation of Eqs. (12) and (14) within a particular time instance can be performed concurrently for all the volume elements N_s . This is an underlying principle of the GPU-based implementation of the computational model. Hundreds or thousands of computing units on a GPU are used for the model acceleration as they evaluate Eqs. (12) and (14) in parallel.

Two CUDA kernels have been implemented in the presented GPU-based computational model. The main kernel is designed for the computation of one time iteration, which provides the evolution of the temperature distribution in one time step lasting Δt . The pseudocode of the main CUDA/C++ kernel reads

```

kernel CALCULATE TEMPERATURE  $T^{n+1}$ 
   $ID \leftarrow$  assign thread in the CUDA grid to a particular control volume
   $k \leftarrow$  update the thermal conductivity in  $ID$ 
   $H^{n+1} \leftarrow$  calculate the enthalpy in  $ID$  for time step  $n + 1$ 
   $T^{n+1} \leftarrow$  determine the temperature from  $H^{n+1}$  for  $ID$ 
end

```

A thread running the main kernel first retrieves its identification, which determines a particular control volume (i, j, k) being calculated. It means that the thread identification determines whether the control volume is the cuboid or curvilinear, its location with respect to the strand (pertaining to the mould, to secondary or tertiary cooling), and whether the control volume is an interior volume, a surface volume, or an edge volume. In the next step, the thermal conductivity of neighbouring control volumes, which are used for the computation of heat transfer rates in Eq. (13), is updated according to the actual temperature distribution. The thread execution continues with the computation of the value of the total enthalpy $H_{i,j,k}^{t+\Delta t}$, which is determined with the use of Eqs. (12) and (14) for the cuboid and curvilinear control volume, respectively. In case of the surface or edge control volume, pertinent heat transfer rates q in Eqs. (12) and (14) are determined in accordance to the actual heat transfer mechanisms as described in Section 3. Once the total enthalpy $H_{i,j,k}^{t+\Delta t}$ is calculated, the thread proceeds with the enthalpy-temperature search, which is the last procedure of the kernel resulting in the determination of the desired temperature $T_{i,j,k}^{t+\Delta t}$.

The auxiliary kernel consists of the code, which ensures regular updates of boundary conditions. The pseudocode of the auxiliary CUDA/C++ kernel reads

```

kernel UPDATE BOUNDARY CONDITIONS
  ID ← assign thread in the CUDA grid to a particular boundary control volume
  BC ← update boundary conditions for ID according to the actual temperature in ID
end
    
```

The update of boundary conditions is essential in case of convective heat transfer due to the cooling nozzles within the secondary cooling. Considering a constant water flow rate through the cooling nozzle, it is well known that the heat transfer coefficient is strongly dependent on the surface temperature (e.g. [Wendelstorf et al., 2008](#)). Particularly in the temperature range including the Leidenfrost temperature, the heat transfer coefficient can significantly alter and directly influence the temperature distribution. It is therefore a crucial task to regularly update the heat transfer coefficient according to the actual surface temperature. As the update of the heat transfer coefficient incorporates a multi-dimensional interpolation and other computationally demanding operations, it is favourable to transfer the execution of the update procedure to the GPU. Since boundary conditions are inputs to the calculation of the temperature distribution, the auxiliary kernel is launched first and it is followed by the execution of the main kernel. These two kernels are sequentially launched on the GPU in a loop, which iterates through the time, and thus provides the transient temperature distribution of the cast strand. The schematic of the GPU-based implementation of the computational model in CUDA is shown in [Fig. 7](#).

5. Verification and validation of the model

Verification and validation are important procedures in development of computer models for real processes. These methods are carried out to ensure that the computer model provides numerical results that are in agreement with the behaviour of an actual system being modelled. Verification of the model is used to check if the computer model – a program – correctly solves the mathematical model of a given problem: “Does the computer model solve equations correctly?”. On the other hand, validation is performed to determine whether the computer model provides results consistent with the behaviour of the real system modelled: “Does the computer model solve correct equations?”.

5.1. Verification for a 1D Stefan problem

The developed model was first verified with the use of a one-dimensional semi-infinite Stefan problem with the solid–liquid moving boundary, for which an exact analytical solution exists. The solid–liquid phase change is assumed to take place at a uniform temperature T_m and the solution of the Stefan problem enables to track the solid–liquid interface in time. [Fig. 9](#) shows the case of the 1D Stefan problem solved. At the beginning, the semi-infinite body is completely in the liquid phase at a temperature T_∞ , which is higher than the phase change temperature T_m . For time $t > 0$, a constant temperature T_0 (Dirichlet boundary condition) is prescribed at the boundary of the semi-infinite body. The liquid gradually solidifies and the solid–liquid interface moves on and recedes from the boundary.

Although considering the 1D semi-infinite body, the investigated case corresponds to a simplified situation, which occurs in the mould during continuous steel casting as presented by [Zhang et al. \(2007\)](#). In fact, the liquid steel in the mould solidifies mainly in the directions perpendicular to the casting direction. A partial solidification occurs within the mould due to heat withdrawal from the

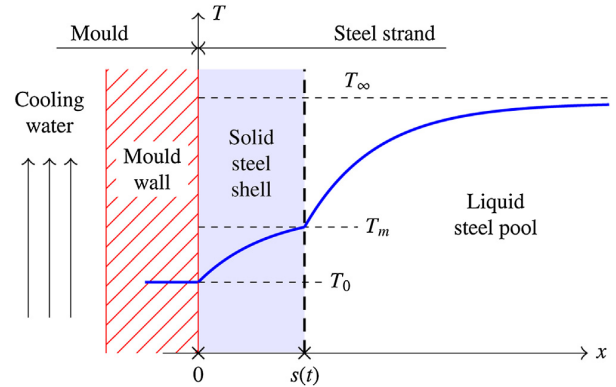


Fig. 9. The investigated 1D Stefan problem with the solid–liquid moving boundary.

strand to the cooling water and the surface of the mould has, at a particular location, approximately a uniform temperature in time.

The considered Stefan problem has the following mathematical formulation ([Hahn and Özişik, 2012](#))

$$\frac{\partial T}{\partial t} = \frac{1}{\alpha} \frac{\partial^2 T}{\partial x^2} \quad \text{for } t > 0 \quad (17)$$

where $\alpha = \frac{k}{\rho c}$ is the thermal diffusivity. Let $s(t)$ be the location of the solid–liquid interface between the phases. For the solid phase $0 < x < s(t)$, $T = T_s$ and $\alpha = \alpha_s$ while for the liquid phase $s(t) < x < \infty$, $T = T_\ell$ and $\alpha = \alpha_\ell$. The Dirichlet boundary condition $T_s(x = 0, t) = T_0$ applies for the solid phase and the initial condition $T_\ell(x > 0, t = 0) = T_\infty$ commits to the liquid phase. Since the body is semi-infinite, obvious implications $T_\ell(x \rightarrow \infty, t > 0) = T_\infty$ and $\frac{\partial T_\ell}{\partial x} |_{x \rightarrow \infty} = 0$ are true. The solid and liquid phases are coupled by means of the heat transfer balance at the interface taking into account the phase change. This balance is called the Stefan condition ([Voller and Cross, 1981](#))

$$k_s \frac{\partial T_s}{\partial x} |_{x=s(t)} - k_\ell \frac{\partial T_\ell}{\partial x} |_{x=s(t)} = \rho L_f \frac{ds(t)}{dt} \quad (18)$$

The phases are also coupled by means of the temperature consistency at the interface $T_s(x = s(t), t > 0) = T_\ell(x = s(t), t > 0) = T_m$.

The exact solution of the problem ([Hahn and Özişik, 2012](#)) gives the time-dependent location of the solid–liquid interface

$$s(t) = 2\psi \sqrt{\alpha_s t} \quad (19)$$

where the parameter ψ is a root of the transcendental equation

$$\frac{e^{-\psi^2}}{\text{erf } \psi} + \frac{k_\ell}{k_s} \sqrt{\frac{\alpha_s}{\alpha_\ell}} \left(\frac{T_m - T_\infty}{T_m - T_0} \right) \frac{e^{-\psi^2(\alpha_s/\alpha_\ell)}}{\text{erfc} \left(\psi \sqrt{\alpha_s/\alpha_\ell} \right)} = \frac{\sqrt{\pi} \psi L_f}{c_s(T_m - T_0)} \quad (20)$$

derived from the energy balance at the solid–liquid interface. The time-dependent temperature distribution in the solid region $0 < x < s(t)$ of the semi-infinite body then results in

$$T_s(x, t) = T_0 + \frac{T_m - T_0}{\text{erf } \psi} \text{erf} \left(\frac{x}{2\sqrt{\alpha_s t}} \right) \quad (21)$$

while for the liquid region $s(t) < x < \infty$

$$T_\ell(x, t) = T_\infty + \frac{T_m - T_\infty}{\text{erfc} \left(\psi \sqrt{\alpha_s/\alpha_\ell} \right)} \text{erfc} \left(\frac{x}{2\sqrt{\alpha_\ell t}} \right) \quad (22)$$

A low carbon steel with 0.1 wt.% of carbon having the phase change temperature of $T_m = 1490^\circ\text{C}$ was considered as the material used in the verification. The values of thermophysical properties

Table 3
Material properties of steel used in verification.

Material property	Value
Thermal conductivity of solid, k_s	31 W/m K
Thermal conductivity of liquid, k_l	35 W/m K
Specific heat capacity of solid, c_s	650 J/kg K
Specific heat capacity of liquid, c_l	830 J/kg K
Density of solid, ρ_s	7550 kg/m ³
Density of liquid, ρ_l	6950 kg/m ³
Temperature of phase change, T_m	1490 °C
Latent heat of phase change, L_f	245 kJ/kg

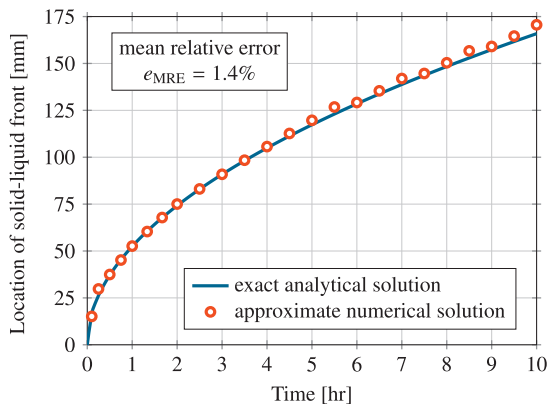


Fig. 10. Location of solid–liquid interface for the studied 1D Stefan problem: simulated and exact results.

are listed in Table 3. The material was initially supposed to be in the liquid state at the temperature $T_\infty = 1550$ °C. For $t > 0$, the temperature $T_0 = 1450$ °C was prescribed at the boundary $x = 0$ of the semi-solid body. The size of the control volumes was configured to 7.5 mm and the time step was set to 0.15 s. Since the enthalpy method cannot in general handle a constant phase change temperature, the phase change was assumed to take place within the temperature interval $(T_m - \Delta T, T_m + \Delta T)$ where $\Delta T = 0.1$ °C.

Fig. 10 shows the simulated and exact results for the time-dependent location of the solid–liquid interface. As can be seen in the figure, the computational model provides a very good approximation of the interface location. The mean relative error between the simulation results and the exact solution is about 1.4%. Fig. 11 presents the simulated and exact temperature distributions within the semi-infinite body. Temperatures for four distinct time instances are plotted in Fig. 11. Similarly as in case of the location of the solid–liquid interface, the computational model predicts a very

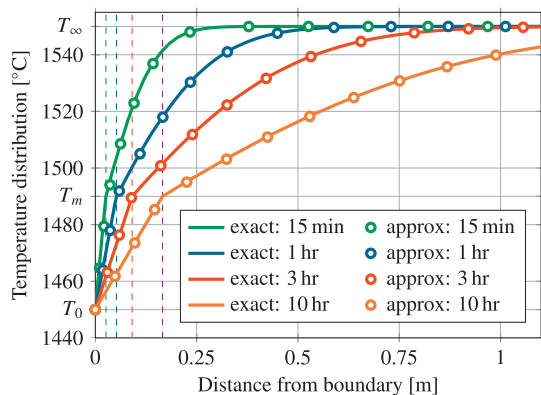


Fig. 11. Temperature distribution within the semi-infinite body at various time instances: simulated and exact results.

good approximation of the temperature distribution within both the solid and liquid phases. The mean relative error of temperature distributions for all four time instances plotted in Fig. 11 is about 0.003%.

Although the agreement between simulated and exact results presented in Figs. 10 and 11 is very good, it could be further improved. The reason for discrepancies related to the position of the solid–liquid interface is mainly due to the phase change at the constant temperature. The enthalpy method is actually intended for problems where the material undergoes the phase change in a temperature interval rather than at a constant temperature. However, an additional treatment proposed by Voller and Cross (1981) allows for the use of the enthalpy in cases with a constant phase change temperature.

5.2. Validation with temperature measurements

Following the verification, the computational model is consequently validated with the use of pyrometer surface measurements carried out in an actual operation of the casting machine in Třinec Iron and Steelworks in the Czech Republic. Two high-temperature pyrometers were placed in the secondary cooling at the distance of 4.69 m from the meniscus (the pyrometer Omega OS 1611 with the temperature range 650–1100 °C) and beyond the bench-straightening mill at the distance of 17.70 m from the meniscus (the pyrometer Siemens Ardocol with the temperature range 800–1200 °C). Both pyrometers measured the surface temperature at the centreline of the right-hand side of the strand.

Operational data from a number of casting melts, various steel grades and distinct casting conditions were acquired for validation from the control system in the steelworks. The data sets include parameters and casting conditions, which are required for the configuration of the computational model: the chemical composition of steel, casting temperature, casting speed, water flow rates in the mould and in the secondary cooling, and the strand surface temperatures measured by the pyrometers. As iron scales form rather unevenly at the surface of the cast strand due to oxidation, the emissivity of the surface alters considerably with the time and location. This makes the non-invasive pyrometer measurements difficult. A mathematical processing of acquired operational data, such as filtering, is therefore necessary to carry out an a priori validation.

The computational model adopted the geometry and configuration of the radial casting machine operated in Třinec Iron and Steelworks. The machine produces steel billets with the cross section of 150 mm × 150 mm, it has the tube water-cooled mould and the secondary cooling incorporates about 200 water cooling nozzles. The length of the mould is 1000 mm and the radius of the radial part of the casting machine is 8900 mm. The heat transfer rate distribution within the mould and the convective heat transfer coefficient of all used cooling nozzles were determined experimentally as described in Section 3. The secondary cooling consists of 6 independent cooling zones and the water flow rates can be adjusted separately for each zone. The computational mesh of the model was set up consistently with the configuration used in the verification; the average size of the computational control volume was 7.5 mm × 7.5 mm × 15 mm with the longest dimension oriented in the casting direction. The mesh therefore consists of about 800 000 volume elements and the time step was set to 0.15 s.

Fig. 12 shows the simulated steady-state temperature distribution along the casting machine for the representative steel grade 9SMN28, which is one of those used in the model validation. The actual chemical composition, which was determined by means of the chemical analysis of a sample taken from the ladle, is presented in Fig. 12 together with the water flow rates through the mould and secondary cooling zones. The temperatures at distinct cross-section locations are plotted in Fig. 12 by coloured solid lines whereas the

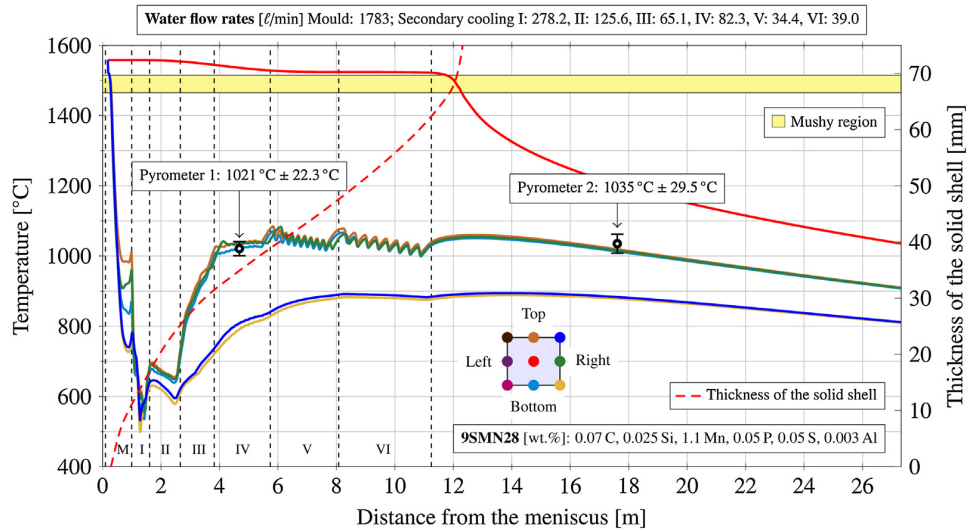


Fig. 12. Temperature distribution of the cast billet along the casting machine: simulated results and experimental measurements.

shell thickness growth is plotted by the red dashed line. According to the processed operational data from the steelworks, the simulation was carried out for the casting speed of 2.81 m/min, the casting temperature of 1558 °C, and for the mould heat withdrawal rate of 1.03 MW.

Values of the surface temperatures measured by the pyrometers at the centreline of the right-hand side of the strand were mathematically processed by means of filtering. The mean values and standard deviations were consequently determined from the filtered data. The mean surface temperature for the pyrometer 1 positioned in the secondary cooling is $\bar{T}_1 = 1021$ °C with the standard deviation $\sigma_1 = 17.4$ °C. For the pyrometer 2 placed beyond the bench-straightening mill, the mean surface temperature is $\bar{T}_2 = 1035$ °C with the standard deviation $\sigma_2 = 23.0$ °C. For each the mean value, the temperature interval ($\bar{T} - 1.281552\sigma$, $\bar{T} + 1.281552\sigma$) was determined, in which 80% values of the measured surface temperatures are expected to be in. The 80% interval for the pyrometer 1 placed in the secondary cooling is (998.7 °C, 1043.3 °C) while for the pyrometer 2 positioned beyond the bench-straightening mill is (1005.5 °C, 1064.5 °C).

The calculated mean values are plotted at the corresponding positions in Fig. 12 as black thick circles while the 80% intervals as vertical lines bounded by short horizontal dashes. As can be seen from Fig. 12, the simulated surface temperature at the centreline of the right-hand side, which is plotted by the green colour, is in good agreement with the determined 80% intervals for both the pyrometers. Well-coincident results have also been attained for other steel grades taken into account in the model validation.

5.3. Conclusion for verification and validation

In conclusion, the developed computational model provides results that are in good agreement with industry measurements

in steelworks as well as with the exact analytical solution of the moving boundary problem. This justifies a consecutive use of the model, e.g. in casting control.

6. Benchmarking and results

6.1. Configuration of benchmarking

A series of benchmarking tests was carried out to assess the computational performance of the developed GPU-based model. The model adopted the identical configuration as used in the validation of the model. Six computational meshes having distinct numbers of volume elements (control volumes) were considered for benchmarking: meshes with 100 thousand, 300 thousand, 500 thousand, 1 million, 3 million, and 5 million volume elements. The characteristic size of the mesh elements, which is determined as the diameter of a sphere having the same volume as the average mesh element, is presented in Table 4 for each mesh. As the explicit time discretization is used in the model formulation, the maximum size of the time step varies with the number of volume elements in the computational mesh according to Eq. (15). The maximum size of the time step is 0.6 s for the coarsest considered mesh with 100 thousand elements. As the number of elements in the mesh increases, the maximum size of the time step decreases due to the reduction of the characteristic size of elements. As for the finest considered mesh with 5 million elements, the maximum size of the time step is 0.1 s. Table 4 summarises the maximum sizes of the time step for all the considered meshes.

The CPU-based computational model previously developed by the authors of the paper was utilized for the comparison of the computational performance between the non-parallel CPU-based model and the highly parallel GPU-based model. The mathematical formulation of the CPU-based model is identical with that

Table 4
Mesh parameters and results of benchmarking.

Number of volume elements	Characteristic element size	Size of time step	Multiple of GPU-acceleration
100 thousand	24.15 mm	0.60 s	33.0
300 thousand	16.43 mm	0.40 s	39.2
500 thousand	13.76 mm	0.35 s	43.1
1 million	10.85 mm	0.25 s	53.3
3 million	7.47 mm	0.15 s	59.2
5 million	6.27 mm	0.10 s	67.7

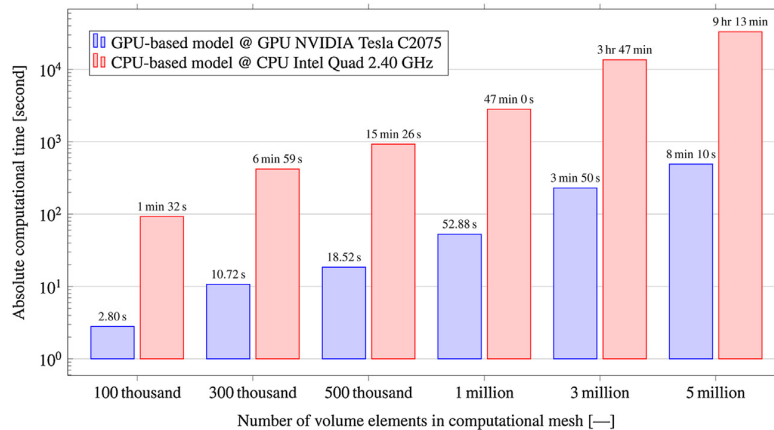


Fig. 13. GPU-model benchmarking—absolute computational time.

of the GPU-based model described in Section 3. Both the models therefore provide identical results. The models, however, differ in the computer implementation. The CPU-based model does not include parallel processing and all the computations are implemented in nested loops. On the contrary the GPU-based model, which is described in detail in Section 4, is highly parallel. Benchmarking of the models was performed with the use of the computer with the Intel Quad 2.40 GHz CPU and 6 GB RAM memory. In addition, the GPU-based model used the NVIDIA Tesla C2075 GPU for launching the kernels. The Tesla C2075 GPU incorporates 448 CUDA cores, each running at the frequency of 1.15 GHz. The GPU had 6 GB RAM of internal memory. The simulation of the casting process lasting 30 min of the wall-clock time was used as the test case for benchmarking.

6.2. Measures for evaluation of benchmarking

Three kinds of the computational time are used in the following section for the assessment of the computational performance between the presented GPU-based model and the common CPU-based model.

- The absolute computational time is the elapsed real time the model requires to complete the simulation.
- The relative computational time is the dimensionless ratio between the absolute computational time and the wall-clock time of the real casting process being simulated.
- The normalized computational time is the absolute computational time related to the computation of a part of the computational mesh having a specified number of volume elements.

The multiple of the GPU-acceleration is then defined as the ratio between either the absolute or the relative computational time of the CPU-based model and of the GPU-based model. The multiple of the GPU-acceleration therefore expresses how many times the presented GPU-based model is faster than the common CPU-based model.

6.3. Benchmarking results and discussion

The absolute computational time for the simulation of the casting process lasting 30 min of the wall-clock time is presented in Fig. 13. The maximum time step listed in Table 4 was used for both the CPU-based and GPU-based models and for the corresponding mesh. As can be seen in Fig. 13 plotted in the logarithmic scale,

the GPU-based model provides a great acceleration of the model computation. In case of the coarsest mesh with 100 thousand elements, the CPU-based model requires about one and half minute to complete the simulation. The GPU-based model, however, completes the simulation in less than 3 s. Very similar conclusions apply when the number of elements in the mesh increases. For the finest computational mesh having 5 million elements, the use of the GPU-based models reduces the computational time from more than 9 h to only 8 min.

The relative computational time of the models, which is the crucial measure for the real-time use of models, is shown in Fig. 14. The presented relative computational time is determined from the results presented in Fig. 13 as the dimensionless ratio between the absolute computational time and the wall-clock time of the simulated casting process. In case the model is intended for the use in real-time control of the casting process, its relative computational time has to be less than one. Moreover, as already mentioned, some control and optimization algorithms require repetitive evaluations of the computational model when searching for the optimal solution. In such cases, the relative computational time of the model has to be significantly less than one, depending on the number of the model evaluations. As apparent from Fig. 14, the developed GPU-based model offers great capabilities for real-time control. For the medium mesh with 500 thousand elements, the relative computational time of the GPU-based model is about 0.01. That implies almost 100 simulations in real time. On the other hand, the relative computational time for the CPU-based model with the identical mesh is more than 0.5, which allows only for one complete simulation in real time. In case of the fine mesh with 3 million elements, the CPU-model is approximately 7.5-times slower than the wall-clock time goes by. However, the GPU-based model is able of completing 7 simulations in real time.

Fig. 15 presents the performance of the models and of the computational hardware in terms of the normalized computational time. This means that all the simulations, regardless of the mesh, were carried out with the time step of 0.1 s, which is feasible for all the tested meshes. The normalized computational time presented in Fig. 15 represents the portion of the computational time required per 10 000 volume elements to complete the simulation of the casting process lasting 30 min of the wall-clock time. A typical distinction between the use of GPUs and CPUs can be observed in Fig. 15. In case of the CPU-based model the normalized computational time magnifies with the increasing number of volume elements as the result of the increased latency. On the other hand, in case of the GPU-based model the normalized computational time decreases with the increasing number of volume elements. This

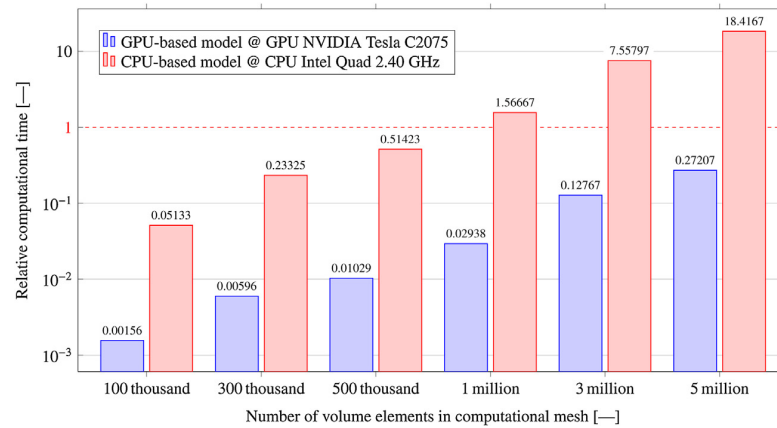


Fig. 14. GPU-model benchmarking—relative computational time.

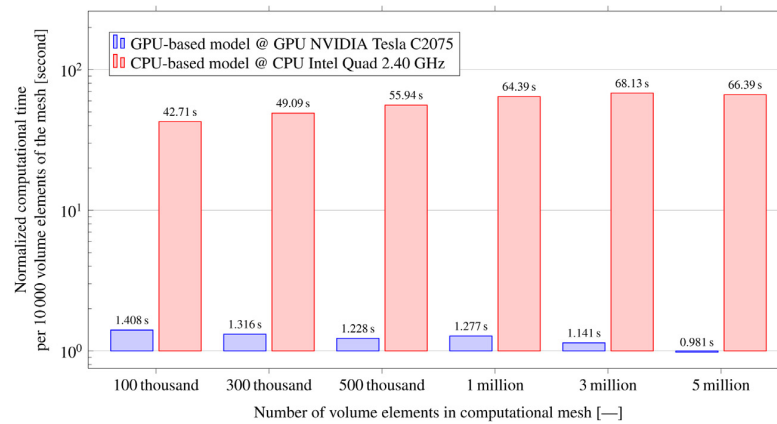


Fig. 15. GPU-model benchmarking—normalized computational time per 10 000 volume elements of the mesh.

behaviour is due to the internal architecture of graphics processing units, which are primarily designed for massively parallel computing. The increase of the number of parallel threads therefore reduces the latency per one thread. This feature is also reflected in the multiple of the GPU-acceleration presented in Table 4. The multiple of the GPU-acceleration, which quantifies how fast the GPU-based model is in comparison to the CPU-based model, is given as the ratio between either the absolute or the relative computational times of the CPU-based and GPU-based models presented in Figs. 13 and 14. The multiple of acceleration is 33 for the coarsest mesh with 100 thousand volume elements and it gradually increases to almost 68 for the finest grid with 5 million volume elements as the computational effectiveness of the GPU increases.

7. Conclusions

The rapid GPU-based heat transfer and solidification model for continuous casting was developed. The model, which implements the parallel code in CUDA/C++, is intended for the use with graphics processing units NVIDIA. The following conclusions can be drawn from the study.

- The very high computational performance of the GPU-based model is due to massively parallel computations, which are performed by means of a large number of computational units on a GPU with CUDA.

- The computational model was verified on Stefan problem and validated with the industry measurements.
- The relative computational time of the developed GPU-based model is between 0.0016 for a coarse mesh and 0.27 for a very fine mesh.
- The corresponding multiple of the GPU-acceleration provided by the GPU-based model is between 33 and 68 in comparison to an equivalent CPU-based model routinely used in the practice.
- The performance characteristics make the GPU-based model suitable for real time applications in casting control and optimization.

Acknowledgement

The authors gratefully acknowledge funding from the Ministry of Education, Youth and Sports of the Czech Republic under the National Sustainability Programme I (Project LO1202 NETME CENTRE PLUS).

References

- Ansoni, J.L., Brandi, A.C., Selegim, P., 2015. Resolution of an inverse thermal problem using parallel processing on shared-memory multiprocessor architectures. *Inverse Probl. Sci. Eng.* 23, 351–375.
- Chen, H., Su, L., Wang, G., Wan, S., Zhang, L., Luo, Z., 2014. Fuzzy estimation for heat flux distribution at the slab continuous casting mold surface. *Int. J. Therm. Sci.* 83, 80–88.
- Cheng, W.L., Sheharyar, A., Sadr, R., Bouhali, O., 2015. Application of GPU processing for Brownian particle simulation. *Comput. Phys. Commun.* 186, 39–47.

- Fic, A., Nowak, A.J., Bialecki, R., 2000. Heat transfer analysis of the continuous casting process by the front tracking BEM. *Eng. Anal. Bound. Elem.* 24, 215–223.
- Fu, W.-S., Wang, W.-H., Huang, S.-H., 2012. An investigation of natural convection of three dimensional horizontal parallel plates from a steady to an unsteady situation by a CUDA computational platform. *Int. J. Heat Mass Transfer* 55, 4638–4650.
- Galizia, A., D'Agostino, D., Clematis, A., 2015. An MPI-CUDA library for image processing on HPC architectures. *J. Comput. Appl. Math.* 273, 414–427.
- Goldsworthy, M.J., 2014. A GPU-CUDA based direct simulation Monte Carlo algorithm for real gas flows. *Comput. Fluids* 94, 58–68.
- Gonzalez, M., Goldschmit, M.B., Assanelli, A.P., Berdaguier, E.F., Dvorkin, E.N., 2003. Modeling of the solidification process in a continuous casting installation for steel slabs. *Metall. Mater. Trans. B* 34, 455–473.
- Ha, J.S., Cho, J.R., Lee, B.Y., Ha, M.Y., 2001. Numerical analysis of secondary cooling and bulging in the continuous casting of slabs. *J. Mater. Process. Technol.* 113, 257–261.
- Hahn, D.W., Özışık, M.N., 2012. *Heat Conduction*, third ed. Wiley, New Jersey.
- Hardin, R.A., Liu, K., Kapoor, A., Beckermann, C., 2003. A transient simulation and dynamic spray cooling control model for continuous steel casting. *Metall. Mater. Trans. B* 34, 297–306.
- Idelsohn, S.R., Storti, M.A., Crivelli, L.A., 1994. Numerical methods in phase-change problems. *Arch. Comput. Method Eng.* 1, 49–74.
- Ji, C., Li, J., Yang, S., Sun, L., 2013. Large eddy simulation of turbulent fluid flow in liquid metal of continuous casting. *J. Iron Steel Res. Int.* 20, 34–39.
- Jiang, B., Dai, W., Khaliq, A., Carey, M., Zhou, X., Zhang, L., 2015. Novel 3D GPU based numerical parallel diffusion algorithms in cylindrical coordinates for health care simulations. *Math. Comput. Simul.* 109, 1–19.
- Kreith, F., Manglik, R.M., Bohn, M.S., 2011. *Principles of Heat Transfer*, seventh ed. Cengage Learning, Stamford.
- Louhenkilpi, S., Mäkinen, M., Vapalahti, S., Räisänen, T., Laine, J., 2005. 3D steady state and transient simulation tools for heat transfer and solidification in continuous casting. *Mater. Sci. Eng. A* 413–414, 135–138.
- Louhenkilpi, S., Laine, J., Miettinen, J., Vesanen, R., 2013. New continuous casting and slab tracking simulators for steel industry. *Phys. Numer. Simul. Mater. Proc.* VII 762, 691–698, <http://dx.doi.org/10.4028/www.scientific.net/MSF.762.691>
- Ma, J.C., Xie, Z., Ci, Y., Jia, G.L., 2009. Simulation and application of dynamic heat transfer model for improvement of continuous casting process. *Mater. Sci. Technol.* 25, 636–639.
- Mauder, T., Šandera, Č., Štětina, J., 2015. Optimal control algorithm for continuous casting process by using fuzzy logic. *Steel Res. Int.*, <http://dx.doi.org/10.1002/srin.201400213>
- Miettinen, J., Louhenkilpi, S., Kytönen, H., Laine, J., 2010. IDS: thermodynamic-kinetic-empirical tool for modelling of solidification, microstructure and material properties. *Math. Comput. Simul.* 80, 1536–1550.
- Meng, Y., Thomas, B.G., 2003. Heat-transfer and solidification model of continuous slab casting: CON1D. *Metall. Mater. Trans. B* 34, 685–705.
- Muhieddine, M., Canot, É., March, R., 2009. Various approaches for solving problems in heat conduction with phase change. *Int. J. Finite Volumes* 6, 66–85.
- Owens, J., Houston, M., Luebke, D., Green, S., Stone, J.E., Phillips, J.C., 2008. GPU computing. *Proc. IEEE* 96, 879–899.
- Patankar, S.V., 1980. *Numerical Heat Transfer and Fluid Flow*, first ed. McGraw-Hill, New York.
- Pyszko, R., Přihoda, M., Fojtík, P., Kováč, M., 2012. Determination of heat flux layout in the mould for continuous casting of steel. *Metalurgija* 51, 149–152.
- Raudenský, M., Pohanka, M., Horský, J., 2002. Combined inverse heat conduction method for highly transient processes. *Adv. Comput. Methods Heat Transf. VII* 4, 35–42.
- Raudenský, M., Horský, J., 2005. Secondary cooling in continuous casting and Leidenfrost temperature effects. *Ironmak. Steelmak.* 32, 159–164.
- Rong, F., Zhang, W., Shi, B., Guo, Z., 2014. Numerical study of heat transfer enhancement in a pipe filled with porous media by axisymmetric TLB model based on GPU. *Int. J. Heat Mass Transfer* 70, 1040–1049.
- Santos, C.A., Spim, J.A., García, A., 2003. Mathematical modeling and optimization strategies (genetic algorithm and knowledge base) applied to the continuous casting of steel. *Eng. Appl. Artif. Intell.* 16, 511–527.
- Šarler, B., Vertnik, R., Lorbiecka, A.Z., Vušanović, I., Senčič, B., 2012. A multiscale slice model for continuous casting of steel. In: Ludwig, A. (Ed.), *Proceedings of International Conference on Modeling of Casting, Welding and Advanced Solidification Processes. Schladming, Austria*, article number 012021.
- Savage, J., Pritchard, W.H., 1954. The problem of rupture of the billet in the continuous casting of steel. *J. Iron Steel Inst.* 178, 269–277.
- Shimada, M., Mitsutsuka, M., 1966. On heat transfer coefficient by forced water cooling to carbon steel. *Tetsu-to-Hagané* 52, 1643–1645.
- Stefanescu, D., 2008. *Science and Engineering of Casting Solidification*, second ed. Springer, New York.
- Touloulian, Y.S., Powell, R.W., Ho, C.Y., Klemens, P.B., 1972. *Thermophysical Properties of Matter*, vol. 8. IFI/Plenum, New York.
- Voller, V.R., Cross, M., 1981. Accurate solutions of moving boundary problems using the enthalpy method. *Int. J. Heat Mass Transfer* 24, 545–556.
- Wendelstorf, J., Spitzer, K.-H., Wendelstorf, R., 2008. Spray water cooling heat transfer at high temperatures and liquid mass fluxes. *Int. J. Heat Mass Transfer* 51, 4902–4910.
- Wilt, N., 2013. *The CUDA Handbook: A Comprehensive Guide to GPU Programming*, first ed. Addison-Wesley, New Jersey.
- Yang, J., Xie, Z., Ji, Z., Meng, H., 2014. Real-time heat transfer model based on variable non-uniform grid for dynamic control of continuous casting billets. *ISIJ Int.* 54, 328–335.
- Yang, J., Xie, Z., Meng, H., Liu, W., Ji, Z., 2014. Multiple time steps optimization for real-time heat transfer model of continuous casting billets. *Int. J. Heat Mass Transfer* 76, 492–498.
- Yoon, J.-K., 2008. Applications of numerical simulation to continuous casting technology. *ISIJ Int.* 48, 879–884.
- Zhang, L., Rong, Y.-M., Shen, H.-F., Huang, T.-Y., 2007. Solidification modeling in continuous casting by finite point method. *J. Mater. Process. Technol.* 192–193, 511–517.

IMPACT OF CASTING SPEED ON THE TEMPERATURE FIELD OF CONTINUOUSLY CAST STEEL BILLETS

VPLIV LIVNE HITROSTI NA TEMPERATURNO POLJE KONTINUIRNO ULITIH GREDEC IZ JEKLA

Lubomir Klimes¹, Josef Stetina¹, Pavol Bucek²

¹Brno University of Technology, Faculty of Mechanical Engineering, Technicka 2896/2, 616 69 Brno, Czech Republic
²Zelezarne Podbrezova, Research and Development Center, Kolkaren 35, 976 81 Podbrezova, Slovakia
klimes@fme.vutbr.cz

Prejem rokopisa – received: 2012-08-31; sprejem za objavo – accepted for publication: 2013-01-04

In continuous casting, the casting speed is one of the most important parameters that influence the entire process of steel production and its productivity. From the physical point of view, the casting speed affects the temperature field formation along the cast steel blank, e.g., the surface and corner temperatures as well as the solidification of the steel, e.g., the shell thickness, the isosolidus and isoliquidus curves, the metallurgical length and the width of the mushy zone. In order to achieve a particular steel structure, the temperature ranges in particular positions (e.g., due to the straightening), and to minimize the occurrence of defects, it is very important to pay attention to a proper determination of the casting speed. The aim of this paper is to investigate the impact of the casting speed on the temperature field formation of continuously cast steel billets, and on the aforementioned parameters. Three steel grades with various chemical compositions and the originally implemented numerical model of the transient temperature field of continuously cast billets in Zelezarne Podbrezova in Slovakia were utilized for the analysis. The results proved the significant influence of the casting speed on the temperature field formation and on related parameters. The conclusions may be utilized, e.g., for the determination of the casting speed and for the setup of the caster.

Keywords: continuous casting, casting speed, dynamic solidification model, temperature field

Pri kontinuirnem ulivanju je hitrost ulivanja eden od odločilnih parametrov, ki vplivajo na celoten proces proizvodnje jekla in na storilnost. Iz fizikalnega vidika hitrost ulivanja vpliva na nastanek temperaturnega polja vzdolž jeklene gredice, kot na primer na temperaturo robov in površine ulitega bloka, kot tudi na strjevanje jekla, kot na primer debelina strjene skorje, krivulje izosolidusa in izoliquidusa, metalurška dolžina in širina kašastega področja. Da bi dosegli želeno strukturo jekla, temperaturno področje v določenih položajih (npr. zaradi ravnanja) in da bi zmanjšali nastanek poškodb, je zelo pomembno, da smo pozorni na pravilno določitev hitrosti ulivanja. Namen prispevka je raziskati vpliv hitrosti ulivanja na oblikovanje temperaturnega polja pri kontinuirno ulitih gredicah in na že navedene parametre. Za analize so bila uporabljena tri različna jekla z različnimi kemijskimi sestavami in originalen numerični model prehodnega temperaturnega polja gredic v Železarni Podbrezova na Slovaškem. Rezultati potrjujejo pomemben vpliv hitrosti ulivanja na nastanek temperaturnega polja in s tem povezanih parametrov. Ugotovitve se lahko uporabijo na primer za določitev hitrosti ulivanja in za postavitev livne naprave.

Ključne besede: kontinuirno ulivanje, hitrost ulivanja, dinamični model strjevanja, temperaturno polje

1 INTRODUCTION

The quality and productivity of continuously cast steel blanks depend on many technological parameters and caster options.¹ The casting speed, which is directly related to the productivity, is one of the most important parameters for continuous steel casting. Its appropriate setting according to the operating conditions, the steel grade being cast and the caster parameters is crucial in order to produce steel blanks with the desired quality and structure, and also to minimize the occurrence of defects. In addition, the produced steel and its properties can be further optimized.² The importance of the proper setting of the casting speed is obvious when taking into account the parameters on which the casting speed may have an influence: mainly the entire temperature distribution (e.g., the surface and corner temperatures that are very often required to fit a certain range of temperatures, e.g., due to the straightening) along the cast blank, the isosolidus and isoliquidus curves that characterize the solidification process, the metallurgical length, or, e.g., the shell thickness along the blank.³

Nowadays, dynamic solidification models are commonly used in steelworks for the control and monitoring of casting.^{4,5} The on-line models for the casting control are fast and rather simple, whereas the off-line models enable an analysis of multiple and detailed factors, but require a long time to run.⁶ Numerical models of the temperature field of continuous casting often utilize the finite-difference method,⁷ the finite-volume method⁸, or the finite-element method.⁹ Recently, new computational approaches are also used, due to their specific advantages, e.g., the meshless finite-point method,¹⁰ the front-tracking boundary-element method,¹¹ or the very fast moving-slice-based models.¹²

The numerical solidification models allow a precise determination of the entire temperature distribution along the cast blank, the prediction of surface defects and the improvement of steel quality.¹³ The numerical model in the off-line mode working as a simulator also makes it possible to perform a case study and an analysis of the operating parameters without any affect on the real caster and the steel production in a steelworks.⁶ Hence, it

is a good idea to utilize the dynamic solidification models in order to determine a suitable casting speed for continuously cast blanks.

The purpose of this paper is to investigate the influence of the casting speed on the temperature field formation and the related parameters of continuously cast billets. For the analysis, three steel grades and the 200 mm × 200 mm billets, which are cast in Zeleziarne Podbrezova in Slovakia, are considered. The analysis was carried out by means of the originally implemented dynamic solidification model of continuously cast billets.

2 DYNAMIC SOLIDIFICATION MODEL

The study of the influence of the casting speed on the thermal behavior of continuously cast steel billets was performed with the use of the originally developed numerical model of the transient temperature field.^{14,15} The model, which is fully 3D, allows a calculation of the transient temperature distribution along the entire, continuously cast billets from the pouring level inside the mould, through the secondary and tertiary cooling zones, to the torch where the semi-infinite billets are cut to desired lengths suitable for the next processing step (**Figure 1**). Since the temperature field is symmetric with respect to the longitudinal vertical plane (**Figure 1**), only one half of the billet is considered.

The transient heat transfer and the solidification of the billet is governed by the Fourier-Kirchhoff equation:

$$\frac{\partial H}{\partial t} = \nabla \cdot (k \nabla T) + v_z \frac{\partial H}{\partial z} \quad (1)$$

where H is the volume enthalpy (J m^{-3}), T is the temperature (K), t is time (s), k is the thermal conductivity ($\text{W m}^{-1} \text{K}^{-1}$), v_z is the casting speed (m s^{-1}) and z is the spatial coordinate along the cast billet (m). The mass transfer and the fluid flow of the melt inside the billet are neglected. The thermodynamic function of the volume enthalpy¹⁶ in Eq. (1), which is defined as follows:

$$H(T) = \int_0^T \left(\rho c - \rho L_f \frac{\partial f_s}{\partial \theta} \right) d\theta \quad (2)$$

where ρ is the density (kg m^{-3}), c is the specific heat ($\text{J kg}^{-1} \text{K}^{-1}$), L_f is the latent heat (J kg^{-1}) and f_s is the solid fraction (1), is used due to the release of the latent heat of structural and mainly phase changes, which the steel undergoes during its solidification.¹⁷

The model is completed with the initial (3) and boundary conditions (4a)–(4d):

$$T_{i,j,k}^0 = T_0 \quad (3)$$

$$T_{i,j,0}^t = T_{\text{cast}} \text{ in the meniscus plane} \quad (4a)$$

$$-k \frac{\partial T}{\partial n} = 0 \text{ in the plane of symmetry} \quad (4b)$$

$$-k \frac{\partial T}{\partial n} = \dot{q} \text{ in the mould and beneath the rollers} \quad (4c)$$

$$-k \frac{\partial T}{\partial n} = h(T - T_\infty) + \sigma \varepsilon (T^4 - T_\infty^4) \text{ in the secondary and tertiary cooling zones} \quad (4d)$$

where T_0 is the initial temperature (K), T_{cast} is the casting temperature (K), \dot{q} is the heat flux (W m^{-2}), h is the heat transfer coefficient ($\text{W m}^{-2} \text{K}^{-1}$), T_∞ is the ambient temperature (K), $\sigma = 5.67 \cdot 10^{-8} \text{ W m}^{-2} \text{K}^{-4}$ is the Stefan-Boltzmann constant and ε is the emissivity (1).

In order to accurately and reliably predict the temperature field of cast blanks by means of solidification models, it is also worth pointing out the variability of the thermophysical properties (H , k , ρ , c : see Eq. (1) and Eq. (2)) according to the chemical composition of the steel being cast and their dependency on the temperature. Due to the mentioned reasons, the developed solidification model utilizes the results of the solidification analysis package IDS.¹⁸ It enables the calculation of the temperature dependency of the aforementioned thermophysical properties according to the chemical composition of the steel. The precise chemical composition can be obtained, e.g., from the chemical analysis of a sample from the tundish.

The dynamic solidification model of continuously cast billets was created with the use of the control-volume method.¹⁹ This approach is based on meshing the entire 3D billet into control volumes, and then the energy balance is established for each control volume of the billet. With the use of the explicit discretization in time,¹⁹ the energy balance of the general control volume (i, j, k) (**Figures 1 and 2**) in the Cartesian coordinates reads:

$$\sum_{i=1}^6 \dot{Q}_i + v_z \Delta x \Delta y (H_{i,j,k-1}^t - H_{i,j,k}^t) = \frac{\Delta x \Delta y \Delta z}{\Delta t} (H_{i,j,k}^{t+\Delta t} - H_{i,j,k}^t) \quad (5)$$

where \dot{Q} denotes the heat transfer rate (W), Δx , Δy , Δz are the spatial dimensions (m) of the control volume and

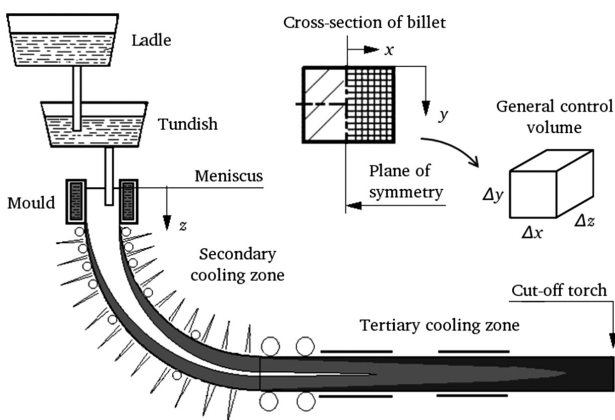


Figure 1: The billet caster and the mesh definition
Slika 1: Naprava za ulivanje gredic in opredelitev mreže

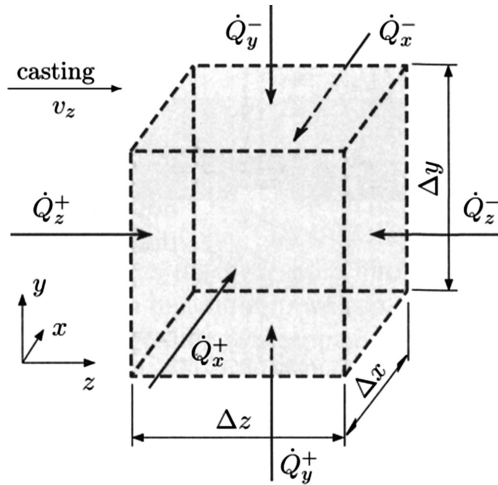


Figure 2: The energy balance of the general control volume in Cartesian coordinates

Slika 2: Energijska bilanca splošnega kontrolnega volumna v kartezičnih koordinatah

Δt is the time step (s). The first term on the left-hand side in Eq. (5) represents the sum of the conduction heat transfer rates given by Fourier's law¹⁹ to the control volume from the neighboring six control volumes (**Figure 2**). For instance, the heat transfer rate to the control volume in the positive direction of the x -axis is then:

$$\dot{Q}_x^+ = -k\Delta y\Delta z \frac{T_{i,j,k}^t - T_{i-1,j,k}^t}{\Delta x} \quad (6)$$

The second term on the left-hand side in Eq. (5) takes into account the energy incoming to the control volume due to the movement of the billet through the caster with the casting speed v_z . The term on the right-hand side in Eq. (5) represents the change of the internal energy of the control volume during the time step Δt , including the release of the latent heat (comprised in the enthalpy) due to the solidification.^{16,17}

In the case of the explicit time discretization,¹⁹ the unknown enthalpy of the general control volume (i, j, k) in time $t + \Delta t$ can be then directly calculated from Eq. (5) with the use of known values of the temperature and enthalpy in time t :

$$H_{i,j,k}^{t+\Delta t} = H_{i,j,k}^t + \frac{\Delta t}{\Delta x\Delta y\Delta z} \sum_{i=1}^6 \dot{Q}_i + v_z \frac{\Delta t}{\Delta z} (H_{i,j,k-1}^t - H_{i,j,k}^t) \quad (7)$$

In the case of the boundary-control volume, the particular heat transfer rates in Eq. (7) are replaced by the corresponding heat transfer rates determined from the boundary conditions (4a)–(4d). The desired temperature in time $t + \Delta t$ is then recalculated from the enthalpy given by Eq. (7) with the use of the temperature-enthalpy relationship provided by the solidification package IDS according to the particular chemical composition of the cast steel.

In the curved region (the radial part) of the caster, the Cartesian coordinate system is transformed to the cylindrical system (the Cartesian coordinates y and z are transformed to the radius coordinate and to the angle coordinate, respectively) and the equations (5)–(7) are appropriately modified.

The model used in the presented analysis utilizes 1136520 control volumes (21 in axis x , 41 in axis y , and 1320 in axis z) with the size of the general control volume of $5 \text{ mm} \times 5 \text{ mm} \times 15 \text{ mm}$. Due to the unconditional stability¹⁹ of the explicit time discretization and the numerical stability also for higher casting speeds, the time step was set to 0.35 s. With the described configuration of the mesh and the time step, the numerical model is still able to run faster than real time. For example, on the HP Z800 workstation the computing time reaches 90 % of the real time.²⁰

The heat transfer coefficients in the boundary condition (4d) for the cooling nozzles in the secondary cooling were determined experimentally in the laboratory on the hot models.²¹ **Figure 3** presents the experimentally measured heat-transfer coefficient for the cooling nozzle TG1 used in the secondary cooling. In order to quantify the heat withdrawal in the mould and the secondary cooling zone,²⁰ the heat flux in the mould given by Eq. (4c) was equivalently expressed to the heat transfer coefficient and plotted in **Figure 4**.

As can be seen from Eq. (1), Eq. (5), and Eq. (7), the casting speed v_z straightforwardly influences the entire transient temperature distribution of cast billets, and therefore the appropriate setting of the casting speed is a crucial issue in continuous casting.

The developed dynamic solidification model was experimentally verified on the billet caster with the use

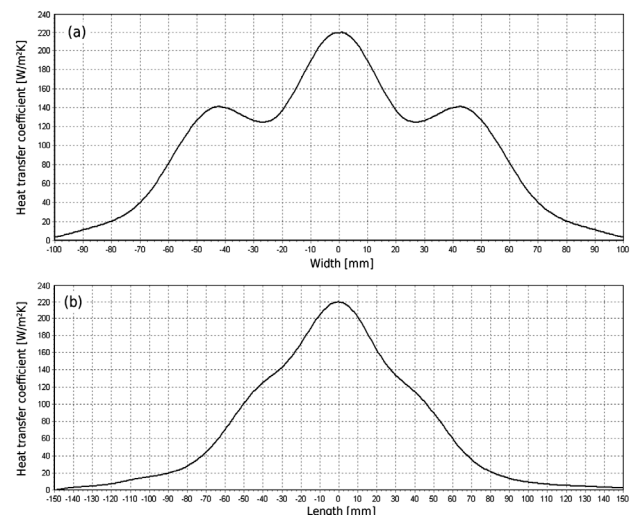


Figure 3: The heat transfer coefficient for the cooling nozzle TG1 and the water flow 0.64 l/min in the centerline of the nozzle: a) perpendicular to the casting direction, b) along the casting direction

Slika 3: Koefficient prenosa toplote za hladilno šobo TG1 in pretok vode 0,64 l/min v simetrični šob: a) pravokotno na smer ulivanja, b) vzdolž smeri ulivanja

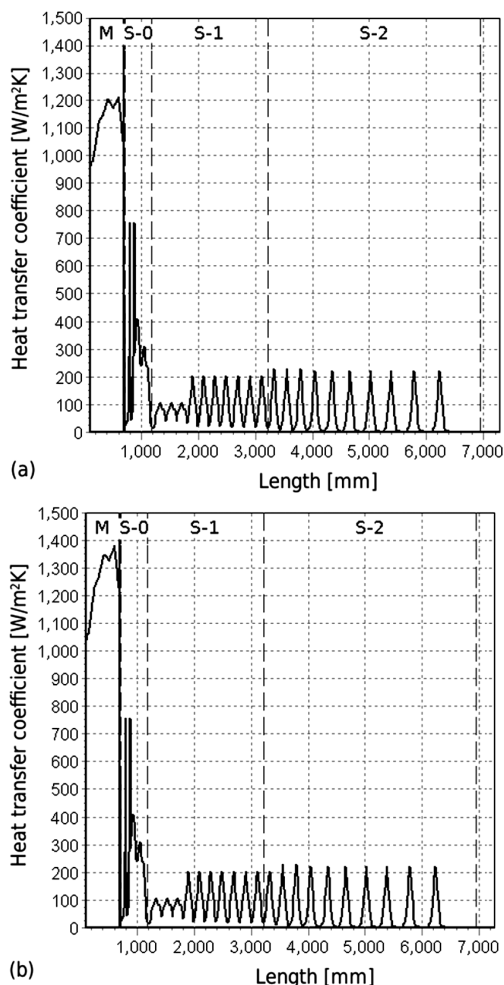


Figure 4: The heat transfer coefficient in the mould and in the secondary cooling zone: a) small radius surface, b) large radius surface of cast billet

Slika 4: Koeficient prenosa toplote v kokili in v sekundarni coni hlajenja: a) površina z majhno ukrivljenostjo, b) površina z veliko ukrivljenostjo lite gredice

of two pyrometers placed behind the mould in the secondary cooling zone (1500 mm from the pour level) and in the tertiary cooling zone (15420 mm from the pour level). Both the pyrometers were positioned in the centerline of the small radius surface of the cast billets. The maximum temperature difference between the measured temperatures by the pyrometers and the calculated temperatures by the solidification model was 40 °C.²⁰

3 ANALYSIS SETUP AND PARAMETERS

The study was carried out for the 200 mm × 200 mm steel billets that are continuously cast in Zeleziarne Podbrezova in Slovakia. The radial billet caster has the tubal mould, it comprises the secondary cooling with three independent cooling zones (denoted by S-0, S-1, and S-2 in figures) including 96 water cooling nozzles of three

types and two straightening mills (denoted by SM-1, SM-2 in figures).

The following three steel grades are considered (only the main elements are listed in mass fractions w): unalloyed fine-grained steel for constructions and welding S355J2G3 (0.187 % C, 1.17 % Mn, 0.22 % Si, 0.016 % P, and 0.012 % S), carbon steel for refining C60 (0.617 % C, 0.73 % Mn, 0.29 % Si, 0.014 % P, 0.013 % S, 0.03 % Cr, 0.05 % Ni, and 0.18 % Cu), and heat-resistant Cr-Mo steel for use at higher temperatures 13CrMo4-5 (0.144 % C, 0.53 % Mn, 0.24 % Si, 0.007 % P, 0.006 % S, 0.98 % Cr, 0.46 % Mo, 0.12 % Cu, and 0.019 % Al). The range of the casting speed was considered to be between 0.7 m/min and 1.1 m/min; all three mentioned steel grades are commonly cast with a casting speed of 0.9-1.0 m/min. In figures, only the casting speeds 0.7 m/min, 0.9 m/min, and 1.1 m/min are pictured for reasons of clarity.

For the analysis the casting temperature was set identically to the real casting process: 1553 °C for the grade S355J2G3, 1515 °C for the grade C60, and 1547 °C for the grade 13CrMo4-5. The analysis was carried out for the identical setting of the caster, mainly the water flow rates through the cooling nozzles in the secondary cooling and through the mould for all the considered steel grades.

4 RESULTS AND DISCUSSION

4.1 Surface and corner temperatures

The analysis confirmed a significant dependency of the temperature field of the cast billets on the casting speed. For all steel grades, a very similar thermal behavior was observed (**Figure 5** for the steel grade S355J2G3): the higher casting speed, the higher both the corner temperature and the surface temperature beneath the nozzles. Moreover, with an increasing casting speed the rise of both the surface and corner temperatures decreases (**Figure 5**). As already mentioned, although all three investigated steel grades have various chemical

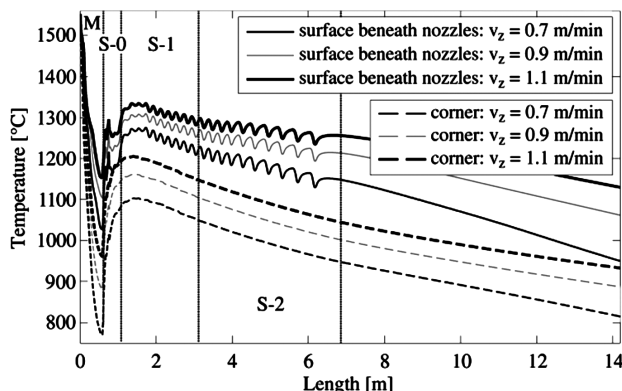


Figure 5: The impact of the casting speed on the surface and corner temperatures for the steel grade S355J2G3

Slika 5: Vpliv hitrosti ulivanja na temperaturo površine in robov pri jeklu S355J2G3

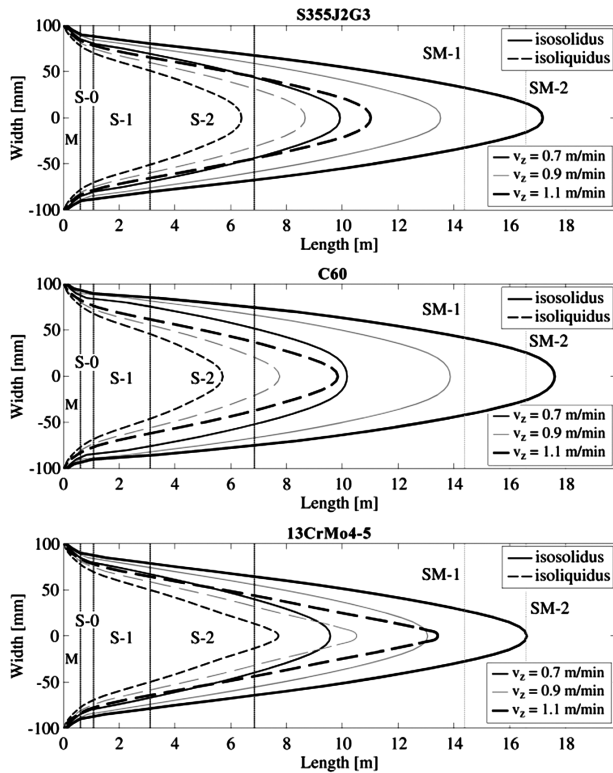


Figure 6: The influence of the casting speed on the isosolidus and isoliquidus curves, and the mushy zone

Slika 6: Vpliv hitrosti ulivanja na izosolidusne, izoliquidusne krivulje in na kašasto področje

compositions and each of them is intended for a different usage, their relative courses of the surface and the corner temperatures along the caster with a casting speed in the range between 0.7 m/min and 1.1 m/min are almost identical. The only significant difference is the temperature shift of both the surface and the corner temperature curves due to the various casting temperatures.

4.2 Isosolidus and isoliquidus curves, metallurgical length, mushy zone

The thermal behavior inside the cast billets, the solidification process, and the influence of the casting

speed on them can be investigated in the longitudinal axial cross-section of the billet with the use of the isosolidus and isoliquidus curves. Moreover, the isosolidus curve is directly related to the metallurgical length, which is an important parameter of continuous casting. **Figure 6** shows the influence of the casting speed on the solidification process of steel in the core of the billets: the isosolidus and isoliquidus curves, and the mushy zone where both the liquid and solid phases coexist.

As can be observed from **Figure 6**, the profile of the isosolidus and isoliquidus curves, the metallurgical length as well as the width of the mushy zone differs for each of the three investigated steel grades. In general, the higher casting speed makes both the isosolidus and isoliquidus longer (a positive shift in the length) and lengthens the metallurgical length as well (**Figure 6**). Moreover, the higher casting speed also enlarges the mushy zone. It implies that the positive shift of the isosolidus curve due to the increasing casting speed is larger than the shift of the isoliquidus curve.

For instance, consider the steel grade C60 (see the middle graph in **Figure 6**): for the casting speed of 0.7 m/min the metallurgical length is 10.1 m and the width of the mushy zone (in the axis of the billet) is 4.5 m. For the casting speed of 0.9 m/min, the metallurgical length increases to 13.9 m and the width of the mushy zone to 6.1 m. However, in the case of the casting speed of 1.1 m/min, the metallurgical length reaches 17.6 m (e.g., in the positions of both the straightening mills SM-1 and SM-2 the billet still contains the liquid phase) and the mushy zones distends to 7.7 m.

4.3 Shell thickness

The casting speed also has an impact on the rate of the shell thickness growth along the caster. A similar shell thickness behavior was observed for all three investigated steel grades. In general, the higher casting speed, the slower rate of the shell thickness growth (**Figure 7**). The shell inside the mould grows almost linearly, and behind the mould the rate of the shell thickness growth declines due to the abrupt reduction of the heat withdrawal. In the secondary cooling the rate of the shell thickness growth slowly increases owing to the

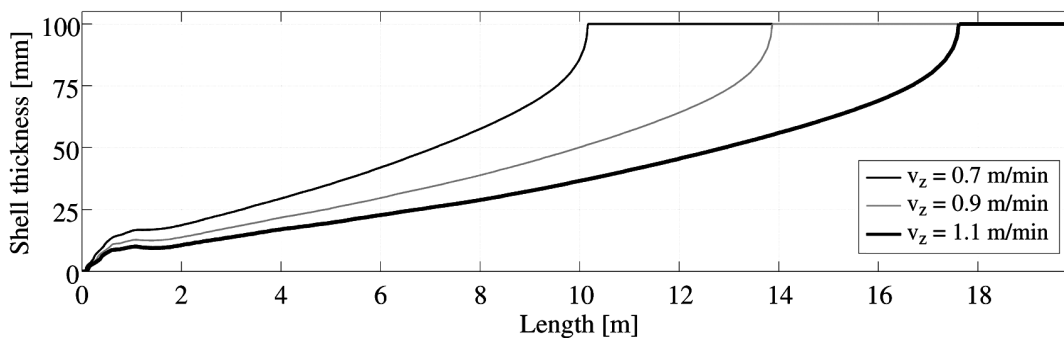


Figure 7: The influence of the casting speed on the shell thickness for the steel grade C60

Slika 7: Vpliv hitrosti ulivanja na debelino skorje pri jeklu C60

heat withdrawal of the cooling nozzles and also of the free convection and radiation heat transfer mechanisms.

For instance, **Figure 7** for the steel grade C60. In the length of 10.1 m where the billet cast with the casting speed of 0.7 m/min is completely solidified (i.e., the shell thickness is 100 mm), the shell thickness of the billet cast with the casting speed of 0.9 m/min is only 50 mm and the shell thickness of the billet cast with the casting speed of 1.1 m/min is even only 35 mm. The billet cast with the casting speed of 0.9 m/min is completely solidified in the length of 13.8 m, where the shell thickness of the billet cast with the casting speed of 1.1 m/min is only 55 mm.

4.4 Local period of solidification

The solidification process of the steel billets can also be investigated by the local period of solidification, which represents the local width of the mushy zone expressed in time related to the casting speed. Thus, for the given point (x, y) in the cross-section of the billet (**Figure 1**), the local period of solidification $lps(x, y)$ expresses the time (s) needed for the solidification (**Figure 6**), i.e., for cooling down from the liquidus temperature (where the first grains of solid phase appear) to the solidus temperature (where the last melt is solidified) along the billet assuming its movement through the caster with the casting velocity:

$$lps(x, y) = \frac{L_{\text{solidus}}(x, y) - L_{\text{liquidus}}(x, y)}{v_z} \quad (8)$$

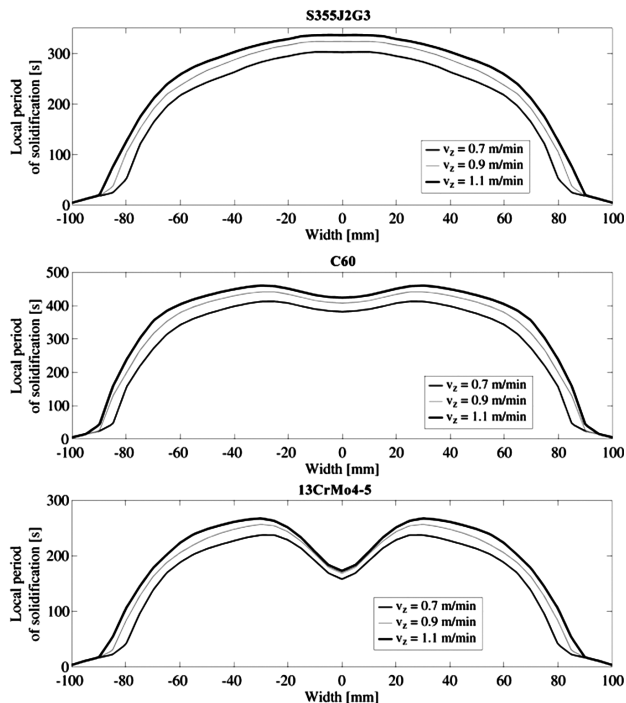


Figure 8: The influence of the casting speed on the local period of solidification in the axial cross-section

Slika 8: Vpliv hitrosti ulivanja na lokalni čas strjevanja v osnem prerezu

where $L_{\text{solidus}}(x, y)$ (m) and $L_{\text{liquidus}}(x, y)$ (m) are the lengths of the isosolidus and isoliquidus curves in the cross-section point (x, y) (**Figure 6** plotted for $y = 100$ mm), and v_z is the casting velocity (m s^{-1}). The local periods of solidification on the horizontal centerline of the cross section (i.e., for the cross section points (x, y) for which $y = 100$ mm) of cast billets are shown in **Figure 8**.

In general, a higher casting speed makes the local period of solidification longer (**Figure 8**). However, the profiles of the local periods of solidification are different for particular steel grades. This behavior is mainly caused by the different steel structure attained during the solidification of the particular steel grade directly related to the chemical composition and by the setup of cooling.²⁰ It was shown that a modification of the chemical composition in the range of the chemical composition given by norms and standards can change the profile of the local period of solidification.²²

In the case of the grade S355J2G3, the slowest solidification is in the core of the billet. However, the slowest solidification of the grade C60 is not in the core, but about 30 mm out of the core (width = ± 30 mm in **Figure 8**). The described behavior is even more evident in the case of the grade 13CrMo4-5, where the slowest solidification is in approximately the same position (width = ± 30 mm) as in the case of C60, but it needs an extra 80 s to be solidified than the core of the billet (width = 0 mm).

5 CONCLUSION

The paper presents the results of an analysis aimed at the impact of the casting speed on the temperature field of continuously cast steel billets and related parameters. The analysis was carried out with the use of the originally implemented dynamic solidification and three various steel grades were taken into account: common unalloyed steel for constructions, carbon steel for refining, and anticorrosive Cr-Mo steel for use at higher temperatures. The casting speed in the range between 0.7 m/min and 1.1 m/min was considered.

The performed analysis proved that the casting speed can significantly influence the temperature field and the solidification during the continuous steel casting. In general, the higher casting speed increases the temperature of the cast billets due to a reduced heat withdrawal. Consequently, the isosolidus and isoliquidus curves become longer and it also causes an increase of the metallurgical length. The higher casting speed also causes a drop in the shell growth as well as making the mushy zone wider, which implies a longer local period of solidification.

The study confirmed that the dynamic solidification models make it possible to perform an analysis of the caster and billets responses to various operating conditions and situations. The results can then be used by operators to set-up the caster.

Acknowledgement

The presented research was supported by the project GACR P107/11/1566 of the Czech Science Foundation and by the BUT project FSI-J-12-22. The main author, the holder of Brno PhD Talent Financial Aid sponsored by Brno City Municipality, also gratefully acknowledges that financial support.

6 REFERENCES

- ¹ A. Cramb Ed., Making, shaping and treating of steel: casting, 11th edition, Assn of Iron & Steel Engineers, 2003
- ² P. Popela, Optimizing mechanical properties of iron during melting process, ZAAM: Zeitschrift fur Angewandte Mathematik und Mechanik, 77 (1997) 2, S649–S650
- ³ M. Sadat, A. H. Gheysari, S. Sadat, The effects of casting speed on steel continuous casting process, Heat and Mass Transfer, 47 (2011) 12, 1601–1609
- ⁴ Y. Meng, B. G. Thomas, Heat-Transfer and Solidification Model of Continuous Slab Casting: CON1D, Metallurgical and materials transactions B, 34 (2003) 5, 685–705
- ⁵ J. Stetina, L. Klimes, T. Mauder, F. Kavicka, Final-structure prediction of continuously cast billets, Mater. Tehnol., 46 (2012) 2, 155–160
- ⁶ B. G. Thomas, Modeling of the continuous casting of steel-past, present, and future, Metallurgical and materials transactions B, 33 (2002) 6, 795–812
- ⁷ B. Petrus, K. Zheng, X. Zhou, B. G. Thomas, J. Bentsman, Real-time, model-based spray-cooling control system for steel continuous casting, Metallurgical and materials transactions B, 42 (2011) 1, 87–103
- ⁸ J. C. Ma, Z. Xie, Y. Ci, G. L. Jia, Simulation and application of dynamic heat transfer model for improvement of continuous casting process, Materials science and technology, 25 (2009) 5, 636–639
- ⁹ M. Gonzalez, M. B. Goldschmit, A. P. Assanelli, E. F. Berdaguer, E. N. Dvorkin, Modeling of the solidification process in a continuous casting installation for steel slabs, Metallurgical and materials transactions B, 34 (2003) 4, 455–473
- ¹⁰ L. Zhang, Y. M. Rong, H. F. Shen, T. Y. Huang, Solidification modeling in continuous casting by finite point method, Journal of materials processing technology, 192–193 (2007), 511–517
- ¹¹ A. Fic, A. J. Nowak, R. Bialecki, Heat transfer analysis of the continuous casting process by the front tracking BEM, Engineering analysis with boundary elements, 24 (2000) 3, 215–223
- ¹² B. Sarler, R. Vertnik, A. Z. Lorbiecka, I. Vusanovic, B. Sencic, A multiscale slice model for continuous casting of steel, International conference on modeling of casting, welding and advanced solidification processes, IOP Conference series – Materials science and engineering, 33 (2012), 012021
- ¹³ C. A. Santos, J. A. Spim, A. Garcia, Mathematical modeling and optimization strategies (genetic algorithm and knowledge base) applied to the continuous casting of steel, Engineering applications of artificial intelligence, 16 (2003) 5–6, 511–527
- ¹⁴ J. Stetina, F. Kavicka, T. Mauder, L. Klimes, Transient simulation temperature field for continuous casting steel billet and slab, Proceedings of METEC InSteelCon 2011, 13–23
- ¹⁵ J. Stetina, F. Kavicka, The influence of the chemical composition of steels on the numerical simulation of a continuously cast slab, Mater. Tehnol., 45 (2011) 4, 363–368
- ¹⁶ C. R. Swaminathan, V. R. Voller, A general enthalpy method for modeling solidification processes, Metallurgical transactions B, 23 (1992) 5, 651–664
- ¹⁷ D. M. Stefanescu, Science and Engineering of Casting Solidification, Second edition, Springer, 2009
- ¹⁸ J. Miettinen, S. Louhenkilpi, H. Kytönen, J. Laine, IDS: Thermodynamic-kinetic-empirical tool for modelling of solidification, microstructure and material properties, Mathematics and computers in simulation, 80 (2010) 7, 1536–1150
- ¹⁹ F. P. Incropera, D. P. DeWitt, T. L. Bergman, A. S. Lavine, Principles of heat and mass transfer, Seventh edition, Wiley, 2012
- ²⁰ J. Stetina, L. Klimes, Analysis of continuous casting of steel billets with the use of the transient 3D numerical model of temperature field, Technical report for Zeleziarne Podbrezova, Slovakia, Brno University of Technology, 2011
- ²¹ M. Raudensky, J. Horsky, Secondary cooling in continuous casting and Leidenfrost temperature effects, Ironmaking and steelmaking, 32 (2005) 2, 159–164
- ²² L. Klimes, J. Stetina, L. Parilak, P. Bucek, Influence of Chemical Composition of Cast Steel on the Temperature Field of Continuously Cast Billets, Proceedings of Metal 2012, Ostrava: Tanger, 2012, 34–39

TWO-STAGE STOCHASTIC PROGRAMMING APPROACH TO A PDE-CONSTRAINED STEEL PRODUCTION PROBLEM WITH THE MOVING INTERFACE

LUBOMÍR KLIMEŠ, PAVEL POPELA, TOMÁŠ MAUDER, JOSEF ŠTĚTINA,
AND PAVEL CHARVÁT

The paper is concerned with a parallel implementation of the progressive hedging algorithm (PHA) which is applicable for the solution of stochastic optimization problems. We utilized the Message Passing Interface (MPI) and the General Algebraic Modelling System (GAMS) to concurrently solve the scenario-related subproblems in parallel manner. The standalone application combining the PHA, MPI, and GAMS was programmed in C++. The created software was successfully applied to a steel production problem which is considered by means of the two-stage stochastic PDE-constrained program with a random failure. The numerical heat transfer model for the steel production was derived with the use of the control volume method and the phase changes were taken into account with the use of the effective heat capacity. Numerical experiments demonstrate that parallel computing facility has enabled a significant reduction of computational time. The quality of the stochastic solution was evaluated and discussed. The developed system seems computationally effective and sufficiently robust which makes it applicable in other applications as well.

Keywords: stochastic programming, progressive hedging, parallel computing, steel production, heat transfer, phase change

Classification: 90C15, 90C06, 80A20, 80A22, 49M27, 93C20

1. INTRODUCTION

A number of decision-making engineering problems lead to optimization models constrained with ordinary or partial differential equations. Such models are frequently large-scale as they consist of physical models derived by means of the finite difference, finite volume, or finite element methods [5, 8, 33]. Applications in various engineering areas can be found; e. g. in systems control [2, 19], in optimal design [30, 37], or in scheduling problems [13, 27]. Moreover, the mentioned problems often include uncertain parameters [1, 6, 26]. Stochastic programming that uses random variables for the uncertainty modelling is a suitable solution approach to such kind of problems. The further analysis of the problems revealed their stage-related decision structure and the possibility to apply the assumption of the discrete probability distribution of random

variables. This leads to the scenario-based approach and multi-stage decision making problems.

In the paper we consider a large-scale steel production problem under uncertainty which is modelled by a two-stage PDE-constrained programme. A computationally effective parallel implementation of the progressive hedging algorithm (PHA) that has been modified for the considered problem by the authors has been adopted for an efficient solution of the problem. The PHA, originally proposed by Rockafellar and Wets [25, 34], decomposes the extensive form of the problem into the scenario-based sub-problems which are linked together by means of penalties. The decomposition also enables a straightforward parallel solution of individual scenario-based sub-problems, and the computational time can significantly be reduced. The PHA therefore mitigates computational problems which can particularly arise in large-scale problems exceeding the computational capability. The PHA is an iterative method which gradually produces a series of aggregated solutions which are implementable. Though the convergence to a globally optimal solution is not guaranteed in case of non-convex non-linear and mixed-integer problems, computational results presented in several studies have demonstrated the applicability of the PHA to those kinds of problems with good results. Carpentier et al. [7] presented the use of the PHA in the solution of the management of the hydroelectric multireservoir systems under uncertainty. The CPLEX solver without parallel computing was used for the solution of scenario-related sub-problems in sequential order. Gul et al. [12] built a stochastic multi-stage mixed-integer model for the surgery planning problem under uncertainty. The authors applied the PHA, they compared it to a heuristic method and evaluated the value of the stochastic solution. Veliz et al. [32] investigated a forest planning problem. A multi-stage stochastic problem was formulated and solved by means of the PHA. The authors demonstrated that the PHA is well applicable and competitive to a direct solution of the extensive form, even in case of non-parallel implementation of the PHA. Goncalves et al. [11] applied the PHA to the solution of the operation scheduling problem of a hydrothermal system. They utilized the CPLEX solver and parallel computing on several processors. The authors reported that they achieved the reduction of 80% of the computational time when comparing the parallel implementation to the serial implementation. Gade et al. [10] reported the assessment of the quality of solutions generated by the PHA by means of the lower bounds. The authors presented a method for the determination of lower bounds for multi-stage mixed-integer problems and they demonstrated computational results in stochastic unit commitment and server location problems.

As for optimization studies related to the control of the continuous casting process, most research papers are related to deterministic optimization with no randomness. A number of studies aim at optimization of operational parameters of the casting machine, of the scheduling, and of the secondary cooling zone, see e. g. [21, 35, 36]. However, only a limited number of papers have been published on the topic of stochastic optimization related to the continuous casting, e. g. [38]. To the best knowledge of the authors, there is no paper related to the application of the PHA to the steel production problem or to a heat transfer problem with the moving interface. The present paper builds on previous research of the authors on the mathematical programming approach and random failures in the continuous casting process [23, 24]. A basis of presented results was conducted in

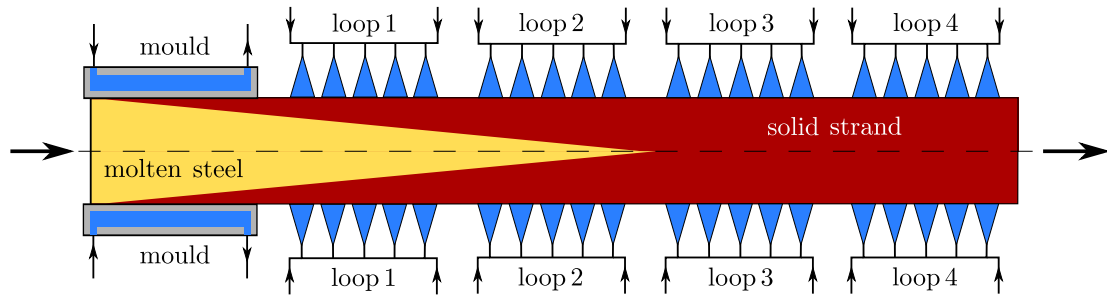


Fig. 1. The schematic of the continuous steel casting method.

the master thesis [15] and some partial results have already been published at scientific conferences [16, 17, 18].

The present paper summarizes the complete application of the stochastic approach to the continuous casting process. A detailed description of the improved heat transfer model based on the effective heat capacity is provided. A computationally efficient parallel implementation of the progressive hedging algorithm is presented and the Message Passing Interface (MPI) was used to solve independent scenario-related sub-problems in the parallel manner. Individual sub-problems are formulated in the General Algebraic Modelling System (GAMS) and solved by the non-linear CONOPT solver. The use and the applicability of the proposed implementation are demonstrated in the two-stage steel production problem with a random failure.

2. STEEL PRODUCTION CONTROL PROBLEM UNDER UNCERTAINTY

2.1. Underlying principle of the steel production problem

The continuous steel casting is a modern production method of steel. Nowadays, more than 95% of the total world steel production is cast by means of the continuous casting [22]. The schematic of the horizontal continuous casting method is shown in Figure 1. The molten steel enters the continuous casting machine through the water-cooled mould. In the mould the initial amount of heat is withdrawn from the steel and this causes the formation of the solid shell at the surface of the cast semi-product, the so-called strand. The steel strand continues from the mould to the secondary cooling zone. The secondary cooling zone consists of several independent cooling loops where the water nozzles producing water sprays are installed. The heat withdrawal in the secondary cooling zone therefore occurs due to the heat convection and radiation. The intensity of the heat convection from the strand is driven by the heat transfer coefficient which is directly dependent on water flow rates through the cooling loops, see e. g. [29].

2.2. Uncertainty in the steel production problem

There are several different categories of parameters under uncertainty which influence the steel production problem. These mainly include the uncertainty in the chemical composition of steel, random faults in parts of the casting machine, and clogging of cooling nozzles. It is well reported [4] that the strand cooling, its distribution and

intensity have a major influence on the steel quality and mechanical properties. Steel-makers therefore pay attention mainly to the secondary cooling and they aim at the gradual cooling in which the temperature of the strand smoothly decreases with no reheating, temperature shocks or zig-zag temperature paths. One of serious faults in the secondary cooling zone is an abrupt stop of water spray cooling within a cooling loop and we investigate this case in the paper. Such a problem is typically caused by a fault in the electric motor of the water pump. In that case there is no cooling of the strand which leads to undesirable steep overheating of the strand and, as a consequence, to irreversible steel quality problems.

2.3. Simplifications and assumptions

Technology. Casting machines can accommodate even more than 20 cooling loops in the secondary cooling zone, particularly in case of large cross-section steel strands. In the paper we consider the problem with a casting machine having four cooling loops as shown in Figure 1. The reason is that requirements for the computational hardware increase rapidly with higher number of cooling loops. Moreover, the goal of the paper is to demonstrate the applicability of the PHA to the steel making problem rather than to solve a huge realistic problem from industry. Nevertheless, the model presented in the paper is formulated without the loss of generality and it can be used for modelling of a problem with the casting machine having an arbitrary number of cooling loops.

Uncertainty and scenario tree. In the paper we focus on the case described above: a cooling system in a loop can fail and as a result the heat withdrawal from the strand stops causing overheating and quality issues. In general, the fail of cooling can occur in an arbitrary cooling loop, even in several loops simultaneously. Hence, such uncertain failures are represented by a random vector and its outcomes form the scenario tree that is suitable for further computations.

3. HEAT AND MASS TRANSFER MODEL FOR CONTINUOUS STEEL CASTING

In the section the mathematical description of the model for the continuous steel casting is provided. Further, the mathematical model is numerically reformulated with the use of the control volume method to the form suitable for the implementation in the modelling system GAMS; see [17, 18] for further details.

3.1. Physical model

The heat and mass transfer model of the continuous steel casting is based on the Fourier-Kirchhoff equation [14]. The governing equation incorporates the heat conduction within the cast strand while the direct modelling of the fluid flow in the melt is omitted. As the continuous steel casting relies on the phase transformation of steel from the liquid phase to the solid phase, the model accounts for phase changes. There are several approaches for phase change modelling, see e.g. [28]. We employ the effective heat capacity method (see [28] for its details) as the method is quite simple and, in particular, easily implementable into the optimization model. Only one half of the strand as shown

in Figure 2 is considered in the model since the spatial domain is symmetrical with respect to the horizontal axis, cf. Figures 1 and 2.

In the paper the casting process of so-called slabs is considered. A slab is a kind of the strand having the rectangular cross-section with a high aspect ratio (usually 8 or more); the width of the slab is therefore several times larger than its height. For such slabs it is justifiable to consider a 2D heat transfer model which neglects interactions in the perpendicular direction of the 2D domain. In the model explained below, the 2D domain is considered as a longitudinal vertical cross-section of the slab in the middle of the width of the slab.

The governing equation describing the 2D heat and mass transfer and phase transformations within the cast strand (the spatial domain Ω) is [28]

$$\varrho c_{\text{eff}} \frac{\partial T}{\partial t} = \frac{\partial}{\partial x} \left(k \frac{\partial T}{\partial x} \right) + \frac{\partial}{\partial z} \left(k \frac{\partial T}{\partial z} \right) + v_z \varrho c_{\text{eff}} \frac{\partial T}{\partial z} \quad \text{in } \Omega \times (0, \tau) \quad (1)$$

where $T(x, z, t)$ is the temperature in a spatial point (x, z) at time $t \in (0, \tau)$, ϱ is the density, c_{eff} is the effective heat capacity, k is the thermal conductivity, v_z is the casting speed and τ is the final time.

The model is completed with the initial (2) condition specifying the initial temperature $T_0(x, z)$ in Ω and boundary conditions (3)–(6)

$$T(x, z, t) = T_0(x, z) \quad \text{in } \Omega \times \{0\}, \quad (2)$$

$$T(x, z, t) = T_{\text{casting}} \quad \text{in } \Gamma_{\text{in}} \times (0, \tau), \quad (3)$$

$$-k \frac{\partial T}{\partial \mathbf{n}} = 0 \quad \text{in } \Gamma_{\text{out}} \times (0, \tau) \text{ and } \Gamma_{\text{sym}} \times (0, \tau), \quad (4)$$

$$-k \frac{\partial T}{\partial \mathbf{n}} = \dot{q}_{\text{mould}} \quad \text{in } \Gamma_{\text{mould}} \times (0, \tau), \quad (5)$$

$$-k \frac{\partial T}{\partial \mathbf{n}} = h_m (T(x, z, t) - T_\infty) + \sigma \varepsilon (T(x, z, t)^4 - T_\infty^4) \quad \text{in } \Gamma_m \times (0, \tau), \quad m = 1, \dots, n_{\text{CC}} \quad (6)$$

which are added to the governing equation (1). In Eq. (4)–(6), the vector \mathbf{n} is the normal vector to the surface. The boundary condition (3) prescribes the constant pouring temperature T_{casting} at the meniscus in the mould (see Γ_{in} in Figure 4) the boundary condition (4) simulates the physical symmetry at the plane of symmetry and the zero heat flux at the end of the strand, see both Γ_{out} and Γ_{sym} boundaries in Figure 4. Further, the defined heat flux \dot{q}_{mould} is prescribed in the mould (see Γ_{mould} boundary part) according to the boundary condition (5). The convective and radiative heat transfer is included in the boundary condition (6) and applied at surfaces of the strand. Here, the cooling occurs due to the forced (in the spraying zones) and the natural (at free surfaces) convection and radiation where h_m is the heat transfer coefficient in the m th cooling loop (see Γ_m in Figure 4), σ is the Stefan-Boltzmann constant, ε is the emissivity, and T_∞ is the ambient temperature. As already mentioned in Section 2 the number of cooling loops n_{CC} in the secondary cooling can vary according to dimensions of cast steel strands and according to the configuration of a casting machine. In the paper we consider, without the loss of generality, the number of cooling loops $n_{\text{CC}} = 4$.

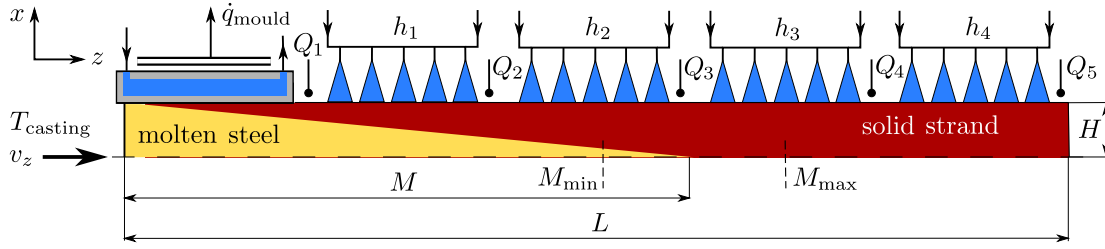


Fig. 2. The spatial domain for the steel production problem.

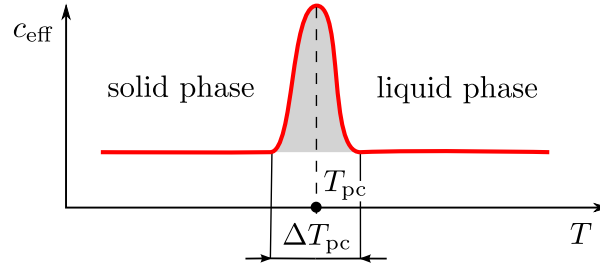


Fig. 3. The idea of the effective heat capacity method.

As mentioned above, the effective heat capacity method is applied to the phase change modelling [28]. The principle of the method relies on the artificial increase of the physical heat capacity in the temperature range of the phase change. The amount of the latent heat accompanying the phase change is then proportional to the shaded area in Figure 3. A typical bell shaped effective heat capacity as a function of the temperature is illustrated in Figure 3. The effective heat capacity can be defined [28] as

$$c_{\text{eff}} = \frac{\partial H}{\partial T} = \rho c - \rho L_f \frac{\partial f_S}{\partial t} \frac{\partial t}{\partial T} \quad (7)$$

where H is the enthalpy, c is a specific heat, L_f is the latent heat of the phase change and f_S is the solid fraction expressing the ratio between the solid and liquid phases during the solidification.

3.2. Numerical continuous casting model and its deterministic formulation

The mathematical model presented in the foregoing section was discretized with the use of the control volume method. The discretization enables an implementation of the model into the modelling system GAMS, and thus it makes possible to find the numerical solution in discrete points within the domain. First, the spatial domain Ω is partitioned into smaller elements, so-called control volumes specified by indices $i = 1, \dots, N_x$ and $j = 1, \dots, N_z$ and denoted as $[i, j]$. The union of all the control volumes is often referred to as the mesh. Similarly, the time domain $(0, \tau)$ is divided into the time steps indexed by $n = 1, \dots, N_\tau$. The energy conservation balance is then applied to each control volume. The balances for all mesh elements form the system of equations and its solution is considered as the numerical solution to the model described by Eqs. (1)–(7).

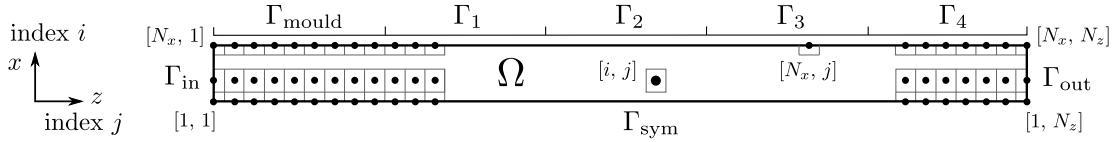


Fig. 4. The discretization of the spatial domain into control volumes.

Let us assume that the time domain $(0, \tau)$ is partitioned into N_τ time intervals, each with the length of Δt (thus $\tau = N_\tau \Delta t$). The energy conservation law [14] states that the sum of energies $E_{[i,j]}$ transferred inward and outward a control volume through its boundaries during any time interval of length Δt must be equal to the change of the internal energy U of that control volume: $\sum_{[i,j]} E_{[i,j]} = \Delta U$. In the considered case, the transferred energy is heat transferred due to heat transfer mechanisms (heat conduction in interior control volumes and also heat convection and radiation in boundary control volumes) and due to the mass transfer as the strand continuously moves through the casting machine. Let us consider the interior control volume $[i, j]$ shown in Figure 4 and the implicit discretization approach for the time scale. The energy conservation law applied to the interior control volume specified by $[i, j]$ and n th time interval where $i = 1, \dots, N_x, j = 1, \dots, N_z$, and $n = 1, \dots, N_\tau$ yields to

$$k\Delta z \frac{T_{i-1,j}^n - T_{i,j}^n}{\Delta x} + k\Delta z \frac{T_{i+1,j}^n - T_{i,j}^n}{\Delta x} + k\Delta x \frac{T_{i,j-1}^n - T_{i,j}^n}{\Delta z} + k\Delta x \frac{T_{i,j+1}^n - T_{i,j}^n}{\Delta z} + v_z \rho c_{\text{eff}} \Delta x (T_{i,j-1}^n - T_{i,j}^n) = \rho c_{\text{eff}} \Delta x \Delta z \frac{T_{i,j}^n - T_{i,j}^{n-1}}{\Delta t} \quad (8)$$

where Δx and Δz are the dimensions of the control volume in the x -axis and z -axis, respectively and $T_{i,j}^n$ values denote unknown temperature distribution. The four terms on the first line of the left-hand side in Eq. (8) are the heat transfer rates that represent the conduction heat transfer from the neighbouring control volumes. The fifth term on the left-hand side of Eq. (8) is the energy input due to the movement of the strand through the casting machine. The right-hand side of Eq. (8) represents the change of the internal energy during the time interval Δt . The energy conservation law is similarly applied to boundary control volumes. For instance, let us consider the boundary control volume $[N_x, j]$ exposed to the water spray cooling in a cooling loop $m = 3$, see Figure 4. The energy conservation law applied to the boundary control volume yields to

$$h_m \Delta z (T_{\text{ambient}} - T_{N_x,j}^n) + \sigma \varepsilon \Delta z (T_{\text{ambient}}^4 - (T_{N_x,j}^n)^4) + k\Delta z \frac{T_{N_x-1,j}^n - T_{N_x,j}^n}{\Delta x} + k \left(\frac{\Delta x}{2} \right) \frac{T_{N_x,j-1}^n - T_{N_x,j}^n}{\Delta z} + k \left(\frac{\Delta x}{2} \right) \frac{T_{N_x,j+1}^n - T_{N_x,j}^n}{\Delta z} + v_z \rho c_{\text{eff}} \frac{\Delta x}{2} (T_{N_x,j-1}^n - T_{N_x,j}^n) = \rho c_{\text{eff}} \left(\frac{\Delta x \Delta z}{2} \right) \frac{T_{N_x,j}^n - T_{N_x,j}^{n-1}}{\Delta t}. \quad (9)$$

The application of the energy conservation law to all control volumes leads to the set of algebraic equations for the unknown temperature distribution $T_{i,j}^n$ with a specified

temperature T_{ambient} . Since the spatial domain is partitioned into $N_x N_z$ control volumes and the time domain into N_τ time intervals, the set consists of the $N_x N_z N_\tau$ algebraic equations for the identical number of the unknown temperatures.

The phase change and the latent heat are implemented in the model by means of the effective heat capacity. A bell-shape function might be used in case of steel having a relatively wide temperature interval of the phase change. The effective heat capacity as the function of the temperature is of the form

$$c_{\text{eff}}(T) = c_0 + \tilde{c} \exp \left\{ -\frac{(T_{i,j}^n - T_{\text{pc}})^2}{\zeta_T} \right\} \quad (10)$$

where c_0 is the heat capacity outside the temperature range of the phase change, \tilde{c} is the parameter characterising the amount of the latent heat of the phase change, T_{pc} is the mean phase change temperature and ζ_T is a parameter related to the temperature interval of the phase change ΔT_{pc} .

Several additional constraints are included to the model due to technological requirements of the continuous casting process. The cooling capacity of the spraying nozzles installed in the secondary cooling zone is limited by the maximum water flow rate provided by the pump and also by the hydrodynamic limits of nozzles. The heat transfer coefficient h_m for the nozzles installed within the cooling loop m is therefore restricted as

$$0 \leq h_m \leq h_{m,\text{max}} \quad m = 1, \dots, n_{\text{CC}} \quad (11)$$

where the value of $h_{m,\text{max}}$ is known. Further, the quality of the produced steel is highly dependent on the thermal history during the casting process, specifically the surface of the strand suffers from defects and cracks due to large thermal gradients. In particular, the surface temperatures of the strand are required to decrease gradually and smoothly in the direction of casting with minimum reheating or temperature shocks. The surface temperatures are therefore required to fit specific temperature ranges in defined control points. Such control points are usually behind the mould and behind each cooling loop as shown in Figure 2 (labelled as Q_m) and thus

$$T_{m,\text{min}} \leq T_{N_x, q_m}^n \leq T_{m,\text{max}} \quad m = 1, \dots, n_{\text{CP}} \quad (12)$$

where q_m is the index of the control volume in the z -axis closest to the control point Q_m and n_{CP} is the number of control points; in our case $n_{\text{CP}} = 5$, see Figure 3. Additionally, $T_{m,\text{min}}$ and $T_{m,\text{max}}$ values are known. Finally, the very important constraint is required for the length of the liquid phase M shown in Figure 2. The distance M must fulfil $M_{\text{min}} \leq M \leq M_{\text{max}}$. In terms of the temperature, it must hold that

$$T_{1, r_{\text{min}}} \geq T_{\text{liquidus}} \quad \text{and} \quad T_{1, r_{\text{max}}} \leq T_{\text{solidus}} \quad (13)$$

where r_{min} and r_{max} are the indices of the control volumes in the z -axis which are the closest ones to the distances M_{min} and M_{max} , respectively. The steel is completely liquid at and above the liquidus temperature T_{liquidus} and it is completely solid at and below the solidus temperature T_{solidus} .

Finally, the deterministic optimization problem for the steady-state continuous casting process can be formulated. The steel-maker requires the maximum productivity with

the preservation of quality, and thus the relevant parameters of the casting process need to be determined. In terms of the above defined quantities and derived relationships, the deterministic model aims to

$$\begin{cases} \text{maximize} & v_z \\ \text{subject to} & (8), (9), (10), (11), (12), (13). \end{cases} \tag{14}$$

The steel-maker is mainly interested in optimal values of operational parameters of the continuous casting machine: the casting speed v_z and the heat transfer coefficients h_m in cooling loops of the secondary cooling zone. A solution to the problem (14) also includes the temperature distribution $T_{i,j}^n$ which can be further investigated by metallurgists or materials engineers.

4. TWO-STAGE STOCHASTIC FORMULATION FOR THE STEEL PRODUCTION PROBLEM AND PARALLEL PROGRESSIVE HEDGING ALGORITHM

In this section we transform the deterministic model discussed in the foregoing section into a two-stage stochastic problem. As already mentioned in Section 2.2, there are several sources of uncertainty in the steel production problem. We will focus on the case with a fail of the water pump which is potentially the most dangerous case in practice. Furthermore, we discuss the progressive hedging algorithm and its parallel implementation suitable for computationally effective processing.

4.1. Stochastic optimization and scenario-based approach

Stochastic programming and the use of random variables is a common approach widely applied in optimization problems with uncertainty [31]. A two-stage stochastic problem is considered in the paper which includes a here-and-now first stage decision and a wait-and-see second stage decision [3]. In general, the solution to a stochastic problem searches for the minimum of an objective function $f(\mathbf{x}, \boldsymbol{\xi})$ subject to equality and inequality constraints $\mathbf{g}(\mathbf{x}, \boldsymbol{\xi}) = \mathbf{0}$ and $\mathbf{h}(\mathbf{x}, \boldsymbol{\xi}) \leq \mathbf{0}$, respectively, where $\mathbf{x} \in X \subset \mathbb{R}^N$ and $\boldsymbol{\xi}$ is a K -dimensional random vector on a probability space (Ω, \mathcal{A}, P) .

The paper is concerned with random variables having a discrete probability distribution and the scenario-based approach is applied to take into account discrete random variables [3]. Assume that the random vector $\boldsymbol{\xi}$ on a probability space (Ω, \mathcal{A}, P) has a finite discrete distribution with $|\Omega| = L < \infty$. Then, outcomes of the random vector are denoted as particular real-valued vectors $\boldsymbol{\xi}_s$ and referred to as scenarios $s \in \mathcal{S}$ with a probability p_s and $\sum_{s \in \mathcal{S}} p_s = 1$. Then, the general deterministic equivalent based on the expected objective with all constraints satisfied almost surely can be written as follows

$$\begin{cases} \text{minimize} & \sum_{s \in \mathcal{S}} p_s f(\mathbf{x}, \boldsymbol{\xi}_s) \\ \text{subject to} & \mathbf{x} \in \bigcap_{s \in \mathcal{S}} C_s \\ & \text{where } C_s = \{ \mathbf{x} \in X \subset \mathbb{R}^N : \mathbf{g}(\mathbf{x}, \boldsymbol{\xi}_s) \leq \mathbf{0}, \mathbf{h}(\mathbf{x}, \boldsymbol{\xi}_s) = \mathbf{0} \}. \end{cases} \tag{15}$$

4.2. Two-stage stochastic formulation of the steel production problem

In this part, the deterministic formulation of the steel production problem described in Section 3.2 is reformulated into a two-stage stochastic problem. A failure situation within the secondary cooling zone is considered and the stochastic approach is used for the modeling of randomness. In particular, failures of water pumps in the cooling loops are assumed to occur. A failure of the pump means that no water is fed into the cooling nozzles, and therefore there are no water sprays generated by the nozzles. This implies that the heat transfer coefficient of the forced convection induced by cooling nozzles drops to zero. Though there is still the natural convection to the ambient air, the total heat transfer coefficient can be assumed zero (i. e. with the neglected natural convection) as the heat transfer coefficient of the natural convection is much lower than that of the forced convection due to cooling nozzles. The model with the scenario-based approach and scenarios $\xi_s, s \in \mathcal{S}$ is utilized to take into account the uncertainty. One scenario models the failure-free casting process while the other scenarios represent the casting process with failures in the cooling loops of the secondary cooling zone. The steel-maker is primarily interested in the first-stage decision which is the set of operational parameters at the beginning of the casting process. However, the first stage decision needs to take into account the possibility that a failure in the secondary cooling zone can occur with a non-zero probability. And if the failure does occur, the second-stage decision is used to revise the first stage decision and to keep the best conditions for the casting process.

Some modifications to the deterministic model (14) are required for its transformation into the two-stage stochastic model. In particular, the objective function in the model (14) (cf. to f in the model (15)) is reformulated as

$$\text{maximize} \quad \sum_{s \in \mathcal{S}} p_s \left[\sum_{n \in \mathcal{N}} v_{z,n}(\xi_s) \right], \quad (16)$$

where $v_{z,n}(\xi_s)$ represents the casting speed under random circumstances that can be specific for different time periods $n \in \mathcal{N} = \{1, \dots, N_\tau\}$ and scenarios $s \in \mathcal{S}$. Let the prime be used for variables related to the first-stage decision while the double prime be used for variables related to the second-stage decision. The stage-related heat transfer coefficients are now also dependent on a particular scenario $\xi_s, s \in \mathcal{S}$ and such dependency is emphasized by the subscript s . For instance, the second-stage heat transfer coefficient for the scenario s_0 in a cooling loop m is denoted as h''_{m,s_0} and it has to be considered constant for all second stage related time indices. So, they can be omitted. Deterministic constraints to the range of heat transfer coefficients in Eq. (11) are updated with respect to the two-stage structure of heat transfer coefficients as

$$0 \leq h'_{m,s} + h''_{m,s} \leq h_{m,\max} \quad \text{for } m = 1, \dots, n_{CC} \quad \text{and } s \in \mathcal{S}. \quad (17)$$

Let t_f be the time when the failure of the pump within the second cooling loop occurs. The set of time related indices $n \in \mathcal{N}$ that identify the period before the failure is denoted by $\mathcal{N}' \subset \mathcal{N}$. Then the heat transfer coefficients h_m in the heat balance equations (9) for the surface control volumes are updated by

$$h_m = h'_{m,s} \quad \text{for } n \in \mathcal{N}', \quad m = 1, \dots, n_{CC}, \quad s \in \mathcal{S}, \quad (18)$$

and similarly the set of time related indices n that identify the period after the failure is denoted by $\mathcal{N}'' \subset \mathcal{N}$. For these indices we replace h_m as follows

$$h_m = h'_{m,s} + h''_{m,s} \quad \text{for } n \in \mathcal{N}'', \quad m = 1, \dots, n_{CC}, \quad s \in \mathcal{S}. \quad (19)$$

Further, note that due to the scenario-based model the temperature variables $T_{i,j}^n$ of the heat transfer model in all equations and constraints presented above are also related to a particular scenario $s \in \mathcal{S}$.

We also assume that the first stage related casting speeds $v_{z,n}(\boldsymbol{\xi}_s)$ and $h'_{m,s}$ variables must satisfy the explicit nonanticipativity constraints. Therefore

$$v_{z,n}(\boldsymbol{\xi}_s) = \sum_{r \in \mathcal{S}} p_r v_{z,n}(\boldsymbol{\xi}_r), \quad \forall s \in \mathcal{S}, \quad n \in \mathcal{N}'. \quad (20)$$

and similarly

$$h'_{m,s} = \sum_{r \in \mathcal{S}} p_r h'_{m,r}, \quad \forall s \in \mathcal{S}. \quad (21)$$

To keep the description compact and general, we will further write about the first stage decision vector \boldsymbol{x}'_s containing first stage components $v_{z,n}, n \in \mathcal{N}'$ and $h'_{m,s}$. Similarly, the second stage related components $v_{z,n}, n \in \mathcal{N}''$ and $h''_{m,s}$ will be contained in the second stage decision vector \boldsymbol{x}''_s . Both vectors \boldsymbol{x}'_s and \boldsymbol{x}''_s form the composed vector \boldsymbol{x}_s .

4.3. Progressive hedging algorithm

The progressive hedging algorithm (PHA) is an optimization method suitable for the solution of multi-stage scenario-based stochastic problems. The PHA, originally proposed by Rockafellar and Wets [25, 34] in 1980s, is a decomposition method which separates the scenario-based problem into smaller independent sub-problems, each related to an individual scenario. The method is therefore particularly applicable in solution of large-scale problems and fits well for parallel computing. The PHA is based on the augmented Lagrangian method with relaxed non-anticipativity constraints. In general, non-anticipativity constraints can be formulated explicitly or implicitly to define an extensive form. An implicit formulation is usually easier for the solution as it introduces shared variables instead of scenario-related variables as in case of the explicit formulation. However, even the implicit formulation can lead to stochastic problems which are difficult for the solution due to their large dimensions as reported in [32].

Let us assume a scenario-based stochastic problem (15) with L scenarios $s \in \mathcal{S}$, each with the probability p_s . Then each particular scenario s forms the sub-problem

$$\begin{cases} \text{minimize} & f(\boldsymbol{x}, \boldsymbol{\xi}_s) \\ \text{subject to} & \boldsymbol{x} \in C_s = \{ \boldsymbol{x} \in X_s \subset \mathbb{R}^N : \boldsymbol{g}(\boldsymbol{x}, \boldsymbol{\xi}_s) \leq \mathbf{0}, \boldsymbol{h}(\boldsymbol{x}, \boldsymbol{\xi}_s) = \mathbf{0} \}. \end{cases} \quad (22)$$

The optimal solution to the problem (15) is denoted as \boldsymbol{x}^* . The progressive hedging algorithm is the iterative algorithm which requires solutions \boldsymbol{x}_s of the sub-problems (22) and generates a sequence of solutions $\hat{\boldsymbol{x}}_k$ converging to the solution \boldsymbol{x}^* of the original scenario-based problem (15). In terms of the steel production problem considered in

the paper, the objective function f aims at the maximization of the production rate v_z (cf. to Eq. (16)). The vector function \mathbf{g} of inequality constraints includes inequality conditions (e. g. Eqs. (12), (13), (17)) while the vector function \mathbf{h} of equality constraints incorporates the heat transfer model (Eqs. (8) and (9)) and other equality conditions (e. g. Eqs. (18) and (19)).

List of symbols for the PHA

D	the error
ε	the termination parameter
L	the number of scenarios $L = \ \mathcal{S}\ $
ϱ	the penalty parameter
$\mathbf{x}'_{k,s}$	the first-stage decision for iteration k and scenario s
$\mathbf{x}''_{k,s}$	the second-stage decision for iteration k and scenario s
$\hat{\mathbf{x}}'_k$	the first-stage “average” decision for iteration k
$\hat{\mathbf{x}}''_{k,s}$	the second-stage iterated decision for iteration k and scenario s
$\mathbf{w}'_{k,s}$	the first-stage weight vector for iteration k and scenario s

TWO-STAGE PROGRESSIVE HEDGING ALGORITHM

Initialization. Choose the penalty parameter $\varrho > 0$ and the termination parameter $\varepsilon > 0$. Set $k = 1$, $\mathbf{w}'_{0,s} = \mathbf{0}$, $\hat{\mathbf{x}}'_0 = \mathbf{0}$ and $\hat{\mathbf{x}}''_{0,s} = \mathbf{0}$ for all $s \in \mathcal{S}$.

Main part.

1. For all $s \in \mathcal{S}$ solve the scenario-based sub-problem

$$\begin{cases} \text{minimize} & f(\mathbf{x}', \mathbf{x}'', \boldsymbol{\xi}_s) + \mathbf{w}'_{k-1,s} \cdot \mathbf{x}' + \frac{1}{2}\varrho \|\mathbf{x}' - \hat{\mathbf{x}}'_{k-1,s}\|^2 \\ \text{subject to} & \mathbf{x}', \mathbf{x}'' \in C_s \end{cases}$$

and let $\mathbf{x}'_{k,s}$ and $\mathbf{x}''_{k,s}$ be its first-stage and second-stage solution, respectively.

2. Calculate the updated first-stage and second-stage solutions $\hat{\mathbf{x}}'_k$ and $\hat{\mathbf{x}}''_{k,s}$, respectively, for all $s \in \mathcal{S}$:

$$\hat{\mathbf{x}}'_k = \sum_{s \in \mathcal{S}} p_s \mathbf{x}'_{k,s} \quad \text{and} \quad \hat{\mathbf{x}}''_{k,s} = \mathbf{x}''_{k,s}.$$

In the case that the termination condition

$$D = \left(L \|\hat{\mathbf{x}}'_{k-1} - \hat{\mathbf{x}}'_k\|^2 + \sum_{s \in \mathcal{S}} \|\hat{\mathbf{x}}''_{k-1,s} - \hat{\mathbf{x}}''_{k,s}\|^2 + \sum_{s \in \mathcal{S}} p_s \|\mathbf{x}'_{k,s} - \hat{\mathbf{x}}'_k\|^2 \right)^{\frac{1}{2}} \leq \varepsilon$$

is fulfilled, then stop, $\hat{\mathbf{x}}'_k$ and $\hat{\mathbf{x}}''_{k,s}$ are the the first-stage and the second-stage solution, respectively, to the scenario-based optimization problem (15). Otherwise, for all $s \in \mathcal{S}$ update the first-stage weights according to

$$\mathbf{w}'_{k,s} = \mathbf{w}'_{k-1,s} + \varrho (\mathbf{x}'_{k,s} - \hat{\mathbf{x}}'_k),$$

set $k = k + 1$ and return to the step 1 of the main part of algorithm.

As can be seen from the detailed description of the PHA, the second-stage decision $\hat{\mathbf{x}}''_{k,s}$ is dependent on a particular scenario while the first-stage “average” decision $\hat{\mathbf{x}}'_k$ is not. The reason is that the first-stage decision is the *here-and-now* decision [3] and it is made at the beginning of the process, i. e. before the decision maker observes a particular outcome of random failure in our case. The first-stage decision is therefore independent on what will happen in the future and represents the initial setup of control variables. This property is referred to as the non-anticipativity [34]. On the other hand, the second-stage decision is the *wait-and-see* decision and it is made after the decision maker has already observed the failure and particular values of the random vector are fully known at that moment.

4.4. Parallel implementation of the progressive hedging algorithm

As already mentioned, the progressive hedging algorithm allows for the direct parallelism. The parallel processing can be accomplished due to the decomposition of the original optimization problem into smaller optimization sub-problems which are independent to each other. The General Algebraic Modelling System (GAMS) was utilized as the optimization solver for the scenario-based sub-problems. The Message Passing Interface (MPI) was used to run the GAMS instances in parallel, each solving an individual sub-problem. The progressive hedging algorithm itself was implemented as the standalone principal application in C++. For detailed information on the implementation, we refer readers to [15, 16].

Principal PHA application. The principal application aggregates the PHA, MPI, and GAMS. The application also

- controls the flow of the PHA,
- creates the scenario-based sub-problems in the form of input files for the GAMS,
- runs the GAMS instances in parallel by means of MPI,
- loads the solutions to sub-problems from the output files produced by the GAMS,
- computes the “average” first-stage and second-stage decisions and
- evaluates the termination condition.

The block diagram and the flow chart of the algorithm are shown in Figure 5 on the left side and on the right side, respectively.

Message Passing Interface. The MPI is an API Windows library which serves the platform for high performance parallel computing. In particular, the LAM/MPI environment was employed for parallel launch of GAMS instances. Each instance of the GAMS is used to solve one of the scenario-based sub-problems. The maximum number of parallel GAMS instances is dependent on the particular hardware. In case the number of scenarios exceeds the maximum number of parallel processes, parallel runs are repeated until all the scenario-based sub-problems are solved.

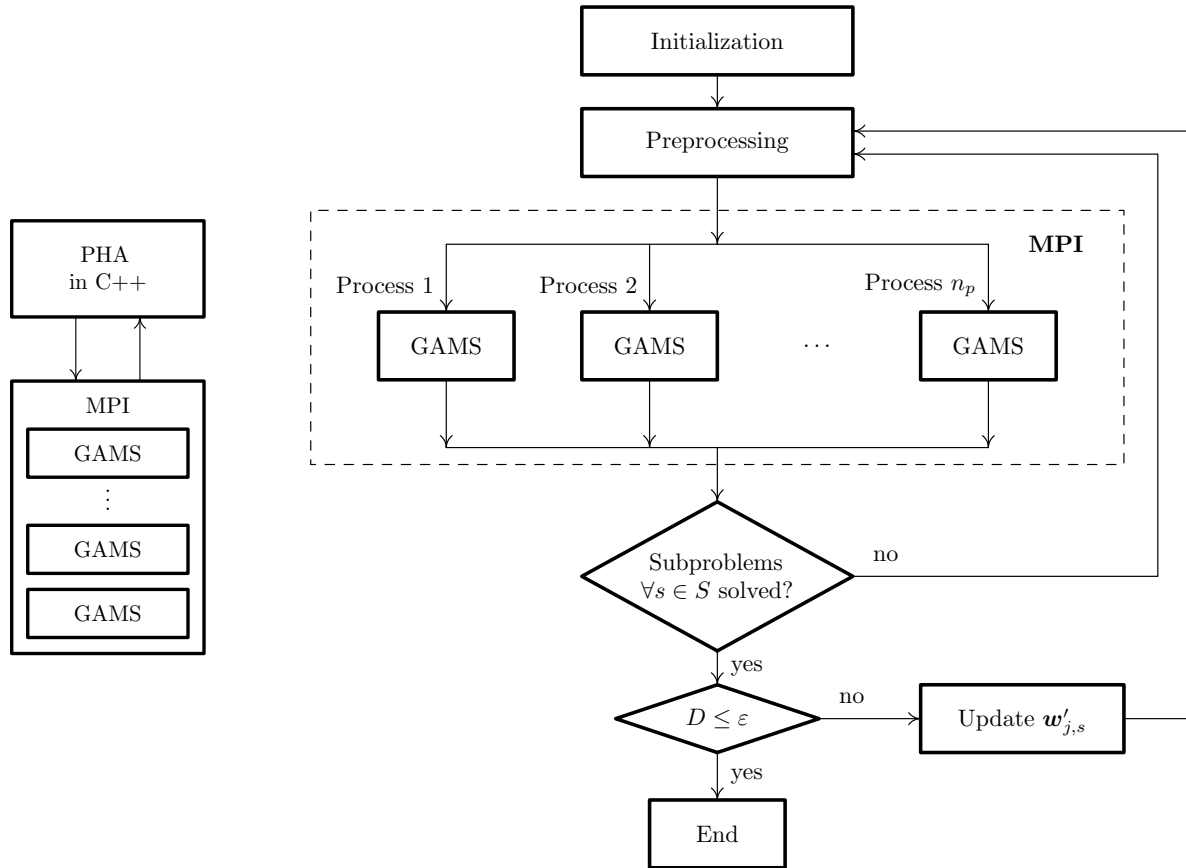


Fig. 5. The block diagram (left) and the flow chart (right) of the parallel implementation of the progressive hedging algorithm.

GAMS. The General Algebraic Modelling System (GAMS) is one of modelling systems applicable to the solution of optimization problems. Various solvers designed for linear, non-linear, integer or mixed integer optimization problems are available. The use of distinct non-linear solvers was investigated. In conclusion, the non-linear solver CONOPT [9] having the best performance was used for the solution of scenario-based sub-problems of the progressive hedging algorithm.

5. NUMERICAL RESULTS AND DISCUSSION

The parallel implementation of the progressive hedging algorithm described in Section 4 was used to solve the two-stage stochastic problem of the steel production described in Section 4.2. The steel-maker is interested in the following questions: “How should the casting machine be set up in order to maximize its productivity but with regard to a failure in the secondary cooling zone which can occur with a given probability?” And in case the failure does occur: “How should the first-stage setup of the machine be modified to preserve optimal casting conditions?”

5.1. Input parameters

As already mentioned in the introduction, we consider the casting machine with four cooling loops, and therefore $n_{CC} = 4$. Further, we consider that the pump fail can occur in the second cooling loop ($i = 2$) of the secondary cooling; two scenarios s_0 and s_2 are therefore taken into account. The selection of the second cooling loop for a random fail of the pump is justifiable from the metallurgical point of view as follows; among all the loops the second cooling loop is crucial for the steel quality since the liquid pool (liquid phase) ends here (see Figure 1) and any fluctuations in the temperature and in the heat withdrawal can cause the formation of separated liquid bulks surrounded by the solid steel leading to serious defects such as interior cracks or non-homogeneity [4].

A low carbon steel grade with the solidus and liquidus temperatures of 1490°C and 1515°C , respectively, was taken into account. The half strand with the height of 125 mm and with the length of 20 m was considered. The spatial domain consisted of 400 control volumes and the time domain of 5 minutes was divided into 300 steps with the time step of 1 s. The scenario-based sub-problem therefore includes about 120 000 variables. The thermal conductivity of steel was 35 W/m K and the ambient air temperature was 20°C . The heat flux withdrawn from the mould of 3 kW/m^2 was assumed. The constraints for the heat transfer coefficients, see Eq. (11), were $h_1 = 500\text{ W/m}^2\text{K}$, $h_2 = 400\text{ W/m}^2\text{K}$, $h_3 = 400\text{ W/m}^2\text{K}$ and $h_4 = 300\text{ W/m}^2\text{K}$. The constraints for the surface temperatures at the control points, see Eq. (12), are presented in Table 1.

Constraint	Control point				
	Q_1	Q_2	Q_3	Q_4	Q_5
$T_{j,\min}$	1300°C	1050°C	900°C	700°C	700°C
$T_{j,\max}$	1480°C	1250°C	1000°C	900°C	800°C

Tab. 1. Temperature constraints for the control points.

5.2. Set-up of scenarios

The problem with two scenarios s_0 and s_2 is considered. The scenario s_0 is used for the failure-free situation in the casting process and its probability was $p_0 = 0.95$. The scenario s_2 models the failure of the pump in the second cooling loop of the secondary cooling zone and its probability is $p_2 = 0.05$. Without the loss of generality of the presented stochastic model, we consider the simplified case with a possible fail in one particular cooling loop. It should be noted here that the above presented stochastic problem is formulated for the two-stage structure with a general number of scenarios and additional scenarios can be added straightforwardly to the model along with constraints. The described simplification will lead to the stochastic steel production problem with two scenarios. A problem including two scenarios may seem to be quite non-comprehensive. However, it should be noted that an attempt to solve the complete (non-decomposed) steel production programme including the two scenarios was made with no success as the problem exceeded the computational capability of the CONOPT solver. On the other

hand, the PHA separates the problem into scenario-related sub-problems which are simpler and solvable by the CONOPT solver. The decomposition principle is therefore a crucial point in the solution of the steel production problem under uncertainty by means of the PHA even for small number of scenarios.

Though the simplified problem with two scenarios was considered, such solution is still quite realistic and applicable in practice. The reason is that the casting problem with a possible failure generally does not require a large number of scenarios for the description of various combinations of failures in cooling loops. The possibility of multiple breakdowns in distinct cooling loops is very low as individual cooling loops are operated by independent pumps and control systems. As explained above, a failure in the second cooling loop was selected since the second cooling loop controls the end of solidification zone in the strand having an important influence on the quality. The second cooling loop can be therefore considered as the most important loop in the secondary cooling zone. As for computational requirements of the proposed PHA implementation, the method is definitely not applicable for real-time applications. However, the PHA implementation can reasonably be used for a pre-calculation of various failure situations in advance and their solutions can be then concatenated into a solution manual applicable by operators of the casting machine in failure cases.

For the failure-free scenario s_0 , the void second-stage decision $h''_{m,s_0} = 0$ for $m = 1, 2, 3, 4$ is obviously required (see Eq. (17)) since the operators of the casting machine modify its setting only in case of the failure. As for the scenario s_2 , the failure situation within the second cooling loop at the time $t_f = 60$ s occurs, and thus $h'_{2,s_2} + h''_{2,s_2} = 0$ (see Eq. (19)).

5.3. Discussion on parameters

The problem was solved with the use of a computer running 64-bit Ubuntu operating system equipped with Intel Quad CPU having four cores and 8 GB of the RAM memory. A crucial point in case of the practical application of the PHA is the choice of the penalty parameter ϱ since the penalty parameter can significantly influence the feasibility of iteratively generated solutions and the convergence of the PHA. An improper value of the penalty parameter can considerably increase the number of iterations required by the PHA, or it may even lead to divergence (oscillatory behaviour) of the algorithm. The penalty parameter can be considered a constant value or it can vary through iterations [25]. Unfortunately, there is no general procedure for the determination of a suitable value of ϱ . Due to this reason a trial-and-error approach is often used by users of the PHA. In the paper we determined the penalty parameter ϱ to 10^{-3} . The termination parameter D was set to 10^{-9} .

5.4. Results

Efficiency of the parallel MPI implementation. The parallel MPI implementation of the PHA was used to solve the presented two-stage stochastic steel production problem. The PHA required 74 iterations performed in about 14 hours and 30 min of the computational time. After 74 iterations the algorithm converged to an optimal solution. The solution of a scenario-related sub-problem (in a particular iteration of the PHA)

Stage	Scenario	Decision	Casting parameters				
			h_1	h_2	h_3	h_4	v_z
First	s_0, s_2	\mathbf{x}'	$476 \frac{\text{W}}{\text{m}^2\text{K}}$	$249 \frac{\text{W}}{\text{m}^2\text{K}}$	$309 \frac{\text{W}}{\text{m}^2\text{K}}$	$87 \frac{\text{W}}{\text{m}^2\text{K}}$	$2.2156 \frac{\text{m}}{\text{min}}$
Second	s_0	\mathbf{x}''_1	$0 \frac{\text{W}}{\text{m}^2\text{K}}$	$0 \frac{\text{W}}{\text{m}^2\text{K}}$	$0 \frac{\text{W}}{\text{m}^2\text{K}}$	$0 \frac{\text{W}}{\text{m}^2\text{K}}$	$2.2156 \frac{\text{m}}{\text{min}}$
Second	s_2	\mathbf{x}''_2	$24 \frac{\text{W}}{\text{m}^2\text{K}}$	$-249 \frac{\text{W}}{\text{m}^2\text{K}}$	$-240 \frac{\text{W}}{\text{m}^2\text{K}}$	$-15 \frac{\text{W}}{\text{m}^2\text{K}}$	$1.8366 \frac{\text{m}}{\text{min}}$

Tab. 2. The first-stage and second-stage decisions to the steel production problem determined with the use of the PHA.

took about 12 min in average and two sub-problems (two scenarios) were concurrently solved via MPI at the same time. On the other hand, the computational time required by the PHA to load results, compute the aggregated solution, update the weights, evaluate the termination condition and to assemble the GAMS files for the next iteration was virtually negligible and less than 1 s. From that point of view the parallel implementation enabled the reduction of the computational time to about a half in the comparison to a sequential (non-parallel) processing.

Solution to the two-stage steel production problem. The scenario-dependent optimal decisions are presented in Table 2. The first-stage “here-and-now” decision \mathbf{x}' is scenario-independent due to the non-anticipativity as mentioned in Section 4.3. The value of the objective function (i. e. the casting speed v_z) corresponding to the first-stage decision is equal to 2.216 m/min.

In case the failure does not occur in the secondary cooling zone (scenario s_0), the second-stage “wait-and-see” decision \mathbf{x}''_1 prescribes no change in the casting parameters. This means that the casting parameters in the second stage are $\mathbf{x}' + \mathbf{x}''_1 = \mathbf{x}'$ with the casting speed unchanged. On the other hand, if the failure in the second loop of the secondary cooling zone does occur, the second stage decision \mathbf{x}''_2 is applied by the operator of the casting machine according to Table 2. In that case the casting parameters are updated to $\mathbf{x}' + \mathbf{x}''_2$. Observe that the heat transfer coefficient for the second cooling loop h_2 is equal to $0 \frac{\text{W}}{\text{m}^2\text{K}}$ as it is used to simulate the failure. Since there is almost no heat withdrawal from the strand in the second loop, the casting speed has to be reduced to 1.8366 m/min in order to fulfil the temperature constraints and the range of the metallurgical length given by Eqs. (12) and (13), respectively.

The resultant temperature distributions of the strand for the failure-free scenario s_0 and for the scenario with the failure s_2 are shown in Figures 6 and 8, respectively. The temperature profiles at the selected longitudinal cross-sections of the strand are pictured in Figures 7 and 9. As can be seen in the figures, the temperature distributions for both the scenarios fulfil quite well the requirement of the gradual decrease of the temperature. In case of the scenario with the failure, there is a small reheating at the surface (see Figure 9) at the distance of about 6 m from the mould. However, such reheating is only local with the peak of about 150 °C and it can therefore be accepted by metallurgists with no negative influence on the surface quality of the strand.

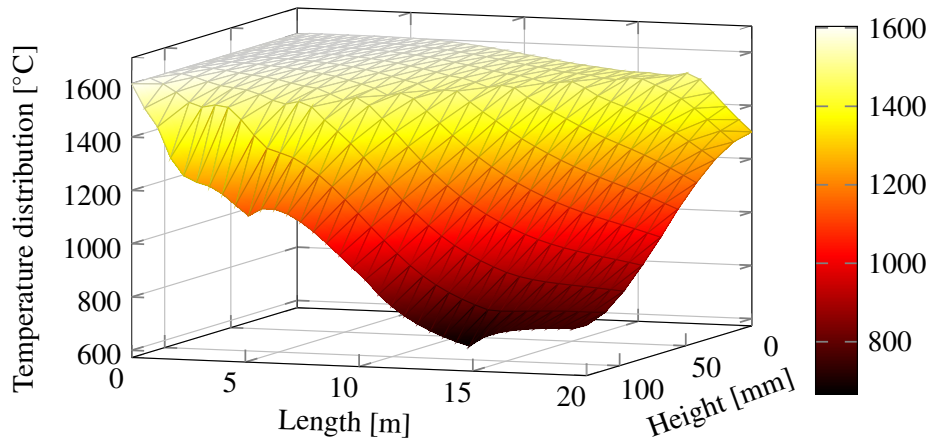


Fig. 6. The resultant temperature distribution of the strand for the failure-free scenario s_0 .

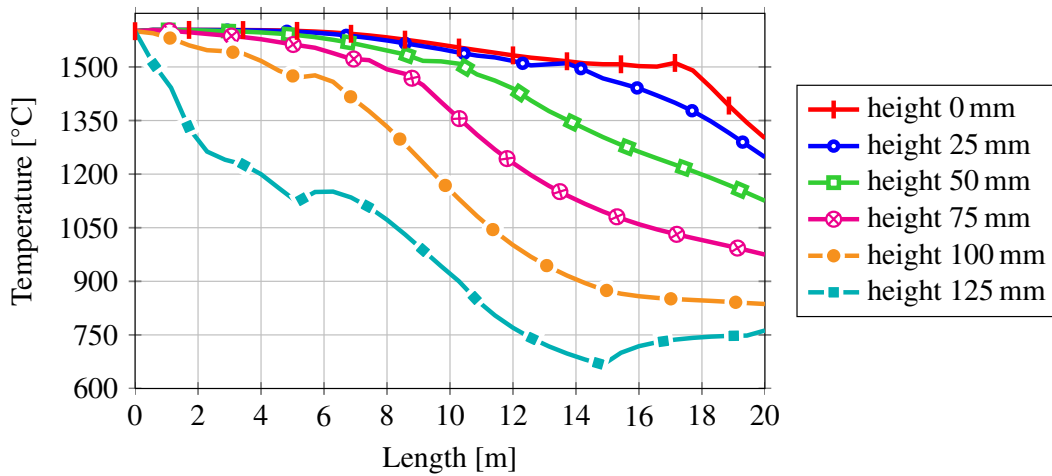


Fig. 7. The temperature profiles in the longitudinal cross-sections of the strand for the failure-free scenario s_0 .

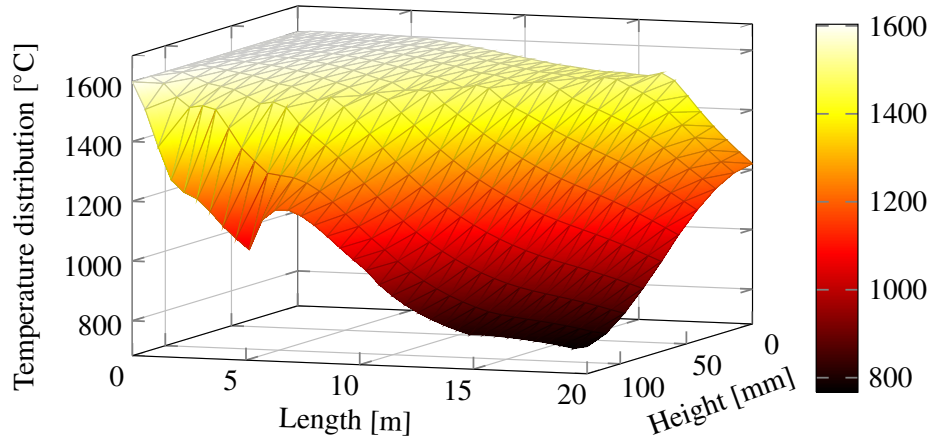


Fig. 8. The resultant temperature distribution of the strand for the scenario s_2 with the failure.

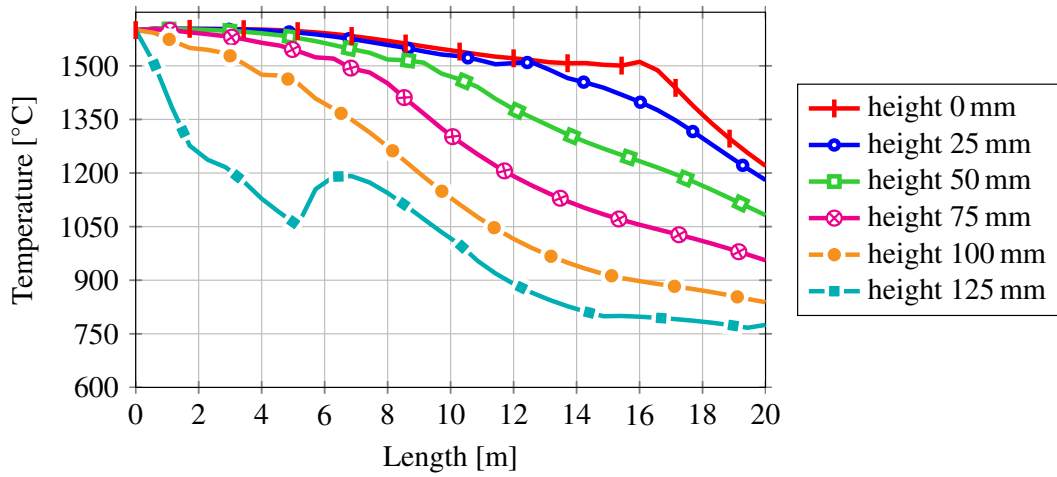


Fig. 9. The temperature profiles in the longitudinal cross-sections of the strand for the scenario s_2 with the failure.

5.5. Evaluation of the results

As mentioned in Section 4 the progressive hedging algorithm was used to determine the solution to the expected objective (EO) problem having the general form

$$\begin{cases} \text{minimize} & \mathbb{E}_{\xi}(f(\mathbf{x}, \xi)) \\ \text{subject to} & \mathbf{x} \in X : \mathbf{g}(\mathbf{x}, \xi) = \mathbf{0}, \mathbf{h}(\mathbf{x}, \xi) \leq \mathbf{0} \text{ almost surely.} \end{cases} \quad (23)$$

In general, it is more difficult to solve the EO problem (23) than the simpler expected value (EV) problem (24)

$$\begin{cases} \text{minimize} & f(\mathbf{x}, \mathbb{E}(\boldsymbol{\xi})) \\ \text{subject to} & \mathbf{x} \in X: \mathbf{g}(\mathbf{x}, \mathbb{E}(\boldsymbol{\xi})) = \mathbf{0}, \mathbf{h}(\mathbf{x}, \mathbb{E}(\boldsymbol{\xi})) \leq \mathbf{0} \end{cases} \quad (24)$$

as the EV formulation reduces the stochastic problem into the deterministic problem because the random variables are replaced by their expected values [3].

Value of stochastic solution (VSS). The VSS is the useful measure for the evaluation of the potential profit which can be obtained if the EO problem (23) is solved instead of the EV problem (24). The VSS is defined as [3]

$$\text{VSS} = \text{EEV} - \mathbb{E}_{\boldsymbol{\xi}}(f(\mathbf{x}_{\text{EO}}, \boldsymbol{\xi})) \quad (25)$$

where \mathbf{x}_{EO} is the optimal solution to the problem (23) and the EEV is called the expected result of using EV solution [3], $\text{EEV} = \mathbb{E}_{\boldsymbol{\xi}}(f(\mathbf{x}_{\text{EV}}, \boldsymbol{\xi}))$ where \mathbf{x}_{EV} is the optimal solution to the problem (24). The EV solution instead of the EO solution can be well applied in cases having small values of the VSS. On the other hand, the higher the value of the VSS the higher the profit that can be acquired using the EO solution instead of the EV solution.

The EV formulation of the steel production problem presented in the paper was solved and the values of the objective function are 2.1885 m/min and 1.8355 m/min for the failure-free scenario s_0 and for the scenario with the failure s_2 , respectively. The value of the EEV is 2.1709 m/min and the VSS for the maximization problem then is

$$\text{VSS} = \mathbb{E}_{\boldsymbol{\xi}}(f(\mathbf{x}_{\text{EO}}, \boldsymbol{\xi})) - \text{EEV} = 0.0258 \text{ m/min}. \quad (26)$$

Though the value of the VSS is rather small, the profit in the strand production of 2.6 cm per minute is not negligible when considering the 24-hour casting operation and the price of the steel strand between 1,000 € and 10,000 € per meter. Moreover, in case of the failure the important aim of steelworkers is not only to optimally solve the problem from the point of the maximum productivity. A crucial task is to maintain the casting process in operation and to provide sufficient time for a repair/solution of the failure. In some cases, a failure in the secondary cooling zone could cause a serious breakout situation in which the solid shell at the surface of the strand cracks and the molten steel inside the strand then leaks out stopping the casting machine for several days.

Expected value of perfect information (EVPI). The EVPI, another useful measure, evaluates the profit which can be acquired in case the full information about the future is available [3]. The EVPI therefore states the maximum amount of “money” which is reasonable to pay for information about the future. The EVPI is defined as

$$\text{EVPI} = \mathbb{E}_{\boldsymbol{\xi}}(f(\mathbf{x}_{\text{EO}}, \boldsymbol{\xi})) - z_{\text{WS}} \quad (27)$$

where z_{WS} is the objective value of the wait-and-see (WS) deterministic formulation to the problem, see [3]. The WS formulation of the steel production problem presented

in the paper was solved. The values of the objective function are 2.2158 m/min and 1.8396 m/min for the failure-free scenario s_0 and for the scenario with the failure s_2 , respectively. The value of z_{WS} is 2.1970 m/min and the EVPI for the maximization problem is then

$$\text{EVPI} = z_{WS} - \mathbb{E}_{\xi}(f(\mathbf{x}_{EO}, \xi)) = 0.0003 \text{ m/min.} \quad (28)$$

Nonetheless, the information about the future is usually not available at any price in technical optimization problems. The VSS is therefore more informative parameter in the studied steel production problem than the EVPI.

6. CONCLUSIONS

The parallel implementation of the two-stage progressive hedging algorithm (PHA) is presented. The Message Passing Interface (MPI) was used for the parallel run of the General Algebraic Modelling System (GAMS) which solves the scenario-based sub-problems. The standalone application wrapping the PHA, MPI, and GAMS was created in C++. The applicability of the developed software was demonstrated for the solution of the two-stage PDE-constrained steel production problem considering a random failure. The discretization of the heat transfer model with phase changes for the steel production by means of the control volume method is discussed. The evaluation of the solution quality is presented and the proposed computational approach seems effective and sufficiently robust for similar kinds of problems. The further research will be mainly aimed at the improvement of the heat transfer model of continuous casting as numerous simplifications were made. Due to requirements from the steel industry, the attention has recently also focused on real-time control algorithms based on predictive control and fuzzy logic approach.

ACKNOWLEDGEMENT

This work was supported by the Czech Science Foundation under the contract GA15-11977S “An adaptive front tracking method for parallel computing of phase change problems”.

(Received December 4, 2016)

REFERENCES

-
- [1] A. Alquarashi, A. H. Etemadi, and A. Khodaei: Treatment of uncertainty for next generation power systems: State-of-the-art in stochastic optimization. *Electr. Power Syst. Res.* *141* (2016), 233–245. DOI:10.1016/j.epsr.2016.08.009
 - [2] M. Barttfeld, N. Alleborn, and F. Durst: Dynamic optimization of multiple-zone air impingement drying process. *Comput. Chem. Engrg.* *30* (2006), 467–489. DOI:10.1016/j.compchemeng.2005.10.016
 - [3] J. R. Birge and F. Louveaux: *Introduction to Stochastic Programming*. Springer, New York 2011.
 - [4] J. K. Brimacombe and K. Sorimachi: Crack formation in continuous-casting of steel. *Metal. Trans. B. Proc. Metal.* *8* (1977), 489–505. DOI:10.1007/bf02696937

- [5] E. P. Carvalho, J. Martínez, J. M. Martínez, and F. Pisnitchenko: On optimization strategies for parameter estimation in models governed by partial differential equations. *Math. Comput. Simul.* *114* (2015), 14–24. DOI:10.1016/j.matcom.2010.07.020
- [6] M. Carrasco, B. Ivorra, and A. M. Ramos: Stochastic topology design optimization for continuous elastic materials. *Comput. Meth. Appl. Mech. Engrg.* *289* (2015), 131–154. DOI:10.1016/j.cma.2015.02.003
- [7] P. L. Carpentier, M. Gendreau, and F. Bastin: Long-term management of a hydroelectric multireservoir system under uncertainty using the progressive hedging algorithm. *Water Resour. Res.* *49* (2013), 2812–2827. DOI:10.1002/wrcr.20254
- [8] Y. M. Cheng, D. Z. Li, N. Li, Y. Y. Lee, S. K. Au: Solution of some engineering partial differential equations governed by the minimal of a functional by global optimization method. *J. Mech.* *29* (2013), 507–516. DOI:10.1017/jmech.2013.26
- [9] A. Drud: CONOPT – A GRG code for large sparse dynamic nonlinear optimization problems. *Math. Program.* *31* (1985), 153–191. DOI:10.1007/bf02591747
- [10] D. Gade, G. Hackebeil, S. M. Ryan, J.-P. Watson, R. J.-B. Wets, and D. L. Woodruff: Obtaining lower bounds from the progressive hedging algorithm for stochastic mixed-integer programs. *Math. Prog.* *157* (2016), 47–67. DOI:10.1007/s10107-016-1000-z
- [11] R. E. C. Gonçalves, E. C. Finardi, and E. L. da Silva: Applying different decomposition schemes using the progressive hedging algorithm to the operation planning problem of a hydrothermal system. *Electr. Power Syst. Res.* *83* (2012), 19–27. DOI:10.1016/j.epsr.2011.09.006
- [12] S. Gul, B. T. Denton, and J. W. Fowler: A progressive hedging approach for surgery planning under uncertainty. *INFORMS J. Comput.* *27* (2015), 755–772. DOI:10.1287/ijoc.2015.0658
- [13] S. Ikeda and R. Ooka: A new optimization strategy for the operating schedule of energy systems under uncertainty of renewable energy sources and demand changes. *Energ. Build.* *125* (2016), 75–85. DOI:10.1016/j.enbuild.2016.04.080
- [14] T. L. Bergman, A. S. Lavine, F. P. Incropera, and D. P. Dewitt: *Fundamentals of Heat and Mass Transfer*. Seventh edition. Wiley, New York 2011.
- [15] L. Klimeš: *Stochastic Programming Algorithms*. Master Thesis. Brno University of Technology, 2010.
- [16] L. Klimeš and P. Popela: An implementation of progressive hedging algorithm for engineering problem. In: *Proc. 16th International Conference on Soft Computing MENDEL, Brno 2010*, pp. 459–464.
- [17] L. Klimeš, P. Popela, and J. Štětina: Decomposition approach applied to stochastic optimization of continuous steel casting. In: *Proc. 17th International Conference on Soft Computing MENDEL, Brno 2011*, pp. 314–319.
- [18] L. Klimeš, T. Mauder, and J. Štětina: Stochastic approach and optimal control of continuous steel casting process by using progressive hedging algorithm. In: *Proc. 20th International Conference on Materials and Metallurgy METAL, Brno 2011*, pp. 146–151.
- [19] M. La Marca, D. Armbruster, M. Herty, and C. Ringhofer: Control of continuum models of production systems. *IEEE Trans. Automat. Control* *55* (2010), 2511–2526. DOI:10.1109/tac.2010.2046925
- [20] A. Lamghari and R. Dimitrakopoulos: Progressive hedging applied as a metaheuristic to schedule production in open-pit mines accounting for reserve uncertainty. *Eur. J. Oper. Res.* *253* (2016), 843–855. DOI:10.1016/j.ejor.2016.03.007

- [21] J. Liu and C. Liu: Optimization of mold inverse oscillation control parameters in continuous casting process. *Mater. Manuf. Process.* *30* (2015), 563–568. DOI:10.1080/10426914.2015.1004696
- [22] K. C. Mills, P. Ramirez-Lopez, P. D. Lee, B. Santillana, B. G. Thomas, and R. Morales: Looking into continuous casting mould. *Ironmak. Steelmak.* *41* (2014), 242–249. DOI:10.1179/0301923313z.000000000255
- [23] T. Mauder, F. Kavička, J. Štětina, Z. Franěk, and M. Masarik: A mathematical & stochastic modelling of the concasting of steel slabs. In: *Proc. International Conference on Materials and Metallurgy, Hradec nad Moravicí 2009*, pp. 41–48.
- [24] T. Mauder and J. Novotný: Two mathematical approaches for optimal control of the continuous slab casting process. In: *Proc. 16th International Conference on Soft Computing MENDEL, Brno 2010*, pp. 41–48.
- [25] R. T. Rockafellar and R. J.-B. Wets: Scenarios and policy aggregation in optimization under uncertainty. *Math. Oper. Res.* *16* (1991), 119–147. DOI:10.1287/moor.16.1.119
- [26] A. Ruszczyński and A. Shapiro: *Stochastic Programming Models*. Handbooks in Operations Research and Management Science, Volume 10: Stochastic Programming, Elsevier, Amsterdam 2003. DOI:10.1016/s0927-0507(03)10001-1
- [27] A. Shioura, N. V. Shakhlevich, and V. A. Strusevich: Application of submodular optimization to single machine scheduling with controllable processing times subject to release dates and deadlines. *INFORMS J. Comput.* *28* (2016), 148–161. DOI:10.1287/ijoc.2015.0660
- [28] D. M. Stefanescu: *Science and Engineering of Casting Solidification*. Second edition. Springer, New York 2009.
- [29] J. Štětina, L. Klimeš, and T. Mauder: Minimization of surface defects by increasing the surface temperature during the straightening of a continuously cast slab. *Mater. Tehnol.* *47* (2013), 311–316.
- [30] H. Ugail and M. J. Wilson: Efficient shape parametrisation for automatic design optimisation using a partial differential equation formulation. *Comput. Struct.* *81* (2003), 2601–2609. DOI:10.1016/s0045-7949(03)00321-3
- [31] P. Varaiya and R. J.-B. Wets: Stochastic dynamic optimization approaches and computation. In: *Proc. 13th International Symposium on Mathematical Programming, Tokio 1989*, pp. 309–331. DOI:10.1007/978-3-642-82450-0_11
- [32] F. B. Veliz, J. P. Watson, A. Weintraub, R. J.-B. Wets, and D. L. Woodruff: Stochastic optimization models in forest planning: a progressive hedging solution approach. *Ann. Oper. Res.* *232* (2015), 259–274. DOI:10.1007/s10479-014-1608-4
- [33] B. G. V. Waanders and B. R. Carnes: Optimization under adaptive error control for finite element based simulations. *Comput. Mech.* *47* (2011), 49–63. DOI:10.1007/s00466-010-0530-0
- [34] R. J.-B. Wets: The aggregation principle in scenario analysis and stochastic optimization. In: *Algorithms and Model Formulations in Mathematical Programming* (S. W. Wallace, ed.), Springer, Berlin 1989. DOI:10.1007/978-3-642-83724-1_4
- [35] Z. Yang, H. L. Qui, X. W. Luo, and D. Shen: Simulating schedule optimization problem in steelmaking continuous casting process. *Int. J. Simul. Model.* *14* (2015), 710–718. DOI:10.2507/ijssimm14(4)co17

- [36] J. Yang, Z.P. Ji, S. Liu, and Q. Jia: Multi-objective optimization based on pareto optimum in secondary cooling and EMS of continuous casting. In: Proc. International Conference on Advanced Robotics and Mechatronics (ICARM), Macau 2016, pp. 283–287. DOI:10.1109/icarm.2016.7606933
- [37] E. Žampachová, P. Popela, and M. Mrázek: Optimum beam design via stochastic programming. *Kybernetika* 46 (2010), 571–582.
- [38] M.H. F. Zarandi, F. Dorry, and F.S. Moghadam: Steelmaking-continuous casting scheduling problem with interval type 2 fuzzy random due dates. In: Proc. IEEE Conference on Norbert Wiener in the 21st Century (21CW), Boston 2014. DOI:10.1109/norbert.2014.6893896

Lubomír Klimeš, Brno University of Technology, Energy Institute, Technická 2896/2, 616 69 Brno. Czech Republic.

e-mail: klimes@fme.vutbr.cz

Pavel Popela, Brno University of Technology, Institute of Mathematics, Technická 2896/2, 616 69 Brno. Czech Republic.

e-mail: popela@fme.vutbr.cz

Tomáš Mauder, Brno University of Technology, Energy Institute, Technická 2896/2, 616 69 Brno. Czech Republic.

e-mail: mauder@fme.vutbr.cz

Josef Štětina, Brno University of Technology, Energy Institute, Technická 2896/2, 616 69 Brno. Czech Republic.

e-mail: stetina@fme.vutbr.cz

Pavel Charvát, Brno University of Technology, Energy Institute, Technická 2896/2, 616 69 Brno. Czech Republic.

e-mail: charvat@fme.vutbr.cz

UNSTEADY MODEL-BASED PREDICTIVE CONTROL OF CONTINUOUS STEEL CASTING BY MEANS OF A VERY FAST DYNAMIC SOLIDIFICATION MODEL ON A GPU

PREDVIDEVANJE KONTROLE KONTINUIRNEGA LITJA NA PODLAGI NERAVNOTEŽNEGA MODELA Z ZELO HITRIM DINAMIČNIM MODELOM STRJEVANJA NA GPU

Lubomir Klimes, Josef Stetina

Brno University of Technology, Faculty of Mechanical Engineering, Energy Institute, Technicka 2896/2, 616 69 Brno, Czech Republic
klimes@fme.vutbr.cz, stetina@fme.vutbr.cz

Prejem rokopisa – received: 2013-10-01; sprejem za objavo – accepted for publication: 2013-10-07

The aim of the paper is to develop and test a model-based predictive control system for continuous casting of steel billets with an emphasis on unsteady casting situations, often accompanied by abrupt changes in the casting speed. A very fast dynamic solidification model was developed for this purpose. This fully 3D model runs on graphics processing units, GPUs, and it is significantly faster than the recently used commercial models. Therefore, a scenario approach can be utilized, which means that the control system, in real time, predicts and evaluates the thermal behavior of cast billets for various scenarios of the control strategy. The concept of the effective casting speed was utilized for the proposed control strategies. The results show that the developed control system can provide an effective control of the casting process and brings new control possibilities for continuous steel casting.

Keywords: continuous casting, model-based predictive control, effective casting speed, dynamic solidification model, GPU, computing

Namen prispevka je razvoj in preizkušanje nadzornega sistema kontinuirnega ulivanja gredic, ki temelji na modelu napovedovanja, z upoštevanjem neenakomernih razmer pri litju, pogosto spremljanih z nenadnimi spremembami hitrosti ulivanja. Za ta namen je bil razvit zelo hiter dinamičen model strjevanja. To je popoln 3D-model, ki teče na grafičnih procesnih enotah GPU in je bistveno hitrejši kot pred kratkim uporabljeni komercialni modeli. Zato se lahko uporabi scenarijski način, kar pomeni, da sistem nadzora v realnem času napoveduje in ocenjuje toplotno vedenje litih gredic pri različnih scenarijih strategije kontrole. Za predlog nadzornih strategij je bil uporabljen koncept učinkovite hitrosti ulivanja. Rezultati kažejo, da razviti sistem nadzora ponuja učinkovito metodo nadzora procesa litja in prinaša nove možnosti nadzora pri kontinuirnem ulivanju jekla.

Ključne besede: kontinuirno ulivanje, napovedovanje na osnovi modela, učinkovita hitrost litja, dinamični model strjevanja, GPU, računalništvo

1 INTRODUCTION

Recently, the optimum control of continuous casting has been among the main objectives of steelmakers around the world. A proper control, especially in the secondary cooling with water or air-mist cooling nozzles, is an essential issue directly related to productivity and quality. Various techniques and approaches can be used for this purpose. An experimental setup of a casting machine is seldom used due to a large complexity of the problem and due to fallible results. Instead, many researchers and steelmakers use numerical dynamic solidification models. These systems enable the calculations of the temperature field of a cast blank and its solidification and they can be, therefore, used for the casting control,^{1,2} its optimization³⁻⁵ and for investigating the thermal behavior.^{6,7}

The crucial issue of dynamic solidification models in relation to casting control is their computational demands limiting their wider use in the production control process. In particular, a dynamic solidification model usually computes the transient heat transfer and the temperature distribution of an entire cast blank in specified

points, in the so-called computing grid. This procedure generates a large amount of calculations (in order of billions) determining the transient temperature field of cast blanks. The recently used commercial dynamic solidification models use the state-of-the-art CPU computing and perform these calculations within tens of minutes. Nevertheless, tens of minutes are rather long times to utilize the solidification models for the real-time control or optimization of a casting process. However, a new computing approach has recently become available for highly parallelizable problems. This technique, called the GPGPU (general-purpose computing on graphics processing units), utilizes the computing on graphics cards, GPUs. A GPU, though primarily intended for the use in computer graphics and gaming, consists of a large number (from hundreds to thousands) of rather simple processors allowing a huge computing performance that can be used for solving various scientific and technical problems. The GPGPU has been mainly used for the simulations of molecular dynamics,⁸ image processing⁹ and Monte Carlo simulations.¹⁰ In spite of this, only a few papers relating to heat-transfer problems have been pub-

lished¹¹ by researchers and none of these covers continuous casting. However, Klimes and Stetina^{12,13} recently published papers on the use of the GPGPU for a parallel dynamic solidification model of continuous casting on a GPU and the results show that the GPGPU can greatly enhance the computing performance of solidification models, allowing a significant reduction in the computing time and, therefore, new opportunities for the use of solidification models in the optimum casting control have become available.

Based on the literature review, researchers have recently used various approaches to the optimum control of the continuous casting process: frequently by applying PI or PID controllers,¹ probabilistic metaheuristics (e.g., simulated annealing²), heuristic searches,³ fuzzy logic techniques⁴ or mathematical programming methods⁵. However, several issues may appear when these methods are used or intended for a practical use in steelworks. One of the most important issues of PI and PID controllers is that they regulate a process according to the history of that process. Considering a system delay, it means that the regulation may react improperly. Heuristic methods and, particularly, the approaches via mathematical programming suffer from huge computational demands, usually because of the repeated computations of the model. This issue can, therefore, significantly prolong the regulation process and, for this reason, the use of these methods is often limited in a real-time regulation.

Due to the above reasons and encouraged by the computational performance of the developed parallel dynamic solidification model running on a GPU, the aim was to propose a new control approach for continuous casting. For this purpose the model-based predictive-control (MPC) approach was selected. One of the features of the MPC is that it uses a model as a numerical sensor to predict the future evolution of a controlled process under certain conditions.

2 PARALLEL DYNAMIC SOLIDIFICATION MODEL RUNNING ON A GPU

Nowadays, commercial dynamic solidification models for continuous steel casting utilize the state-of-the-art computing on central processing units (CPUs). These models usually solve heat transfer and solidification of cast blanks in discretized points (in a number of hundreds of thousands or millions) and these models require tens of minutes to compute the stationary state under constant casting conditions.¹² These models are, therefore, rather awkward for a fast and real-time regulation due to time-consuming computations. However, many computational problems with a possibility to be parallelized can be computed more efficiently with the use of GPGPU techniques and graphics processing units (GPUs).¹⁴ The GPGPU divides a computational problem into independent parts that can be computed concurrently in a parallel manner. For this reason a GPU

consists of many simple computing units that are designed to process an identical code, but on different data. The number of units depends on the type of the GPU, generally varying between several hundreds and several thousands.

The transient heat transfer and the solidification of cast blanks can be modeled with the Fourier-Kirchhoff equation:

$$\frac{\partial H}{\partial t} = \nabla \cdot (k \nabla T) + v_z \frac{\partial H}{\partial z} \quad (1)$$

where H is the volume enthalpy (J m^{-3}), T is the temperature (K), t is the time (s), k is the thermal conductivity ($\text{W m}^{-1} \text{K}^{-1}$), v_z is the casting speed (m s^{-1}) and z is the spatial coordinate (m) in the direction of casting. The mass-transfer and fluid-flow phenomena inside a blank are usually neglected, but they can also be considered, e.g., with the use of the effective heat-conductivity approach. The volume enthalpy that appears in Equation (1) is used to include the latent heat released during the solidification.¹⁵ This thermodynamic function can be defined as:

$$H(T) = \int_0^T \left(\rho c - \rho L_f \frac{df_s}{d\theta} \right) d\theta \quad (2)$$

where ρ is the density (kg m^{-3}), c is the specific heat ($\text{J kg}^{-1} \text{K}^{-1}$), L_f is the latent heat (J kg^{-1}) and f_s is the solid fraction (1).

The developed parallel dynamic solidification model for continuous casting of steel billets (**Figure 1**) based on Equation (1) and the necessary initial and boundary conditions was created using the control-volume method and explicit time discretization.^{12,13} The heat withdrawal from the mould, within the secondary cooling zones with the cooling nozzles and other casting conditions, can be adjusted through the initial and boundary conditions. The explicit discretization in time is an essential condition for the parallel model, allowing it to run on GPUs. Basically, the calculations related to various control volumes are solved concurrently by various computing units of a GPU.^{12,13} The CUDA C/C++ computing architecture was

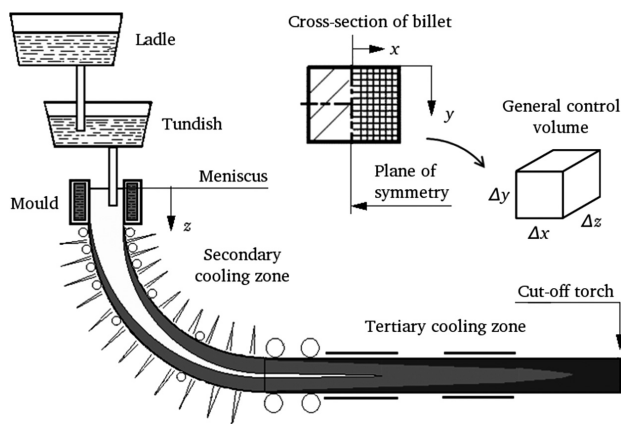


Figure 1: Billet caster and the mesh definition

Slika 1: Naprava za ulivanje gredic in določanje mreže

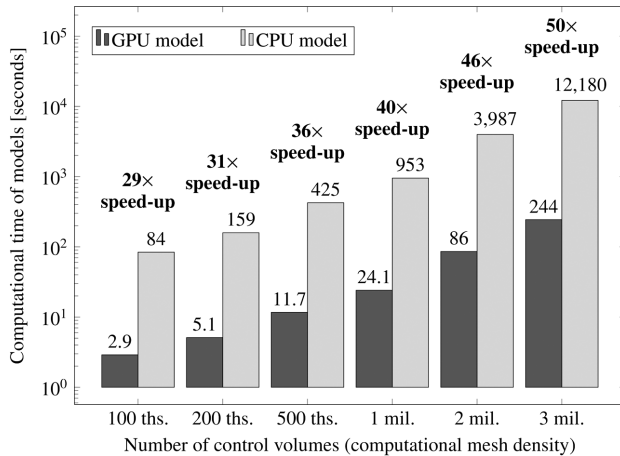


Figure 2: Comparison of computational performances between GPU and CPU dynamic solidification models

Slika 2: Primerjava računske zmogljivosti med GPU in CPU pri dinamičnih modelih strjevanja

used for the development of the presented solidification model.¹⁶

A comparison of the computing performances between the developed parallel solidification model running on a GPU and an identical model utilizing the state-of-the-art computing on a CPU is shown in **Figure 2**. The results are presented for various numbers of control volumes (i.e., for various computational mesh densities) and identical casting conditions.¹² GPU NVIDIA Tesla C2075 having 448 computing units was used as the representative of GPUs. The CPU model was run on a computer with Intel Core 2 Quad CPU with 4 cores, each having a frequency of 2.4 GHz. As can be seen from **Figure 2**, the GPGPU computing can greatly enhance the computational performance of the solidification models. For the mesh with 100000 control volumes, the GPU model processes the computations in only about 3 s which is 30-times faster than in the case of the model running on a CPU. Moreover, with an increasing mesh density the parallelism and the computational performance of the GPU become more significant: in the case of 3 million control volumes, the model running on a GPU is even about 50-times faster than the CPU model. In this case, the GPU model performs all the computations with a very fine mesh in only 4 min. On the contrary, the CPU model needs more than 200 min to do the same job. These results unambiguously prove the benefits of the parallel GPU solidification model, opening new possibilities for its real-time use in continuous-casting control.

3 MODEL-BASED PREDICTIVE CONTROL FOR CONTINUOUS CASTING

3.1 Model-based predictive control systems

On the basis of the literature review, the model-based predictive control approach^{17,18} was chosen to be utilized with the developed GPU model for the optimum control

of continuous casting process. Though primarily utilized in the petroleum industry, the model-based predictive control has been recently used in many engineering applications, mainly due to a rapid development of computers and their performance.^{17–19} The main principle of the general model-based predictive control (MPC) system is as follows: in defined consecutive time instants with the measurements of the current and past process outputs and with the past values of the control inputs, the control inputs for the current and future instants are determined with the model, so that these control inputs minimize the differences between the predicted controlled outputs and the required reference values, the so-called set-points over a certain control horizon¹⁷. In other words, the MPC utilizes the model of the process to predict the behavior of the system resulting from the changes in the inputs and to evaluate the consequences of these modifications. This is actually an opposite to the PI and PID controllers that control and regulate the process according to the known behavior in the past. A very illustrative comparison between the PI and PID versus the MPC is as follows: the PI and PID controlling is like driving a car using the rear-view mirror. On the other hand, the MPC approach, in the context of driving a car, is like the normal driving using the windshield of the car.¹⁷

Inspired by the described idea of the MPC, we propose an MPC system for the continuous casting of steel utilizing the developed, very fast GPU model. The scenario approach and the effective casting speeds are then used for determining the control inputs.

3.2 Proposal of the model-based predictive control system for continuous steel casting

The main idea of the proposed MPC system for continuous steel casting is based on using the developed parallel GPU model as a numeric sensor of the real casting machine. However, due to the developed, very

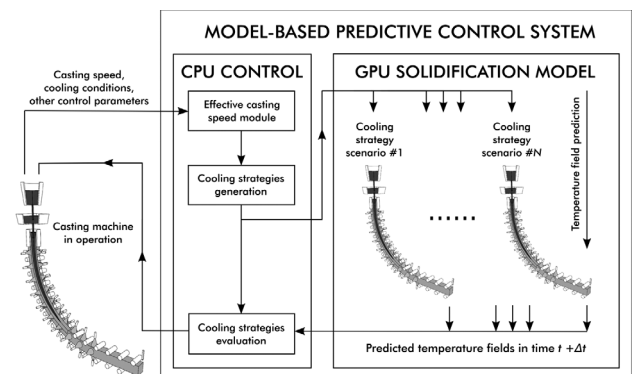


Figure 3: Concept of the model-based predictive control system for continuous casting using a very fast dynamic solidification model running on a GPU

Slika 3: Zasnova kontrolnega sistema napovedovanja na osnovi modela pri kontinuirnem ulivanju z uporabo modela zelo hitrega dinamičnega modela strjevanja, ki teče na GPU

fast dynamic solidification model running on a GPU, the concept of the MPC can be extended and modified. The entire concept of the control system is presented in **Figure 3**. The main idea is to use the scenario approach. It means that in every time step the MPC system retrieves the actual casting parameters (e.g., the casting speed, the casting temperature, etc.) from the casting machine. The control system then generates several control strategies, the so-called control scenarios in order to control the process. Each of these scenarios represents a possible control of the casting machine, particularly the cooling setup (i.e., the water-flow volume) of the cooling nozzles in the cooling circuits within the secondary zone. The control scenarios are generated making use of the experiences provided by the experts, the traditional relationships between the water-flow volume through the nozzles and the casting speed, and the concept of the effective casting speed²⁰. The control system then predicts the future thermal behavior of cast billets for a certain future-time horizon and for all the generated control scenarios. This task can be performed in real time (between tens of seconds and several minutes depending on the number of scenarios) solely due to the very fast GPU dynamic solidification model. The control system consequently analyses the results of the scenario thermal behaviors and chooses the resultant control strategy used for the real casting process. The main objective of the resultant control strategy is to ensure that the surface temperatures of cast billets fit the predefined temperature intervals (to avoid subcooling or overcooling because of a low ductility of steel²¹ resulting in surface defects, e.g., cracks) and that the metallurgical length fits the defined range.^{3,4} The control loop is, thereby, closed and the procedure is repeated in the next time instant.

3.3 Effective casting speed

The concept of the effective casting speed was adopted for the determination of the control cooling strategies in secondary cooling.²⁰ When the actual cast-

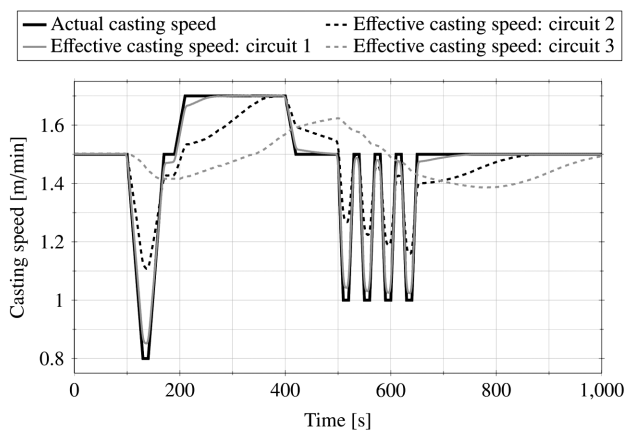


Figure 4: Concept of the effective casting speed
Slika 4: Zasnova učinkovite hitrosti litja

ing speed rapidly varies in time (e.g. due to a change of tundishes), the determination of the water-flow volume through the nozzles as a function of the actual casting speed may result in inappropriate cooling, particularly in the cooling circuits far from the mould.²⁰ Researchers and steelworkers usually tend to use the dependencies of the water-flow volume in the cooling circuits as the quadratic functions of the casting speed.²⁰ The mentioned problem can be overcome with the use of the effective casting-speed approach, based on considering the dwell time that a blank divided into slices spends in each of the cooling circuits. The effective casting speed $v_{e,i}$ for the i -th cooling circuit (m min⁻¹) can be calculated as:

$$v_{e,i} = \varepsilon_i v_{a,i} + (1 - \varepsilon_i) v_z \quad (3)$$

where ε_i is the weight coefficient (1), v_z is the actual casting speed (m min⁻¹) and the average casting speed $v_{a,i}$ for the i -th cooling circuit (m min⁻¹) is determined as:

$$v_{a,i} = \frac{n_i L_i}{\sum_{j=1}^{n_i} t_{r,i,j}} \quad (4)$$

where n_i is the number of slices, L_i is the distance from the mould (m) and $t_{r,i,j}$ is the residential time (s).²⁰ **Figure 4** shows the effective casting speed for the fluctuating actual casting speed and for the casting machine with three cooling circuits within the secondary cooling zone.

As can be seen from **Figure 4**, the effective casting-speed approach can be suitably used for the characterization of the fluctuating casting conditions. Particularly in the cooling circuits far from the mould, the effective casting speed has a smoothness effect, which fairly corresponds to the reality.

4 USE OF THE CONTROL SYSTEM, RESULTS, DISCUSSION

The developed MPC system was tested for the control of the secondary cooling in the case of a temporary change in the casting speed, e.g., due to the change of tundishes. The dynamic solidification model was configured for a caster with 6 cooling circuits within the secondary cooling incorporating 180 JATO cooling nozzles of several types. The caster casts 200 mm × 200 mm steel billets, normally with the casting speed of 1.5 m/min. The temporary drop in the casting speed from 1.5 m/min to 0.8 m/min was assumed for 6 min as depicted in **Figure 5** where the effective casting speeds for each of the cooling circuits are presented as well.

The aim of the control was to determine the cooling strategy of the cooling nozzles within the secondary cooling so that the surface temperatures on the cast billets would be maintained as close as possible to the surface temperatures in the case when no change is made to the casting speed. Thereby, the steady-state surface

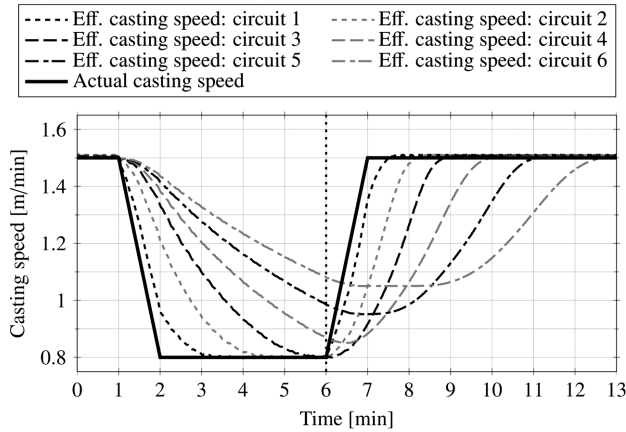


Figure 5: Actual casting speed and the corresponding effective casting speeds for all the cooling circuits

Slika 5: Dejanska hitrost litja in ustrezne hitrosti litja za vse hladilne kroge

temperatures were considered as the optimum target temperatures. The resultant surface temperatures on the top (small-radius) surface of the control process are shown in **Figure 6**. These temperatures for the cooling circuits 4, 5, 6 are plotted for the time when 5 min have elapsed from the beginning of the change in the casting speed (depicted by the vertical dotted line in **Figure 5**) and when the actual casting speed begins to increase from 0.8 m/min back to 1.5 m/min.

As for the described control problem of the temporary change in the casting speed, the developed model-based control system generated 15 cooling scenarios for the cooling strategy within the secondary cooling. These scenarios were generated taking into account the effective casting speeds. The system then predicted the future thermal behavior (calculating the complete temperature distribution) for all these cooling scenarios. The computations were performed for a computational mesh with 1 million control volumes and all these computations for all the cooling scenarios were performed within 1 min

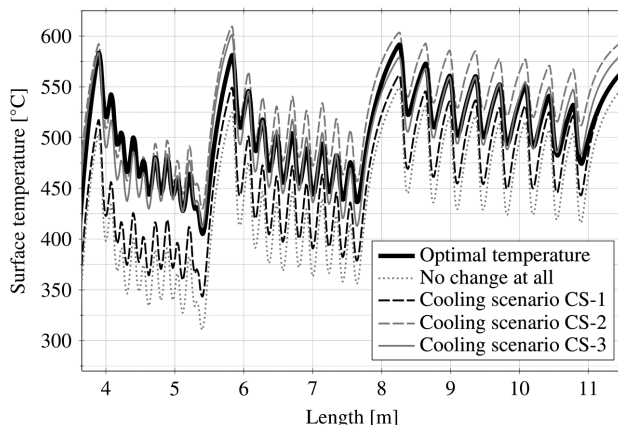


Figure 6: Surface temperatures on the top (small-radius) surface resulting from the use of the MPC system

Slika 6: Temperature površine na vrhu grede (manjši polmer), ki so dobljene z uporabo MPC-sistema

using GPU NVIDIA Tesla C2075. The temperature distributions for three representative scenarios (denoted as CS-1, CS-2, and CS-3) are plotted in **Figure 6** together with the optimum steady-state temperature distribution and with the temperature distribution for the case when no change in the cooling strategy is performed. As can be seen from **Figure 6**, when no change in the cooling strategy is considered, a significant subcooling occurs within the secondary cooling. Further, the generated cooling strategy CS-1 is also rather inappropriate due to the subheating, mainly occurring within the fourth cooling circuit. Similarly, the cooling strategy CS-2 is also rather inconvenient owing to the overheating, especially in the fifth and sixth cooling circuits. But in the case of the cooling strategy CS-3, the distribution of the temperature is very close to the target temperature distribution in all three cooling circuits plotted in **Figure 6**. The cooling scenario SC-3 can, therefore, be considered as the optimum cooling strategy for the investigated situation.

5 CONCLUSION

The paper presents a proposal for a model-based predictive control system for the continuous casting of steel. The system is based on the dynamic solidification model as the numerical sensor for predicting the future thermal behavior of cast billets under specific casting conditions. The control system utilizes the developed very fast dynamic solidification model that runs on graphics processing units, GPUs. The solidification model, using the concepts of the scenario-based cooling strategies and the effective casting speed was then used for the optimum control of continuous casting. The control system was tested for the case of a temporary drop in the casting speed and the results show that the proposed system is a promising tool for solving these control problems. The next research will aim at tuning up the developed control system and testing it in various production control situations in the continuous casting of steel.

Acknowledgement

The presented research was supported by project GACR P107/11/1566 of the Czech Science Foundation, by the NETME Centre, ED0002/01/01, by the NETME CENTRE PLUS (LO1202), and by the BUT project FSI-J-13-1977 for young researchers. The principal author, the former holder of the Brno PhD Talent Financial Aid sponsored by the Brno City Municipality, also gratefully acknowledges the financial support.

6 REFERENCES

- ¹ B. Petrus, K. Zheng, X. Zhou, B. G. Thomas, J. Bentsman, Real-time model based spray-cooling control system for steel continuous casting, *Metallurgical and Materials Transactions B*, 42 (2011) 1, 78–103

- ² M. S. Kulkarni, A. S. Babu, Managing quality in continuous casting process using product quality model and simulated annealing, *Journal of Materials Processing Technology*, 166 (2005) 2, 294–306
- ³ N. Cheung, A. Garcia, The use of a heuristic search technique for the optimization of quality of steel billets produce by continuous casting, *Engineering Applications of Artificial Intelligence*, 14 (2001) 2, 229–238
- ⁴ T. Mauder, C. Sandera, J. Stětina, A fuzzy-based optimal control algorithm for a continuous casting process, *Mater. Tehnol.*, 46 (2012) 4, 325–328
- ⁵ T. Mauder, J. Novotny, Two mathematical approaches for optimal control of the continuous slab casting process, *Proc. of 16th International Conference on Soft Computing MENDEL, Brno, 2010*, 395–400
- ⁶ L. Klimes, J. Stetina, P. Bucek, Impact of casting speed on the temperature field of continuously cast steel billets, *Mater. Tehnol.*, 47 (2013) 4, 507–513
- ⁷ Y. J. Xia, F. M. Wang, C. R. Li, J. L. Wang, Simulation of thermo-mechanical behaviour during continuous casting process based on MiLE method, *Journal of Central South University*, 19 (2012) 9, 2403–2410
- ⁸ J. A. Baker, J. D. Hirst, Molecular dynamics simulations using graphics processing units, *Molecular Informatics*, 30 (2011) 6–7, 498–504
- ⁹ K. E. A. van der Sande, T. Gevers, C. G. M. Snoek, Empowering visual categorization with the GPU, *IEEE Transactions on Multimedia*, 13 (2011) 1, 60–70
- ¹⁰ Y. Uejima, T. Terashima, R. Maezono, Acceleration of a QM/MM-QMC simulation using GPU, *Journal of Computational Chemistry*, 32 (2011) 10, 2264–2272
- ¹¹ W. S. Fu, W. H. Wang, S. H. Huang, An investigation of natural convection of three dimensional horizontal parallel plates for a steady to an unsteady situation by a CUDA computation platform, *International Journal of Heat and Mass Transfer*, 55 (2012) 17–18, 4638–4650
- ¹² L. Klimes, J. Stetina, Parallel dynamic solidification model of continuous steel casting on GPU, *Proc. of 22nd Conference on Metallurgy and Materials METAL, Brno, 2013*, 6
- ¹³ L. Klimes, J. Stetina, Transient heat transfer problem with phase changes solved by means of GPGPU with CUDA and MATLAB, *Proc. of 19th International Conference on Soft Computing MENDEL, Brno, 2013*, 397–402
- ¹⁴ J. D. Owens, M. Houston, D. Luebke, S. Green, J. E. Stone, J. C. Phillips, GPU computing, *Proceedings of the IEEE*, 96 (2008) 5, 879–899
- ¹⁵ L. Klimeš, P. Charvat, M. Ostry, Challenges in the computer modeling of phase change materials, *Mater. Tehnol.*, 46 (2012) 4, 335–338
- ¹⁶ N. Wilt, *CUDA Handbook: A comprehensive guide to GPU programming*, 1st ed., Addison-Wesley, 2013
- ¹⁷ P. Tatjewski, *Advanced Control of Industrial Processes: Structures and Algorithms*, Springer, London 2007
- ¹⁸ A. Ivanova, Model predictive control of secondary cooling modes in continuous casting, *Proc. of 22nd Conference on Metallurgy and Materials METAL, Brno, 2013*, 6
- ¹⁹ S. J. Qin, T. A. Badgwell, A survey of industrial model predictive control technology, *Control Engineering Practice*, 11 (2003) 7, 733–764
- ²⁰ Z. Dou, Q. Liu, B. Wang, X. Zhang, J. Zhang, Z. Hu, Evolution of control models for secondary cooling in continuous casting process of steel, *Steel Research International*, 82 (2011) 10, 1220–1227
- ²¹ S. G. Jansto, Steelmaking and continuous casting process metallurgy factors influencing hot ductility behaviour of niobium bearing steels, *Proc. of International Conference on Metallurgy and Materials METAL, Brno, 2013*, 7

4

Conclusions and further work

HHEAT TRANSFER WITH PHASE CHANGES represents an important task in many technical applications and industrial processes. Nowadays, research and development not only in areas including heat transfer and phase changes are twofold: experimental and computational. In fact, these two approaches are commonly combined together as it is rather difficult to develop and optimise an engineering system just with the use of (usually expensive and time-consuming) experimental investigations, and similarly computer simulations without proper validation and verification by means of experimental data are hardly applicable as a reliable design and optimisation tool.

The thesis provides an insight into two areas, in which heat transfer with phase changes takes place: latent heat thermal energy storage (LHTES) employing phase change materials (PCMs), and the steelmaking process by means of continuous steel casting. The focus is concentrated on the computational solution and on the development of computer models of these systems, in which the phase change represents a crucial issue. Though the two applications may seem rather distinct at the first glance, they have many common properties, and similar modelling approaches can be applied to both of them. The contribution of the author to the field is demonstrated by ten journal papers, which are included in the thesis. Each paper co-authored by the author of the thesis has been published in a peer-review journal having an impact factor according to Web of Science.

LHTES represents a way for thermal energy storage by means of the latent heat accompanying the phase change. Suitable PCMs including e.g. paraffins and salt hydrates are often utilised in such systems. The latent heat (the heat of fusion) of the phase change is used to accumulate, store, and release heat. In the thesis, thermal storage units with a PCM designed for the use with solar air heaters, and a thermally activated building system containing a microencapsulated PCM were investigated by means of computer simulations. The effective heat capacity method and the enthalpy method were mostly used in the created models. However, it was found that the front tracking approach allows

for about two orders of the magnitude higher computational accuracy, but its coding and implementation are significantly more challenging than in case of the commonly used enthalpy method and the effective heat capacity method. Further, the models were proposed and implemented in a way, which allows for their high computational efficiency. This means that they are well applicable for long-term simulations (the case of LHTEs systems), and their computational efficiency makes them suitable for their coupling with optimisation algorithms. The developed computer models were validated with the use of experimental data or verified against other simulation data, and the models were used for analyses of the systems and their assessment and optimisation. In all cases, a good agreement between the created models and data from other sources was achieved. Further, it was concluded that LHTEs and PCMs represent a viable way, which allows for efficient heat storage and for the utilisation of renewable energy resources (solar energy). In case of thermal storage units, their use enables the mitigation of mismatch between the energy demand and energy supply, for peak load shaving, and they can be used for "free" cooling. In case of building structures, an integrated PCM allows for an improved thermal comfort, for preventing a room from overheating and temperature fluctuations, and for the increase of thermal inertial of lightweight buildings.

In case of steelmaking and continuous steel casting process, the phase change and the release of the heat of fusion during the solidification of steel represent an important issue, which needs to be properly addressed in computer modelling as well as in the real casting process. The reason is that the heat of fusion released during the solidification is a significant source of heat, which has to be withdrawn from the cast strand. Moreover, besides the liquid-to-solid phase change (the solidification), also solid-to-solid phase changes (e.g. the austenite–ferrite transformation) of steel has to be addressed properly in some cases. In recent years, the use of computer models for continuous steel casting is a common practice in research as well as directly in steel plants for the casting control and optimisation. In the thesis, the main achievement in modelling of continuous steel casting is the developed rapid GPU-based computer model, which enables very fast computer simulations allowing for the real-time casting control, e.g. by means of the model predictive control approach as demonstrated in the thesis. The GPU-based model provides the acceleration (when compared to a CPU-based model) in the order of tens (in particular, between $33\times$ and $68\times$ for the computational grid with 10^5 and $5 \cdot 10^6$ nodes). Further, it was also shown that stochastic programming is also applicable for optimisation of continuous steel casting under uncertainty, though not in the real-time use and having some limitations.

Various computer models and tools have been developed by the author for systems incorporating heat transfer with phase changes. As for the future work, the aim of the author is to continue with the improvement of existing models, and with the development of new models for other systems. Currently, two papers related to a computer model of the solar air collector with a PCM-based absorber and to a computer model of a PCM-based attenuator of the fluid temperature fluctuations are in a review process. Another objective of the further author's research will focus on optimisation: coupling of developed computer models with optimisation algorithms. The use of nature-inspired methods, metaheuristics and their implementations, e.g., in the open-source DEAP (Distributed Evolutionary Algorithms in Python) library for Python seem to be a promising way, already confirmed by results of other investigators.

Nomenclature

Symbol	Unit	Description
c_{eff}	[J/kg·K]	Effective heat capacity
c_p	[J/kg·K]	Heat capacity at constant pressure
c_v	[J/kg·K]	Heat capacity at constant volume
f_s	[1]	Solid fraction
ΔH_m	[J/kg]	Heat of fusion
H	[J/kg, J/m ³]	Enthalpy
k	[W/m·K]	Thermal conductivity
m	[kg]	Mass
n	[1]	Normal vector
p	[Pa]	Pressure
ρ	[kg/m ³]	Density
s	[m]	Position
t	[s]	Time
T	[K, °C]	Temperature
V	[m ³]	Volume
v_n	[m/s]	Normal velocity
v_z	[m/s]	Casting speed
Q	[J]	Heat
x, y, z	[m]	Cartesian spatial coordinates

List of abbreviations

1D	one-dimensional
2D	two-dimensional
3D	three-dimensional
CFD	computational fluid dynamics
CSM	compact storage module
DEAP	distributed evolutionary algorithms in Python
LHTES	latent heat thermal energy storage
LNG	liquefied natural gas
NG	natural gas
MFC	mixed fluid cascade
MPC	model predictive control
MPI	message passing interface
PCM	phase change material
PID	proportional integral derivative
SST	shear stress transport
TABS	thermally activated building system
TES	thermal energy storage
TWP	total world production

References

- [1] Abuska M, Sevik S, Kayapunar A. A comparative investigation of the effect of honeycomb core on the latent heat storage with PCM in solar air heater. *Applied Thermal Engineering* **148**: 684–693.
- [2] Agyenim F, Hewitt N, Eames P, Smyth M. 2010. A review of materials, heat transfer and phase change problem formulation for latent heat thermal energy storage systems (LHTESS). *Renewable & Sustainable Energy Reviews* **14** (2): 615–628.
- [3] Akeiber H, Nejat P, Majid MZA, Wahid MZ, Jomehzadeh F, Famileh IZ, Calautit JK, Hughes BR, Zaki SA. 2016. A review on phase change material (PCM) for sustainable passive cooling in building envelopes. *Renewable and Sustainable Energy Reviews* **60**: 1470–1497.
- [4] Al-Abidi AA, Mat SB, Sopian K, Sulaiman MY, Lim CH, Th A. 2012. Review of thermal energy storage for air conditioning systems. *Renewable and Sustainable Energy Reviews* **16** (8): 5802–5819.
- [5] Al-Abidi AA, Mat SB, Sopian K, Sulaiman MY, Mohammed AT. CFD applications for latent heat thermal energy storage: a review. *Renewable and Sustainable Energy Reviews* **20**: 353–363.
- [6] Al-Saadi SN, Zhai Z. 2013. Modeling phase change materials embedded in building enclosure: A review. *Renewable and Sustainable Energy Reviews* **21**: 659–673.
- [7] Al-Saadi SN, Zhai Z. 2015. Systematic evaluation of mathematical methods and numerical schemes for modeling PCM-enhanced building enclosure. *Energy and Buildings* **92**: 374–388.
- [8] Ansuini R, Larghetti R, Giretti A, Lemma M. 2011. Radiant floors integrated with PCM for indoor temperature control. *Energy and Buildings* **43** (11): 3019–3026.
- [9] Arfaoui N, Bouadila S, Guizani A. 2017. A highly efficient solution of off-sunshine solar air heating using two packed beds of latent storage energy. *Solar Energy* **155**: 1243–1253.
- [10] Arkar C, Medved S. 2007. Free cooling of a building using PCM heat storage integrated into the ventilation system. *Solar Energy* **81** (9): 1078–1087.
- [11] Baetens R, Jelle BP, Gustavsen A. 2010. Phase change materials for building applications: A state-of-the-art review. *Energy and Buildings* **42** (9): 1361–1368.
- [12] Battaglioli S, Robinson AJ, McFadden S. 2017. Axisymmetric front tracking model for the investigation of grain structure evolution during directional solidification. *International Journal of Heat and Mass Transfer* **115**: 592–605.
- [13] Bartz-Beielstein T, Zaefferer M. 2017. Model-based methods for continuous and discrete global optimization. *Applied Soft Computing* **55**: 154–167.

- [14] Bellabdaoui A, Teghem J. 2006. A mixed-integer linear programming model for the continuous casting planning. *International Journal of Production Economics* **104**: 260–270.
- [15] Belmonte JF, Izquierdo-Barrientos MA, Molina AE, Almendros-Ibáñez JA. 2016. Air-based solar systems for building heating with PCM fluidized bed energy storage. *Energy and Buildings* **130**: 150–165.
- [16] Bratu V, Mortici C, Oros C, Ghiban N. Mathematical model of solidification process in steel continuous casting taking into account the convective heat transfer at liquid–solid interface. *Computational Materials Science* **94**: 2–7.
- [17] Cabeza LF, Castell A, Barreneche C, de Gracia A, Fernandez AI. 2011. Materials used as PCM in thermal energy storage in buildings: A review. *Renewable & Sustainable Energy Reviews* **15** (3): 1675–1695.
- [18] Cárdenas B, León N. 2013. High temperature latent heat thermal energy storage: Phase change materials, design considerations and performance enhancement techniques. *Renewable and Sustainable Energy Reviews* **27**: 724–737.
- [19] Chakraborty S, Ganguly S, Talukdar P. 2019. Determination of optimal taper in continuous casting billet mould using thermo-mechanical models of mould and billet. *Journal of Materials Processing Technology* **270**: 132–141.
- [20] Charvát P. 2015. Latent heat thermal energy storage in solar air heating. Habilitation thesis. Brno University of Technology, Czech Republic.
- [21] Charvát P, Klimeš L, Ostrý M. 2014. Numerical and experimental investigation of a PCM-based thermal storage unit for solar air systems. *Energy and Buildings* **68**: 488–497.
- [22] Charvát P, Klimeš L, Zálešák M. 2019. Utilization of an air-PCM heat exchanger in passive cooling of buildings: A simulation study on the energy saving potential in different European climates. *Energies* **12** (6): article 1133.
- [23] Chen H, Long M, Chen D, Liu T, Duan H. 2018. Numerical study on the characteristics of solute distribution and the formation of centerline segregation in continuous casting (CC) slab. *International Journal of Heat and Mass Transfer* **126**: 843–853.
- [24] Cramb A. 2003. *Making, Shaping and Treating of Steel: Casting*. Eleventh edition. Assn of Iron & Steel Engineers; ISBN 978-0930767044.
- [25] da Cunha JP, Eames P. 2016. Thermal energy storage for low and medium temperature applications using phase change materials—a review. *Applied Energy* **177**: 227–238.
- [26] de Gracia A. 2019. Dynamic building envelope with PCM for cooling purposes — Proof of concept. *Applied Energy* **235**: 1245–1253.
- [27] de Gracia A, Cabeza LF. 2015. Phase change materials and thermal energy storage for buildings. *Energy and Buildings* **103**: 414–419.
- [28] Dinker A, Agarwal M, Agarwal GD. 2017. Heat storage materials, geometry and applications: A review. *Journal of the Energy Institute* **90** (1): 1–11.

- [29] Dirand M, Bouroukba M, Briard A-J, Chevallier V, Petitjean D, Corriou J-P. 2002. Temperatures and enthalpies of (solid + solid) and (solid + liquid) transitions of *n*-alkanes. *Journal of Chemical Thermodynamics* **34**: 1255–1277.
- [30] Du FM, Wang XD, Liu Y, Li TY, Yao M. 2016. Analysis of non-uniform mechanical behavior for a continuous casting mold based on heat flux from inverse problem. *Journal of Iron and Steel Research International* **23** (2): 83–91.
- [31] Du K, Calautit J, Wang Z, Wu Y, Liu H. 2018. A review of the applications of phase change materials in cooling, heating and power generation in different temperature ranges. *Applied Energy* **220**: 242–273.
- [32] Dusanberre GM. 1945. Numerical methods for transient heat flows. *Transactions of ASME* **67**: 703–712.
- [33] Elnajjar E. 2017. Using PCM embedded in building material for thermal management: Performance assessment study. *Energy and Buildings* **151**: 28–34.
- [34] Emi T. 2003. Making, Shaping and Treating of Steel: Casting. Chapter Surface defects on continuously cast strands. ASSN of Iron & Steel Engineers, ISBN 978-0930767044.
- [35] *Energy Efficiency in Buildings*. 2009. World business council for sustainable development. Atar Roto Presse SA, Switzerland, August 2009.
- [36] Fachinotti VD, Le Corre S, Triolet N, Bobadilla M, Bellet M. 2006. Two-phase thermo-mechanical and macrosegregation modelling of binary alloys solidification with emphasis on the secondary cooling stage of steel slab continuous casting processes. *International Journal for Numerical Methods in Engineering* **67** (10): 1341–1384.
- [37] Farah S, Liu M, Saman W. 2019. Numerical investigation of phase change material thermal storage for space cooling. *Applied Energy* **239**: 526–535.
- [38] Farid MM, Khudhair AM, Razack SAK, Al-Hallaj S. 2004. A review on phase change energy storage: materials and applications. *Energy Conversion and Management* **45** (9–10): 1597–1615.
- [39] Feng G, Huang K, Xie H, Li H, Liu X, Liu S, Cao C. 2016. DSC test error of phase change material (PCM) and its influence on the simulation of the PCM floor. *Renewable Energy* **87** (Part 3): 1148–1153.
- [40] Furtmüller C, Colaneri P, del Re L. 2012. Adaptive robust stabilization of continuous casting. *Automatica* **48** (1): 225–232.
- [41] Gao X, Yang S, Li J. 2016. Effects of micro-alloying elements and continuous casting parameters on reducing segregation in continuously cast slab. *Materials & Design* **110**: 284–295.
- [42] Gissey GC, Subkhankulova D, Dodds PE, Barrett M. 2019. Value of energy storage aggregation to the electricity system. *Energy Policy* **128**: 685–696.
- [43] Gulfam R, Zhang R, Meng Z. 2019. Advanced thermal systems driven by paraffin-based phase change materials – A review. *Applied Energy* **238**: 582–611.

- [44] Halawa E, Saman W. 2011. Thermal performance analysis of a phase change thermal storage unit for space heating. *Renewable Energy* **36** (1): 259–264.
- [45] Han Y, Zhang X-B, Yu E, Sun L, Gao Y. 2017. Numerical analysis of temperature field and structure field in horizontal continuous casting process for copper pipes. *International Journal of Heat and Mass Transfer* **115** (B): 294–306.
- [46] Hao J, Liu M, Jiang S, Wu C. 2015. A soft-decision based two-layered scheduling approach for uncertain steelmaking-continuous casting process. *European Journal of Operational Research* **244**: 966–979.
- [47] Hardin RA, Liu K, Kapoor A, Beckermann C. 2003. A transient simulation and dynamic spray cooling control model for continuous steel casting. *Metallurgical and Materials Transactions B* **34** (3): 297–306.
- [48] He F, Zhou L, Deng Z-H. 2015. Novel mold breakout prediction and control technology in slab continuous casting. *Journal of Process Control* **29**: 1–10.
- [49] Herbinger F, Bhourri M, Groulx D. 2017. Investigation of heat transfer inside a PCM-air heat exchanger: a numerical parametric study. *Heat and Mass Transfer* **54** (8): 2433–2442.
- [50] Hetmaniok E, Slota D, Zielonka A. 2015. Restoration of the cooling conditions in a three-dimensional continuous casting process using artificial intelligence algorithms. *Applied Mathematical Modelling* **39** (16): 4797–4807.
- [51] Hietanen PT, Louhenkilpi S, Yu S. 2016. Investigation of solidification, heat transfer and fluid flow in continuous casting of steel using an advanced modeling approach. *Steel Research International* **88** (7): article 1600355.
- [52] Hou A-G, Zhang Q-L, Xu G-D, Jiang M-F. 2015. Study and Application of Advanced Secondary Control Model for Continuous Casting at Baosteel. *Journal of Iron and Steel Research International* **22** (S1): 98–103.
- [53] Hughes BR, Cheuk-Ming M. 2011. A study of wind and buoyancy driven flows through commercial wind towers. *Energy and Buildings* **43** (7): 1784–1791.
- [54] Incropera FP, DeWitt DP, Bergman TL, Lavine AS. 2013. *Principles of Heat and Mass*. Seventh edition. Wiley, ISBN 978-0-470-64615-1.
- [55] Iten M, Liu S, Shukla A. 2016. A review on the air-PCM-TES application for free cooling and heating in the buildings. *Renewable and Sustainable Energy Reviews* **61**: 175–186.
- [56] Iten M, Liu S, Shukla A. 2016. Experimental study on the thermal performance of air-PCM unit. *Building and Environment* **105**: 128–139.
- [57] Jaworski M, Lapka P, Furmanski P. 2014. Numerical modelling and experimental studies of thermal behaviour of building integrated thermal energy storage unit in a form of a ceiling panel. *Applied Energy* **113**: 548–557.
- [58] Ji C, Luo S, Zhu M. 2014. Analysis and application of soft reduction amount for bloom continuous casting process. *ISIJ International* **54** (3): 504–510.

- [59] Ji C-B, Li J-S, Yang S-F, Sun L-Y. 2013. Large eddy simulation of turbulent fluid flow in liquid metal of continuous casting. *International Journal of Iron and Steel Research* **20** (1): 34–39.
- [60] Jiang D, Wang W, Luo S, Ji C, Zhu M. 2018. Numerical simulation of slab centerline segregation with mechanical reduction during continuous casting process. *International Journal of Heat and Mass Transfer* **122**: 315–323.
- [61] Jiang S-L, Liu M, Lin J-H, Zhong H-X. 2016. A prediction-based online soft scheduling algorithm for the real-world steelmaking-continuous casting production. *Knowledge-Based Systems* **111**: 159–172.
- [62] Jiang S-L, Zheng Z, Liu M. 2017. A multi-stage dynamic soft scheduling algorithm for the uncertain steelmaking-continuous casting scheduling problem. *Applied Soft Computing* **60**: 722–736.
- [63] Jobli MI, Yao R, Luo Z, Shahrestani M, Li N, Liu H. 2019. Numerical and experimental studies of a capillary-tube embedded PCM component for improving indoor thermal environment. *Applied Thermal Engineering* **148**: 466–477.
- [64] Kenisarin M, Mahkamov K. Solar energy storage using phase change materials. *Renewable and Sustainable Energy Reviews* **11** (9): 1913–1965.
- [65] Khudhir AM, Farid MM. 2004. A review on energy conservation in building applications with thermal storage by latent heat using phase change materials. *Energy Conversion and Management* **45** (2): 263–275.
- [66] Klimeš L. 2014. Optimization of secondary cooling parameters of continuous steel casting. PhD thesis. Brno University of Technology, Czech Republic.
- [67] Klimeš L, Charvát P, Ostrý M. 2019. Thermally activated wall panels with microencapsulated PCM: comparison of 2D and 3D models. *Journal of Building Performance Simulation* **12** (4): 404–419. DOI: 10.1080/19401493.2018.1543350.
- [68] Klimeš L, Mauder T, Charvát P, Štětina J. 2018. Front tracking in modelling of latent heat thermal energy storage: Assessment of accuracy and efficiency, benchmarking and GPU-based acceleration. *Energy* **155**: 297–311.
- [69] Klimeš L, Popela P, Mauder T, Štětina J, Charvát P. 2017. Two-stage stochastic programming approach to a PDE-constrained steel production problem with the moving interface. *Kybernetika* **53** (6): 1047–1070.
- [70] Klimeš L, Štětina J. 2014. Unsteady model-based predictive control of continuous steel casting by means of a very fast dynamic solidification model on a GPU. *Materials and Technology* **48** (4): 525–530.
- [71] Klimeš L, Štětina J. 2015. A rapid GPU-based heat transfer and solidification model for dynamic computer simulations of continuous steel casting. *Journal of Materials Processing Technology* **226**: 1–14.
- [72] Klimeš L, Štětina J, Buček P. 2013. Impact of casting speed on the temperature field of continuously cast steel billets. *Materials and Technology* **47** (4): 507–513.

- [73] Konuklu Y, Ostry M, Paksoy HO, Charvat P. 2015. Review on using microencapsulated phase change materials (PCM) in building applications. *Energy and Buildings* **106**: 134–155.
- [74] Koric S, Hibbeler LC, Liu R, Thomas BG. 2010. Multiphysics model of metal solidification on the continuum level. *Numerical Heat Transfer B* **58**: 371–392.
- [75] Kumirai T, Dirker J, Meyer J. 2019. Experimental analysis for thermal storage performance of three types of plate encapsulated phase change materials in air heat exchangers for ventilation applications. *Journal of Building Engineering* **22**: 75–89.
- [76] Li B, Zhai X, Cheng X. 2019. Thermal performance analysis and optimization of multiple stage latent heat storage unit based on entransy theory. *International Journal of Heat and Mass Transfer* **135**: 149–157.
- [77] Li C, Thomas BG. 2004. Thermomechanical finite-element model of shell behavior in continuous casting of steel. *Metallurgical and Materials Transactions B* **35** (6): 1151–1172.
- [78] Li C-Y, Garimella SV, Simpson JE. 2003. Fixed-Grid Front-Tracking Algorithm For Solidification Problems, Part I: Method And Validation. *Numerical Heat Transfer B* **43**: 117–141.
- [79] Li G, Yu W, Cai Q. 2016. Investigation of reduction pretreatment process for continuous casting. *Journal of Materials Processing Technology* **227**: 41–48.
- [80] Lin W, Ma Z, Ren H, Gschwander S, Wang S. 2019. Multi-objective optimisation of thermal energy storage using phase change materials for solar air systems. *Renewable Energy* **130**: 1116–1129.
- [81] Lin Y, Alva G, Fang G. 2018. Review on thermal performances and applications of thermal energy storage systems with inorganic phase change materials. *Energy* **165** (Part A): 685–708.
- [82] Liu S, Li Y, Zhang Y. 2014. Mathematical solutions and numerical models employed for the investigations of PCMs phase transformations. *Renewable and Sustainable Energy Reviews* **33**: 659–674.
- [83] Liu W-H, Xie Z. 2011. Design and Simulation Test of Advanced Secondary Cooling Control System of Continuous Casting Based on Fuzzy Self-Adaptive PID. *Journal of Iron and Steel Research International* **18** (1): 26–30.
- [84] Liu X, Zhu M. 2006. Finite element analysis of thermal and mechanical behavior in a slab continuous casting mold. *ISIJ International* **46** (11): 1652–1659.
- [85] Liu YK, Tao YB. 2018. Thermodynamic analysis and optimization of multistage latent heat storage unit under unsteady inlet temperature based on entransy theory. *Applied Energy* **227**: 488–496.
- [86] Liu Z, Yu Z, Yang T, Qin D, Li S, Zhang G, Haghghat F, Joybari MM. 2018. A review on macro-encapsulated phase change material for building envelope applications. *Building and Environment* **144**: 281–294.
- [87] Liu ZQ, Qi FS, Li BK, Cheung SCP. 2016. Modeling of bubble behaviors and size distribution in a slab continuous casting mold. *International Journal of Multiphase Flow* **79**: 190–201.

- [88] Long MJ, Chen DF, Wang QX, Luo DH, Han ZW, Liu Q, Gao WX. 2012. Determination of CC slab solidification using nail shooting technique. *Ironmaking & Steelmaking* **39** (2): 370–377.
- [89] Lopez JPA, Kuznik F, Baillis D, Virgone J. 2013. Numerical modeling and experimental validation of a PCM to air heat exchanger. *Energy and Buildings* **64**: 415–422.
- [90] Louhenkilpi S. 2014. Treatise on Process Metallurgy: Industrial Processes. Chapter Continuous casting of steel. Elsevier, pp. 373–434. ISBN 978-0-08-096988-6.
- [91] Louhenkilpi S, Laitinen E, Nieminen R. 1993. Real-time simulation of heat-transfer in continuous-casting. *Metallurgical Transactions B* **24** (4): 685–693.
- [92] Louhenkilpi S, Makinen M, Vapalahti S, Raisanen T, Laine J. 2005. 3D steady state and transient simulation tools for heat transfer and solidification in continuous casting. *Materials Science A* **413**: 135–138.
- [93] Luo S, Zhu M, Louhenkilpi S. 2012. Numerical simulation of solidification structure of high carbon steel in continuous casting using cellular automaton method. *ISIJ International* **52** (5): 823–830.
- [94] Luo X, Xie Q, Wang Y, Yang C. 2017. Estimation of heat transfer coefficients in continuous casting under large disturbance by Gaussian kernel particle swarm optimization method. *International Journal of Heat and Mass Transfer* **111**: 1087–1097.
- [95] Maurya A, Jha PK. 2017. Influence of electromagnetic stirrer position on fluid flow and solidification in continuous casting mold. *Applied Mathematical Modelling* **48**: 736–748.
- [96] Mi X, Liu R, Cui H, Memon SA, Xing F, Lo Y. 2016. Energy and economic analysis of building integrated with PCM in different cities of China. *Applied Energy* **175**: 324–336.
- [97] Miki Y, Takeuchi S. 2003. Internal Defects of Continuous Casting Slabs Caused by Asymmetric Unbalanced Steel Flow in Mold. *ISIJ International* **43** (10): 1548–1555.
- [98] Milkowska-Piszczek K, Falkus J, Drozd P. 2014. The influence of enthalpy and specific heat on the distribution of temperature in the continuous steel casting process. *Acta Metallurgica Slovaca* **4**: 82–89.
- [99] Mitchell SL, Vynnycky M. 2017. Verified reduction of a model for a continuous casting process. *Applied Mathematical Modelling* **48**: 476–490.
- [100] Mochnacki B, Lara S. 2003. Application of generalized finite difference method in numerical modelling of moving boundary problems. *Scientific Research of the Institute of Mathematics and Computer Science* **2**: 129–143.
- [101] Mosayebidorchen S, Gorji-Bandpy M. 2017. Local and averaged-area analysis of steel slab heat transfer and phase change in continuous casting process. *Applied Thermal Modelling* **118**: 724–733.
- [102] Muhieddine M, Canot E, March R. 2009. Various approaches for solving problems in heat conduction with phase change. *International Journal on Finite Volumes* **6** (1).

- [103] Nazir H, Batool M, Osorio FJB, Isaza-Ruiz M, Xu X, Vignarooban K, Phelan P, Inamuddin, Kanna AM. 2019. Recent developments in phase change materials for energy storage applications: A review. *International Journal of Heat and Mass Transfer* **129**: 491–523.
- [104] Olivieri L, Tenorio JA, Revuelta D, Navarro L, Cabeza LF. 2018. Developing a PCM-enhanced mortar for thermally active precast walls. *Construction and Building Materials* **181**: 638–649.
- [105] Osterman E, Butala V, Stritih U. 2015. PCM thermal storage system for ‘free’ heating and cooling of buildings. *Energy and Buildings* **106**: 125–133.
- [106] Pan Q-K. 2018. An effective co-evolutionary artificial bee colony algorithm for steelmaking-continuous casting scheduling. *European Journal of Operational Research* **250** (3): 702–714.
- [107] Peixoto JJ, Gabriel WV, Ribeiro LQ, da Silva CA, da Silva IA, Seshadri V. 2016. Computational and physical simulation of fluid flow inside a beam blank continuous casting mold. *Journal of Materials Processing Technology* **233**: 89–99.
- [108] Peng K, Pan Q, Zhang B. 2018. An improved artificial bee colony algorithm for steelmaking-refining-continuous casting scheduling problem. *Chinese Journal of Chemical Engineering* **26** (8): 1727–1735.
- [109] Petrus B, Zheng K, Zhou X, Thomas BG, Bentsman J. 2011. Real-time, model-based spray-cooling control system for steel continuous casting. *Metallurgical and Materials Transactions B* **42** (1):87–103.
- [110] Pielichowska K, Pielichowski K. 2014. Phase change materials for thermal energy storage. *Progress in Materials Science* **65**: 67–123.
- [111] Poltarak G, Ferro S, Cicutti C. 2017. Estimation of internal cracking risk in the continuous casting of round bars. *Steel Research International* **88** (4): article 1600223.
- [112] Pomianowski M, Heiselberg P, Zhang Y. 2013. Review of thermal energy storage technologies based on PCM application in buildings. *Energy and Buildings* **67**: 56-69.
- [113] Pospíšil J, Charvát P, Arsenyeva O, Klimeš L, Špiláček M, Klemeš JJ. 2019. Energy demand of liquefaction and regasification of natural gas and the potential of LNG for operative thermal energy storage. *Renewable and Sustainable Energy Reviews* **99**: 1–15.
- [114] Rajagopal M, Velraj R. 2016. Experimental investigation on the phase change material-based modular heat exchanger for thermal management of a building. *International Journal of Green Energy* **13** (11): 1109–1119.
- [115] Ramstorfer F, Roland J, Chimani C, Morwald K. 2009. Modelling of air-mist spray cooling heat transfer for continuous slab casting. *International Journal of Cast Metals Research* **22** (1–4): 39–42.
- [116] Rao VR, Dalyankar VD, Waghmare G. 2014. Parameters optimization of selected casting processes using teaching–learning-based optimization algorithm. *Applied Mathematical Modelling* **38** (23): 5592–5608.
- [117] Rao VV, Parameshwaran R, Ram VV. 2018. PCM-mortar based construction materials for energy efficient buildings: A review on research trends. *Energy and Buildings* **158**: 95–122.

- [118] Raudenský M, Horský J. 2005. Secondary cooling in continuous casting and Leidenfrost temperature effects. *Ironmaking & Steelmaking* **32** (2): 159–164. 9233.
- [119] Ridolfi MR, Frascetti S, De Vito A, Ferro LA. 2010. Mathematical modeling of hot tearing in the solidification of continuously cast round billets. *Metallurgical and Materials Transactions B* **41**: 1293–1309.
- [120] Rockafellar RT, Wets RJB. 1991. Scenarios and policy aggregation in optimization under uncertainty. *Mathematics of Operations Research* **16**: 119–147.
- [121] Royon L, Karim L, Bontemps A. 2014. Optimization of PCM embedded in a floor panel developed for thermal management of the lightweight envelope of buildings. *Energy and Buildings* **82**: 385–390.
- [122] Saffari M, de Gracia A, Fernández C, Belusko M, Boer D, Cabeza LF. 2018. Optimized demand side management (DSM) of peak electricity demand by coupling low temperature thermal energy storage (TES) and solar PV. *Applied Energy* **211**: 604–616.
- [123] Saffari M, de Gracia A, Fernández C, Cabeza LF. 2017. Simulation-based optimization of PCM melting temperature to improve the energy performance in buildings. *Applied Energy* **202**: 420–434.
- [124] Saffari M, de Gracia A, Ushak S, Cabeza LF. 2017. Passive cooling of buildings with phase change materials using whole-building energy simulation tools: A review. *Renewable and Sustainable Energy Reviews* **80**: 1239–1255.
- [125] Santos CA, Spim JA, Ierardi MCF, Garcia A. 2002. The use of artificial intelligence technique for the optimisation of process parameters used in the continuous casting of steel. *Applied Mathematical Modelling* **26**: 1077–1092.
- [126] Sarbu I, Sebarchievici S. 2018. A comprehensive review of thermal energy storage. *Sustainability* **10** (1): article 191. DOI: 10.3390/su10010191.
- [127] Šarler B, Vertnik R, Lorbiecka AZ, Vusanovic I, Sencic B. 2012. A multiscale slice model for continuous casting of steel. Proceedings of International Conference on Modeling of Casting, Welding and Advanced Solidification Processes MCWASP XIII. *IOP Conference Series-Materials Science and Engineering* **33** (editor Ludwig A).
- [128] Sengupta J, Thomas BG, Wells MA. 2005. The use of water cooling during the continuous casting of steel and aluminum alloys. *Metallurgical Transactions A* **36A** (1): 187–204.
- [129] Sharma A, Tyagi VV, Chen CR, Buddhi D. 2009. Review on thermal energy storage with phase change materials and applications. *Renewable and Sustainable Energy Reviews* **13** (2): 318–345.
- [130] Sharma RK, Ganesan P, Tyagi VV, Metselaar HSC, Sandaran SC. Developments in organic solid–liquid phase change materials and their applications in thermal energy storage. *Energy Conversion and Management* **95**: 193–228.
- [131] Singh A, Sørensen K, Condra T, Batz SS, Kristensen S. 2019. Investigation on transient performance of a large-scale packed-bed thermal energy storage. *Applied Energy* **239**: 1114–1129.

- [132] Souayfane F, Fardoun F, Biwole P-H. 2016. Phase change materials (PCM) for cooling applications in buildings: A review. *Energy and Buildings* **129**: 396–431.
- [133] Stefanescu DM. 2009. *Science and Engineering of Casting Solidification*. Second edition. Springer, 400 p. ISBN 978-1441945099.
- [134] Stritih U, Charvát P, Koželj R, Klimeš L, Osterman E, Ostrý M, Butala V. 2018. PCM thermal energy storage in solar heating of ventilation air—Experimental and numerical investigations. *Sustainable Cities and Society* **37**: 104–115.
- [135] Stritih U, Tyagi VV, Stropnik R, Paksoy H, Haghghat F, Joybari MM. 2018. Integration of passive PCM technologies for net-zero energy buildings. *Sustainable Cities and Society* **41**: 286–295.
- [136] Sun X, Chu Y, Medina MA, Mo Y, Fan S, Liao S. 2019. Experimental investigations on the thermal behavior of phase change material (PCM) in ventilated slabs. *Applied Thermal Engineering* **148**: 1359–1369.
- [137] Swaminathan CR, Voller VR. 1992. A general enthalpy method for modeling solidification processes. *Metallurgical and Materials Transactions B* **23** (5): 651–664.
- [138] Tan HB, Li C, Li YZ. 2011. Simulation research on PCM freezing process to recover and store the cold energy of cryogenic gas. *International Journal of Thermal Sciences* **50** (11): 2220–2227.
- [139] Tian Y, Zhao CY. 2013. A review of solar collectors and thermal energy storage in solar thermal applications. *Applied Energy* **104**: 538–553.
- [140] Thomas BG. 2002. Modeling of the continuous casting of steel—past, present, and future. *Metallurgical and Materials Transactions B* **33** (6): 795–812.
- [141] Thomas BG. 2018. Review on modeling and simulation of continuous casting. *Steel Research International* **89**: article 1700312.
- [142] Troler-McKinstry S, Newnham RE. 2017. *Materials Engineering: Bonding, Structure, and Structure-Property Relationships*. First edition. Cambridge University Press, ISBN 978-1107103788.
- [143] Udaykumar HS, Mittal R, Shyy W. 1999. Computation of solid-liquid phase fronts in the sharp interface limit on fixed grids. *Journal of Computational Physics* **153**: 535–574.
- [144] Udaykumar HS, Shyy W, Rao MM. 1996. ELAFINT: a mixed Eulerian-Lagrangian method for fluid flows with complex and moving boundaries. *International Journal of Numerical Methods in Fluids* **22**: 691–712.
- [145] Vertnik R, Šarler B. 2009. Simulation of continuous casting of steel by a meshless technique. *International Journal of Cast Metals Research* **22** (1–4): 311–313.
- [146] Vertnik R, Šarler B. 2014. Solution of a continuous casting of steel benchmark test by a meshless method. *Engineering Analysis with Boundary Elements* **45**: 45–61.
- [147] Vorster WJJ, Schwindt SA, Schupp J, Korsunsky AM. 2009. Analysis of the spray field development on a vertical surface during water spray-quenching using a flat spray nozzle. *Applied Thermal Engineering* **29**: 1406–1416.

- [148] Wang C, Wang R, Hertwich E, Liu Y. 2017. A technology-based analysis of the water-energy-emission nexus of China's steel industry. *Resources, Conservation and Recycling* **124**: 116–128.
- [149] Wang X, Wang Z, Liu Y, Du F, Yao M, Zhang X. 2016. A particle swarm approach for optimization of secondary cooling process in slab continuous casting. *International Journal of Heat and Mass Transfer* **93**: 250–256.
- [150] Wang Y, Luo X, Zhang F, Wang S. 2019. GPU-based model predictive control for continuous casting spray cooling control system using particle swarm optimization. *Control Engineering Practice* **84**: 349–364.
- [151] Waqas A, Ali M, Din ZU. 2017. Performance analysis of phase-change material storage unit for both heating and cooling of buildings. *International Journal of Sustainable Energy* **36** (4): 379–397.
- [152] Weinläder H, Klinker F, Yasin M. 2017. PCM cooling ceilings in the Energy Efficiency Center — Regeneration behaviour of two different system designs. *Energy and Buildings* **156**: 70–77.
- [153] Wendelstorf J, Spitzer KH, Wendelstorf R. 2008. Spray water cooling heat transfer at high temperatures and liquid mass fluxes. *International Journal of Heat and Mass Transfer* **51** (19-20): 4902–4910.
- [154] Wets RJB. 1989. The aggregation principle in scenario analysis and stochastic optimization. *Algorithms and Model Formulations in Mathematical Programming*, editor Wallace SW. Springer, Berlin.
- [155] World Steel in Figures 2018. Report of World Steel Association, 17 p. Available at www.worldsteel.org. Accessed on February 21, 2019.
- [156] Xie J, Wang W, Liu J, Pan S. 2018. Thermal performance analysis of PCM wallboards for building application based on numerical simulation. *Solar Energy* **162**: 533–540.
- [157] Yasin M, Scheidemantel E, Klinker F, Weinläder H, Weismann S. 2019. Generation of a simulation model for chilled PCM ceilings in TRNSYS and validation with real scale building data. *Journal of Building Engineering* **22**: 372–382.
- [158] Yoshiya M, Watanabe M, Nakajima K, Ueshima N, Hashimoto K, Nagira T, Yasuda H. 2015. Concurrent γ -phase nucleation as a possible mechanism of δ - γ massive-like phase transformation in carbon steel: Numerical analysis based on effective interface energy. *Materials Transactions* **56** (9): 1467–1474.
- [159] You B, Kim M, Lee D, Lee J, Lee JS. 2011. Iterative learning control of molten steel level in a continuous casting process. *Control Engineering Practice* **19** (3): 234–242.
- [160] Yuan Q, Zhao B, Vanka SP, Thomas BG. 2005. Study of computational issues in simulation of transient flow in continuous casting. *Steel Research International* **76** (1): 33–43.
- [161] Zeinelabdein R, Omer S, Gan G. 2018. Critical review of latent heat storage systems for free cooling in buildings. *Renewable and Sustainable Energy Reviews* **82** (Part 3): 2843–2868.

- [162] Zhang J, Chen D-F, Zhang C-Q, Wang S-G, Hwang W-S. 2016. Dynamic spray cooling control model based on the tracking of velocity and superheat for the continuous casting steel. *Journal of Materials Processing Technology* **229**: 651–658.
- [163] Zhang J, Chen D-F, Zhang C-Q, Wang S-G, Hwang W-S, Han M-R. 2015. Effects of an even secondary cooling mode on the temperature and stress fields of round billet continuous casting steel. *Journal of Materials Processing Technology* **222**: 315–326.
- [164] Zhang N, Yuan YP, Cao XL, Du YX, Zhang ZL, Gu YW. 2018. Latent heat thermal energy storage systems with solid-liquid phase change materials: A review. *Advance Engineering Materials* **20** (6): article 1700753.
- [165] Zhao Y, Qin R, Chen D, Wan X, Li Y, Ma M. 2015. A three dimensional cellular automata model for dendrite growth in non-equilibrium solidification of binary alloy. *Steel Research International* **86**: 1490–1497.
- [166] Zhou D, Zhao CY, Tian Y. 2012. Review on thermal energy storage with phase change materials (PCMs) in building applications. *Applied Energy* **92**: 593–605.
- [167] Zwanzig SD, Lian Y, Brehob EG. 2013. Numerical simulation of phase change material composite wallboard in a multi-layered building envelope. *Energy Conversion and Management* **69**: 27–40.